Kinetic and Mechanistic Studies of Rh(Bis(diazaphospholane))-Catalyzed Asymmetric Hydroformylation

By

Anna Christine Brezny

A dissertation submitted in partial fulfillment of

the requirements for the degree of

Doctor of Philosophy

(Chemistry)

at the

UNIVERSITY OF WISCONSIN–MADISON

2018

Date of final oral examination: 01/15/2018

The dissertation is approved by the following members of the Final Oral Committee:

Clark R. Landis, Professor, Chemistry
Samuel H. Gellman, Professor, Chemistry
Jennifer M. Schomaker, Associate Professor, Chemistry
Shannon S. Stahl, Professor, Chemistry

Kinetic and Mechanistic Studies of Rh(Bis(diazaphospholane))-Catalyzed Asymmetric Hydroformylation

Anna Christine Brezny

Under the supervision of Professor Clark R. Landis

at the University of Wisconsin–Madison

Asymmetric hydroformylation (AHF) to yield α-chiral, branched aldehydes is a primary area of research in the Landis group. This work has led to the development of state-of-the-art rhodium bis(diazaphospholane) catalysts. Despite the fact that the mechanism of hydroformylation has been well accepted since the 1960s, what steps control both rate and selectivity has remained unclear. The work discussed in this thesis focuses on developing a deeper understanding of the kinetics and origins of selectivity for Rh(bis(diazaphospholane))-catalyzed AHF. We trapped and characterized catalyst intermediates revealing competing kinetic and thermodynamic preferences. Non-catalytic study of these species in the Wisconsin High Pressure NMR Reactor enabled us to quantify the percent of catalyst that goes off-cycle during catalytic reactions—a quantitative example of Halpern's rules. Furthermore, we used these data in combination with a variety of other non-catalytic experiments to build a full microkinetic model of AHF. Finally, we synthesized a library of bis(diazaphospholane) ligands to explore a structure-selectivity relationship and designed more effective ligands for AHF. Together these studies help to elucidate the origins of selectivity in Rh(bis(diazaphospholane))-catalyzed hydroformylation.

Acknowledgments

First, and foremost, I would like to thank my advisor, Clark Landis. You have taught me to be a more critical and effective scientist. I am extremely fortunate to have had you as a mentor in graduate school, and I cannot thank you enough for being so dedicated to helping me along the way.

I would also like to acknowledge the other members of my committee: Profs. Sam Gellman, Jen Schomaker, and Shannon Stahl. You have all helped me grow as a teacher and a scientist, and thank you for taking the time to serve on this committee.

I owe many thanks to everyone that maintains the instrumentation and support facilities. but I especially need to thank Drs. Charlie Fry, Heike Hofstetter, and Lingchao Zhu. None of this work could have been possible without the outstanding NMR facility and staff at UW–Madison.

I must thank both past and present Landis group members that have helped to make this a collaborative and friendly environment. I would like to acknowledge my mentors, Drs. Eleanor Nelsen and Leigh Abrams, who were incredibly patient and helpful during my first year. Additionally, I want to acknowledge both Drs. Eleanor Nelsen and Julia Wildt for collaborating with me—I was fortunate to work with two incredibly intelligent scientists. I have made many friends in this group and the department, and you all have made graduate school more fun in and out of the office.

Thank you to my family who has given me so much love and encouragement. My parents have taught me the value of education and to pursue my passion, and I would not be where I am without you. Finally, I want to thank my fiancé, Kaz Skubi. You have helped me become a better scientist, and your love and support have made graduate school a much happier place. (P.S. You win).

Table of Contents

List of Figures

List of Schemes

List of Tables

Chapter 1

WISL Introduction for Communicating Doctoral Research to the Public: Understanding Selectivity in Asymmetric Rhodium-Catalyzed Hydroformylation

1.1 Introduction

The overall goal of my Ph.D. was to *understand the selectivity in asymmetric rhodium-catalyzed hydroformylation*. Likely, very few of the words of this one sentence description made much sense—chemistry is absolutely like a foreign language. There are terminologies and phrases that become second nature to chemists, but we need to explain them in order to discuss our research with a lay audience. Therefore, the goal of this chapter is to break down the explanation of my Ph.D. goals so that the reader can walk away from this having a better idea of what I spent the last 4.5 years working on, obsessing over, and talking about non-stop.

1.2 What is "Asymmetric?"

The first word that I want to expand is "asymmetric." Before explaining that, we need to discuss some physical characteristics of molecules—specifically that they can be left- or right-handed. Your hands are non-superimposable mirror images of one another. There is no way to orient your hands such that they both have the knuckles up and thumb pointing to the left. In the same manner, molecules can be right- or left-handed. An example of this (with balls instead of atoms) is shown in Figure 1-1, in the bottom is the way a chemist would depict this. We use a wedge to indicate that an atom is coming out of the plane of the page, and a dash means it is going backwards behind the page. As you can see, there is no way to rotate the molecule on the right to overlay with the molecule on the left.

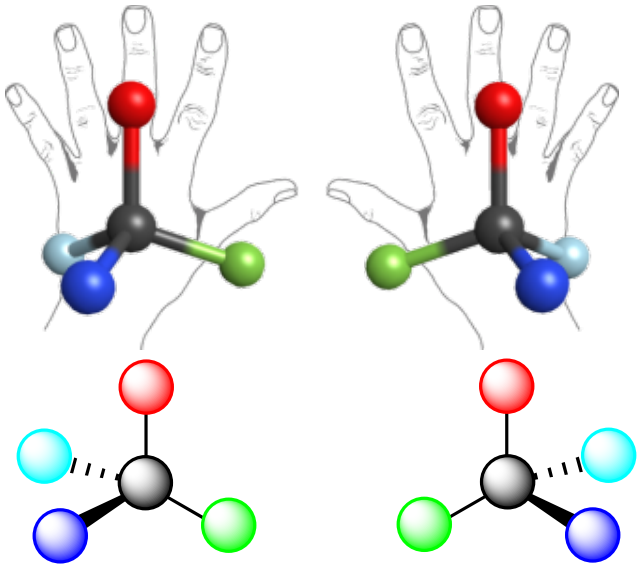

Figure 1-1. Example of left- and right-handed molecules (top) with a 2-dimensional depiction of the same molecules (bottom).

At this point, you might be asking yourself, "Why do I care if molecules are right- or left-handed?" The simplest answer is because our bodies react differently with the two hands. The amino acids in our bodies that make up proteins are handed.[1] This means that they will interact differently with molecules of opposite handedness. A classic example of this is the molecule carvone: the left-handed molecule smells like caraway; the right-handed molecule smells like spearmint (Figure 1-2).

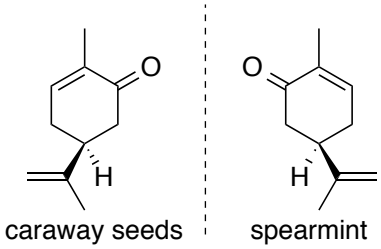

Figure 1-2. Left- and right-handed carvone smell different to humans.

Although different smells are interesting, a more important, and potentially dangerous, way handedness affects our bodies is when it comes to medicine. In many cases, the wrong hand

of a drug is ineffective, but harmless. For example, only the left-handed version of ibuprofen (Advil) treats pain, but the drug is sold as a 50:50 ratio of both hands. The way ibuprofen is made, it is obtained as a equal mixture of the two hands. Because separating them is not trivial, the companies keep each tablet as a mixture: if you are taking a 200 mg tablet, only 100 mg is actually helping your headache.

A far less innocuous example is the pharmaceutical thalidomide; it was prescribed from 1957–1961 for insomnia, tension, and morning sickness. The commercial drug was sold as a 50:50 mixture of the two hands. Scientists were unaware of the side effects until women started giving birth to babies with severe birth defects (usually deformed limbs). Since then, we have learned that it was the left-handed thalidomide molecule that caused these devastating effects (Figure 1-3), but the right-handed version was relatively benign.

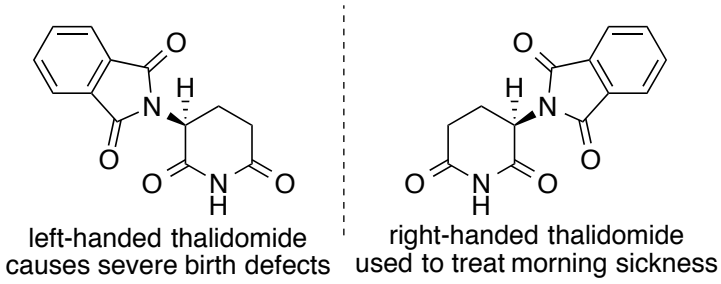

Figure 1-3. Left- and right-handed thalidomide molecules have extremely different effects on the body.

In part due to examples such as thalidomide, there has been a push from pharmaceutical companies to sell drugs that are only one hand (instead of a 50:50 mixture of both). This brings us back to the original point of this chapter: asymmetry. If a reaction is asymmetric, it simply means that it forms one hand of the product preferentially over the other.

Asymmetric synthesis is challenging because under normal reaction conditions, we will always form a 50:50 mixture of the two hands. In order to make one hand in excess over the

other, we need something else in the reaction that *also* is handed. The easiest way to think about this is literally with hands. If you had a hook for hand, it wouldn't matter to you if you shook someone's left or right hand. If you are only going to use your right hand, you know that it will be much easier to only shake someone else's right hand. That's the same for synthesis. If you perform a non-asymmetric reaction, meaning you don't add anything handed to the reaction flask (a hook), you will obtain equal amounts of both left and right molecules. If instead, you add something right-handed, the reaction will preferentially make right-handed molecules.

In theory, if you did a non-asymmetric reaction (using a hook) to form equal amounts of both the left- and right-handed molecules, they could be separated and you could obtain just the one you want. If you think about this from the viewpoint of a pharmaceutical company, that means they are throwing away half of their reaction product every time. Because this is extremely wasteful, they would rather just make one of the hands in the first place. Therefore, they want to utilize asymmetric reactions as much as possible.

Bringing this back to my Ph.D. research, I was studying *asymmetric* rhodium-catalyzed hydroformylation. At this point, you should understand that I was making handed molecules, and more specifically, making one in excess over the other. But the next issue we need to tackle is what does it mean to be catalyzed.

1.3 What is "Rhodium-Catalyzed?"

If you imagine a reaction as going over a mountain, you will understand that it takes energy to do such a process. As we know, in a reaction, we break some bonds and form new ones. The act of breaking bonds requires a lot of energy—just like climbing up the mountain.

When we form the new bonds, it is like going down the other side. In some cases, the mountain might be so tall that it would be impossible for you to climb over the top on your own. This is true of a reaction as well—sometimes the energy required is so great that the bonds will not break under any normal conditions. This is the case in which a catalyst is crucial. A catalyst is something that lowers the energy barrier to a reaction, but is not consumed in it. In our analogy of a mountain, it would be a trolley that utilizes a tunnel that cuts through the center of the mountain, drops you off at the end (the products), and then picks up new people (starting material) to bring across (Figure 1-4).

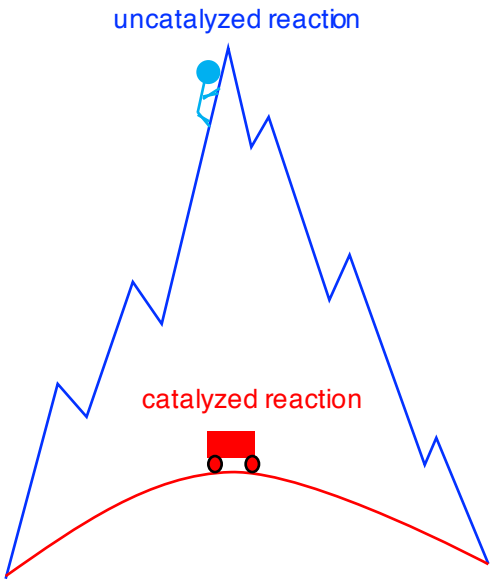

Figure 1-4. Climbing a mountain as an analogy for an uncatalyzed reaction versus a trolley as a catalyst.

Of course in reality, the catalyst is another molecule that is present during the reaction. In my case, we use rhodium metal, hence the term "rhodium-catalyzed." There are other atoms in the catalyst (hydrogen, carbon, phosphorus, nitrogen, and oxygen) that are attached to the rhodium, but chemists typically refer to the metal as the catalyst in these types of species.

Up until now, I have not discussed the actual reaction that I am studying. You know that it is asymmetric and catalyzed by rhodium, but not the specifics—which leads us to the next section.

1.4 What is Hydroformylation?

Hydroformylation is the reaction of a molecule with a carbon–carbon (C–C) double bond, carbon monoxide, and hydrogen gas. A generic reaction is shown in Scheme 1-1; instead of showing the rest of the molecule, I am simplifying it as a green circle. This reaction would normally take far too much energy to accomplish, so we need to add a catalyst to the reaction to speed it up. Without a catalyst, you could mix these three starting materials together and let them stir in a flask forever, but nothing would happen. With our rhodium catalyst, the reaction is complete in an hour.

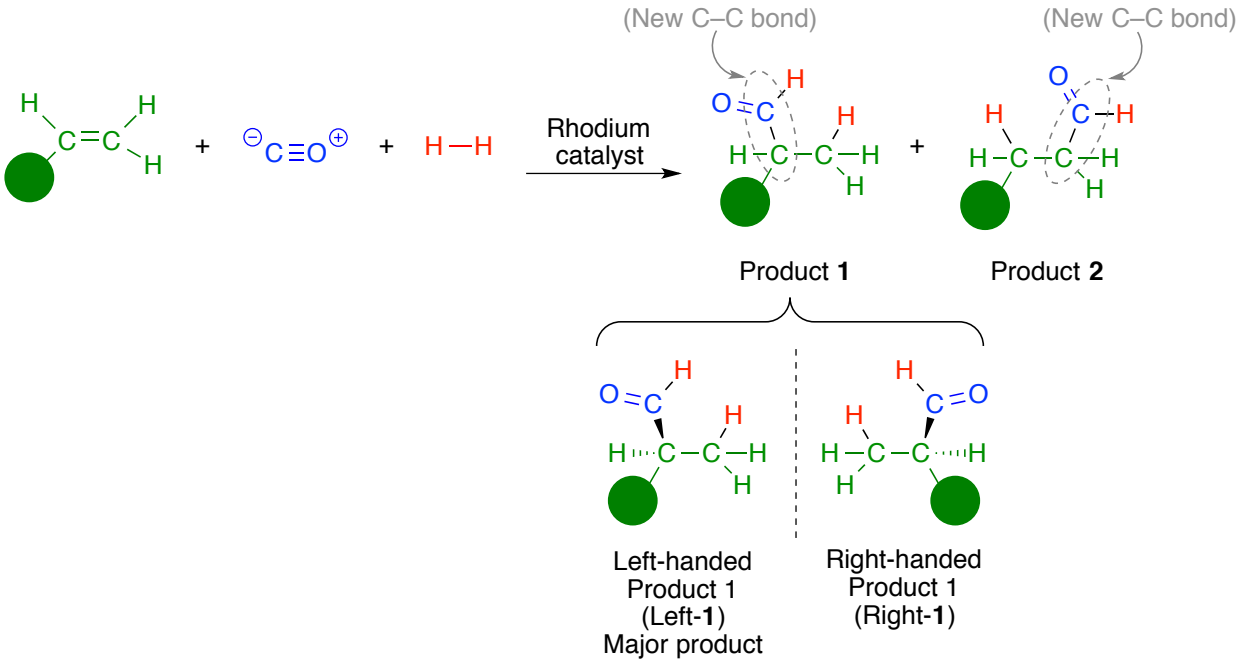

Scheme 1-1. Generic hydroformylation reaction.

Product **1** is formed when the new C–C bond is formed closest to the rest of the molecule. Product **2** is generated when it is formed on the carbon atom farther away from the rest of the molecule. There are not really only two products, though; **1** is actually a handed molecule. Therefore, there are 3 products from hydroformylation of this starting material: Left-**1**, Right-**1**, and **2**.[2] Product **2** is only formed in small amounts in our reaction. As I have already told you, this reaction is asymmetric: when using the Landis catalyst, the reaction yields much more of Left-**1** than Right-**1**. Bringing it all together, it should now make sense when I say that I studied rhodium-catalyzed asymmetric hydroformylation!

Why would I want to study this reaction? As we've already discussed, asymmetric reactions are extremely useful for pharmaceutical synthesis because we make one hand of the molecule in preference over the other. The reason hydroformylation is so useful is because the products we form are extremely versatile. A group that contains carbon, oxygen, and hydrogen bonded together in this way is called an aldehyde; these can be easily transformed it into a wide variety of other type of molecules (Figure 1-5).

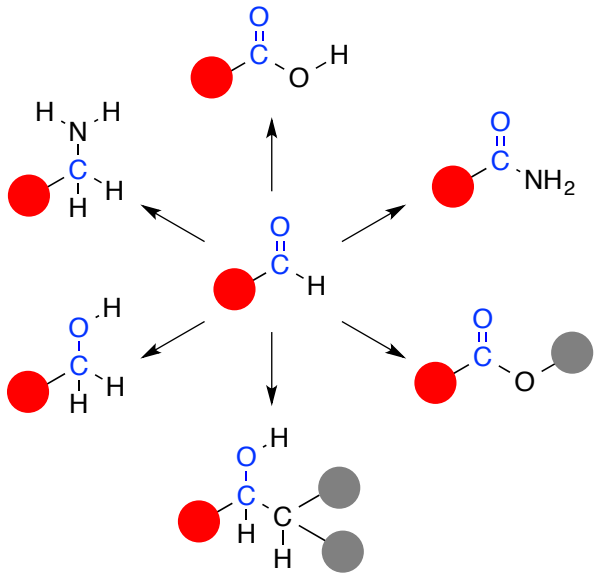

Figure 1-5. Aldehydes (center) can be easily transformed into other molecules.

At this point, you might be asking yourself what exactly I study about this reaction. As I mentioned previously, our catalyst is quite good at making only the Left-**1** product. The major question I asked in my research is: why? If we can understand why this catalyst is effective, we can learn how to make even better ones.

1.5 How Do We Understand this Reaction?

All of my projects in graduate school have centered on trying to understand what makes the Landis catalyst selective for the Left-**1** product. The reason this is a complicated topic is that the mechanism for transforming the starting materials to these products is complex. Scheme 1-1 shows the overall transformation for hydroformylation, but not the individual steps; not all of the atoms move at once, there are intermediate molecules formed along the way. An analogy that I will use throughout the section is simply doing the dishes. You cannot immediately go from dirty dishes in the sink to clean, dry dishes in the cabinet (you just wish you could!). There are several steps along the way: wash, dry, and then finally put the dishes away. In this case, our 'starting material' is dirty dishes. The first intermediate is clean, wet dishes. The second is dry dishes on the counter. The final products are dishes in the cabinet (Scheme 1-2).

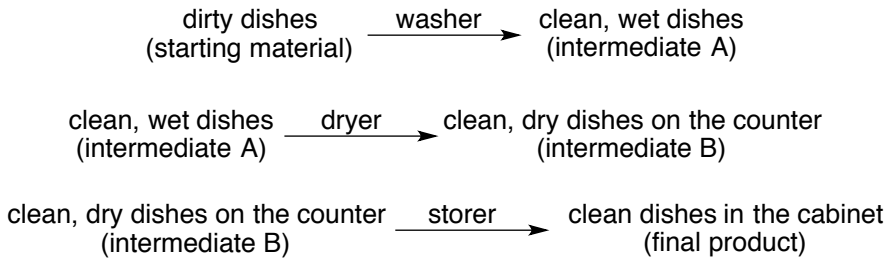

Scheme 1-2. Analogy for forming intermediates in a chemical reaction.

In this example, if mostly bowls are getting put away into the cabinet, this is analogous to the Left-**1** product being mostly formed in hydroformylation. The question I wanted to study is: what step (or steps) is controlling this selectivity? In our analogy, this is essentially asking: is it the washer, the dryer, or the person putting dishes away (the storer) that keeps choosing to handle bowls and not plates or cups?

The first way I studied this reaction was by characterizing the intermediates along the pathway. In order to understand how they are formed, it was imperative to know what they were. This is kind of silly when it comes to the dishes, but makes more sense when we are talking about chemicals that you cannot actually see.

How do you visualize these compounds? We used a technique called 'nuclear magnetic resonance spectroscopy' or NMR. You don't need to know how the instrument works to understand how I used it. NMR spectrometers are the forefather of the MRI machine; instead of visualizing your body, it is used to visualize molecules. It is complicated because the output for an NMR spectrometer doesn't look like a picture of a molecule. It is a series of lines that need to be interpreted to determine the structure (Figure 1-6).[3]

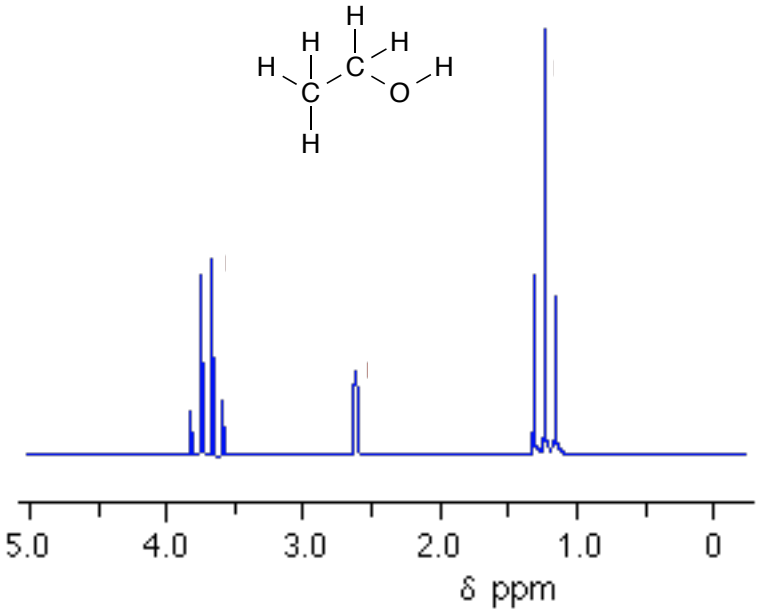

Figure 1-6. Example NMR spectrum of ethanol.

In many chemical reactions, we cannot normally observe the intermediates along the way because they are very short-lived (i.e. as soon as they are formed, they react away). This would be like being only able to see the pile of dirty dishes in the sink and clean ones in the cabinet. The rest of the process would be invisible to you—it is unknown who keeps choosing bowls. Thus, the only way to observe the intermediates is to leave out one or more of the starting materials. In my case, hydroformylation cannot go to completion in the absence of hydrogen, just as clean, dry dishes cannot appear in the cabinet without the storer. Therefore, in the absence of hydrogen, the reaction *had* to stop part way through, because not all of the reactants were there to form the product—allowing me to observe the intermediates using NMR spectroscopy (Scheme 1-3). Without the storer, you could actually see the pile of clean dishes on the counter. As I noted previously, an NMR spectrum is a series of peaks that need to be interpreted. Thus, an important part of this project was deciphering exactly what I had made.

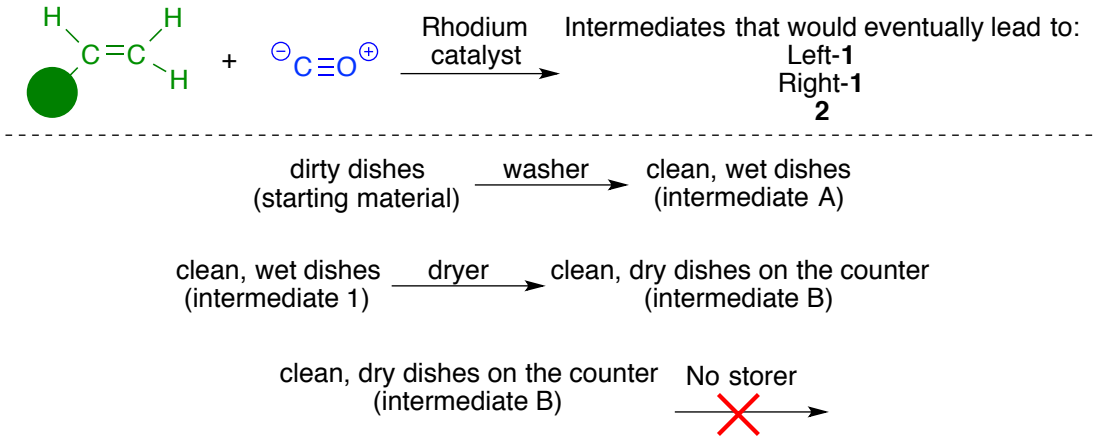

Scheme 1-3. Formation of intermediates in the absence of hydrogen gas.

The next step was to assess the selectivity for the intermediates being formed. Was there an excess of clean, dry bowls on the counter at this stage? If so, it means that either the washer or the dryer is choosing to only handle bowls—and it is probably not the storer being selective. Was there a random assortment of all types of dishes on the counter? This would imply that the storer was the one choosing (setting selectivity) for bowls, and the washer and dryer handled anything without being particular. What I actually observed in the absence of hydrogen was a lot of the intermediate being formed that eventually gives the Left-**1** product. This implies that the earlier steps are selective toward forming Left-**1**.

As you might have noticed, I am not differentiating the washer and dryer. The way these experiments are set up, I cannot tell the difference between the washer and dryer's selectivity. I can tell from my experiments that one (or both) of them is choosing mostly bowls, but not which one. This is a limitation of my experiments. And in fact, this remained a problem throughout my Ph.D.; there was no direct way for me to separate these two steps.

I could tell from my data that it was not only the first two steps that were setting the selectivity. In our example, the percentage of bowls after the dryer (let's say 70% bowls) was

lower than what was in the cabinet (90%). This implied that the storer was *also* choosing primarily bowls in this step of the process.

I studied this by taking those same intermediates formed in the absence of H_2 then adding hydrogen to see how they react (Scheme 1-4). By following this reaction in the NMR spectrometer, I was able to tell that, yes, in fact the last part of the reaction was also being selective for forming the Left-**1** product. In the analogy, this would be like giving the storer a huge stack of clean, dry dishes of all types and watching him to see which ones he chooses to put away.

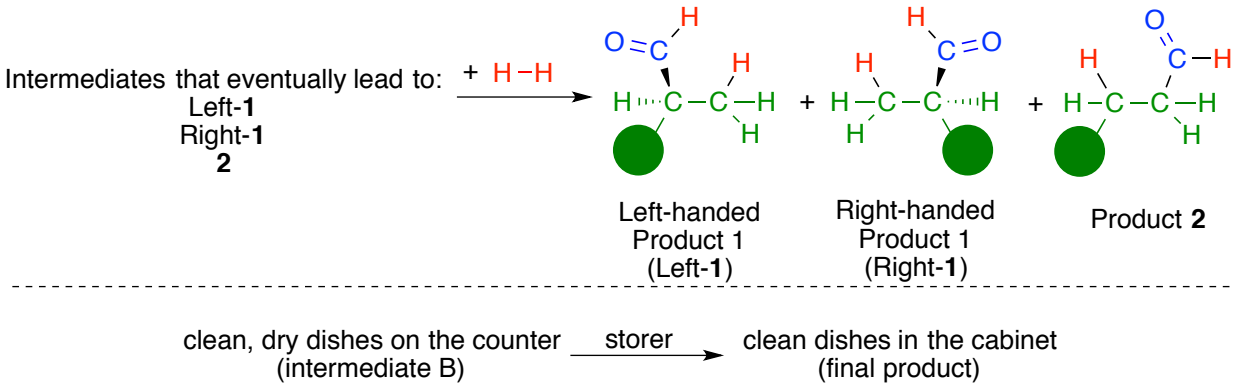

Scheme 1-4. Reaction of intermediates with hydrogen gas.

Consistent with my hypothesis, I observed that the last step of the reaction was also selective for the Left-**1** product. What this meant is that both forming the intermediates was selective, as well as the reaction taking them away. Both the washer/dryer combination was selecting mostly bowls, and the storer was also choosing mostly bowls to put in the cabinet!

This was really interesting (in my opinion) because chemists usually like to choose one step of the reaction and say, "That one step is determining selectivity!" For example, saying it was only the washer choosing bowls, and everyone else was indiscriminate. But my Ph.D.

research showed us that, in fact, it was a combination of all of the steps that were involved in setting the selectivity for the Left-**1** product. We think this conclusion can be relevant to other reactions, as well. Maybe it is more common than we think to have all the steps cooperate to yield a highly selective reaction.

I hope this Chapter has made my last 4.5 years slightly more digestible. I want you to take away knowing what I mean when I tell you that I studied the selectivity of rhodium-catalyzed asymmetric hydroformylation. This reaction is a powerful method for making useful products for pharmaceuticals, and I wanted to understand how the Landis catalyst was so selective for forming only one product. In the end, we learned that it wasn't only one step that was good, but a combination of all of them that together make it work so well.

1.6 Notes

(1) Interestingly, almost all living things on Earth produce molecules of the same hand. There are theories about the origins of handedness (homochirality), but there is no consensus, yet.

(2) Product **2** is not a handed molecule. The mirror image of it can be superimposed.

(3) Groups of atoms connected in certain ways essentially leave a fingerprint that you can assign. How far something is to the left or right of the spectrum tells us something about the nearby atoms in the molecule. The shape of the signal tells me different information about the nearby atoms. Solving a spectrum like this is basically a complicated, but really fun, puzzle.

Chapter 2

Recent Developments in the Scope, Practicality, and Mechanistic Understanding of Enantioselective Hydroformylation

Portions of this Chapter were submitted to Brezny, A.C.; Landis C.R. *Acc. Chem. Res*. 2018.

2.1 Introduction

Since its discovery in 1938,[1] hydroformylation (Scheme 2-1) has grown to be one of the largest scale organotransition metal catalyzed processes in chemical industry. Common catalysts are based on cobalt or rhodium complexes.[2-6] Hydroformylation constitutes a catalytic, atom-economic, one-step, one-carbon homologation of alkene feedstocks that produces versatile aldehydes. The value of aldehydes stems from their oxidation level, which lies between that of an alcohol and a carboxylic acid, and their facile conversion into a variety of functional groups including amines, alcohols, and acids.

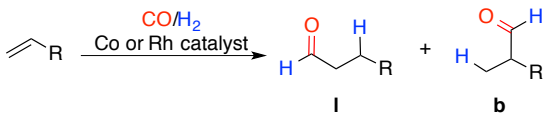

Scheme 2-1. Hydroformylation of alkenes.

Commodity scale applications of hydroformylation focus on the production of the achiral, linear aldehydes. These products serve as intermediates for the production of solvents, plasticizers, and detergents.[7] Enantioselective or asymmetric hydroformylation (AHF) for the synthesis of chiral, branched products is comparatively underdeveloped, but these aldehydes are attractive precursors for fine chemical synthesis and pharamceuticals.[8] A major challenge for these reactions is the need to obtain high regio- and enantioselectivity as well as useful rates. Although there has been considerable progress in the development of new ligands for this transformation,[9-37] a variety of limitations still remain.

First, the substrate scope of AHF is generally limited to activated, terminal alkenes. In order for this reaction to find widespread use in both academia and industry, high selectivity must be possible for both unactivated and more complex substrates. Second, the catalysts required for AHF are often viewed as expensive, difficult to synthesize, and unable to be

recycled, which has limited their use.[38] Furthermore, the industrial need for flow reactors with good gas/liquid mixing, and the need for high pressures of toxic gases has made AHF inaccessible to researchers without specialized equipment. This chapter will highlight several of the major advancements in these areas over the last 10 years.

In addition to its synthetic applications, the mechanism of hydroformylation has been the subject of considerable study. For linear selective hydroformylation, a variety of experiments have been performed to understand the mechanism and origins of selectivity. Some of these involve indirect methods such as deuteroformylation of alkenes[39-46] while others include direct observation of catalyst species by high-pressure IR and NMR.[47-55] There has been far less exploration of asymmetric hydroformylation catalysts, and thus the origins of both regio- and enantioselectivity have remained unclear. In this chapter we will also describe our group's progress toward understanding the complex kinetics and mechanism of AHF.

2.2 Recent Advancements in the Accessibility of AHF

Although the development of *asymmetric* hydroformylation lags behind the linear-selective process, advances over the last decade have expanded significantly the practical applications of AHF. These advances include: expansion of the substrate scope, immobilization of catalysts, development of flow processes, and lowering the reaction pressure. Such developments make AHF more attractive to both academic and industrial researchers and provide a convenient, atom-efficient route to α-chiral aldehydes.

2.2.1 Substrate Scope

The most common 'benchmark' substrates for asymmetric hydroformylation are functionalized, prochiral terminal alkenes such as vinyl arenes or vinyl acetates.[6] Terminal alkenes bearing inductively electron-withdrawing substituents commonly direct reaction to the branched product[56,2,57-59,6] and constitute many of the substrates in successful applications of AHF. Broader application of AHF in organic synthesis requires expansion of the useful substrate class beyond terminal, activated alkenes. In this section we highlight a few important advances at the expense of a comprehensive review.

2.2.1.1 Simple 1-Alkenes

Simple 1-alkenes represent a historically difficult class of substrates for AHF because they lack the electron-withdrawing groups that direct formylation to the branched position. Therefore, common ligands for AHF tend to either favor the linear product or are unselective. For example, Rh(binaphos)[60] and Rh((*S,S,S*)-BDP)[61] give branched:linear ratios of 1:4 and 1:2.8, respectively for hydroformylation of unactivated 1-alkenes (Figure 2-1). Recent work from Clarke and coworkers using Rh(acac)$(CO)_2$ and (S_{ax},*S,S*)-bobphos achieved significant regioselectivities and enantioselectivities for a variety of 1-alkenes (Table 2-1).[33] In order to obtain reasonable b:l ratios, low temperatures and long reaction times were required. Although the regioselectivity for 1-hexene is still relatively moderate (b:l = 3:1) compared to activated alkenes, this was a significant improvement over state-of-the-art ligands and was a major step forward in the scope of Rh-catalyzed asymmetric hydroformylation.

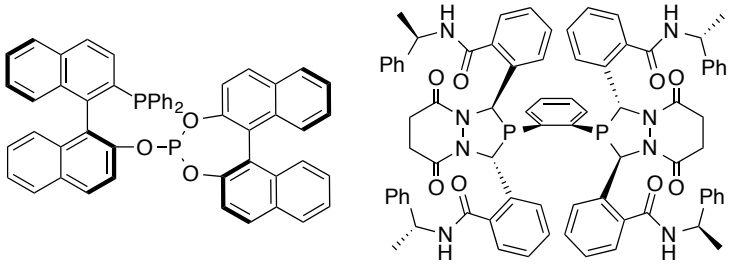

Figure 2-1. Structures of (*S*,*R*)-binaphos and (*S*,*S*,*S*)-BDP.

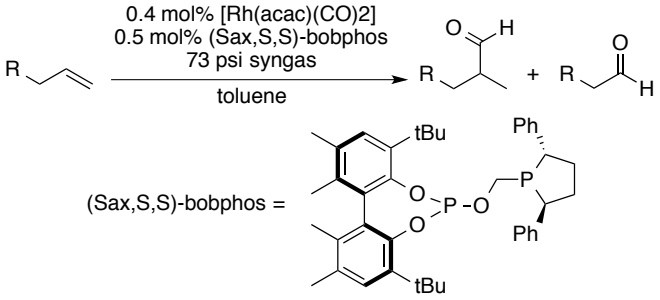

R=	Temp (°C)	Conv. (%)	t (h)	b:l	ee (%)
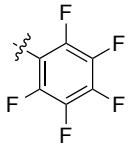	16	81	21	6.2:1	91
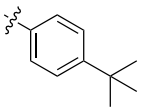	16	99	66	3.0:1	92
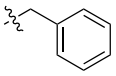	16	89	70	2.5:1	75
$CH_2CH_2CH_3$	16	78	46	3.0	93
CN	30	>99	14	10.0:1	81
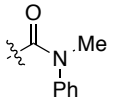	16	72	71	4.5:1	92

Table 2-1. Hydroformylation of alkyl olefins by Rh(bobphos).

2.2.1.2 1,2-Disubstituted Alkenes

In the AHF of terminal alkenes, the branched product necessarily includes a methyl group at the stereogenic center. AHF of 1,2-disubstituted alkenes generates stereogenic centers with greater complexity. With the increased steric bulk at both positions of the olefin, obtaining products with high regioselectivity and rates is inherently more difficult. Both the Tan and Breit groups have used a scaffolding catalyst strategy to impart regiocontrol.[62-67] For example, Tan and coworkers achieved high enantioselectivities for allyl amines through use of a scaffolding ligand that undergoes reversible, covalent attachment of the substrate to the phosphine ligand. (Scheme 2-2).[68]

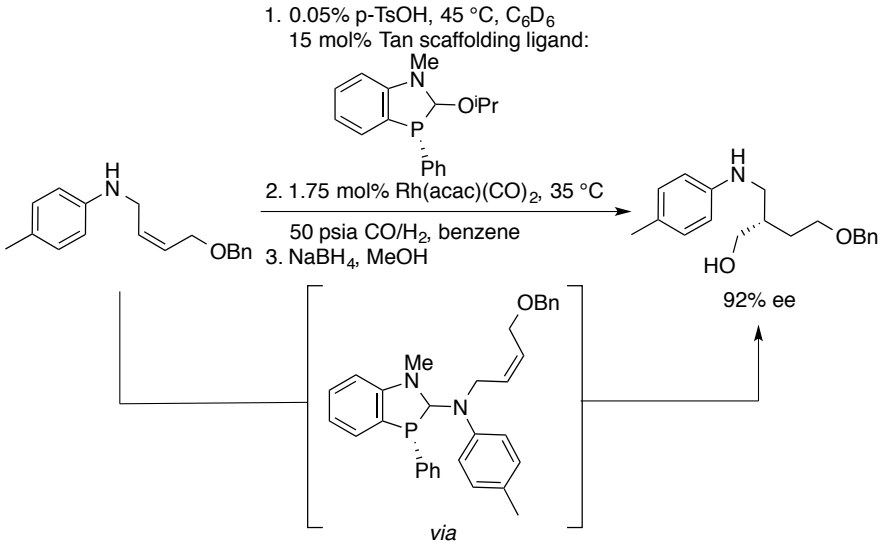

Scheme 2-2. Hydroformylation of 1,2-disubstituted alkene with Tan's scaffolding ligand.

In addition to the scaffolding approach, both binaphos and BDP have been successfully used for AHF of activated internal alkenes.[14,69-70] A recent advance from our group is the AHF of *Z*-enamides and enol esters yielding α-functionalized aldehydes with high regioselectivity and *ee* values (Scheme 2-3).[71] In these reactions, the electron-withdrawing group enables regio control in the absence of a scaffold.

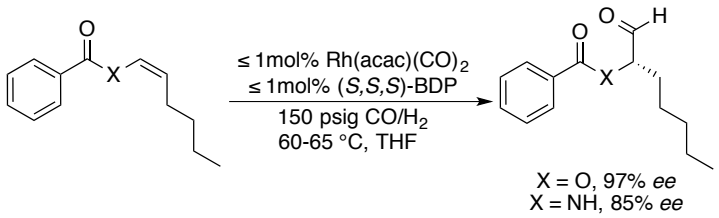

Scheme 2-3. Hydroformylation of *Z*-enamides and enol esters with (*S,S,S*)-BDP.

2.2.1.3 1,1-Disubstituted Alkenes

A third challenging class of substrates is 1,1-disubstituted alkenes. Due to increased steric bulk at the α position, the majority of examples give rise to the linear product, but unlike with terminal alkenes, this product still creates a stereogenic center.[72] Although difficult, formation of the branched product is attractive because it creates a chiral tetrasubstituted center. Because facial discrimination of the alkene is challenging with two substituents, these substrates tend to give minimal *ee*.[73-75] An exception can be found in the work of the Buchwald group, in which AHF of α-trifluoromethyl vinyl acetate gives good selectivity for the branched aldehyde in high *ee* (Scheme 2-4).[76] This result appears to be unique to 1,1-disubstituted alkenes with two small sigma electron-withdrawing substituents (e.g., $–CF_3$ and –OAc), as other 1,1-disubstituted alkenes yield linear hydroformylation products with these ligands.[30] Our group is currently investigating other substrates with a variety of catalyst systems that can produce branched, α-tetrasubstituted aldehydes.[77]

These recent advances demonstrate that AHF of structurally complex alkenes can be achieved with a suitable catalyst, and suggest that further advances can be achieved through new ligand design. However, wider adoption of AHF requires more than ligands with good selectivity and activity profiles. More common application of AHF to organic synthesis, whether in

academic or industrial environments, is promoted by advances in the safety, scalability, and cost for the process.

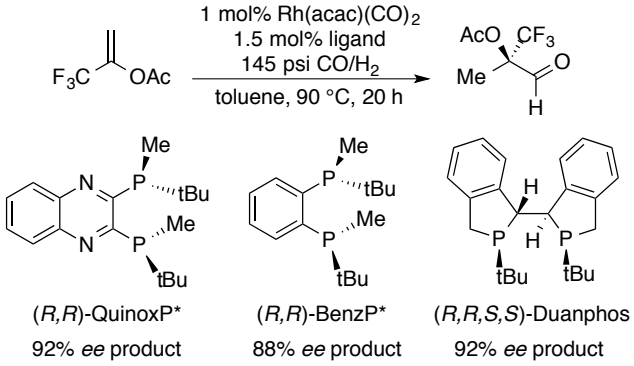

Scheme 2-4. Branched-selective AHF of 3,3,3-trifluoroprop-1-en-2-yl acetate.

2.2.2 Improving Practicality and Ease of Use

2.2.2.1 Bis(diazaphospholane) Ligands

Bis(diazaphospholane) (BDP) ligands exhibit high reactivity and selectivity in rhodium-catalyzed asymmetric hydroformylation.[78] However, the original synthesis of resolved BDP ligands was inconvenient due to the number of steps, low yield, and difficult resolution, which limited application of the ligand by both bench chemists and industrial users.[38] Recently our group, in collaboration with Eli Lilly, reported an improved, scalable synthesis and resolution procedure that avoids the need for chromatography or specialized equipment.[79] This procedure uses fewer steps and increases the yield and purity of the ligand.

Immobilization of catalysts on a solid support can improve the ease of recycling, which is especially important for expensive, precious metal catalysts. The carboxylic acid functional groups of the BDP ligands enable immobilization of the ligands to resins via simple coupling reactions. Rh(BDP) catalysts supported on Tentagel resin exhibit high selectivity and activity,

similar to the homogenous system.[80] By pumping a well-stirred solution of substrate and synthesis gas from a glass pressure bottle through a column of immobilized catalyst, one can achieve high turnover numbers and obviate the need to separate catalyst and aldehyde product in a simple apparatus.

2.2.2.2 Flow Reactors

Larger scale application of hydroformylation in a pharmaceutical environment must address the safety concerns of using flammable and toxic gases, and the challenge of maintaining good gas-liquid mixing. Flow processes represent an attractive approach to scaling intrinsically dangerous processes, but gas-liquid mixing can be problematic for flow reactors. In collaboration with Eli Lilly, we reported a pipes-in-series flow reactor for asymmetric hydroformylation, which mitigates the safety hazards by minimizing the quantity of reagent gas.[81-82] Additionally, this design enables good gas/liquid mixing, an important feature because regio- and enantioselectivity strongly depend on gas concentrations.[83] Ley and coworkers have developed related continuous flow reactors based on a tube-in-tube gas-liquid design.[84] Thus, flow reactors that are optimized for gas-liquid reactions can enable practical application of AHF in industrial settings.

2.2.2.3 Asymmetric Transfer Hydroformylation

To be truly accessible to a bench chemist in an academic setting, AHF without pressurized gases is ideal. To this end, both the Clarke and Morimoto groups have demonstrated successful asymmetric transfer hydroformylation.[85-86] These systems use formalin or paraformaldehyde (Scheme 2-5) which undergo catalytic conversion to CO/H_2 *in situ*, which

then react in AHF. These reactions can be performed in microwave tubes or glass pressure bottles, eliminating the need for gas cylinders and manifolds. Useful selectivity has been demonstrated for some substrates.

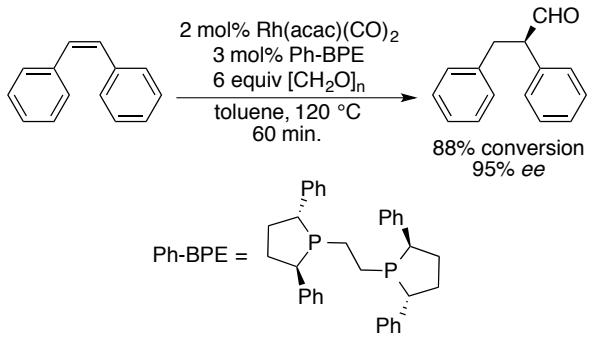

Scheme 2-5. Asymmetric transfer hydroformylation of *cis*-stilbene from Clarke and coworkers.

The advances summarized above make AHF a more attractive and practical process. To date, progress in AHF has been driven by empiricism. As a result, there are few general rules to guide new ligand design or to match substrates with an optimal catalyst structure or reaction conditions. This lack of rational design is largely due to the complexity of the reaction mechanism, which involves three reactants and a catalyst precursor that traverse three isomeric catalytic cycles, each comprising multiple elementary steps. Whether the goal is reaction design or simply understanding the origins of catalytic activity and selectivity, deeper examination of the mechanistic intricacies of AHF is required.

2.3 Mechanistic Studies of Rh(bis(diazaphospholane)) Catalysts

Recently, our group has focused on understanding the origins of selectivity in rhodium BDP-catalyzed AHF. The mechanism depicted in Scheme 2-6 was first proposed by Breslow and Heck in 1961 for Co-catalyzed hydroformylation.[87] Although this mechanism provides a general

framework for hydroformylation using either rhodium or cobalt catalysts, the origins of both regio- and enantioselectivity remain unclear. For example, is regioselectivity fixed when the rhodium hydride alkene complex (**3**) undergoes insertion to yield **4l** or **4b**, or is this step reversible? At what temperatures and pressures are these steps reversible?[39-46]

Compared to the linear-selective systems, less work has been done to probe the origins of selectivity in asymmetric hydroformylation. Using deuteroformylation studies, Nozaki and coworkers investigated the reversibility of alkene insertion for a Rh(binaphos) system with several alkenes (see Figure 2-1).[88] With styrene as the substrate at 40 °C, they reported irreversible hydride migration at high CO pressures (150 and 730 psi). However, at lower CO pressure (<10 psi), alkyl formation becomes reversible, at least for the branched alkyl. This was evidenced by significant deuterium incorporation at the β-carbon of the unconverted styrene and other deuterium distribution data. Additionally, at these lower gas pressures, they observed a decrease in both regio- and enantioselectivity.

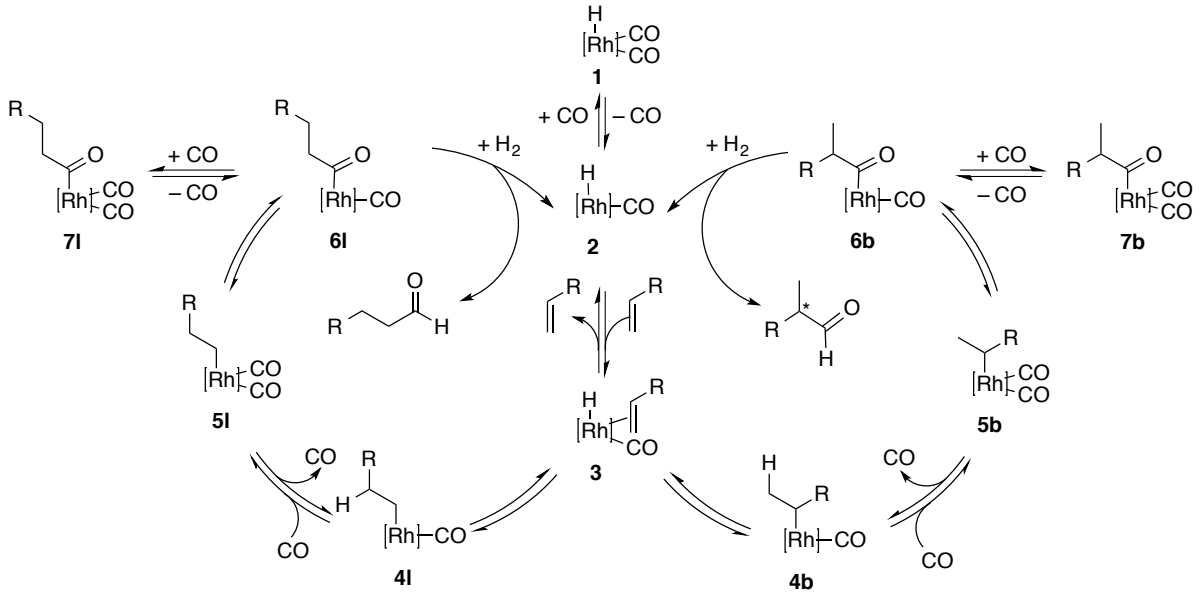

Scheme 2-6. Accepted mechanism for hydroformylation.

We have also observed an effect of the CO pressure on selectivity for styrene hydroformylation by the standard Landis Rh(*S,S,S*–BDP) catalyst (see Figure 2-1).[83] An increase in CO pressure leads to a significant increase in both the regio- and enantioselectivity of the reaction (Figure 2-2). The rate and selectivity are apparently independent of H_2 pressure. In combination with the observed first order dependence on the [styrene], the cumulative data suggest that the resting state of the catalyst is the hydrido dicarbonyl (**1**).

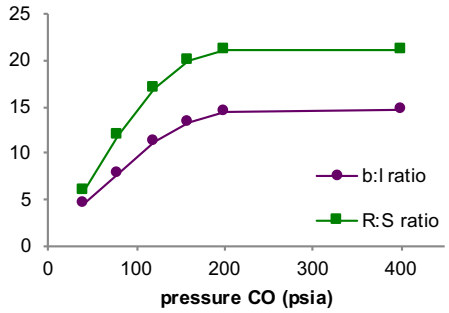

Figure 2-2. Effect of CO pressure on selectivity in styrene hydroformylation by Rh(*S,S,S*)-BDP.

In order to explain the effect of CO pressure, Watkins and Landis proposed a kinetic model outlining the origins of selectivity (Scheme 2-7). It includes a reversible insertion of styrene from **3(*R*)** to give the kinetically favored branched alkyl **4b(*R*)**. Insertion from the same intermediate Rh-alkene complex (**3(*R*)**) is proposed to be irreversible when leading to the linear alkyl **4l**. Additionally, they suggest an irreversible hydride migration from **3(*S*)** to both the minor branched alkyl (**4b(*S*)**) and the linear isomer (**4(l)**). Thus, in this mechanistic proposal the kinetic competition of **4b(*R*)** undergoing deinsertion to **3(*R*)** or binding CO to lead to aldehyde is crucial for setting the selectivity of the reaction because the fates of both **4b(*S*)** and **4l** are already set. This model is consistent with their experimental kinetic and isotopic labeling data (*vide infra*).

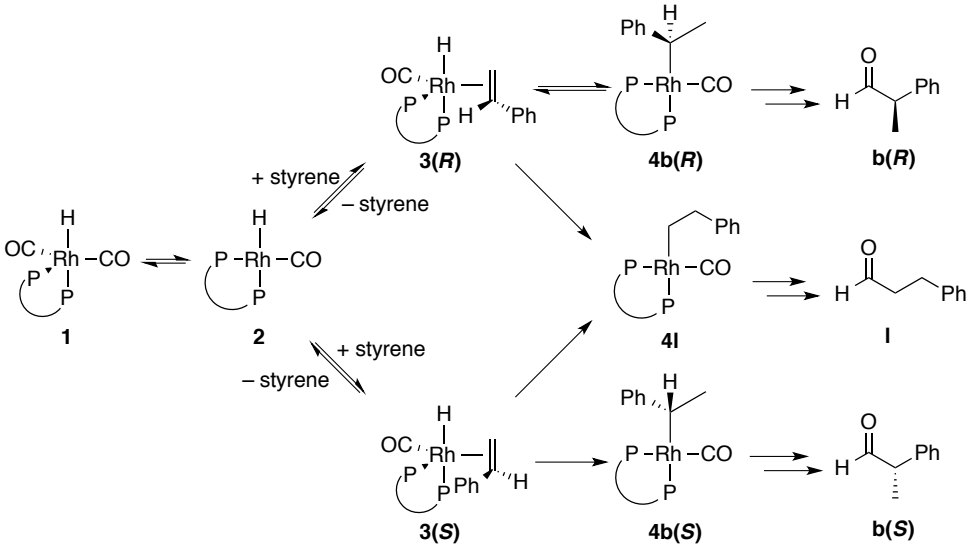

Scheme 2-7. Proposed kinetic model for determining selectivity in AHF of styrene.

2.3.1 Hydroformylation Using Deuterium Labeling

2.3.1.1 Hydroformylation of α-deuterostyrene

In order to provide evidence that the linear alkyl **4l** was produced from both the Rh-alkene complexes (**3(*R*)** and **3(*S*)**), the products from hydroformylation of α-deuterostyrene were examined (Scheme 2-8).[83] The stereochemistry of the *linear* product was used to determine the face of the alkene to which the migrating hydride added. Experimentally, they observed that 70% of the aldehyde products came from hydride addition to the *re* face and exhibited good selectivity for the branched product (22:1 b:l). Hydride migration to the *si* face was unselective, yielding an approximately 1:1 b:l ratio. The kinetic model therefore reflects these results, which demonstrates that the linear aldehyde can arise from hydride addition to either face of styrene.

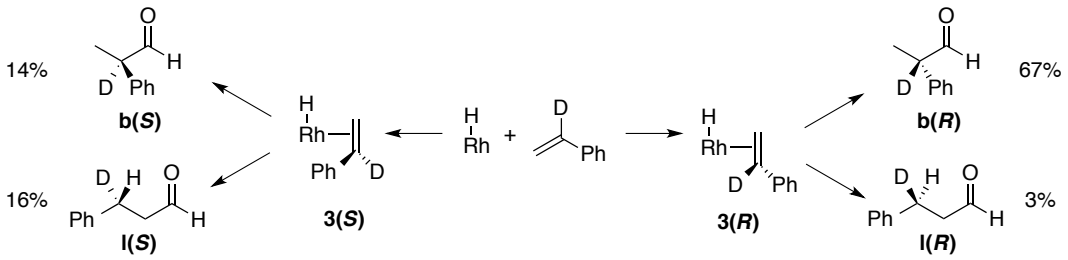

Scheme 2-8. Product distribution from the hydroformylation of α-deuterostyrene.

2.3.1.2 Deuteroformylation of styrene

The reversibility of styrene insertion was probed using a series of deuteroformylation experiments that are similar in design to those of Nozaki and coworkers.[88] In the limit of irreversible deuteride migration, one would expect deuterium only at the aldehyde and β-positions, whereas scrambling of the label requires reversible formation of the alkyl species (Figure 2-3).[83]

Watkins and Landis found that the deuteroformylation of styrene at 80 °C with Rh((*S,S,S*)-BDP) yielded a significant amount of both the β-deuterostyrene (**E**) and d_1-aldehydes (**G**, **H**). This result provides indirect evidence for the reversible formation of the branched alkyl intermediate (**4b(*R*)**). Taking into account the observation that seven times as much β-deuterostyrene (**E**) was formed as aldehyde (**D**), and the intrinsic labeling statistics (only 1/3 of reversions from the branched alkyl leave an isotopic trace), the branched alkyl complex reverts to styrene 21 times faster than it converts to aldehyde. No significant amount of α-deuterostyrene (**B**) was observed in these experiments, which suggests that when the linear Rh-alkyl isomer (**4l**) is formed, it is more likely to go on to product than revert to the Rh-alkene complex. One caveat to this analysis is that because the methylene hydrogens of the linear alkyl complex are

diastereotopic, **4l** could undergo a stereospecific β-deuteride elimination without leaving a deuterium label.

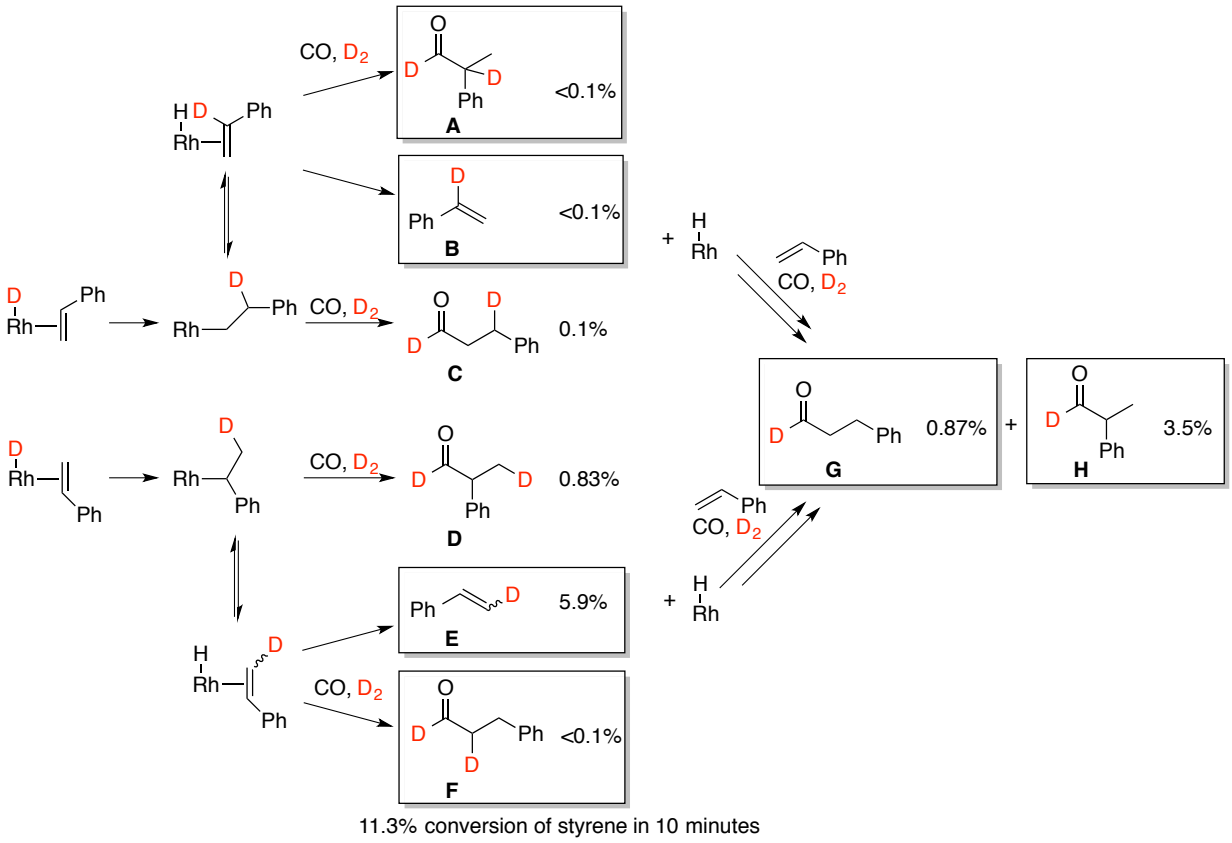

Figure 2-3. Observed product distribution on the deuteroformylation of styrene at 80 °C, 80 psia CO/D_2, 0.01 mol% Rh((*S,S,S*)-BDP), 10 minutes. Products outlined by boxes require reversible deuteride/hydride migration.

The kinetics of deuteroformylation reveal that an increase in the partial pressure of CO leads to a slower isomerization of the branched alkyl species (**4b(*R*)**) to β-deuterostyrene (**E**) (Figure 2-4).[83] These findings can be explained by more efficient trapping of **4b** at higher CO concentrations to produce the Rh-acyl intermediate (**6b(*R*)**) and eventually aldehyde.

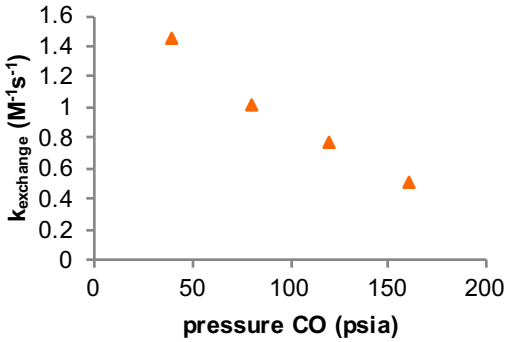

Figure 2-4. Influence of CO pressure on observed rate for formation of β-deuterostyrene. All reactions performed at 80 °C, $[styrene]_0$ = 2.9 M, [Rh(TMBA-BDP)] = 6.7 x10^{-4} M, P_{H2} = 40 psia.

The effect of CO pressure on rates of product formation supports the proposed kinetic model (Figure 2-5). The rates for producing both the linear and *S*-branched aldehydes are inhibited by CO, which is plausibly due to the need for the resting state complex (hydrido dicarbonyl **1**) to lose CO before entering the catalytic cycle.

The rate of formation of the (*R*)-branched product is roughly independent of [CO] with slight inhibition at high pressures. In the low-pressure regime, the rate for trapping **4b(*R*)** with CO should increase with higher [CO], limiting reversion to **3(*R*)**, and therefore lead to faster product formation. It was proposed that the increased rate of trapping **4b(*R*)** is offset by the inhibitory effect of CO, thus yielding a rate for (*R*)-branched product that is independent of this gas pressure. In contrast, formation of both **4l** and **4b(*S*)** is irreversible, and thus there is no rate increase for trapping these alkyl species because reversion is noncompetitive.

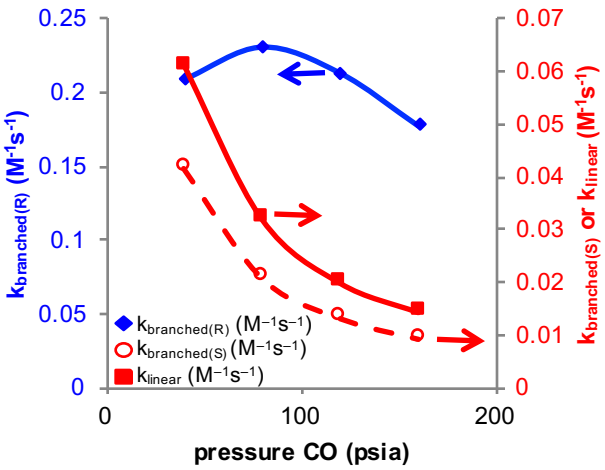

Figure 2-5. The effect of CO pressure on rates of linear, branched(*R*), and branched(*S*) product formation. Lines connecting points are guides only. All reactions performed at 80 °C, $[\text{styrene}]_0$ = 2.9 M, [Rh(TMBA-BDP)] = 6.7 x10^{-4} M, P_{H2} = 40 psia.

In the high-pressure limit, trapping of **4b(*R*)** presumably outcompetes β-hydride elimination to give **3(*R*)** and thus there is no longer a promoting effect of CO. Still, the CO-promoted shifting of catalyst to the off-cycle resting state persists. Therefore, the overall rate is inhibited by CO at higher pressures, as shown in Figure 2-5.

These kinetic data together help to explain the effect of CO pressure on selectivity. Due to the irreversible formation of **4l** and **4b(*S*)**, the rates of formation of linear and *S*-branched aldehydes are solely inhibited by CO. In contrast, increasing [CO] has little effect on the rate of the *R*-branched aldehyde. Furthermore, with irreversible hydride migration to all alkyl intermediates at high pressure, the relative transition states for alkene insertion become selectivity-determining and therefore the regio- and enantiomeric ratios become independent of [CO] at high pressures (see Figure 2-2).

2.3.2 Ultra Low-Pressure Hydroformylation

Studies of ultra low-pressure hydroformylation also are consistent with the proposed model (Scheme 2-7). Tonks and Landis reported that the hydroformylation of styrene at very low CO pressures led to an inversion of the regioselectivity and a loss of enantiomeric excess (Figure 2-6).[89] Interestingly, they obtained a different rate law than that observed at high gas pressures. The rate was apparently first order in [CO] (compared to 0 or –1 order at high pressures, *vide supra*) and inhibited by styrene.

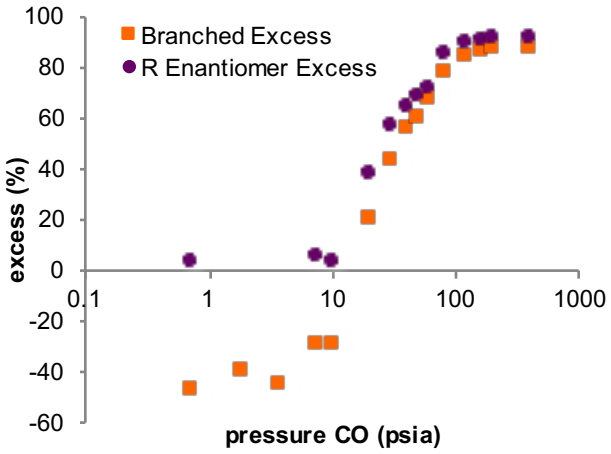

Figure 2-6. Regio- and enantioselectivity in the AHF of styrene at varied CO pressures ($[\text{styrene}]_0$ = 2.2 M, [Rh(BDP)] = 5 x10^{-4}, 80 °C, $P_{H2} = P_{CO}$).

This rate law suggested a Rh(BDP)(alkyl)(CO)(styrene) complex (**4**-styrene adduct) as the catalyst resting state at high styrene pressures. Under the ultra low-pressure CO conditions, [styrene]>>[CO], making this proposal feasible.

The change in selectivity is consistent with Watkins and Landis's model in which the kinetically favored branched alkyl **4b** is formed reversibly. Under lower CO pressures, this intermediate can revert to the alkene complex, and reinsert to form the thermodynamically favored species. We note that both of these works provided indirect measures of catalyst

reactivity and assumed the kinetic preference for branched species. In moving forward with our studies, we sought to observe catalyst species and directly determine their kinetic and thermodynamic preferences.

2.3.3 Observation of Catalyst Species

In order to directly observe catalyst species by NMR spectroscopy, a slightly different BDP ligand was used. The tetraphenyl-BDP (Figure 2-7) has increased solubility and improved lineshape in the ^{31}P NMR spectrum compared to (*S,S,S*)-BDP as used above.

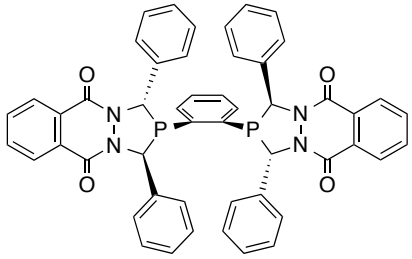

Figure 2-7. Tetraphenyl-BDP (racemic) used in NMR spectroscopy studies for improved solubility and lineshape.

Under low temperature and low CO pressure (no H_2) conditions, reaction of hydrido dicarbonyl **1** with styrene enabled observation and detailed characterization of several on- and off-cycle catalyst species by ^{1}H and ^{31}P NMR spectroscopy (Figure 2-8).[90] At –20 °C upon addition of styrene, the hydrido dicarbonyl compound (**1**) disappeared in an approximately first-order fashion ($t_{1/2}$ = 30 minutes) and was replaced primarily by acyl dicarbonyl species **7**. At early reaction times, a kinetic preference for the branched isomer (**7b**) was observed, which is consistent with the assumption in Watkins and Landis's kinetic model (*vide supra*).[83,89] At longer reaction times, the linear acyl dicarbonyl (**7l**) was the predominant species, indicating that it is thermodynamically preferred.

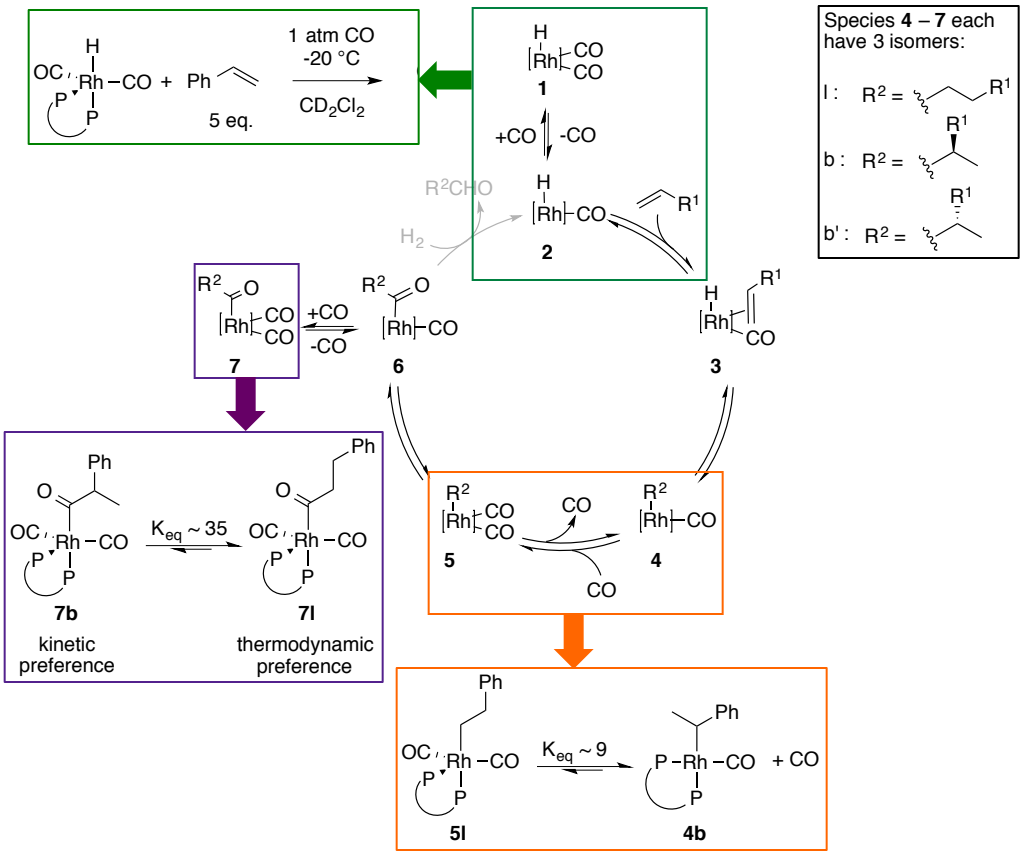

Figure 2-8. The generalized catalytic cycle for rhodium-catalyzed hydroformylation of styrene, with intercepted intermediates highlighted. Reaction of hydrido dicarbonyl **1** with styrene (60 mM **1**, 5 equivalents styrene, P_{CO} (initial) ~ 15 psia, –20 °C, CH_2Cl_2) enabled interception and characterization of intermediates **4**, **5**, and **7**. The kinetic and thermodyanmic perferences of the acyl dicarbonyl intermediates (**7**) and alkyls (**5l** and **4b**) could be observed directly.

Inherent to the setup of these NMR tube experiments, only passive gas-liquid mixing could occur during the reaction. Therefore, at longer reaction times, the solution became starved of CO (the formation of **7** from **1** consumes one equivalent of CO). Under these conditions, the four-coordinate branched alkyl monocarbonyl **4b** and the five-coordinate linear alkyl dicarbonyl **5l** were observed. These data demonstrated more favorable coordination of CO to the linear alkyl species (**4l**) compared to the branched isomer (**4b**). The differing number of terminal CO ligands

between the observed alkyl species (**4b** and **5l**), prevented a quantitative comparison of the kinetics for their formation. Nonetheless, this work provided the first direct observation of alkyl catalyst intermediates for any rhodium hydroformylation system. Furthermore, it provided direct evidence of the kinetic preference for the branched acyl dicarbonyl (**7b**), the reversibility of its formation, and a thermodynamic preference for the linear isomer (**7l**). Still the question remained: how relevant are these off-cycle species during catalysis?

2.3.4. Wisconsin High Pressure NMR (WiHP-NMRR) Studies

The WiHP-NMRR[91] developed by Landis and coworkers is particularly well suited to explore these catalyst species under high pressure (Figure 2-9). This reactor enables reaction monitoring at high, known gas pressures and with active gas-liquid mixing.

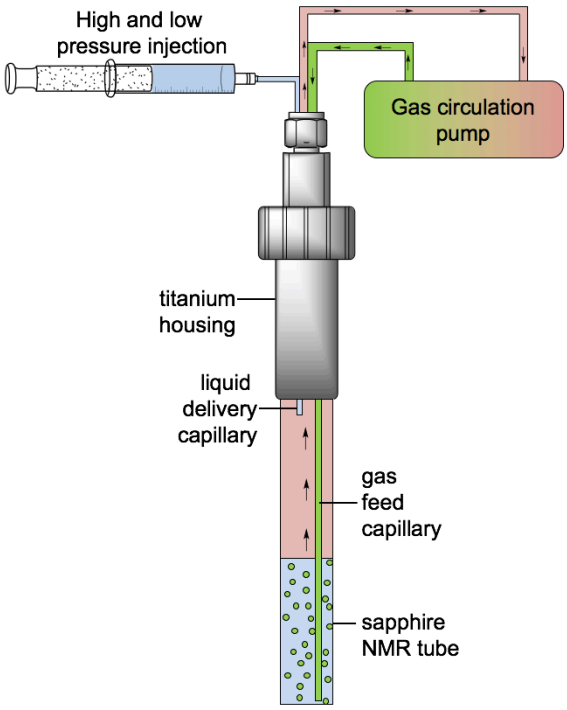

Figure 2-9. Wisconsin High Pressure NMR Reactor (WiHP-NMRR) developed by Landis and coworkers for studying gas-fed reactions.

2.3.4.1 Operando Study of Catalytic Hydroformylation

Recently, we utilized this apparatus to explore the role of off-cycle acyl dicarbonyl species (**7**) during catalysis.[92] The data from catalytic hydroformylation reactions collected by *operando* spectroscopy allowed us to monitor both starting material and product concentrations as a function of time (Figure 2-10), and we found a zeroth order dependence on [styrene]. This contrasts with the previous work from Watkins and Landis at higher temperatures, in which a first order dependence was observed, indicating a rhodium hyrdide (**1**) resting state.[83] In our case, the acyl complexes (**7**) were instead found to be the resting state, which is consistent with a catalytic rate law that is independent of [styrene].

At high CO pressures (200 psia (Figure 2-10A) and 115 psia (Figure 2-1B)) in the steady-state region, the catalyst was observed as **7b** and **7l** in a 3:1 ratio. Under these conditions, the reaction rate was inhibited by [CO], which is consistent with the need for CO dissociation from **7** before reaction with dihydrogen.

At low CO pressure (20 psia (Figure 2-10 C)), the selectivity decreased significantly. This was consistent with the findings from both Watkins et. al.[83] and Tonks et. al.[89] Interestingly, we observed a *decrease* in the rate under these lower pressure conditions. This was correlated to the change in resting state from a 3:1 **7b**:**7l** ratio to an approximately thermodynamic mixture of acyl dicarbonyls (<1:10 **7b**:**7l**). At lower CO pressures, it has been shown with both (*S,S,S*)-BDP[83] (*vida supra*) and tetraphenyl-BDP[92] that acyl isomerization is facile. Thus under low CO pressure conditions, more catalyst pools in the slower, linear pathway that contains the thermodynamic sink (**7l**), thereby retarding the overall rate of hydroformylation.

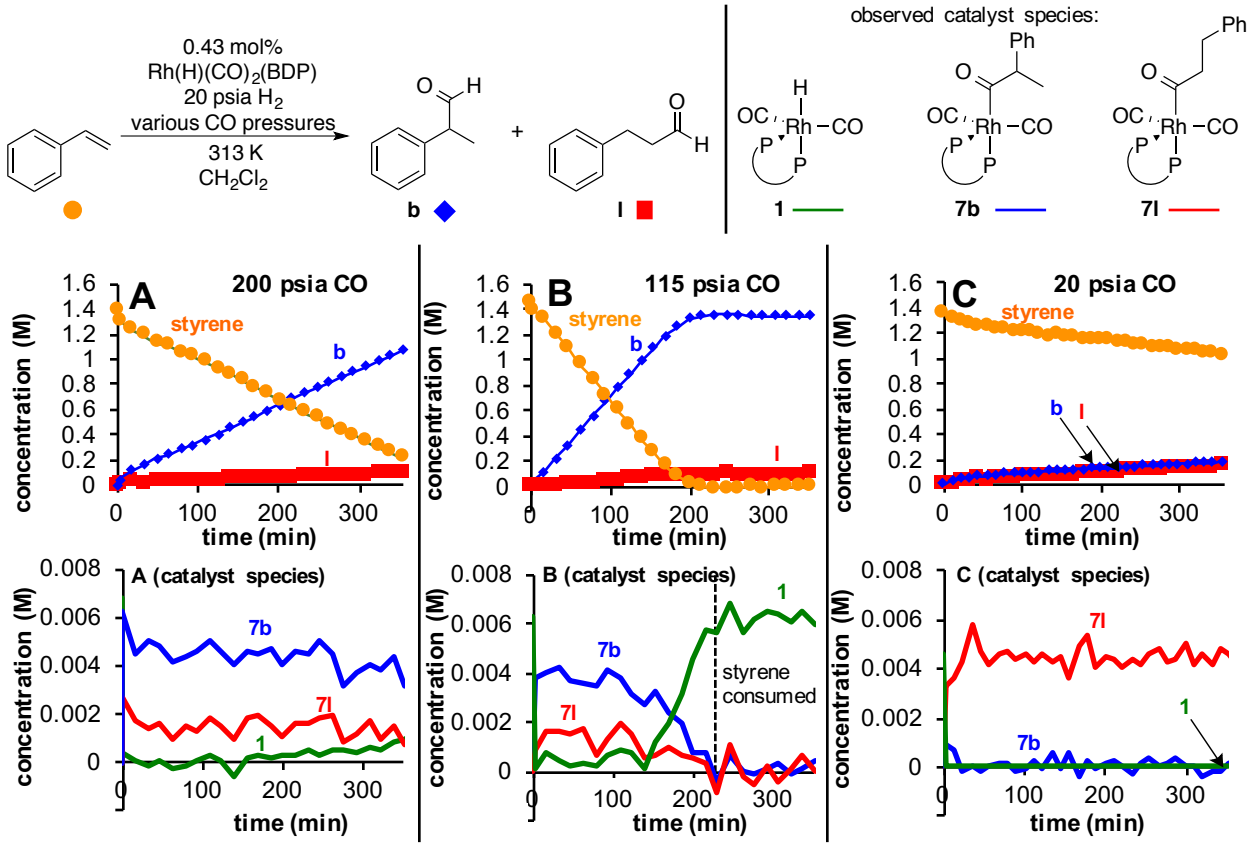

Figure 2-10. Time course data for catalytic hydroformylation reactions collected using the WiHP-NMRR. For each set of conditions: disappearance of styrene, appearance of product (top) and catalyst speciation (bottom) are presented. (1.4 M styrene, 6 mM $Rh(H)(CO)_2$(tetraphenyl-BDP) (1), 313 K, 20 psia H_2, varied CO pressures: 20 psia CO (A), 115 psia CO (B), 200 psia CO (C)).

The observed mismatch in selectivity between the catalyst resting state (**7b**:**7l**) versus aldehyde products (**b**:**l**) was less expected. For example, at low CO pressure (20 psia CO, Figure 2-10C) in the steady-state regime, the catalyst was observed as a <1:10 **7b**:**7l** ratio, but the products appeared in a 1:1 ratio. One potential explanation for these results is that the branched acyl dicarbonyl (**7b**) undergoes faster CO dissociation and/or reaction with H_2 than the linear isomer (**7l**), which requires hydrogenolysis to be the turnover-limiting step. This analysis is

complicated by the fact that **7** is an off-cycle species and, therefore, the more important intermediate is the sixteen electron acyl monocarbonyl, **6**, which can react with H_2. Therefore, we also considered the possibility that the catalyst does not necessarily form **7** at every turnover and thus there is both a 'shunted' and 'direct' pathway for product formation.

2.3.4.2 Non-catalytic Hydrogenolysis Experiments (NCH)

By performing non-catalytic experiments, we were able to directly measure the kinetics of hydrogenolysis of the acyl dicarbonyl species. These complexes were formed in the WiHP-NMRR in the absence on H_2 and then exposed to reaction conditions; the disappearance of **7b** and **7l** as well as the corresponding product formation (**b** and **l**) was monitored (Figure 2-11).[92]

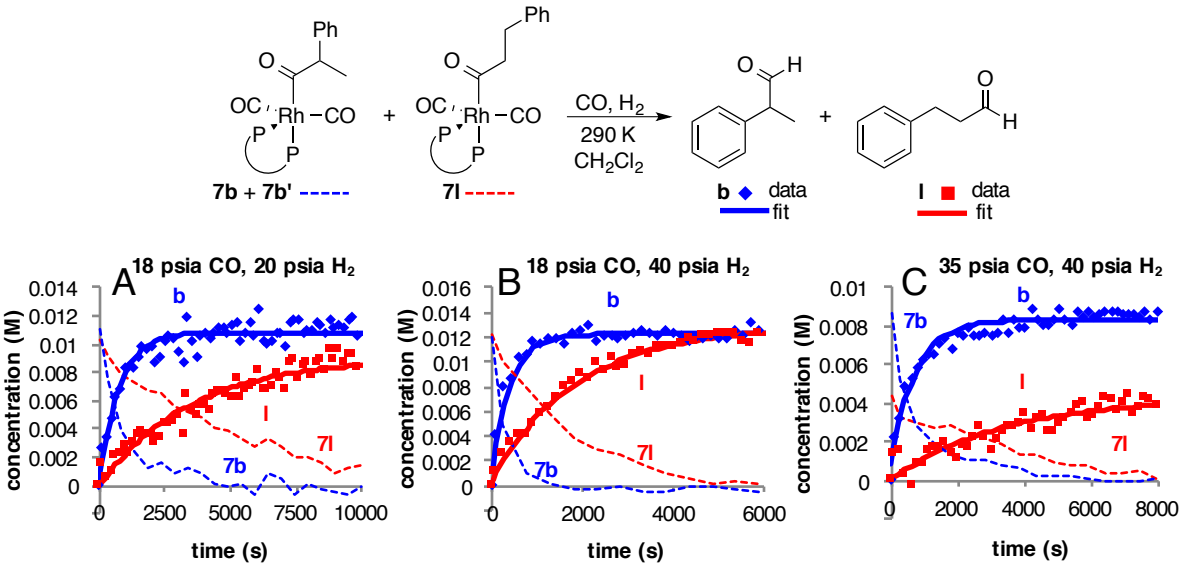

Figure 2-11. Non-catalytic hydrogenolysis experiments in the WiHP-NMRR. (~22 mM Rh(acyl)(tetraphenyl-BDP) as 1:1 mixture, 290 K, varied CO and H_2 pressures: 18 psia CO, 20 psia H_2 (A), 18 psia CO, 40 psia H_2 (B), 35 psia CO, 40 psia H_2 (C)).

Previously, we referred to these experiments as "single turnover" studies,[92] but in this Chapter we use the term non-catalytic hydrogenolysis experiments (NCH) so as to avoid

confusion with the enzymological use of the term. In the enzymology literature, single turnover experiments refer to the reaction of a substrate with excess enzyme under normal reaction conditions which allows for formation of product without reaching a steady state.[93] In this work, although we combined **1** with less than one equivalent of styrene, we formed **7b** and **7l** in the absence of H_2 under one set of conditions, then changed the conditions and reacted the off-cycle species with dihydrogen.

Kinetic modeling of NCH data yields empirical rate constants for the hydrogenolysis of both the branched and linear acyl dicarbonyls (**7**). By comparing these values with data under catalytic conditions at the same temperature, we determined that the rate of catalytic product formation was *faster* than hydrogenolysis of the acyl dicarbonyls (**7**). Thus, it is inaccurate to characterize the catalytic reaction rate as limited by hydrogenolysis of the catalyst resting state. Under NCH conditions, the acyl monocarbonyls (**6**), which react with H_2, form *only* by dissociation of CO from the dicarbonyl, **7**. Under catalytic conditions, **6** can form directly from the preceding alkyl species (**4**) as well. Accordingly, there are different steady-state concentrations of key intermediates under the different types of reactions (eq 2-1–2-4).

$$[\mathbf{6}]_{SS,\ single\ turnover} = \frac{k_{7\rightarrow 6}[\mathbf{7}]}{k_{6\rightarrow product}[H_2]+k_{6\rightarrow 7}[CO]} \qquad (2\text{-}1)$$

$$[\mathbf{6}]_{SS,\ catalytic} = \frac{k_{7\rightarrow 6}[\mathbf{7}]+k_{4\rightarrow 6}[\mathbf{4}][CO]}{k_{6\rightarrow product}[H_2]+k_{6\rightarrow 7}[CO]} \qquad (2\text{-}2)$$

$$\frac{d[product]}{dt}\ (single\ turnover) = \frac{k_{6\rightarrow product}k_{7\rightarrow 6}[\mathbf{7b}][H_2]}{k_{6\rightarrow product}[H_2]+k_{6\rightarrow 7}[CO]} \qquad (2\text{-}3)$$

$$\frac{d[product]}{dt}\ (catalytic) = \frac{(k_{7\rightarrow 6}[\mathbf{7b}]+k_{4\rightarrow 6}[\mathbf{4}][CO])k_{6\rightarrow product}[H_2]}{k_{6\rightarrow product}[H_2]+k_{6\rightarrow 7}[CO]} \qquad (2\text{-}4)$$

Another way to view this information is that not all catalyst is 'shunted' to the off-cycle resting state (**7**) during catalysis. In fact, the majority of the aldehyde product originates from

direct, on-cycle trapping of **6** by H_2, thus avoiding conversion to the off-cycle resting state **7**. For example, at 17 °C and 40 psia syn gas, we showed that 70% of the branched aldehyde and 55% of the linear product are formed from the direct, on-cycle pathway. Despite the fact that the only observable catalyst species lie off-cycle, there must be a small amount that remains on-cycle at any given time. Such on-cycle species are highly reactive, leading to the conclusion that what one observes is largely irrelevant to the productive mechanism; the analysis is a quantitative example of Halpern's rules.[94] This 'shunted' versus 'direct' interpretation helps to explain the mismatch between the catalyst resting state and aldehyde product distributions. Faster hydrogenolysis of the branched acyl dicarbonyl compared to the linear isomer does contribute to this discrepancy, but a significant factor is the faster formation of the branched alkyl complexes (**4** and **5**) and acyl monocarbonyl (**6**) relative to the linear species.

2.3.4.3 General Implications of 'Shunted' versus 'Direct' Reaction

The conclusions of this study may be general to other catalysts. However, dissection of the 'shunted' versus 'direct' pathways requires detailed information concerning catalyst speciation and direct measurement of the conversion of off-cycle species to products. Such information is rare.

2.3.5 Summarizing the Origins of Selectivity

Together, these studies paint a complex picture for the origins of regioselectivity in Rh(BDP) catalyzed hydroformylation. In this system, there are many transition state barriers that are similar in energy, causing the kinetics of many steps to be competitive; therefore we cannot choose a single step to be either turnover-limiting or selectivity-determining under common

conditions. As shown by both Watkins et. al.[83] and Tonks et al.,[89] under high CO pressures, the kinetic preference for the branched alkyl and acyl species (**4b** and **6b**, respectively) gives rise to high selectivity for the branched aldehyde because isomerization is slow. At lower CO pressures, not only is the kinetic preference for the branched pathway important, but so is the rate of isomerization to the linear pathway (containing **7l**, a thermodynamic sink). Finally, under all reaction conditions, the differing rates of hydrogenolysis from the branched and linear pathways play a role in determining the product selectivity because these rates affect the catalyst that is off-cycle.

2.4 Conclusions

Many of the attractive features of AHF are obvious, for example non-enantioselective hydroformylation is a proven commodity-scale process, two of the reactants are renewable gases that can be easily separated from the products, and the one-carbon homologation creates both a new stereogenic center and a versatile aldehyde functional group. While the practical application of AHF currently is not widespread, the developments and demonstrations summarized herein have improved prospects for more applications of AHF at both bench- and production-scale. Prominent examples include new ligand development, gas-less hydroformylation technologies, application of AHF in flow reactors, heterogenization of AHF catalysts, and broadened substrate scope.

How does AHF work? Elucidating the of origin of selectivity and rate control in complex catalytic systems facilitates problem-solving and satisfies the basic human urge to understand how nature works. Complexity is abundant in AHF; even a minimal mechanism requires three

isomeric catalytic cycles and more than a dozen catalyst-containing species. As summarized in this Chapter, the interception and characterization of key intermediates, application of operando NMR spectroscopy, kinetic analysis, and isotopic labelling techniques provide insights into the mechanism of AHF, along with strategies and principles that apply to catalytic reaction mechanisms in general.

2.5 References

(1) (a) Roelen, O. Process for the preparation of oxygen-containing compounds. German Patent DE 849548, 1938/1952. (b) Roelen, O. Production of oxygenated carbon compounds. U.S. Patent US 2327066, 1943.

(2) Agbossou, F.; Carpentier, J.-F.; Mortreux, A. Asymmetric Hydroformylation. *Chem. Rev.* **1995**, *95*, 2485–2506.

(3) van Leeuwen, P. W. N. M.; Claver, C. *Rhodium Catalyzed Hydroformylation*; Kluwer Academic Publishers: Dordrecht, The Netherlands 2000.

(4) Diéguez, M.; Pàmies, O.; Claver, C. Recent advances in Rh-catalyzed asymmetric hydroformylation using phosphite ligands. *Tetrahedron: Asymmetry* **2004**, *15*, 2113–2122.

(5) Wiese, K.-D.; Obst, D. In *Top. Organomet. Chem.*; Beller, M., Ed. 2006; Vol. 18, p 1–33.

(6) Franke, R.; Selent, D.; Börner, A. Applied Hydroformylation. *Chem. Rev.* **2012**, *112*, 5675–5732.

(7) Bohnen, H.-W.; Cornils, B. Hydroformylation of alkenes: An industrial view of the status and importance. *Advances in Catalysis* **2002**, *47*, 1–64.

(8) Botteghi, C.; Paganelli, S.; Schionato, A.; Marchetti, M. The asymmetric hydroformylation in the synthesis of pharmaceuticals. *Chirality* **1991**, *3*, 355–369.

(9) Wink, D. J.; Kwok, T. J.; Yee, A. Practical syntheses of chelating bis(dioxaphospholane) ligands through chlorodioxaphospholane intermediates and demonstration of catalytic competence of bis(phosphite)rhodium cation. *Inorg. Chem.* **1990**, *29*, 5006–5008.

(10) Gladiali, S.; Pinna, L. Asymmetric hydroformylation of N-acyl 1-aminoacrylic acid derivatives by rhodium/chiral diphosphine catalysts. *Tetrahedron: Asymmetry* **1991**, *2*, 623–632.

(11) Sakai, N.; Nozaki, K.; Mashima, K.; Takaya, H. Asymmetric hydroformylation of vinyl acetate by use of chiral bis(triarylphosphite)-rhodium(I) complexes. *Tetrahedron: Asymmetry* **1992**, *3*, 583–586.

(12) Babin, J. E.; Whiteker, G. T.. Asymmetric Syntheses. World Patent WO1993003839, 1993.

(13) Sakai, N.; Mano, S.; Nozaki, K.; Takaya, H. Highly enantioselective hydroformylation of olefins catalyzed by new phosphine phosphite-rhodium(I) complexes. *J. Am. Chem. Soc.* **1993**, *115*, 7033–7034.

(14) Sakai, N.; Nozaki, K.; Takaya, H. Asymmetric hydroformylation of 1,2-disubstituted olefins catalysed by chiral phosphinephosphite-rhodium(I) complexes. *J. Chem. Soc., Chem. Commun.* **1994**, 395–396.

(15) Nanno, T.; Sakai, N.; Nozaki, K.; Takaya, H. Asymmetric hydroformylations of sulfur-containing olefins catalyzed by BINAPHOS—Rh(I) complexes. *Tetrahedron: Asymmetry* **1995**, *6*, 2583–2591.

(16) Masdeu-Bultó, A. M.; Orejón, A.; Castellanos, A.; Castillón, S.; Claver, C. Asymmetric hydroformylation of styrene using a rhodium catalyst with BDPP as the chiral ligand. *Tetrahedron: Asymmetry* **1996**, *7*, 1829–1834.

(17) Horiuchi, T.; Ohta, T.; Shirakawa, E.; Nozaki, K.; Takaya, H. Asymmetric Hydroformylation of Heterocyclic Olefins Catalyzed by Chiral Phosphine−Phosphite−Rh(I) Complexes. *J. Org. Chem.* **1997**, *62*, 4285–4292.

(18) Nozaki, K.; Li, W.-g.; Horiuchi, T.; Takaya, H. Asymmetric hydroformylation of allylic alcohols catalyzed by Rh(I)-(R,S)-BINAPHOS. *Tetrahedron Lett.* **1997**, *38*, 4611–4614.

(19) Nozaki, K.; Sakai, N.; Nanno, T.; Higashijima, T.; Mano, S.; Horiuchi, T.; Takaya, H. Highly Enantioselective Hydroformylation of Olefins Catalyzed by Rhodium(I) Complexes of New Chiral Phosphine−Phosphite Ligands. *J. Am. Chem. Soc.* **1997**, *119*, 4413–4423.

(20) Breeden, S.; Cole-Hamilton, D. J.; Foster, D. F.; Schwarz, G. J.; Wills, M. Rhodium-Mediated Asymmetric Hydroformylation with a Novel Bis(diazaphospholidine) Ligand. *Angew. Chem. Int. Ed.* **2000**, *39*, 4106–4108.

(21) Cobley, C. J.; Gardner, K.; Klosin, J.; Praquin, C.; Hill, C.; Whiteker, G. T.; Zanotti-Gerosa, A.; Petersen, J. L.; Abboud, K. A. Synthesis and Application of a New Bisphosphite Ligand Collection for Asymmetric Hydroformylation of Allyl Cyanide. *The Journal of Organic Chemistry* **2004**, *69*, 4031–4040.

(22) Castillon, S.; Claver, C.; Diaz, Y. C 1 and C2-symmetric carbohydrate phosphorus ligands in asymmetric catalysis. *Chem. Soc. Rev.* **2005**, *34*, 702–713.

(23) Yan, Y.; Zhang, X. A Hybrid Phosphorus Ligand for Highly Enantioselective Asymmetric Hydroformylation. *J. Am. Chem. Soc.* **2006**, *128*, 7198–7202.

(24) Rubio, M.; Suárez, A.; Álvarez, E.; Bianchini, C.; Oberhauser, W.; Peruzzini, M.; Pizzano, A. Asymmetric Hydroformylation of Olefins with Rh Catalysts Modified with Chiral Phosphine−Phosphite Ligands. *Organometallics* **2007**, *26*, 6428–6436.

(25) Chikkali, S. H.; Bellini, R.; Berthon-Gelloz, G.; van der Vlugt, J. I.; de Bruin, B.; Reek, J. N. H. Highly enantioselective hydroformylation of dihydrofurans catalyzed by hybrid phosphine-phosphonite rhodium complexes. *Chem. Commun.* **2010**, *46*, 1244–1246.

(26) Gual, A.; Godard, C.; Castillón, S.; Claver, C. Highly Efficient Rhodium Catalysts for the Asymmetric Hydroformylation of Vinyl and Allyl Ethers using C1-Symmetrical Diphosphite Ligands. *Adv. Synth. Catal.* **2010**, *352*, 463–477.

(27) Robert, T.; Abiri, Z.; Wassenaar, J.; Sandee, A. J.; Romanski, S.; Neudörfl, J.-M.; Schmalz, H.-G.; Reek, J. N. H. Asymmetric Hydroformylation Using Taddol-Based Chiral Phosphine−Phosphite Ligands. *Organometallics* **2010**, *29*, 478–483.

(28) Wassenaar, J.; de Bruin, B.; Reek, J. N. H. Rhodium-Catalyzed Asymmetric Hydroformylation with Taddol-Based IndolPhos Ligands. *Organometallics* **2010**, *29*, 2767–2776.

(29) Zhang, X.; Cao, B.; Yan, Y.; Yu, S.; Ji, B.; Zhang, X. Synthesis and Application of Modular Phosphine–Phosphoramidite Ligands in Asymmetric Hydroformylation: Structure–Selectivity Relationship. *Chem. Eur. J.* **2010**, *16*, 871–877.

(30) Wang, X.; Buchwald, S. L. Rh-Catalyzed Asymmetric Hydroformylation of Functionalized 1,1-Disubstituted Olefins. *J. Am. Chem. Soc.* **2011**, *133*, 19080–19083.

(31) Chikkali, S. H.; Bellini, R.; de Bruin, B.; van der Vlugt, J. I.; Reek, J. N. H. Highly Selective Asymmetric Rh-Catalyzed Hydroformylation of Heterocyclic Olefins. *J. Am. Chem. Soc.* **2012**, *134*, 6607–6616.

(32) Clarke, M. 2012. Ligands for selective asymmetric hydroformylation, World Patent, WO2012016147, 2012.

(33) Noonan, G. M.; Fuentes, J. A.; Cobley, C. J.; Clarke, M. L. An Asymmetric Hydroformylation Catalyst that Delivers Branched Aldehydes from Alkyl Alkenes. *Angew. Chem. Int. Ed.* **2012**, *51*, 2477–2480.

(34) Fernández-Pérez, H.; Benet-Buchholz, J.; Vidal-Ferran, A. Enantiopure Narrow Bite-Angle P−OP Ligands: Synthesis and Catalytic Performance in Asymmetric Hydroformylations and Hydrogenations. *Chem. Eur. J.* **2014**, *20*, 15375–15384.

(35) Noonan, G. M.; Cobley, C. J.; Mahoney, T.; Clarke, M. L. Rhodium/phospholane-phosphite catalysts give unusually high regioselectivity in the enantioselective hydroformylation of vinyl arenes. *Chem. Commun.* **2014**, *50*, 1475–1477.

(36) Allmendinger, S.; Kinuta, H.; Breit, B. Easily Accessible TADDOL-Derived Bisphosphonite Ligands: Synthesis and Application in the Asymmetric Hydroformylation of Vinylarenes. *Adv. Synth. Catal.* **2015**, *357*, 41–45.

(37) Schmitz, C.; Holthusen, K.; Leitner, W.; Franciò, G. Highly Regio- and Enantioselective Hydroformylation of Vinyl Esters Using Bidentate Phosphine,P-Chiral Phosphorodiamidite Ligands. *ACS Catalysis* **2016**, *6*, 1584–1589.

(38) Ho, S.; Bucher, C.; Leighton, J. L. A highly step-economical synthesis of dictyostatin. *Angew. Chem. Int. Ed. Engl.* **2013**, *52*, 6757–6761.

(39) Lazzaroni, R.; Uccello-Barretta, G.; Benetti, M. Reversibility of metal-alkyl intermediate formation in the rhodium-catalyzed deuterioformylation of 1-hexene. *Organometallics* **1989**, *8*, 2323–2327.

(40) Raffaelli, A.; Pucci, S.; Settambolo, R.; Uccello-Barretta, G.; Lazzaroni, R. Inter- and intramolecular protium-deuterium exchange in the rhodium-catalyzed deuterioformylation of styrene. *Organometallics* **1991**, *10*, 3892–3898.

(41) Uccello-Barretta, G.; Lazzaroni, R.; Settambolo, R.; Salvadori, P. The use of 2H NMR in the elucidation of the catalytic pathway of the hydroformylation reaction. *J. Organomet. Chem.* **1991**, *417*, 111–119.

(42) Casey, C. P.; Petrovich, L. M. (Chelating diphosphine)rhodium-Catalyzed Deuterioformylation of 1-Hexene: Control of Regiochemistry by the Kinetic Ratio of Alkylrhodium Species Formed by Hydride Addition to Complexed Alkene. *J. Am. Chem. Soc.* **1995**, *117*, 6007–6014.

(43) Lazzaroni, R.; Settambolo, R.; Uccello-Barretta, G. .beta.-Hydride Elimination and Regioselectivity in the Rhodium-Catalyzed Hydroformylation of Open Chain Unsaturated Ethers. *Organometallics* **1995**, *14*, 4644–4650.

(44) Lazzaroni, R.; Uccello-Barretta, G.; Scamuzzi, S.; Settambolo, R.; Caiazzo, A. 2H NMR Investigation of the Rhodium-Catalyzed Deuterioformylation of 1,1-Diphenylethene: Evidence for the Formation of a Tertiary Alkyl−Metal Intermediate. *Organometallics* **1996**, *15*, 4657–4659.

(45) Lazzaroni, R.; Settambolo, R.; Uccello-Barretta, G.; Caiazzo, A.; Scamuzzi, S. Rhodium-catalyzed hydroformylation of vinylidenic olefins: the different behaviors of the isomeric alkyl–metal intermediates as the origin of the β-regioselectivity. *J. Mol. Catal. A: Chem.* **1999**, *143*, 123–130.

(46) van der Slot, S. C.; Duran, J.; Luten, J.; Kamer, P. C. J.; van Leeuwen, P. W. N. M. Rhodium-Catalyzed Hydroformylation and Deuterioformylation with Pyrrolyl-Based

Phosphorus Amidite Ligands: Influence of Electronic Ligand Properties. *Organometallics* **2002**, *21*, 3873–3883.

(47) Feng, J.; Garland, M. Unmodified Homogeneous Rhodium-Catalyzed Hydroformylation of Styrene. The Detailed Kinetics of the Regioselective Synthesis. *Organometallics* **1999**, *18*, 417–427.

(48) Aghmiz, A.; Orejón, A.; Diéguez, M.; Miquel-Serrano, M. D.; Claver, C.; Masdeu-Bultó, A. M.; Sinou, D.; Laurenczy, G. Rhodium-sulfonated diphosphine catalysts in aqueous hydroformylation of vinyl arenes: high-pressure NMR and IR studies. *J. Mol. Catal. A: Chem.* **2003**, *195*, 113–124.

(49) Silva, S. M.; Bronger, R. P. J.; Freixa, Z.; Dupont, J.; van Leeuwen, P. W. N. M. High pressure infrared and nuclear magnetic resonance studies of the rhodium-sulfoxantphos catalysed hydroformylation of 1-octene in ionic liquids. *New J. Chem.* **2003**, *27*, 1294.

(50) Damoense, L.; Datt, M.; Green, M.; Steenkamp, C. Recent advances in high-pressure infrared and NMR techniques for the determination of catalytically active species in rhodium- and cobalt-catalysed hydroformylation reactions. *Coord. Chem. Rev.* **2004**, *248*, 2393–2407.

(51) Bianchini, C.; Oberhauser, W.; Orlandini, A.; Giannelli, C.; Frediani, P. Operando High-Pressure NMR and IR Study of the Hydroformylation of 1-Hexene by 1,1'-Bis(Diarylphosphino)metallocene-Modified Rhodium(I) Catalysts. *Organometallics* **2005**, *24*, 3692–3702.

(52) Kubis, C.; Ludwig, R.; Sawall, M.; Neymeyr, K.; Börner, A.; Wiese, K.-D.; Hess, D.; Franke, R.; Selent, D. A Comparative In Situ HP-FTIR Spectroscopic Study of Bi- and Monodentate Phosphite-Modified Hydroformylation. *ChemCatChem* **2010**, *2*, 287–295.

(53) Bellini, R.; Reek, J. N. Application of supramolecular bidentate hybrid ligands in asymmetric hydroformylation. *Chem. Eur. J.* **2012**, *18*, 13510–13519.

(54) Kubis, C.; Selent, D.; Sawall, M.; Ludwig, R.; Neymeyr, K.; Baumann, W.; Franke, R.; Borner, A. Exploring between the extremes: conversion-dependent kinetics of phosphite-modified hydroformylation catalysis. *Chem. Eur. J.* **2012**, *18*, 8780–8794.

(55) Güven, S.; Nieuwenhuizen, M. M. L.; Hamers, B.; Franke, R.; Priske, M.; Becker, M.; Vogt, D. Kinetic Explanation for the Temperature Dependence of the Regioselectivity in the Hydroformylation of Neohexene. *ChemCatChem* **2014**, *6*, 603–610.

(56) Lazzaroni, R.; Bertozzi, S.; Pocai, P.; Troiani, F.; Salvadori, P. Factors affecting the regioselectivity in the rhodium-catalysed hydroformylation of vinyl ethers. *J. Organomet. Chem.* **1985**, *295*, 371–376.

(57) Settambolo, R.; Pucci, S.; Bertozzi, S.; Lazzaroni, R. Remarkable α-regioselectivity in the rhodium-catalyzed hydroformylation of 2-vinylpyridine. *J. Organomet. Chem.* **1995**, *489*, C50–C51.

(58) Botteghi, C.; Marchetti, M.; Paganelli, S.; Sechi, B. Study on the regioselectivity in the rhodium-catalyzed hydroformylation of vinyl-pyridine derivatives. *J. Mol. Catal. A: Chem.* **1997**, *118*, 173–179.

(59) Nozaki, K.; Takaya, H.; Hiyama, T. Enantioselective hydroformylation of olefins catalyzed by rhodium(I) complexes of chiral phosphine–phosphite ligands. *Top. Catal.* **1997**, *4*, 175.

(60) Yu, Z.; Eno, M. S.; Annis, A. H.; Morken, J. P. Enantioselective Hydroformylation of 1-Alkenes with Commercial Ph-BPE Ligand. *Org. Lett.* **2015**, *17*, 3264–3267.

(61) Nelsen, E.R. Ph.D. Thesis, University of Wisconsin, Madison, WI, 2014.

(62) Grunanger, C. U.; Breit, B. Branched-regioselective hydroformylation with catalytic amounts of a reversibly bound directing group. *Angew. Chem. Int. Ed.* **2008**, *47*, 7346–7349.

(63) Lightburn, T. E.; Dombrowski, M. T.; Tan, K. L. Catalytic Scaffolding Ligands: An Efficient Strategy for Directing Reactions. *J. Am. Chem. Soc.* **2008**, *130*, 9210–9211.

(64) Grunanger, C. U.; Breit, B. Remote control of regio- and diastereoselectivity in the hydroformylation of bishomoallylic alcohols with catalytic amounts of a reversibly bound directing group. *Angew. Chem. Int. Ed.* **2010**, *49*, 967–970.

(65) Worthy, A. D.; Joe, C. L.; Lightburn, T. E.; Tan, K. L. Application of a Chiral Scaffolding Ligand in Catalytic Enantioselective Hydroformylation. *J. Am. Chem. Soc.* **2010**, *132*, 14757–14759.

(66) Usui, I.; Nomura, K.; Breit, B. Diastereoselective Hydroformylation of 2,5-Cyclohexadienyl-1-carbinols with Catalytic Amounts of a Reversibly Bound Directing Group. *Org. Lett.* **2011**, *13*, 612–615.

(67) Joe, C. L.; Blaisdell, T. P.; Geoghan, A. F.; Tan, K. L. Distal-selective hydroformylation using scaffolding catalysis. *J. Am. Chem. Soc.* **2014**, *136*, 8556–8559.

(68) Joe, C. L.; Tan, K. L. Enantioselective hydroformylation of aniline derivatives. *J. Org. Chem.* **2011**, *76*, 7590–7596.

(69) Watkins, A. L.; Hashiguchi, B. G.; Landis, C. R. Highly Enantioselective Hydroformylation of Aryl Alkenes with Diazaphospholane Ligands. *Org. Lett.* **2008**, *10*, 4553–4556.

(70) McDonald, R. I.; Wong, G. W.; Neupane, R. P.; Stahl, S. S.; Landis, C. R. Enantioselective Hydroformylation of N-Vinyl Carboxamides, Allyl Carbamates, and Allyl Ethers Using Chiral Diazaphospholane Ligands. *J. Am. Chem. Soc.* **2010**, *132*, 14027–14029.

(71) Abrams, M. L.; Foarta, F.; Landis, C. R. Asymmetric Hydroformylation of Z-Enamides and Enol Esters with Rhodium-Bisdiazaphos Catalysts. *J. Am. Chem. Soc.* **2014**, *136*, 14583–14588.

(72) Deng, Y.; Wang, H.; Sun, Y.; Wang, X. Principles and Applications of Enantioselective Hydroformylation of Terminal Disubstituted Alkenes. *ACS Catalysis* **2015**, *5*, 6828–6837.

(73) Gladiali, S.; Pinna, L. Completely regioselective hydroformylation of methyl n-acetamidoacrylate by chiral rhodium phosphine catalysts. *Tetrahedron: Asymmetry* **1990**, *1*, 693–696.

(74) Basoli, C.; Botteghi, C.; Cabras, M. A.; Chelucci, G.; Marchetti, M. Hydroformylation of some functionalized olefins catalyzed by rhodium(I) complexes with pydiphos and its P-oxide. *J. Organomet. Chem.* **1995**, *488*, C20–C22.

(75) Lee, C. W.; Alper, H. Influence of 1,4-Bis(diphenylphosphino)butane on the Hydroformylation of α,β-Unsaturated Esters Catalyzed by Zwitterionic, Cationic, and Neutral Rhodium(I) Complexes. The Asymmetric Hydroformylation of .alpha.-Methylene-.gamma.-Butyrolactone. *J. Org. Chem.* **1995**, *60*, 499–503.

(76) Wang, X.; Buchwald, S. L. Synthesis of optically pure 2-trifluoromethyl lactic acid by asymmetric hydroformylation. *J. Org. Chem.* **2013**, *78*, 3429–3433.

(77) Floriana Foarta, PhD Dissertation, University of Wisconsin–Madison, 2017.

(78) Klosin, J.; Landis, C. R. Ligands for Practical Rhodium-Catalyzed Asymmetric Hydroformylation. *Acc. Chem. Res.* **2007**, *40*, 1251–1259.

(79) Jones, B. R.; Abrams, M. L.; Landis, C. R.; May, S. A.; Campbell, A. N.; Martinelli, J. R.; Calvin, J. R. Scalable Synthesis of Enantiopure Bis-3,4-diazaphospholane Ligands for Asymmetric Catalysis. *J. Org. Chem.* **2016**, *81*, 11965–11970.

(80) Adint, T. T.; Landis, C. R. Immobilized bisdiazaphospholane catalysts for asymmetric hydroformylation. *J. Am. Chem. Soc.* **2014**, *136*, 7943–7953.

(81) Abrams, M. L.; Buser, J. Y.; Calvin, J. R.; Johnson, M. D.; Jones, B. R.; Lambertus, G.; Landis, C. R.; Martinelli, J. R.; May, S. A.; McFarland, A. D.; Stout, J. R. Continuous Liquid Vapor Reactions Part 2: Asymmetric Hydroformylation with Rhodium-Bisdiazaphos Catalysts in a Vertical Pipes-in-Series Reactor. *Org. Process Res. Dev.* **2016**, *20*, 901–910.

(82) Johnson, M. D.; May, S. A.; Calvin, J. R.; Lambertus, G. R.; Kokitkar, P. B.; Landis, C. R.; Jones, B. R.; Abrams, M. L.; Stout, J. R. Continuous Liquid Vapor Reactions Part 1: Design and Characterization of a Reactor for Asymmetric Hydroformylation. *Org. Process Res. Dev.* **2016**, *20*, 888–900.

(83) Watkins, A. L.; Landis, C. R. Origin of Pressure Effects on Regioselectivity and Enantioselectivity in the Rhodium-Catalyzed Hydroformylation of Styrene with (S,S,S)-BisDiazaphos. *J. Am. Chem. Soc.* **2010**, *132*, 10306–10317.

(84) Kasinathan, S.; Bourne, S.; Tolstoy, P.; Koos, P.; O'Brien, M.; Bates, R.; Baxendale, I.; Ley, S. Syngas-Mediated C-C Bond Formation in Flow: Selective Rhodium-Catalysed Hydroformylation of Styrenes. *Synlett* **2011**, *2011*, 2648–2651.

(85) Fuentes, J. A.; Pittaway, R.; Clarke, M. L. Rapid Asymmetric Transfer Hydroformylation (ATHF) of Disubstituted Alkenes Using Paraformaldehyde as a Syngas Surrogate. *Chem. Eur. J.* **2015**, *21*, 10645–10649.

(86) Morimoto, T.; Fujii, T.; Miyoshi, K.; Makado, G.; Tanimoto, H.; Nishiyama, Y.; Kakiuchi, K. Accessible protocol for asymmetric hydroformylation of vinylarenes using formaldehyde. *Org. Biomol. Chem.* **2015**, *13*, 4632–4636.

(87) Heck, R. F.; Breslow, D. S. The Reaction of Cobalt Hydrotetracarbonyl with Olefins. *J. Am. Chem. Soc.* **1961**, *83*, 4023–4027.

(88) Horiuchi, T.; Shirakawa, E.; Nozaki, K.; Takaya, H. Mechanistic Aspects of Asymmetric Hydroformylation of Olefins Catalyzed by Chiral Phosphine−Phosphite−Rhodium(I) Complexes. *Organometallics* **1997**, *16*, 2981–2986.

(89) Tonks, I. A.; Froese, R. D.; Landis, C. R. Very Low Pressure Rh-Catalyzed Hydroformylation of Styrene with (S,S,S-Bisdiazaphos): Regioselectivity Inversion and Mechanistic Insights. *ACS Catalysis* **2013**, *3*, 2905–2909.

(90) Nelsen, E. R.; Landis, C. R. Interception and Characterization of Alkyl and Acyl Complexes in Rhodium-Catalyzed Hydroformylation of Styrene. *J. Am. Chem. Soc.* **2013**, *135*, 9636–9639.

(91) Beach, N. J.; Knapp, S. M. M.; Landis, C. R. A reactor for high-throughput high-pressure nuclear magnetic resonance spectroscopy. *Rev. Sci. Instrum.* **2015**, *86*, 104101–104109.

(92) Brezny, A. C.; Landis, C. R. Unexpected CO Dependencies, Catalyst Speciation, and Single Turnover Hydrogenolysis Studies of Hydroformylation via High Pressure NMR Spectroscopy. *J. Am. Chem. Soc.* **2017**, *139*, 2778–2785.

(93) Johnson, K. A. 1 Transient-State Kinetic Analysis of Enzyme Reaction Pathways. *The Enzymes* **1992**, *20*, 1–61.

(94) Halpern's rule or guidlines were first discussed in relation to studies of Wilkinson's catalyst in which the observable species are off-cycle intermediates. For examples, see (a) Du, G.; Fanwick, P. E.; Abu-Omar, M. M. *J. Am. Chem. Soc*. **2007**, *129*, 5180-5187. (b) Yang, X.; Stern, C.; Marks, T. J. *J. Am. Chem. Soc.* **1994**, *116*, 10015. (c) Landis, C. R.; Rosaaen, K. A.; Kimberly, A.; Sillars, D. R. *J. Am. Chem. Soc*. **2003**, *125*, 1710. (d) Sillars, D. R.; Landis, C. R. *J. Am. Chem. Soc*. **2003**, *125*, 9894. (e) Maughon, B. R.; Grubbs, R. H. *Macromolecules* **1997**, *30*, 3459. (f) Dias, E. L.; Nguyen, S. T.; Grubbs, R. H. *J. Am. Chem. Soc*. **1997**, *119*, 3887. (g) Wu, Z.; Benedicto, A. D.; Grubbs, R. H. *Macromolecules* **1993**, *26*, 4975. (h) Tallarico, J. A.; Bonitatebus, P. J., Jr.; Snapper, M. L. *J. Am. Chem. Soc*. **1997**, *119*, 7157.

Chapter 3

Interception and Characterization of Catalyst Species in Rhodium Bis(diazaphospholane)-Catalyzed Hydroformylation of Octene, Vinyl Acetate, Allyl Cyanide, and 1-Phenyl-1,3-butadiene

Portions of this work were published as Nelsen, E. R.;‡ Brezny, A. C.;‡ Landis, C. R. Interception and Characterization of Catalyst Species in Rhodium Bis(diazaphospholane)-Catalyzed Hydroformylation of Octene, Vinyl Acetate, Allyl Cyanide, and 1-Phenyl-1,3-butadiene. *J. Am. Chem. Soc.* **2015**, *137*, 14208-14219.

‡Denotes co-authors with equal contribution

Eleanor R. Nelsen characterized intermediates for vinyl acetate, allyl cyanide, and octene. Anna C. Brezny performed catalytic reactions at 0 °C, carried out control experiments with [Rh(OAc)(BDP)] and acetyl acetone, characterized intermediates for 1-phenyl-1,3-butadiene, and performed high pressure NMR spectroscopy studies.

3.1 Introduction

Since its discovery more than seventy five years ago, the hydroformylation of alkenes has become one of the largest-scale applications of homogeneous catalysis in industry.[1-4] Rhodium complexes modified with phosphorus-based ligands yield highly active and selective catalysts, facilitating the production of millions of tons per year of aldehydes – predominantly the linear product, a versatile feedstock for the production of other commodity chemicals.

The comparatively underdeveloped asymmetric reaction shows promise for enantiopure chemical production, because chiral aldehydes are attractive precursors for pharmaceutical and other fine-chemical products.[5] The 3,4-bis(diazaphospholane) (BDP) class of ligands introduced in 2004 combine high activity – greater than one turnover per second – and useful selectivities for the enantioselective hydroformylation of various alkene substrates (Figure 3-1).[6-11]

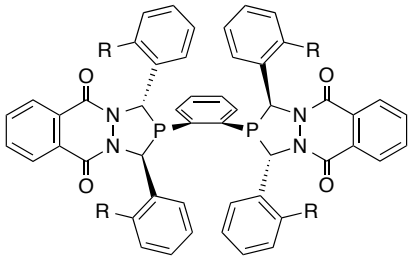

Figure 3-1. Structure of (*S*,*S*)-3,4-bis(diazaphospholane) (BDP). This work uses racemic BDP with R = H.

The general mechanism for hydroformylation was proposed by Breslow and Heck for cobalt-catalyzed hydroformylation over fifty years ago (Scheme 3-1), and remains accepted today.[12] Our ultimate goal is to understand how the kinetic and thermodynamic selectivities of the individual steps of this mechanism influence the net regio- and enantioselectivity of AHF and their response to reaction conditions.

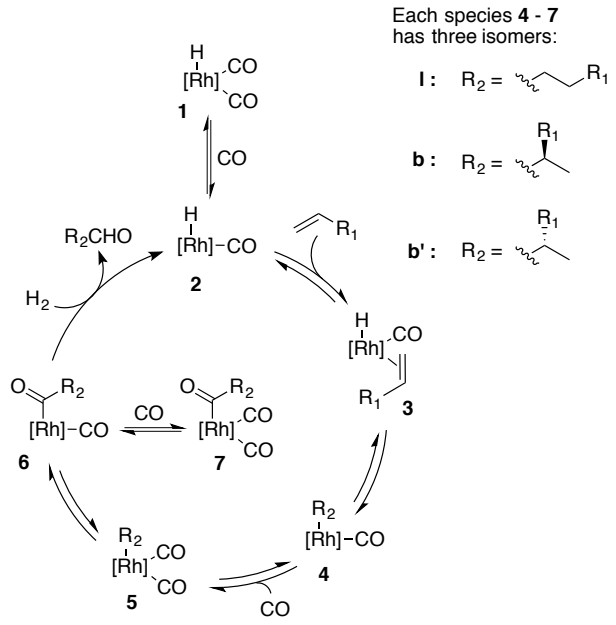

Scheme 3-1. General mechanism for hydroformylation.

One empirical approach to elucidating the origins of selectivity in a catalytic reaction involves the detailed characterization of rate laws for the formation of all products over a wide variety of reaction conditions. Using these data, the mechanistic step (or collections of steps) that control(s) selectivity may be inferred; we call this an outside-in approach. The level of detail of the mechanistic inference depends on the complexity of the observed rate laws, with more complex rate laws providing greater intrinsic information. Additional information may be extracted by using isotopic labels and measuring their distributions in different products as a function of reaction conditions. Many such studies have been performed for non-enantioselective hydroformylation reactions with mono- or bidentate phosphorus ligands.[13-27] For the AHF of styrene with Rh(BDP) catalysts, we have reported empirical rate laws over a wide variety of reaction pressures.[28-29]

The other empirical extreme for elucidation of detailed catalytic mechanisms involves isolating and characterizing key intermediates and examining their kinetic and thermodynamic

properties. If enough of these intermediates and their properties can be studied, the origins of selectivity can be deduced. This may be called an inside-out approach because understanding of what comes out of a catalytic cycle is revealed by direct observation of what lies inside the cycle. Few studies report direct characterization of the intermediates in useful hydroformylation reactions. Brown and Kent's pioneering NMR studies of the reaction of styrene with $[Rh(H)(CO)(PPh_3)_3]$ (the catalyst precursor and resting state) revealed formation of branched and linear acyls of the formula $Rh(acyl)(PPh_3)_2(CO)_2$, with the branched acyl formed first and followed by equilibration to the more stable linear acyl.[30-31] Since that time, however, there have been few cases in which catalyst species are directly observed[32] and most of these have been limited to slow and/or unselective catalysts[24] or analogous iridium complexes.[33-35] Previously, we examined the reaction of $[RhH(BDP)(CO)_2]$ with styrene in the absence of H_2 and reported the first interception of linear and branched rhodium alkyl, as well as acyl, intermediates in AHF (Figure 3-2).[36] These intermediates were characterized by multinuclear NMR spectroscopy, their relative thermodynamic stabilities were estimated, and we demonstrated that the thermodynamic preference for linear vs. branched isomers inverts upon conversion of the rhodium alkyls to the rhodium acyls.

The most complete understanding of the origins of selectivity in a catalytic reaction comes from a combination of outside-in and inside-out approaches. For example, direct observation of catalyst resting state by *operando* spectroscopic methods provides an invaluable check on the interpretation of empirical rate laws (see Chapter 4).

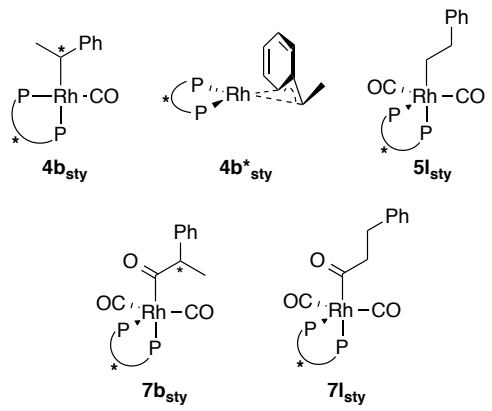

Figure 3-2. Alkyl and acyl rhodium bis(diazaphospholane) complexes identified following the reaction of **1** with styrene.

This Chapter comprises two major sections. Following a brief presentation of some benchmarking catalytic results, the first section reports the interception and NMR characterization of catalytic intermediates that include common substrates for AHF: vinyl acetate, allyl cyanide, 1-octene, and *trans*-1-phenyl-1,3-butadiene. Such data provide an essential foundation for more in-depth analysis of kinetic and thermodynamic selectivity in AHF. The conditions of these experiments, low temperature and inconstant CO solution concentration, enable characterization of species such as Rh-alkyls and Rh-acyl monocarbonyls that are not generally accessible. However, these conditions are very different from those of actual catalysis. The second major section of this work applies high pressure NMR techniques to probe (1) the equilibration of Rh-allyls and acyl dicarbonyl intermediates for the hydroformylation of *trans*-1-phenyl-1,3-butadiene and (2) the interplay of kinetic and thermodynamic selectivity for the formation of linear and branched acyl intermediates, and their subsequent hydrogenolyses.

3.2 Results and Discussion

3.2.1 Catalytic Results

The alkenes chosen for this study are all monosubstituted but span a modest range of substituent electronic effects, from sigma electron-withdrawing (vinyl acetate) to electron-donating (1-octene). Styrene, vinyl acetate, and allyl cyanide appear intrinsically selective for the branched product under common reaction conditions. For the tetraphenyl BDP catalyst (Figure 3-1, R = H), the catalytic selectivities are reported under standard (150 psi CO/H_2, 75 °C) and low temperature conditions (30 psi CO/H_2, 0 °C) (Table 3-1). Catalytic reactions at low temperatures and pressures (relevant to this work), give higher selectivity towards the branched products than reactions under more common conditions (Table 3-1). Dienes such as 1-phenyl-1,3-butadiene are selective for the branched 3-formyl-1-phenyl-1-butene product.[11] A π-allyl complex (analogous to **4b*$_{sty}$**) was proposed as an intermediate in this mechanism.

substrate	150 psi CO/H_2, 75 °C	30 psi CO/H_2, 0 °C
vinyl acetate	b:l = 13.1:1[a]	b:l = 49:1[c]
allyl cyanide	b:l = 4.9:1[a]	b:l = 12:1[c]
phenyl-butadiene	60% 3-formyl product[b,c]	only 3-formyl product obsd[c]
1-octene	b:l = 0.66:1[a]	b:l = 0.92:1[c]

[a]Jerzy Klosin, Dow Chemical Company, 2004. [b]Other products correspond to the double-bond isomers of primary product. [c]Based on 1H NMR spectroscopy.

Table 3-1. Selectivities for catalytic AHF under two different sets of conditions for four substrates with the tetraphenyl BDP catalyst.

Simple alkenes such as 1-octene commonly favor the linear product. For example, 1-octene hydroformylation with the tetraphenyl BDP catalyst under the same conditions cited above yields b : l = 0.66.[37] Common rationalizations for regioselectivity in AHF invoke a general steric preference for the linear aldehyde that can be overridden by electronic factors. Thus, the

high branched selectivity for electron-deficient olefins results from stabilization of branched alkyl complexes **4** by the electron-withdrawing substituents. In these species, the methine carbon, metal center, and trans phosphorus atom comprise a three-center, four-electron bond in which the phosphorus atom donates electron density onto the alkyl carbon. For substrates such as styrene, the electron withdrawing group mitigates charge buildup on that carbon, stabilizing the branched alkyl species. The alkyl chain of 1-octene has the opposite effect, destabilizing $\mathbf{4b_{oct}}$ relative to $\mathbf{4l_{oct}}$ and reinforcing the steric preference for linear insertion.

3.2.2 Noncatalytic Experiments

3.2.2.1 Experiment Description

Noncatalytic experiments in the absence of dihydrogen under low temperature and pressure conditions (-20 to 0 °C, 15 psia CO) proceed from [RhH(BDP)$(CO)_2$] to the acyl dicarbonyls (**7**) but cannot go on to aldehyde products. With only passive mixing (i.e., unstirred or diffusive), in these experiments the total dissolved CO concentration is not known and changes significantly during the reaction. Reactions performed with active gas-liquid mixing (using WiHP-NMRR, *vide infra*) will be referred to as actively mixed. There are advantages and disadvantages of experiments run under low temperature, passively mixed conditions. First the low temperature and absence of H_2 enable direct observation of various acyl and, in some cases, alkyl isomers at convenient time scales.[38] These intermediates persist under these conditions sufficiently long for detailed characterization. However, it is not clear how the kinetic and thermodynamic selectivities obtained at low pressure and temperature with passive mixing relate to catalytic conditions.

Preliminary experiments for the reaction of RhH(BDP)$(CO)_2$ and alkene at –10 °C and 15 psi CO revealed different apparent half-lives for the four substrates: ca. 2 min (1-octene), 4 min (allyl cyanide), 18 min (vinyl acetate), and 30 min (*trans*-1-phenyl-1,3-butadiene) (Figure 3-3). Because the rates vary so much, detailed analysis of thermodynamic and kinetic selectivity required different temperatures for different substrates. In all reactions, greater than 90% mass balance was observed as demonstrated in Figures A-1–A-4 in Appendix A.

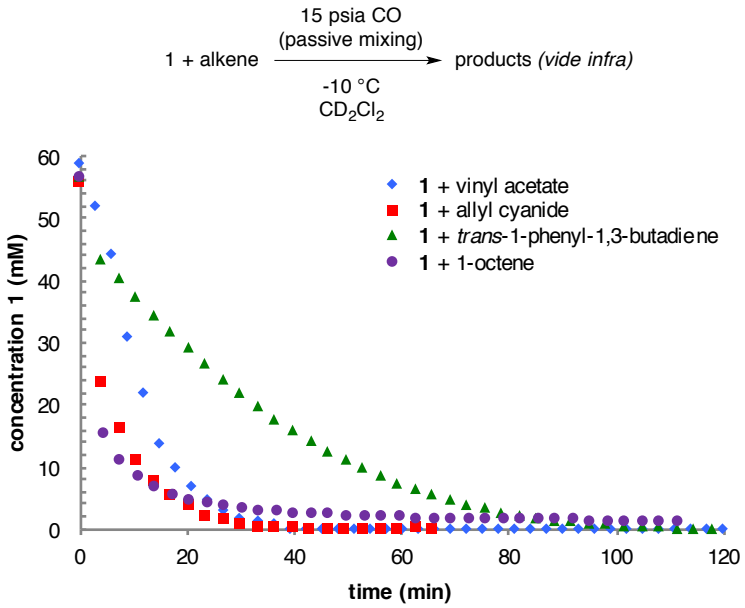

Figure 3-3. Disappearance of Rh(H)(CO)2(BDP) (**1**) with different substrates (–10 °C, 15 psia CO, 60 mM **1**, 240 mM alkene).

3.2.2.2 Vinyl Acetate

The reaction of vinyl acetate with rhodium hydride **1** at –10 °C under a CO atmosphere can be monitored easily by ^{1}H and ^{31}P NMR spectroscopy. As seen with styrene, **1** disappears over the course of 30 minutes to yield five-coordinate acyl dicarbonyl species (Figure 3-4). The qualitative half-life of the disappearance of **1** is approximately 10 minutes. However, exact rates and kinetics are not perfectly reproducible due to the variable and unknown concentration of

dissolved CO in a passively mixed standard NMR tube during reactions in which CO is consumed.

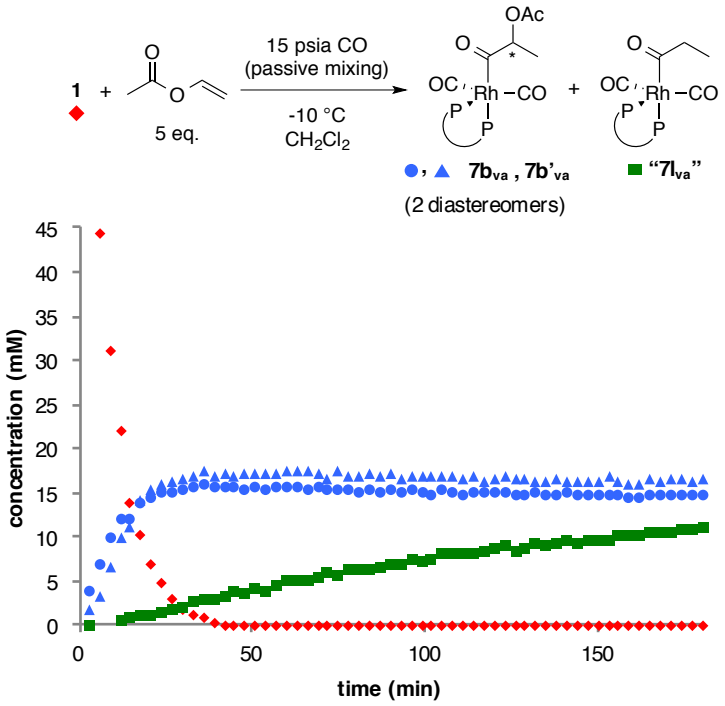

Figure 3-4. Catalyst speciation following the reaction of **1** (red diamonds) with vinyl acetate; the remaining mass balance comprises alkyl complexes (*vide infra*). (-10 °C, 15 psia CO, 65 mM **1**, 320 mM vinyl acetate, CH_2Cl_2). For plots demonstrating total mass balance, see Appendix A-1–A-4.

The diastereomeric branched acyl species **7b$_{va}$** and **7b'$_{va}$** appear as eight-line patterns in the $^{31}P\{1H\}$ NMR spectrum at δ 69.5, 60.4 ppm and δ 68.5, 57.8 ppm, respectively. Another acyl species **"7l$_{va}$"** is responsible for the eight-line patterns at δ 70.1, 62.4 ppm (see Appendix A for complete NMR data), and increases in concentration over a longer time period than the branched acyls (Figure 3-4). As the signal for **"7l$_{va}$"** grows in, the catalyst precursor [Rh(acac)(BDP)] forms at the same rate and the alkyl species, **4b$_{va}$**, **4b*$_{va}$**, and **5b$_{va}$**, disappear from solution (Figure 3-5).

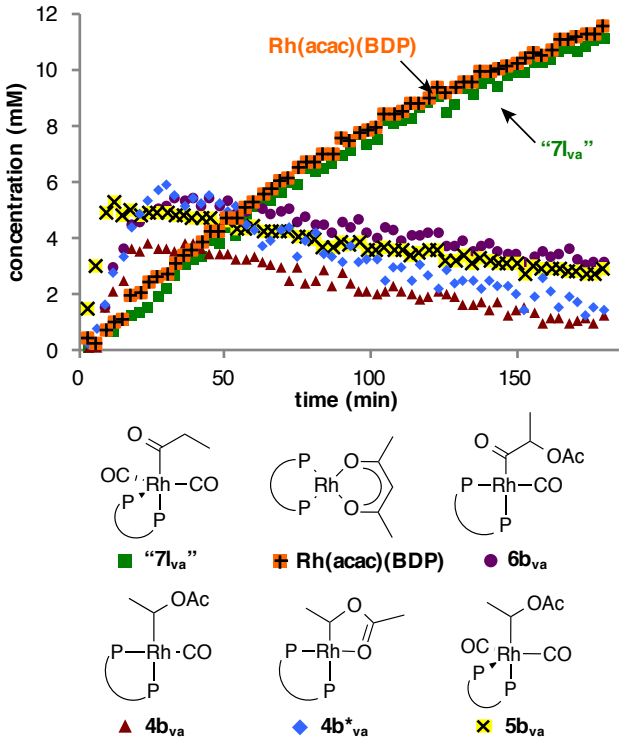

Figure 3-5. Disappearance of observed Rh-alkyl species and formation of **"7l$_{va}$"** and [Rh(acac)(BDP)] during reaction of 1 with vinyl acetate under the same conditions previously reported. (-10 °C, 15 psia CO, 65 mM **1**, 320 mM vinyl acetate, CH_2Cl_2).

Characterization of acyl complexes. ^{31}P-^{1}H HMBC experiments show through-bond coupling from each set of ligand phosphorus atoms of **7b$_{va}$** and **7b'$_{va}$** to methine quartets and methyl doublets in the ^{1}H NMR spectrum. This experiment also revealed that, notably, *the linear acyl complex* ***"7l$_{va}$"*** *is not the β-acetoxypropionyl complex as expected, but the unsubstituted propionyl species* (see Figure 3-4). The HMBC spectrum shows correlations to two diastereotopic methylene protons at δ 2.62 and 1.67 ppm, as expected, but a COSY spectrum shows that these protons, rather than being correlated to an adjacent methylene group, are vicinal instead to a methyl group, which appears as a triplet at δ 0.5 ppm (^{1}H-^{13}C HSQC shows that these protons are attached to a carbon atom with a signal at 10 ppm, also consistent with a

methyl group). Thus, the linear acyl dicarbonyl **"7l$_{va}$"** appears to result from the reaction of ethene with **1** (*vide infra*).

A variety of other one- and two-dimensional NMR experiments, including ^{31}P-^{31}P COSY and ^{13}C-^{1}H HSQC, corroborate these assignments of **7b**$_{va}$ and **7b'**$_{va}$ as five-coordinate, branched acyl dicarbonyl complexes. The methine carbons of **7b$_{va}$** and **7b'$_{va}$** are visible at δ 86.2 and 83.9 ppm, respectively. The acyl and terminal carbonyl carbons of these complexes are also observable; chemical shifts and coupling constants are similar to those reported for complexes **7$_{sty}$**. The coordination number of complexes **7b**$_{va}$ and **7b'**$_{va}$ was determined by labeling with ^{13}CO; the upfield ^{31}P signal (P$_{eq}$) shows three new $^{1}J_{PC}$, consistent with an acyl dicarbonyl. The J_{PRh} values for these complexes (81 and 152 Hz for **7b$_{va}$** and 80 and 167 Hz for **7b'$_{va}$**) are consistent with five-coordinate trigonal bipyramidal species.

The characterization of these off-cycle species raises the question: is the observation of these intermediates relevant to catalysis? The significance of quantitatively observing these off-cycle diastereomers at low temperature, non-catalytic conditions is that their kinetic selectivities correlate with the product selectivity for both sets of conditions. For example, high branched selectivity for acyl dicarbonyls mirrors the high selectivity for branched aldehyde under catalytic conditions. Interestingly, we also find that acyl dicarbonyl complexes **7b**$_{va}$ and **7b'$_{va}$** are formed even in the presence of H_2 and persist for hours under an atmosphere of syngas with passive mixing at –10 °C. For the unobserved acyl monocarbonyl intermediates produced by insertion of coordinated CO into the branched Rh-alkyl, there is competition between CO coordination, reaction with dihydrogen, and isomerization. Evidently the oxidative addition of H_2 (and subsequent reductive elimination of the product) is not competitive with CO association under these conditions of low temperature and low concentration of dissolved dihydrogen.

Replacement of the branched acyls with linear acyl **"7l$_{va}$"** occurs slowly over the course of the reaction; however, the branched isomers predominate by a ratio of 2.6:1 after four hours, a time at which equilibrium has not been achieved.

For vinyl acetate, the ratio of the diastereomeric acyl complexes reveals a slight kinetic preference (1.2:1) for **7b$_{va}$** which is eventually overtaken by a slight thermodynamic preference (1.1:1) for **7b'$_{va}$**. These small countervailing preferences are consistent with the low *ee* for vinyl acetate under tyical asymmetric catalytic reaction conditions. This equilibration between acyl complexes, along with continuing isomerization to the linear isomer, indicates that all steps leading to the formation of the acyl complexes are reversible under these conditions.

Characterization of alkyl complexes. The ^{31}P{1H} NMR spectrum shows at least five additional species, in addition to [Rh(acac)(BDP)] and a rhodium dimer. Three of these can be tentatively identified as alkyl complexes, as indicated by the absence of any additional signals in the acyl region of the ^{13}C NMR spectrum (Figure 3-6). Identification of alkyl intermediates along the hydroformylation catalytic cycle is rare.

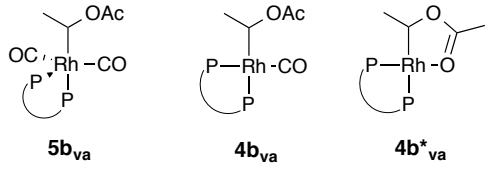

5b$_{va}$ **4b$_{va}$** **4b*$_{va}$**

Figure 3-6. Alkyl complexes formed following the reaction of 1 with vinyl acetate.

The species we have assigned as **4b$_{va}$** has phosphorus signals at δ 82.6 and 39.2 ppm, and the upfield peak exhibits one new 89 Hz ^{31}P-^{13}C coupling following the reaction of vinyl acetate with [Rh(H)(^{13}CO)$_2$(BDP)]. Along with its two large $^1J_{PRh}$ values (101 and 213 Hz), this suggests it is a four-coordinate alkyl complex (Figure 3-7).[39] ^{1}H-^{31}P HMBC shows correlation of the upfield phosphorus resonance to an apparent triplet at δ 1.58 ppm in the ^{1}H NMR spectrum,

which shows through-bond coupling to a multiplet at δ 4.69 ppm. We propose that the upfield signal is actually a doublet of doublets belonging to a methyl group; the second 6.5-Hz coupling is created by the *trans* ligand phosphorus atom. While a triplet might seem to be more consistent with the methyl group of an ethyl fragment, the ^{1}H-^{1}H COSY correlation to a single downfield signal belies this simple assignment; methylene protons would almost certainly be further upfield. Moreover, in all other linear [Rh(BDP)] complexes characterized thus far, the diastereotopic methylene protons have a substantial (ca. 1 ppm) difference in chemical shift. Therefore, we ascribe these signals to branched alkyl **4b$_{va}$**. The signal from the methine proton at 4.69 ppm is not observable in the simple 1D spectrum, although it is clearly observed in the 2D COSY and ^{1}H-^{31}P HMBC spectra. However, because this signal would be at least a doublet of quartets (and possibly a *ddq*) in a crowded region of the spectrum, the absence of a clear peak for the methine proton in the simple 1D NMR spectrum is not surprising.

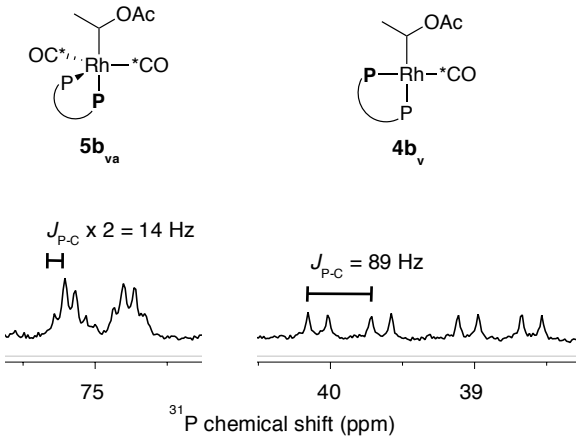

Figure 3-7. Partial ^{31}P{1H} NMR spectrum taken following the reaction of [Rh(H)(^{13}CO)$_2$(BDP)] with vinyl acetate. Ligand phosphorus atoms show two new $^{2}J_{PC}$ for **5b$_{va}$** (left) and one for **4b$_{va}$** (right). ^{13}C-labeled carbons denoted by (*). (202.5 MHz, -40 °C, CD_2Cl_2).

Five-coordinate branched alkyl complex **5b$_{va}$** was identified by its moderate (83- and 159-Hz) phosphorus-rhodium coupling constants, the presence of two CO ligands (both *cis* to the ligand's phosphorus atoms, as established by labeling with ^{13}CO), and as above, through-bond coupling to an apparent triplet at δ 1.4 ppm in the ^{1}H NMR spectrum which is itself coupled to a downfield (δ 4.7 ppm) signal. In the ^{31}P NMR spectrum (see Figure 3-7), another small doublet-of-doublets appears just upfield of each ^{31}P signal for **5b$_{va}$**. The signals are too small to provide any useful characterization information, but because of the similarity of their spectral features to those of **5b$_{va}$**, they could plausibly belong to the other diastereomer, **5b'$_{va}$**. If that is the case, the diastereomeric ratio for these alkyl complexes is 3.9:1 – much greater than that observed at the acyl stage.

The final alkyl species has no CO ligands, which, along with its large (256 and 129 Hz) $^{1}J_{PRh}$ and apparent correlation to a broad quartet in the ^{1}H NMR spectrum leads us to assign it as **4b*$_{va}$**, in which the acetate group occupies the fourth coordination site. In the absence of additional characterization data this assignment is speculative because there is no spectroscopic indication of carbonyl coordination. The regiochemistry of this species is clearly branched and the coupling data are indicative of a square planar or perhaps T-shaped complex.

There is a fourth, unidentified species, with broad phosphorus signals at δ 78.5 and 54.6 ppm. Its large (107 and 221 Hz) phosphorus-rhodium coupling constants suggest that it is a four-coordinate species (although the peaks are too broad following labeling with ^{13}CO to provide any conclusive information). Through-bond coupling to a quartet and doublet in the ^{1}H NMR spectrum are consistent with a branched species. These peaks are tentatively assigned to four-coordinate branched acyl **6b$_{va}$**. For NMR data for alkyl and acyl complexes generated from the reaction of **1** with vinyl acetate, see Appendix A.

Proposal for the formation of "7l$_{va}$". Propionyl complex **"7l$_{va}$"** could plausibly be formed by the reaction of hydride **1** (or monocarbonyl hydride **2**, not observed) with ethene. We propose that the unseen linear alkyl intermediate **4l$_{va}$** is formed from the isomerization of the kinetically favored branched alkyl complexes. **4l$_{va}$** undergoes β-acetoxy elimination to form ethene, which subsequently dissociates and goes on to react with another rhodium hydride to generate **"7l$_{va}$"** (Scheme 3-2). (Even after dicarbonyl hydride **1** has been consumed, the equilibration of alkyl and acyl complexes implies that **2** persists in solution, albeit below the limit of detection). The β-acetoxy elimination reaction is commonly cited in transition-metal mediated reactions, although most commonly for Group 10 metals;[40-46] however, it has been specifically invoked to explain the reaction of a variety of metal hydrides (including rhodium) with vinyl acetate to generate ethylene.[47-48] Also, our group has reported observation of β-elimination of trifluoroacetoxy groups (a better leaving group than acetate) during the AHF of enol trifluoroacetate esters.[49]

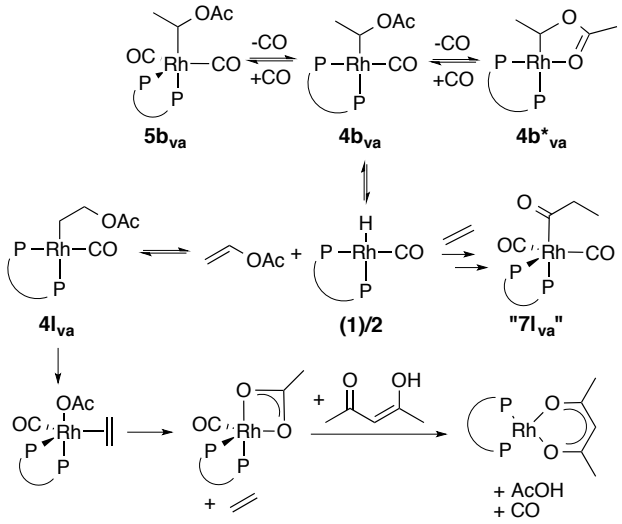

Scheme 3-2. Proposal for the formation of propionyl complex **"7l$_{va}$"**.

β-acetoxy elimination from **4l$_{va}$** yields a rhodium acetate complex as well as ethene (see Scheme 3-2). We hypothesize that the reaction of ethene with **2** is fast because no free ethene is observed in the ^{1}H NMR spectrum. We do not see any evidence for a rhodium acetate species, however, we do see [Rh(acac)(BDP)] build up at a rate that is identical to the rate of formation of **"7l$_{va}$"** (Figure 3-5). This could suggest that any Rh-acetate intermediate undergoes fast exchange with acetylacetone which is present from the initial generation of [RhH(CO)$_2$(BDP)] (Scheme 3-2). Thus, the loss of branched alkyl complexes, **4b$_{va}$**, **5b$_{va}$**, and **4b$_{va}$**, is replaced by a 1:1 mixture of [Rh(acac)(BDP)] and **"7l$_{va}$"**. Control experiments establish that *in situ* generated [Rh(OAc)(BDP)] and acetyl acetone react to form [Rh(acac)(BDP)] (see Appendix A).

The high selectivity for the branched product in catalytic hydroformylation of vinyl acetate seems to be reflected in the strong kinetic preference for branched alkyl and acyl complexes versus their linear counterparts. In fact, the only linear species observed is propionyl acyl complex **"7l$_{va}$"**, and this species is presumably formed from ethylene addition to the hydride **2** (which produces degenerate insertion products).

3.2.2.3 Allyl Cyanide

Addition of allyl cyanide to a solution of **1** at –10 °C under an atmosphere of CO gives the five-coordinate linear acyl complex **7l$_{ac}$** as the major product (regiochemistry determined by ^{1}H-^{31}P HMBC spectroscopy). The apparent half-life for the disappearance of **1** in this experiment is approximately 4 minutes (see Figure 3-3). The reaction timecourse at –20 °C is shown in Figure 3-8. Colder temperatures were used to observe the branched acyl dicarbonyl species. The remaining mass balance comprises uncharacterized complexes in low concentrations (see Appendix A).

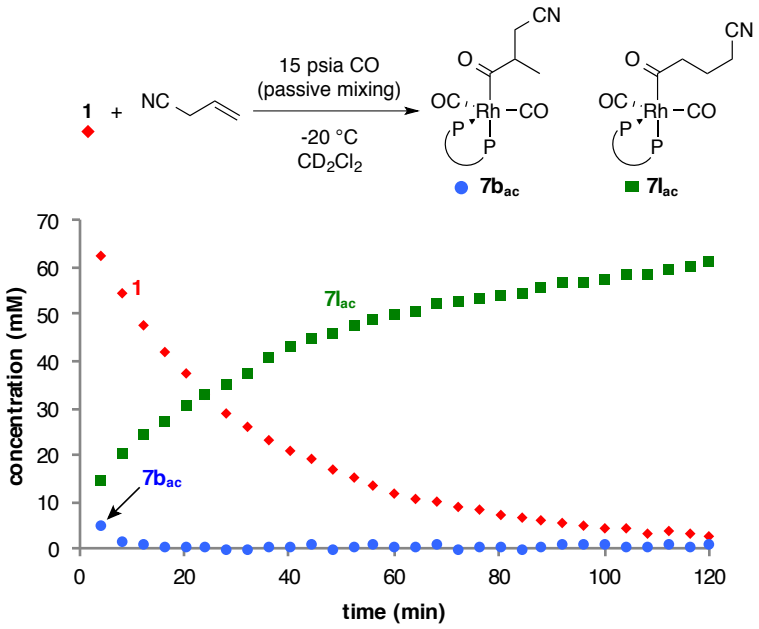

Figure 3-8. Reaction of **1** (red diamonds) with allyl cyanide gives predominantly linear acyl **7l$_{ac}$**. (–20 °C, 15 psia CO, 90 mM **1**, 400 mM allyl cyanide, CH_2Cl_2).

The coordination number of **7l$_{ac}$** was determined by labeling with ^{13}CO as described above. While the minor species produced by this reaction proved difficult to characterize definitively, the most promising candidate for branched acyl **7b$_{ac}$** based on chemical shift and coupling constants is the set of two doublets-of-doublets at δ 68.6 ppm ($^1J_{PRh}$ = 80 Hz, $^2J_{PP}$ = 17 Hz) and δ 59.7 ppm ($^1J_{PRh}$ = 169 Hz, $^2J_{PP}$ = 17 Hz). The apparent thermodynamic instability of this species, which is already decreasing in concentration when the first spectrum is recorded (see Figure 3-8), is consistent with this assignment, since we expect allyl cyanide to exhibit the typical steric preference for the linear acyl. The challenge in synthesizing the ^{13}C-labeled structure made it difficult to further characterize these species.

3.2.2.4 Trans-1-Phenyl-1,3-Butadiene

The reaction of *trans*-1-phenyl-1,3 butadiene with **1** at 0 °C under an atmosphere of CO gives five-coordinate acyl complexes and an allyl complex as the major products (Figure 3-9). The diastereomeric acyl complexes **7b$_{diene}$** and **7b'$_{diene}$** are responsible for the eight-line patterns at δ 68.9, 60.8 ppm and δ 67.0, 59.1 ppm, respectively in the $^{31}P\{1H\}$ NMR spectrum. The allyl complex, **4b*$_{diene}$**, appears as a four-line pattern at δ 78.3 and 48.1 ppm. At –10 °C, the qualitative half-life for the disappearance of **1** is 20 minutes (see Figure 3-3).

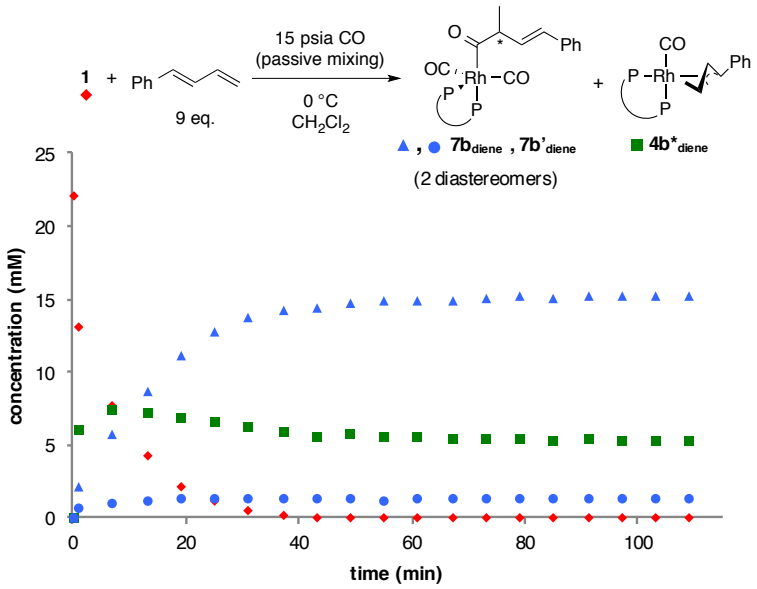

Figure 3-9. Reaction of **1** (red diamonds) with *trans*-1-phenyl-1,3-butadiene leads to primarily the 2-formyl acyl **7b$_{diene}$** and the allyl species **4b*$_{diene}$**. (0 °C, 15 psia CO, 22 mM **1**, 200 mM *trans*-1-phenyl-1,3-butadiene, CH_2Cl_2). For plot highlighting mass balance, see Appendix A.

Characterization of acyl complexes. As with the other substrates, the regiochemistry of acyl complexes formed from 1-phenyl-1,3-butadiene was determined using ^{1}H-^{31}P HMBC spectroscopy. The ligand phosphorus atoms show long-range coupling to methine protons for both observed acyl complexes. Selective 1D-TOCSY spectra with irradiation at these proton

peaks elucidated the regiochemistry. Other two-dimensional NMR spectra, including ^{31}P-^{31}P COSY and ^{1}H-^{13}C HSQC, are consistent with these assignments.

The characterization of these species as acyl, rather than alkyl, complexes was made using ^{1}H-^{13}C HSQC spectroscopy. The methine protons of **7b$_{diene}$** and **7b'$_{diene}$** were correlated to carbon atoms at δ 70.8 ppm. For comparison, in the branched styrenyl acyl complex **7b$_{sty}$**, the methine carbon appears at δ 74.0 ppm versus δ 37.7 ppm for the alkyl species.[36]

The coordination number for these complexes was determined by labeling with ^{13}CO. For **7b$_{diene}$** the axial phosphorus resonance is an apparent triplet of quartets with another multiplet underneath obscuring the structure slightly; *J*=81.8, 15.9 Hz (Figure 3-10). This multiplet is correctly interpreted as a *dddt*, but one $^{2}J_{PC}$ happens to be equal to the $^{1}J_{PRh}$ coupling constant, and the other two $^{2}J_{PC}$ are equal to the $^{2}J_{PP}$ value. The downfield multiplet for **7b'$_{diene}$** appears to have a similar structure; however, its relatively low concentration prevents exact determination of coupling constants.

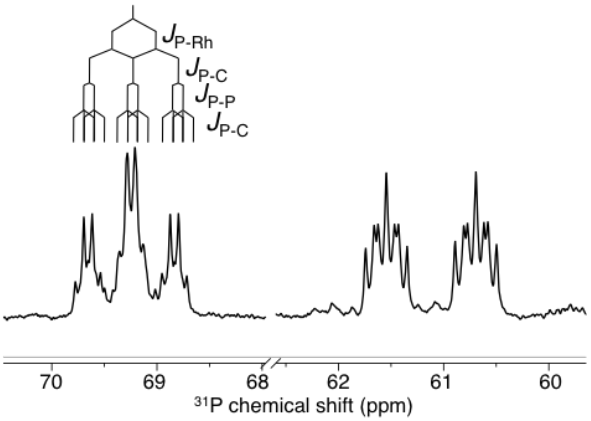

Figure 3-10. ^{31}P{1H} NMR spectrum demonstrating the use of ^{13}C labeling to determine the coordination number of **7b$_{diene}$**. The multiplet is an apparent triplet of quartets. (0 °C, 15 psia ^{13}CO, 30 mM **1**, 260 mM *trans*-1-phenyl-1,3-butadiene, CH_2Cl_2)**.**

Characterization of allyl complex 4b*$_{diene}$. The regiochemistry of the allyl species was determined by ^{1}H-^{31}P HMBC and selective 1D-TOCSY experiments. The proton peaks appear at δ 1.57, 1.72, 3.82, and 5.34 ppm, which are consistent with other reported Rh-allyl complexes.[32,50] DEPT experiments assisted in the assignments shown in Figure 3-11. ^{1}H-^{13}C HMBC spectroscopy supports the presence of an allyl species by the lack of an acyl carbon peak; the proton signal at δ 3.82 ppm showed no ^{13}C crosspeaks above δ 150 ppm in the ^{1}H-^{13}C HMBC spectrum.

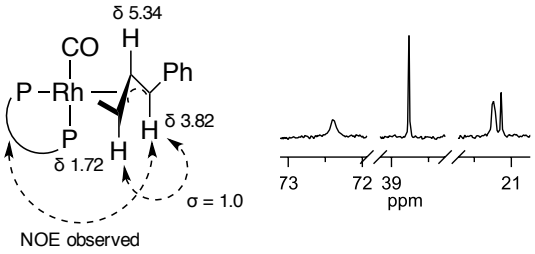

Figure 3-11. ^{1}H NMR assignments of allyl protons and observed NOE between *anti* protons and the ligand (left). ^{13}C NMR spectrum of allyl carbon peaks in **4b*$_{diene}$** (right). (0 °C, 15 psia CO, 22 mM **1**, 200 mM *trans*-1-phenyl-1,3-butadiene, CH_2Cl_2).

The coordination number of **4b*$_{diene}$** was determined by labeling with ^{13}CO. Both of the ^{31}P signals for **4b*$_{diene}$** show one additional coupling in the reaction with *trans*-1-phenyl-1,3-butadiene and Rh(H)(^{13}CO)$_2$(BDP). The phosphorus atom trans to CO has $^{2}J_{PC}$ = 38.0 Hz, and the *cis* phosphorus gives $^{2}J_{PC}$ = 10.3 Hz.

Selective 1D-NOESY experiments were used to determine the *syn/anti* relationship of the substituents. When the peak at δ 3.82 ppm was irradiated, an NOE was observed with the proton that appears at δ 1.72 ppm with an initial build-up rate of σ = 1.0 s^{-1}. The lack of NOE to the proton resonating at 5.34 ppm and the significant NOE between the protons resonating at 1.72 and 3.82 ppm provides evidence for the structure shown in Figure 3-11.

We have assigned this complex as an η^3-allyl, but an η^1 complex also was considered. ^{1}H-^{13}C HSQC spectroscopy was used to identify the ^{13}C NMR signals for the allyl ligand. In the ^{13}C{1H} NMR spectrum, these peaks are broad multiplets; while the peaks' low intensity prevents exact determination of coupling constants, their shape suggests an η^3-allyl species with $^1J_{CRh}$ and $^2J_{CP}$ coupling.

3.2.2.5 1-Octene

Because 1-octene undergoes AHF to give predominantly linear product, stoichiometric NMR studies of this substrate provide an instructive counterpoint to results obtained with styrene and other more electron-deficient substrates.

It is also important to point out that, unlike styrene, 1-octene can isomerize under hydroformylation conditions to give internal alkenes, primarily 2-octene. For example, in hydroformylation with the methylbenzylamide BDP ligand, at 50 °C and 150 psig H_2/CO, 32 % of the starting material had isomerized to 2-octene after 24 hours.[37] Therefore, alkyl and acyl complexes derived from the reaction of **1** with internal alkenes should be considered as possible products.

As with the other substrates, the major product of the reaction between 1-octene and **1** is a five-coordinate dicarbonyl acyl complex. At –10 °C, the half-life for the disappearance of hydride is approximately 3 minutes (see Figure 3-3). The reaction was monitored at lower temperatures to better observe the kinetic selectivity early in the reaction. At –20 °C in the absence of H_2, the linear acyl $\mathbf{7l_{oct}}$ product dominates (Figure 3-12), as seen for styrene and allyl cyanide. The branched acyl $\mathbf{7b_{oct}}$ could only be observed when the reaction temperature was lowered to –30 °C to monitor speciation very early in the reaction. Again, the regiochemistry of

7l$_{oct}$ was determined by ^{1}H-^{31}P HMBC (see Appendix A). The concentration of **7b$_{oct}$** was too low to give a crosspeak in the 2-D spectrum; however, our assignment is corroborated by the observation of a doublet in the ^{1}H NMR spectrum early in the reaction at δ 0.37 ppm, and comparison of the chemical shifts and coupling constants in the ^{31}P NMR spectrum.

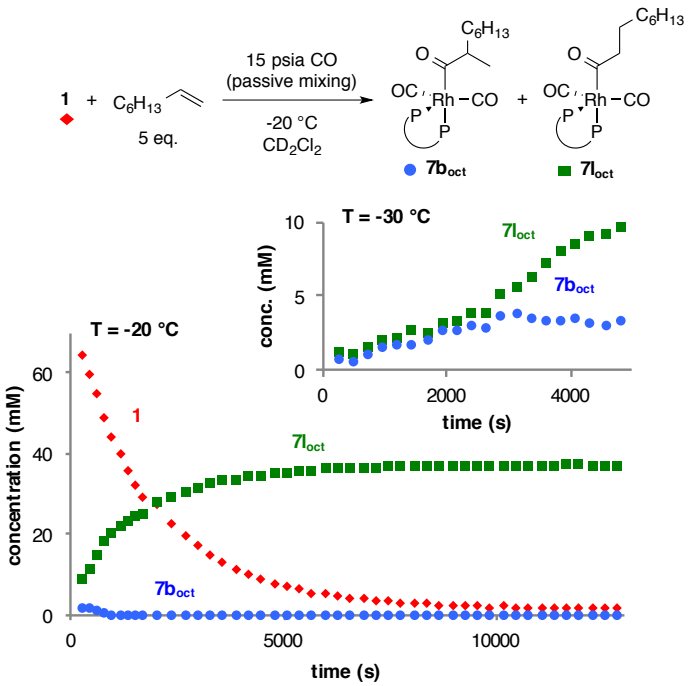

Figure 3-12. Plots demonstrating apparent kinetic b:l selectivity for 1-octene can be resolved at –30 °C but not –20 °C under passive mixing conditions. Reaction of **1** (red diamonds) with 1-octene gives predominantly linear acyl **7l$_{oct}$** (-20 °C, 15 psia CO, 80 mM **1**, 400 mM 1-octene, CH_2Cl_2). Spectra acquired at lower temperature and shorter reaction times (inset) show no kinetic preference for either regioisomer, in constrast with the results for styrene (-30 °C, 15 psia CO, 65 mM **1**, 320 mM 1-octene, CH_2Cl_2). R = C_6H_{13}. For plot highlighting mass balance, see Appendix A.

The minor species were more difficult to characterize and quantify, leading to a slight loss of mass balance (ca. 5-10%) (see Appendix A). Most minor species were not well-resolved

until the temperature was lowered to –40 or –80 °C. The two most prominent minor species have eight-line patterns at δ 70.8 and 67.4 ppm and δ 63.2 and 57.6 ppm. We have tentatively assigned these as **5b$_{oct}$** and **4b$_{oct}$**, respectively (Figure 3-13). Generating these species with 1-^{13}C-octene demonstrates that neither is a linear isomer (insertion at the 1-position of the alkene would result in measurable ^{31}P-^{13}C coupling for both alkyl and acyl species). However, it is important to point out that while these species have been drawn with methyl branches, the data from this ^{13}C-labeling experiment are also consistent with complexes formed by the insertion of internal octenes (the products of alkene isomerization) into the R-H bond of **1**. We do not currently have any data that would rule out species of this type. Indeed, the presence of at least two distinct types of ^{13}C-labeled methyl groups in the ^{1}H and ^{13}C NMR spectra shows that isomerization does occur under these conditions. Of course, isomerization must also occur during the reaction of **1** with unlabeled substrate; however, the crowded alkyl and vinyl region of these spectra make detection of isomerization virtually impossible without isotopic enrichment.

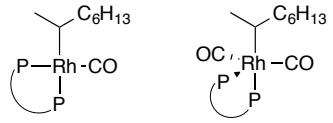

4b$_{oct}$ **5b$_{oct}$**

Figure 3-13. Alkyl species tentatively characterized following the reaction of 1 with 1-octene.

The NMR spectrum of **5b$_{oct}$** taken after addition of 1-octene to ^{13}CO-labeled [Rh(H)(^{13}CO)$_2$(BDP)] shows two new poorly-resolved ^{31}P-^{13}C couplings, consistent with an alkyl dicarbonyl, where the phosphorus atom (P_{eq}) showing the new coupling shares the equatorial plane with the two labeled carbon atoms. Complex **4b$_{oct}$**, on the other hand, shows one new 34 Hz phosphorus-carbon coupling to the upfield phosphorus signal (P_{ax}) while the downfield peak (P_{eq}) shows a larger 81 Hz coupling. These data are consistent with an alkyl

monocarbonyl structure for which the large coupling belongs to the phosphorus atom *trans* to the labeled carbonyl group. Curiously, for the other alkyl complexes we identified, the phosphorus atom that is positioned *trans* to the organic fragment is responsible for the downfield signal. If the structural assignment of **4b$_{oct}$** is correct, the downfield signal belongs instead to the phosphorus atom *trans* to the carbonyl ligand. We do not currently have an explanation for this change in chemical shift trends; however, the difference in magnitude of the phosphorus-carbon coupling constants would make a different assignment of the coordination geometry implausible.

Unfortunately, the absence of strong correlations in the ^{1}H-^{31}P HMBC spectrum prevents the use of ^{1}H NMR data to further substantiate these assignments. The ^{13}C NMR spectra of the material generated using either ^{13}CO or 1-^{13}C-octene are similarly unhelpful. However, the acyl region of the former seems to have at least two minor acyl signals in the baseline (in addition to the major peak for **7l$_{oct}$**), suggesting that at least one of the unresolved species in the baseline may be another acyl complex. See Table 3-3 for NMR data for **7b$_{oct}$**, **7l$_{oct}$**, **4b$_{oct}$**, and **5b$_{oct}$**.

At equilibrium, rhodium complex speciation in the non-catalytic reaction of **1** with 1-octene generally resembles that seen with styrene: the five-coordinate linear acyl dominates, accounting for more than 50 percent of the total ^{31}P integration. However, the data early in the reaction, under conditions where **7b$_{oct}$** is observable, reveal an important distinction. Whereas for styrene there was a clear kinetic preference for the branched acyl **7b$_{sty}$** (presumably reflecting a preference for the branched intermediate **4b$_{sty}$**),[36] 1-octene displays no such preference (see Figure 3-12). The two species grow in at roughly the same rate.

If we assume that the kinetic behavior of the acyl species reflects the kinetic behavior of the alkyl species, and that the relative rates of alkene insertion to give alkyl complexes **4** is the

primary factor governing selectivity, the results presented in Figure 3-12 are consistent with the experimental observation of low selectivity in 1-octene hydroformylation by Rh(BDP) catalysts.

3.2.3 NMR Studies at Higher Pressure with Active Mixing

*3.2.3.1 Equilibration of the Allyl Complex **4b*$_{diene}$** and the Acyl Dicarbonyl **7b**$_{diene}$*

A limitation of low-pressure studies with passive mixing is that the concentration of CO in solution is unknown and not controlled during the reaction. Our group has recently reported the development of the Wisconsin high-pressure NMR reactor (WiHP-NMRR). The apparatus allows for the collection of data under a known pressure with active gas-liquid mixing.[51]

The reaction of **1** with *trans*-1-phenyl-1,3-butadiene at 0 °C was monitored under a constant pressure of 5 psig CO with active mixing (Figure 3-14). The WiHP-NMRR experiment shows a higher concentration of **4b*$_{diene}$** than in the low-pressure studies. We attribute this to the uncertain and variable [CO] in the passively mixed low-pressure experiments. The lower sensitivity of the 360 MHz spectrometer used for WiHP-NMRR studies results in lower signal-to-noise ratios for ^{31}P NMR spectra than the other examples reported herein, and thus, the diastereomer, **7b'$_{diene}$** was below the detection limit under these conditions.

After the reaction of the diene and [RhH(BDP)(CO)$_2$] reached equilibrium, the CO pressure was increased and the changes in the [**7b$_{diene}$**]/[**4b*$_{diene}$**] ratio were measured. As expected, as the pressure of CO (and consequently, the dissolved CO concentration) increases, the equilibrium favors **7b$_{diene}$** (Figure 3-15). Based on reaction 2 in **Figure 3-16**, K_{eq} was determined. The equilibrium expression was rearranged such that plotting $[CO]^2$ versus [**7b$_{diene}$**]/[**4b*$_{diene}$**] gives a line with a slope of $K_{eq} = k_2/k_{-2} = 6973$.

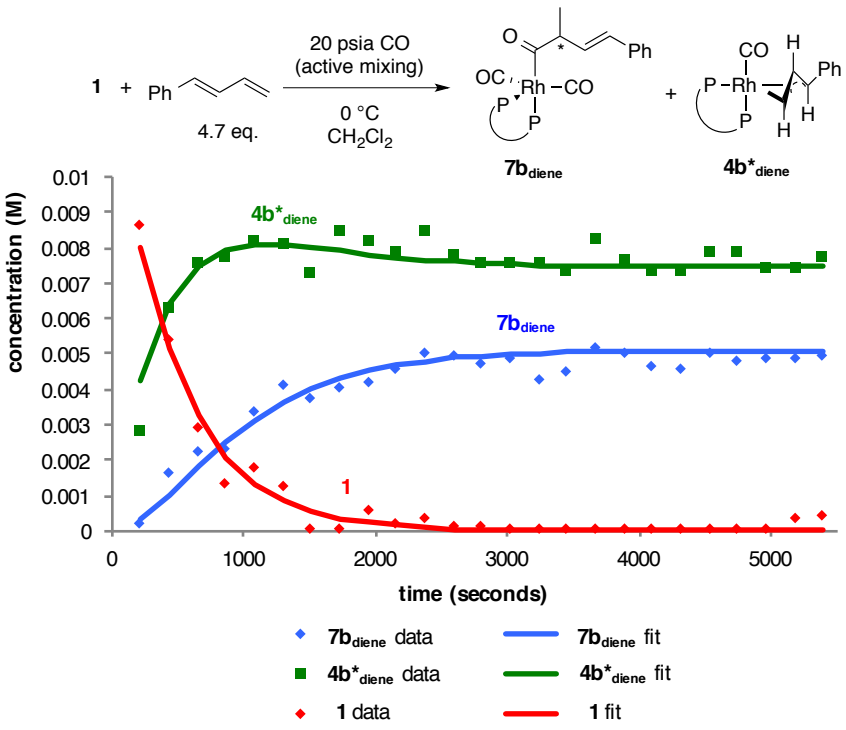

Figure 3-14. Reaction of **1** (13 mM) with *trans*-1-phenyl-1,3-butadiene (61 mM) at 0 °C under a constant pressure of 20 psia as measured by WiHP-NMRR. The data were modeled in COPASI.

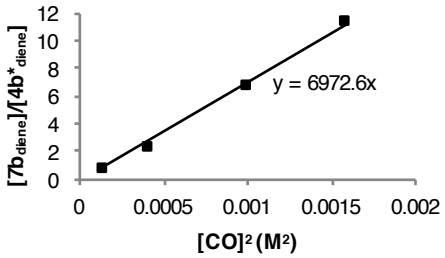

Figure 3-15. Effect of CO pressure on product distribution. By rearrangement of equilibrium expression, the slope is equal to K_{eq} (6973).

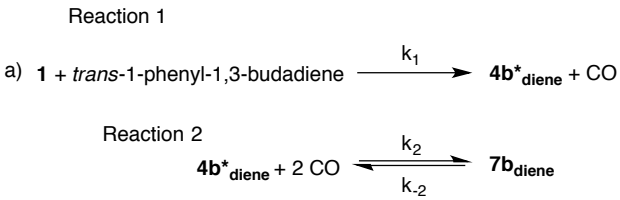

b)

	Value	Standard Deviation
k_1	$2.09 \times 10^{-3}\ M^{-1}s^{-1}$	5×10^{-5}
k_2	$7.4\ M^{-2}\ s^{-1}$	7×10^{-1}
k_{-2}	$1.1 \times 10^{-3}\ s^{-1}$	1×10^{-4}

Figure 3-16. a) Simplified kinetic model for determination of rate constants of formation of products of the reaction of **1** and *trans*-1-phenyl-1,3-butadiene at 0 °C in the absence of H_2 and approximately 17 psia CO and b) rate constants and standard deviations estimated by non-linear least squares fitting.

Simplified reactions were entered into the kinetic modeling program COPASI for determination of rate constants for the formation of **4b*$_{diene}$** and **7b$_{diene}$**.[52] The rate constants for k_1, k_{-1}, and k_2 were calculated by fitting the data; k_{-2} was set based on k_2 and the known value for K_{eq} (see Figure 3-16). The data were fit best when a pressure of CO of 17 psia was entered into the model. The pressure transducer used has an accuracy of ± 3 psi, thus 17 psia falls within this range. See Appendix A for other plots.

These calculations show that the rate constant for formation of the allyl complex (k_1) is significantly smaller than its trapping by CO (k_2) to form an acyl dicarbonyl complex. A rate constant (k_{-1}, not shown) for deinsertion of the allyl complex to form **1** and *trans*-1-phenyl-1,3-butadiene was optimized, but found to be insignificantly small; therefore this step was modeled as irreversible. The calculated equilibrium constant indicates that under the higher CO pressures used in standard hydroformylation reactions, the acyl dicarbonyl species is favored thermodynamically over the allyl complex. However, this equilibrium distribution may not be

achieved under catalytic conditions because dihydrogen may competitively trap the acyl monocarbonyl intermediate to ultimately yield **1** and aldehyde.

The WiHP-NMRR apparatus enables analysis of the kinetics and thermodynamics of the equilibration of **1**, **4b*$_{diene}$**, and **7b$_{diene}$**, which were previously unattainable. Under increasingly high pressures of CO, the equilibrium is shifted toward the acyl dicarbonyl complex. In contrast with our previous studies, the WiHP-NMRR assures that the CO partial pressure is known and that the equilibrium concentration of dissolved CO (i.e., Henry's law equilibrium) is rigorously maintained throughout the reaction.

3.2.3.2 Selectivity of Acyl 7 Formation for Allyl Cyanide

At temperatures below 0 °C and at one atmosphere of passively-mixed CO, reaction with allyl cyanide proceeds with a half-life of a few minutes, thermodynamics clearly favor linear acyl dicarbonyl **7l$_a$**, and the kinetic selectivity seems to slightly favor the branched acyl. What happens if the reaction is performed with active CO mixing?

As shown in Figure 3-17, reaction of hydrido dicarbonyl with one equivalent of allyl cyanide at 17 psia CO at 0 °C in the presence of active gas mixing yields a distinct kinetic preference for the formation of one diastereomer **7b$_{ac}$** of the *branched* acyl dicarbonyl with an overall branched:linear ratio of about 3:1; the two branched diastereomers are distinguishable and appear in a ratio of about 5:1.[53] With active mixing at 0 °C these ratios are maintained for three hours with little change. However, warming the solution to room temperature with active mixing initiates isomerization of the branched acyls to the linear (see Appendix A). Isomerization can be effectively stopped by cooling back to 0 °C. These data conclusively demonstrate that (a) the branched acyl dicarbonyls are the kinetic products (b) the linear acyl

dicarbonyl **7l$_a$** is the thermodynamic product (c) the rate of isomerization is inhibited by CO and (d) the reaction of **1** with allyl cyanide is inhibited by CO.

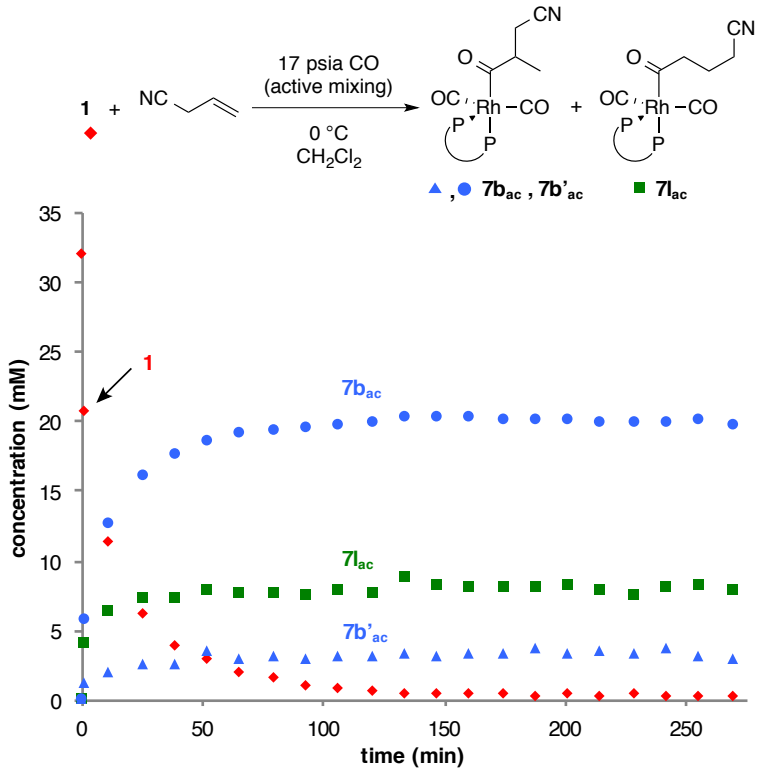

Figure 3-17. Reaction of **1** (32 mM) with allyl cyanide (32 mM) at 0 °C under a constant pressure of 17 psia CO as measured by WiHP-NMRR with active mixing.

3.2.3.3 Selectivity of Hydrogenolysis for Allyl Cyanide

What about selectivity in the presence of H_2? By "freezing" a nonequilibrium ratio of linear and branched acyl dicarbonyls at roughly 1:1 and adding H_2 with active mixing, we can directly examine the relative hydrogenolysis rates of linear and branched acyl dicarbonyls. The results are shown in Figure 3-18. Starting from nearly equal amounts of linear and branched acyl dicarbonyls, the branched aldehyde clearly forms faster than the linear isomer. Furthermore, the data demonstrate that little isomerization of linear and branched acyls occurs over the five hour

reaction time (as seen in the absence of H_2, *vide supra*). Hydrogenolysis rates differ significantly for the two branched diastereomers with **7b$_a$** disappearing three-fold faster than **7b'$_a$**. Such reactions with dihydrogen demonstrate substantial intrinsic selectivities for hydrogenolysis of acyl dicarbonyls. Furthermore, at these temperatures and pressures, the rate of hydrogenolysis is faster than equilibration amongst the various acyl dicarbonyls (non-Curtin-Hammett conditions). For more detailed analysis on how differing rates of hydrogenolysis affect catalytic conditions, see Chapter 4.

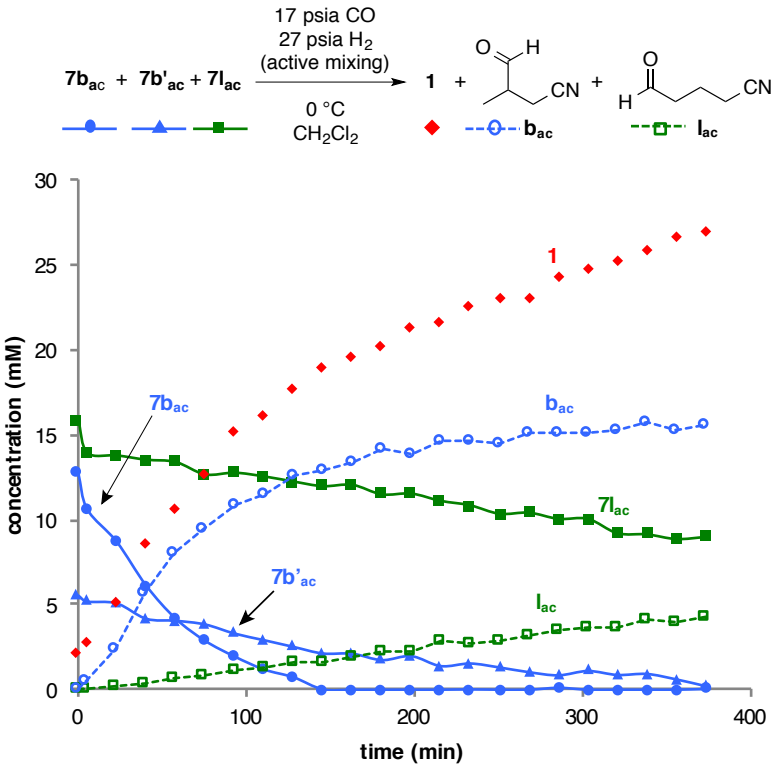

Figure 3-18. Hydrogenolysis of a nonequilibrium distribution of acyl dicarbonyl species (**7l$_{ac}$**, **7b$_{ac}$**, **7b'$_{ac}$**) (32 mM, b:l ~1) to produce linear (**l$_{ac}$**) and branched (**b$_{ac}$**) aldehydes at 0 °C under a constant pressure of 17 psia CO and 27 psia H_2 as measured by WiHP-NMRR with active mixing.

3.3 Conclusions

One motivation of these studies was to determine the spectroscopic signatures of alkyl, acyl, and allylic intermediates relevant to AHF for a representative sampling of different substrate types. Such data are essential to establish the relative rates and thermodynamic stabilities of catalyst intermediates that constitute the "inside-out" mechanistic approach. These studies have been facilitated by adopting low temperature and low pressure reaction conditions without H_2 present and passive gas-liquid mixing. Many catalytic intermediates have been intercepted and characterized by detailed NMR studies. These intermediates include the rarely observed alkyl and acyl monocarbonyl intermediates of catalytically active complexes. These studies and analyses are limited to one particular BDP ligand (Figure 1, R=H) structure. We note that substitutions of this ligand (R=carboxamides), the use of chelates with large bite angles, or phosphite groups may affect the spectroscopic and kinetic details.

The data reported herein indicate that at low temperatures, modest CO pressures, and without H_2 present, acyl dicarbonyl complexes form rapidly and with thermodynamic preference over the intermediary alkyl and acyl monocarbonyl complexes. Indeed, alkyl and acyl monocarbonyl complexes only appear under conditions where dissolved CO becomes nearly completely depleted. A notable exception occurs with *trans*-1-phenyl-1,3-butadiene as the substrate; intramolecular η^3-coordination competes with bimolecular CO association in this case. The data compellingly demonstrate that for simple α-olefins (styrene, octene, allyl cyanide), thermodynamics prefer linear acyl dicarbonyls over branched, but that kinetics generally favor the branched isomers. With vinyl acetate and *trans*-1-phenyl-1,3-butadiene, analysis is complicated by β-acetoxy elimination and by formation of stable η^3-allyls, respectively.

High pressure NMR equipment, such as the WiHP-NMR, enables informative examination of acyl formation and hydrogenolysis under actively mixed conditions. For *trans*-1-phenyl-1,3-butadiene, the kinetics of equilibration between η^3-allyl and acyl dicarbonyls can be probed directly. More significantly, single turnover experiments involving actively mixed gases at superambient pressures enable us to determine the selectivity of acyl dicarbonyl formation and hydrogenolysis steps independently. For allyl cyanide, the data demonstrate that the kinetically favored branched acyl dicarbonyl also reacts fastest with H_2.

The significance of this work is three-fold. First, it represents the broadest effort thus far to characterize catalyst intermediates that are relevant to one of the largest industrial applications of homogeneous, organotransition metal catalysts. Second, the data provide strong evidence that the kinetics and selectivities of forming off-cycle acyl dicarbonyl isomers under low temperature, non-catalytic conditions reflect the catalytic selectivities at higher temperatures. Finally, single turnover experiments performed at superambient pressures with active gas-liquid mixing and NMR detection constitute a powerful divide-and-conquer strategy to understanding the origins of catalytic activity and selectivity in hydroformylation. Such studies are discussed in more detail in Chapter 4.

3.4 Experimental Details

3.4.1 General Considerations

All manipulations were carried out under nitrogen using standard Schlenk, high vacuum, and glovebox techniques. All solvents and liquid reagents were degassed by at least three freeze-pump-thaw cycles unless otherwise noted. Dichloromethane and CD_2Cl_2 were distilled from

P_2O_5 and degassed. Tetrahydrofuran was distilled from sodium benzophenone ketyl and degassed. Vinyl acetate was dried over $CaCl_2$, vacuum-transferred, and degassed. Allyl cyanide (Sigma) was distilled under nitrogen, redistilled under vacuum, and degassed. *S*-Acetoxypropionyl chloride, 2-bromoethylacetate, and 1-octene were degassed. Butyllithium, acetyl chloride, benzoyl chloride, and $^{13}CH_3I$ (all from Sigma), were used as received. ^{13}CO was purchased from Cambridge Isotope Laboratories and used as received. 1:1 CO:H_2, CO, and H_2 were purchased from Airgas. [Rh(acac)$(CO)_2$] was used as received from Dow and stored in the glovebox. *trans*-1-Phenyl-1,3-butadiene synthesized as reported in the literature.[11]

Rh(acac)(BDP) and [Rh$(CO)_2$(BDP)]K (BDP = tetraphenyl bis(diazaphospholane) were synthesized and stored in the glovebox. Rh(H)$(CO)_2$(BDP) was synthesized as needed and used immediately. These complexes were synthesized as reported in the literature.[36]

Routine ^1H and ^{31}P NMR spectra were recorded on a Bruker AV-400 MHz spectrometer; ^{13}C, ^{19}F, and all reaction-monitoring and two-dimensional experiments were performed using Varian Inova-500 MHz or Unity-500 MHz spectrometers, or Bruker Avance-500 spectrometers. Proton spectra were referenced to residual protio solvent; an xref macro was used to reference ^{13}C and ^{31}P spectra to accompanying proton spectra.

3.4.2 Syntheses of Rhodium Complexes and Substrates

Rh(H)($^{13}CO)_2$(BDP): *Method A*: In the glovebox, 51 mg (50 μmol) of Rh(acac)(tetraphenyl BDP) was dissolved in 0.8 mL CH_2Cl_2 in a 5-mL pressure bottle. The pressure bottle was attached to a reactor head, removed from the glovebox, and connected to the Schlenk line and to a lecture bottle of ^{13}CO. The solution was frozen and the reactor evacuated. The solution was allowed to warm to room temperature; the valve to the gas tank was opened,

and the reactor was pressurized to 20 psi (the maximum delivery pressure of the lecture bottle). The valve to the gas tank was closed and the pressure bottle cooled with liquid nitrogen until the gauge pressure dropped below 10 psi. The valve to the gas tank was opened and quickly closed, and the solution and headspace were allowed to warm to room temperature. This allowed the ^{13}CO pressure in the lecture bottle to reach 40 psi. The reactor was then pressurized with 40 psi H_2 and allowed to stir in a 60 °C oil bath overnight. Conversion: 80%. Spectral data match the reports in the literature.[36]

Method B: A solution of $Rh(H)(CO)_2(BDP)$ was transferred to a dry, H_2 purged NMR tube. After cooling to 0 °C in an ice bath, the solution was purged for 3-5 minutes with ^{13}CO. Conversion: 95-100%. Spectral data match the reports in the literature.[36]

1-^{13}C-octene: To a Schlenk flask containing 3g (7.4 mmol) [$^{13}CH_3PPh_3$]I and 827 mg KO*t*Bu (7.2 mmol) was added 30 mL dry ether. This created a yellow suspension, which was stirred for two hours under nitrogen. Heptanal (1 mL, 7.2 mmol) was added via syringe. The suspension immediately became colorless and the solvent refluxed slightly. This mixture was stirred under nitrogen overnight, and then filtered and concentrated under reduced pressure. The product, a colorless oil, was removed from residual $Ph_3P=O$ by distillation. ^1H NMR (400.18 MHz, CD_2Cl_2, 24 °C): δ 5.83 ppm (m, 1H, -C*H*CH_2); δ 4.99 ppm (dddt, J_{HC} = 153.3 Hz, J_{HH} = 16.8, 1.8, 2 x 1.8 Hz, 1H, H_{trans}); δ 4.92 ppm (dddt, J_{HC} = 156.9 Hz, J_{HH} = 10.4, 2.0, 2 x 1.0 Hz, 1H, H_{cis}). For synthesis of [$^{13}CH_3PPh_3$]I, see Nozaki, K.; Sato, N.; Tonomura, Y.; Yasutomi, M.; Takaya, H.; Hiyama, T.; Matsubara, T.; Koga, N. *J. Am. Chem. Soc.* **1997**, *119*, 12779–12795.

3.4.3 General Procedure for NMR Experiments

A pressure reactor containing a 60 or 30 μM solution of $Rh(H)(CO)_2(BDP)$ was depressurized and refilled with 20 psi CO. It was connected via a cannula to an oven-dried septum-capped NMR tube equipped with a vent, and the pressure reactor/NMR tube system was purged with the desired gas (generally CO) for several minutes. The cannula was then used to transfer the solution to the NMR tube, and the tube was sealed with Parafilm. The NMR spectrometer was cooled to the desired temperature (actual temperature determined using a methanol standard), and initial spectra were taken. The sample was ejected from the spectrometer, and the desired alkene was added via a gastight syringe; the tube was inverted three times and quickly returned to the spectrometer. For kinetic experiments, the time elapsed between mixing and taking the first spectrum was recorded (typically less than one minute).

3.4.4 General Procedure for WiHP-NMRR Experiments

$Rh(H)(CO)_2(BDP)$ was prepared as reported and depressurized to 5 psig. The reactor was brought into a N_2-purged glovebox. The solution was added to a vial of triphenylphosphine oxide and 1,4-bistrimethylsilyl benzene (^{31}P and ^{1}H internal standards, respectively). The contents were pulled into a threaded, gas-tight syringe (syringe one). The vial was rinsed with dichloromethane, which was pulled into a second syringe. The total volume of the two catalyst-containing syringes (catalyst and rinse) was 2.0 mL. The desired volume of substrate was put into the third syringe, and the fourth contained a dichloromethane rinse. The combined volume of syringes three and four was 500 μL.

The WiHP-NMRR was purged with nitrogen with three vent/refill cycles. The catalyst and rinse (syringes one and two) were injected into the high-pressure NMR tube. Gas was

circulated for 15 seconds to assure the solutions reached the NMR active region. The system was purged with CO with three vent/refill cycles. The spectrometer was set to the desired temperature and pressure of CO with an over pressure in the antecylinder. The initial spectra were acquired. Substrate and rinse (syringes three and four) were injected with the system under pressure with an over-pressure of N_2. Acquisition with circulation during NMR pulse sequence delays was started. The time between injection and data collection was recorded.

3.4.5 General Procedure for Low-Temperature Catalytic Experiments

In a N_2-purged glovebox, 0.015 mmol Rh(acac)(BDP) was dissolved in 950 μL dichloromethane and combined with 50 μL (0.3 mmol) diphenylmethane (as internal standard) in a pressure bottle. The reactor head was attached and removed from the glovebox. The system was pressurized and vented three times with synthesis gas. The reactor was pressurized to 140 psig 1:1 H_2/CO and stirred in 60 °C oil bath for three hours. The reactor was removed from the oil bath, cooled to room temperature, and placed in ice bath. It was vented and 0.3 mmol substrate was injected via gastight syringe. The system was pressurized and vented three times with synthesis gas, then finally pressurized to 30 psig and reacted in ice bath for 3 hours. The reactor was vented and the crude mixture was analyzed by ^{1}H NMR spectroscopy.

3.4.6 Control Experiment for [Rh(OAc)] to [Rh(acac)]

In a N_2-purged glovebox, 0.041 mmol $[Rh(COD)Cl]_2$ and 0.085 mmol BDP were dissolved in 3.0 mL dichloromethane and allowed to stir overnight. The solution was analyzed by NMR spectroscopy in a J. Young tube and brought back into the glovebox. Silver acetate (0.20 mmol) was added, the mixture was stirred for 5 minutes, filtered, and analyzed by NMR

spectroscopy. In the glovebox, 0.120 mmol acetylacetone was added and the resulting solution was analyzed by NMR spectroscopy.

3.4.7 Tabulated NMR Data

Vinyl acetate					
Nucleus	*Complex*	*Assignment*	*δ (ppm)*	*J_{CRh} (Hz)*	*J_{CP} (Hz)*
^{13}C	**7b**	acyl C=O	232.1	90	21.5
		methine	86.2	2.1	33.8
		methyl	14.6	-	-
	7b'	acyl C=O	236.2	87.8	21.7
		methine	83.9	2.7	36.7
		methyl	15.7	-	-
	7l	acyl C=O	232.5	18.3	79.8
		methylene	60.2	2.1	33.9
		methyl	10	-	-
Nucleus	*Complex*	*Assignment*	*δ (ppm)*	*J_{PRh} (Hz)*	*J_{PP} (Hz)*
^{31}P	**7b$_{va}$**	P_{ax}	69.5	81	19
		P_{eq}	60.4	152	19
	7b'$_{va}$	P_{ax}	68.5	80	17
		P_{eq}	57.8	167	17
	7l$_{va}$	P_{ax}	70.1	82	21
		P_{eq}	62.4	172	21
	5b$_{va}$	P_{ax}	74.8	83	17
		P_{eq}	53.9	159	17
	6b$_{va}$	P_{trans}	78.5	107	24
		P_{cis}	54.6	221	24
	4b*$_{va}$	P_{trans}	83.2	256	27
		P_{cis}	67.7	129	27
	4b$_{va}$	P_{trans}	82.6	101	28
		P_{cis}	39.2	213	28
Nucleus	*Complex*	*Assignment*	*δ (ppm)*	*mult.*	*J (Hz)*
^{1}H	**7b$_{va}$**	methine	4.14	q	6.5
		methyl	0.77	d	6.5
	7b'$_{va}$	methine	4.38	q	6.9
		methyl	0.73	d	6.9
	7l$_{va}$	methyl	0.5	t	6.9
		methylene	1.67	dq	18.2, 6.9
			2.61	dq	18.2, 6.9
	5b$_{va}$	methine	4.70	-	-
		methyl	1.37	dd	8, 7
	4b$_{va}$	methine	4.69	-	-
		methyl	1.58	dd	6.5
	4b*$_{va}$	methine	4.19	m, broad	-
Allyl cyanide					
Nucleus	*Complex*	*Assignment*	*δ (ppm)*	*J_{PRh} (Hz)*	*J_{PP} (Hz)*
^{31}P	**7l$_{ac}$**	P_{ax}	70.4	82	21
		P_{eq}	63.1	173	21
Nucleus	*Complex*	*Assignment*	*δ (ppm)*	*mult.*	*J (Hz)*
^{1}H	**7l$_{ac}$**	γ-methylene	2.74	dt	17.9, 7.3
			1.65	ddd	17.9, 7,7, 5.0
		β-methylene	1.17	m	-
		α-methylene	1.5	m	-

Table 3-2. Tabulated NMR data for complexes formed in the reactions of 1 with vinyl acetate and allyl cyanide.

1-octene					
Nucleus	*Complex*	*Assignment*	*δ (ppm)*	*J_{PRh} (Hz)*	*J_{PP} (Hz)*
^{31}P	**7l$_{oct}$**	P_{ax}	69.1	80	16
		P_{eq}	59.3	171	16
	7b$_{oct}$	P_{ax}	68.7	81	15
		P_{eq}	59.5	173	15
	5b$_{oct}$	P_{trans}	70.8	203	68
		P_{cis}	67.4	152	68
	4b$_{oct}$	P_{trans}	63.2	183	40
		P_{cis}	57.6	181	40
Nucleus	*Complex*	*Assignment*	*δ (ppm)*	*mult.*	*J (Hz)*
^{1}H	**7l$_{oct}$**	β-methylene	2.59	m	-
			1.56	m	-
	7b$_{oct}$	methyl	0.37	d	6
Nucleus	*Complex*	*Assignment*	*δ (ppm)*	*J_{CRh} (Hz)*	*J_{CP} (Hz)*
^{13}C	**7l$_{oct}$**	acyl C=O	232.2	18.7	81.1
		β-methylene	67.3	-	32.4
***trans*-1-phenyl-1,3-butadiene** (spectra acquired at 0 °C)					
Nucleus	*Complex*	*Assignment*	*δ (ppm)*	*J_{PRh} (Hz)*	*J_{PP} (Hz)*
^{31}P	**7b$_{diene}$**	P_{ax}	68.93	81.3	16.3
		P_{eq}	60.81	172.3	16.3
	7b'$_{diene}$	P_{ax}	66.96	81.2	14.6
		P_{eq}	59.07	172.3	14.5f
	4b*$_{diene}$	P_{cis}	78.29	147.8	-
		P_{trans}	48.12	190	-
Nucleus	*Complex*	*Assignment*	*δ (ppm)*	*mult.*	*J (Hz)*
^{1}H	**7b$_{diene}$**	methyl	0.7	d	6.5
		methine	3.07	dq	9.2, 6.4
		3-vinyl	5.92	dd	15.9. 9.2
		4-vinyl	6.42	d	15.9
	7b'$_{diene}$	methyl	1.02	d	7
		methine	3.41	dq	8.6, 6.9
		3-vinyl	5.64	dd	16.0, 8.6
		4-vinyl	6.22	d	16
	4b*$_{diene}$	methyl	1.57	m	-
		CHMe-allyl	1.72	m	-
		meso	5.34	m	-
		CHPh-allyl	3.82	dd	9.9, 6.9
Nucleus	*Complex*	*Assignment*	*δ (ppm)*	*J_{CRh} (Hz)*	*J_{CP} (Hz)*
^{13}C	**7b$_{diene}$**	methine	70.8	-	32.7
	7b'$_{diene}$	methine	70.8	(baseline)	(baseline)
	4b*$_{diene}$	methyl	21.24	(mult. unresolved)	(mult. unresolved)
		CHMe-allyl	38.76	(mult. unresolved)	(mult. unresolved)
		CHPh-allyl	72.40	(mult. unresolved)	(mult. unresolved)

Table 3-3. Tabulated NMR data for complexes formed in the reactions of 1 with 1-octene and *trans*-1-phenyl-1,3-butadiene.

3.5 References

(1) Agbossou, F.; Carpentier, J.-F.; Mortreux, A. Asymmetric Hydroformylation. *Chem. Rev.* **1995**, *95*, 2485–2506.

(2) Franke, R.; Selent, D.; Börner, A. Applied Hydroformylation. *Chem. Rev.* **2012**, *112*, 5675–5732.

(3) van Leeuwen, P. W. N. M.; Claver, C. *Rhodium Catalyzed Hydroformylation*; Kluwer Academic Publishers: Dordrecht, The Netherlands 2000.

(4) Wiese, K.-D.; Obst, D. In *Top. Organomet. Chem.*; Beller, M., Ed. 2006; Vol. 18, p 1–33.

(5) Botteghi, C.; Paganelli, S.; Schionato, A.; Marchetti, M. The asymmetric hydroformylation in the synthesis of pharmaceuticals. *Chirality* **1991**, *3*, 355–369.

(6) Adint, T. T.; Wong, G. W.; Landis, C. R. Libraries of Bisdiazaphospholanes and Optimization of Rhodium-Catalyzed Enantioselective Hydroformylation. *J. Org. Chem.* **2013**, *78*, 4231–4238.

(7) Clark, T. P.; Landis, C. R.; Freed, S. L.; Klosin, J.; Abboud, K. A. Highly Active, Regioselective, and Enantioselective Hydroformylation with Rh Catalysts Ligated by Bis-3,4-diazaphospholanes. *J. Am. Chem. Soc.* **2005**, *127*, 5040–5042.

(8) Klosin, J.; Landis, C. R. Ligands for Practical Rhodium-Catalyzed Asymmetric Hydroformylation. *Acc. Chem. Res.* **2007**, *40*, 1251–1259.

(9) McDonald, R. I.; Wong, G. W.; Neupane, R. P.; Stahl, S. S.; Landis, C. R. Enantioselective Hydroformylation of N-Vinyl Carboxamides, Allyl Carbamates, and Allyl Ethers Using Chiral Diazaphospholane Ligands. *J. Am. Chem. Soc.* **2010**, *132*, 14027–14029.

(10) Watkins, A. L.; Hashiguchi, B. G.; Landis, C. R. Highly Enantioselective Hydroformylation of Aryl Alkenes with Diazaphospholane Ligands. *Org. Lett.* **2008**, *10*, 4553–4556.

(11) Watkins, A. L.; Landis, C. R. Regioselective Rhodium-Catalyzed Hydroformylation of 1,3-Dienes to Highly Enantioenriched β,γ-Unsaturated Aldehyes with Diazaphospholane Ligands. *Org. Lett.* **2010**, *13*, 164–167.

(12) Heck, R. F.; Breslow, D. S. The Reaction of Cobalt Hydrotetracarbonyl with Olefins. *J. Am. Chem. Soc.* **1961**, *83*, 4023–4027.

(13) Casey, C. P.; Paulsen, E. L.; Beuttenmueller, E. W.; Proft, B. R.; Matter, B. A.; Powell, D. R. Electronically Dissymmetric DIPHOS Derivatives Give Higher n:i Regioselectivity in Rhodium-Catalyzed Hydroformylation Than Either of Their Symmetric Counterparts. *J. Am. Chem. Soc.* **1999**, *121*, 63–70.

(14) Casey, C. P.; Paulsen, E. L.; Beuttenmueller, E. W.; Proft, B. R.; Petrovich, L. M.; Matter, B. A.; Powell, D. R. Electron Withdrawing Substituents on Equatorial and Apical Phosphines Have Opposite Effects on the Regioselectivity of Rhodium Catalyzed Hydroformylation. *J. Am. Chem. Soc.* **1997**, *119*, 11817–11825.

(15) Casey, C. P.; Petrovich, L. M. (Chelating diphosphine)rhodium-Catalyzed Deuterioformylation of 1-Hexene: Control of Regiochemistry by the Kinetic Ratio of Alkylrhodium Species Formed by Hydride Addition to Complexed Alkene. *J. Am. Chem. Soc.* **1995**, *117*, 6007–6014.

(16) Casey, C. P.; Whiteker, G. T.; Melville, M. G.; Petrovich, L. M.; Gavney, J. A.; Powell, D. R. Diphosphines with natural bite angles near 120.degree. increase selectivity for n-

aldehyde formation in rhodium-catalyzed hydroformylation. *J. Am. Chem. Soc.* **1992**, *114*, 5535–5543.

(17) Freixa, Z.; van Leeuwen, P. W. N. M. Bite angle effects in diphosphine metal catalysts: steric or electronic? *Dalton Trans.* **2003**, 1890–1901.

(18) Horiuchi, T.; Shirakawa, E.; Nozaki, K.; Takaya, H. Mechanistic Aspects of Asymmetric Hydroformylation of Olefins Catalyzed by Chiral Phosphine–Phosphite–Rhodium(I) Complexes. *Organometallics* **1997**, *16*, 2981–2986.

(19) Kranenburg, M.; van der Burgt, Y. E. M.; Kamer, P. C. J.; van Leeuwen, P. W. N. M.; Goubitz, K.; Fraanje, J. New Diphosphine Ligands Based on Heterocyclic Aromatics Inducing Very High Regioselectivity in Rhodium-Catalyzed Hydroformylation: Effect of the Bite Angle. *Organometallics* **1995**, *14*, 3081–3089.

(20) Kubis, C.; Baumann, W.; Barsch, E.; Selent, D.; Sawall, M.; Ludwig, R.; Neymeyr, K.; Hess, D.; Franke, R.; Börner, A. Investigation into the Equilibrium of Iridium Catalysts for the Hydroformylation of Olefins by Combining In Situ High-Pressure FTIR and NMR Spectroscopy. *ACS Catalysis* **2014**, *4*, 2097–2108.

(21) Lazzaroni, R.; Raffaelli, A.; Settambolo, R.; Bertozzi, S.; Vitulli, G. Regioselectivity in the rhodium-catalyzed hydroformylation of styrene as a function of reaction temperature and gas pressure. *J. Mol. Catal.* **1989**, *50*, 1–9.

(22) Lazzaroni, R.; Settambolo, R.; Uccello-Barretta, G. .beta.-Hydride Elimination and Regioselectivity in the Rhodium-Catalyzed Hydroformylation of Open Chain Unsaturated Ethers. *Organometallics* **1995**, *14*, 4644–4650.

(23) van der Slot, S. C.; Duran, J.; Luten, J.; Kamer, P. C. J.; van Leeuwen, P. W. N. M. Rhodium-Catalyzed Hydroformylation and Deuterioformylation with Pyrrolyl-Based

Phosphorus Amidite Ligands: Influence of Electronic Ligand Properties. *Organometallics* **2002**, *21*, 3873–3883.

(24) van der Slot, S. C.; Kamer, P. C. J.; van Leeuwen, P. W. N. M.; Iggo, J. A.; Heaton, B. T. Mechanistic Studies of the Hydroformylation of 1-Alkenes Using a Monodentate Phosphorus Diamide Ligand. *Organometallics* **2001**, *20*, 430–441.

(25) van der Veen, L. A.; Boele, M. D. K.; Bregman, F. R.; Kamer, P. C. J.; van Leeuwen, P. W. N. M.; Goubitz, K.; Fraanje, J.; Schenk, H.; Bo, C. Electronic Effect on Rhodium Diphosphine Catalyzed Hydroformylation: The Bite Angle Effect Reconsidered. *J. Am. Chem. Soc.* **1998**, *120*, 11616–11626.

(26) van der Veen, L. A.; Keeven, P. H.; Schoemaker, G. C.; Reek, J. N. H.; Kamer, P. C. J.; van Leeuwen, P. W. N. M.; Lutz, M.; Spek, A. L. Origin of the Bite Angle Effect on Rhodium Diphosphine Catalyzed Hydroformylation. *Organometallics* **2000**, *19*, 872–883.

(27) del Río, I.; Pàmies, O.; van Leeuwen, P. W. N. M.; Claver, C. Mechanistic study of the hydroformylation of styrene catalyzed by the rhodium/BDPP system. *J. Organomet. Chem.* **2000**, *608*, 115–121.

(28) Tonks, I. A.; Froese, R. D.; Landis, C. R. Very Low Pressure Rh-Catalyzed Hydroformylation of Styrene with (S,S,S-Bisdiazaphos): Regioselectivity Inversion and Mechanistic Insights. *ACS Catalysis* **2013**, *3*, 2905–2909.

(29) Watkins, A. L.; Landis, C. R. Origin of Pressure Effects on Regioselectivity and Enantioselectivity in the Rhodium-Catalyzed Hydroformylation of Styrene with (*S,S,S*)-BisDiazaphos. *J. Am. Chem. Soc.* **2010**, *132*, 10306–10317.

(30) Brown, J. M.; Kent, A. G. Structure and dynamics of the stable rhodium-acyl complex formed during hydroformylation. *J. Chem. Soc., Chem. Commun.* **1982**, 723–725.

(31) Brown, J. M.; Kent, A. G. Structural characterisation in solution of intermediates in rhodium-catalysed hydroformylation and their interconversion pathways. *J. Chem. Soc. Perk. Trans. 2* **1987**, 1597–1607.

(32) Schmidt, S.; Baráth, E.; Prommnitz, T.; Rosendahl, T.; Rominger, F.; Hofmann, P. Synthesis and Characterization of Crotyl Intermediates in Rh-Catalyzed Hydroformylation of 1,3-Butadiene. *Organometallics* **2014**, *33*, 6018–6022.

(33) Abkai, G.; Schmidt, S.; Rosendahl, T.; Rominger, F.; Hofmann, P. Iridium Models of Rhodium Intermediates in Hydroformylation Catalysis: Isolation and Molecular Structures of Fluxional ae and ee Isomers. *Organometallics* **2014**, *33*, 3212–3214.

(34) Chan, A. S. C.; Shieh, H.-s. A mechanistic study of the homogeneous catalytic hydroformylation of formaldehyde: synthesis and characterization of model intermediates. *Inorg. Chim. Acta* **1994**, *218*, 89–95.

(35) Deutsch, P. P.; Eisenberg, R. Synthesis and reactivity of propionyliridium complexes. Competitive reductive elimination of carbon-hydrogen and hydrogen-hydrogen bonds from a propionyldihydridoiridium complex. *Organometallics* **1990**, *9*, 709–718.

(36) Nelsen, E. R.; Landis, C. R. Interception and Characterization of Alkyl and Acyl Complexes in Rhodium-Catalyzed Hydroformylation of Styrene. *J. Am. Chem. Soc.* **2013**, *135*, 9636–9639.

(37) Adint, Tyler. PhD Dissertation, University of Wisconsin–Madison, 2014.

(38) The formation of acyl dicarbonyls appears to be thermodynamically favorable under these conditions, but this process requires consumption of one equivalent of CO from solution. The concentration of **1** at the beginning of the reaction exceeds the estimated [CO] in solution and, because gas-liquid mixing is slow, the reaction becomes starved of gas as acyl

dicarbonyl complexes are produced. This enables observation of the alkyl complexes, which do not require additional CO from solution.

(39) Note: this designation should not be taken to imply that **4b$_{va}$** and **7b$_{va}$** have the same absolute stereochemistry; we are not currently able to determine the configuration of any of these species.

(40) Cheng, J. C. Y.; Daves, G. D. Control of organopalladium glycal adduct decomposition reactions. Role of conformational restriction and .beta.-carbon substituents. *Organometallics* **1986**, *5*, 1753–1755.

(41) Heck, R. F. The palladium-catalyzed arylation of enol esters, ethers, and halides. A new synthesis of 2-aryl aldehydes and ketones. *J. Am. Chem. Soc.* **1968**, *90*, 5535–5538.

(42) Ogiwara, Y.; Tamura, M.; Kochi, T.; Matsuura, Y.; Chatani, N.; Kakiuchi, F. Ruthenium-Catalyzed Ortho-Selective C–H Alkenylation of Aromatic Compounds with Alkenyl Esters and Ethers. *Organometallics* **2014**, *33*, 402–420.

(43) Williams, B. S.; Leatherman, M. D.; White, P. S.; Brookhart, M. Reactions of Vinyl Acetate and Vinyl Trifluoroacetate with Cationic Diimine Pd(II) and Ni(II) Alkyl Complexes: Identification of Problems Connected with Copolymerizations of These Monomers with Ethylene. *J. Am. Chem. Soc.* **2005**, *127*, 5132–5146.

(44) Yu, J. Y.; Kuwano, R. Rhodium-catalyzed cross-coupling of organoboron compounds with vinyl acetate. *Angew. Chem. Int. Ed. Engl.* **2009**, *48*, 7217–7220.

(45) Zhang, Z.; Lu, X.; Xu, Z.; Zhang, Q.; Han, X. Role of Halide Ions in Divalent Palladium-Mediated Reactions: Competition between β-Heteroatom Elimination and β-Hydride Elimination of a Carbon−Palladium Bond. *Organometallics* **2001**, *20*, 3724–3728.

(46) Zhu, G.; Lu, X. Reactivity and Stereochemistry of .beta.-Heteroatom Elimination. A Detailed Study through a Palladium-Catalyzed Cyclization Reaction Model. *Organometallics* **1995**, *14*, 4899–4904.

(47) Komiya, S.; Yamamoto, A. C-O bond cleavage in alkenyl carboxylates promoted by transition-metal hydrides. *J. Chem. Soc., Chem. Commun.* **1974**, 523–524.

(48) Komiya, S.; Yamamoto, A. Carbon−oxygen bond cleavage of alkenyl carboxylate promoted by transition metal hydrides. *J. Organomet. Chem.* **1975**, *87*, 333–339.

(49) Abrams, M. L.; Foarta, F.; Landis, C. R. Asymmetric Hydroformylation of Z-Enamides and Enol Esters with Rhodium-Bisdiazaphos Catalysts. *J. Am. Chem. Soc.* **2014**, *136*, 14583–14588.

(50) Fryzuk, M. D. Synthesis and characterization of substituted-allyl-rhodium complexes incorporating bidentate phosphine and phosphinite ligands. *Inorg. Chem.* **1982**, *21*, 2134–2139.

(51) Beach, N. J.; Knapp, S. M. M.; Landis, C. R. A reactor for high-throughput high-pressure nuclear magnetic resonance spectroscopy. *Rev. Sci. Instrum.* **2015**, *86*, 104101–104109.

(52) Hoops, S.; Sahle, S.; Gauges, R.; Lee, C.; Pahle, J.; Simus, N.; Singhal, M.; Xu, L.; Mendes, P.; Kummer, U. COPASI—a COmplex PAthway SImulator. *Bioinformatics* **2006**, *22*, 3067–3074.

(53) The WiHPP-NMR uses dinitrogen for injection of substrate. When this experiment was performed, this resulted in some initial degassing of dissolved CO, such that even with active mixing there is a brief time of approximately 2 minutes where the dissolved CO concentration was lower than the equilibrium value. As a result the ratio of acyl dicarbonyls observed does not represent the limiting kinetic selectivity. Additionally, the observed b:l = 5:1

ratio observed may be lower than the observed catalytic product selectivity (b:l = 12:1) due to faster hydrogenolysis of **7b** over **7l** (see section 3.2.3.3 and Chapter 4).

Chapter 4

Unexpected CO Dependenices, Catalyst Speciation, and Single Turnover Hydrogenolysis Studies of Hydroformylation *via* High Pressure NMR Spectroscopy

Portions of this work were published as Brezny, A. C.; Landis, C. R. Unexpected CO Dependencies, Catalyst Speciation, and Single Turnover Hydrogenolysis Studies of Hydroformylation via High Pressure NMR Spectroscopy. *J. Am. Chem. Soc.* **2017**, *139*, 2778-2785.

4.1 Introduction

In 1961, Heck and Breslow proposed a mechanism for cobalt-catalyzed hydroformylation that remains generally accepted for rhodium systems (Scheme 4-1).1 Although this mechanism outlines the sequence of transformations that constitute the overall reaction, only more detailed kinetic and extra-kinetic analyses can reveal the origins of regioselectivity, enantioselectivity, and rate control. Such analyses include applications of isotopic labels, interception and characterization of catalyst intermediates, *operando* examination of catalyst speciation, and kinetic studies of the catalytic reaction. For example, deuteroformylation studies probe the reversibility of the formation of Rh-alkyls (**4**). With some catalysts and reaction conditions, this step is irreversible, thus indicating that selectivity is fixed at the alkene insertion step.[2-11]

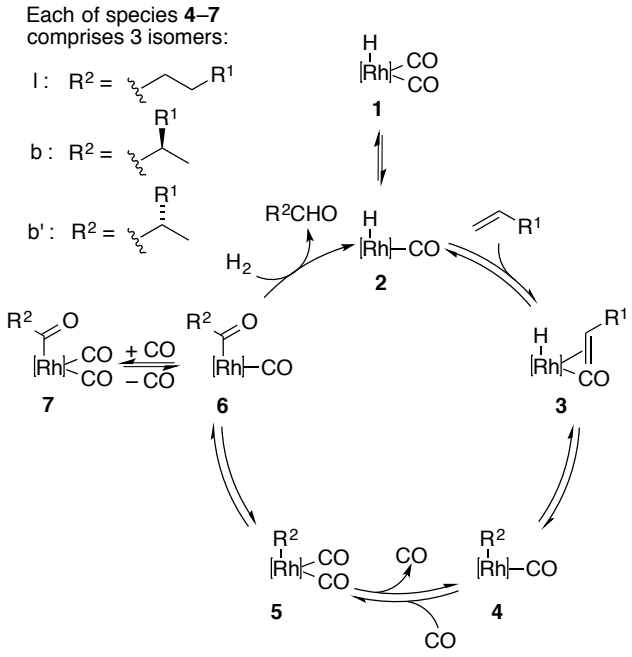

Scheme 4-1. General mechanism for hydroformylation.

However, in Rh(BDP)-catalyzed hydroformylation, the alkyl intermediates are known to isomerize for a variety of olefin substrates. Reversible formation of **4** has been demonstrated

under catalytic conditions by analysis of product isotope distributions in the presence of D_2 and CO. Under non-catalytic conditions, the acyl dicarbonyl isomers (**7**) have been intercepted, characterized, and observed to interconvert.[11-13] According to the Heck and Breslow mechanism, such interconversion must proceed *via* alkyl species. In such cases, the product selectivity cannot be attributed to the control of a single elementary step.

In many studies of bisphosphine-modified rhodium catalysts for hydroformylation the rate laws can be classified as type-I or type-II as coined by van Leeuwen and Claver.[14] Characteristics of type-I kinetics include a rate law (eq 4-1) that is independent of $[H_2]$, first-order in [catalyst] and [alkene] and inhibited by [CO], and $RhH(CO)_2(L)_2$ is observed as the primary resting state. For type-II kinetics the reaction rate (eq 4-2) commonly exhibits a first-order dependence on $[H_2]$ and inhibition by [CO] with catalyst pooling in the form of $Rh(acyl)(CO)_2(L)_2$ **7** at high [alkene]. These observations are interpreted to mean that the overall rate is controlled by the rate of hydrogenolysis of **7**.

$$\text{Type-I Rate} = \frac{k[\text{cat}][\text{alkene}]}{[\text{CO}]} \qquad (4\text{-}1)$$

$$\text{Type-II Rate} = \frac{k[\text{cat}][H_2]}{[\text{CO}]} \qquad (4\text{-}2)$$

Of particular interest to the themes of this Chapter are recent studies of hydroformylation catalysts that feature elegant, quantitative, and simultaneous analysis of catalyst speciation and reaction rates.[15-17] For example, Vogt's work combined kinetic and *operando* IR spectroscopic studies of the hydroformylation of 3,3-dimethylbut-1-ene, catalyzed by rhodium complexes of monodentate phosphites. This study demonstrated that (1) catalyst primarily populates the acyl dicarbonyl **7** with hydrido dicarbonyl **1** appearing in greater concentration as the alkene is consumed; (2) at high alkene concentrations the catalytic reaction obeys type-II kinetics with the rate of aldehyde appearance strictly correlating with the steady-state concentration of acyl

dicarbonyl **7**; (3) the branched:linear ratio of the acyl dicarbonyl species remained in the range of 1:1-2 over the 298–342 K while the branched:linear ratio of the aldehyde product remained constant over an individual experiment and ranged from ca. 1:6-22 over a 320–370 K temperature range.[16,18] These data were interpreted as indicating that hydrogenolysis of the linear acyl dicarbonyl **7** is faster than the branched acyl dicarbonyl and that "the rate-limiting step for both the linear and branched aldehydes was shown to be the hydrogenolysis of the Rh-acyl species."[19]

Selent and coworkers also studied the hydroformylation of 3,3-dimethylbut-1-ene using a different bulky monophosphite ligated rhodium catalyst. This work utilizes a Michaelis-Menten analysis in which "the rate of product formation is limited by the hydrogenolytic step of the mechanism over the entire conversion range."[17] Garland's examination of the hydroformylation of styrene by an unmodified rhodium catalyst also led to a similar conclusion, "hydrogenolysis of the two acyl rhodium intermediates represents the rate-limiting step for aldehyde formation."[15]

However the observed off-cycle acyls **7** do not lie on the catalytic cycle, which raises a fundamental question that is general to all catalytic reactions: to what extent is the catalytic rate controlled by conversion of off-cycle species to the product? Because the acyl dicarbonyl species are present as both linear and branched isomers, it is important to consider the role of off-cycle species in the control of regioselectivity.

Herein we report kinetic studies of the non-asymmetric hydroformylation of styrene as catalyzed by racemic Rh(BDP) complexes. Our report begins with a summary of prior *operando* studies of hydroformylation kinetics and catalyst speciation. We then describe new catalytic results obtained by *operando* NMR using the Wisconsin High Pressure NMR Reactor (WiHP-NMRR) that demonstrate unexpected overall kinetics. The data presentation concludes with

kinetic characterization of the non-catalytic hydrogenolysis of linear and branched isomers and the development of a robust kinetic model that describes both catalytic and non-catalytic kinetic data. We finish with an analysis of direct vs. shunted pathways to product formation that demonstrates the confusion that may result when a catalyst primarily accumulates as off-cycle species.

4.2 Results and Discussion

4.2.1 Operando Spectroscopy and Hydroformylation

The two most common *operando* methods for study of catalytic hydroformylation are IR and NMR spectroscopy. IR is a natural choice due to the relatively high sensitivity (detection of less than 1 mM concentrations) afforded by the strongly absorbing C–O and M–H stretches, the lower expense of IR spectrometers, and the development of principal component decompositions that enable the extraction of spectra for individual components from complex spectra. Excellent examples of combined kinetic/operando IR spectroscopic studies of hydroformylation are provided by recent work of Garland, Selent, and Vogt (vide supra).[15-17,20-22] NMR methods, while less sensitive and more expensive, bring tools for elucidating detailed structures, simple correlation of peak areas with concentrations, and applicability for cases where IR spectra are crowded or structurally insensitive. The Wisconsin High Pressure NMR Reactor (WiHP-NMRR) enables the observation of reactions under known, constant gas concentration with active gas-liquid mixing and injection of reagents under pressure.[23] Previously we have shown that key intermediates can be intercepted and rigorously characterized by NMR under low-

pressure conditions; these assignments facilitate the interpretation of data collected by operando NMR methods.[12-13]

4.2.1.1 Operando Study of the Catalytic Hydroformylation of Styrene as Studied by WiHP-NMRR at 313 K

In our previous studies of the Rh(BDP)-catalyzed hydroformylation of styrene, several alkyl and acyl on- and off-cycle intermediates were characterized in the absence of H_2, under low CO pressure, without active gas-liquid mixing, and at low temperature.[12] Formation of the branched acyl dicarbonyl (**7b**) is kinetically favored, but this species isomerizes to the thermodynamically preferred linear species (**7l**) under these CO-starved conditions. For quantitative analysis of the kinetic selectivity, see Appendix A. These studies demonstrate intrinsic kinetic and thermodynamic selectivities for acyl formation but do not necessarily apply to catalytic conditions.

Data collected for catalytic hydroformylation by operando ^{1}H NMR spectroscopy at 313 K and 20 psia H_2 are presented in Figure 4-1. The data of plots B and C are consistent with type-II kinetics[14] for which the resting state is an acyl dicarbonyl (**7**) and the reaction rate is dependent on [H_2] with inhibition by CO (see Appendix A for the dependence of the rate on dihydrogen concentration). Thus, increasing the CO pressure from 115 psia CO to 200 psia results in approximate halving of the reaction rate. However, the changes upon *decreasing* the CO pressure from 115 psia CO to 20 psia are unexpected: a dramatic *decrease* of both the reaction rate *and* regioselectivity is observed. Does the catalyst change resting state over the three different kinetic regimes represented?

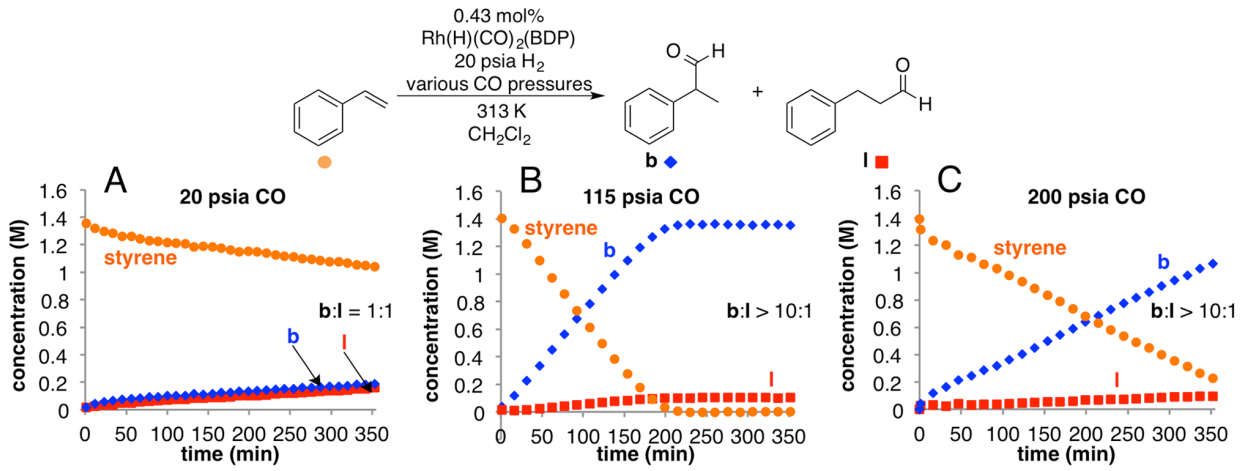

Figure 4-1. Effect of CO pressure on rates and selectivity in hydroformylation. Time course data were collected using the Wisconsin High Pressure NMR reactor (WiHP-NMRR) (1.4 M styrene, 6 mM $Rh(H)(CO)_2(BDP)$, 313 K, 20 psia H_2, and varied CO pressures: 20 psia CO (A), 115 psia CO (B), and 200 psia CO (C)).

The reactions described in Figure 4-1 use concentrations of catalyst that enable direct observation of catalyst speciation by $^{31}P\{^1H\}$ NMR spectroscopy. In these experiments, the branched and linear acyl dicarbonyl species are the primary catalyst resting states (Figure 4-2). Under low CO pressures (20 psia, plot A), rhodium pools primarily as the linear acyl dicarbonyl **7l**, but under higher CO pressures (115 and 200 psia, plots B and C), it sits as a ~3:1 **7b**:**7l** mixture. These data are consistent with thermodynamic control of the **7b**:**7l** ratio at the lowest CO pressure and kinetically controlled ratios at the two higher pressures. Low CO pressures allow sufficiently rapid interconversion of linear and branched acyls **7** such that an equilibrium distribution is attained. Previous non-catalytic studies established a strong thermodynamic preference for **7l** over **7b**, yielding a 33:1 ratio of **7l**:**7b** at –20 °C. For the catalytic conditions of Figures 4-1 and 4-2 it is reasonable that higher CO pressures suppress isomerization of the Rh-alkyls **4l** and **4b**, because CO trapping of **4** to ultimately to yield **6** is more efficient.

Additionally, isomerization by reversion of the acyl **6** to the alkyl **4** likely is slower at high pressure because such reversion requires CO dissociation.

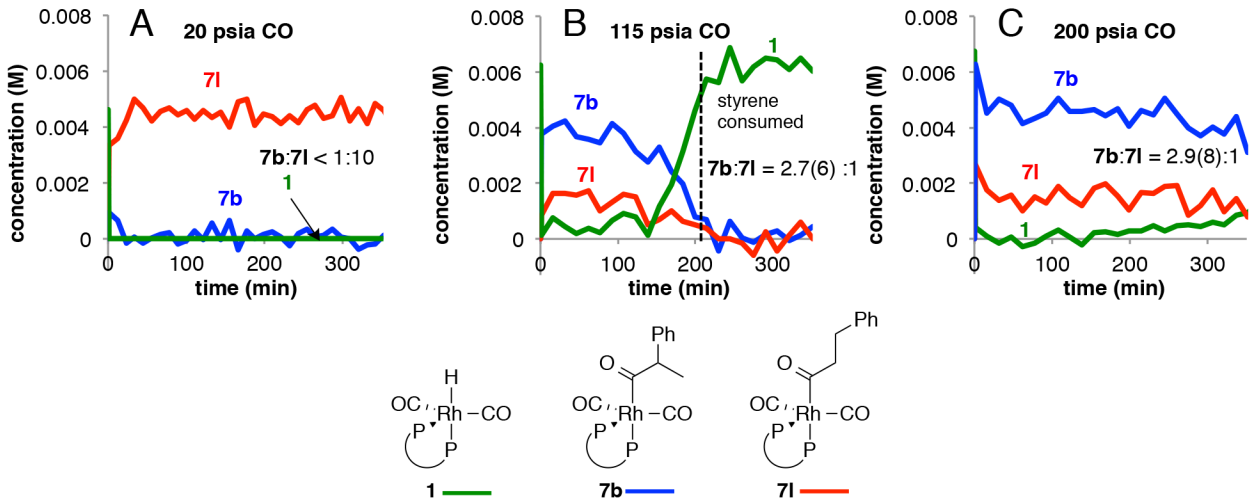

Figure 4-2. Catalyst speciation observed during hydroformylation reactions in the WiHP-NMRR under same conditions shown in Figure 4-1 (1.4 M styrene, 6 mM $Rh(H)(CO)_2(BDP)$, 313 K, 20 psia H_2, and varied CO pressure: 20 psia CO (A), 115 psia CO (B), and 200 psia CO (C)).

We have conducted deuteroformylation studies at 40 and 80 psia CO, the results of which are consistent with this interpretation: deuterium scrambling, hence alkyl isomerization, is inhibited by increased CO pressure and decreased temperatures (Table 4-1). The data in Figure 4-1 and Figure 4-2 reveal three key observations: (1) the rate law is not described fully by either type-I or type-II scenarios; (2) different conditions lead to large differences in rate and catalyst speciation; (3) the steady-state ratio of the acyls (**7b**:**7l**) does not equal the ratio of aldehyde products (**b**:**l**).

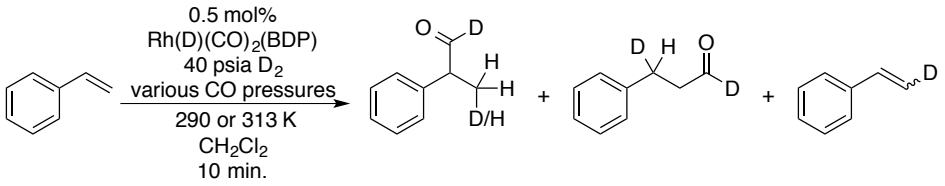

Temperature (K)	Pressure CO (psia)	Aldehydes : *d*-styrene
290 K	40	0.75 : 1
290 K	80	4.2 : 1
313 K	40	1:5 : 1
313 K	80	6.3 : 1

Table 4-1. Deuteroformylation of styrene at low conversion (<10%).

The difference in overall rates between the reactions at 115 and 200 psia CO most simply is attributed to CO inhibition consistent with type-II kinetics. The common interpretation is that acyl dicarbonyl species (**7**) or hydrido dicarbonyl (**1**) must lose one ligand to re-enter the cycle, thus at higher pressures of CO, the rate is slower.

The dramatic differences in rate between the low CO pressure (20 psia, Figure 4-1A) versus the higher pressure reactions (115 psia or 200 psia, Figure 4-1B,C) clearly correlate with changes in the catalyst resting state. Interestingly, at low (20 psia) CO pressures the ratio **7l**:**7b** is ~20:1 but yields a 1:1 b:l ratio of product aldehydes. *Only at low CO pressures* do the catalytic data superficially correspond to Curtin-Hammett kinetics, in which there is rapid isomerization between the acyl dicarbonyls **7** and the rates of product formation are described by eq 4-3–4-4 (Figure 4-3).

$$\frac{d[\mathrm{b}]}{dt} = \mathrm{k_b}[\mathbf{7b}] \qquad (4\text{-}3)$$

$$\frac{d[\mathrm{l}]}{dt} = \mathrm{k_l}[\mathbf{7l}] \qquad (4\text{-}4)$$

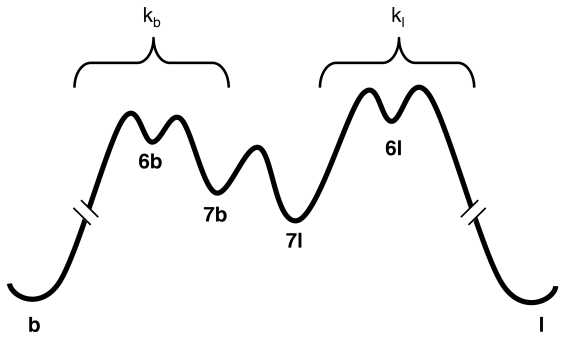

Figure 4-3. A Curtin-Hammett free energy scheme that may describe catalytic data in low [CO] regime.

In order to explain the 1:1 ratio of linear and branched aldehyde products, **7b** must undergo faster hydrogenolysis than **7l**.[24] Strictly speaking, at the higher pressures of Figures 4-1B, 4-1C, 4-2B, and 4-2C, Curtin-Hammett behavior does not explain the regioselectivity because **7b** and **7l** are not in equilibrium. Regardless of whether or not the acyls are in equilibrium, equations 3 and 4 can still be true under conditions of turnover-limiting hydrogenolysis.

4.2.1.2 Direct Measurement of the Kinetics of Hydrogenolysis of Acyl Dicarbonyls 7 at 290K

In Vogt's analysis of hydroformylation,[16] the appearance of branched and linear products was modeled by equations 3 and 4. The steady state concentrations of **7b** and **7l** were determined by direct *operando* observation; the apparent rate constants k_b and k_l depend on [CO] and [H_2]. In order to evaluate the role of off-cycle species **7b** and **7l** in determining the reaction kinetics and selectivity, it is useful to know their intrinsic rates of hydrogenolysis. Therefore, we devised single turnover experiments that directly measure these rates.

In the WiHP–NMRR, a 1:1 mixture of **7b** and **7l** was formed in the absence of hydrogen by allowing 1 equivalent of styrene to react with hydride **1** at 310K and 18 psia of CO. When the **7b**:**7l** ratio reached approximately 1:1, the reaction was cooled to 290 K and additional CO and H_2 were added to the reactor with active gas–liquid mixing. Under these conditions the acyls produce the aldehyde products without any further interconversion of acyl dicarbonyl **7**, i.e. the initial concentrations of **7b** + **7b'** and **7l** correspond to the final concentrations of branched and linear aldehydes, respectively (Figure 4-4). We note that the minor branched diastereomer **7b'** is barely visible under these conditions and is not considered in our subsequent analysis. Temperatures lower than those in the catalytic experiments of Figure 4-1 and Figure 4-2 are necessary to slow the rate of hydrogenolysis for convenient monitoring by ^{1}H and ^{31}P NMR spectroscopies. Data were collected under three CO pressures (18, 35 and 70 psia CO) and a wide range of H_2 pressures ranging from 20 psia to 530 psia. As expected, based on the rate laws assuming a steady state approximation on **6** (eq 4-5–4-10), higher pressures of hydrogen increase the rate of hydrogenolysis, and CO inhibits the reaction. These data corroborate the hypothesis that **7b** undergoes hydrogenolysis faster than **7l**.

The data show that increasing pressures of H_2 effect saturation of the rate of hydrogenolysis. Such saturation indicates efficient competitive trapping of **6** by dihydrogen vs. reassociation of CO. In this limit, the rate of hydrogenolysis is controlled by the rate of CO dissociation from **7** (k_{1b} and k_{1l}, see Figure 4-5).

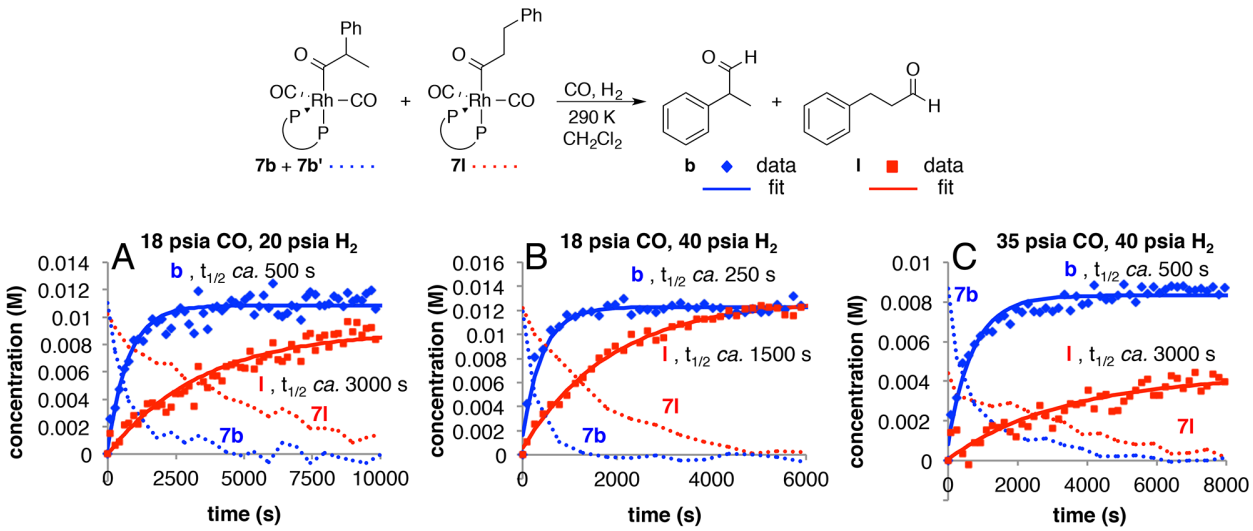

Figure 4-4. Single turnover experiments in the WiHP–NMRR. The branched acyl dicarbonyl undergoes hydrogenolysis faster than the linear isomer (CO loss and/or reaction with H_2). (~22 mM Rh(BDP) as 1:1 mixture of acyls, 290 K, varied CO and H_2 pressures: 18 psi CO, 20 psi H_2 (A); 18 psi CO, 40 psi H_2 (B); 35 psi CO, 40 psi H_2 (C)). The points indicate the experimental data and solid lines represent the modeled fits.

$$[\mathbf{6b}] = \frac{k_{1b}[\mathbf{7b}]}{k_{2b}[H_2] + k_{-1b}[CO]} \qquad (4\text{-}5)$$

$$\frac{d[\mathbf{b}]}{dt} = k_{2b}[\mathbf{6b}][H_2] \qquad (4\text{-}6)$$

$$\frac{d[\mathbf{b}]}{dt} = \frac{k_{2b}k_{1b}[\mathbf{7b}][H_2]}{k_{2b}[H_2] + k_{-1b}[CO]} \qquad (4\text{-}7)$$

$$[\mathbf{6l}] = \frac{k_{1l}[\mathbf{7l}]}{k_{2l}[H_2] + k_{-1l}[CO]} \qquad (4\text{-}8)$$

$$\frac{d[\mathbf{l}]}{dt} = k_{2l}[\mathbf{6l}][H_2] \qquad (4\text{-}9)$$

$$\frac{d[\mathbf{l}]}{dt} = \frac{k_{2l}k_{1l}[\mathbf{7l}][H_2]}{k_{2l}[H_2] + k_{-1l}[CO]} \qquad (4\text{-}10)$$

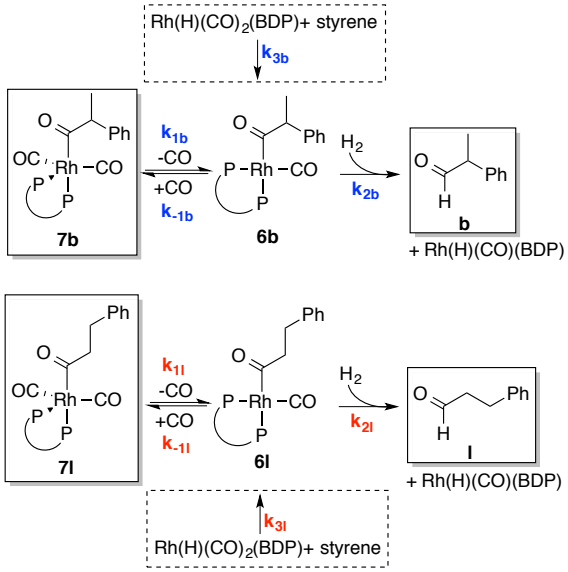

Figure 4-5. Kinetic model for hydrogenolysis of acyl dicabonyl complexes **7b** and **7l**. Species indicated with solid boxes are directly observable by NMR spectroscopy; reactions indicated with dashed boxes are only relevant to catalytic reactions.

Global modeling of all the empirical kinetic data for the single turnover hydrogenolysis experiments with the program COPASI,[25] in accordance with the kinetic model represented by equations 4-5–4-10, led to values for the rate constants k_{1b}, k_{1l}, k_{-1b}/k_{2b} and k_{-1l}/k_{2l} (Table 4-2). Because the acyl monocarbonyl species (**6b** and **6l**) are not observed by NMR, only the ratios k_{-1b}/k_{2b} and k_{-1l}/k_{2l} (but not the values of the individual rate constants) could be determined. Representative modeled fits are shown in Figure 4-4; for all modeled data, see Appendix A.

	value	standard deviation
k_{1b}	2.3 x10^{-2} (s^{-1})	1 x10^{-3}
k_{1l}	6.4 x10^{-3} (s^{-1})	5 x10^{-4}
k_{-1b}/k_{2b}	8.2	0.2
k_{-1l}/k_{2l}	10.5	0.3

Table 4-2. Computed rate constants for hydrogenolysis of acyl dicarbonyl complexes.

These data quantitatively show that CO loss from the branched acyl dicarbonyl is approximately four-fold faster than from the linear isomer. At equal concentrations of H_2 and CO, the branched acyl monocarbonyl (**6b**) is just eight times more likely to be trapped by CO than react with dihydrogen; the linear acyl monocarbonyl (**6l**) is ten times more likely to be trapped by CO. These data indicate only modest differences (factors of 4-5) in the hydrogenolysis rates of **7b** and **7l**. Application of these rates to catalytic data at 313 K cannot account for the mismatch between steady-state acyl concentrations and the aldehyde product distributions. In order to draw quantitative conclusions and because the rates of the single turnover experiments are too fast at 313 K, we chose to examine catalytic data at 290 K.

4.2.1.3 WiHP-NMRR Catalytic Hydroformylation at 290K

In order to compare the rates of non-catalytic hydrogenolysis with catalytic rates, *operando* NMR studies of the catalytic reaction were performed. Both the catalyst speciation and the rates of linear and branched aldehyde were monitored over a range of CO and H_2 pressures (20 or 200 psia of each gas) (Figure 4-6). The catalytic data at 290 K were successfully fit using the kinetic model of Figure 4-5 and the rate constants obtained from single-turnover hydrogenolysis experiments. For this simplified model, the reaction of **1** and styrene to form **6b** and **6l** are represented as irreversible pseudo-elementary steps. Because the effect of [CO] on these pseudo-elementary steps is not known, the phenomenological rate constants, k_{3b} and $k_{3l,}$ for these steps were fitted for each set of catalytic reaction conditions. The results are shown in Table 4-3 and Figure 4-6. Consistent with CO inhibition, the apparent rate constants for acyl formation ($k_{3b/l}$) are inversely proportional to CO pressure, i.e. increasing the CO pressure from

20 psia to 200 psia decreases the rate constant by an order of magnitude. These rate constants are approximately independent of [H_2].

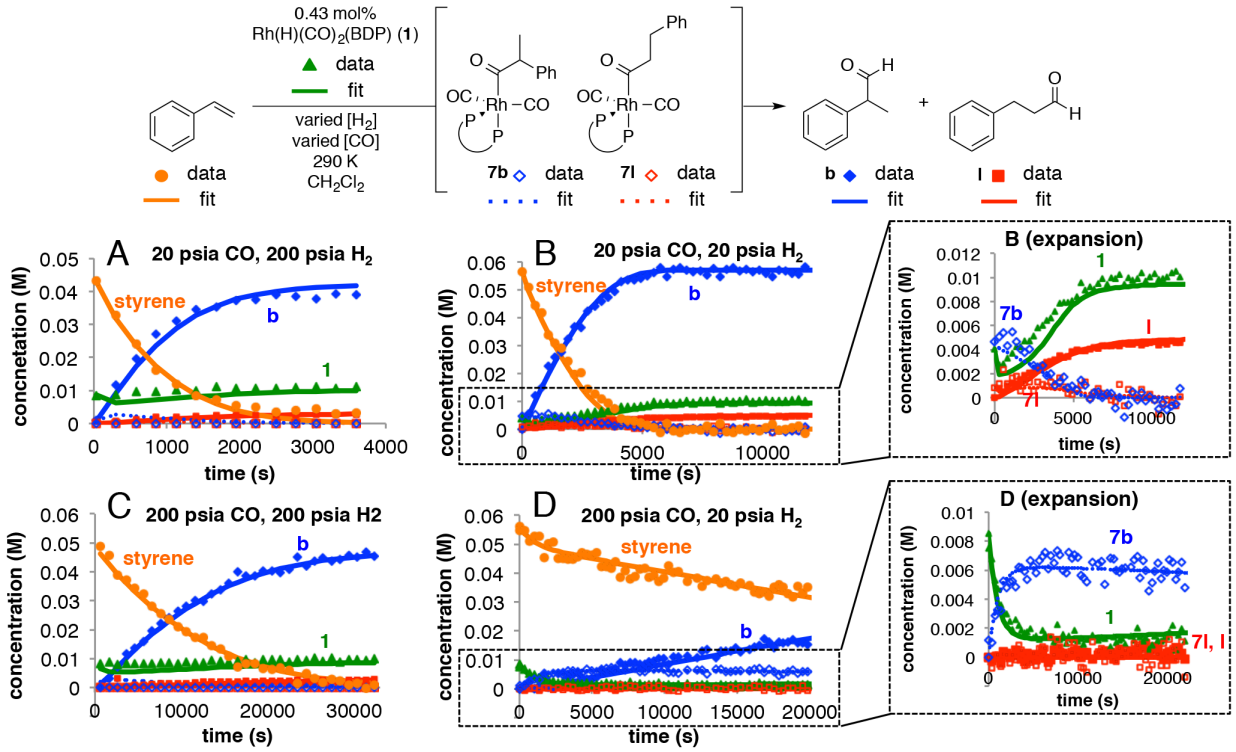

Figure 4-6. Time courses for hydroformylation of styrene collected in the WiHP-NMRR at 290 K. (0.06 M styrene, 0.01M Rh(H)$(CO)_2$(BDP), 290 K, and varied gas pressures: 20 psia CO, 200 psia H_2 (A), 20 psia CO, 20 psia H_2 (B), 200 psia CO, 200 psia H_2 (C), 200 psia CO, 20 psia H_2 (D). Experimental data shown as points; modeled fits displayed as lines.

P_{CO}	P_{H2}	k_{3b} value ($M^{-1}s^{-1}$)	standard deviation	k_{3l} value ($M^{-1}s^{-1}$)	standard deviation
20	20	0.110	0.003	7.0×10^{-3}	3×10^{-4}
200	20	0.0151	0.0003	6.1×10^{-4}	5×10^{-5}
20	200	0.122	0.005	8.3×10^{-3}	6×10^{-4}
200	200	0.0113	0.0002	6.6×10^{-4}	3×10^{-5}

Table 4-3. Computed rate constants (k_{3b}, k_{3l}, see Figure 4-5) for formation of acyl monocarbonyl complexes.

4.2.2 Interpretation of the Difference in Catalytic Kinetics at 313 K and 290 K

In Figure 4-1, catalytic data at 313 K show large and complex changes in selectivity and rate upon changing the CO pressure. In contrast, the data at 290 K (Figure 4-6) exhibit much smaller effects; for the CO pressure ranges explored, the product selectivity remains almost constant. As discussed above, deuteroformylation experiments show greater H/D scrambling at higher temperatures and lower CO pressures (Table 4-1). Therefore, the reactions at higher temperature (313 K) and low CO pressure (20 psia) allow for greater isomerization of the catalyst to the slower linear pathway that contains the thermodynamic sink (**7l**). The result is low regioselectivity (b:l = 1:1) and slow product formation. At higher CO pressures (115 or 200 psia), the isomerization is slowed such that the majority of the catalyst remains on the faster, branched pathway. In contrast, at 290 K, even at the low CO pressures, the isomerization of alkyls is slow enough such that the product distribution is relatively unaffected and the rates display the expected CO inhibition.

4.2.3 Does the Observed Catalytic Rate Correspond to Rate-Limiting Hydrogenolysis?

Comparison of the non-catalytic hydrogenolysis rate (using the steady-state concentrations of $[\mathbf{7b}]_{ss}$=4.8(5) mM and $[\mathbf{7l}]_{ss}$=1.36(6) mM) with the catalytic rate over the first 50% conversion conclusively demonstrates that the catalytic rate is *faster* than hydrogenolysis. For example, at 20 psia CO and 20 psia H_2 the catalytic rates for making linear and branched products are $8.3(1)\times10^{-7}$ Ms^{-1} and $1.8(1)\times10^{-5}$ Ms^{-1}, respectively, whereas the hydrogenolysis rates are computed to be $3.6(3)\times10^{-7}$ Ms^{-1} and $5.2(6)\times10^{-6}$ Ms^{-1}, respectively[15]. In other words, the hydrogenolysis rates are just 44(4)% and 29(4)% of the catalytic rates for branched and linear

products, respectively. Thus, we conclude that the catalytic rates are not controlled solely by the hydrogenolysis of **7**.

If the catalyst pools in the form of the acyl dicarbonyls **7b** and **7l** and the observed rate law is independent of [alkene], first order in [H_2], and inhibited by CO, why is the rate not predicted by a model of rate-limiting hydrogenolysis? Although intermediates **6b** and **6l** precede product formation in both catalytic hydroformylation and non-catalytic, single turnover hydrogenolysis experiments, steady-state concentrations of these intermediates differ between catalytic and non-catalytic experiments. Under the single-turnover conditions, **6** can only be formed by dissociation of CO from the acyl dicarbonyl (**7**). In contrast, under catalytic conditions, **6** can also be formed directly from the alkyl **4**. Thus, there is a more efficient pathway to aldehyde in which the catalyst goes directly from **6** to aldehyde product without being diverted off-cycle to **7**. Applying the steady state approximation to [**6**], the concentrations and rate laws in equations 4-11–4-14 result for the model depicted in Figure 4-7. This kinetic model represents the CO association and insertion steps that convert the alkyl monocarbonyl (**4**) to the acyl monocarbonyl (**6**) as a single pseudoelementary step with the composite rate constant k_4. The reaction of **2** and styrene to give the alkyl (**4**) is represented without a rate constant because it is presumed to be fast by the 0^{th} order dependence on styrene and no observation of **2** during catalysis. The forms of the catalytic rate law demonstrate that the rates of linear and branched aldehyde formation under catalytic conditions are (a) controlled by the steady-state concentrations of **6l** and **6b**, respectively (eq 4-12 and 4-14), and that (b) the steady-state concentrations of **6** are greater under catalytic than non-catalytic conditions (eq 4-11, 4-13 versus 4-5, 4-8). Indeed, relative to the single turnover conditions, the catalytic steady-state concentration of **6b** increases more that of **6l**. This differential increase occurs because formation

of the branched alkyl **4b** is kinetically preferred over the linear alkyl **4b**, as conclusively demonstrated by our previous studies.[12]

$$[\mathbf{6b}] = \frac{k_{1b}[\mathbf{7b}] + k_{4b}[\mathbf{4b}][CO]}{k_{2b}[H_2] + k_{-1b}[CO]} \qquad (4\text{-}11)$$

$$\frac{d[\mathbf{b}]}{dt} = \frac{(k_{1b}[\mathbf{7b}] + k_{4b}[\mathbf{4b}][CO])k_{2b}[H_2]}{k_{2b}[H_2] + k_{-1b}[CO]} \qquad (4\text{-}12)$$

$$[\mathbf{6l}] = \frac{k_{1l}[\mathbf{7l}] + k_{4l}[\mathbf{4l}][CO]}{k_{2l}[H_2] + k_{-1l}[CO]} \qquad (4\text{-}13)$$

$$\frac{d[\mathbf{l}]}{dt} = \frac{(k_{1l}[\mathbf{7l}] + k_{4l}[\mathbf{4l}][CO])k_{2l}[H_2]}{k_{2l}[H_2] + k_{-1l}[CO]} \qquad (4\text{-}14)$$

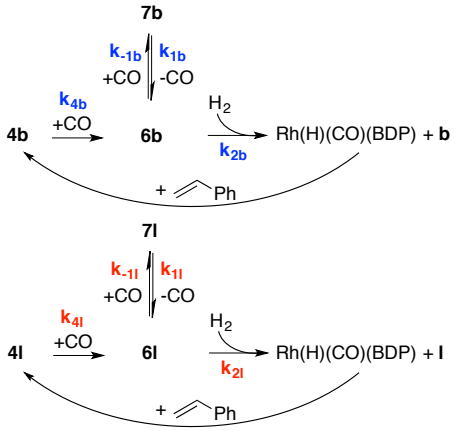

Figure 4-7. Simplified model for catalytic hydroformylations highlighting the importance of [alkyl] (**4**) in the rate of formation of aldehyde.

The analysis above describes scenarios that apply to *any* catalytic reaction with off-cycle species. The most efficient catalysis occurs for the scenario whereby all of the catalytic species are on-cycle. Any distribution of catalyst off-cycle, or even to the slower of concurrent cycles, must decrease the catalytic rate. As catalyst and substrate circuit the catalytic cycle there are junctions where the catalyst temporarily may go off-cycle (e.g. intermediates **2** and **6**). We refer to these as a "shunted" pathways to product, in opposition to the "direct" pathway for which the catalyst remains on-cycle. The direct pathway may contribute substantially to the overall rate

even under conditions in which the only *detectable* catalyst is off-cycle. For the hydroformylation catalysts and conditions examined here, even though all detectable catalyst species lie off-cycle (as **7l**, **7b**, and **1**) and the catalytic rate law *appears* to indicate rate-limiting hydrogenolysis, detailed analysis reveals that the majority of products (55% of the linear and 70% of the branched aldehydes) originate from direct, on-cycle pathways. These percentages vary with reaction conditions. For example, the reaction at 200 psia CO (Figure 4-6D) using the same analysis reveals that only 20% of the branched acyl monocarbonyl reacts directly while 80% is shunted off-cycle.

The hydroformylation data presented herein demonstrate that it is inappropriate to identify the reaction as rate-limited by the hydrogenolysis of acyl dicarbonyls **7**. Such dissection of the rates into "direct" and "shunted" components was possible only because elementary steps of the full catalytic reaction could be characterized independently.

The analysis given above directly relates to "Halpern's rules" which cast doubt on the role of observable catalyst-derived species under catalytic conditions: species sufficiently stable to accumulate are likely to lie off-cycle. For the example of Rh(BDP)-catalyzed hydroformylation under the conditions reported above, many of the alkene molecules are transformed to aldehyde without ever existing as the off-cycle **7**, even though the acyl dicarbonyl species are the primary observed catalyst species.

4.3 Conclusions

Operando observation of hydroformylation by WiHP-NMRR reveals complex kinetics and an apparent mismatch between the b:l ratio of the acyl resting states and the product

distribution. This discrepancy led us to study the rates of hydrogenolysis of branched and linear acyls *via* single turnover experiments. Although the branched acyl dicarbonyl (**7b**) undergoes faster hydrogenolysis than the linear isomer (**7l**), these differences in rates cannot fully explain the observed catalytic behavior. Detailed analysis distinguishes between direct and shunted pathways to product. Shunted pathways are those in which intermediates go off-cycle prior to forming product. Even under conditions where all of the detectable catalyst lies off-cycle, this analysis at 290 K reveals that 70% of the branched product and 55% of the linear product form by the direct pathway and bypassing **7b** and **7l**. These differences in catalytic activity are consistent with our observation of higher **7l** concentrations relative to **7b** than are observed in the final product distribution; these mismatches are more prevalent at higher reaction temperatures.

These results highlight the complex mechanism of the hydroformylation reaction and the value of *operando* NMR studies of both single-turnover and catalytic kinetics for a prototypical hydroformylation reaction. More generally the results provide quantitative illustration for why superficially labeling a step as selectivity-determining, rate-limiting, rate-controlling, or turnover-limiting can be problematic, especially when only the apparent catalytic rate law is known without knowledge of rates and rate laws for individual steps nor the speciation of catalyst under a variety of conditions. These considerations apply to all catalytic reactions.

4.4 Experimental Details

4.4.1 General Considerations

All reactions and manipulations were carried out under nitrogen using standard Schlenk and glovebox techniques. Work up and purification procedures were performed open to air.

Dichloromethane was used from a solvent purification system packed with activated alumina. CD_2Cl_2 was distilled from P_2O_5 and degassed. Solvents for column chromatography were used as received. Styrene was filtered through silica and sparged. Tetraphenyl bisdiazaphospholane, Rh(acac)(BDP), and Rh(H)$(CO)_2$(BDP) were synthesized following literature procedure.[12]

Routine ^1H and $^{31}P\{^1H\}$ spectra were recorded on a Bruker Avance-400 MHz spectrometer; WiHP-NMRR ^1H and $^{31}P\{1H\}$ spectra were performed on a Bruker Avance-360 MHz spectrometer with a Bruker 10 mm BB probe. Proton spectra were referenced to residual protio solvent. Phosphorus spectra were referenced to the corresponding proton spectrum using an xref macro.

4.4.2 General Method for Catalytic WiHP-NMRR Experiments

Rh(H)$(CO)_2$(BDP) was prepared as reported and depressurized to 5 psig. The reactor was brought into a N_2-purged glovebox. The solution was added to a vial of triphenylphosphine oxide and 1,4-bis(trimethylsilyl)benzene (^{31}P and ^1H internal standards, respectively). The contents were pulled into a threaded, gas-tight syringe (syringe one). The vial was rinsed with dichloromethane, which was pulled into a second syringe. The total volume of the two catalyst containing syringes (catalyst and rinse) was 2.0 mL. The desired volume of styrene was put into the third syringe, and the fourth contained a dichloromethane rinse. The combined volume of syringes three and four was either 150 or 500 μL (depending on required volume of styrene).

The WiHP-NMRR was purged with nitrogen with three vent/refill cycles. The catalyst and rinse (syringes one and two) were injected into the high-pressure NMR tube. The probe was set to the desired temperature and pressure of CO and H_2 with an over pressure in the antecylinder. The initial spectra were acquired. Styrene and rinse (syringes three and four) were

injected with the system under an over-pressure of N_2. Acquisition with circulation during NMR pulse sequence delays was started.

4.4.3 General Method for Single Turnover WiHP-NMRR Experiments

$Rh(H)(CO)_2(BDP)$ was prepared as reported and depressurized to 5 psig. The reactor was brought into a N_2-purged glovebox. The solution was added to a vial of triphenylphosphine oxide and 1,4-bis(trimethylsilyl)benzene (^{31}P and ^{1}H internal standards, respectively). The contents were pulled into a threaded, gas-tight syringe (syringe one). The vial was rinsed with dichloromethane, which was pulled into a second syringe. The total volume of the two catalyst containing syringes (catalyst and rinse) was 2.0 mL. A solution of styrene in dichloromethane was prepared and pulled into the third syringe, and the fourth contained a dichloromethane rinse. The total volume of syringes three and four was 150 μL.

The WiHP-NMRR was purged with nitrogen with three vent/refill cycles. The catalyst and rinse (syringes one and two) were injected into the high-pressure NMR tube. The reactor was pressurized, circulated, and vented five times with CO. The system was pressurized to 17 psia CO, warmed to 310 K, and styrene and rinse (syringes 3 and 4) were injected with an overpressure of N_2. The formation of acyl dicarbonyl species was monitored by ^{1}H and $^{31}P\{^{1}H\}$ NMR spectroscopy. Upon reaching an approximately 1:1 mixture of the two isomeric acyl dicarbonyl species, the system was cooled to 290 K and the pressure of CO was changed to the desired reaction pressure. The appropriate pressure of H_2 was added to the reactor and acquisition with circulation during NMR pulse sequence delays was started. ^{1}H NMR spectroscopy was used to monitor the formation of aldehydes, and $^{31}P\{^{1}H\}$ was used to monitor

the disappearance of acyl dicarbonyl species. Reactions with relatively short half-lives (<10 min) were followed by ^{1}H NMR only.

4.4.4 General Method for Deuteroformylation Experiments

The experimental setup was adapted from the method reported in the literature.[11] In a N_2-purged glovebox, solutions for deuteroformylation were prepared by combining Rh(acac)(BDP) (0.0015 mmol) stock solution, diphenylmethane internal standard (0.3 mmol), and dichloromethane to an oven-dried 50 mL pressure bottle equipped with a magnetic stir bar (total volume = 0.9 mL). The pressure bottle was then connected to a gauged pressure reactor assembly, and the reactor was removed from the glovebox. The reactor was purged five times with CO, charged with 40 psia CO followed by 40 psia D_2, and allowed to stir in a 60 °C oil bath for 2 hours. After 2 hours, the reactor was vented and purged 5 times with CO. With a slight overpressure in the reactor (15 psig) styrene (0.3 mmol) was added via gastight syringe. The reactor was pressurized with the appropriate CO pressure (40 or 80 psia) and 40 psia D_2. The reactions stirred at the appropriate temperature (290 K or 313 K) for 20 minutes. The reactions were cooled for one minute in an ice bath and vented. Mixtures were analyzed by ^{1}H and ^{2}H NMR spectroscopy on a Avance-500 spectrometer with DCH cryoprobe.

4.5 References

(1) Heck, R. F.; Breslow, D. S. The Reaction of Cobalt Hydrotetracarbonyl with Olefins. *J. Am. Chem. Soc.* **1961**, *83*, 4023-4027.

(2) Lazzaroni, R.; Uccello-Barretta, G.; Benetti, M. Reversibility of metal-alkyl intermediate formation in the rhodium-catalyzed deuterioformylation of 1-hexene. *Organometallics* **1989**, *8*, 2323-2327.

(3) Raffaelli, A.; Pucci, S.; Settambolo, R.; Uccello-Barretta, G.; Lazzaroni, R. Inter- and intramolecular protium-deuterium exchange in the rhodium-catalyzed deuterioformylation of styrene. *Organometallics* **1991**, *10*, 3892-3898.

(4) Uccello-Barretta, G.; Lazzaroni, R.; Settambolo, R.; Salvadori, P. The use of 2H NMR in the elucidation of the catalytic pathway of the hydroformylation reaction. *J. Organomet. Chem.* **1991**, *417*, 111-119.

(5) Lazzaroni, R.; Settambolo, R.; Uccello-Barretta, G. β-Hydride Elimination and Regioselectivity in the Rhodium-Catalyzed Hydroformylation of Open Chain Unsaturated Ethers. *Organometallics* **1995**, *14*, 4644-4650.

(6) Casey, C. P.; Petrovich, L. M. (Chelating diphosphine)rhodium-Catalyzed Deuterioformylation of 1-Hexene: Control of Regiochemistry by the Kinetic Ratio of Alkylrhodium Species Formed by Hydride Addition to Complexed Alkene. *J. Am. Chem. Soc.* **1995**, *117*, 6007-6014.

(7) Lazzaroni, R.; Uccello-Barretta, G.; Scamuzzi, S.; Settambolo, R.; Caiazzo, A. 2H NMR Investigation of the Rhodium-Catalyzed Deuterioformylation of 1,1-Diphenylethene: Evidence for the Formation of a Tertiary Alkyl–Metal Intermediate. *Organometallics* **1996**, *15*, 4657-4659.

(8) Horiuchi, T.; Shirakawa, E.; Nozaki, K.; Takaya, H. Mechanistic Aspects of Asymmetric Hydroformylation of Olefins Catalyzed by Chiral Phosphine–Phosphite–Rhodium(I) Complexes. *Organometallics* **1997**, *16*, 2981-2986.

(9) Lazzaroni, R.; Settambolo, R.; Uccello-Barretta, G.; Caiazzo, A.; Scamuzzi, S. Rhodium-catalyzed hydroformylation of vinylidenic olefins: the different behaviors of the isomeric alkyl–metal intermediates as the origin of the β-regioselectivity. *J. Mol. Catal. A: Chem.* **1999**, *143*, 123-130.

(10) van der Slot, S. C.; Duran, J.; Luten, J.; Kamer, P. C. J.; van Leeuwen, P. W. N. M. Hydroformylation and Deuterioformylation with Pyrrolyl-Based Phosphorus Amidite Ligands: Influence of Electronic Ligand Properties. *Organometallics* **2002**, *21*, 3873-3883.

(11) Watkins, A. L.; Landis, C. R. Origin of Pressure Effects on Regioselectivity and Enantioselectivity in the Rhodium-Catalyzed Hydroformylation of Styrene with (S,S,S)-BisDiazaphos. *J. Am. Chem. Soc.* **2010**, *132*, 10306-10317.

(12) Nelsen, E. R.; Landis, C. R. Interception and Characterization of Alkyl and Acyl Complexes in Rhodium-Catalyzed Hydroformylation of Styrene. *J. Am. Chem. Soc.* **2013**, *135*, 9636-9639.

(13) Nelsen, E. R.; Brezny, A. C.; Landis, C. R. Interception and Characterization of Catalyst Species in Rhodium Bis(diazaphospholane)-Catalyzed Hydroformylation of Octene, Vinyl Acetate, Allyl Cyanide, and 1-Phenyl-1,3-butadiene. *J. Am. Chem. Soc.* **2015**, *137*, 14208-14219.

(14) van Leeuwen, P. W. N. M.; Claver, C. *Rhodium Catalyzed Hydroformylation*; Kluwer Academic Publishers: Dordrecht, The Netherlands 2000.

(15) Feng, J.; Garland, M. Unmodified Homogeneous Rhodium-Catalyzed Hydroformylation of Styrene. The Detailed Kinetics of the Regioselective Synthesis. *Organometallics* **1999**, *18*, 417-427.

(16) Güven, S.; Nieuwenhuizen, M. M. L.; Hamers, B.; Franke, R.; Priske, M.; Becker, M.; Vogt, D. Kinetic Explanation for the Temperature Dependence of the Regioselectivity in the Hydroformylation of Neohexene. *ChemCatChem* **2014**, *6*, 603-610.

(17) Kubis, C.; Selent, D.; Sawall, M.; Ludwig, R.; Neymeyr, K.; Baumann, W.; Franke, R.; Borner, A. Exploring between the extremes: conversion-dependent kinetics of phosphite-modified hydroformylation catalysis. *Chem. Eur. J.* **2012**, *18*, 8780-8794.

(18) Rate laws: $d[b]/dt= (k_{6b\rightarrow 1}[\mathbf{7b}][H_2])/(K_{6b\rightarrow 7b}[CO])$; $d[l]/dt= (k_{6l\rightarrow 1}[\mathbf{7l}][H_2])/(K_{6l\rightarrow 7b}[CO])$. In situ high-pressure IR spectroscopy experimental conditions: T = 298–343 K, [3,3-dimethyl-1-butene] = 0.54 M, [Rh] = $3.14\text{x}10^{-4}$ M, L/Rh = 26, P_{CO} = 29.75–35.15 bar, P_{H2} = 3.75–6.59 bar. Deuteroformylation experimental conditions: T = 323–373 K, [3,3-dimethyl-1-butene] = 2.7 M, [Rh] = $1.0\text{x}10^{-4}$ M, L/Rh = 27, P_{CO} = 20 bar, P_{D2} = 20 bar. Semibatch experimental conditions: T = 334–363 K, [3,3-dimethyl-1-butene] = 1.25–2.93 M, [Rh] = $0.59\text{x}10^{-4}$–$2.95\text{x}10^{-4}$ M, L/Rh = 15–30, P_{CO} = 9–35.9 bar, P_{H2} = 20–42 bar.

(19) The term hydrogenolyis does not strictly refer to the reaction of 6 with H_2, only; rapid equilibration of **7** and **6** are assumed such that one could equivalently describe hydrogenolysis of $_7$ as rate-determining where hydrogenolysis as a composite two-step process

(20) Kubis, C.; Baumann, W.; Barsch, E.; Selent, D.; Sawall, M.; Ludwig, R.; Neymeyr, K.; Hess, D.; Franke, R.; Börner, A. Investigation into the Equilibrium of Iridium Catalysts for the Hydroformylation of Olefins by Combining In Situ High-Pressure FTIR and NMR Spectroscopy. *ACS Catalysis* **2014**, *4*, 2097-2108.

(21) Kubis, C.; Sawall, M.; Block, A.; Neymeyr, K.; Ludwig, R.; Borner, A.; Selent, D. An operando FTIR spectroscopic and kinetic study of carbon monoxide pressure influence on rhodium-catalyzed olefin hydroformylation. *Chem. Eur. J.* **2014**, *20*, 11921-11931.

(22) Kubis, C.; Ludwig, R.; Sawall, M.; Neymeyr, K.; Börner, A.; Wiese, K.-D.; Hess, D.; Franke, R.; Selent, D. A Comparative In Situ HP-FTIR Spectroscopic Study of Bi- and Monodentate Phosphite-Modified Hydroformylation. *ChemCatChem* **2010**, *2*, 287-295.

(23) Beach, N. J.; Knapp, S. M. M.; Landis, C. R. A reactor for high-throughput high-pressure nuclear magnetic resonance spectroscopy. *Rev. Sci. Instrum.* **2015**, *86*, 104101–104109.

(24) We refer to hydrogenolysis as the overall reaction from resting state **7** to aldehyde; it includes the (reversible) loss of CO and the irreversible reaction with hydrogen to form aldehyde.

(25) Hoops, S.; Sahle, S.; Gauges, R.; Lee, C.; Pahle, J.; Simus, N.; Singhal, M.; Xu, L.; Mendes, P.; Kummer, U. COPASI—a COmplex PAthway SImulator. *Bioinformatics* **2006**, *22*, 3067-3074.

Chapter 5

Progress Towards a Full Microkinetic Model of Rh(BDP)-Catalyzed Hydroformylation of Styrene

Computations were performed by Prof. Frank Neese at the Max Planck Institute and Dr. Robert Froese at Dow Chemical Company.

5.1 Introduction

The mechanism for hydroformylation was first proposed in 1961 by Breslow and Heck and outlines the elementary steps of the overall transformation (Scheme 5-1).[1] This proposal does not account for the origins of selectivity, and as discussed previously (Chapters 2, 3, and 4), a long standing goal in the field has been to understand how both rate and selectivity are controlled in asymmetric hydroformylation (AHF) catalyzed by rhodium bis(diazaphospholane) (BDP) catalysts.

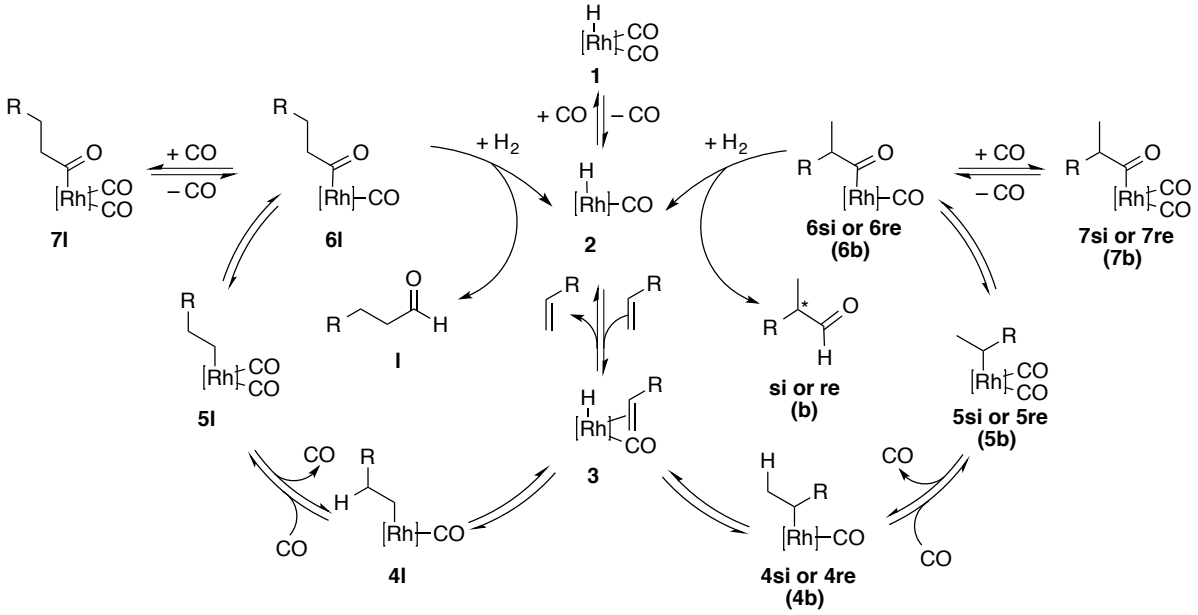

Scheme 5-1. Mechanism for hydroformylation proposed by Breslow and Heck.

Previous work revealed a complex picture regarding selectivity of styrene hydroformylation by Rh(BDP) catalysts. Watkins and Landis demonstrated that selectivity depends on CO pressure (Figure 5-1), and detailed mechanistic studies reinforce their proposal that the competition between CO trapping of the branched alkyl intermediate (**4si**) versus reversion to styrene was crucial to account for this complex dependence on gas concentration.[2]

This hypothesis implies a kinetic preference for forming the branched alkyl, but a competing thermodynamic preference for a linear intermediate.

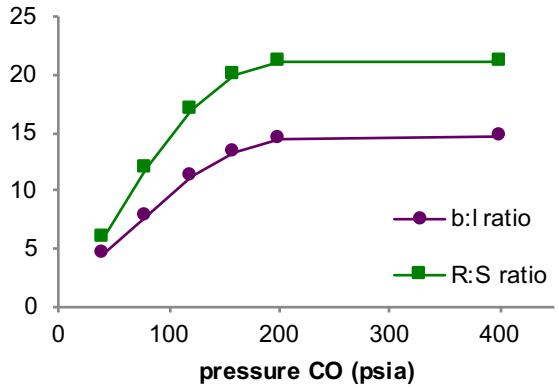

Figure 5-1. Selectivity versus CO pressure as demonstrated by Watkins and Landis.

Work from Nelsen and Landis support this hypothesis. Several on- and off-cycle intermediates were trapped and characterized under low-pressure and low-temperature conditions.[3] They observed kinetic selectivity for a branched acyl dicarbonyl complex (**7b**) and a competing thermodynamic preference for the linear isomer (**7l**) (Scheme 5-2).

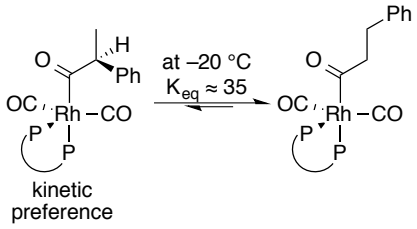

Scheme 5-2. Kinetic versus thermodynamic preference of acyl dicarbonyl species.

Extension of this work to studies in the Wisconsin High-Pressure NMR Reactor (WiHP-NMRR)[4] revealed that while off-cycle species are observed as resting states, there is a competition between catalyst going off-cycle and remaining on-cycle at the acyl bifurcation point (Chapter 4).[5] Additionally, this work highlights the complicated competition between

isomerization of the kinetic, branched species to the slower linear pathway that contains the thermodynamic sink (**7l**).

The competition between isomerization and CO trapping of alkyl species indicates that several transition state barriers are similar in energy, meaning that multiple steps impact selectivity. While the previously discussed work *qualitatively* explains the origins of selectivity in asymmetric hydroformlylation, we desire a *quantitative* understanding of how various steps impact AHF. Therefore, the goal of this Chapter is to develop a robust microkinetic model that can explain all of our data. Microkinetic analysis refers to examining a catalytic reaction in terms of the elementary steps. The reaction kinetics are calculated by numerically solving the differential equations that define the reaction network.

Transition state theory provides a procedure for calculating rate constants from a free energy surface, and *vice versa* (eq 5-1). Therefore, a microkinetic model allows one to predict rate, selectivity, and catalyst distribution under any conditions. This is beneficial from a practical standpoint, because one can quickly determine the ideal operating conditions to achieve a given reactivity profile, including temperature, pressure, and concentration. Furthermore, the way we express our understanding of a reaction is through the free energy surface. With an accurate microkinetic model, we can quantitatively explain what governs selectivity in this complicated reaction. This allows us to explore fundamental questions about the reversibility of a step under any set of reaction conditions, the transient concentrations of intermediates not observed spectroscopically, and the selectivity changes as a function of reaction conditions. While microkinetic models are ubiquitous in heterogeneous catalysis, there are far fewer examples in the homogeneous literature.[6-13] This is particularly surprising given the well-defined nature of the catalysts and intermediates, which in theory lends more readily itself to detailed quantitation.

$$k=2.0837x10^{10}(T)e^{-\left(\frac{\Delta H^{\ddagger}-\Delta S^{\ddagger}(T)}{1.987(T)}\right)} \quad (5\text{-}1)$$

5.1.1 Computational Data

Modern computational methods enable the calculation of full free energy surfaces for complex catalytic reactions such as AHF. Thus, the simplest approach to a microkinetic model is to use these types of computed data. Collaborators Prof. Frank Neese and Dr. Robert Froese calculated the energies of every intermediate and transition state in Rh(BDP)-catalyzed styrene AHF using CCSD and DFT *ab initio* methods, respectively. The computations involve the same BDP ligand described in Chapters 3 and 4. These high-level computations revealed three steps with significant activation enthalpies: 1) alkene insertion into the Rh–H bond of **3** to form an alkyl complex (**4**), 2) CO insertion from **5** to form an acyl species (**6**), and 3) the reductive elimination of aldehyde from the Rh(acyl)$(H)_2$(BDP) species (**9**) (Figure 5-2).

Using the program COPASI,[14] we created a kinetic model utilizing the computed activation enthalpies ($\Delta H^{\ddagger}$) and estimated activation entropies ($\Delta S^{\ddagger}$) to give rate constants at a given temperature. Because it is difficult to accurately calculate $\Delta S^{\ddagger}$ using these computational methods, entropy of activation values were set based on the molecularity of the elementary step. For instance, a bimolecular reaction forming a single product is assumed to have an overall entropy change of –30 cal·mol^{-1}K^{-1}. This value is split evenly at the transition state, thus in the forward direction $\Delta S^{\ddagger}$ = –15 cal·mol^{-1}K^{-1} and 15 cal·mol^{-1}K^{-1} in the reverse. Unimolecular reactions forming a single product are given an entropy of 0 cal·mol^{-1}K^{-1} in both the forward and reverse directions. In order to assess the accuracy of this model, the predicted values were compared to experimental catalytic data (Figure 5-3).

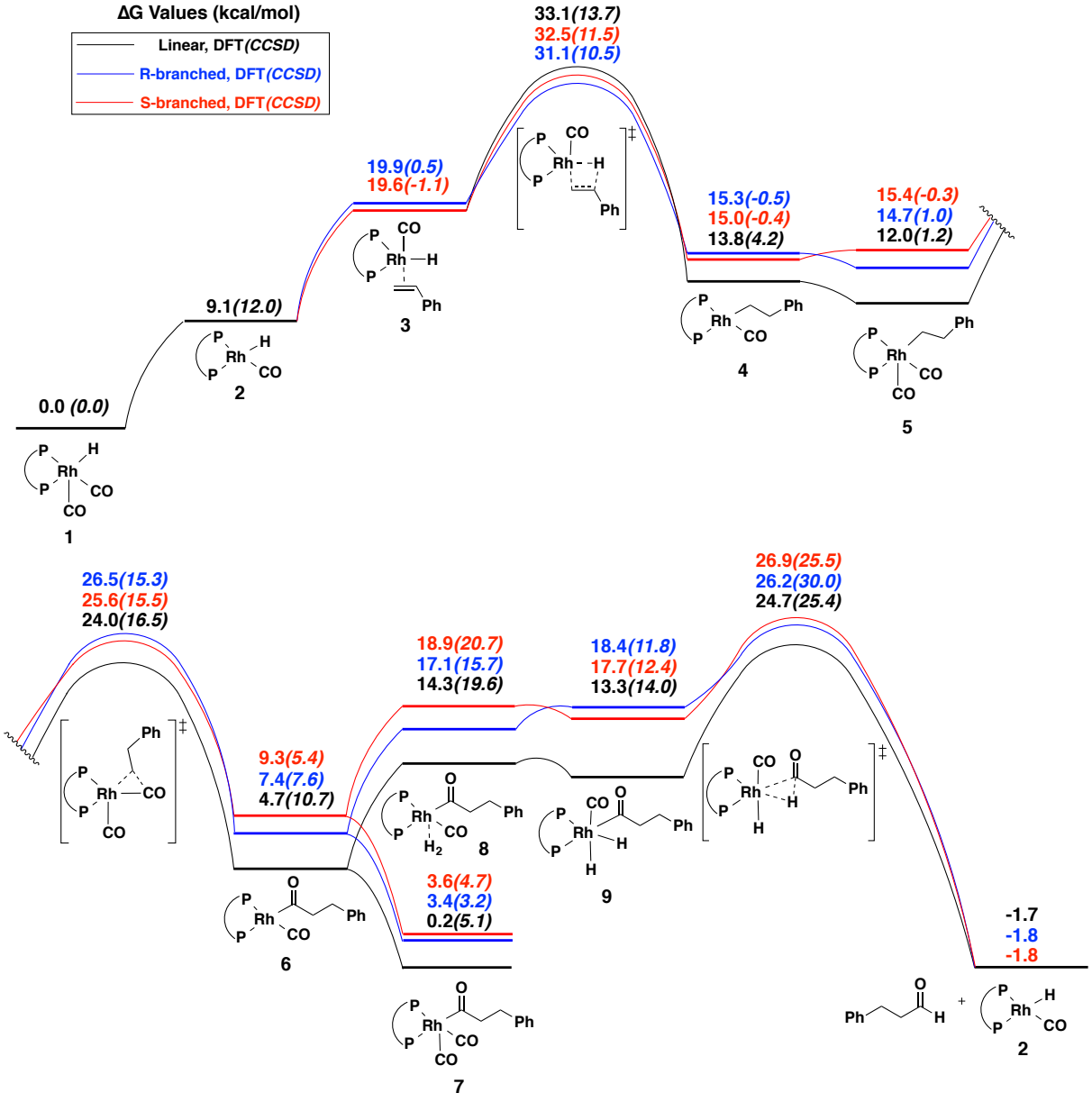

Figure 5-2. Free energy surface computed by Prof. Frank Neese and Dr. Robert Froese.

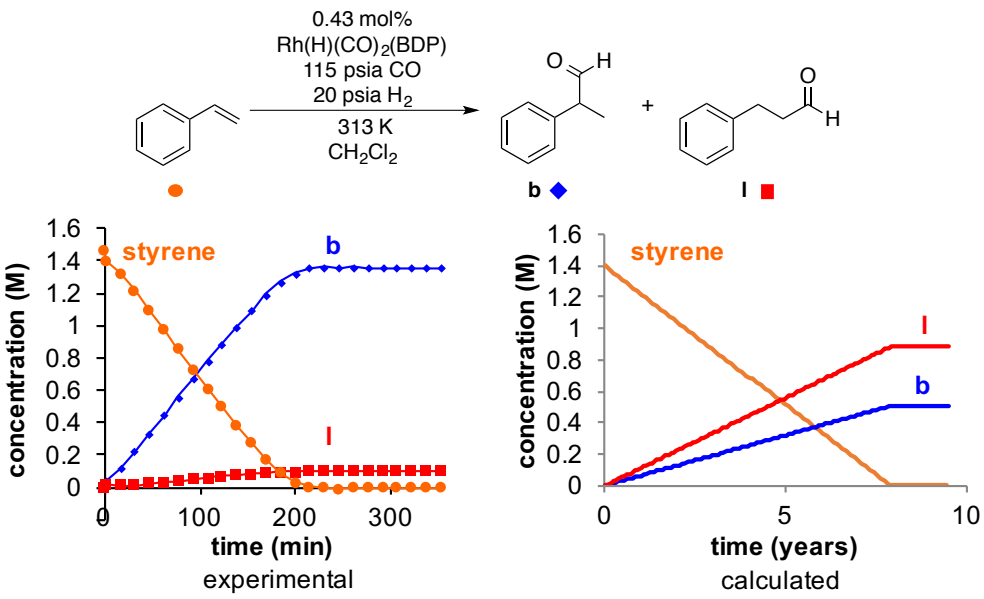

Figure 5-3. Experimental versus calculated time courses highlighting the inaccuracies of computations.

It is apparent from comparison of the experimental and calculated values that these computations do not have the accuracy required for a microkinetic model. Although no single barrier is obviously too extreme, the accumulation of error gives rise to a rate that is off by orders of magnitude. Some of these discrepancies arise from the computational method failing to sample all conformational states of the transition states and intermediates. Other issues are caused by the difficulty of computing CO association with these types of calculations. Thus, the simplest form of this microkinetic model is insufficient to fit our data and the free energy surface must be adjusted by experimental data. We envisioned using the *ab initio* computations in combination with a variety of experimental data to develop a model (Figure 5-4). What is the best approach for empirically adjusting computations to achieve an accurate and robust microkinetic model?

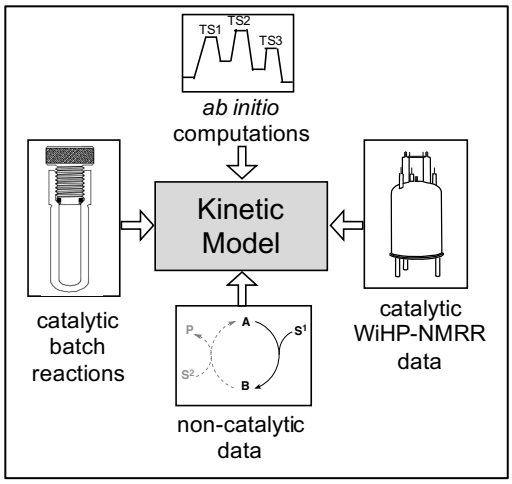

Figure 5-4. Overall goal of developing an empirically adjusted *ab initio* kinetic model for AHF.

5.1.2 Empirically Adjusted Ab Initio Microkinetic Model

Concurrent with our efforts to develop an empirically-adjusted microkinetic model, an elegant example was published by Ho *et al.* at the Pacific Northwest National Laboratory focusing on the electrocatalytic proton reduction catalyzed by a homogeneous nickel catalyst.[13] Similar to our observations, a kinetic model based on raw *ab initio* kinetic parameters was not accurate enough to fit their experimental data. The authors used a sensitivity analysis to determine which rate constants had the greatest impact on the overall rate of reaction. They identified four protonation steps that had the largest influence on the rate of H_2 production, and upon optimization of $\Delta G^{\ddagger}$ for these steps against experimental data, they were able to achieve improved fits and correct turnover frequencies. We wondered if this relatively simple approach would also work in modeling AHF. This Chapter describe how we approached this complicated problem and what methods were most successful in modeling AHF.

5.2 Results and Discussion

We began by conducting a similar sensitivity analysis as Ho *et al.* to determine what parameters most affected the rate and selectivity of hydroformylation, but found that it was not particularly helpful. The rate of styrene consumption and product selectivity were relatively sensitive to all parameters, which highlights that many steps are in competition with one another and thus many barriers are involved in controlling AHF. More practically, it indicated that we needed to find a new approach to developing this full microkinetic model. Unlike the H_2 production example above, AHF includes 3 concurrent pathways, meaning that both selectivity and overall rate must be accurately predicted in order to obtain a useful model. The AHF model includes substantially more parameters and intermediates, which also increases its complexity. Furthermore, while the work from Ho *et al.* modeled only $\Delta G^{\ddagger}$, we desired to obtain both $\Delta H^{\ddagger}$ and $\Delta S^{\ddagger}$ so that our model could be extrapolated to any temperature. Therefore, we were required to collect data at multiple ($\geq$3) temperatures to obtain these activation parameters.

5.2.1 Approach 1: General Activation Parameters

As discussed in Chapter 4, the WiHP-NMRR enables the collection of *operando* catalytic reactions. The rates of formation and consumption of intermediates can be measured as well as concentrations of starting materials and products. Therefore, catalytic data contain the maximum amount information in one experiment. We first aimed to model these types of data sets because they would, in theory, allow us to build the model using the fewest number of experiments.

In order to minimize the number of transition states to be optimized, we removed the differentiation between isomeric pathways and aimed to model the general activation parameters to fit the correct catalyst speciation (hydride **1** versus the sum of acyl dicarbonyl complexes, **7**)

and the overall rate of product formation (Figure 5-5). With fewer parameters and intermediates, we hoped that we could more easily optimize activation enthalpies and obtain fits for the generalized reaction. After achieving reasonable overall rates, we would reintroduce the added complexity of isomeric pathways and adjust each barrier slightly from the general activation parameters. As discussed above, $\Delta S^{\ddagger}$ for each elementary step was set based on the molecularity of the reaction.

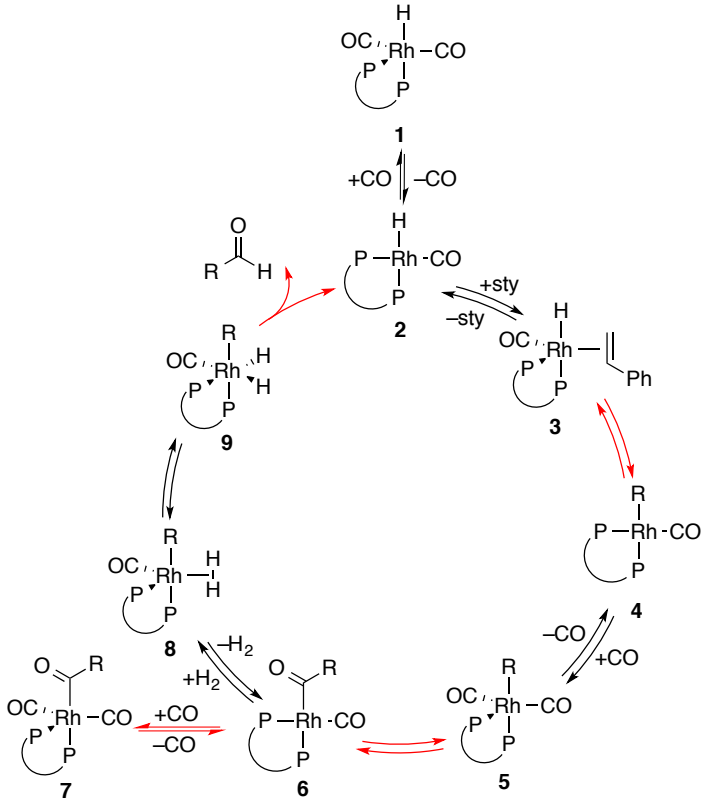

Figure 5-5. Simple model for optimizing general, non-isomeric activation parameters. Adjusted barriers highlighted in red.

In COPASI, we built the model in Figure 5-5 with rate constants for each step set based on the enthalpies and entropies of activation (by eq 5-1). We provided experimental, catalytic data and allowed the fitting program to optimize $\Delta H^{\ddagger}$ for the three significant barriers (**3**→**4**, **5**→**6**, **9**→**2** *vide supra*) as well as the thermodynamics for CO association to Rh(acyl)(CO)(BDP)

(**6**). This works by minimizing the error between the data and fit by adjusting the floated parameters. This optimization led to greatly improved fits in comparison to the raw *ab initio* model (Figure 5-6, cf. Figure 5-3). The *ab initio* values were used for all other steps in the reaction. We hoped that any inaccuracies of the assumed steps could be overcome by the adjustments to the four optimized parameters. Although these fits were not perfect, they showed promise for this approach.

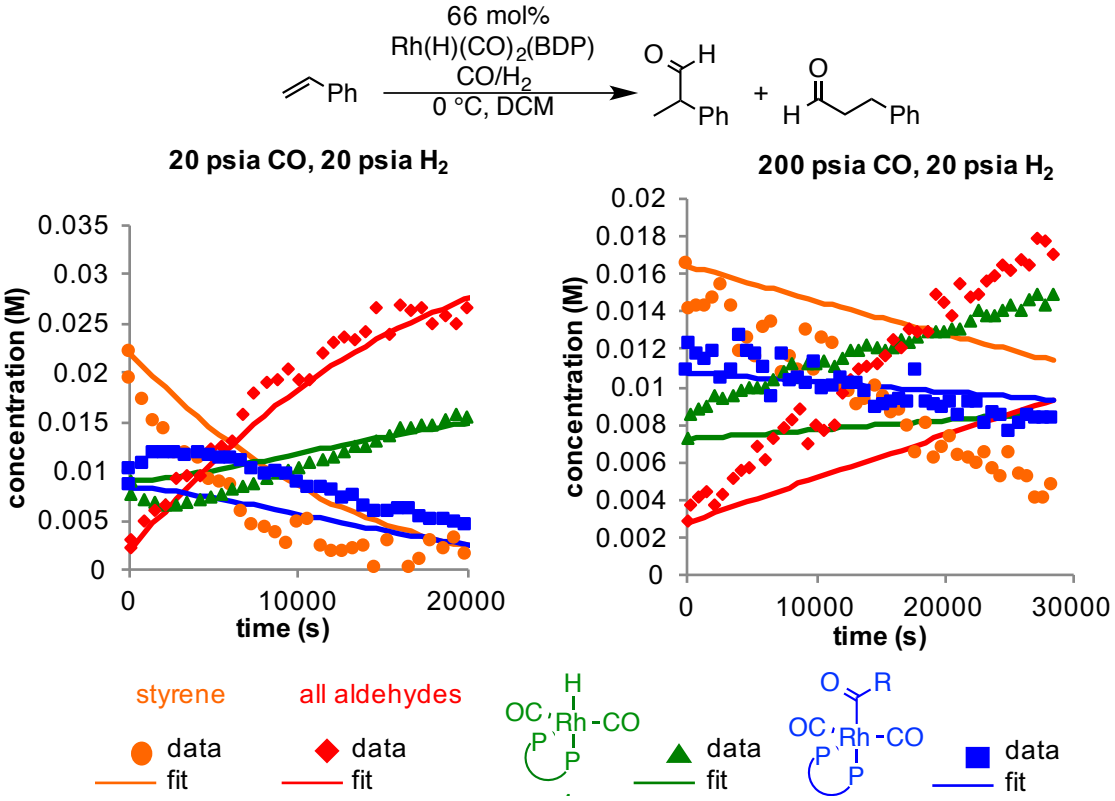

Figure 5-6. Data and fits for sample data at 0 °C using the general activation model. (0.03 M styrene, 0.02 M Rh(H)(CO)$_2$(BDP), 273 K, 20 psia H_2, and varied CO pressures: 20 psia CO (left) and 200 psia CO (right). Note: acyl intermediate and aldehyde present at t_0 due degassing of solution upon injection with this early generation of the WiHP-NMRR.

However, as we continued to collect data at other temperatures, it became apparent that this general activation parameter approach was intrinsically flawed . Catalytic experiments at 40

°C show unusual CO dependencies (see Chapter 4, Figures 4-1 and 4-2). Whether the catalyst rests as a branched or linear acyl dicarbonyl complex results in *drastic* differences in overall rate.[5] The non-isomeric model cannot account for this type of kinetic behavior, because the resting state would be entered into the model as 100% acyl dicarbonyl complex, regardless of which isomer predominates. This indicated that the isomeric pathways needed to be reintroduced into the model into order to fit these high temperature catalytic data.

5.2.2 Approach 2: Reintroducing Three Isomeric Pathways

The complexity of all three pathways was added back into the model with the goal of fitting catalytic experiments at warmer temperatures (40 °C). This model included 22 intermediates, 45 rate constants, and thus, 90 activation parameters (see Figure 5-2). Attempts to model catalytic data by optimizing the same four steps were unsuccessful. Rather than estimating four steps (Section 5.2.1), 12 were required to adjust all three isomeric pathways. This approach was successful in that it vastly improved the overall rate of the reaction to the correct order of magnitude (from years to hours). The intricacies of catalyst speciation and relative rates of branched *versus* linear product formation were not accurately reproduced and thus not a useful model.

There are several potential issues with this approach. First, the large number of adjustable parameters results in the calculations optimizing into local minima, rather than finding the actual global minimum. Second, we relied on the computations for the majority of the barriers, which are not necessarily accurate. In fact, our raw *ab initio* model suggests that they are most likely incorrect. Third, we assumed the values for $\Delta S^{\ddagger}$, but these parameters likely need to be adjusted as well. In order to not rely on computations, but also not adjust the energy barriers for every

elementary step, this indicates that a simplified model is necessary to correctly determine the values for fewer adjustable parameters.

5.2.3 Approach 3: Simplifying the Kinetic Model

In order to limit the number of adjustable parameters and rely less heavily on potentially inaccurate *ab initio* computations, we simplified the model by combining several elementary steps. Because many of the intermediates cannot be directly observed spectroscopically, we chose to fold them together into a reaction with a significant calculated barrier. We hypothesized that the adjustable parameters would be able to compensate for the energies of the preceding, combined intermediates, thus providing an observed rate constant value for these steps. For example, loss of CO from **1**, styrene association, and alkene insertion were combined into one pseudoelementary step that was modeled with a phenomenological rate law (eq 5-2–5-5). Similarly, association of CO to the alkyl **4** and insertion to give acyl **6** were combined. The H_2 association to **6**, oxidative addition, and reductive elimination to give product were also condensed. These changes are reflected in the model in Figure 5-7.

$$\frac{d[\mathbf{4si}]}{dt} = \frac{k^{si}_{for}[\mathbf{1}][\text{styrene}]}{[\text{CO}]} - k^{si}_{back}[\mathbf{4si}] \qquad (5\text{-}2)$$

$$\frac{d[\mathbf{4re}]}{dt} = \frac{k^{re}_{for}[\mathbf{1}][\text{styrene}]}{[\text{CO}]} - k^{re}_{back}[\mathbf{4re}] \qquad (5\text{-}3)$$

$$\frac{d[\mathbf{4l}]}{dt} = \frac{k^{l}_{for}[\mathbf{1}][\text{styrene}]}{[\text{CO}]} - k^{l}_{back}[\mathbf{4l}] \qquad (5\text{-}4)$$

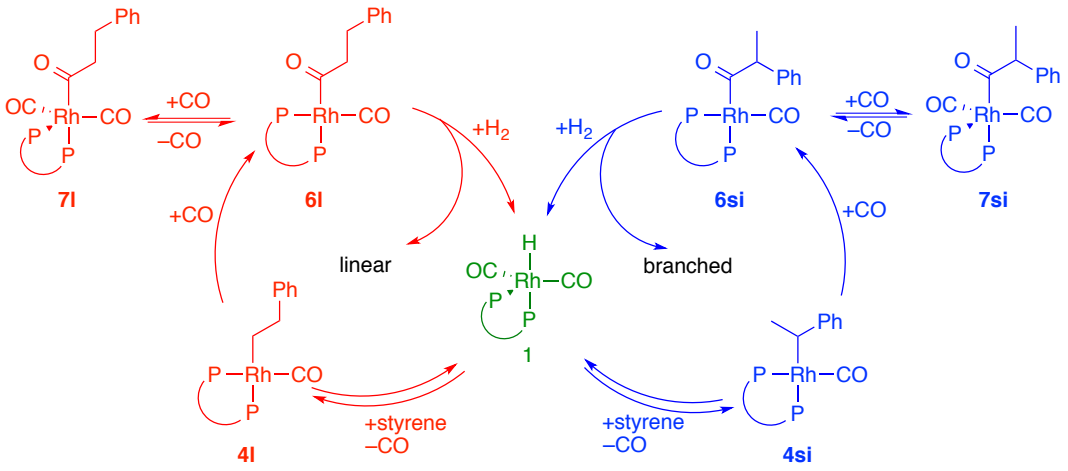

Figure 5-7. Simplified kinetic model by combining several reactions into pseudoelementary steps.

In order to address another flaw of the previous kinetic modeling approaches, we aimed to adjust both $\Delta H^{\ddagger}$ and $\Delta S^{\ddagger}$, rather than rely on assumptions about transition state entropy. To limit the number of simultaneously adjusted parameters, we modeled each catalytic temperature separately in terms of rate constants, then planned to back calculate the activation parameters afterwards. Concurrent with this approach, we also modeled the hydrogenolysis steps (**7**→**2**, aldehyde) from non-catalytic reactions at 290 K (see Chapter 4). Using these values in combination with catalytic experiments at the same temperature, we were able to fit the 290 K experimental data exceptionally well (Figure 5-8).

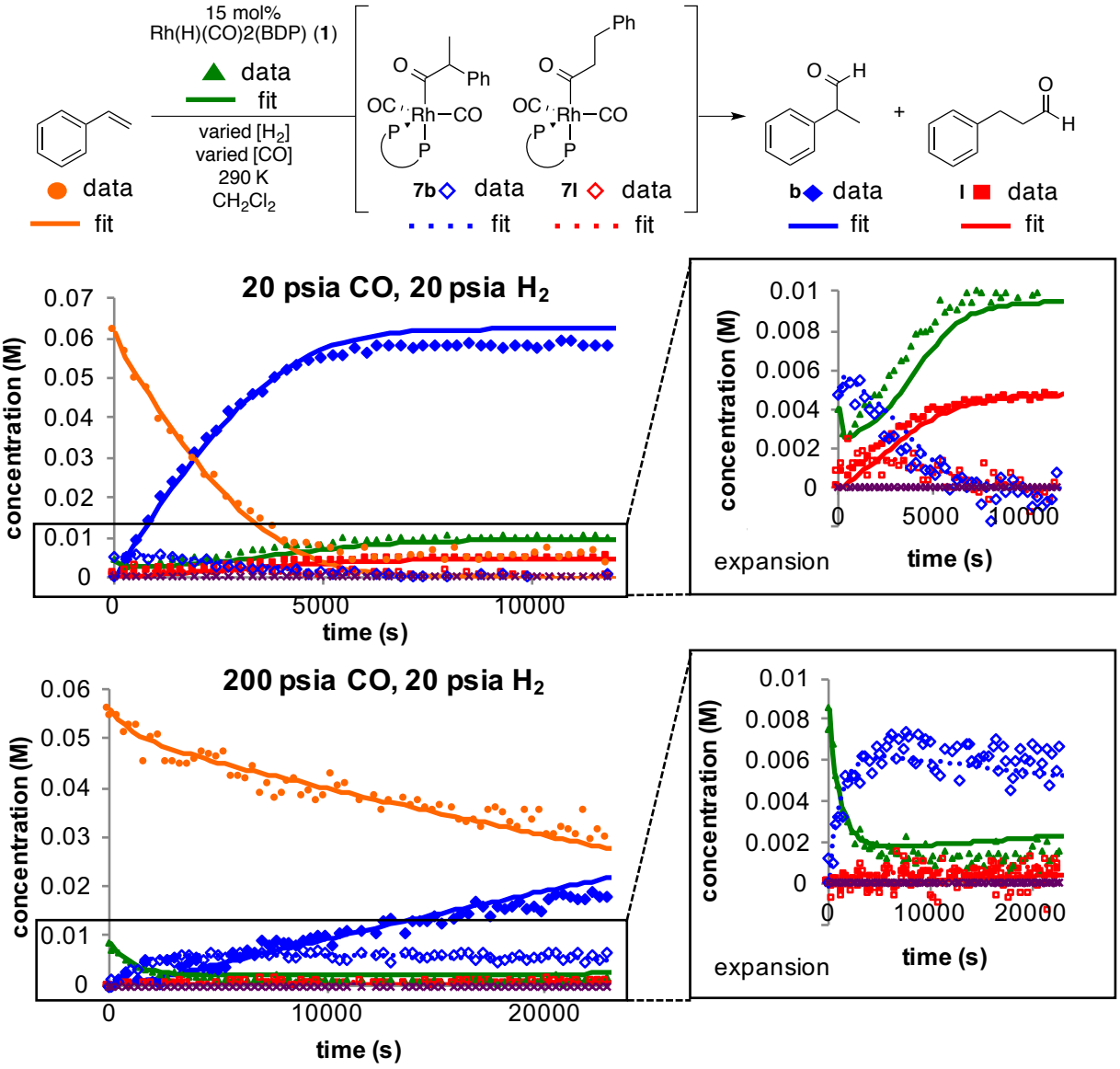

Figure 5-8. Example data and fits of catalytic experiments at 290 K using simplified model. (0.6 M styrene, 10 mM $Rh(H)(CO)_2(BDP)$, 290 K, 20 psia H_2, and varied CO pressures: 20 psia CO (top) and 200 psia CO (bottom).

However, this approach was ineffective for modeling other temperatures predominantly because the hydrogenolysis experiments described in Chapter 4 could not be performed at higher temperature. This is because 1) the reactions would be too fast to be monitored in the WiHP-NMRR and 2) isomerization of the acyl dicarbonyl starting materials would complicate the

analysis. Therefore, we attempted the model the 313 K catalytic data without the independent hydrogenolysis experiments and thus simultaneously optimize those parameters. In order to match the overall rate of the reactions, the catalyst speciation was fit extremely poorly (Figure 5-9). Once again there were likely too many parameters and only a local minimum could be obtained. Comparison of the successful 290 K model versus that at 313 K highlights the power of breaking down the model into the different types of data to build up the full catalytic reaction. Thus, moving forward, we sought to use this type of approach for all temperature data with a wider variety of non-catalytic experiments.

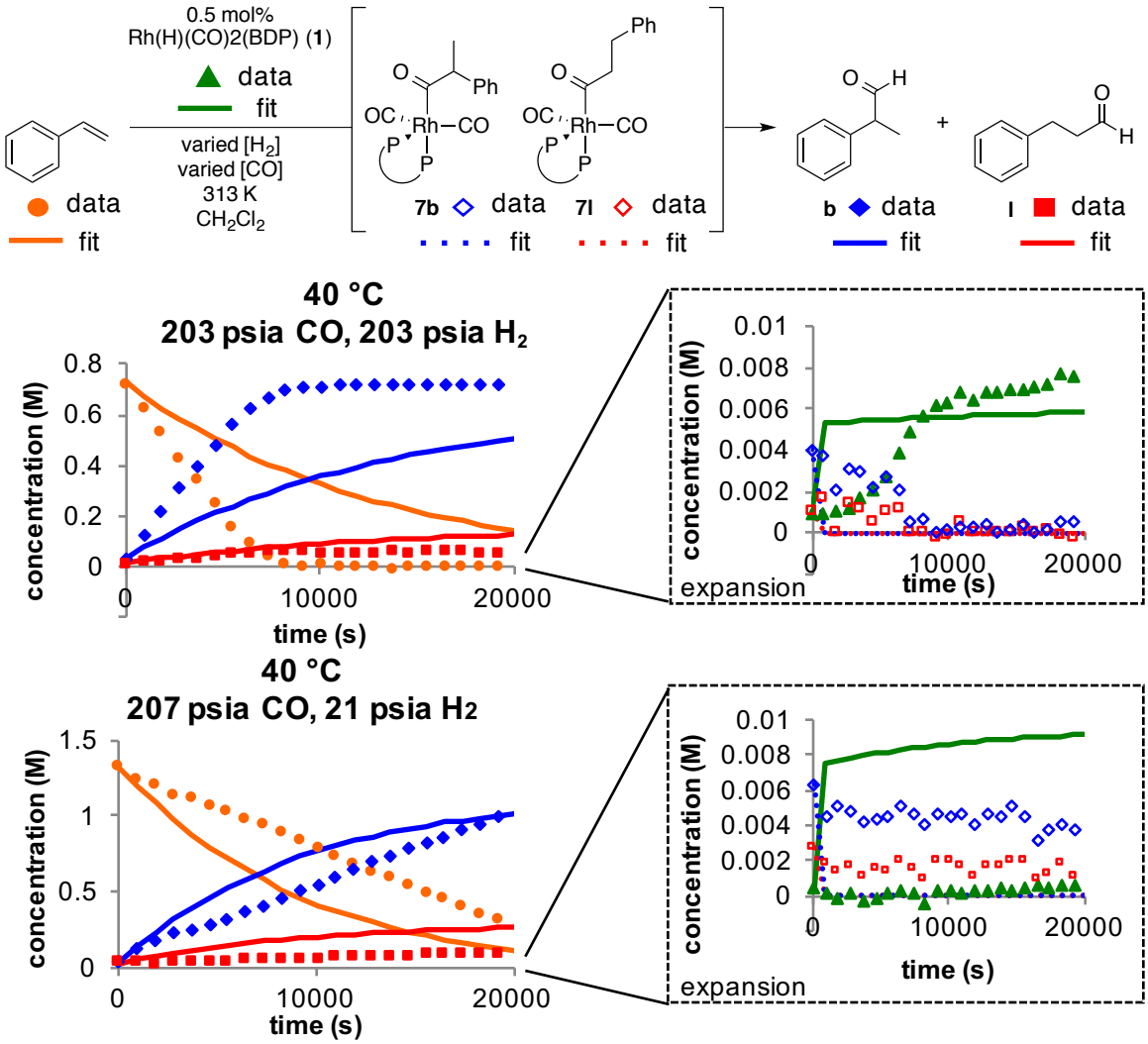

Figure 5-9. Data and fits of example catalytic experiments at 313 K using the simplified model. (1.4 M styrene, 6 mM $Rh(H)(CO)_2(BDP)$, 313 K, 200 psia CO, and varied H_2 pressures: 203 psia H_2 (top) and 201 psia H_2 (bottom).

5.2.4 Approach 4: Divide and Conquer

Inspired by the success of combining non-catalytic hydrogenolysis experiments with catalytic data, we developed a kinetic model in which different types of non-catalytic data could be pieced together to develop the full reaction (Figure 5-10). In order to develop this full model and obtain activation parameters for every step we needed to collect several types of non-

catalytic data at multiple temperatures. First, we expanded the hydrogenolysis experiments from Chapter 4 to other temperatures to obtain $\Delta H^{\ddagger}$ and $\Delta S^{\ddagger}$ for these steps. Second, we included hydrido monocarbonyl **2** in the model and obtained information about the rate of CO loss from **1**. Because we had previously demonstrated that the catalyst does not always go off-cycle at the acyl monocarbonyl intermediate,[5] we also could not assume that **2** always binds CO to give **1**. Third, using the WiHP-NMRR we collected data about the rates of formation of **7** from the hydrido dicarbonyl and styrene. Previous work (see Chapter 4) highlighted the importance of alkyl isomerization during catalysis, and therefore we collected data regarding the fate of **4**. Finally, under catalytic conditions at warm temperatures, the acyl dicarbonyl species are known to isomerize. Thus, using the WiHP-NMRR we obtained data following the isomerization of **7si** to **7l**. Note: errors reported are computed standard deviations of the modeled fits from COPASI.

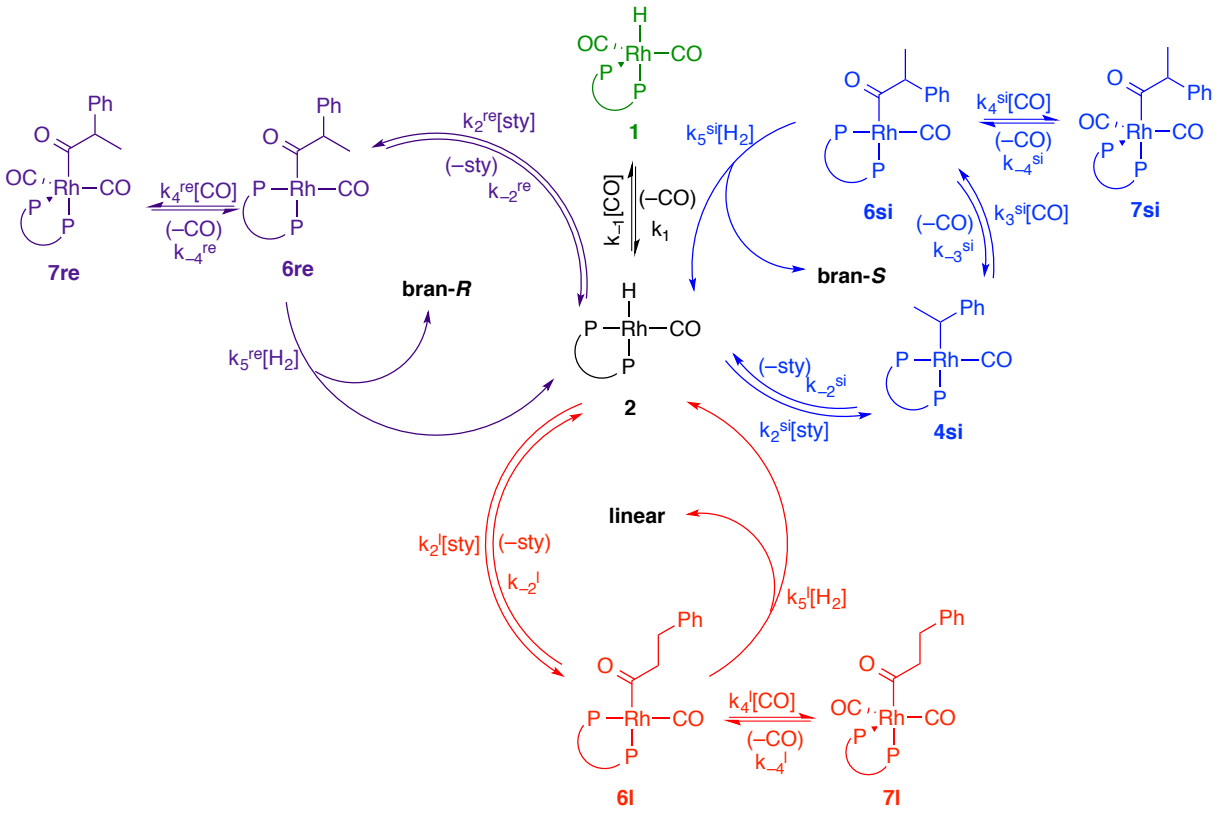

Figure 5-10. Full kinetic model used in the 'divide and conquer' approach.

5.2.4.1 Hydrogenolysis of Acyl Dicarbonyl Species (7)

In order to obtain activation parameters for the hydrogenolysis steps of AHF, we collected single turnover data from –15 to 17 °C, CO pressures from 18 to 70 psia, and H_2 pressures from 20 to >400 psia (Figure 5-11). The data were modeled in the same manner as described in Chapter 4, but rather than rate constants, $\Delta H^{\ddagger}$ and $\Delta S^{\ddagger}$ were optimized (Figure 5-12). As with our previous model, because **6** is not directly observable spectroscopically, k_4 and k_5 cannot be modeled independently, but we obtain their relative rates. Rather than a ratio of rate constants (as in Chapter 4), the difference between $\Delta H^{\ddagger}_4$ and $\Delta H^{\ddagger}_5$ as well as $\Delta S^{\ddagger}_4$ and $\Delta S^{\ddagger}_5$ are obtained (eq 5-5–5-6). Ideally, these values can be accurately extrapolated to warmer temperatures where the same non-catalytic hydrogenolysis experiments cannot be performed.

These results are in direct contrast to the computational values. The *ab initio* data show that reaction with H_2 is one of the significant barriers in AHF while CO association to the acyl monocarbonyl complex is barrierless (i.e. diffusion controlled) (Figure 5-2). In our refined model, the barriers are competitive. In fact, the enthalpic barrier for CO association to **6** is *higher* than for reaction with dihydrogen. In retrospect, this is not surprising; if reaction with H_2 was not competitive, fast catalytic rates would not be observed. With a model of these experiments in hand, we sought to continue modeling other non-catalytic experiments.

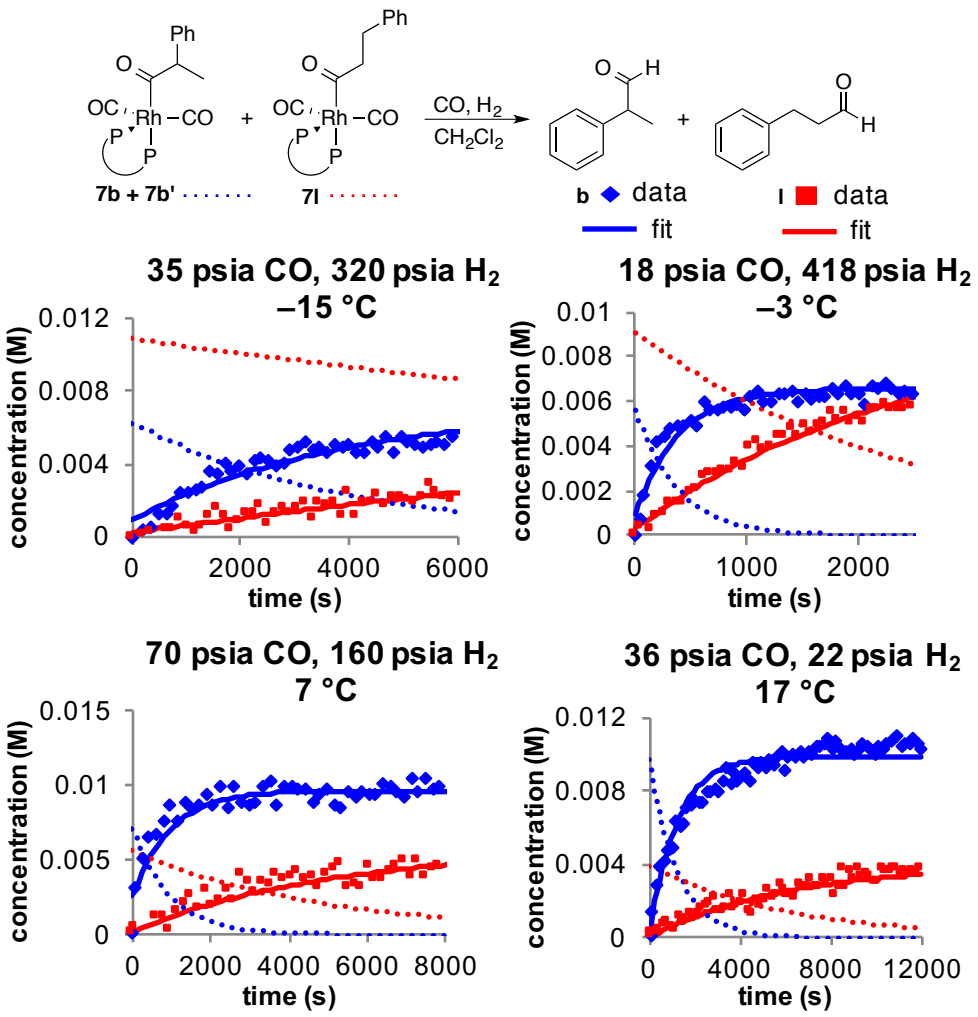

Figure 5-11. Example non-catalytic hydrogenolysis data and modeled fits. (~20 mM Rh(BDP) as ~1:1 mixture of acyls, varied temperature and CO/H_2 pressures: 258 K, 35 psi CO, 320 psi H_2 (top left); 270 K, 18 psi CO, 418 psi H_2 (top right); 280 K, 70 psi CO, 160 psi H_2 (bottom left); 290 K, 36 psi CO, 22 psi H_2 (bottom left)). Experiments chosen to highlight temperature and pressure ranges modeled. Points indicate the experimental data and solid lines represent the modeled fits.

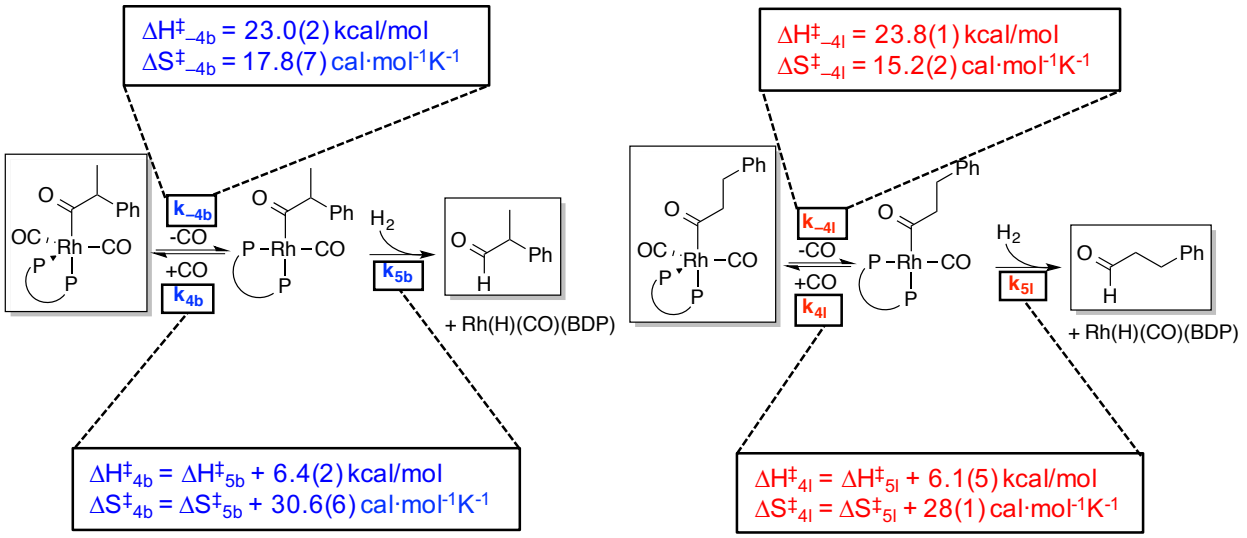

Figure 5-12. Model used to optimize activation parameters for non-catalytic hydrogenolysis experiments. Species in boxes are observable in the WiHP-NMRR.

$$\frac{k_4}{k_5} = \frac{2.0837\text{x}10^{10}(T)e^{-\left(\frac{\Delta H_4^{\ddagger}-(\Delta S_4^{\ddagger}(T))}{1.987(T)}\right)}}{2.0837\text{x}10^{10}(T)e^{-\left(\frac{\Delta H_5^{\ddagger}-(\Delta S_5^{\ddagger}(T))}{1.987(T)}\right)}} \qquad (5\text{-}5)$$

$$\frac{k_4}{k_5} = e^{\left(\frac{-\Delta H_4^{\ddagger}+\Delta H_5^{\ddagger}+(\Delta S_4^{\ddagger}-\Delta S_5^{\ddagger})(T)}{1.987(T)}\right)} \qquad (5\text{-}6)$$

*5.2.4.2 CO Dissociation from the Hydrido Dicarbonyl Species (**1**)*

As discussed above, we could not include monocarbonyl **2** in the model without first knowing the rate of CO loss from the hydrido dicarbonyl species (**1**). There are multiple ways to envision collecting these data. The first is to use a ^{13}CO labeled hydrido dicarbonyl complex in the WiHP-NMRR, add a known concentration of unlabeled CO, and monitor the loss of label as the free CO exchanges. Although this procedure would provide the desired information, it is a relatively inefficient approach. Each solution of RhH(^{13}CO)$_2$(BDP) could only be used once and

is thus both wasteful of an expensive label and time consuming. Instead, we used saturation transfer $^{13}C\{^{1}H\}$ NMR experiments of the same $RhH(^{13}CO)_2(BDP)$ complex. Using this pulse program, ^{13}C-labeled **1** is continuously saturated for a known length of time then pulsed to detect. The signal for free ^{13}CO decreases over time, due to exchange between the saturated ligands of **1** and free dissolved gas (Figure 5-13).[15] By collecting many of these experiments for varied saturation times (d5) we can obtain a time course for the loss of magnetization of free CO (Figure 5-14). Although this experiment is theoretically possible in the WiHP-NMRR, we used a J-young tube in a higher field instrument, which gives better signal-to-noise in the ^{13}C NMR spectrum. Due to the relatively slow exchange compared to the NMR time scale, a < 1 mM change in concentration is observed. These studies are limited to lower temperatures (where exchange is slower) because at higher temperatures, the hydrido dicarbonyl 1 dimerizes. For these reasons, the data are extremely noisy and the modeled fits are not perfect, but they provide a reasonable estimation of the rate for CO exchange.

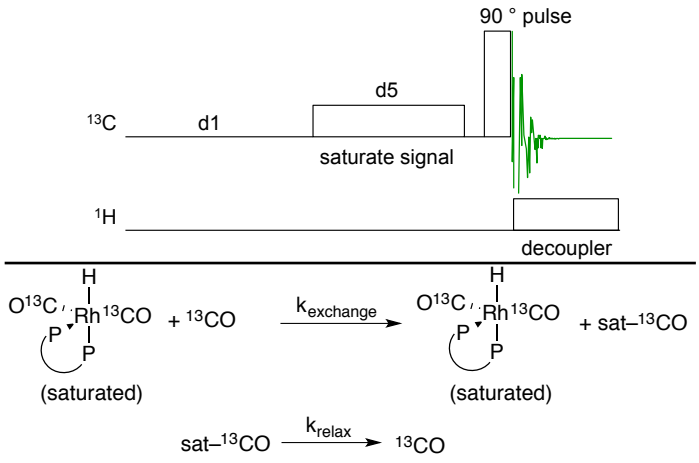

Figure 5-13. Pulse program for saturation transfer $^{13}C\{^{1}H\}$ NMR experiment (top) and kinetic model for the exchange of ^{13}CO in this experiment (bottom).

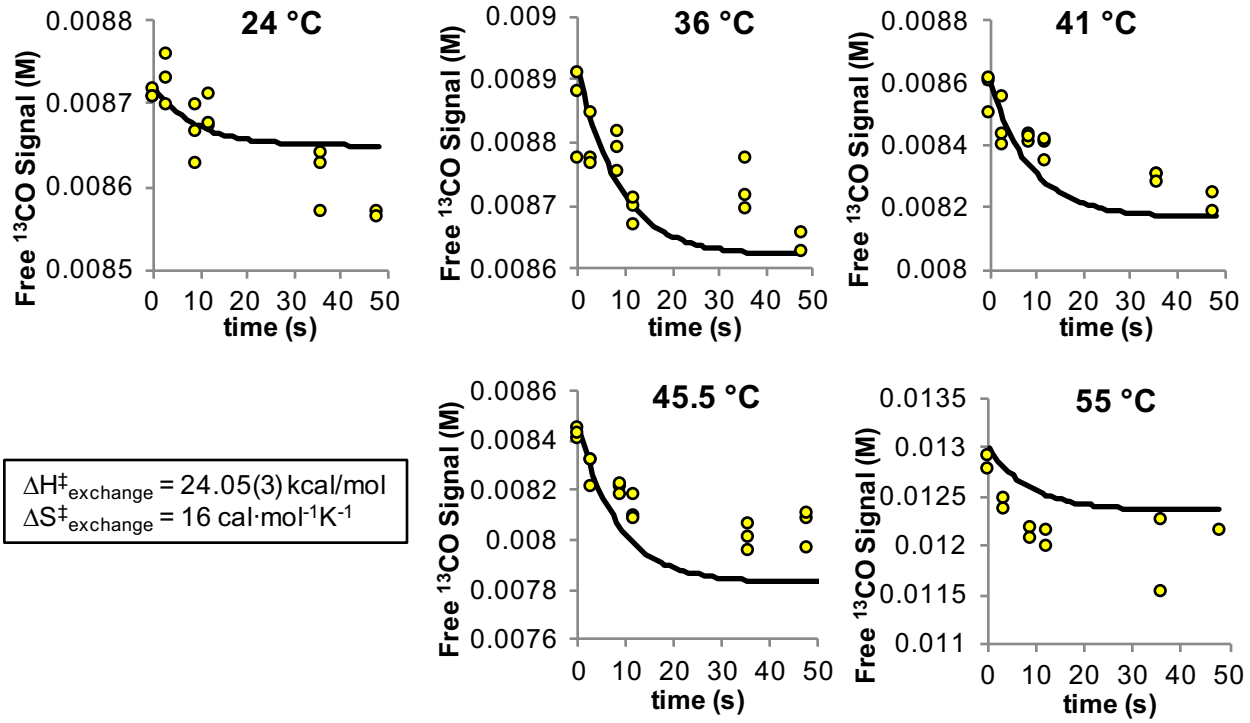

Figure 5-14. Saturation transfer data and fits modeling the rate of exchange of ligand ^{13}CO and free ^{13}CO. The noise in the data is due to measuring low (< 1mM) changes in concentration.

The model includes a species "sat-CO," which refers to free ^{13}CO without magnetization (i.e. saturated). Although this species is NMR silent, it is necessary to include its concentration to maintain mass balance in the model. The pulse program continuously saturates **1**, and therefore, this species is saturated on both sides of the equation (even after it exchanges with magnetized ^{13}CO). We modeled [^{13}CO] as a function of time at a range of temperatures (Figure 5-14). The rate constant k_{relax} is known from measuring T1 of free CO, so only $k_{exchange}$ was optimized in terms of $\Delta H^{\ddagger}$ and $\Delta S^{\ddagger}$ such that the data could be extrapolated to other temperatures. We can safely assume that the rate controlling exchange is loss of CO from **1**, rather than CO association to **2** because under all conditions we explored, the equilibrium between **1** and **2** lies far toward the dicarbonyl species; even under extremely low CO pressures, no hydrido monocarbonyl complex has been observed.

Due to the amount of noise in the data, $\Delta S^{\ddagger}$ could not be obtained independently of $\Delta H^{\ddagger}$. The activation entropy was assumed to be 16 cal·mol^{-1}K^{-1} because 1) that is a reasonable value based on the molecularity of the reaction and 2) similar values were obtained for CO loss from the acyl dicarbonyl species. With reasonable activation parameters in hand, these results were used to help model the formation of acyl dicarbonyl complexes.

5.2.4.3 Formation of Acyl Dicarbonyl Complexes (7)

The acyl dicarbonyl species (**7**) are a common resting state during AHF (see Chapter 4), and thus independently measuring their formation under non-catalytic conditions is valuable for building up to the full catalytic model. As shown previously, the reaction of the hydrido dicarbonyl species (**1**) with styrene produces the acyl dicarbonyl complexes (**7**) (Chapter 3). Under CO-starved conditions, this leads to predominantly the linear isomer, but at constant CO pressures in the WiHP-NMRR, the branched complexes are favored (Figure 5-15).[3,5,16]

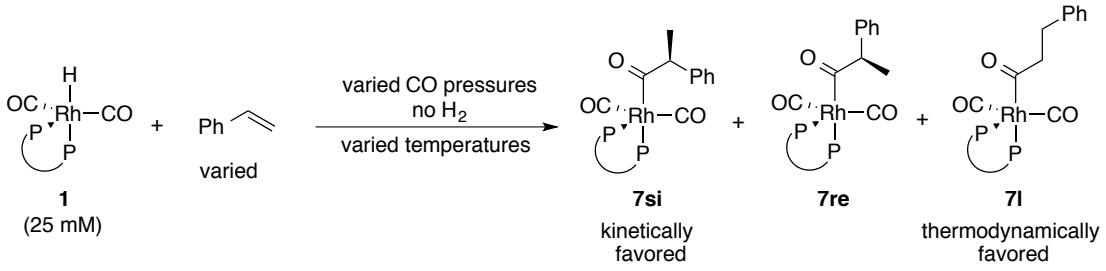

Figure 5-15. General reaction conditions for forming acyl dicarbonyl complexes in the WiHP-NMRR.

These reactions were carried out in the WiHP-NMRR under a variety of styrene concentrations (10–100 mM), CO pressures (180–465 psia), and temperatures (6–27 °C). These conditions formed the acyl species at reasonable rates, allowing us to monitor the reactions in the WiHP-NMRR without competing isomerization of **7si** to the thermodynamically favored **7l**. The

data revealed a first order dependence on [styrene], and surprisingly, a simple first order inhibition by [CO]. This indicates that the CO associations to alkyl **4** or to acyl monocarbonyl **6** are relatively fast compared to reaction with styrene. For this reason, we modeled these data phenomenlogically as a reaction of **2** and styrene, despite the fact that CO is required for acyl **7** formation (Figure 5-16). The activation parameters for the loss of CO from **1** were set based on the results from the previous model. Because **2** is not observed during the reaction, activation parameters for k_{-1} cannot be obtained independently from k_2. Therefore, $\Delta H^{\ddagger}_{-1}$ and $\Delta S^{\ddagger}_{-1}$ were set to 7 kcal/mol and –16 cal·mol^{-1}K^{-1}, respectively. The entropy activation value was chosen based on the assumed entropy value for the reverse reaction (*vide supra*) and the enthalpic parameter was arbitrarily chosen to be a relatively low barrier for this step. The entropic activation parameters for the three steps involving styrene ($\Delta S^{\ddagger}_2$) were set equal to one another because the concentrations of **7re** and **7l** were too low and therefore not sensitive enough to obtain these values independently of the enthalpic contribution. Thus, we assume that these entropic values will be similar to the major pathways (k_2^{si}, **7si**).

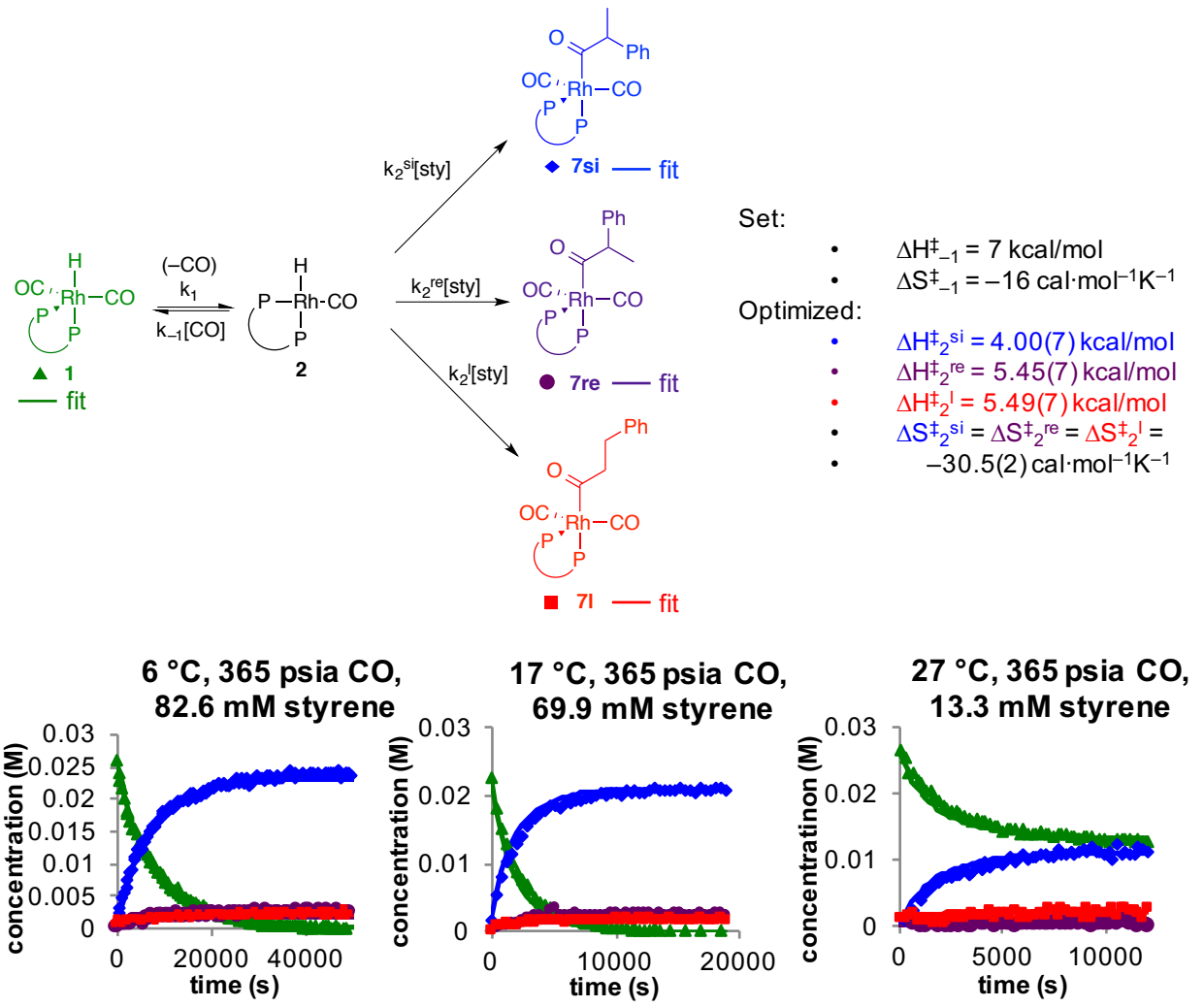

Figure 5-16. Kinetic model, example fits, and optimized activation parameters for the formation of acyl dicarbonyls **7** under non-catalytic conditions. (~25 mM **1**, 365 psia CO, varied temperature and styrene concentrations: 279 K and 82.6 mM styrene (left); 290 K and 69.9 mM styrene (middle); 300 K and 13.3 mM styrene (right)). Experiments chosen to highlight temperature and concentration ranges modeled. Points indicate the experimental data and solid lines represent the modeled fits.

Computations (*vide supra*) show that reaction with styrene (insertion into the Rh–H bond) has a significant enthalpic barrier, but CO association is barrierless (i.e. diffusion controlled). Interestingly, the modeling results reveal that the reaction with styrene is highly

competitive with CO association. These values must be competitive in order to obtain the rates we observe in catalytic AHF. While we cannot draw any conclusions from the exact values reported because we can only model the relative barriers, these results highlight the discrepancies between the model and computations.

These experiments were unable to determine the fate of the alkyls **4**, because we only observed a simple first order inhibition by [CO]. This indicated that the barrier for CO association/insertion (**4→6**) was lower than for styrene association/insertion (**2→4**), but does not provide an exact values. Because **4** cannot be observed directly in the WiHP-NMRR, we employed indirect methods to probe this intermediate.

*5.2.4.4 Isomerization of the Major Alkyl Complex (**4si**)*

Deuteroformylation of alkenes has proven to be an effective technique for probing the reversibility of alkyl **4** formation (Scheme 5-3).[2,17-21] Our previous work (Chapter 4) demonstrated that styrene insertion into the Rh–H bond is reversible with this same catalyst,[5] but we sought to extend these studies to quantify the fate the of alkyl intermediate. These batch reactions are conducted in standard pressure bottles (not the WiHP-NMRR), meaning that only one time point is collected per experiment. By determining the ratio of *d*-alkene to *d*-aldehyde at a given time, we can determine the relative rates for k_{-2} and k_3 shown in Figure 5-10. Deuteroformylation reactions need to be stopped at low conversion to prevent multiple label scrambling events, but at these early time points, only *d*-branched aldehyde and β-deuterostyrene are observed in the ^{2}H NMR spectrum. Therefore, the quantitation of k_{-2}/k_3 is limited to the major, si pathway.

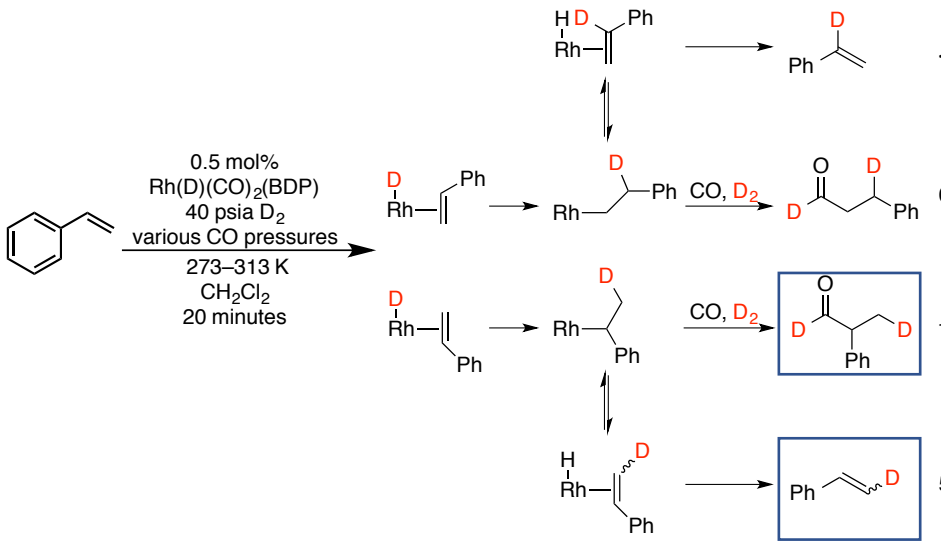

Scheme 5-3. Potential and observed (boxed) products from the deuteroformylation of styrene.

A simple model was used to determine the ratio of k_{-2}^{si}/k_3^{si}. In a similar manner to the hydrogenolysis experiments (*vide supra*), the differences between the activation enthalpies and entropies were optimized (eq 5-7–5-9). The model results are shown in Table 5-1.

$$\frac{[d\text{-alkene}]}{[d\text{-aldehyde}]} = \frac{[\mathbf{4si}]k_{-2}^{si}}{[\mathbf{4si}][CO]k_3^{si}} \qquad (5\text{-}7)$$

$$\frac{k_{-2}^{si}}{k_3^{si}} = \frac{2.0837\text{x}10^{10}(T)e^{-\left(\frac{\Delta H_{-2}^{\ddagger}-(\Delta S_{-2}^{\ddagger}(T))}{1.987(T)}\right)}}{2.0837\text{x}10^{10}(T)e^{-\left(\frac{\Delta H_{3}^{\ddagger}-(\Delta S_{3}^{\ddagger}(T))}{1.987(T)}\right)}} \qquad (5\text{-}8)$$

$$\frac{k_{-2}^{si}}{k_3^{si}} = e^{\left(\frac{-\Delta H_{-2}^{\ddagger}+\Delta H_{3}^{\ddagger}+(\Delta S_{-2}^{\ddagger}-\Delta S_{3}^{\ddagger})(T)}{1.987(T)}\right)} \qquad (5\text{-}9)$$

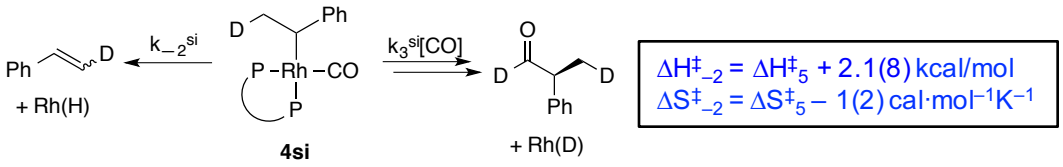

Temperature (K)	Pressure CO (psia)	measured *d*-alkene:*d*-aldehyde	computed *d*-alkene:*d*-aldehyde
288	40	0.676	0.618
288	80	0.245	0.309
293	40	0.625	0.653
293	80	0.322	0.327
313	40	0.842	0.801
313	80	0.329	0.400

Table 5-1. Measured and computed *d*-alkene:*d*-aldehyde ratios for deuteroformylation batch reactions under several temperatures and CO pressures.

Consistent with our previous assumptions (Chapter 4), the barriers for β–hydride elimination and CO insertion are highly competitive with each other and thus alkyl **4** isomerization is relevant compared to CO addition under catalytic reaction conditions. At high temperatures and low CO pressures, both acyls **6** and **7** isomerization is also rapid enough to affect catalysis, thus the final barriers we need to measure and optimize are those for the reversion of the acyl monocarbonyls to the hydride **2** and styrene.

*5.2.4.5 Isomerization of the Acyl Complexes (**6**)*

The last rate constants to model in the "divide and conquer" approach are the reversions of the three acyl monocarbonyl species **6si**, **6re**, and **6l** (k_{-3}^{si}, k_{-2}^{re}, and k_{-2}^{l}) in Figure 5-10. The isomerization of the acyl dicarbonyl complexes **7** can be monitored in the WiHP-NMRR (Figure 5-17). Because the CO loss from **7** to **6** was previously modeled, the reactivity of **6** could be separated from that of **7**. The kinetic distribution of acyls **7** was formed as previously shown

(Section 5.2.4.3). Then the temperature was increased to 20–41 °C and the pressure in the reactor decreased to 10–80 psia CO in order to begin the reaction. The isomerization of **7si** and **7re** to **7l** was monitored by $^{31}P\{^{1}H\}$ NMR spectroscopy.

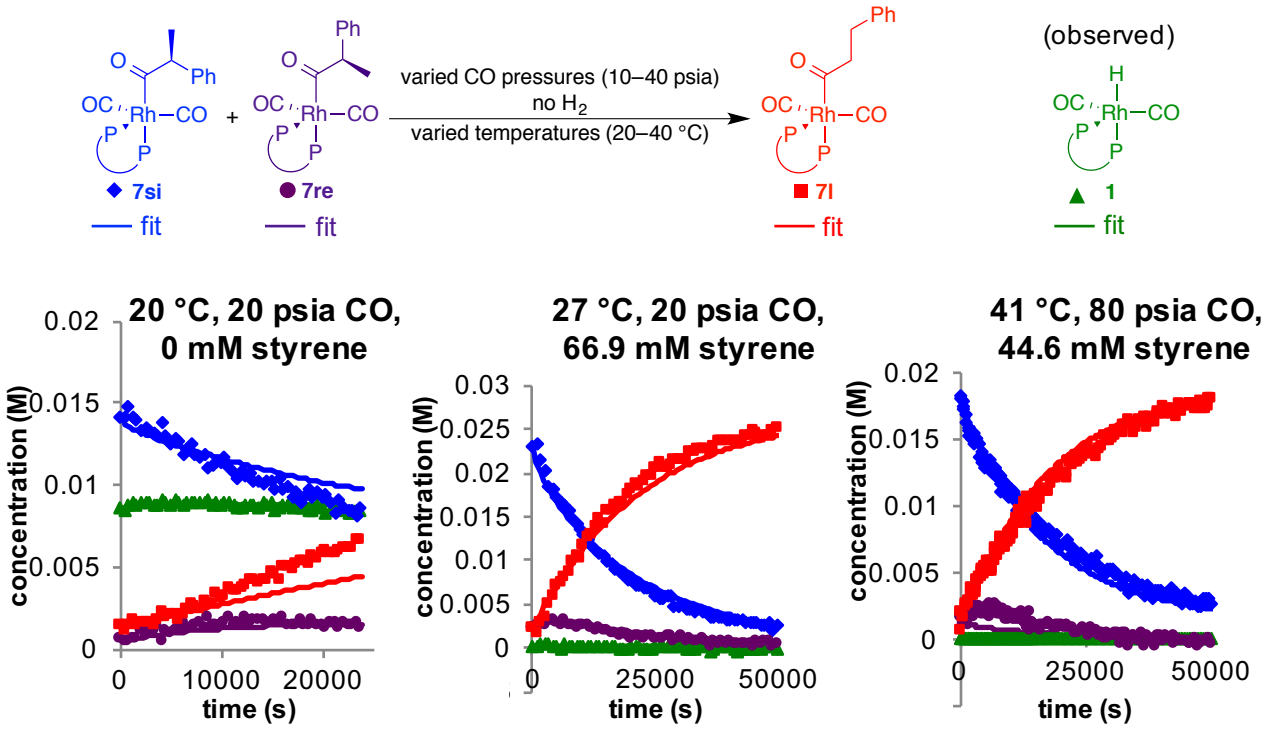

Figure 5-17. Isomerization of acyls **7si** and **7re** to thermodynamically favored **7l**. (~20 mM **7si**, , varied temperature, CO pressure, and styrene concentrations: 294 K, 20 psia CO and 0 mM excess styrene (left); 300 K, 20 psia CO, and 66.9 mM excess styrene (middle); 314 K, 80 psia CO, and 44.6 mM excess styrene (right)). Experiments chosen to highlight temperature, pressure, and concentration ranges modeled. Points indicate the experimental data and solid lines represent the modeled fits.

By using all the previously modeled parameters in the "divide and conquer" approach, we optimized the activation enthalpies for the reversion of the acyl monocarbonyls **6** to either the alkyl **4** or hydride **2** (si or re/l pathways, respectively) (Figure 5-18). The entropies were based on the optimized value in the opposite direction. For example, $\Delta S^{\ddagger}_{2}{}^{re}$ = –30.5 cal/mol·K,

therefore in the reverse direction the molecularity of the reaction implies that $\Delta S^{\ddagger}_{-2}{}^{re} \approx 0$ cal·mol^{-1}K^{-1}. To ensure that the acyl formation steps were not incorrectly impacted by adjusting the isomerization barriers, we included these data while optimizing the activation parameters for $k_{-3}{}^{si}$, $k_{-2}{}^{re}$, and $k_{-2}{}^{l}$. This guarantees that significant isomerization would not occur in the model at the colder temperatures when extrapolating $\Delta S^{\ddagger}$ and $\Delta H^{\ddagger}$.

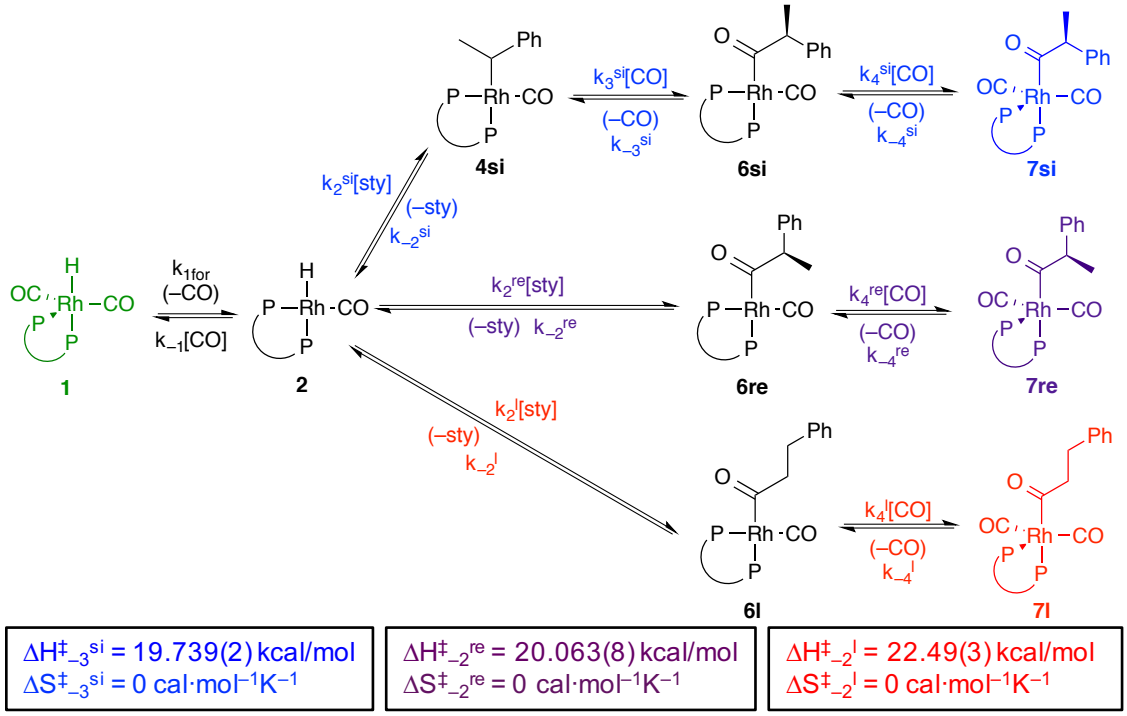

Figure 5-18. Model for isomerization of acyl dicarbonyls **7**. Modeled activation parameters for $k_{-3}{}^{si}$, $k_{-2}{}^{re}$, $k_{-2}{}^{l}$. All other parameters set based on previous models.

The values obtained in this model demonstrate that while acyl reversion of the si pathway is faster than that of the linear, there is only a 3 kcal/mol difference in enthalpic barriers. In fact, there is no direct evidence of the linear isomer reverting—only that the thermodynamic mixture does not solely prefer **7l**. This emphasizes the fact that small changes in energies can lead to significant changes to catalysis and overall rates and selectivity of the reaction.

5.2.4.6 Summary of Modeled Parameters

We were able to successfully model acyl formation, isomerization, and hydrogenolysis simultaneously. This is a significant advance in the understanding of AHF. Our results highlight that the importance of considering each step in AHF. The overall selectivity of the reaction is controlled by all of these, rather than a single step dominating the process. While there is a kinetic preference for the si pathway, at colder temperatures (0–27 °C), while alkyl **4si** can isomerize, most of the catalyst remains on the major pathway because CO insertion is faster than β-hydride elimination. Additionally, the reversion of the acyls **6** is essentially non-existent at these temperatures. As the temperature is raised (40 °C), isomerization of alkyl **4** outcompetes CO insertion to give **6**. Furthermore, the reversion of **6** is competitive with the overall rates of reaction, leading to more catalyst on the slower, linear pathway that contains a thermodynamic sink. A summary of optimized parameters in Table 5-2.

Parameter	Value	Set or Optimized?	Section
$\Delta H^{\ddagger}_{1}$	24.05(3) kcal/mol	optimized	5.2.4.2
$\Delta S^{\ddagger}_{1}$	16 cal·mol^{-1}K^{-1}	set	5.2.4.2
$\Delta H^{\ddagger}_{-1}$	7 kcal/mol	set	5.2.4.3
$\Delta S^{\ddagger}_{-1}$	–16 cal·mol^{-1}K^{-1}	set	5.2.4.3
$\Delta H^{\ddagger}_{2}{}^{si}$	4.00(7) kcal/mol	optimized	5.2.4.3
$\Delta S^{\ddagger}_{2}{}^{si}$	-30.5(2) cal·mol^{-1}K^{-1}	optimized	5.2.4.3
$\Delta H^{\ddagger}_{-2}{}^{si}$	13.90 kcal/mol	set based on relationship to $\Delta H^{\ddagger}_{3}{}^{si}$	5.2.4.2
$\Delta H^{\ddagger}_{-2}{}^{si}$	–1.1 cal·mol^{-1}K^{-1}	set based on relationship to $\Delta S^{\ddagger}_{3}{}^{si}$	5.2.4.2
$\Delta H^{\ddagger}_{2}{}^{re}$	5.45(7) kcal/mol	optimized	5.2.4.3
$\Delta S^{\ddagger}_{2}{}^{re}$	-30.5 cal·mol^{-1}K^{-1}	set equal to $\Delta S^{\ddagger}_{2}{}^{si}$	5.2.4.3
$\Delta H^{\ddagger}_{-2}{}^{re}$	20.063(8) kcal/mol	optimized	5.2.4.5

$\Delta S^{\ddagger}_{-2}{}^{re}$	0 cal·mol^{-1}K^{-1}	set based on $\Delta S^{\ddagger}_{2}{}^{re}$	5.2.4.5
$\Delta H^{\ddagger}_{2}{}^{l}$	5.49(7) kcal/mol	optimized	5.2.4.3
$\Delta S^{\ddagger}_{2}{}^{l}$	-30.5 cal·mol^{-1}K^{-1}	set equal to $\Delta S^{\ddagger}_{2}{}^{si}$	5.2.4.3
$\Delta H^{\ddagger}_{-2}{}^{l}$	22.49(3) kcal/mol	optimized	5.2.4.5
$\Delta S^{\ddagger}_{-2}{}^{l}$	0 cal·mol^{-1}K^{-1}	set based on $\Delta S^{\ddagger}_{2}{}^{l}$	5.2.4.5
$\Delta H^{\ddagger}_{3}{}^{si}$	11.80 kcal/mol	set	5.2.4.2
$\Delta S^{\ddagger}_{3}{}^{si}$	0 cal·mol^{-1}K^{-1}	set	5.2.4.2
$\Delta H^{\ddagger}_{-3}{}^{si}$	19.739(2) kcal/mol	optimized	5.2.4.5
$\Delta S^{\ddagger}_{-3}{}^{si}$	0 cal·mol^{-1}K^{-1}	set	5.2.4.5
$\Delta H^{\ddagger}_{4}{}^{si}$	9 kcal/mol	set	5.2.4.1
$\Delta S^{\ddagger}_{4}{}^{si}$	–12.2 cal·mol^{-1}K^{-1}	set based on $\Delta S^{\ddagger}_{-4}{}^{si}$	5.2.4.1
$\Delta H^{\ddagger}_{-4}{}^{si}$	23.0(2) kcal/mol	optimized	5.2.4.1
$\Delta S^{\ddagger}_{-4}{}^{si}$	17.8(7) cal·mol^{-1}K^{-1}	optimized	5.2.4.1
$\Delta H^{\ddagger}_{4}{}^{re}$	9 kcal/mol	set	5.2.4.1
$\Delta S^{\ddagger}_{4}{}^{re}$	–12.2 cal·mol^{-1}K^{-1}	set based on $\Delta S^{\ddagger}_{-4}{}^{si}$	5.2.4.1
$\Delta H^{\ddagger}_{-4}{}^{re}$	23.0(2) kcal/mol	optimized	5.2.4.1
$\Delta S^{\ddagger}_{-4}{}^{re}$	17.8(7) cal·mol^{-1}K^{-1}	optimized	5.2.4.1
$\Delta H^{\ddagger}_{4}{}^{l}$	9 kcal/mol	set	5.2.4.1
$\Delta S^{\ddagger}_{4}{}^{l}$	–14.8 cal·mol^{-1}K^{-1}	set based on $\Delta S^{\ddagger}_{-4}{}^{l}$	5.2.4.1
$\Delta H^{\ddagger}_{-4}{}^{l}$	23.8(1) kcal/mol	optimized	5.2.4.1
$\Delta S^{\ddagger}_{-4}{}^{l}$	15.5(2) cal·mol^{-1}K^{-1}	optimized	5.2.4.1
$\Delta H^{\ddagger}_{5}{}^{si}$	2.6 kcal/mol	set based on $\Delta H^{\ddagger}_{4}{}^{si}$	5.2.4.1
$\Delta S^{\ddagger}_{5}{}^{si}$	–42.8 cal·mol^{-1}K^{-1}	set based on $\Delta S^{\ddagger}_{4}{}^{si}$	5.2.4.1
$\Delta H^{\ddagger}_{5}{}^{re}$	2.6 kcal/mol	set based on $\Delta H^{\ddagger}_{4}{}^{re}$	5.2.4.1
$\Delta S^{\ddagger}_{5}{}^{re}$	–42.8 cal·mol^{-1}K^{-1}	set based on $\Delta S^{\ddagger}_{4}{}^{re}$	5.2.4.1

$\Delta H^{\ddagger}_{5}{}^{re}$	2.9 kcal/mol	set based on $\Delta H^{\ddagger}_{4}{}^{l}$	5.2.4.1
$\Delta S^{\ddagger}_{5}{}^{re}$	–43.4 cal·mol^{-1}K^{-1}	set based on $\Delta S^{\ddagger}_{4}{}^{l}$	5.2.4.1

Table 5-2. Summary of set and optimized parameters in Section 5.2.4. Reported errors are standard deviations from the modeled fits in COPASI.

5.2.4.7 Catalytic Fits

These optimized values for acyl formation, isomerization and hydrogenolysis describe a full catalytic reaction. As a check of our whole model, we used the activation parameters laid out in Table 5-2 to test how well the model fit our catalytic data collected in the WiHP-NMRR. We optimized no values in this section, but simply overlaid the fits and experimental data.

At colder temperatures (0–17 °C), we obtained relatively good fits of the catalytic reactions (Figure 5-19). The data at 0 °C are a factor of ~2 off in rate, but the 17 °C data are matched exceptionally well. The fits match catalyst speciation as well as overall rate and selectivity. Although both temperatures were not fit perfectly, these results were a promising proof of concept for our model.

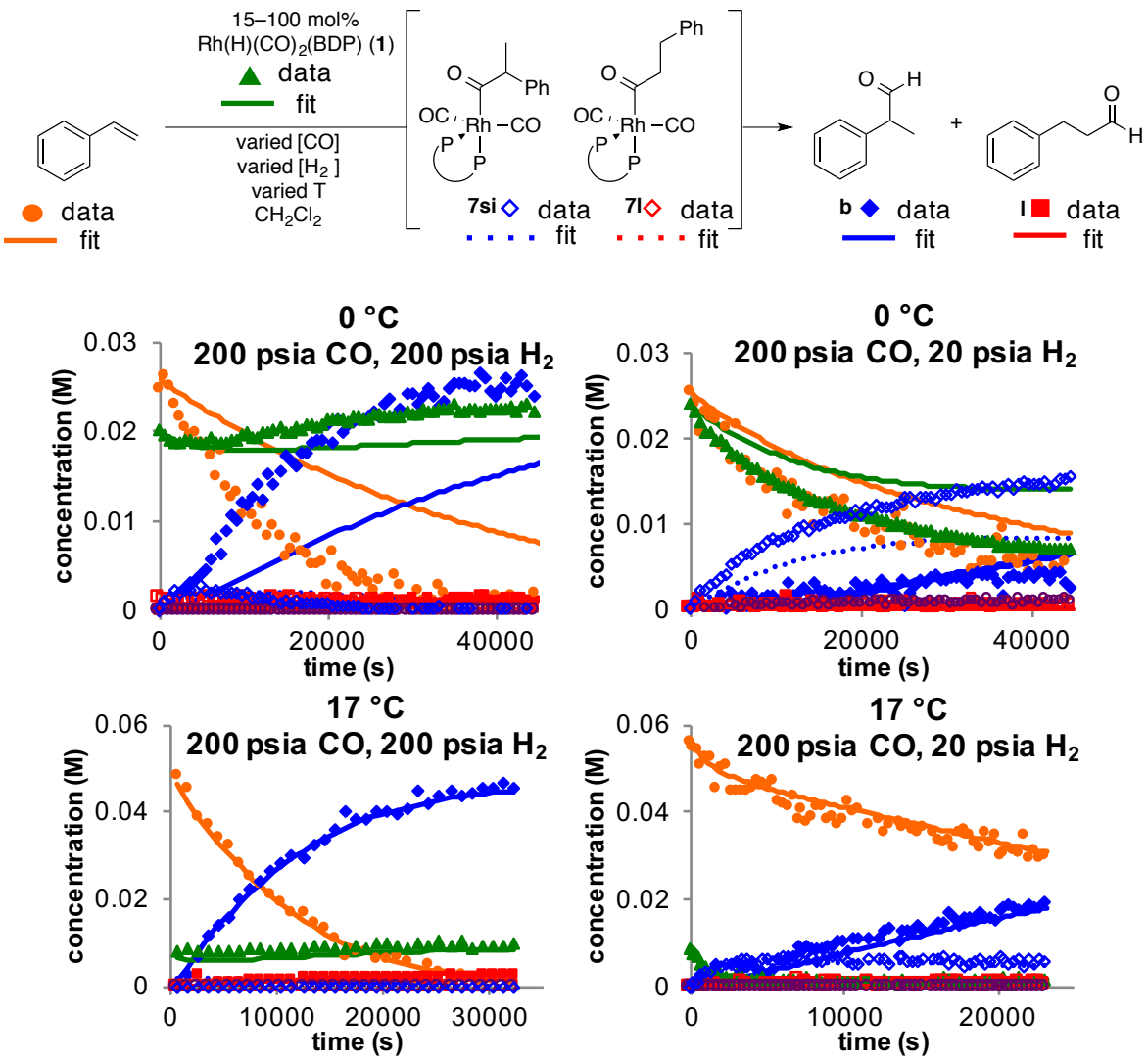

Figure 5-19. Example fits for catalytic reactions at 0 °C and 17 °C using previously optimized parameters. Top: 0.25 M styrene, 0.25 M **1**, 273 K, 200 psia CO and varied H_2 pressure: 200 psia H_2 (top left); 20 psia H_2 (top right). Bottom: 0.055 M styrene, 0.01 M **1**, 290 K, 200 psia CO and varied H_2 pressure: 200 psia H_2 (bottom left); 20 psia H_2 (bottom right). Points indicate the experimental data and solid lines represent the modeled fits.

In contrast, our model does not fit the catalytic data at 40 °C as well as the lower temperature data (Figure 5-20). Unfortunately, these data indicate that the modeled temperature dependencies of some steps are substantially different from the true values. Because the

extrapolations to high temperatures are more problematic, it appears that parameters modeled at low temperatures are most likely incorrect. Based on the significant difference in the fits of the two examples at 40 °C by only changing the [H_2], it implies that the hydrogenolysis steps are not modeled well enough: the rate constants for competition between binding CO and reaction with dihydrogen from **6** are not correct. This is unsurprising because the values for CO association to acyl monocarbonyls **6** were arbitrarily set. Although we know that this step is relatively fast (no **6** is ever observed), the thermodynamic equilibrium between **6** and **7** is likely incorrect for all three pathways.

This same issue is likely problematic elsewhere in the model as well. For example, the activation parameters for CO association to the hydrido monocarbonyl **1** were assumed. Although we know this rate must be fast, the modeled thermodynamic equilibrium between **1** and **2** is potentially incorrect, but because we cannot observe **1**, we cannot measure K_{eq} directly. We also assumed values for CO association to **4si** to give the acyl **6si** (k_3^{si}). We set this to a relatively fast value compared to formation of **4si** based on the phenomenological rate law observed in the formation of acyl species (Section 5.2.4.3), but the exact value is unknown. In order to improve the kinetic model at higher temperatures, we need to better model the temperature dependence of these steps. This will include changing these assumed values and remodeling all experimental data simultaneously (*vide infra*).

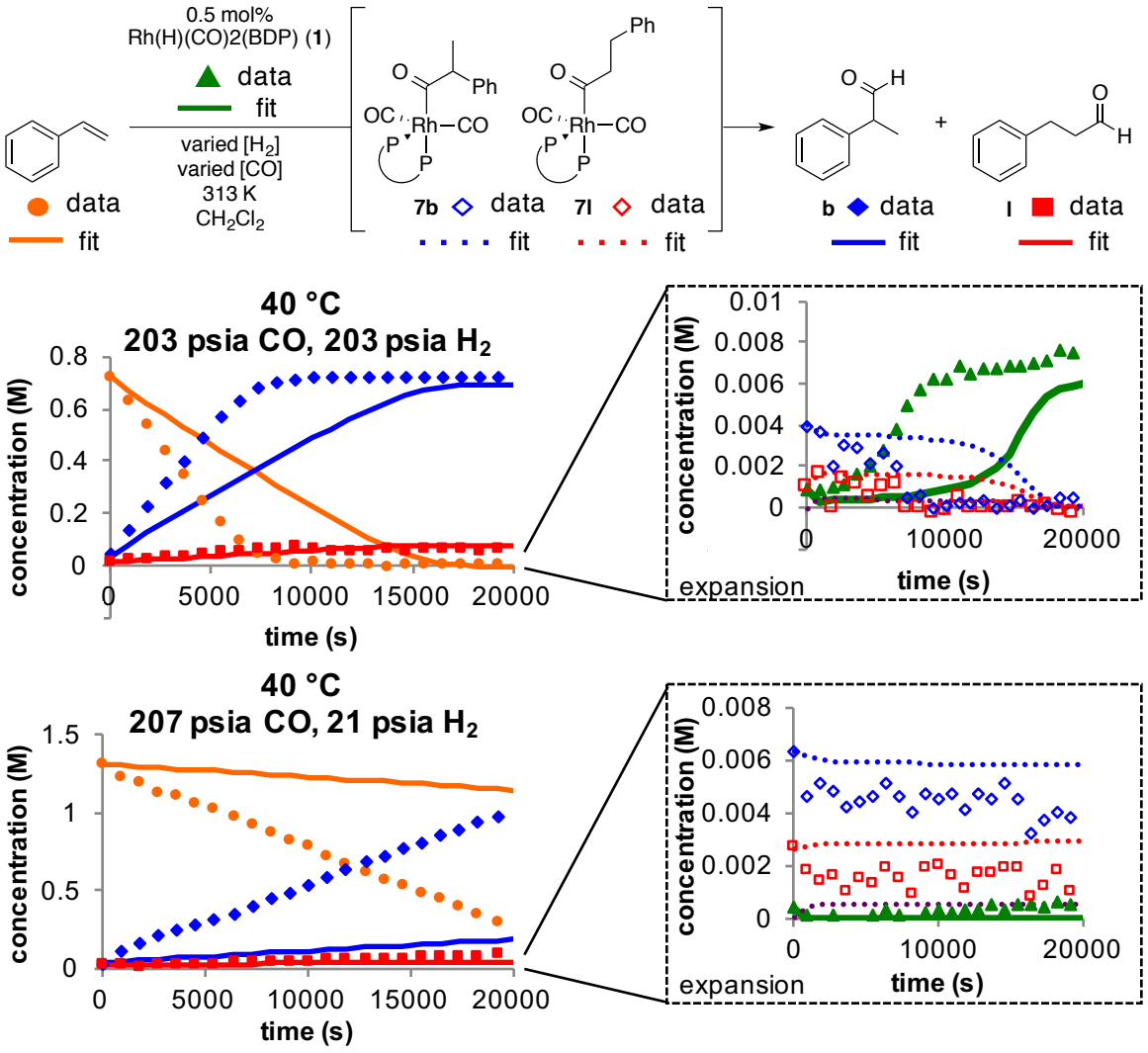

Figure 5-20. Example fits for catalytic reactions at 40 °C using previously optimized parameters. Top: 0.75 M styrene, 0.008 M **1**, 313 K, 200 psia CO and 200 psia H_2. Bottom: 1.4 M styrene, 0.008 M **1**, 313 K, 200 psia CO 20 psia H_2. Points indicate the experimental data and solid lines represent the modeled fits.

5.3 Conclusions

The goal of this Chapter was to develop an approach for microkinetic modeling of asymmetric hydroformylation. We first used the experimentally simplest model, which was

based solely on *ab initio* computations. Comparison of modeled catalytic reactions versus experimental data revealed that the computed free energy barriers were not accurate enough to be used in a kinetic model. The predicted rates were orders of magnitudes slower than the empirical data, therefore, it was apparent that a different approach was required.

By testing several models, we determined that a simplified model with some elementary reactions combined into pseudoelementary steps was effective, as it 1) includes all three isomeric pathways, and 2) limits the number of adjustable parameters. Furthermore, we demonstrated that combining both catalytic and non-catalytic data in a single model could be beneficial to developing the full reaction. This led us to the "divide and conquer" approach, in which we collected a variety of non-catalytic data, modeled them independently, and then attempted to use those results to fit catalytic experiments.

The non-catalytic modeling results revealed that many barriers are close in energy, which affects selectivity. For example, there is only a 3 kcal/mol difference in enthalpic barriers between the acyl reversion of the si and linear pathways, but there is only direct evidence of the si pathway reverting; this indicates that a small difference in barriers leads to a great difference in rates. There is only a 1.5 kcal/mol difference in the enthalpic activation entropy for binding and inserting styrene to **1** between the si and linear pathways. Less than 1 kcal/mol difference in CO loss from the acyl dicarbonyls **7** leads to the faster hydrogenolysis of **7b** over **7l**. This highlights the difficulty in modeling these data, as small errors in computed or modeled energy barriers lead to inaccurate fitting of selectivity and rates.

In disagreement with the *ab initio* computations, the non-catalytic models revealed that CO association is not a barrierless process. These models show that alkene association/insertion to **1**, alkyl reversion, and H_2 association/reaction with **6** are actually competitive with the CO

coordination steps. In fact, in some cases, the enthalpic barrier is modeled to be lower for the non-CO containing steps. While the absolute values for these steps may be modeled incorrectly in the final model presented here, the modeling results emphasize that CO association steps are poorly computed by these *ab initio* methods.

The three CO association barriers were arbitrarily set, and therefore these are likely a major contributor to the problems fitting catalytic data at warm (40 °C) temperatures. Because hydrido monocarbonyl **2**, alkyl monocarbonyl **4**, and acyl monocarbonyl **6** are not directly observed under reaction conditions, only the ratios between CO association and the non-CO steps could be computed. Thus, we likely have the relative values correctly modeled, though the absolute values may still be incorrect. In order to address this deficiency, current efforts are focused on systematically scanning through a range of possible enthalpic CO association barriers for each of the three steps and reoptimizing the adjustable parameters at each combination. With this approach, we hope to determine which CO-containing steps are the most problematic in the model and establish more accurate values.

While this model is not yet accurate for catalytic reactions at all temperatures, the rate constants at 17 °C are likely close to correct. The fact that we can fit catalytic reactions at a range (20–200 psia) of CO and H_2 pressures is evidence for an accurate model. Therefore, we can still learn about the selectivity determining steps of these reactions. Furthermore, the fact that all types of non-catalytic data are fit well, allows us to understand how small the differences in energy barriers are for the three isomeric pathways. This work was successful in identifying the most effective approach to a complex problem, indicating the discrepancies between computations and empirical data, as well as emphasizing that small differences in energy barriers can lead to large differences in selectivity and rate.

5.4 Experimental Details

5.4.1 General Considerations

All reactions and manipulations were carried out under nitrogen using standard Schlenk and glovebox techniques. Work up and purification procedures were performed open to air. Dichloromethane was used from a solvent purification system packed with activated alumina. CD_2Cl_2 was distilled from P_2O_5 and degassed. Solvents for column chromatography were used as received. Styrene was filtered through silica and sparged. Tetraphenyl bis(diazaphospholane), Rh(acac)(BDP), and $Rh(H)(CO)_2$(BDP) were synthesized following literature procedure.[12]

Routine ^1H and $^{31}P\{^1H\}$ spectra were recorded on a Bruker Avance-400 MHz spectrometer; WiHP-NMRR ^1H and $^{31}P\{^1H\}$ spectra were performed on a Bruker Avance-360 MHz spectrometer with a Bruker 10 mm BB probe. Proton spectra were referenced to residual protio solvent. Phosphorus spectra were referenced to the corresponding proton spectrum using an xref macro.

5.4.2 General Method for Catalytic WiHP-NMRR Experiments

$Rh(H)(CO)_2$(BDP) was prepared as reported and depressurized to 5 psig. The reactor was brought into a N_2-purged glovebox. The solution was added to a vial of triphenylphosphine oxide and 1,4-bis(trimethylsilyl)benzene (^{31}P and ^1H internal standards, respectively). The contents were pulled into a threaded, gas-tight syringe (syringe one). The vial was rinsed with dichloromethane, which was pulled into a second syringe. The total volume of the two catalyst containing syringes (catalyst and rinse) was 2.0 mL. The desired volume of styrene was put into

the third syringe, and the fourth contained a dichloromethane rinse. The combined volume of syringes three and four was either 150 or 500 μL (depending on required volume of styrene).

The WiHP-NMRR was purged with nitrogen with three vent/refill cycles. The catalyst and rinse (syringes one and two) were injected into the high-pressure NMR tube. The probe was set to the desired temperature and pressure of CO and H_2 with an over pressure in the antecylinder. The initial spectra were acquired. Styrene and rinse (syringes three and four) were injected with the system under an over-pressure of N_2. Acquisition with circulation during NMR pulse sequence delays was started.

5.4.3 General Method for Single Turnover WiHP-NMRR Experiments

$Rh(H)(CO)_2(BDP)$ was prepared as reported and depressurized to 5 psig. The reactor was brought into a N_2-purged glovebox. The solution was added to a vial of triphenylphosphine oxide and 1,4-bis(trimethylsilyl)benzene (^{31}P and ^{1}H internal standards, respectively). The contents were pulled into a threaded, gas-tight syringe (syringe one). The vial was rinsed with dichloromethane, which was pulled into a second syringe. The total volume of the two catalyst containing syringes (catalyst and rinse) was 2.0 mL. A solution of styrene in dichloromethane was prepared and pulled into the third syringe, and the fourth contained a dichloromethane rinse. The total volume of syringes three and four was 150 μL.

The WiHP-NMRR was purged with nitrogen with three vent/refill cycles. The catalyst and rinse (syringes one and two) were injected into the high-pressure NMR tube. The reactor was pressurized, circulated, and vented five times with CO. The system was pressurized to 17 psia CO, warmed to 310 K, and styrene and rinse (syringes 3 and 4) were injected with an

overpressure of N_2. The formation of acyl dicarbonyls was monitored by ^1H and $^{31}P\{^1H\}$ NMR spectroscopy. Upon reaching an approximately 1:1 mixture of the two isomeric acyl dicarbonyls, the system was cooled and pressurized to the desired temperature and CO pressure, respectively. The appropriate pressure of H_2 was added to the reactor and acquisition with circulation during NMR pulse sequence delays was started. ^1H NMR spectroscopy was used to monitor the formation of aldehydes, and $^{31}P\{^1H\}$ was used to monitor the disappearance of acyl dicarbonyls. Reactions with relatively short half-lives (<10 min) were followed by ^1H NMR only.

5.4.4 General Method for Deuteroformylation Experiments

The experimental setup was adapted from the method reported in the literature.[11] In a N_2-purged glovebox, solutions for deuteroformylation were prepared by combining Rh(acac)(BDP) (0.0015 mmol) stock solution, diphenylmethane internal standard (0.3 mmol), and dichloromethane to an oven-dried 50 mL pressure bottle equipped with a magnetic stir bar (total volume = 0.9 mL). The pressure bottle was then connected to a gauged pressure reactor assembly, and the reactor was removed from the glovebox. The reactor was purged five times with CO, charged with 40 psia CO followed by 40 psia D_2, and allowed to stir in a 60 °C oil bath for 2 hours. After 2 hours, the reactor was vented and purged 5 times with CO. With a slight overpressure in the reactor (15 psig) styrene (0.3 mmol) was added via gastight syringe. The reactor was pressurized with the appropriate CO pressure (40 or 80 psia) and 40 psia D_2. The reactions stirred at the appropriate temperature for 20 minutes. The reactions were cooled for one minute in an ice bath and vented. Mixtures were analyzed by ^1H and ^2H NMR spectroscopy on a Avance-500 spectrometer with DCH cryoprobe.

5.4.5 General Method for Acyl Formation Reactions

$Rh(H)(CO)_2(BDP)$ was prepared as reported and depressurized to 5 psig. The reactor was brought into a N_2-purged glovebox. The solution was added to a vial of triphenylphosphine oxide and 1,4-bis(trimethylsilyl)benzene (^{31}P and ^{1}H internal standards, respectively). The contents were pulled into a threaded, gas-tight syringe (syringe one). The vial was rinsed with dichloromethane, which was pulled into a second syringe. The total volume of the two catalyst containing syringes (catalyst and rinse) was 2.0 mL. The desired volume of styrene was put into the third syringe, and the fourth contained a dichloromethane rinse. The combined volume of syringes three and four was 150 μL**.**

The WiHP-NMRR was purged with nitrogen with three vent/refill cycles. The catalyst and rinse (syringes one and two) were injected into the high-pressure NMR tube. The reactor was pressurized, circulated, and vented five times with CO. The system was pressurized with CO, set to the desired reaction temperatures, and styrene and rinse (syringes 3 and 4) were injected with an overpressure of N_2. The formation of acyl dicarbonyls species was monitored by $^{31}P\{^{1}H\}$ NMR spectroscopy.

5.4.6 General Method for Acyl Isomerization Reaction

After forming the acyl dicarbonyl species (section 4.4.5), the reactor was warmed to the desired temperature for the isomerization experiment. The isomerization was initiated by depressuring the reactor to reach the desired CO pressure. The isomerization of acyl dicarbonyls species was monitored by $^{31}P\{^{1}H\}$ NMR spectroscopy. After equilibrium was achieved, the reactor was pressurized with H2 to react with the acyl dicarbonyl complexes as well as any excess styrene and followed by ^{1}H and $^{31}P\{^{1}H\}$ NMR spectroscopy. After all styrene was

consumed, $Rh(H)(CO)_2(BDP)$ was reformed, and the solution was used again in the formation of acyl dicarbonyl species (section 4.4.5); one solution was used up to 6 times (reaching a total volume of 3 mL).

5.5 References

(1) Heck, R. F.; Breslow, D. S. The Reaction of Cobalt Hydrotetracarbonyl with Olefins. *J. Am. Chem. Soc.* **1961**, *83*, 4023–4027.

(2) Watkins, A. L.; Landis, C. R. Origin of Pressure Effects on Regioselectivity and Enantioselectivity in the Rhodium-Catalyzed Hydroformylation of Styrene with (S,S,S)-BisDiazaphos. *J. Am. Chem. Soc.* **2010**, *132*, 10306–10317.

(3) Nelsen, E. R.; Landis, C. R. Interception and Characterization of Alkyl and Acyl Complexes in Rhodium-Catalyzed Hydroformylation of Styrene. *J. Am. Chem. Soc.* **2013**, *135*, 9636–9639.

(4) Beach, N. J.; Knapp, S. M. M.; Landis, C. R. A reactor for high-throughput high-pressure nuclear magnetic resonance spectroscopy. *Rev. Sci. Instrum.* **2015**, *86*, 104101–104109.

(5) Brezny, A. C.; Landis, C. R. Unexpected CO Dependencies, Catalyst Speciation, and Single Turnover Hydrogenolysis Studies of Hydroformylation via High Pressure NMR Spectroscopy. *J. Am. Chem. Soc.* **2017**, *139*, 2778–2785.

(6) Deshmukh, S. R.; Mhadeshwar, A. B.; Vlachos, D. G. Microreactor Modeling for Hydrogen Production from Ammonia Decomposition on Ruthenium. *Ind. Eng. Chem. Res.* **2004**, *43*, 2986–2999.

(7) Mhadeshwar, A. B.; Wang, H.; Vlachos, D. G. Thermodynamic Consistency in Microkinetic Development of Surface Reaction Mechanisms. *J. Phys. Chem. B* **2003**, *107*, 12721–12733.

(8) Mhadeshwar, A. B.; Vlachos, D. G. Is the water–gas shift reaction on Pt simple?: Computer-aided microkinetic model reduction, lumped rate expression, and rate-determining step. *Catal. Today* **2005**, *105*, 162–172.

(9) Dossin, T. F.; Reyniers, M.-F.; Marin, G. B. Kinetics of heterogeneously MgO-catalyzed transesterification. *Applied Catalysis B: Environmental* **2006**, *62*, 35–45.

(10) Greeley, J.; Jaramillo, T. F.; Bonde, J.; Chorkendorff, I.; Nørskov, J. K. Computational high-throughput screening of electrocatalytic materials for hydrogen evolution. *Nature Materials* **2006**, *5*, 909–913.

(11) Nørskov, J. K.; Bligaard, T.; Rossmeisl, J.; Christensen, C. H. Towards the computational design of solid catalysts. *Nature Chemistry* **2009**, *1*, 37–46.

(12) Marin, G. B.; Yablonsky, G. S. *Kinetics of chemical reactions : decoding complexity*; Weinheim, Germany : Wiley-VCH, 2011.

(13) Ho, M.-H.; Rousseau, R.; Roberts, J. A. S.; Wiedner, E. S.; Dupuis, M.; DuBois, D. L.; Bullock, R. M.; Raugei, S. Ab Initio-Based Kinetic Modeling for the Design of Molecular Catalysts: The Case of H2 Production Electrocatalysts. *ACS Catalysis* **2015**, *5*, 5436–5452.

(14) Hoops, S.; Sahle, S.; Gauges, R.; Lee, C.; Pahle, J.; Simus, N.; Singhal, M.; Xu, L.; Mendes, P.; Kummer, U. COPASI—a COmplex PAthway SImulator. *Bioinformatics* **2006**, *22*, 3067–3074.

(15) Note: This is not equivalent to EXchange SpectroscopY (EXSY). In EXSY, one signal is saturated with a 90° pulse, allowed to mix (i.e. exchange), then pulsed again to detect.

Therefore, in EXSY, the relaxation of both the saturated and exchanging signals affect what rates can be monitored. In saturation transfer, because one signal is continuously saturated, the T1 value of this resonance does not matter. In our case, the T1 for 1 was only 0.5 seconds, but the half-life for relaxation of free CO was 11 seconds. For this reason we chose to continuously saturate 1 to allow the slower exchange rates to be monitored.

(16) Nelsen, E. R.; Brezny, A. C.; Landis, C. R. Interception and Characterization of Catalyst Species in Rhodium Bis(diazaphospholane)-Catalyzed Hydroformylation of Octene, Vinyl Acetate, Allyl Cyanide, and 1-Phenyl-1,3-butadiene. *J. Am. Chem. Soc.* **2015**, *137*, 14208–14219.

(17) Lazzaroni, R.; Uccello-Barretta, G.; Benetti, M. Reversibility of metal-alkyl intermediate formation in the rhodium-catalyzed deuterioformylation of 1-hexene. *Organometallics* **1989**, *8*, 2323–2327.

(18) Lazzaroni, R.; Settambolo, R.; Uccello-Barretta, G. .beta.-Hydride Elimination and Regioselectivity in the Rhodium-Catalyzed Hydroformylation of Open Chain Unsaturated Ethers. *Organometallics* **1995**, *14*, 4644–4650.

(19) Horiuchi, T.; Shirakawa, E.; Nozaki, K.; Takaya, H. Mechanistic Aspects of Asymmetric Hydroformylation of Olefins Catalyzed by Chiral Phosphine−Phosphite−Rhodium(I) Complexes. *Organometallics* **1997**, *16*, 2981–2986.

(20) van der Slot, S. C.; Duran, J.; Luten, J.; Kamer, P. C. J.; van Leeuwen, P. W. N. M. Rhodium-Catalyzed Hydroformylation and Deuterioformylation with Pyrrolyl-Based Phosphorus Amidite Ligands: Influence of Electronic Ligand Properties. *Organometallics* **2002**, *21*, 3873–3883.

(21) Casey, C. P.; Petrovich, L. M. (Chelating diphosphine)rhodium-Catalyzed Deuterioformylation of 1-Hexene: Control of Regiochemistry by the Kinetic Ratio of Alkylrhodium Species Formed by Hydride Addition to Complexed Alkene. *J. Am. Chem. Soc.* **1995**, *117*, 6007–6014.

Chapter 6

Backbone-Modified Bis(diazaphospholanes) for Regioselective Rhodium-Catalyzed Hydroformylation of Alkenes

Portions of this work were published as Wildt, J.; Brezny, A. C.; Landis, C. R. Backbone-Modified Bisdiazaphospholanes for Regioselective Rhodium-Catalyzed Hydroformylation of Alkenes. *Organometallics* **2017**, *36*, 3142–3151.

Julia Wildt synthesized ligands **1**, **2**, **4**, **5**, and **6**. She performed hydroformylation reactions of benchmark substrates with ligands **3** and **4** and reactions of all substrates with ligands **1**, **2**, **5**, and **6**. Dr. Wildt calculated all *ab initio* computations of ligand geometries and WINDNMR simulations. Anna Brezny synthesized ligands **3**, **7** and **8**. She performed hydroformylation reactions of allylic and cyclic substrates with ligands **3** and **4** and of all substrates with ligands **7** and **8**.

6.1 Introduction

Hydroformylation of alkenes, also known as the oxo reaction, is catalyzed by homogeneous organotransition metal complexes and produces over 18 billion pounds of oxo-products annually.[1] Enantioselective hydroformylation is an atom economic process for converting inexpensive feedstocks (alkenes and syngas) into chiral aldehydes under neutral reaction conditions.[2] Although chiral aldehydes can be important intermediates in the synthesis of fine chemicals, pharmaceuticals, and agrochemicals,[3] asymmetric hydroformylation (AHF) is not commonly practiced on an industrial scale. The inherent challenge is to create robust catalysts that enable hydroformylation with high regio- and enantioselectivities for a wide range of alkene substrates (Scheme 6-1).

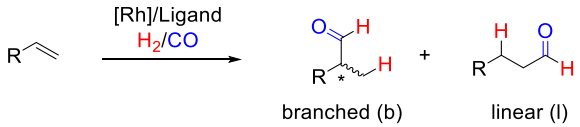

Scheme 6-1. Rhodium-catalyzed hydroformylation.

The general themes of regioselectivity control and ligand design are pervasive in the hydroformylation literature.[1,4] A variety of phosphorous-containing ligands have been shown to influence regioselectivity, including those with large chelate bite angles,[5,6-8] hydrogen-bond directed monophosphine dimerization,[9-11] reversible covalent attachment of substrate to phosphine ligand,[12-20] macromolecular encapsulation,[21-24] electrostatic substrate-ligand secondary interactions,[25-26] and mixed phosphine-phosphite ligands.[27-30] Other factors that influence hydroformylation regioselectivity include gas pressures (especially the CO partial pressures), and the steric and electronic nature of the alkenes. Commonly, mono- and disubstituted alkenes with one inductively electron-withdrawing substituent preferentially yield aldehydes with that substituent positioned α to the formyl group. For some substrates the regioselectivity of

hydroformylation is strongly dependent on the reaction pressures. For example, the hydroformylation of styrene as catalyzed by bis(diazaphospholane) complexes of rhodium produces branched aldehydes with 14.5:1 b:l ratios at high pressures (100 psia CO)[31] but reversed regioselectivity 1:40 b:l at very low pressures (<5 psia CO).[32] The general goal of AHF is to control the regioselectivity such that a high branched (b) to linear (l) ratio is achieved along with high enantioselectivity. Bis(diazaphospholane) (BDP) ligands with rhodium catalyst precursors enable high catalytic rates and generally good selectivity for a variety of substrate types under mild conditions.[33-38]

Closely related to the BDP class of phosphines are bisphospholanes such as (*R*,*R*)-Ph-BPE ((*R*,*R*)-1,2-Bis(2,5-diphenylphospholano)ethane) and DuPhos. In a ligand screen, (*R*,*R*)-Ph-BPE was found to provide high regio- and enantioselectivities for three benchmark substrates: styrene (b : l = 45 : 1 and 94% *ee*), vinyl acetate (b : l = 340 : 1 and 82% *ee*) and allyl cyanide (b : l = 7.1 : 1 and 90% *ee*).[39] One major structural difference between BDPs and Ph-BPE lies in the hybridization of the atoms in the phospholane ring. Whereas the BDP ligands comprise both sp^2-hybridized N-atoms and sp^3-hybridized C-atoms, in Ph-BPE all ring atoms have sp^3 hybridization (Figure 6-1). It appears that changes in ring puckering associated with different hybridization influence the reaction regioselectivity, with the (*R*,*R*)-Ph-BPE ligand commonly producing a higher fraction of branched product relative to the BDP ligands. In order to understand the relationship between phospholane ring puckering and hydroformylation regioselectivity, we explored modification of bis(diazaphospholane) ligands to all-sp^3 hybridized phospholane rings. This modification was accomplished by the reduction of the acylhydrazine group to an alkylhydrazine backbone.

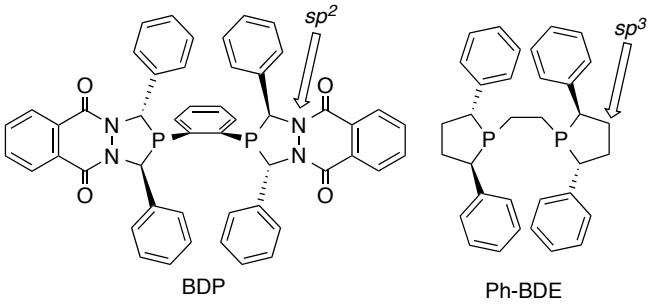

Figure 6-1. Hybridization of the backbone in BDP and Ph-BPE ligands.

Herein, we report the synthesis of reduced, alkylhydrazine-derived bis(diazaphospholanes) (red-BDP) containing an all sp^3-hybridized diazaphospholane ring. Regioselectivity of red-BDPs in the hydroformylation of several alkene substrates are compared to their sp^2-hybridized acylhydrazine BDP derivatives, demonstrating the effect of phospholane ring conformation on regioselectivity.

6.2 Results and Discussion

6.2.1 Synthesis and Characterization and of Bis(diazaphospholanes) and their Reduced Derivatives

6.2.1.1 General Synthesis

The parent acylhydrazine backbone bis(diazaphospholanes) were synthesized from the primary phosphine, aryl azine, and acyl chloride species.[34,40] A mixture of stereoisomers was obtained; after purification by column chromatography the racemic, C_2-symmetric BDP was obtained in 20–29% yield (Scheme 6-2). Treatment of a diacyl-3,4-hydrazine with $BH_3 \cdot SMe_2$ produced an *N,N'*-dialkyl-3,4-hydrazine without rupture of the hydrazine N–N bond.[41] This

reduction method has been previously applied to monodiazaphopholanes by Nelson and Landis.[40] We have expanded the borane reduction to bis(diazaphospholane) ligands. To assure a clean reduction of all acyl groups, we found that BH_3·THF is a more suitable reagent than BH_3·SMe_2. Reacting the bis(diazaphospholanes) (BDP) with a 2.5-fold excess of borane leads first to the reduced alkylhydrazine phospholane as its phosphine-borane adduct. This adduct is broken by heating it with $HNEt_2$ to obtain the desired reduced bis(diazaphospholanes) (red-BDPs) (Scheme 6-3).

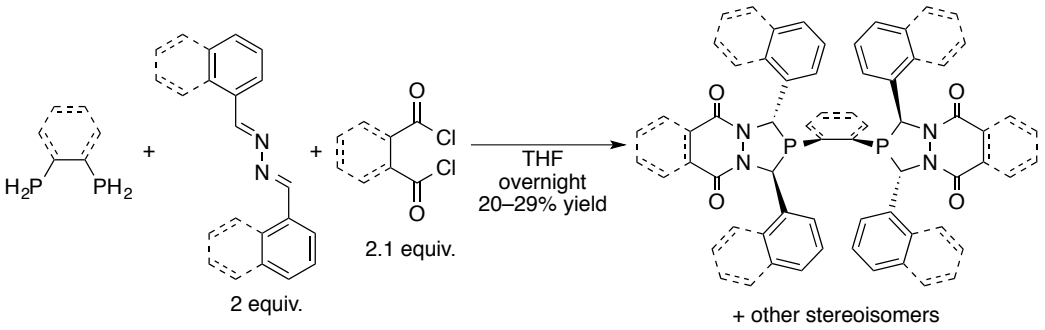

Scheme 6-2. Synthesis of acylhydrazine backbone bis(diazaphospholanes) from corresponding primary phosphines, azines, and acyl chlorides.

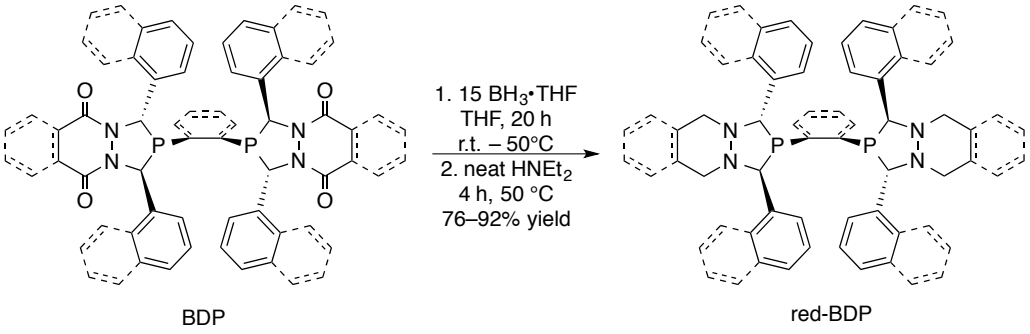

Scheme 6-3. Reduction of the acylhydrazine backbone of bis(diazaphospholanes) to an alkylhydrazine red-BDPs using BH_3·THF.

The bis(diazaphospholanes) chosen for this study vary in their backbone (succinyl or phthaloyl), the bridge between the phosphorous atoms (phenylene or ethylene) as well as the

substituents in the 2- and 5- positions (phenyl or naphthyl) (Figure 6-2). All bis(diazaphospholanes) examined underwent quantitative reduction to their alkylhydrazine derivatives. The reduction of BDPs **1** and **3** was performed at 55 °C for 20 h, whereas the tetranaphthyl derivative requires reaction at room temperature to prevent over-reduction of the diazaphospholane moiety back to the primary phosphine. In the synthesis of non-reduced BDPE **5**, which bears an ethano bridge between the two P atoms, most of the material was isolated as its phosphine oxide, presumably due to the high air sensitivity of 1,2-bisphosphinoethane and/or the product **5**. Reaction of a mixture of BDPE **5** phosphine and phosphine oxide with BH_3•THF at room temperature reduced both the acylhydrazine and phosphine oxide functionalities to yield **6**. This was unexpected because reductions of phosphine oxides typically require reaction with activated LAH or hydrosilanes, such as Ph_3SiH.[42]

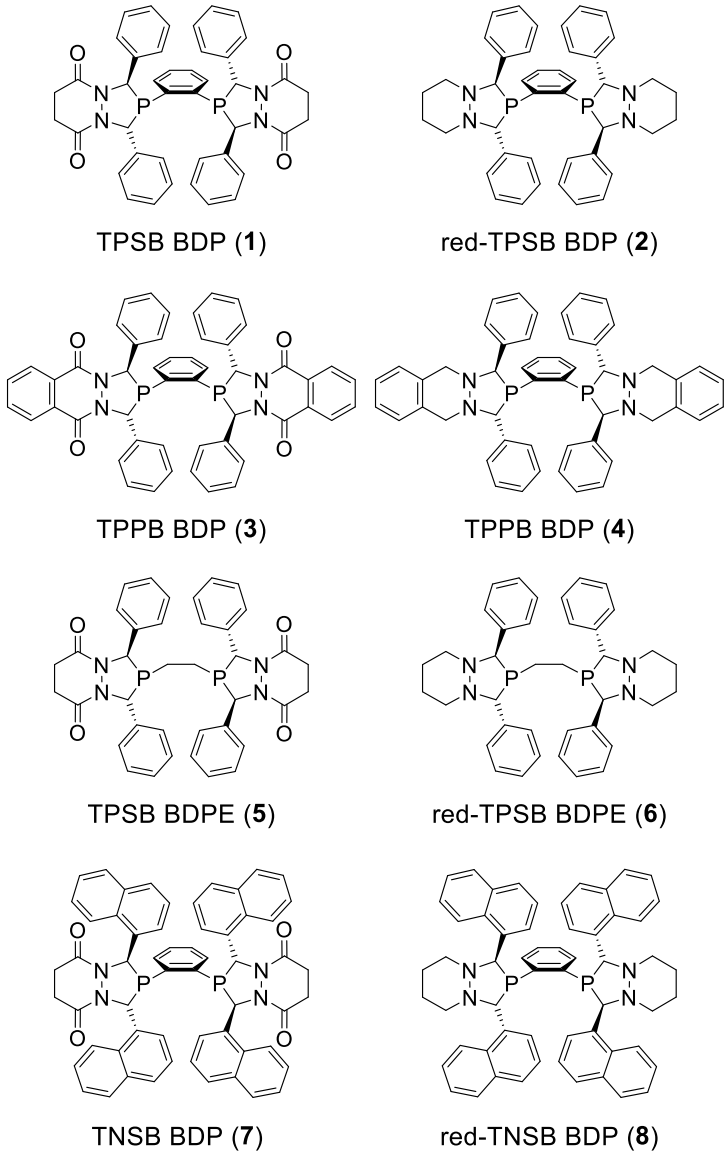

Figure 6-2. Bis(diazaphospholanes) **1**, **3**, **5** and **7** and their reduced derivatives **2**, **4**, **6** and **8**.

6.2.1.2 NMR Analysis and Modeling of Methine Protons

In the process of characterizing phenylene- and ethano-bridged BDPs, we observed significant differences in the appearance of the ^{1}H NMR resonances corresponding to the methine protons in the diazaphospholane ring for the different bridge types. For phenylene-bridged BDPs (**1**, **3**, and **7)** the two methine protons at the 2- and 5-positions within a

phospholane ring are inequivalent. For ligand **1**, the methine resonances appear as a broad apparent singlet next to a triplet (Figure 6-3, top). The triplet methine resonance is due to virtual coupling which results from three factors: (1) one of the methine protons is coupled to the proximal P atom (J_{H-P} = 10-25Hz) (2) which itself is strongly coupled to the P atom of the other phospholane ring (J_{P-P} > 150 Hz) and (3) the chemical shifts of the two P centers are identical by symmetry. In the BDPs, despite being magnetically equivalent, the two P-atoms are strongly coupled, meaning that $J_{P-P} > \Delta\nu_{P-P}$ and virtual coupling is commonly seen for one of the two inequivalent methine ^{1}H resonances.[43,44-45] The other methine resonance has weak two-bond coupling to the proximal P atom and the coupling is not resolved.

In contrast, the methine resonances of the ethano-bridged BDP **5** display an apparent doublet of doublets along with a broad apparent singlet (Figure 6-3, bottom). Comparable virtual splitting patterns have been observed for other ethano- bridged bisphosphines.[46] To understand the coupling pattern and the size of the coupling constant between the phosphorous atoms, the experimental spectra (red) were simulated for ligands **1** and **5** using the WINDNMR program[47] starting from a '4-spin' coupling simulation (blue).

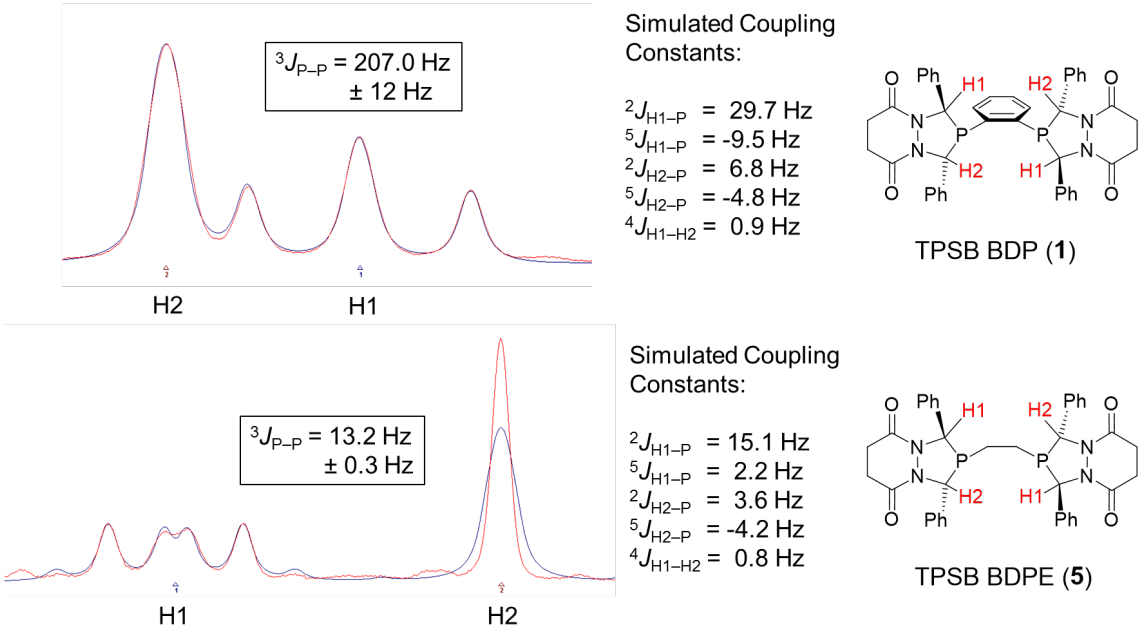

Figure 6-3. Methine protons in the ^{1}H NMR spectra of ligands **1** and **5**, coupling constants determined with the WINDNMR simulation program (red: experimental; blue: simulated).

The splitting pattern can be assigned as AA'XX' and the size of the coupling constant $^3J_{P-P}$ in phenylene-bridged **1** is on the order of 200 Hz, whereas $^3J_{P-P}$ for ethano-bridged **5** is approximately 13 Hz. The height of each peak is sensitive to the sign of the coupling constants and to obtain the correct height and shape of the peak, the $^5J_{H-P}$ coupling constants must be negative. In addition, the broadness and overall shape of the peaks are further adjusted by adding a small coupling constant of 0.8 and 0.9 Hz between the two methine protons, common for a proton-proton coupling in five-membered rings. Perfect simulation of the apparent singlet methine resonance for **5** could not be achieved due to the complex, interactive nature of the spectrum with respect to adjustment of the coupling and chemical shift parameters. This signal can be simulated independently when the coupling constant $^3J_{P-P}$ is 45.5 Hz, while the doublet of doublets shape of H1 is lost and is converted to a triplet-like pattern.

The overall difference in P–P coupling constants for the phenylene- and ethano-bridges is not surprising given the relative orientation of the P-atoms for the different bridges. While the phenylene bridge is more rigid and forces a P–C(sp^2)–C(sp^2)–P torsion angle of ~0°, the ethano bridge allows rotational flexibility resulting in a calculated P–C(sp^3)–C(sp^3)–P torsion angle of 146° (Figure 6-4) and lowered coupling of the P-nuclei.

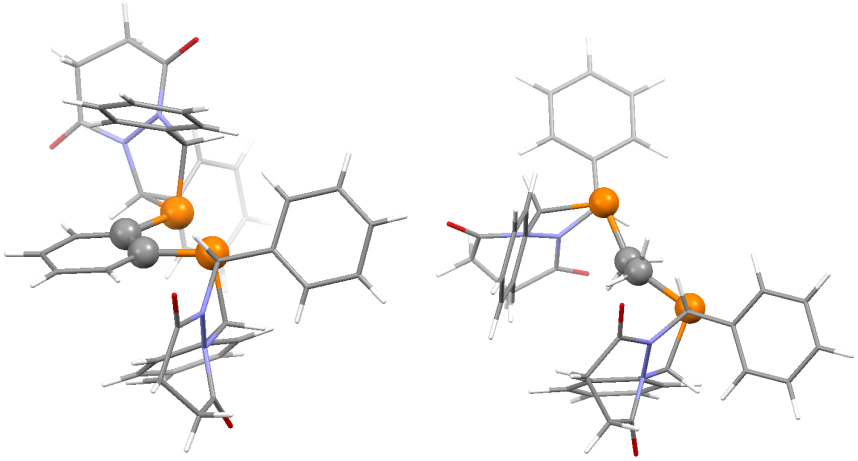

Figure 6-4. BDP ligands TPSB BDP **1** (left) and TPSB BDPE **5** (right) indicating the conformational difference due to the bridge between the P-atoms (P–C–C–P shown as spheres).

6.2.2 Hydroformylation of Benchmark Substrates Styrene, Vinyl Acetate and Allyl Cyanide

It is known that reduction of the sp^2-hybridized N-atom to an sp^3-hybridized N-atom in the diazaphospholane ring changes the ring puckering.[40] The influence of such structural changes on the selectivity of Rh-catalyzed hydroformylation has not been explored. The new red-BDP ligands **2**, **4**, **6** and **8** were tested with a variety of substrates and compared to their BDP control ligands **1**, **3**, **5** and **7**. The active catalyst was prepared by mixing a solution of $[Rh(acac)(CO)]_2$ and 1.5 equiv. of ligand to ensure full rhodium complexation. This solution was pressurized with syngas (1:1 molar ratio of H_2:CO) to 150 psig and heated at 60 °C for at least 1 h under vigorous

stirring to give the hydride complex, [RhH(CO)$_2$BDP]. Initially, hydroformylation of bench mark substrates with ligands **1** – **4** was performed at 80 °C, 150 psig of syngas pressure and 3 h reaction time in order to directly compare with data previously obtained for the ligands (*R*,*R)*-Ph-BPE and (*S*,*S*,*S*)-BisDiazaPhos (Table 6-1).[48] Remarkably, the reduced bis(diazaphospholane) analogues yield significantly increased regioselectivity (entries 2 and 4), outperforming (*S*,*S*,*S*)-BisDiazaPhos (entry 6). Under the test conditions the branched selectivities do not exceed those observed with Ph-BPE in entry 7, however, it is clear that reduction of ligands **1** ,**3**, **5**, and **7** to all-*sp*^{3} hybridized phospholanes **2, 4, 6,** and **8** produces catalysts that perform similarly to Ph-BPE. In addition, the reduced diazaphospholane ligands show higher activity compared to Ph-BPE, as revealed by higher conversions under the trial conditions.

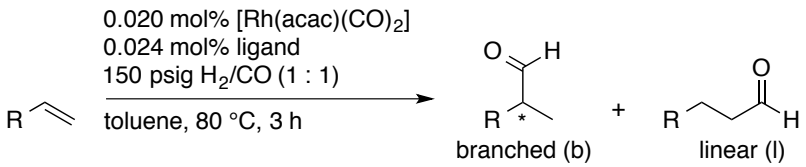

Entry	Ligand	conv (%)	b : l ratio	conv (%)	b : l ratio	conv (%)	b : l ratio
1	**1**	>99	7.7:1	98	8.2:1	>99	4.3:1
2	**2**	98	30:1	89	>50:1	98	7.2:1
3	**3**	100	5.7:1	95	9.2:1	>99	4.6:1
4[b]	**4**	>99	25:1	93	>50:1	>99	6.4:1
5[c]	BPE	57	45:1	52	370:1	96	7.1:1
6[c]	BDP	100	6.6:1	100	37:1	100	4.0:1

[a] Conditions: one pot screen of all 3 substrates, total alkene/Rh = 5000 : 1, [alkene] = 1.5 M, Rh/L = 1 : 1.5; conversions and b : l ratios determined by ^{1}H NMR spectroscopy. [b] ligand used as Rh(acac)(4)-complex. [c] same standard conditions.[49] (BPE = (*R*,*R*)-Ph-BPE; BDP = (*S*,*S*,*S*)-BisDiazaPhos-SPE).

Table 6-1. Hydroformylation of benchmark substrates styrene, vinyl acetate and allyl cyanide.[a]

Testing of the benchmark substrates styrene, vinyl acetate and allyl cyanide was extended to the lower reaction temperature of 60 °C, 150 psig syngas pressure, 0.02 mol% catalyst loading, and 16 h reaction time for ligands **1** – **8** (Table 6-2). These reactions were performed with two substrates per run (styrene/allyl cyanide or vinyl acetate/allyloxy-*tert*-butyldimethylsilane).[49] The results are shown for individual substrates in Tables 6-2 and 6-3. All ligands show nearly quantitative conversion (98 to 100% for BDP ligands (entry 1, 3, 5 and 7) and 80 to 100% for red-BDPs (entry 2, 4, 6, and 8)) at standard conditions of 60 °C. The regioselectivity for all benchmark substrates significantly increases with red-BDPs (entry 2, 4, 6 and 8) relative to the non-reduced ligands, in favor of the branched isomer (Table 6-2). For styrene hydroformylation, non-reduced BDP ligands exhibit branched to linear ratios on the order of 10 : 1. In contrast, the reduced ligands favor the branched styrene aldehyde over the linear product by at least 39 : 1. The most regioselective ligand for styrene hydroformylation is red-TNSB BDP **8** with a >50 : 1 branched to linear ratio (entry 8). All reduced ligands are highly branched selective for vinyl acetate (b : l = >50 : 1), however, slightly lower conversions are observed with all reduced ligands compared to their non-reduced parents. The only other ligand leading to selectivities of these magnitudes is (*R*,*R*)-Ph-BPE (at 80 °C: styrene b : l = 45 : 1; vinyl acetate b : l = 370 : 1).[50]

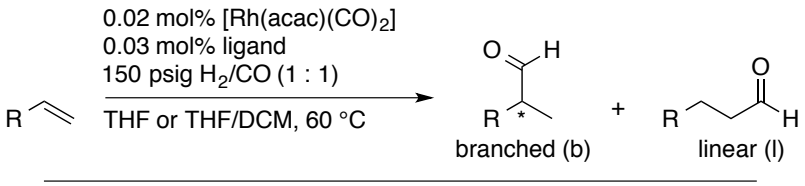

Entry	Ligand	conv (%)	b : l	conv (%)	b : l	conv (%)	b : l
1[b]	**1**	100	13.6:1	98	12.3:1	100	4.7:1
2	**2**	>99	49:1	89	>50:1	>99	9.4:1
3[b]	**3**	100	8.5:1	98	13.2:1	100	5.0:1
4	**4**	100	39:1	94	>50:1	100	7.5:1
5[b]	**5**	>99	9.1:1	98	16.0:1	>99	3.6:1
6	**6**	99	47:1	90	>50:1	99	7.8:1
7[b]	**7**	100	10:1	100	22:1	99	4.0:1
8	**8**	80	50:1	93	>50:1	99	20:1
9[c]	BDP	87	18.3:1	98	>50:1	---	---

[a] Conditions: total alkene/Rh = 5000 : 1, [alkene] = 1.5 M, Rh/L = 1 : 1.5 to ensure full ligation of Rh, 16 h; run as one pot reaction with styrene/allyl cyanide and vinyl acetate/allyloxy *tert*-butyldimethylsilane; branched to linear ratios and conversion determined by ^{1}H NMR spectroscopy. [b] ligand added as stock solution in DCM for solubility. [c] standard conditions except of 1600 : 1 total alkene/Rh; 4 h reaction time, run as a one-pot screen with styrene, vinyl acetate and allyloxy-*tert*-butyldimethylsilane (BDP = (*S*,*S*,*S*)-BisDiazaPhos-SPE).[38]

Table 6-2. Hydroformylation of benchmark substrates styrene, vinyl acetate and allyl cyanide.[a]

Regioselectivity control for allyl cyanide is approximately doubled by using the reduced ligands **2**, **4** and **6** (entry 2, 4 and 6) over their non-reduced derivatives **1**, **3** and **5** (entry 1, 3 and 5). Remarkably, red-TNSB BDP **8** exhibits a 5-fold increase of the branched to linear ratio from 4 : 1 to 20 : 1 compared to its control ligand **7** for allyl cyanide. The only other regioselectivities with a branched to linear ratio of around 10 : 1 or higher were found with (*R*,*R*)-BDPP (b : l = 16 : 1), JosiPhos (b : l = 14.1 : 1) and (*S*,*S*)-Kelliphite (b : l = 9.9 : 1) at 80 °C.[39,50]

Overall, the reduced ligands outperform the BDP control ligands with respect to regioselectivity control. Ligands **2** and **8** are notable for their high selectivity. Amongst the reduced ligands, factors that appear to *lower* regioselectivity include the presence of the ethano- vs. phenylene-bridge (i.e. **6** vs. **2**) or the rigid phthaloyl backbone (i.e. **4** vs. **2**).

6.2.3 Hydroformylation of Allylic Alkenes

Regioselective control of allylic substrates commonly is challenging. Due to the improved regioselectivities for allyl cyanide hydroformylation using reduced ligands, we investigated the hydroformylation of the allylic substrates allyl alcohol, allyloxy-*tert*-butyldimethylsilane and 3-butenoic acid (Table 6-3). Previous work has shown an intrinsic preference for the linear aldehyde in the hydroformylation of allyl alcohol. For example, (*S*,*S*,*S*)-BisDiazaPhos yields predominantly the linear aldehyde in a branched to linear ratio of 1 : 3.4 (entry 9).[37] Nozaki's phosphine-phosphite BinaPhos ligand shows a branched to linear ratio of 1 : 9.[51] Selectivity of allyl alcohol hydroformylation for the branched aldehyde product was observed for the first time by Tan and coworkers with a cyclic aminal phosphine through directed and intramolecular hydroformylation (b : l = 6.7 : 1).[52] Hydroformylation with the non-reduced BDPs **1**, **3** and **7** demonstrate a slight preference for the branched aldehyde product (b : l = 1.7 : 1, 1.5 : 1 and 2.0 : 1, respectively). The amount of branched aldehyde product increased with the reduced ligands, in particular with red-TPSB BDP **1** and red-TNSB BDP **8** by 4.4 and 5.0-fold, respectively, giving rise to the notably increased branched to linear ratio of 10 : 1 with red-TNSB BDP. Allyl alcohol can isomerize to propanal under hydroformylation conditions. However, the reduced ligands have a lower tendency to isomerize this substrate compared to the non-reduced BDP ligands; propanal is commonly formed in around 10% with the BDPs but only

ca. 2% with the reduced ligands. The highest amount of propanal of 10% is observed with ligand **5**.

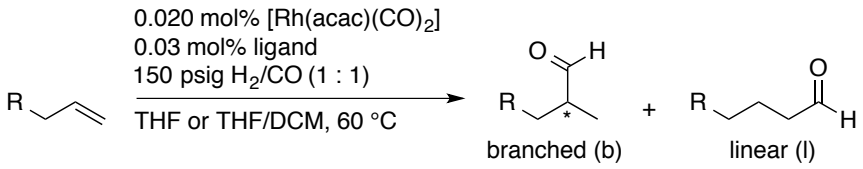

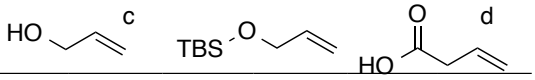

Entry	Ligand	conv (%)	b : l	conv (%)	b : l	conv (%)	b : l
1[b]	**1**	39	1.7:1	>99	1.1:1	>99	2.1:1
2	**2**	70	7.4:1	98	3.5:1	>99	5.8:1
3[b]	**3**	30	1.5:1	95	1:1	>99	2.6:1
4	**4**	70	4.4:1	100	3.1:1	>99	6.5:1
5[b]	**5**	34	1:1.1	>99	1:1.2	>99	1.1:1
6	**6**	67	3.8:1	>99	3.5:1	99	4.9:1
7[b]	**7**	100	2:1	83	1:1	>99	2.3:1
8	**8**	65	10:1	100	4.0:1	83	8.8:1
9[e]	BDP	99	1:3.4	99	2.0:1	---	---

[a] Conditions: 60 °C, total alkene/Rh = 5000 : 1, [alkene] = 1.5 M, Rh/L = 1 : 1.5 to ensure full ligation of Rh, 16 h; ligand added as stock solution in DCM for solubility; allyloxy-*tert*-butyldimethylsilane was run as one pot reaction with vinyl acetate; conversion and b : l ratios determined by ^{1}H NMR spectroscopy. [b] ligand added as stock solution in DCM for solubility. [c] allyl alcohol was run at 40 °C, hydroformylation products were converted to the pinacolyl acetal; % of 1-propanal of total product mixture formed: BDPs **1**: 7%, **3**: 2%, **5**: 10%, **7**: 2%, red-BDPs **2**: 1%, **4**: <1%, **6**: 3%, **8**: 1%. [d] a few drops of NEt_3 were added to the hydroformylation product mixture before obtaining ^{1}H NMR spectrum. [e] conditions: [alkene] = 0.75 M in toluene, total alkene/Rh = 200 : 1; 4 h reaction time, 140 psig syngas pressure (BDP = (*S*,*S*,*S*)-BisDiazaPhos).[37]

Table 6-3. Screening of allylic alkene substrates.[a]

Hydroformylation of allyloxy-*tert*-butyldimethylsilane represents an attractive and alternate route to "Roche Aldehydes," which are common building blocks in the synthesis of biologically active compounds.[37,53-55] Even though (*S*,*S*,*S*)-BisDiazaPhos leads to a higher

branched to linear ratio for allyloxy-*tert*-butyldimethylsilane compared to the unprotected allyl alcohol, this trend is not observed with the BDP ligands discussed herein. Non-reduced ligands **1**, **3**, **5**, and **7** give only a 1 : 1 ratio for the aldehyde product (entry 1, 3, 5 and 7). Using the red-BDPs, these ratios increase to about 3–4 : 1, with the highest value being obtained by red-TNSB BDP **8** (b : l = 4 : 1, entry 8).

Hydroformylation of 3-butenoic acid has been previously reported by Breit and coworkers using a guanidine-substituted monophosphine favoring the linear aldehyde product (b : l = 1 : 23).[56] Reek and coworkers also showed a linear preference of 1: 1.9 with the DIMPhos ligand.[25] The BDP ligands slightly favor the branched aldehyde product (entries 1, 3, 5 and 7). Hydroformylation with the reduced ligands leads to an increase in regioselectivity to over 5 : 1, the highest selectivity is observed with red-TPPB BDP **4** (b : l = 6.5 : 1) and red-TNSB BDP **8** (b : l = 8.8 : 1).

6.2.4 Hydroformylation of Cyclic, Heteroatom-Containing Alkenes

The hydroformylation products of cyclic alkenes, such as *N*-Boc-2,3-dihydropyrrole and 2,3- and 2,5-dihydrofurans are useful precursors and intermediates in organic synthesis.[57-61] This substrate class has remained challenging[62-67] and was evaluated with ligands **1** – **8** (Table 6-4). Hydroformylation of *N*-Boc-2,3-dihydropyrrole shows preference for the α-aldehyde (because only branched products are possible for these disubstituted alkenes, the regioisomeric products are labeled as α and β with respect to the heteroatom) product with all tested ligands. Ligands **2**, **4**, and **6** favor the α-product by approximately 1.1 – 1.6 times. The highest regioselectivity is observed with ligands **5** and **6**, providing α : β = 11.0 : 1 and 12.2 : 1, respectively. Interestingly,

TNSB BDP **7** shows good selectivity for the α-aldehyde product with 9.1 : 1 ratio, but an increase in regioselectivity was not observed using the reduced ligand **8**. Rather the α : β ratio *decreased* to 5.9 : 1.

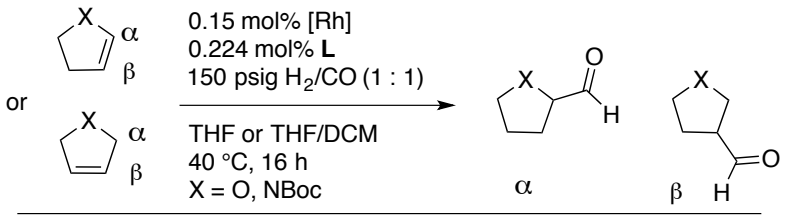

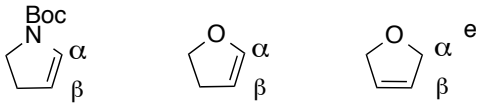

Entry	Ligand	conv (%)	b : l	conv (%)	b : l	conv (%)	b : l
1[b]	**1**	91	5.7:1	74	1:1.2	42	1:50
2	**2**	20	8.2:1	11	1:1.4	62	<1:50
3[b]	**3**	98	4.6:1	90	1:1.7	21	1:44
4	**4**	15	7.5:1	13	1:1.9	80	<1:44
5[b]	**5**	93	11.0:1	74	1.6:1	24	<1:50
6	**6**	55	12.2:1	46	1:1	58	1:30
7[b]	**7**	90	9.1:1	84	2.5:1	3	1:14.0
8	**8**	4	5.9:1	4	1.6:1	6	1:6.5
9	BDP	99	10.4:1[d]	25	2.8:1[c]	80	1:15.0[c]

[a] Conditions: total alkene/Rh = 670 : 1, [alkene] = 1.5 M, Rh/L = 1 : 1.5 to ensure full ligation of Rh, 16 h; conversion and b : l ratios determined by ^{1}H NMR spectroscopy. [b] ligand added as stock solution in DCM for solubility. [c] conditions: 60 °C, 15 h, 140 psig syngas, total alkene/Rh = 200 : 1, [alkene] = 0.75 M in toluene, Rh/Ligand = 1 : 1.1.[9] [d] conditions: 40 °C, 4 h, 150 psig syngas, total alkene/Rh = 670 : 1, [alkene] = 2.6 M in toluene/THF, Rh/Ligand = 1 : 1.1.[10] [e] % of 2,3-dihydrofuran of total product mixture formed: ligands **1**: 6%, **3**: 16%, **5**: 8%, **7**: 6% , red-BDPs **2**: 1%, **4**: 4%, **6**: 1%, **8**: 1% (BDP=(*S,S,S*)-BisDiazaPhos).

Table 6-4. Hydroformylation of cyclic alkenes.[a]

In contrast to the selectivity α : β = 2.8 : 1 obtained with (*S,S,S*)-BisDiazaPhos for the hydroformylation of 2,3-dihydrofuran (entry 9), BDPs **1**, **2**, **3** and **4** exhibit slight preference for the β-aldehyde product. Under the conditions examined, the highest α : β ratio of 2.5 : 1 is

observed with TNSB BDP **7**. In contrast with our observations with previous substrates, all reduced ligands are less selective than their non-reduced equivalents for 2,3-dihydrofuran hydroformylation. Conversions with the reduced ligands are lower for both cyclic 2,3-dihydro substrates and hydroformylation proceeds 2 to 4-times slower (entries 2, 4, 6 and 8); red-TNSB BDP is 20 times slower.

The 2,5-dihydrofuran substrate, unlike the 2,3-isomer, produces the α-aldehyde product *only* via isomerization of the initially formed Rh-alkyl. Reduced ligands **2**, **4** and **6** retard such isomerization and give high selectivity for the 2,5-dihydrofuran β-aldehyde product with α : β ratios on the order of 1 : 50, which is more selective than was reported with (*S*,*S*,*S*)-BisDiazaPhos (1 : 15, entry 9). Compared to the tetranaphthyl derivative **7**, red-TNSB BDP **8** exhibits lowered preference for the β-product with selectivity changing from 1 : 14 to 1 : 6.5. Ligand **7** yields selectivities comparable to (*S*,*S*,*S*)-BisDiazaPhos.

Opposite to the 2,3-dihydro alkenes, 2,5-dihydrofuran exhibits higher conversion when using the reduced ligands (entries 2, 4, 6, and 8). Minor (16% or less) formation of 2,3-dihydrofuran through isomerization of the double bond in 2,5-dihydrofuran is observed. As seen for the hydroformylation of allyl alcohol, the reduced ligands **2**, **4**, **6**, and **8** exhibit much lower isomerization. Isomerization product 2,3-dihydrofuran is typically formed in around 6 – 16% yield with the BDPs and only to 1 – 4% yield with the reduced ligands.

6.2.5 Summary of Hydroformylation Reactions

Overall, the regioselectivity for terminal alkenes increases by using the reduced ligands **2**, **4**, **6** and **8**. An even higher amount of branched aldehyde is observed than when using the state-

of-the-art (*S*,*S*,*S*)-BisDiazaPhos. The total changes in regioselectivities are summarized in Table 6-5. The highest branched to linear ratios for all terminal alkenes are observed with red-TNSB BDP **8**. Ligand **8**, however, is not suitable for selective hydroformylation of the cyclic alkenes. In fact, regioselectivities decline for all cyclic alkenes (entries 7, 8 and 9) with this ligand.

Entry	Substrate	**2**	**4**	**6**	**8**
1	styrene	3.7	4.6	5.2	5.0
2	vinyl acetate	>4.1	>3.8	>3.1	>2.3
3	allyl cyanide	2.0	1.5	2.2	5.0
4	allyl alcohol	4.4	2.9	3.8	5.0
5	allyloxy silane	3.2	3.1	3.6	4.0
6	3-butenoic acid	2.8	2.5	4.4	3.8
7	N-boc-2,3- pyrrole	1.4	1.6	1.1	(1.5)
8	2,3-dihydrofuran	(1.2)	(1.1)	(1.5)	(1.6)
9	2,5-dihydrofuran	>1	>1	>1.4	(2.2)

Table 6-5. Ratio of regioselectivities $((b:l)^{red\text{-}BDP}/(b:l)^{BDP})$ of red-BDP compared to BDP. Numbers in () indicating a decrease in the selectivity for the α-product.

Reduction of the BDP ligands to red-BDP ligands generally slows the hydroformylation. Two factors may be at play. First, the more electron-donating character of the reduced ligands may slow CO dissociation, a process that is required for common dicarbonyl resting states ($[RhH(BDP)(CO)]_2$ or $[Rh(acyl)(BDP)(CO)_2]$) to move onto the catalytic cycle. The other factor is increased steric repulsion of the 2,5 aryl groups with the substrate upon reduction of the sp^2-hybridized N centers to sp^3-hybridization (*vide infra*).

6.2.6 Conformational Analysis of Reduced Ligands

To gain more insight into the structural changes induced by ligand reduction, the conformation of the diazaphospholane ring of red-BDPs and BDPs were compared. Crystallographic structures of **1** – **4** as well as **7** and **8** were obtained and the C–N–N–C torsion angle (θ) in the diazaphospholane ring of each structure was evaluated. The torsion angle (θ) is the observed dihedral angle when the diazaphospholane ring is oriented in the Newman-projection along the N–N bond (Figure 6-5). The perspective view of ligands **1** and **2** in Figure 6-2 is oriented along an N–N bond of one of the diazaphospholane rings so that the structural changes in the ring conformation are clearly visible. The torsion angle (θ) of the C–N–N–C-connection in the reduced ligands is by far greater than their non-reduced equivalents. The BDP ligands **1** and **3** have a torsion angle of 19.2° and 10.4°, respectively, whereas the red-BDP ligands **2** and **4** show a torsion angle of 62.1° and 56.0°, respectively (Figure 6-6). TNSB BDP **7** displays a torsion angle of 33.4° and red-TNSB BDP **8** has 58.6°. The conformation of the reduced ligands resembles the typical half-chair conformation in cyclopentane rings.

In addition to the solid state structures, the geometries of **1** – **8** were calculated using *ab initio* DFT calculation (B3LYP/6-31G(d)). These calculations allow for the structural determination of ligands TPSB BDPE **5** and red-TPSB BDPE **6**, whose crystal structures were not obtained. The experimental and calculated torsion angles are depicted in Figure 6-6. The computed and experimental values are in good agreement. With the reduction of the acylhydrazine group to the alkylhydrazine, the red-BDPs structurally resemble phospholanes such as Ph-BPE, which has a calculated torsion angle of 52.2°.

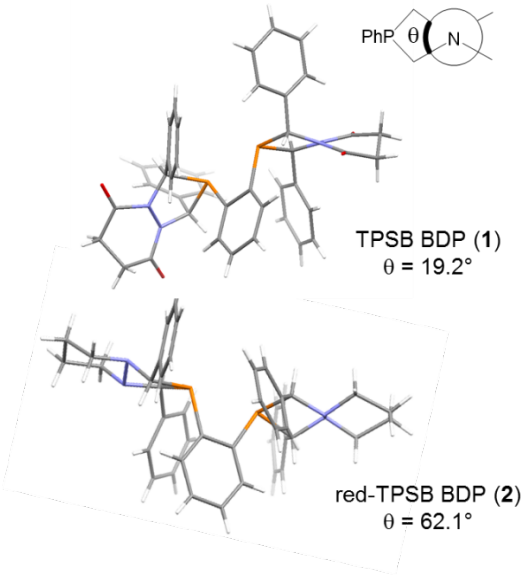

Figure 6-5. Comparison of the torsion angle (θ) within the diazaphospholane moiety of TPSB BDP **1** (θ = 19.2°, top) and red-TPSB BDP **2** (θ = 62.1°, bottom). Crystal structures are oriented along the N–N bond of one of the diazaphospholane rings (blue: nitrogen atoms, orange: phosphorous atoms, red: oxygen atoms).

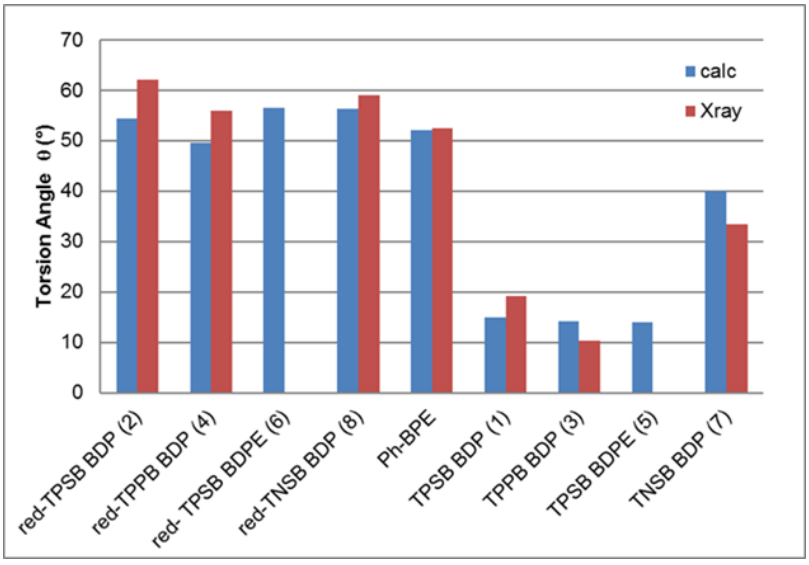

Figure 6-6. Calculated (blue bars, B3LYP/6-31G(d)) and experimental (red bars, X-ray crystallography) torsion angle of diazaphospholane rings in reduced BDPs, Ph-BPE and BDPs.

The crystal structure of the [Rh(acac)(BDP)] complex of **1** was also obtained (Appendix C). The torsion angle within the phospholane ring is 21.7°, similar to the free ligand value of 19.2°, which enabled us to estimate the torsion angle in the diazaphospholane ring of the Rh-complexes from the free ligand structures. As has been demonstrated previously with monodiazaphospholanes,[40] the change from an sp^2-hydridized N-atom in the acylhydrazine to an sp^3-hydridized N-atom gives rise to a large change in the puckering of the six-membered diazacyclohexane, as well as the diazaphospholane rings. A subsequent variation in the conformation concerns the orientation of the phenyl rings in the 2- and 5-positions.

The origins of the correlation between increased phospholane ring puckering with increased b:l regioselectivity is not easily understood. Several factors caution against overinterpretation. First, the observed regioselectivity of hydroformylation depends on reaction conditions and commonly reflects interplay amongst several catalytic steps: the intrinsic kinetic selectivity of forming linear vs. branched Rh-alkyls, the rate of Rh-acyl formation vs. the rate of Rh-alkyl isomerization, and rates of hydrogenolysis vs. isomerization for the Rh-acyl regioisomers.[68] The b:l ratio of aldehyde products typically increases with increasing CO partial pressure, especially for aryl alkenes such as stryrene, and reaches a limiting value that represents the intrinsic kinetic selectivity for forming branched vs. linear Rh-alkyls. We note that the *ca.* 50:1 b:l ratios for styrene observed with the reduced diazaphospholanes under standard conditions exceed those for the non-reduced ligands, even in cases where the partial pressure was adjusted to achieve optimal branched selectivity (*ca*. 25:1 for the BDP ligand).[31] This result implies that reduced diazaphospholanes have higher intrinsic kinetic preference for forming the corresponding branched vs. linear alkyl relative to the unreduced diazaphospholanes. Second, it

is not clear that more detailed analysis can be convincing given the small transition state energy differences and extensive conformational degrees of freedom involved. .

Previously, we proposed an *empirical* quadrant map to visualize the steric and electronic contributions to the transition state energies responsible for the alkene insertion into the Rh–H bond.[31,34-35] Although this empirical map has proven useful for predicting the absolute stereochemistry of aldehyde products in AHF it does not lend any detailed insight into quantifiable correlations of structure and selectivity for different phospholane ring structures.

6.3 Conclusions

A borane reduction procedure has been applied to four racemic tetraaryl bis(diazaphospholanes) varying in the phosphine-bridge, the backbone, and the substituents in the 2- and 5-positions. The acylhydrazine backbones were converted to alkylhydrazines, leading to a change in the hybridization of the N-atoms from sp^2 to sp^3 and therefore mimicking the all sp^3 ring of (*R,R*)-Ph-BPE. The resulting twist in the diazaphospholane ring leads to both an increased C–N–N–C-torsion angle and reorientation of the aryl-ring substituents in 2- and 5-positions. This conformational change dramatically influences the regioselectivity of rhodium-catalyzed hydroformylation of a variety of alkenes, including styrene, vinyl acetate, allyl cyanide, allyl alcohol, allyloxy-*tert*-butyldimethylsilane, 3-butenoic acid, *N*-Boc-2,3-dihydropyrrole, 2,3- and 2,5-dihydrofuran. Indeed, regioselectivity ratios increased by up to 5-fold, favoring the branched aldehyde product. Thus this reduction procedure yielded improved ligands for AHF that combine the higher intrinsic regioselectivity of (*R,R*)-Ph-BPE ligand with the high activity of bis(diazaphospholanes).

The tetranaphthyl ligand red-TNSB **8** exhibits the highest regioselectivities for all terminal alkene substrates, but at the cost of slightly lower conversions at 16 h. Obtaining high regioselectivities for the cyclic alkenes is challenging. The ligand that best combines good overall activity and regioselectivity for all tested substrates is red-TPSB BDP **2**. Overall, the ligands combining the phenylene bridge and the succinyl backbone, red-TPSB BDP **2** and red-TNSB BDP **8**, exhibit the best regioselectivities. The torsion angles of the diazaphospholane moieties were analyzed by crystallographic and computational methods that reveal a strong correlation between the regioselectivity and the puckering of the phospholane rings. The significance of this work is that it establishes a simple pathway for increasing the regioselectivity of the broad and easily accessible BDP class of ligands. The reduced ligands reported herein have yet to be tested in their enantiopure forms. The data presented herein support extension of reduced BDP ligands to enantioselective hydroformylations.

6.4 Experimental Details

6.4.1 General Considerations

All ligand preparations and manipulations were performed under air-free conditions using standard Schlenk line techniques or an N_2-filled glovebox. Most workups and flash column chromatography were performed in air. Air-free extractions were performed by sparging the 1 M HCl (aq.) and K_2CO_3 (aq.) vigorously with N_2 for 30 – 40 min prior to use. THF was distilled from Na/benzophenone, DCM was distilled from CaH_2 and sparged with N_2. $CDCl_3$ was purchased from Sigma-Aldrich, dried over CaH_2 and stored in a bomb flask over 3 Å molecular sieves under an N_2 atmosphere. [Rh(acac)$(CO)_2$] was provided by the Dow Chemical Company

and was recrystallized from toluene. Succinyl and phthaloyl chloride were distilled under reduced pressure and stored in an N_2 filled glovebox. All alkenes were purchased from Sigma-Aldrich and purged with N_2 before use. ^{1}H and ^{31}P NMR spectra were recorded on a Bruker Avance-400 MHz spectrometer. ^{13}C NMR spectra were recorded on a Bruker Avance-500 MHz spectrometer. ^{1}H and ^{13}C NMR spectra were referenced to the residual protio-solvent. ^{31}P NMR shifts were referenced from the corresponding ^{1}H NMR frequency. ^{1}H splitting patterns are designated as singlet (s), broad singlet (brs), doublet (d), doublet of doublets (dd), virtual doublet of doublets (vdd), doublet of triplets (dt), triplet (t), triplet of doublets (td), virtual triplet (vt) or multiplet (m). Mass spectra were obtained at the Paul Bender Chemical Instrumentation Center of the Chemistry Department of the University of Wisconsin–Madison using a Thermo Q Exactive™ Plus ESI-MS. Crystallographic data were obtained with Bruker Smart Quazar with an APEX2 detector and a Mo-microsource. The azine and ligand **3** were prepared following known literature procedures.[36]

6.4.2 Synthesis of 1,2-Bis(phosphino)ethane

The title compound was prepared following a modified literature procedure.[69] A solution of $Li[AlH_4]$ (1 M in ether, 19.56 mL, 8 equiv) in ether (24 mL) was cooled to –78 °C. The phosphine 1,2-bis(dichlorophosphino)ethane (369.1 μL, 2.45 mmol, 1 equiv) was added dropwise *via* syringe over a period of 20 min. The solution was allowed to warm to rt overnight. N_2-sparged water was slowly added dropwise while the reaction mixture was cooled with an ice bath. The white precipitate was filtered off using a Schlenk frit, and the solid was washed with ether (6 x 8 mL). The ether solution was cannulated into a Schlenk flask containing degassed

$MgSO_4$, which was filtered off using a Schlenk frit and washed with ether (5 x 3 mL). The product was isolated as a colorless oil (82% yield) by distilling out the lower boiling ether solvent at 40 °C. NMR spectroscopic data were in agreement with the reported values.[70-71]

6.4.3 General Synthesis of Tetraaryl-bis(diazaphospholanes) 1, 3, 5 and 7

In an oven-dried 50 mL Schlenk flask, the diaryl azine (1.00 g, 4.8 mmol, 2 equiv) and the primary bisphosphine (2.4 mmol, 1 equiv) were combined in THF (30 mL). The corresponding diacyl chloride (5.1 mmol, 2.1 equiv) was added dropwise to the yellow homogeneous solution *via* syringe. The solution turned almost colorless over time. BDP **1**, **3** and **5** precipitated as white solids; BDP **7** stayed dissolved in solution.

TPSB BDP (1). The product formed as a white solid from the reaction mixture, was filtered off in air and washed with THF (4 x 7 mL) (503.0 mg, 29% yield). X-ray quality crystals (colorless needles) were obtained from a gas-phase diffusion of pentane into a DCM-solution of 1 at 4 °C. ^{1}H NMR ($CDCl_3$, 400 MHz, ppm): δ 7.45 – 7.30 (m, 8H), 7.16 (d, $^3J_{H\text{-}H}$ = 7.5 Hz, 4H), 7.11 – 7.01 (m, 4H), 6.87 (t, $^3J_{H\text{-}H}$ = 7.6 Hz, 4H), 6.62 (d, $^3J_{H\text{-}H}$ = 7.3 Hz, 4H), 5.75 (brs, 2H), 5.74 (vt, $^2J_{H\text{-}P}$ = 10.1 Hz, 2H), 2.84 – 2.56 (m, 8H). ^{13}C(1H) NMR ($CDCl_3$, 126 MHz, ppm): δ 167.5, 165.1, 138.7 (vt, $^2J_{C\text{-}P}$ = 2.0 Hz), 137.2 (vt, $^2J_{C\text{-}P}$ = 9.0 Hz), 135.7, 130.78, 130.1 (vt, $^2J_{C\text{-}P}$ = 2.1 Hz), 129.2, 128.3, 127.8, 127.2, 126.0 (vt, $^1J_{C\text{-}P}$ = 4.4 Hz), 125.9 (vt, $^1J_{C\text{-}P}$ = 2.2 Hz), 61.9 (vt, $^1J_{C\text{-}P}$ = 18.5 Hz), 57.1 (vt, $^1J_{C\text{-}P}$ = 4.3 Hz), 30.3, 29.7. ^{31}P(1H) NMR ($CDCl_3$, 162 MHz, ppm): δ -1.4. HRMS (ESI, m/z): $[M+H]^+$ calcd. for $C_{42}H_{37}N_4O_4P_2$: 723.2285, found: 723.2278 (Δ = 1.0 ppm).

TPPB BDP (3). All data were in agreement with reported values.[36]

TPSB BDPE (5). The product crashed out of the THF solution, was filtered in air and washed with THF (5 x 3 mL) (333.9 mg, 20% yield). The majority of **5** was recovered from the filtrate as its phosphine oxide derivative. **^{1}H NMR** ($CDCl_3$, 400 MHz, ppm): δ 7.40 – 7.27 (m, 12H), 7.17 (d, $^{3}J_{H\text{-}H}$ = 7.5 Hz, 4H), 7.02 (d, $^{3}J_{H\text{-}H}$ = 7.5 Hz, 4H), 5.59 (vdd, $^{2}J_{H\text{-}P}$ = 8.7 Hz, 2H), 5.49 (bs, 2H), 3.10 – 2.89 (m, 2H), 2.83 – 2.70 (m, 6H), 1.04–0.94 (m, AA'BB'XX', 2H), 0.54–0.44 (m, AA'BB'XX', 2H). **^{13}C(1H) NMR** ($CDCl_3$, 126 MHz, ppm): δ 167.9, 165.9, 137.2 (vt, $J_{C\text{-}P}$ = 7.2 Hz), 133.2, 129.4, 129.2, 128.3, 127.6, 125.7 (vt, $J_{C\text{-}P}$ = 3.9 Hz), 125.0 (br), 59.8 (vdd, $J_{C\text{-}P}$ = 14.0 Hz), 59.2 (vt, $J_{C\text{-}P}$ = 9.3 Hz), 30.8, 29.9. **^{31}P(1H) NMR** ($CDCl_3$, 162 MHz, ppm): δ 9.8. **HRMS** (ESI, m/z): $[M+H]^+$ calcd. for $C_{38}H_{37}N_4O_4P_2$: 675.2285, found: 675.2290 (Δ = 0.7 ppm).

TPSB BDPEO. The solution containing **5** was concentrated *in vacuo* to yield a crude solid, which was suspended in EtOAc. The phosphine oxide was filtered and washed with EtOAc (4 x 3 mL) (389.6 mg, 24% yield). **^{1}H NMR** ($CDCl_3$, 400 MHz, ppm): δ 7.40 – 7.32 (m, 12H), 7.25 (m, 4H, overlapped with $CHCl_3$), 7.92 (m, 4H), 5.80 (vdd, $^{2}J_{H\text{-}P}$ = 10.0 Hz, 2H), 5.41 (vdd, $^{2}J_{H\text{-}P}$ = 16.2 Hz, 2H), 3.95 – 2.82 (m, 2H), 2.81 – 2.62 (m, 6H), 1.85–1.73 (AA'BB'XX', 2H), 1.29–1.16 (m, AA'BB'XX', 2H). **^{13}C(1H) NMR** ($CDCl_3$, 126 MHz, ppm): δ 167.3, 166.1, 131.4, 131.4, 129.8, 129.5, 129.1, 128.8, 127.0, 125.0, 58.4 (vdd, $J_{C\text{-}P}$ = 31.4 Hz), 55.4 (vdd, $J_{C\text{-}P}$ = 32.5 Hz). **^{31}P(1H) NMR** ($CDCl_3$, 162 MHz, ppm): δ 54.3. **HRMS** (ESI, m/z): $[M-H]^-$ calcd. for $C_{38}H_{35}N_4O_6P_2$: 705.2037. found: 705.2040 (Δ = 0.4 ppm).

TNSB BDP (7). Compound **7** was purified *via* column chromatography (EtOAc:DCM = 1 : 9, R_f = 0.38) Colorless needles were obtained by gas-phase diffusion of pentane into a CH_2Cl_2 solution of **7** (234.2 mg, 20% yield, contains solvents in the crystal lattice). **^{1}H NMR** ($CDCl_3$, 400 MHz, ppm): δ 8.25 (d, $^{3}J_{H\text{-}H}$ = 8.4 Hz, 2H), 7.96 (app. dd, *J* = 18.0, 7.8 Hz, 6H), 7.70 (app.

dt, J = 19.8, 6.9 Hz, 4H), 7.48 (t, $^{3}J_{H\text{-}H}$ = 7.7 Hz, 2H), 7.25 (app. dd, J = 23.4, 7.6 Hz, 4H), 7.10 (s, 4H), 6.92 – 6.85 (m, 4H), 6.71 (t, $^{3}J_{H\text{-}H}$ = 11.6 Hz, 2H), 6.57 (t, $^{3}J_{H\text{-}H}$ = 7.7 Hz, 2H), 6.46 (d, $^{3}J_{H\text{-}H}$ = 7.2 Hz, 2H), 6.11 (vt, $^{2}J_{H\text{-}P}$ = 6.9 Hz, 2H), 5.86 (s, 2H), 2.78 (td, $^{2}J_{H\text{-}H}$ = 15.9, $^{3}J_{H\text{-}H}$ = 15.9, $^{3}J_{H\text{-}H}$ = 4.9 Hz, 2H), 2.49 (dd, $^{2}J_{H\text{-}H}$ = 16.7, $^{3}J_{H\text{-}H}$ = 3.2 Hz, 2H), 2.36 (dd, $^{2}J_{H\text{-}H}$ = 16.7, $^{3}J_{H\text{-}H}$ = 3.2 Hz, 2H), 2.08 (td, $^{2}J_{H\text{-}H}$ = 16.1, $^{3}J_{H\text{-}H}$ = 16.1, $^{2}J_{H\text{-}H}$ = 4.7 Hz, 2H). **^{13}C(1H) NMR** ($CDCl_3$, 126 MHz, ppm): δ 167.7, 165.6, 140.0 (vt, $^{2}J_{C\text{-}P}$ = 1.8 Hz), 134.53 (vt, $^{2}J_{C\text{–}P}$ = 10.0 Hz), 134.3, 132.7, 131.1 (vt, $^{2}J_{C\text{–}P}$ = 2.0 Hz), 130.84 (vt, $^{2}J_{C\text{-}P}$ = 2.1 Hz), 130.82, 130.4, 129.5, 128.9, 128.6, 128.1, 127.7, 126.6, 126.5, 126.0, 125.7, 125.5, 125.2, 125.1 (vt, $^{1}J_{C\text{–}P}$ = 8.3 Hz), 124.31, 123.1 (vt, $^{1}J_{C\text{–}P}$ = 3.1 Hz), 121.55, 59.8 (vt, $^{1}J_{C\text{–}P}$ = 18.5 Hz), 55.1 (vt, $^{1}J_{C\text{–}P}$ = 4.2 Hz), 30.4, 26.9. **^{31}P(1H) NMR** ($CDCl_3$, 162 MHz, ppm): δ 3.27. **HRMS** (ESI, m/z): $[M+H]^+$ calcd. for $C_{58}H_{45}N_4O_4P_2$: 923.2911, found: 923.2914 (Δ = 0.3 ppm).

6.4.4 General Borane Reduction Procedure

To a mixture of the BDP ligand (437.9 mg, 0.606 mmol, 1 equiv.) in THF (7 mL), BH_3•THF (1 M in THF, 9.10 mL, 9.10 mmol, 15 equiv.) was added *via* syringe. The Schlenk flask was sealed and the mixture was stirred at 55 °C or at room temperature for 20 h. The reaction mixture was allowed to cool to room temperature and all volatiles were removed *in vacuo*. The remaining solid was dissolved in $HNEt_2$ (3 mL) and the solution was heated at 50 °C for at least 4 h. Upon cooling, all volatiles were removed *in vacuo*. The crude product was dissolved in EtOAc (15 mL) and stirred with aq. HCl (1 M, 10 mL) and the mixture was stirred for at least 30 min. Aq. K_2CO_3 (10 wt%,) was added until the aqueous layer was basic (pH ~ 10). The aqueous layer was extracted and washed with EtOAc (at least 2 x 5 mL). The combined

organic layers were washed with aq. K_2CO_3 (10 wt%, 2 x 7 mL) and dried over $MgSO_4$. The solvent was removed *in vacuo* to obtain the desired crude product as an off-white solid, which was further purified by column chromatography or recrystallization.

red-TPSB BDP (2). 2 was obtained as colorless block crystals upon slow evaporation of EtOAc (89% yield). ^{1}H NMR ($CDCl_3$, 400 MHz, ppm): δ 7.69 (m, 2H), 7.37 – 7.16 (m, 12H), 6.72 – 6.60 (m, 6H), 6.40 (t, J = 7.4 Hz, 4H), 4.09 (vt, $^2J_{H\text{-}P}$ = 12.5 Hz, 2H), 3.96 (brs, 2H), 2.94 (app. dd, J = 23.5, 11.4 Hz, 4H), 2.47 (app. td, J = 11.4, 2.9 Hz, 2H), 2.01 (app. td, J = 11.4, 2.9 Hz, 2H), 1.62 – 1.33 (m, 8H). **^{13}C(1H) NMR** ($CDCl_3$, 126 MHz, ppm): δ 141.9 (brs), 141.0 (brs), 136.6, 132.8 (vt, $^2J_{C\text{-}P}$ = 1.9 Hz), 129.2 (vt, $^1J_{C\text{-}P}$ = 3.7 Hz), 128.0, 127.8, 127.5 (brs), 127.0, 126.8 (brs), 71.8 (vt, $^1J_{C\text{-}P}$ = 10 Hz), 71.2, 55.4, 54.9, 24.7, 24.0. **^{31}P(1H) NMR** ($CDCl_3$, 162 MHz, ppm): δ -0.9. **HRMS** (ESI, m/z): $[M+H]^+$ calcd. for $C_{42}H_{45}N_4P_2$: 667.3114. found: 667.3105 (Δ = 1.3 ppm).

red-TPPB BDP (4). The pure product was obtained by recrystallization from liquid-liquid diffusion of EtOAc and pentane at room temperature (92% yield). **^{1}H NMR** ($CDCl_3$, 400 MHz, ppm): δ 7.78 (m, 2H), 7.37 – 7.20 (m, 12H), 7.15 – 7.04 (m, 6H), 6.99 (d, $^3J_{H\text{-}H}$ = 7.2 Hz, 2H), 6.89 (d, $^3J_{H\text{-}H}$ = 7.2 Hz, 2H), 6.85 (t, $^3J_{H\text{-}H}$ = 7.2 Hz, 2H), 6.80 (d, $^3J_{H\text{-}H}$ = 7.4 Hz, 4H), 6.64 (t, $^3J_{H\text{-}H}$ = 7.7 Hz, 4H), 4.25 (vt, $^2J_{H\text{-}P}$ = 11.7 Hz, 2H), 4.20 (bs, 2H, overlapped with 4.18 ppm signal), 4.10 (d, $^2J_{H\text{-}H}$ = 14.5 Hz, 2H), 3.98 (d, $^2J_{H\text{-}H}$ = 14.5 Hz, 2H), 3.51 (d, $^2J_{H\text{-}H}$ = 14.5 Hz, 2H). **^{13}C(1H) NMR** ($CDCl_3$, 126 MHz, ppm): δ 142.1, 141.1 (vt, $J_{C\text{-}P}$ = 8.6 Hz), 135.8, 133.7, 133.3, 133.2, 128.7 (vt, $J_{C\text{-}P}$ = 3.5 Hz), 128.4, 128.2, 127.5, 127.0, 126.2, 126.1, 126.0, 125.8, 72.7 (vt, $J_{C\text{-}P}$ = 9.2 Hz), 71.6, 58.7, 57.6. **^{31}P(1H) NMR** ($CDCl_3$, 162 MHz, ppm): δ 1.1. **HRMS** (ESI, m/z): $[M+H]^+$ calcd. for $C_{50}H_{45}N_4P_2$: 763.3114. found: 763.3105 (Δ = 1.4 ppm).

red-TPSB BDPE (6). Product **6** was obtained through air-free extraction using N_2-sparged EtOAc, aq. HCl (1 M) and aq. K_2CO_3. $MgSO_4$ was degassed prior to use. The sample also contains small amounts of other phosphorous compounds in the ^{31}P NMR. **^{1}H NMR** ($CDCl_3$, 400 MHz, ppm): δ 7.40 – 7.27 (m, 12H), 7.17 (app. d, J = 7.5 Hz, 4H), 7.02 (app. d, J = 7.5 Hz, 4H), 5.59 (vdd, 2H), 5.49 (bs, 2H), 3.10 – 2.89 (m, 2H), 2.83 – 2.70 (m, 6H), 0.99 (AA'BB'XX', 2H), 0.49 (AA'BB'XX', 2H). **^{31}P(1H) NMR** ($CDCl_3$, 162 MHz, ppm): δ 6.5. **^{13}C(1H) NMR** ($CDCl_3$, 126 MHz, ppm): δ 140.3 (vt, $^{1}J_{C\text{-}P}$ = 7.0 Hz), 134.5 (vt, $^{2}J_{C\text{-}P}$ = 1.7 Hz), 127.5, 127.4 (vt, $^{2}J_{C\text{-}P}$ = 3.7 Hz), 127.3, 127.2, 126.1 (bs), 125.9, 125.3, 74.6 (vdd), 68.7 (vdd), 54.6, 54.5, 23.4, 23.1, 19.0 (d, $^{1}J_{C\text{-}P}$ = 8.0 Hz). **HRMS** (ESI, m/z): $[M+H]^+$ calcd. for $C_{38}H_{45}N_4P_2$: 619.3114, found: 619.3114 (Δ = <0.1 ppm).

red-TNSB BDP (8). (47.5 mg, 76% yield). Colorless needles were obtained by gas-phase diffusion of pentane into a CH_2Cl_2 solution of **8.** **^{1}H NMR** ($CDCl_3$, 400 MHz, ppm): δ 8.10 (m, 2H), 7.95 (m, 4H), 7.77 (d, $^{3}J_{H\text{-}H}$ = 8.1 Hz, 2H), 7.54 (t, $^{3}J_{H\text{-}H}$ = 7.5 Hz, 4H), 7.49 – 7.28 (m, 10H), 6.48 (bs, 2H), 6.67 (bs, 6H), 6.40 (bs, 2H), 4.62 (bs, 4H), 2.88 (app. bd, J = 11.6 Hz, 2H), 2.60 (app. bd, J = 8.0 Hz, 2H), 2.47 (app. bt, J = 10.4 Hz, 2H), 1.80 (app. bt, J = 11.1 Hz, 2H), 1.50 – 1.24 (m, 8H). **^{13}C(1H) NMR** ($CDCl_3$, 126 MHz, ppm): δ 144.5, 134.0 (br s), 133.7, 13.32 (br s), 133.28, 131.32, 131.29, 130.5, 128.8, 128.8 (vt, $^{1}J_{C\text{-}P}$ = 5.0 Hz), 128.1, 127.3, 127.2, (br s) 126.2, 125.9 (br s), 126.5 (br s), 125.2, 125.0, 124.4, 124.3, 123.6, 122.6 (vt, $^{2}J_{C\text{-}P}$ = 2.3 Hz), 69.6, 55.7, 55.1, 29.9, 25.9, 24.1. **^{31}P(1H)** NMR ($CDCl_3$, 162 MHz, ppm): δ -2.2. **HRMS** (ESI, m/z): $[M+H]^+$ calcd. for $C_{58}H_{53}N_4P_2$: 867.3740, found: 867.3737 (Δ = 0.3 ppm).

6.4.5 General Hydroformylation Procedure

Inside an N_2-filled glovebox, a solution of [Rh(acac)$(CO)_2$] in THF (20 mM), a solution of the bis(diazaphospholane) ligand in DCM (5 –20 mM) or the reduced bis(diazaphospholane) in THF (20 mM) and THF were combined into an oven-dried 15 mL Ace Glass pressure bottle equipped with a magnetic stir bar using 1000 μL and 200 μL Eppendorf® pipets. The pressure bottle was attached to a pressure reactor and removed from the glovebox. In a fume hood, the reactor was purged with syngas (3 x 120 psig) and then filled to 150 psig of syngas. The yellow solution was vigorously stirred at 60 °C for at least 60 min. Upon cooling, the reactor was depressurized to 10 psig and the alkene was injected *via* a gas-tight syringe. Solid alkenes were injected as a solution in THF. The reactor was then purged with syngas (3 x 120 psig) and filled to 150 psig of syngas. The reaction was heated at 40, 60 or 80 °C. After the desired reaction time, the reactor was allowed to cool to room temperature and vented to atmospheric pressure. NMR spectra of the crude reaction mixture were taken in $CDCl_3$ or toluene-d_8 to obtain conversions of the alkenes and branched to linear ratios of the produced aldehydes.

6.5 References

(1) van Leeuwen, P. W. N. M.; Claver, C. *Rhodium Catalyzed Hydroformylation*; Kluwer Academic Publishers: Dordrecht, The Netherlands 2000.

(2) Trost, B. M. The atom economy--a search for synthetic efficiency. *Science* **1991**, *254*, 1471–1477.

(3) Botteghi, C.; Paganelli, S.; Schionato, A.; Marchetti, M. The asymmetric hydroformylation in the synthesis of pharmaceuticals. *Chirality* **1991**, *3*, 355–369.

(4) Börner, A.; Franke, R. *Hydroformylation: Fundamentals, Processes, and Applications in Organic Synthesis*; Wiley-VCH Verlag GmbH & Co. KGaA: Weinheim, Germany, 2016.

(5) Billig, E.; Abatjoglou, A. G.; Bryant, D. R. Bis-phosphite compounds. EP 0213639 A2. March 11, 1987.

(6) Casey, C. P.; Whiteker, G. T.; Melville, M. G.; Petrovich, L. M.; Gavney, J. A.; Powell, D. R. Diphosphines with natural bite angles near 120.degree. increase selectivity for n-aldehyde formation in rhodium-catalyzed hydroformylation. *J. Am. Chem. Soc.* **1992**, *114*, 5535–5543.

(7) van der Veen, L. A.; Keeven, P. H.; Schoemaker, G. C.; Reek, J. N. H.; Kamer, P. C. J.; van Leeuwen, P. W. N. M.; Lutz, M.; Spek, A. L. Origin of the Bite Angle Effect on Rhodium Diphosphine Catalyzed Hydroformylation. *Organometallics* **2000**, *19*, 872–883.

(8) Li, Y.-Q.; Wang, P.; Zhang, H.; Zhao, X.-L.; Lu, Y.; Popović, Z.; Liu, Y. Influence of electrostatic repulsive force and electron-withdrawing effect in ionic diphosphine on regioselectivity of rhodium-catalyzed hydroformylation of 1-octene. *J. Mol. Catal. A: Chem.* **2015**, *402*, 37–45.

(9) Breit, B.; Seiche, W. Hydrogen Bonding as a Construction Element for Bidentate Donor Ligands in Homogeneous Catalysis: Regioselective Hydroformylation of Terminal Alkenes. *J. Am. Chem. Soc.* **2003**, *125*, 6608–6609.

(10) Breit, B.; Seiche, W. Self-Assembly of Bidentate Ligands for Combinatorial Homogeneous Catalysis Based on an A-T Base-Pair Model. *Angew. Chem. Int. Ed.* **2005**, *44*, 1640–1643.

(11) Seiche, W.; Schuschkowski, A.; Breit, B. Bidentate Ligands by Self-Assembly through Hydrogen Bonding: A General Room Temperature/Ambient Pressure Regioselective Hydroformylation of Terminal Alkenes. *Adv. Synth. Catal.* **2005**, *347*, 1488–1494.

(12) Grunanger, C. U.; Breit, B. Branched-regioselective hydroformylation with catalytic amounts of a reversibly bound directing group. *Angew. Chem. Int. Ed.* **2008**, *47*, 7346–7349.

(13) Grunanger, C. U.; Breit, B. Remote control of regio- and diastereoselectivity in the hydroformylation of bishomoallylic alcohols with catalytic amounts of a reversibly bound directing group. *Angew. Chem. Int. Ed.* **2010**, *49*, 967–970.

(14) Joe, C. L.; Blaisdell, T. P.; Geoghan, A. F.; Tan, K. L. Distal-selective hydroformylation using scaffolding catalysis. *J. Am. Chem. Soc.* **2014**, *136*, 8556–8559.

(15) Joe, C. L.; Tan, K. L. Enantioselective hydroformylation of aniline derivatives. *J. Org. Chem.* **2011**, *76*, 7590–7596.

(16) Lightburn, T. E.; Dombrowski, M. T.; Tan, K. L. Catalytic Scaffolding Ligands: An Efficient Strategy for Directing Reactions. *J. Am. Chem. Soc.* **2008**, *130*, 9210–9211.

(17) Sun, X.; Frimpong, K.; Tan, K. L. Synthesis of Quaternary Carbon Centers via Hydroformylation. *J. Am. Chem. Soc.* **2010**, *132*, 11841–11843.

(18) Ueki, Y.; Ito, H.; Usui, I.; Breit, B. Formation of quaternary carbon centers by highly regioselective hydroformylation with catalytic amounts of a reversibly bound directing group. *Chem. Eur. J.* **2011**, *17*, 8555–8558.

(19) Usui, I.; Nomura, K.; Breit, B. Diastereoselective Hydroformylation of 2,5-Cyclohexadienyl-1-carbinols with Catalytic Amounts of a Reversibly Bound Directing Group. *Org. Lett.* **2011**, *13*, 612–615.

(20) Worthy, A. D.; Joe, C. L.; Lightburn, T. E.; Tan, K. L. Application of a Chiral Scaffolding Ligand in Catalytic Enantioselective Hydroformylation. *J. Am. Chem. Soc.* **2010**, *132*, 14757–14759.

(21) Bellini, R.; Reek, J. N. Application of supramolecular bidentate hybrid ligands in asymmetric hydroformylation. *Chem. Eur. J.* **2012**, *18*, 13510–13519.

(22) Kuil, M.; Soltner, T.; van Leeuwen, P. W. N. M.; Reek, J. N. H. High-Precision Catalysts: Regioselective Hydroformylation of Internal Alkenes by Encapsulated Rhodium Complexes. *J. Am. Chem. Soc.* **2006**, *128*, 11344–11345.

(23) Slagt, V. F.; Kamer, P. C. J.; van Leeuwen, P. W. N. M.; Reek, J. N. H. Encapsulation of Transition Metal Catalysts by Ligand-Template Directed Assembly. *J. Am. Chem. Soc.* **2004**, *126*, 1526–1536.

(24) Slagt, V. F.; Reek, J. N. H.; Kamer, P. C. J.; van Leeuwen, P. W. N. M. Assembly of Encapsulated Transition Metal Catalysts. *Angew. Chem. Int. Ed.* **2001**, *40*, 4271–4274.

(25) Dydio, P.; Dzik, W. I.; Lutz, M.; de Bruin, B.; Reek, J. N. Remote supramolecular control of catalyst selectivity in the hydroformylation of alkenes. *Angew. Chem. Int. Ed.* **2011**, *50*, 396–400.

(26) Dydio, P.; Reek, J. N. Supramolecular control of selectivity in hydroformylation of vinyl arenes: easy access to valuable beta-aldehyde intermediates. *Angew. Chem. Int. Ed.* **2013**, *52*, 3878–3882.

(27) Noonan, G. M.; Cobley, C. J.; Mahoney, T.; Clarke, M. L. Rhodium/phospholane-phosphite catalysts give unusually high regioselectivity in the enantioselective hydroformylation of vinyl arenes. *Chem. Commun.* **2014**, *50*, 1475–1477.

(28) Noonan, G. M.; Fuentes, J. A.; Cobley, C. J.; Clarke, M. L. An Asymmetric Hydroformylation Catalyst that Delivers Branched Aldehydes from Alkyl Alkenes. *Angew. Chem. Int. Ed.* **2012**, *51*, 2477–2480.

(29) Nozaki, K.; Sakai, N.; Nanno, T.; Higashijima, T.; Mano, S.; Horiuchi, T.; Takaya, H. Highly Enantioselective Hydroformylation of Olefins Catalyzed by Rhodium(I) Complexes of New Chiral Phosphine–Phosphite Ligands. *J. Am. Chem. Soc.* **1997**, *119*, 4413–4423.

(30) Nozaki, K.; Takaya, H.; Hiyama, T. Enantioselective hydroformylation of olefins catalyzed by rhodium(I) complexes of chiral phosphine–phosphite ligands. *Top. Catal.* **1997**, *4*, 175–185.

(31) Watkins, A. L.; Landis, C. R. Origin of Pressure Effects on Regioselectivity and Enantioselectivity in the Rhodium-Catalyzed Hydroformylation of Styrene with (S,S,S)-BisDiazaphos. *J. Am. Chem. Soc.* **2010**, *132*, 10306–10317.

(32) Tonks, I. A.; Froese, R. D.; Landis, C. R. Very Low Pressure Rh-Catalyzed Hydroformylation of Styrene with (S,S,S-Bisdiazaphos): Regioselectivity Inversion and Mechanistic Insights. *ACS Catal.* **2013**, *3*, 2905–2909.

(33) Abrams, M. L.; Foarta, F.; Landis, C. R. Asymmetric Hydroformylation of Z-Enamides and Enol Esters with Rhodium-Bisdiazaphos Catalysts. *J. Am. Chem. Soc.* **2014**, *136*, 14583–14588.

(34) Adint, T. T.; Wong, G. W.; Landis, C. R. Libraries of Bisdiazaphospholanes and Optimization of Rhodium-Catalyzed Enantioselective Hydroformylation. *J. Org. Chem.* **2013**, *78*, 4231–4238.

(35) Clark, T. P.; Landis, C. R.; Freed, S. L.; Klosin, J.; Abboud, K. A. Highly Active, Regioselective, and Enantioselective Hydroformylation with Rh Catalysts Ligated by Bis-3,4-diazaphospholanes. *J. Am. Chem. Soc.* **2005**, *127*, 5040–5042.

(36) Landis, C. R.; Jin, W.; Owen, J. S.; Clark, T. P. Rapid Access to Diverse Arrays of Chiral 3,4-Diazaphospholanes. *Angew. Chem. Int. Ed.* **2001**, *40*, 3432–3434.

(37) McDonald, R. I.; Wong, G. W.; Neupane, R. P.; Stahl, S. S.; Landis, C. R. Enantioselective Hydroformylation of N-Vinyl Carboxamides, Allyl Carbamates, and Allyl Ethers Using Chiral Diazaphospholane Ligands. *J. Am. Chem. Soc.* **2010**, *132*, 14027–14029.

(38) Watkins, A. L.; Hashiguchi, B. G.; Landis, C. R. Highly Enantioselective Hydroformylation of Aryl Alkenes with Diazaphospholane Ligands. *Org. Lett.* **2008**, *10*, 4553–4556.

(39) Axtell, A. T.; Klosin, J.; Abboud, K. A. Evaluation of Asymmetric Hydrogenation Ligands in Asymmetric Hydroformylation Reactions. Highly Enantioselective Ligands Based on Bis-phosphacycles. *Organometallics* **2006**, *25*, 5003–5009.

(40) Landis, C. R.; Nelson, R. C.; Jin, W.; Bowman, A. C. Synthesis, Characterization, and Transition-Metal Complexes of 3,4-Diazaphospholanes. *Organometallics* **2006**, *25*, 1377–1391.

(41) Feuer, H.; Brown, F. Chemistry of hydrazides. X. The reduction of cyclic and acyclic hydrazides with diborane. *J. Org. Chem.* **1970**, *35*, 1468-1471.

(42) Herault, D.; Nguyen, D. H.; Nuel, D.; Buono, G. Reduction of secondary and tertiary phosphine oxides to phosphines. *Chem. Soc. Rev.* **2015**, *44*, 2508–2528.

(43) Reich, H. J. http://www.chem.wisc.edu/areas/reich/nmr /notes-5-hmr-16-virtual-coupling.pdf.

(44) Fackler, J. P.; Fetchin, J. A.; Mayhew, J.; Seidel, W. C.; Swift, T. J.; Weeks, M. Chemical exchange in "virtually coupled" systems. Metal-ion-induced relaxation of methyl-phosphorus coupling in phosphine complexes. *J. Am. Chem. Soc.* **1969**, *91*, 1941–1947.

(45) Pidcock, A. Coupling and "virtual" coupling in the nuclear magnetic resonance spectra of phosphine complexes. *Chem. Commun.* **1968**, *0*, 92-92.

(46) Hersh, W. H. False AA'X Spin-Spin Coupling Systems in 13C NMR: Examples Involving Phosphorus and a 20-Year-Old Mystery in Off-Resonance Decoupling. *J. Chem. Educ.* **1997**, *74*, 1485.

(47) Reich, H. J. http://www.chem.wisc.edu/areas/reich/ plt/windnmr.htm.

(48) Klosin, J.; Landis, C. R. Ligands for Practical Rhodium-Catalyzed Asymmetric Hydroformylation. *Acc. Chem. Res.* **2007**, *40*, 1251–1259.

(49) All most reactions proceeded to near complete conversion, precluding comparison of relative rates.

(50) Axtell, A. T.; Cobley, C. J.; Klosin, J.; Whiteker, G. T.; Zanotti-Gerosa, A.; Abboud, K. A. Highly regio- and enantioselective asymmetric hydroformylation of olefins mediated by 2,5-disubstituted phospholane ligands. *Angew. Chem. Int. Ed.* **2005**, *44*, 5834–5838.

(51) Nozaki, K.; Li, W.-g.; Horiuchi, T.; Takaya, H. Asymmetric hydroformylation of allylic alcohols catalyzed by Rh(I)-(R,S)-BINAPHOS. *Tetrahedron Lett.* **1997**, *38*, 4611–4614.

(52) Lightburn, T. E.; De Paolis, O. A.; Cheng, K. H.; Tan, K. L. Regioselective Hydroformylation of Allylic Alcohols. *Org. Lett.* **2011**, *13*, 2686–2689.

(53) Fürstner, A.; Nevado, C.; Waser, M.; Tremblay, M.; Chevrier, C.; Teplý, F.; Aïssa, C.; Moulin, E.; Müller, O. Total Synthesis of Iejimalide A–D and Assessment of the

Remarkable Actin-Depolymerizing Capacity of These Polyene Macrolides. *J. Am. Chem. Soc.* **2007**, *129*, 9150–9161.

(54) Smith, A. B.; Brandt, B. M. Total Synthesis of (–)-Callystatin A. *Org. Lett.* **2001**, *3*, 1685–1688.

(55) Koskinen, A. M. P.; Karisalmi, K. Polyketide stereotetrads in natural products. *Chem. Soc. Rev.* **2005**, *34*, 677–690.

(56) Šmejkal, T.; Breit, B. A Supramolecular Catalyst for Regioselective Hydroformylation of Unsaturated Carboxylic Acids. *Angew. Chem. Int. Ed.* **2008**, *47*, 311–315.

(57) List, B. Proline-catalyzed asymmetric reactions. *Tetrahedron* **2002**, *58*, 5573–5590.

(58) Woodward, R. B.; Logusch, E.; Nambiar, K. P.; Sakan, K.; Ward, D. E.; Au-Yeung, B. W.; Balaram, P.; Browne, L. J.; Card, P. J.; Chen, C. H. Asymmetric total synthesis of erythromcin. 1. Synthesis of an erythronolide A secoacid derivative via asymmetric induction. *J. Am. Chem. Soc.* **1981**, *103*, 3210–3213.

(59) Stemmler, R. CBS Oxazaborolidines – Versatile Catalysts for Asymmetric Synthesis*Synlett* **2007**, *6*, 997-998.

(60) Carley, S.; Brimble, M. A. A Novel Approach to the CDE Ring System of Pectenotoxin-4 Triggered by VO(acac)2-Induced Epoxy-Acetalization. *Org. Lett.* **2009**, *11*, 563–566.

(61) Stepan, A. F.; Karki, K.; McDonald, W. S.; Dorff, P. H.; Dutra, J. K.; DiRico, K. J.; Won, A.; Subramanyam, C.; Efremov, I. V.; O'Donnell, C. J.; Nolan, C. E.; Becker, S. L.; Pustilnik, L. R.; Sneed, B.; Sun, H.; Lu, Y.; Robshaw, A. E.; Riddell, D.; O'Sullivan, T. J.; Sibley, E.; Capetta, S.; Atchison, K.; Hallgren, A. J.; Miller, E.; Wood, A.; Obach, R. S.

Metabolism-Directed Design of Oxetane-Containing Arylsulfonamide Derivatives as γ-Secretase Inhibitors. *J. Med. Chem.* **2011**, *54*, 7772–7783.

(62) Chikkali, S. H.; Bellini, R.; de Bruin, B.; van der Vlugt, J. I.; Reek, J. N. H. Highly Selective Asymmetric Rh-Catalyzed Hydroformylation of Heterocyclic Olefins. *J. Am. Chem. Soc.* **2012**, *134*, 6607–6616.

(63) Horiuchi, T.; Ohta, T.; Shirakawa, E.; Nozaki, K.; Takaya, H. Asymmetric Hydroformylation of Heterocyclic Olefins Catalyzed by Chiral Phosphine–Phosphite–Rh(I) Complexes. *J. Org. Chem.* **1997**, *62*, 4285–4292.

(64) Mazuela, J.; Pàmies, O.; Diéguez, M.; Palais, L.; Rosset, S.; Alexakis, A. Fine-tunable monodentate phosphoroamidite and aminophosphine ligands for Rh-catalyzed asymmetric hydroformylation. *Tetrahedron: Asymmetry* **2010**, *21*, 2153–2157.

(65) Rovira, L.; Vaquero, M.; Vidal-Ferran, A. Asymmetric Hydroformylation of Heterocyclic Olefins Mediated by Supramolecularly Regulated Rhodium-Bisphosphite Complexes. *J. Org. Chem.* **2015**, *80*, 10397–10403.

(66) Zheng, X.; Xu, K.; Zhang, X. Highly selective bisphosphine ligands for asymmetric hydroformylation of heterocyclic olefins. *Tetrahedron Lett.* **2015**, *56*, 1149–1152.

(67) Mazuela, J.; Coll, M.; Pàmies, O.; Diéguez, M. Rh-Catalyzed Asymmetric Hydroformylation of Heterocyclic Olefins Using Chiral Diphosphite Ligands. Scope and Limitations. *J. Org. Chem.* **2009**, *74*, 5440–5445.

(68) Brezny, A. C.; Landis, C. R. Unexpected CO Dependencies, Catalyst Speciation, and Single Turnover Hydrogenolysis Studies of Hydroformylation via High Pressure NMR Spectroscopy. *J. Am. Chem. Soc.* **2017**, *139*, 2778–2785.

(69) Reiter, S. A.; Nogai, S. D.; Karaghiosoff, K.; Schmidbaur, H. Insignificance of P–H···P Hydrogen Bonding: Structural Chemistry of Neutral and Protonated 1,8-Di(phosphinyl)naphthalene. *J. Am. Chem. Soc.* **2004**, *126*, 15833–15843.

(70) Maier, L. Organische Phosphorverbindungen XXII. Darstellung und Eigenschaften von diprimären α,ω-Bis-phosphino-alkanen. *Helv. Chim. Acta* **1966**, *49*, 842–851.

(71) Marzano, C.; Gandin, V.; Pellei, M.; Colavito, D.; Papini, G.; Lobbia, G. G.; Del Giudice, E.; Porchia, M.; Tisato, F.; Santini, C. In Vitro Antitumor Activity of the Water Soluble Copper(I) Complexes Bearing the Tris(hydroxymethyl)phosphine Ligand. *J. Med. Chem.* **2008**, *51*, 798–808.

Appendix A

NMR Spectra and Supporting Information for Chapters 3-4, and 6

A.1 Chapter 3: Interception and Characterization of Catalyst Species in Rhodium Bis(diazaphospholane)-Catalyzed Hydroformylation of Octene, Vinyl Acetate, Allyl Cyanide, and 1-Phenyl-1,3-butadiene

A.1.1 Additional Time Course Data

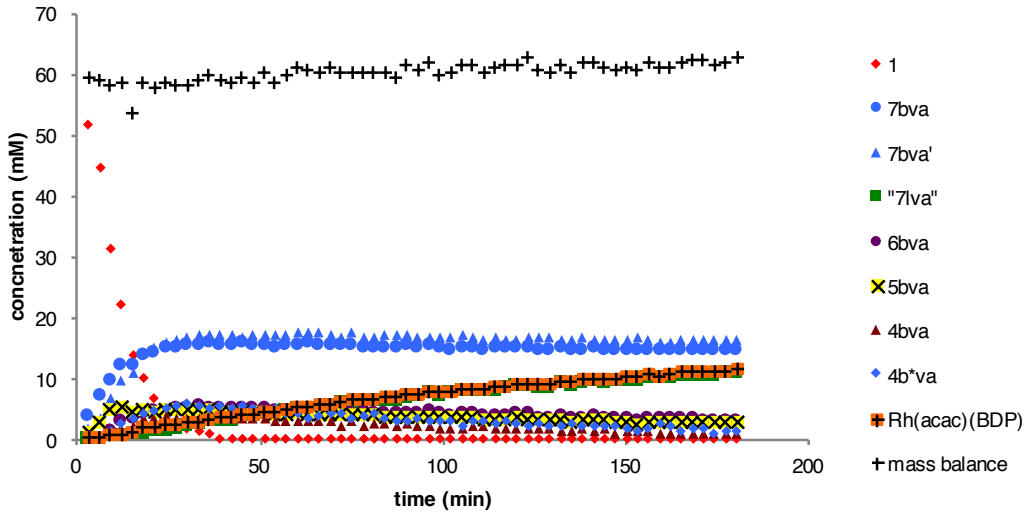

Figure A-1. Catalyst speciation and mass balance following the reaction of **1** (red diamonds) with vinyl acetate (-10 °C, 15 psia CO, 65 mM **1**, 320 mM vinyl acetate, CH_2Cl_2).

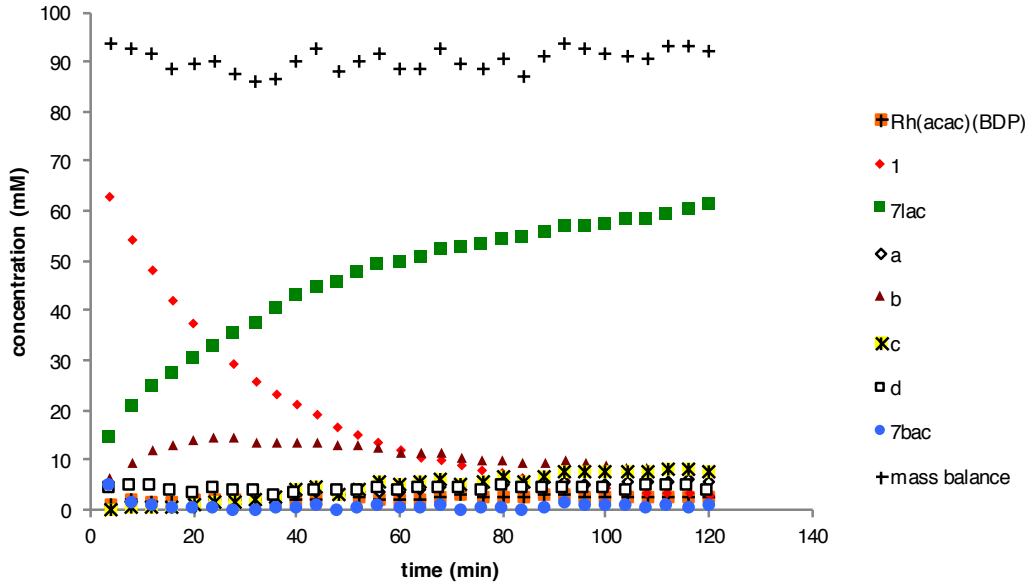

Figure A-2. Catalyst speciation and mass balance following the reaction of **1** (red diamonds) with allyl cyanide (-20 °C, 15 psia CO, 90 mM 1, 400 mM allyl cyanide, CH_2Cl_2).

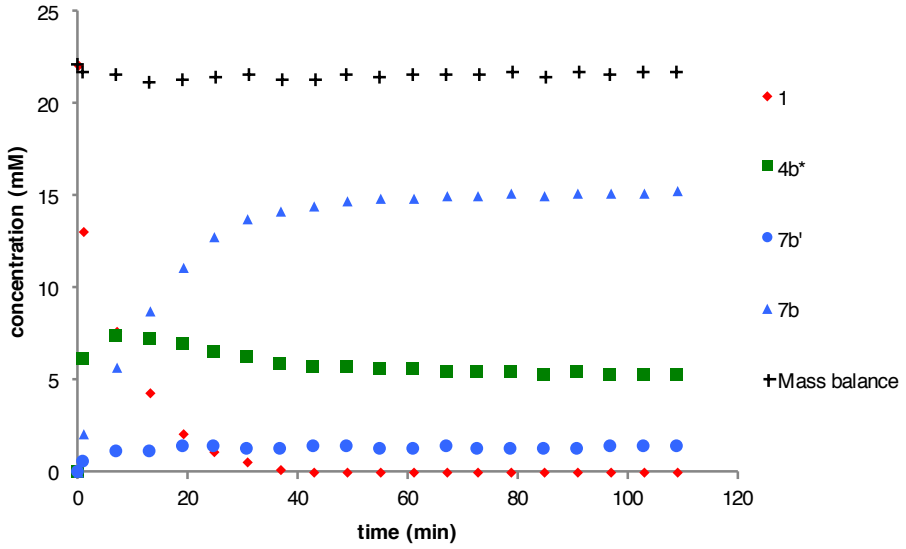

Figure A-3. Catalyst speciation and mass balance following the reaction of **1** (red diamonds) with *trans*-1-phenyl-1,3-butadiene (0 °C, 15 psia CO, 22 mM **1**, 200 mM *trans*-1-phenyl-1,3-butadiene, CH_2Cl_2).

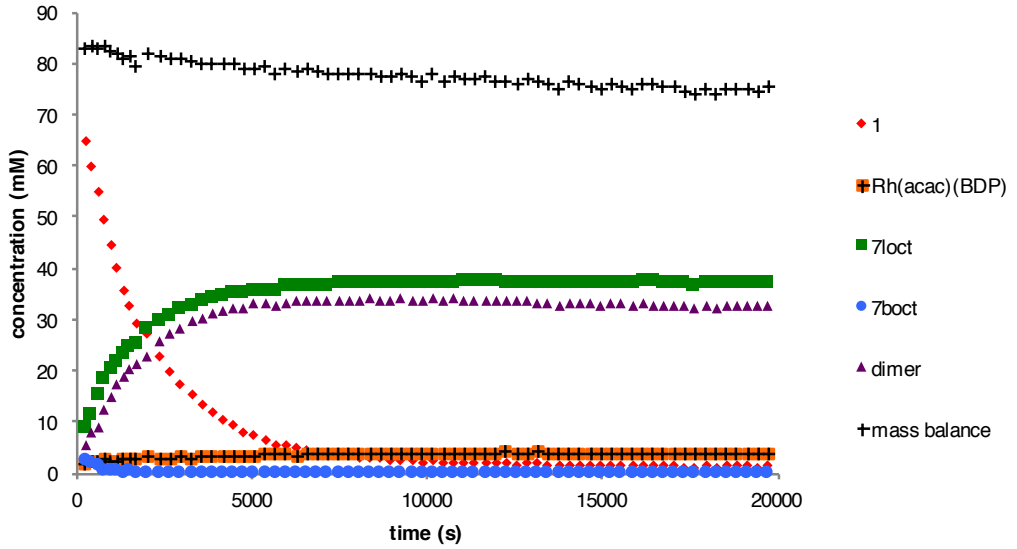

Figure A-4. Catalyst speciation and mass balance following the reaction of **1** (red diamonds) with 1-octene (-20 °C, 15 psia CO, 80 mM **1**, 400 mM 1-octene, CH_2Cl_2).

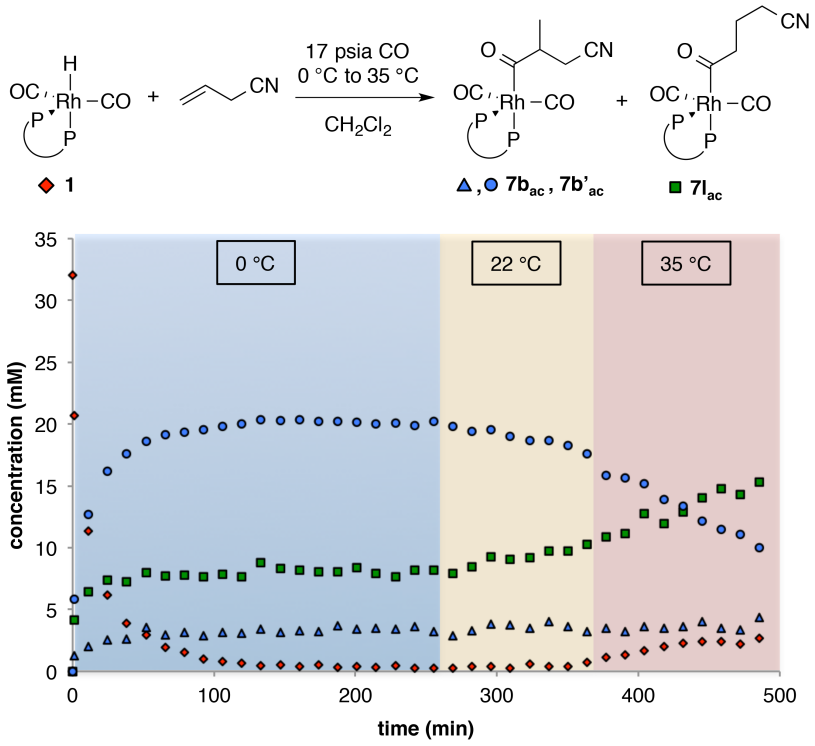

Figure A-5. Reaction of **1** (32 mM) with allyl cyanide (32 mM) with increasing temperature under a constant pressure of 17 psia CO as measured by WiHP-NMRR with active mixing.

A.1.2 Selected NMR Spectra

A.1.2.1 General Spectra

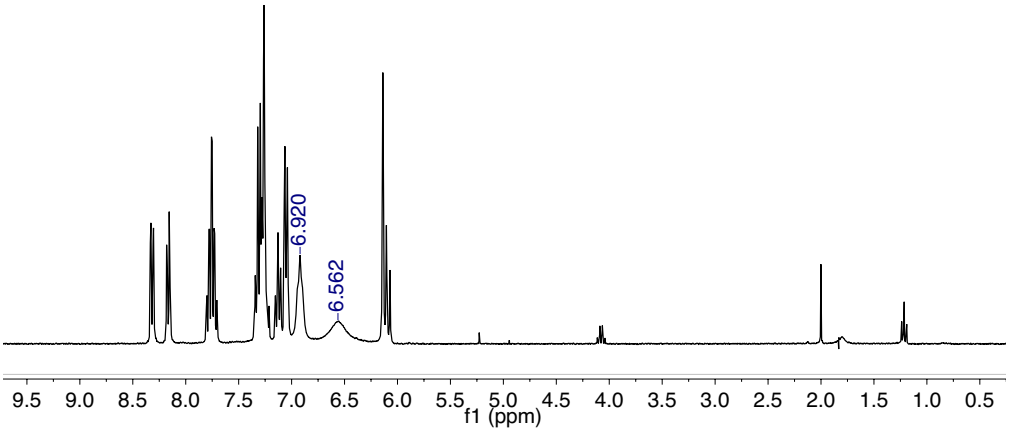

Figure A-6. ^{1}H NMR spectrum (300 MHz) of tetraphenyl bis(diazaphospholane); methine protons indicated. 24 °C, $CDCl_3$.

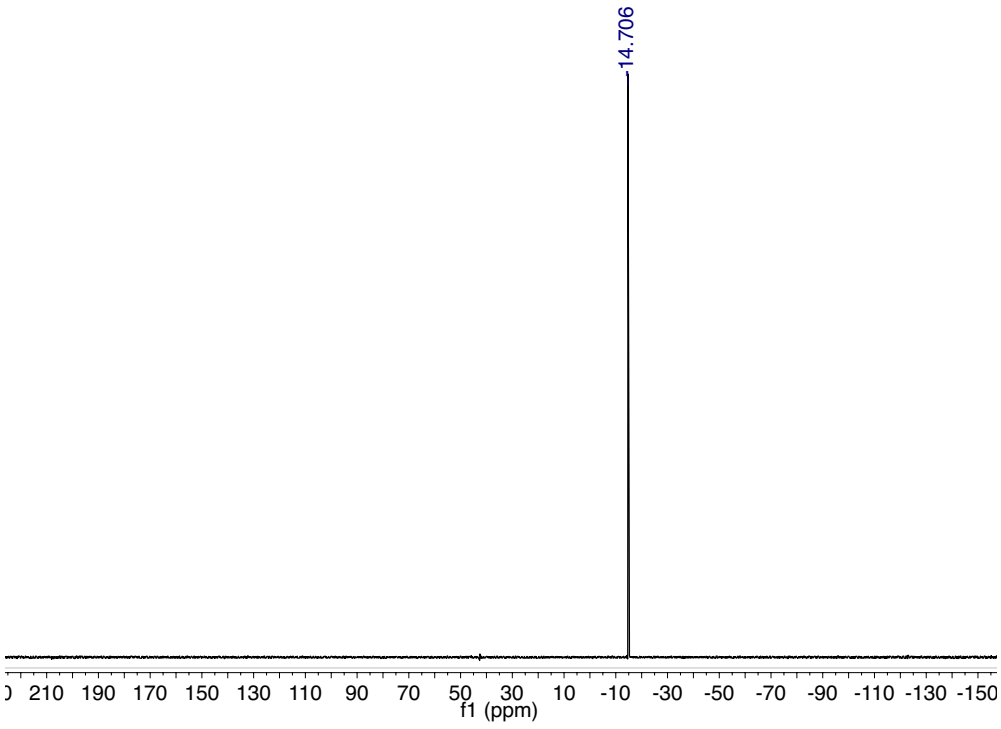

Figure A-7. $^{31}P\{^{1}H\}$ NMR spectrum (121.4 MHz) of tetraphenyl bis(diazaphospholane). 24 °C, $CDCl_3$.

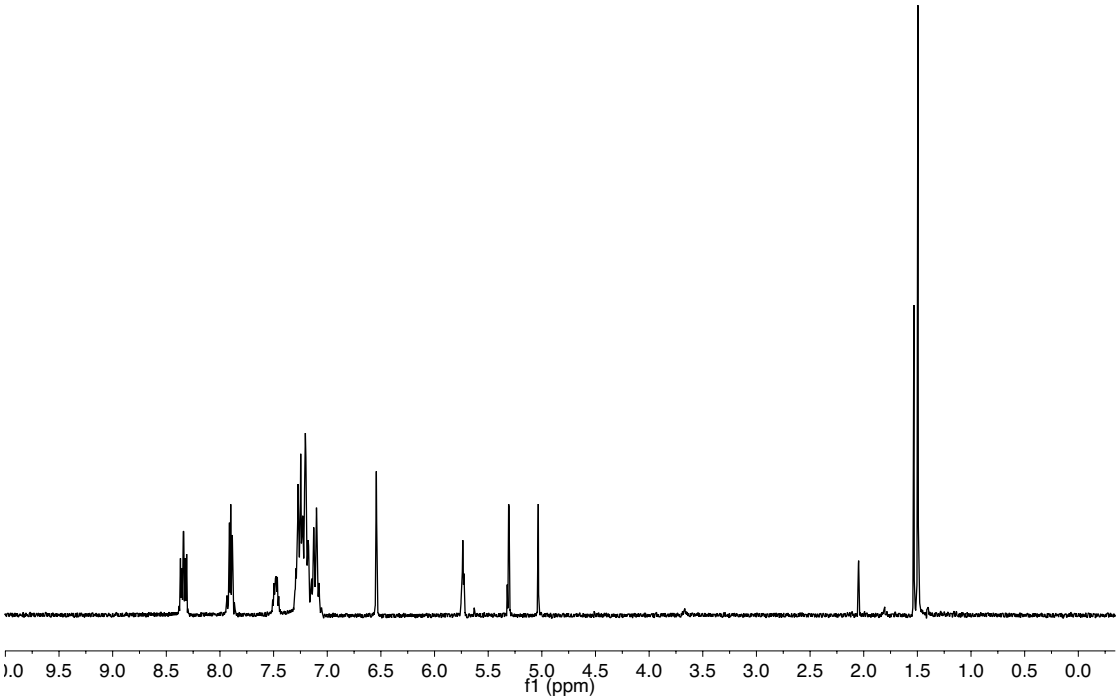

Figure A-8. ^{1}H NMR spectrum of [Rh(acac)(BDP)] (300 MHz, $CDCl_3$, 24 °C).

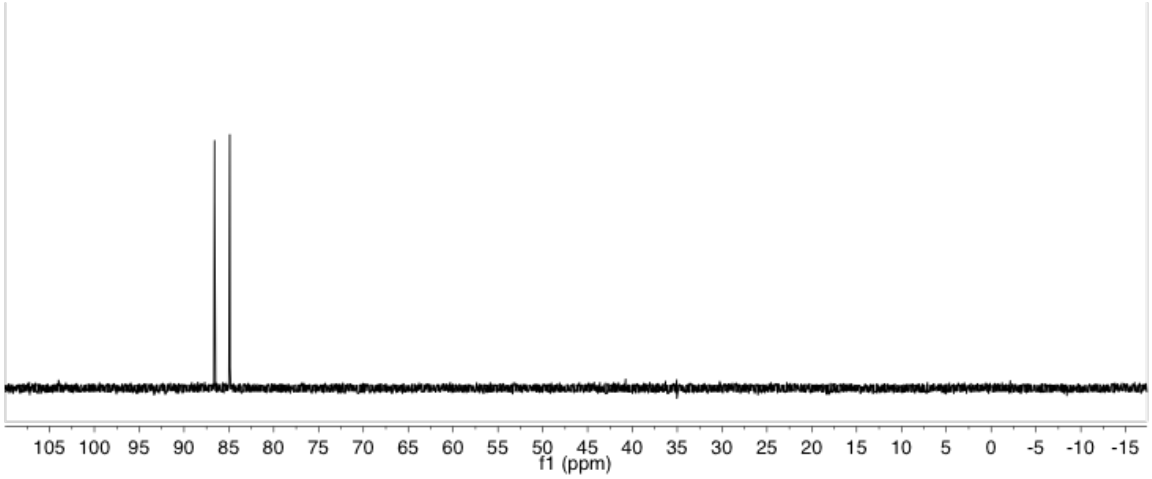

Figure A-9. $^{31}P\{^{1}H\}$ NMR spectrum of [Rh(acac)(BDP)] (121.5 MHz, $CDCl_3$, 24 ° C).

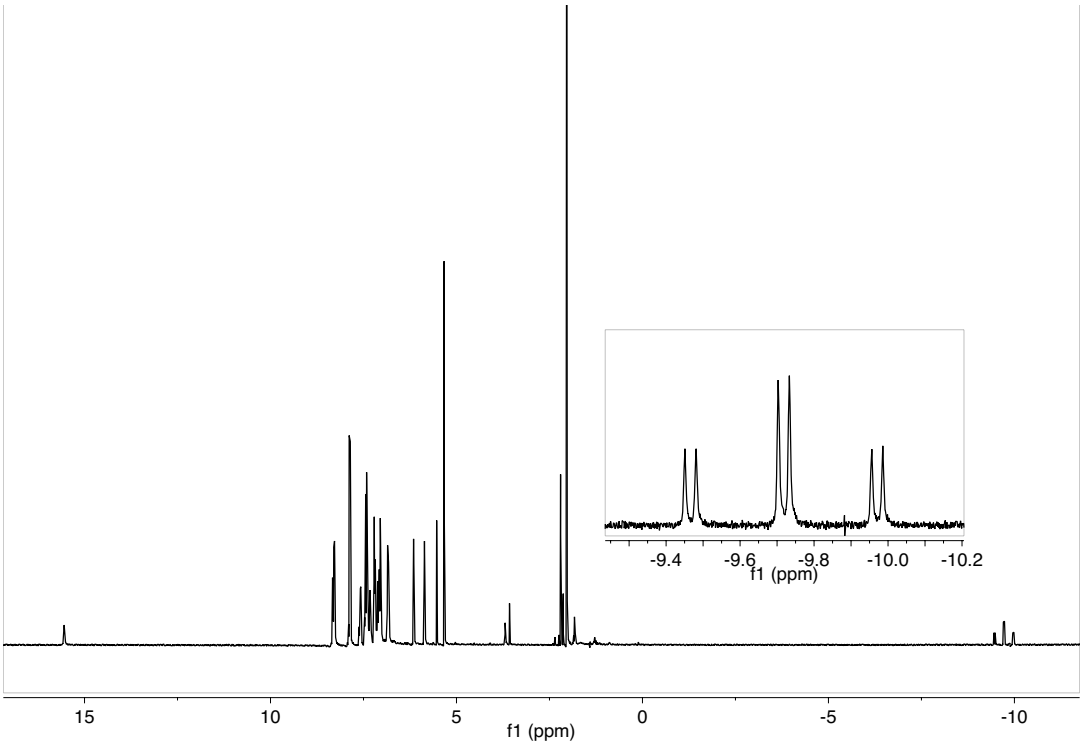

Figure A-10. ^{1}H NMR spectrum of [Rh(H)(CO)$_2$(BDP)] (**1**) (500 MHz, CD_2Cl_2, 24 °C).

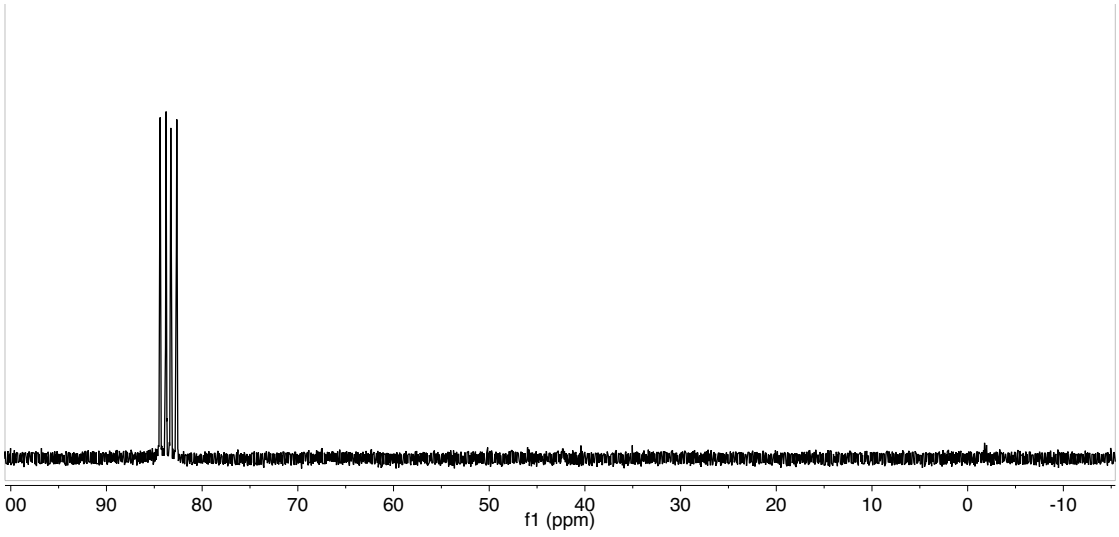

Figure A-11. ^{31}P NMR spectrum of **1** (121.5 MHz, CD_2Cl_2, 24 °C).

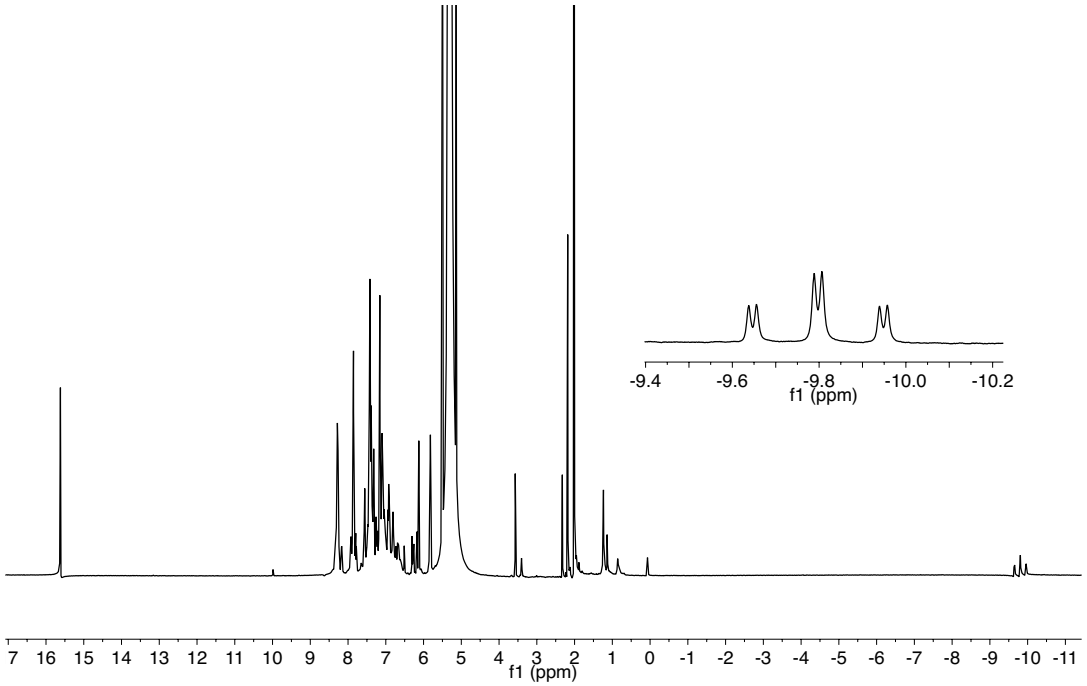

Figure A-12. ^{1}H NMR spectrum of [Rh(H)($^{13}CO)_2$(BDP)] (500 MHz, CH_2Cl_2, -20 °C).

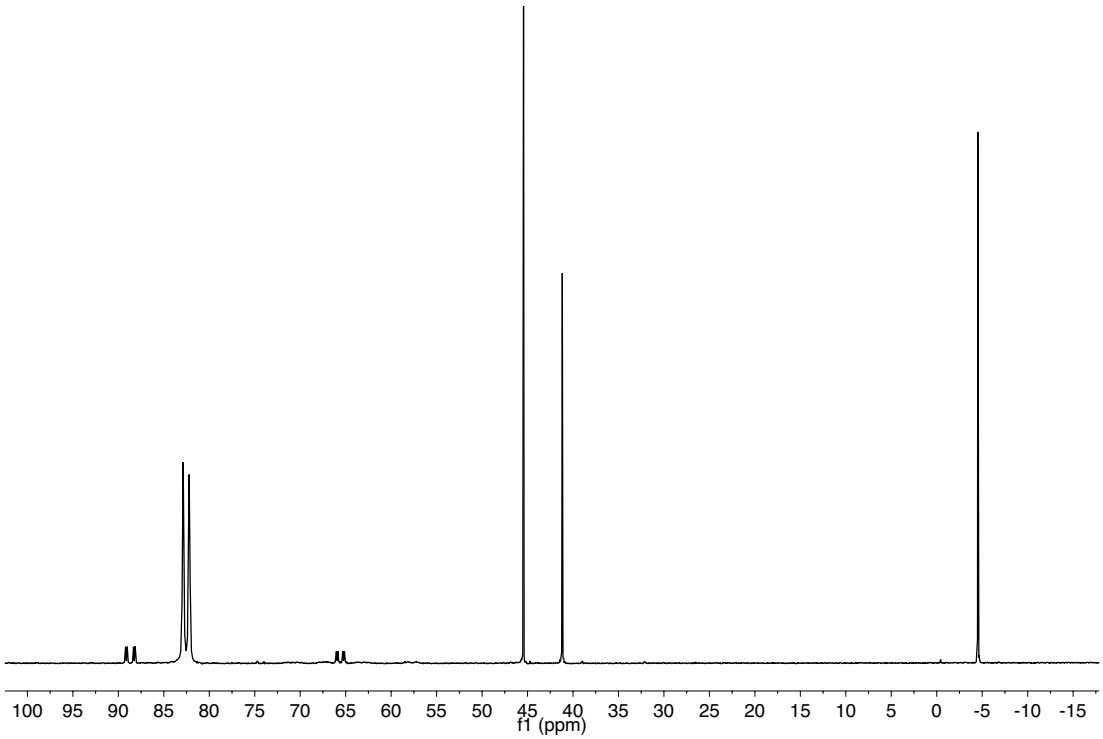

Figure A-13. $^{31}P\{^{1}H\}$ NMR spectrum of [Rh(H)($^{13}CO)_2$(BDP)] (202.5 MHz, CH_2Cl_2, -20 °C).

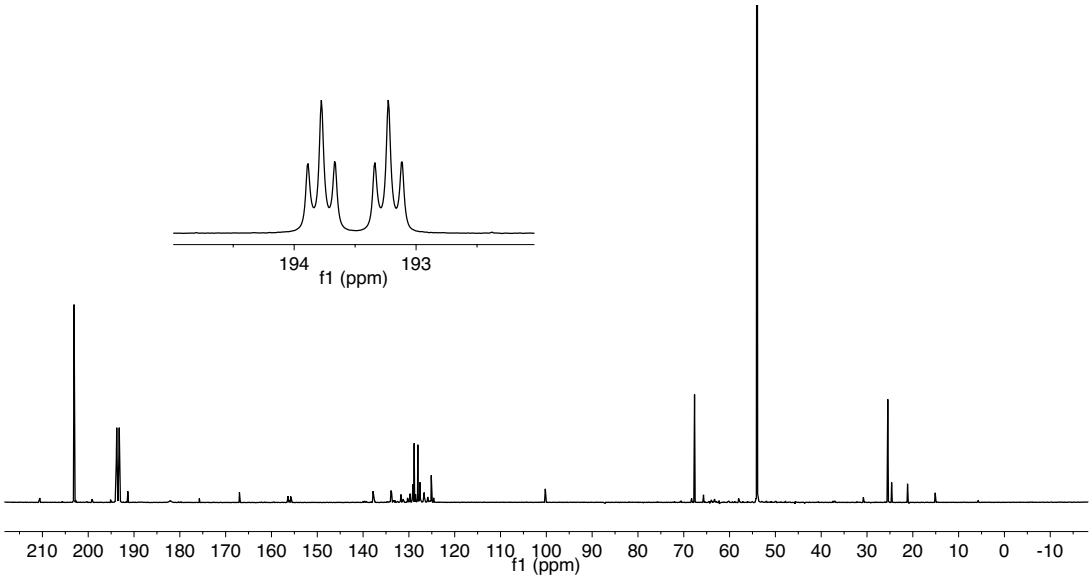

Figure A-14. $^{13}C\{1H\}$ NMR spectrum of [Rh(H)($^{13}CO)_2$(BDP)] (125.8 MHz, CH_2Cl_2, -20 °C). Inset shows terminal carbonyl resonances; $^2J_{CP} = \pm$ 14Hz.

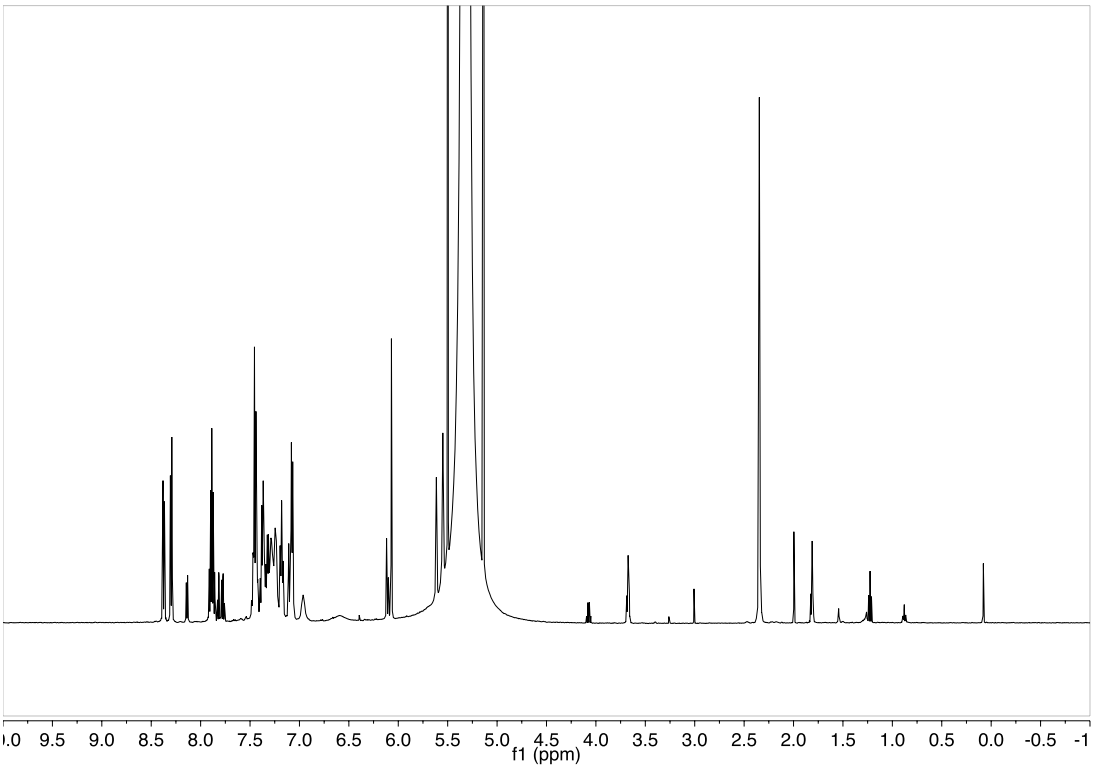

Figure A-15. ^1H NMR spectrum acquired after the reaction of $[Rh(COD)Cl]_2$ and BDP (500 MHz, CH_2Cl_2, 24 °C).

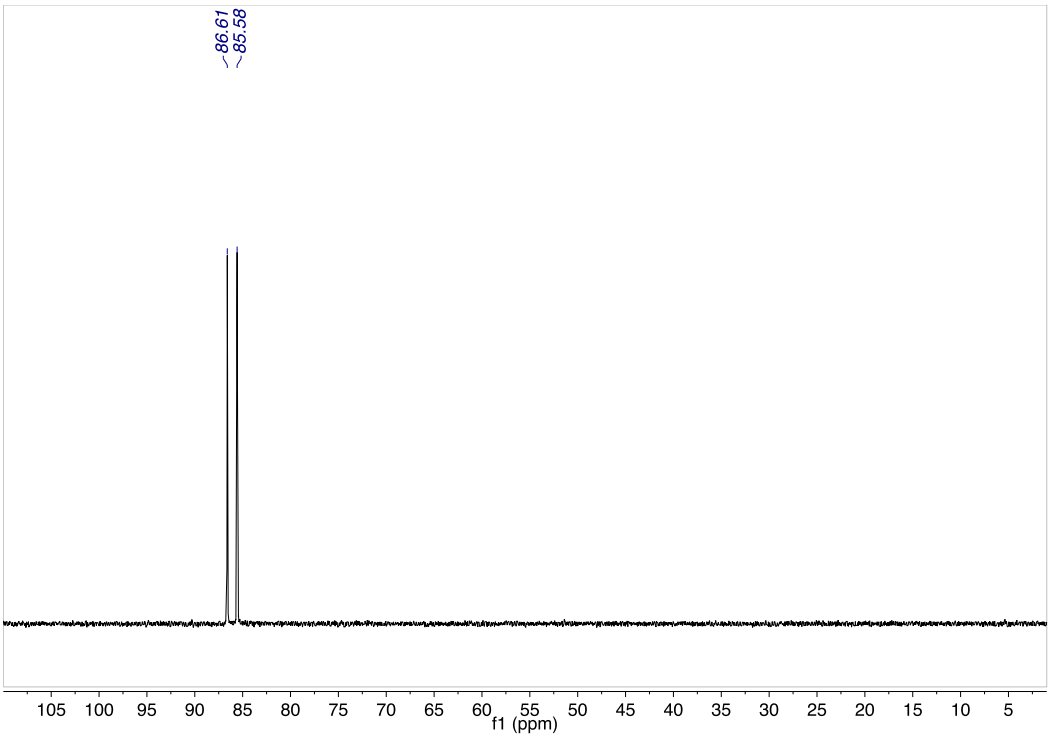

Figure A-16. $^{31}P\{1H\}$ NMR spectrum acquired after the reaction of $[Rh(COD)Cl]_2$ and BDP (202.5 MHz, CH_2Cl_2, 24 °C).

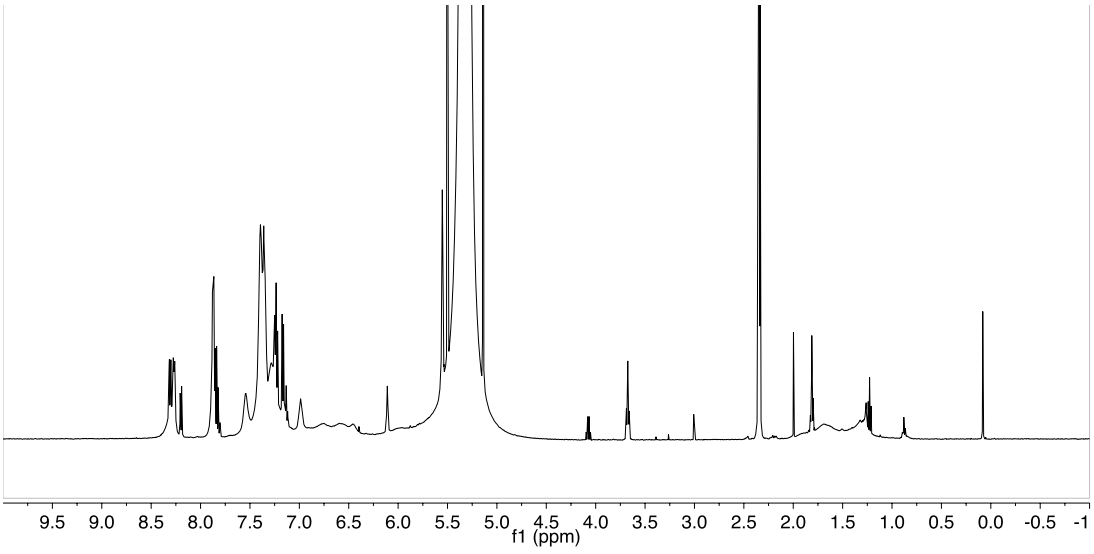

Figure A-17. ^{1}H NMR spectrum of a [Rh(OAc)] species acquired after the reaction of $[Rh(BDP)Cl]_2$ and silver acetate (500 MHz, CH_2Cl_2, 24 °C).

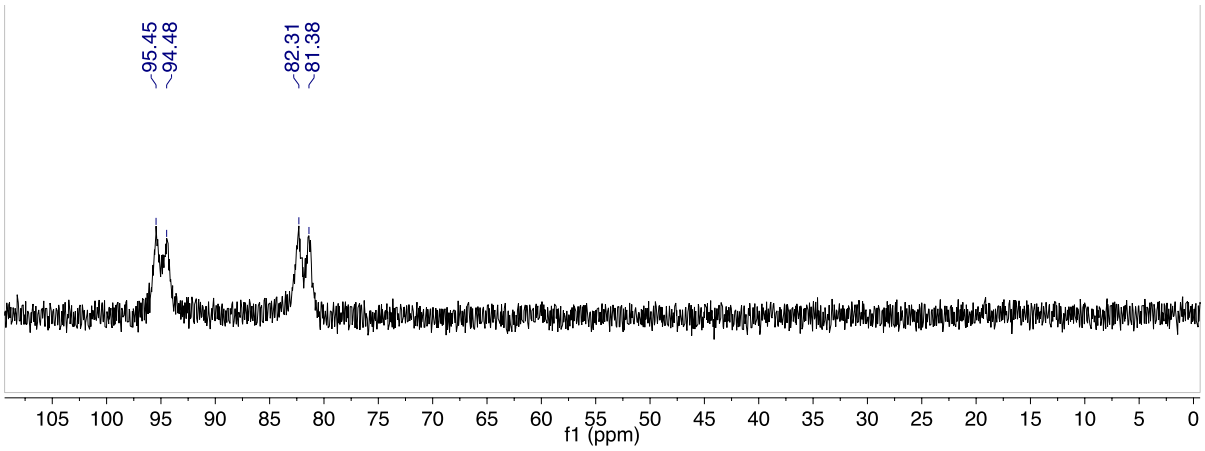

Figure A-18. $^{31}P\{1H\}$ NMR spectrum of a [Rh(OAc)] species acquired after the reaction of $[Rh(BDP)Cl]_2$ and silver acetate (202.5 MHz, CH_2Cl_2, 24 °C).

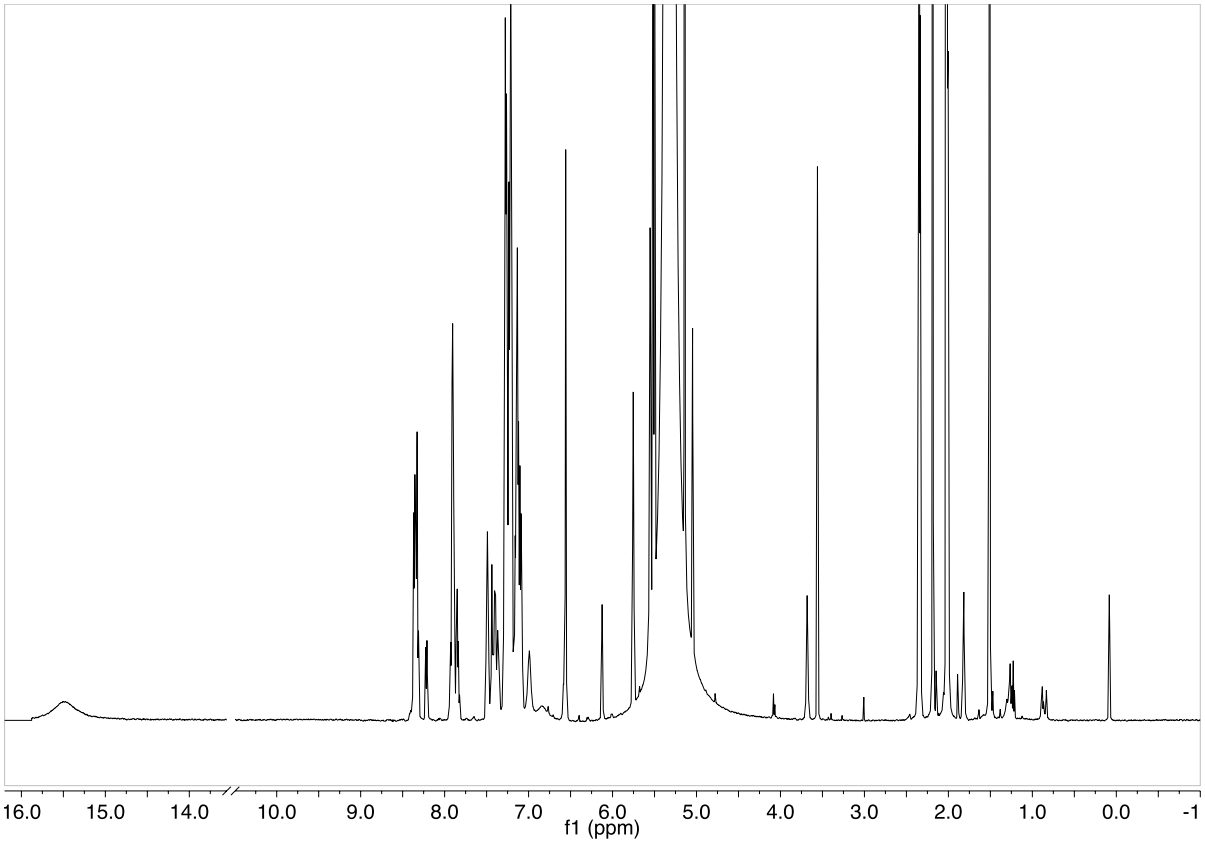

Figure A-19. ^{1}H NMR spectrum of [Rh(acac)(BDP)] acquired after the reaction of a [Rh(OAc)] species and acetylacetone (500 MHz, CH_2Cl_2, 24 °C).

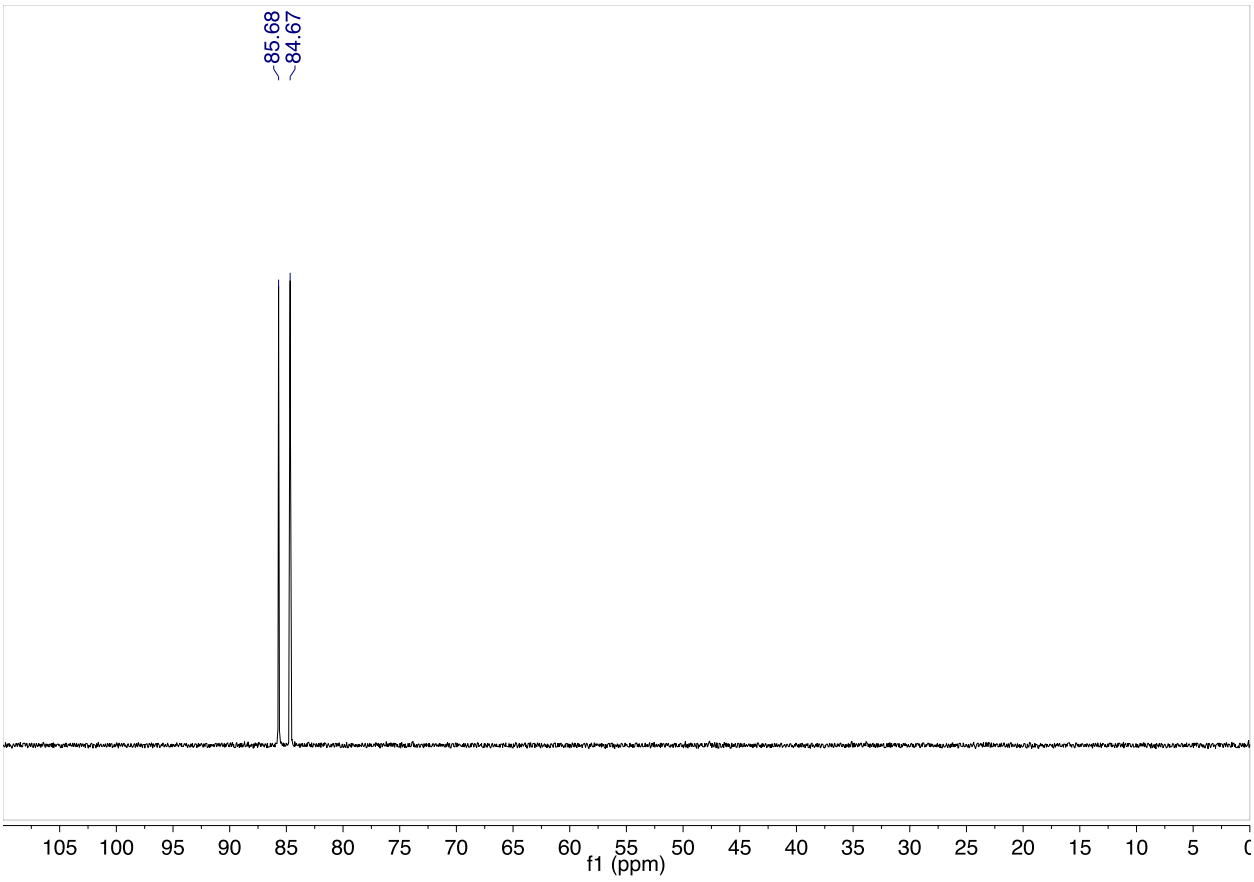

Figure A-20. $^{31}P\{1H\}$ NMR spectrum of [Rh(acac)(BDP)] acquired after the reaction of a [Rh(OAc)] species and acetylacetone (202.5 MHz, CH_2Cl_2, 24 °C).

A.1.2.2 Vinyl Acetate

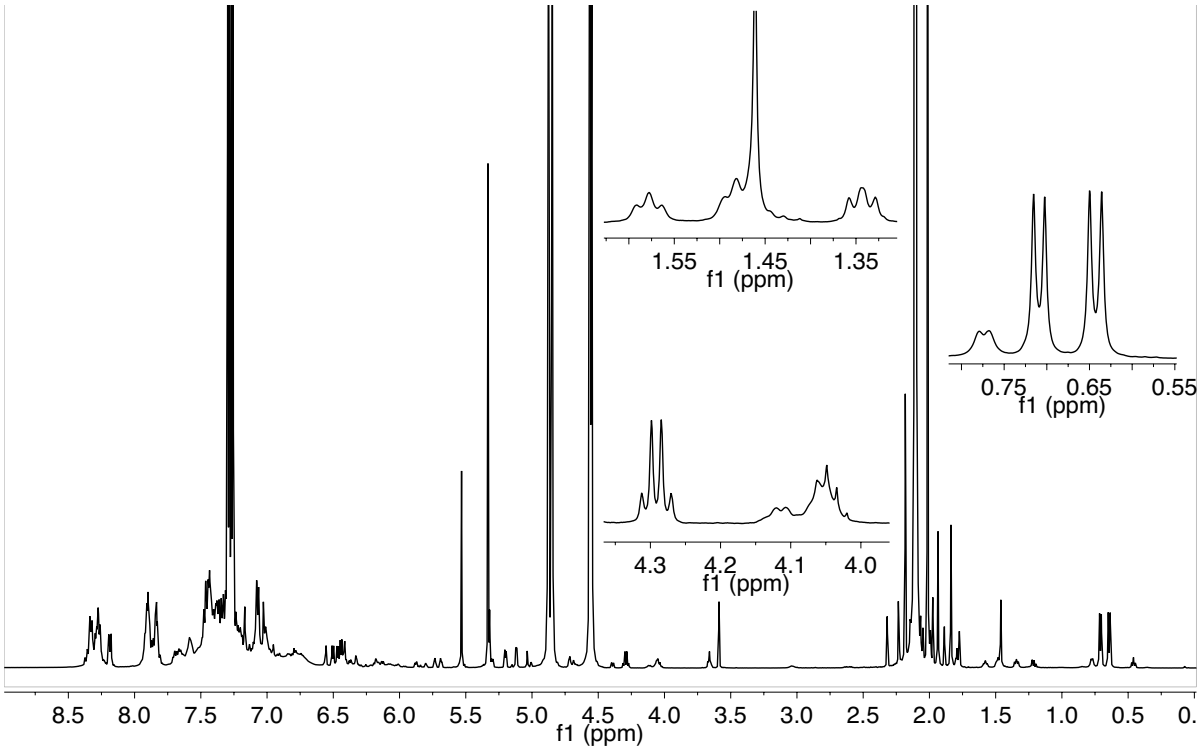

Figure A-21. ^{1}H NMR spectrum taken after the reaction of **1** with vinyl acetate. Insets show the methyl (right) and methine (center, lower) resonances of **7b,b'**$_{va}$ and methyl resonances (center, upper) of **4b**$_{va}$, **5b**$_{va}$ (500.22 MHz, -40 °C, CD_2Cl_2).

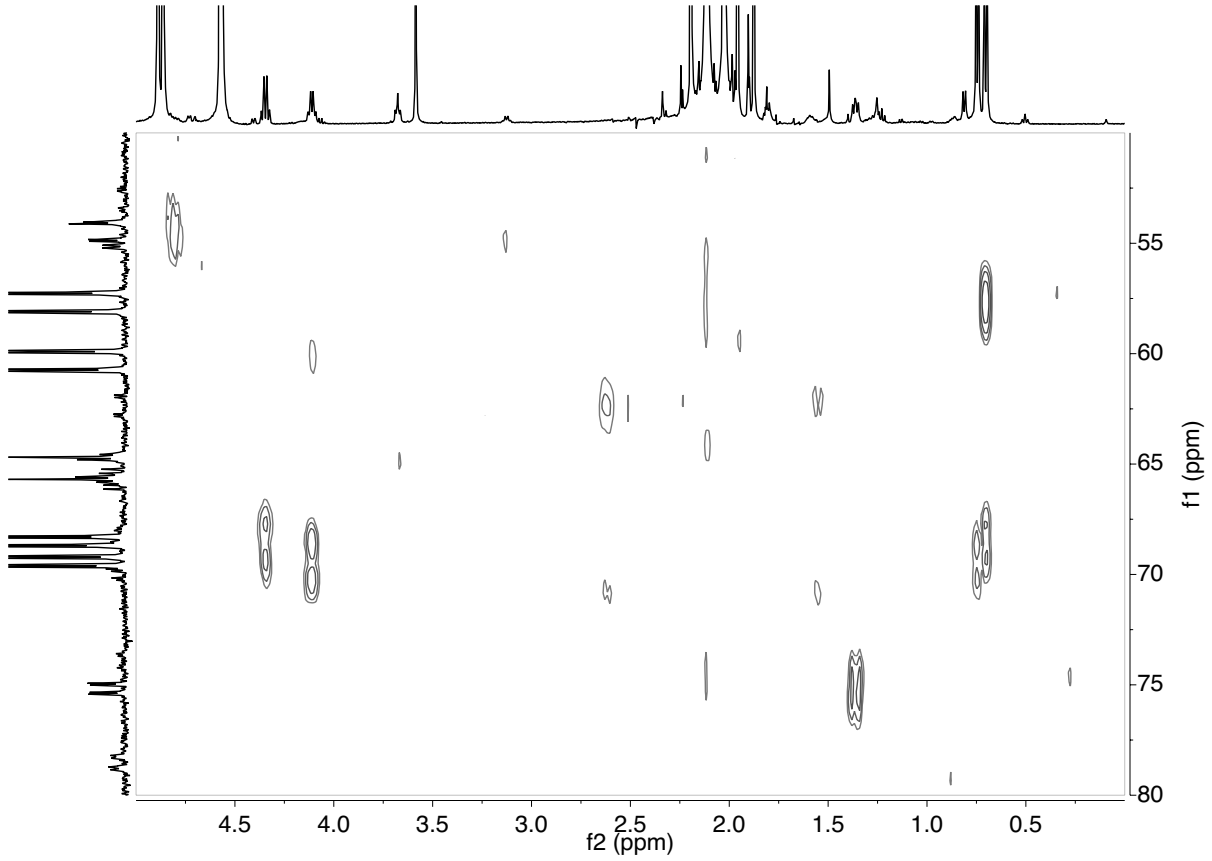

Figure A-22. ^{1}H-^{31}P gHMBC during the reaction of **1** with vinyl acetate (1 atm CO, 202.5 MHz, CO atmosphere, -10 °C; nt = 8, ni = 128, jnxh = 3.0 Hz, D1 = 3.0 sec).

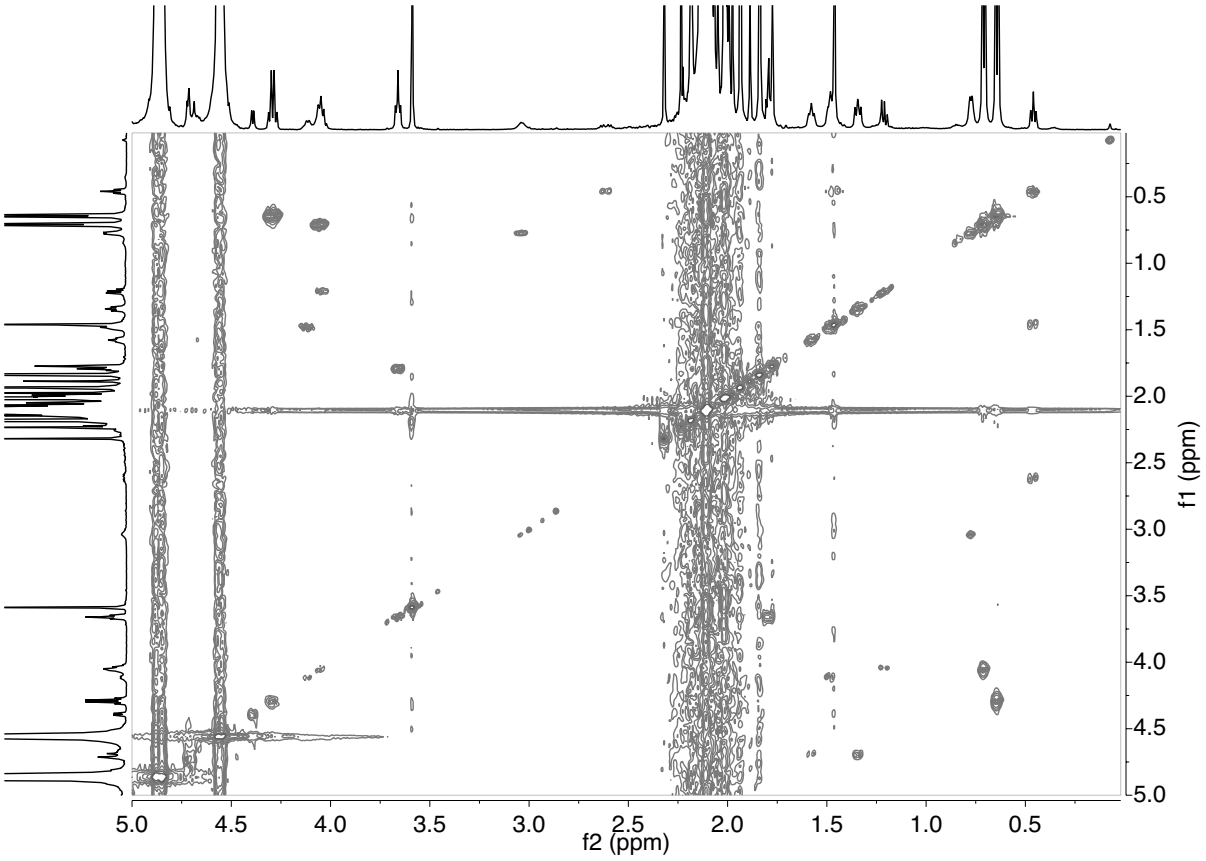

Figure A-23. ^{1}H-^{1}H gCOSY taken after the reaction of **1** with vinyl acetate. (500.2 MHz, CH_2Cl_2, -40 °C; nt = 2, ni = 256).

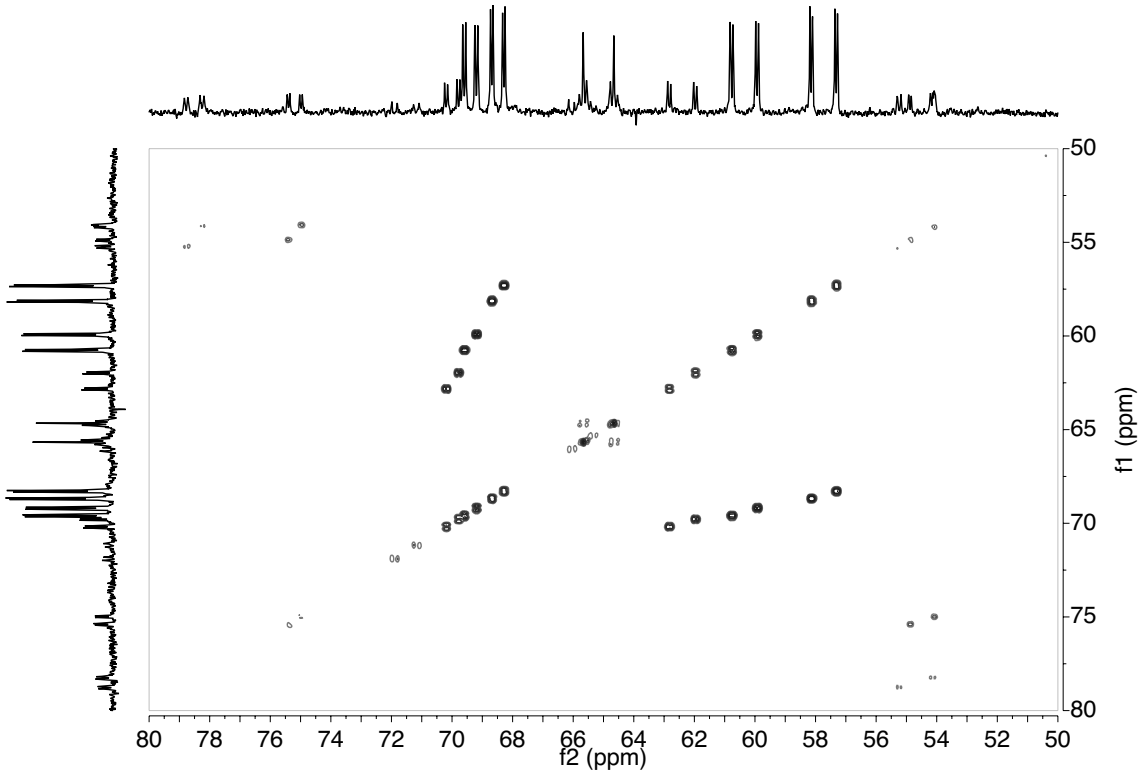

Figure A-24. ^{31}P-^{31}P gCOSY taken after the reaction of **1** with vinyl acetate (1 atm CO, 202.5 MHz, CH_2Cl_2, -10 °C; nt = 8, ni = 512).

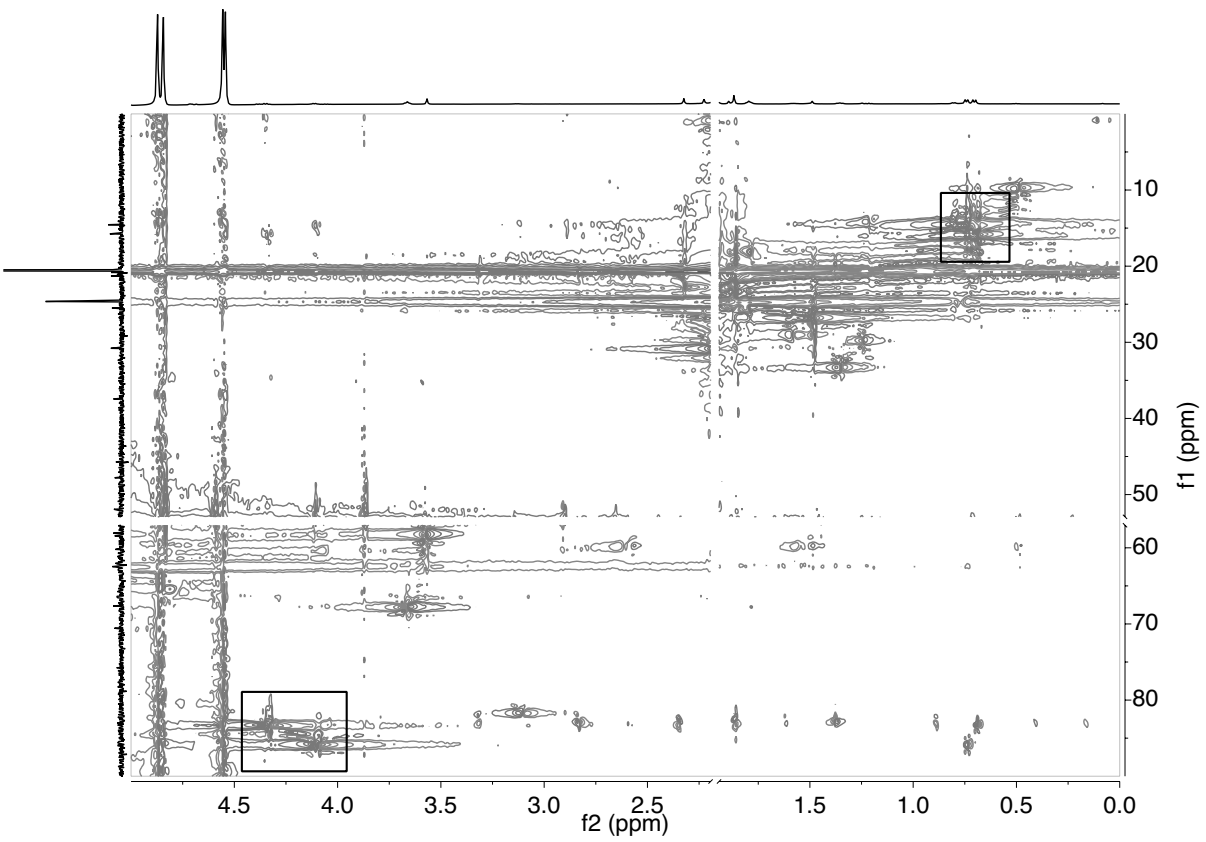

Figure A-25. ^{1}H-^{13}C HSQC taken following the reaction of **1** with vinyl acetate. Correlations for the methyl (upper right) and methine (lower left) groups indicated. ((f2, f1) = (500.22, 125.79 MHz), 1 atm CO, CH_2Cl_2, -20 °C).

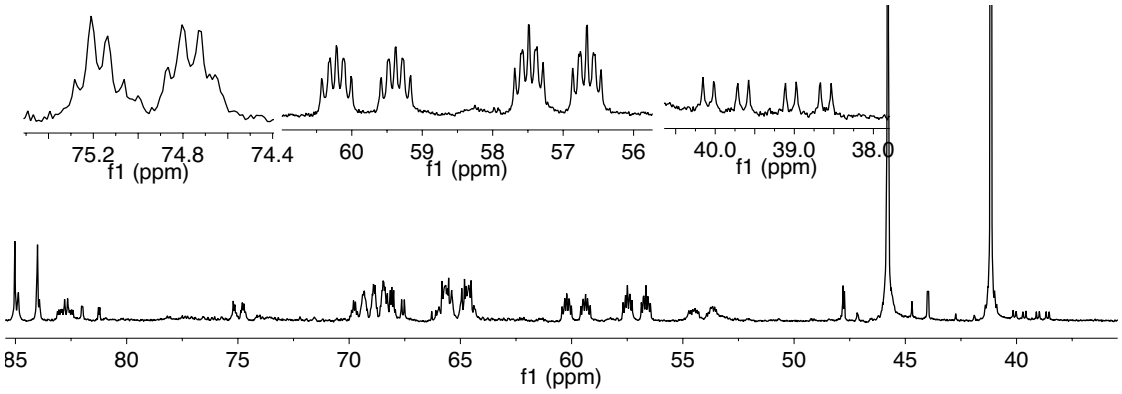

Figure A-26. $^{1}P\{^{1}H\}$ NMR spectrum taken following the reaction of $[Rh(H)(^{13}CO)_2(BDP)]$ with vinyl acetate. Insets show two new $^{2}J_{PC}$ for 5bva (left), three each for $\mathbf{7b_{va}}$ and $\mathbf{7b'_{va}}$ (center), and one for $\mathbf{4b_{va}}$ (right) (202.5 MHz, -40 °C, CD_2Cl_2).

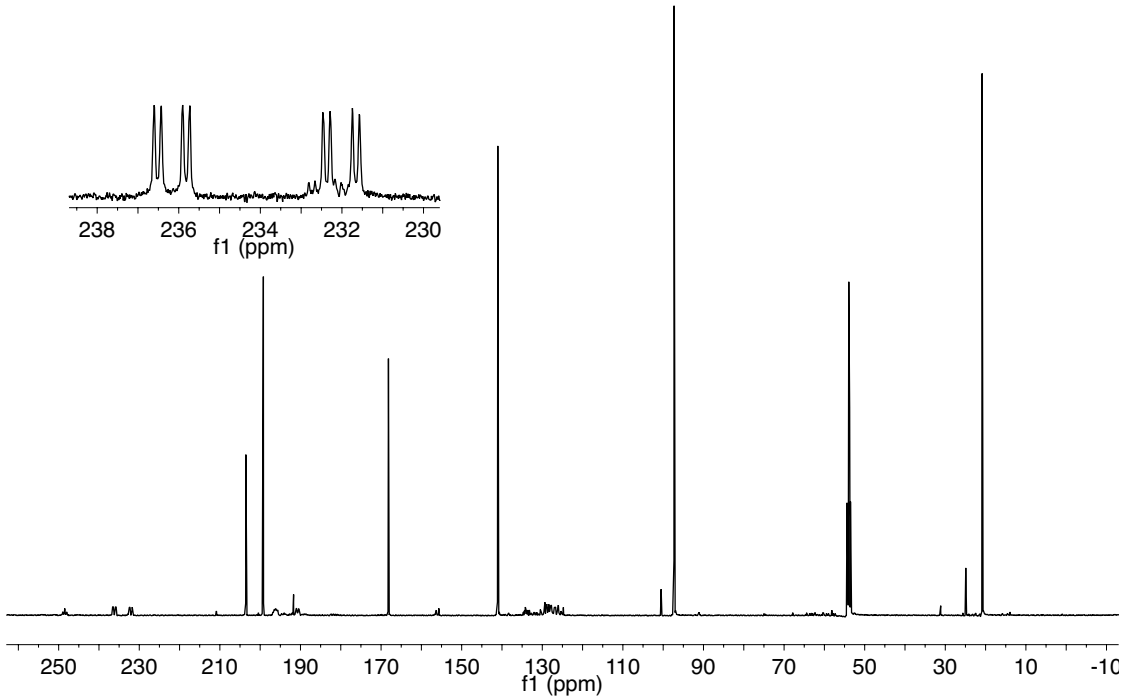

Figure A-27. $^{13}C\{^{1}H\}$ NMR spectrum taken following the reaction of $[Rh(H)(^{13}CO)_2(BDP)]$ with vinyl acetate. Inset shows acyl carbonyl resonances of (left to right) $\mathbf{7b'_{va}}$, $\mathbf{7l_{va}}$, $\mathbf{7b_{va}}$ (125.79 MHz, -40 °C, CD_2Cl_2).

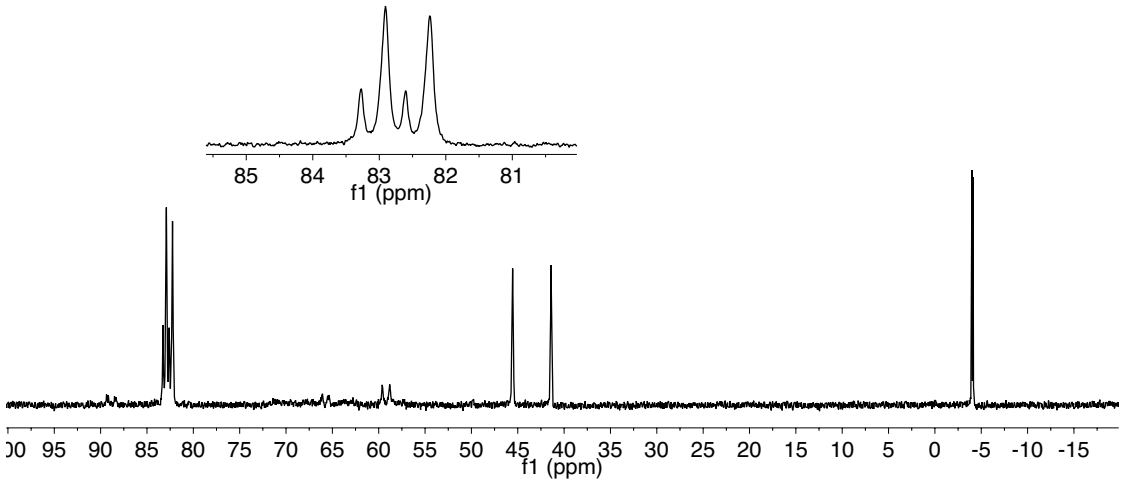

Figure A-28. $^{31}P\{^{1}H\}$ NMR spectrum of $[Rh(D)(CO)_2(BDP)]$. Inset shows that both the deuteride (upfield doublet) and hydride (downfield doublet) are present (202.5 MHz, -10 °C, CH_2Cl_2).

A.1.2.3 Allyl Cyanide

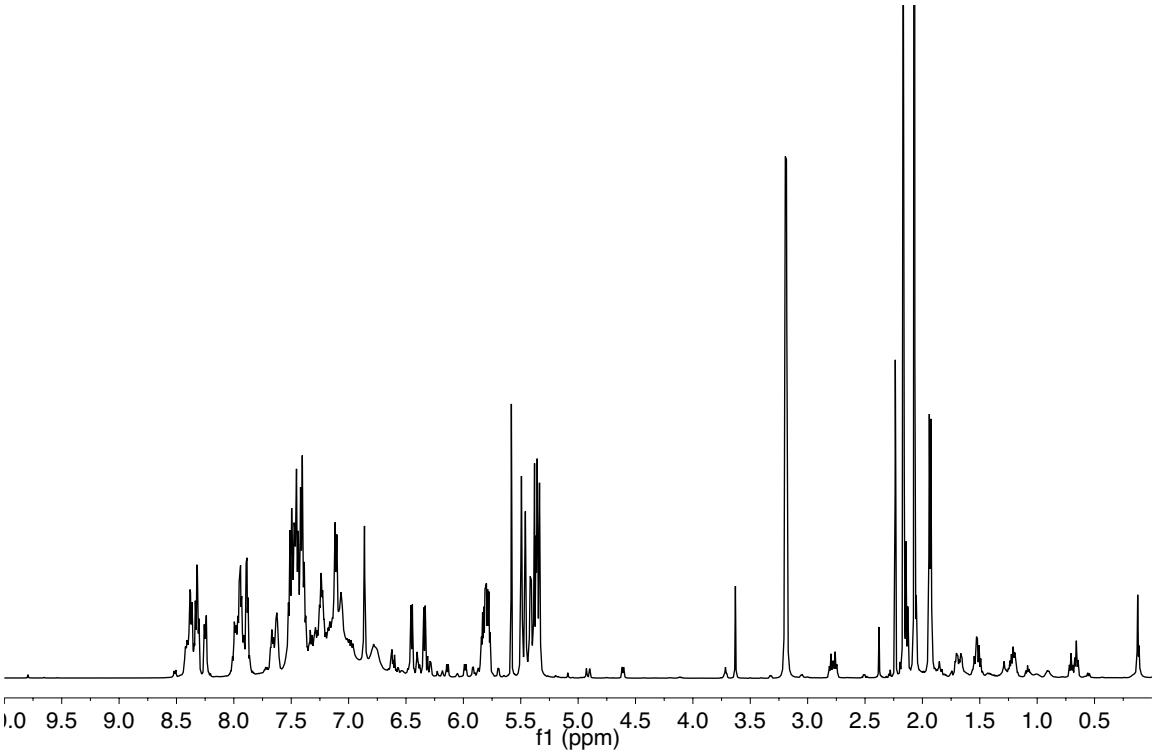

Figure A-29. ^{1}H NMR spectrum taken following the reaction of **1** with allyl cyanide (500.22 MHz, -20 °C, CD_2Cl_2).

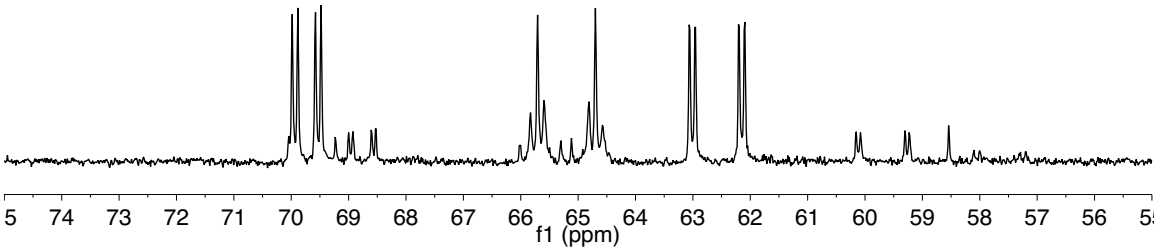

Figure A-30. $^{31}P\{^{1}H\}$ NMR spectrum taken during the reaction of **1** with allyl cyanide at -30 °C. The larger eight-line pattern is $\mathbf{7l_{ac}}$; the smaller is $\mathbf{7b_{ac}}$ (1 atm CO, 202.5 MHz, -30 °C, CD_2Cl_2).

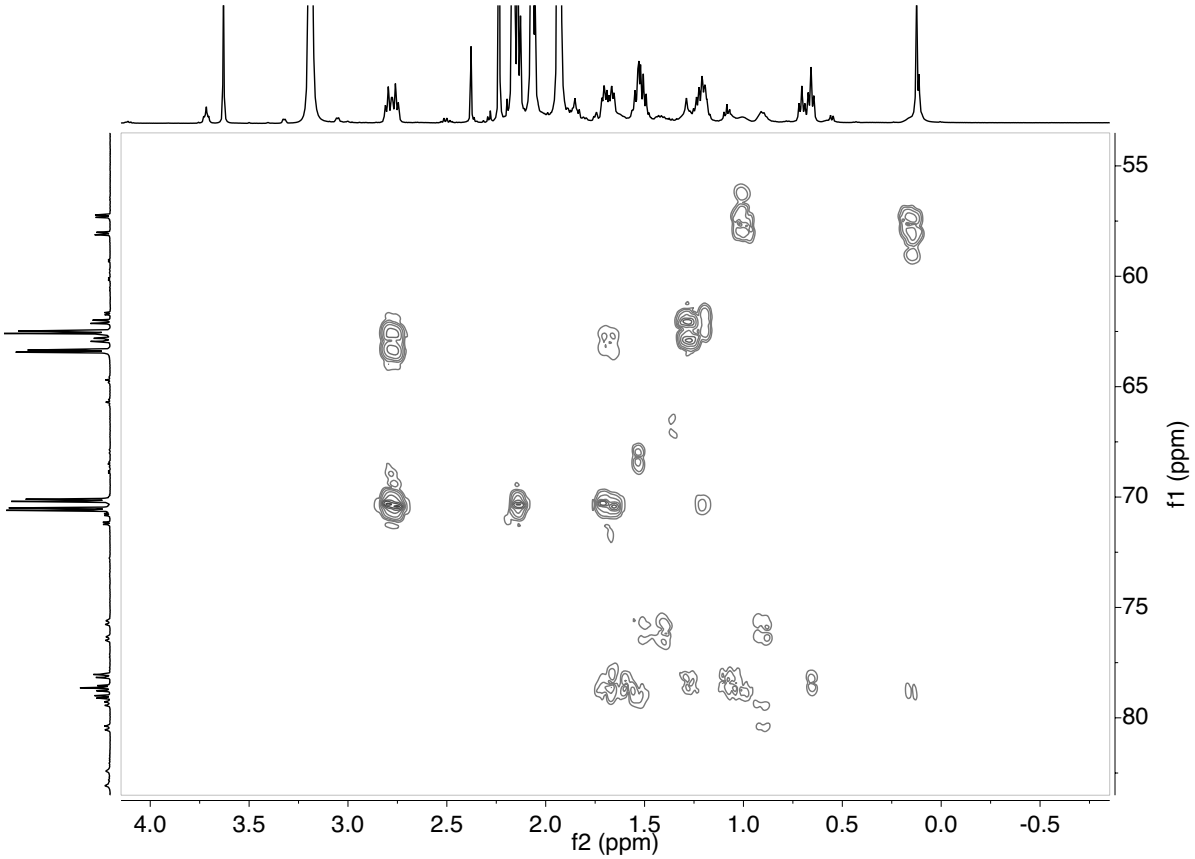

Figure A-31. ^{1}H-^{31}P gHMBC during the reaction of **1** with allyl cyanide (1 atm CO, (f2,f1) = 500.22, 202.5 MHz, -20 °C; nt = 8, ni = 256, jnxh = 3.0 Hz).

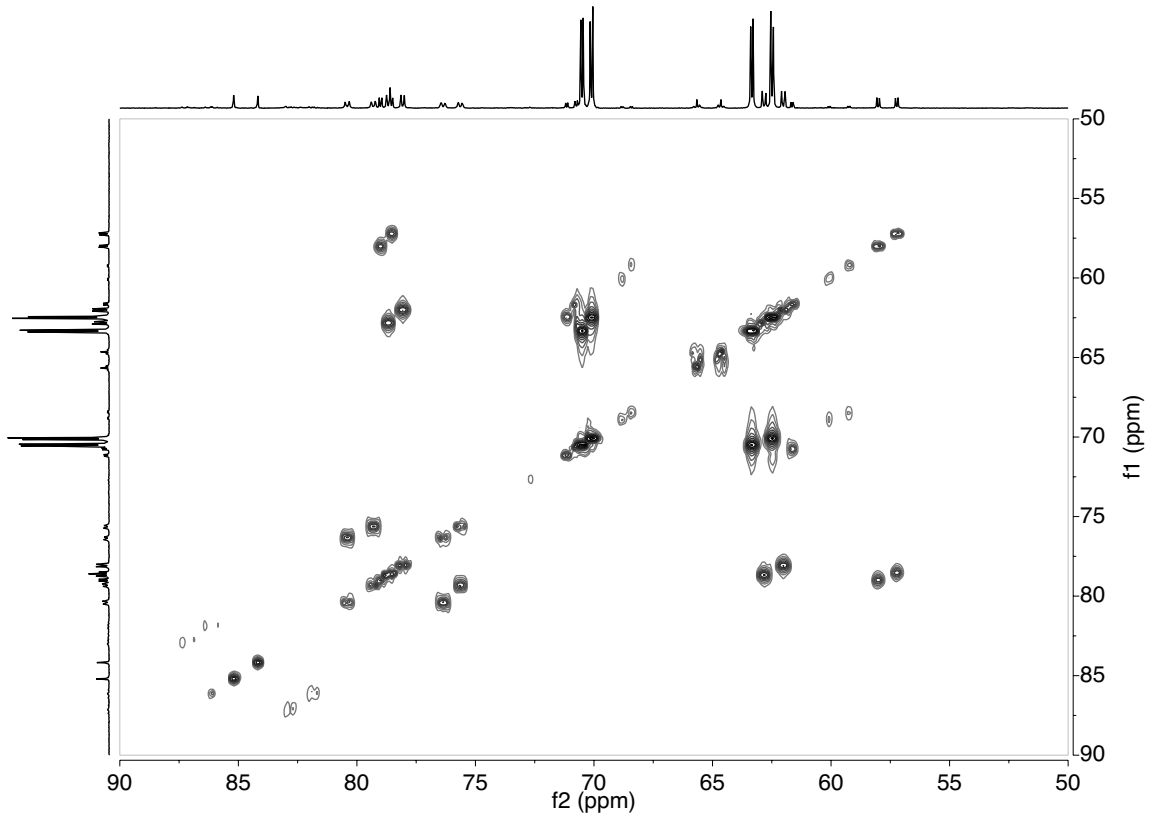

Figure A-32. ^{31}P-^{31}P gCOSY taken after the reaction of **1** with allyl cyanide (1 atm CO, 202.5 MHz, CH_2Cl_2, -20 °C; nt = 8, ni = 256).

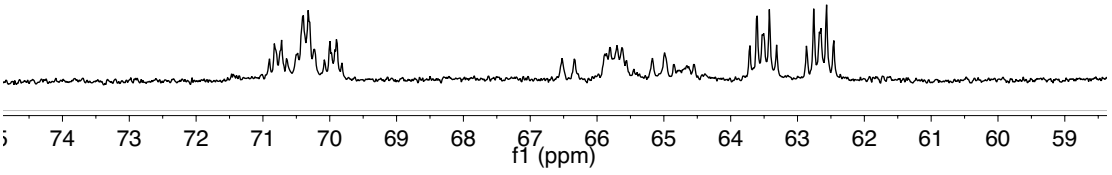

Figure A-33. $^{31}P\{^{1}H\}$ NMR spectrum taken following the reaction of [Rh(H)($^{13}CO)_2$(BDP)] with allyl cyanide. The axial (downfield) peak of **7l$_{ac}$** shows three new $^{2}J_{PC}$, indicating that **7l$_{ac}$** is an acyl dicarbonyl species (1 atm H_2, 202.5 MHz, -10 ° C, CD_2Cl_2).

A.1.2.4 Trans-1-phenyl-1,3-butadiene

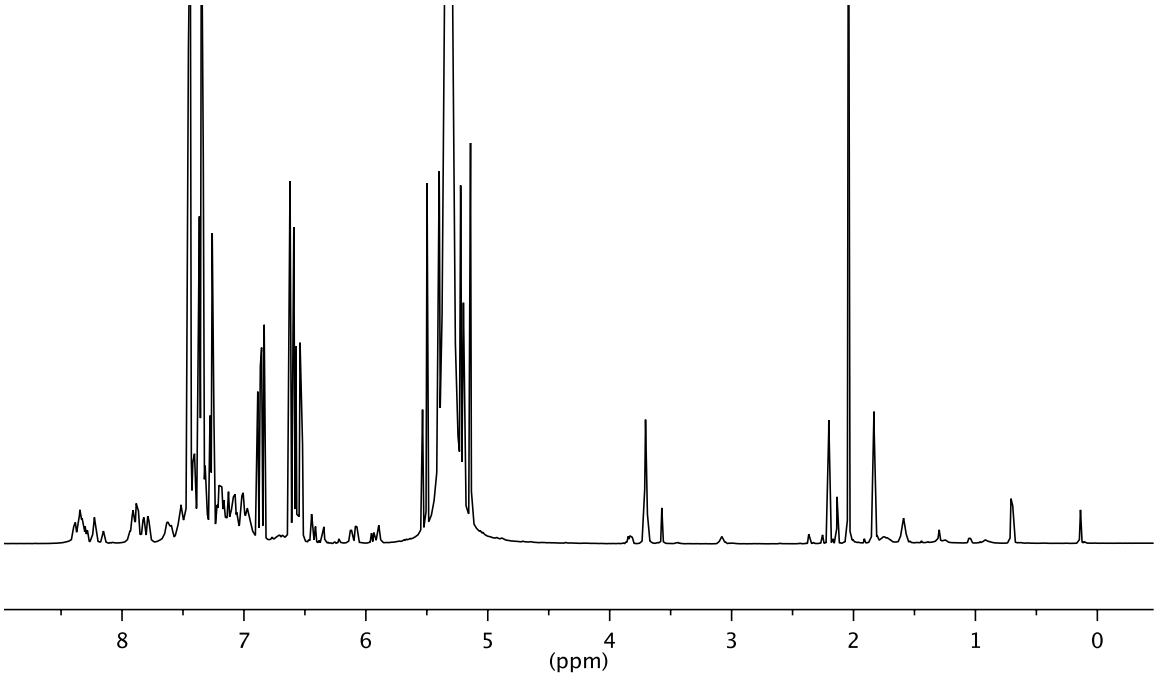

Figure A-34. ^{1}H NMR spectrum taken following the reaction of **1** with *trans*-1-phenyl-1,3-butadiene (500.22 MHz, 0 °C, CH_2Cl_2).

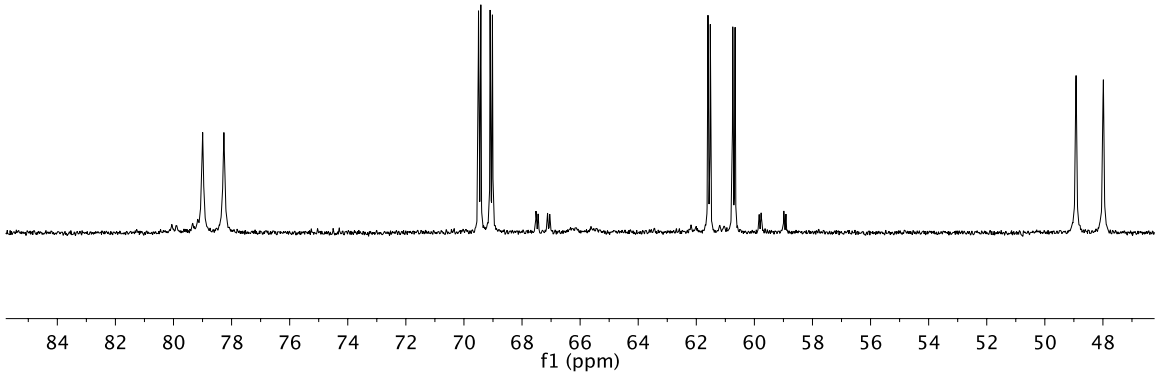

Figure A-35. $^{31}P\{^{1}H\}$ NMR spectrum taken following the reaction of **1** with *trans*-1-phenyl-1,3-butadiene at 0 °C. The larger eight-line pattern is $\mathbf{7b_{diene}}$; the smaller is $\mathbf{7b'_{diene}}$; the four-line pattern is $\mathbf{4b^{*}_{diene}}$. (1 atm CO, 202.5 MHz, 0 °C, CH_2Cl_2).

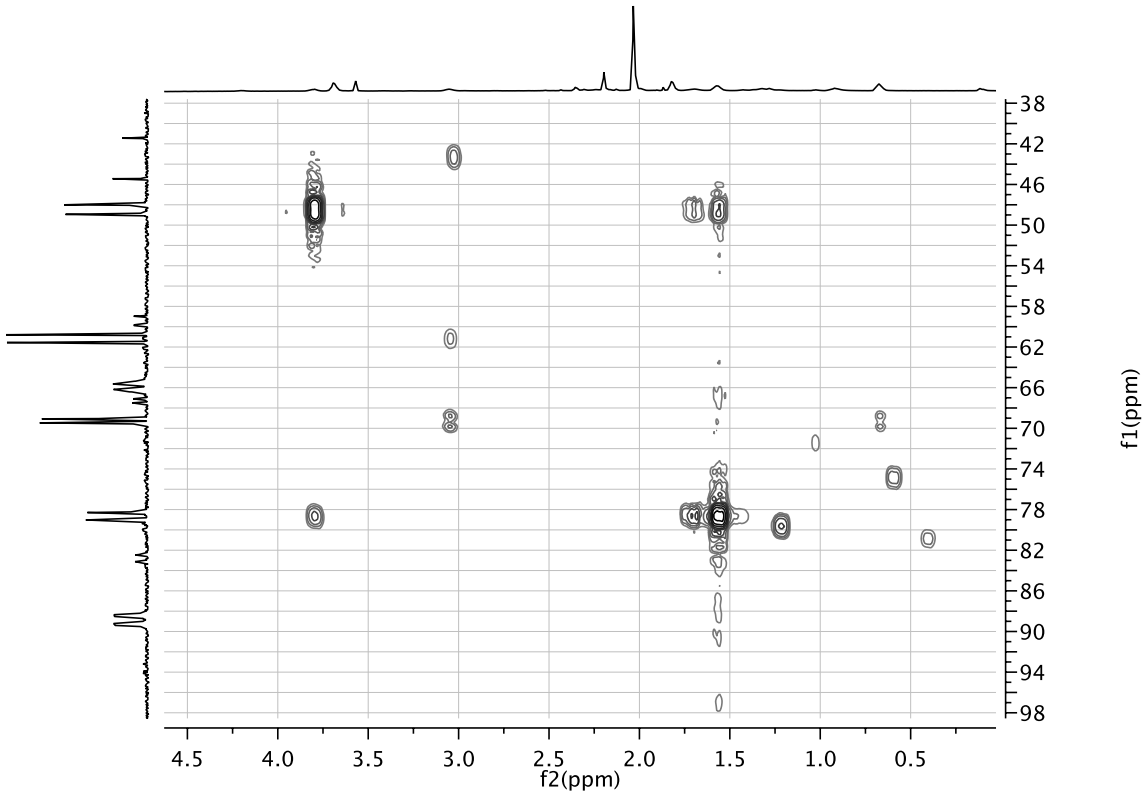

Figure A-36. ^{1}H-^{31}P gHMBC following the reaction of **1** with *trans*-1-phenyl-1,3-butadiene (1 atm CO, (f2,f1) = 500.22, 202.5 MHz; 0 °C; nt = 8, ni = 256, jnxh = 3.0 Hz).

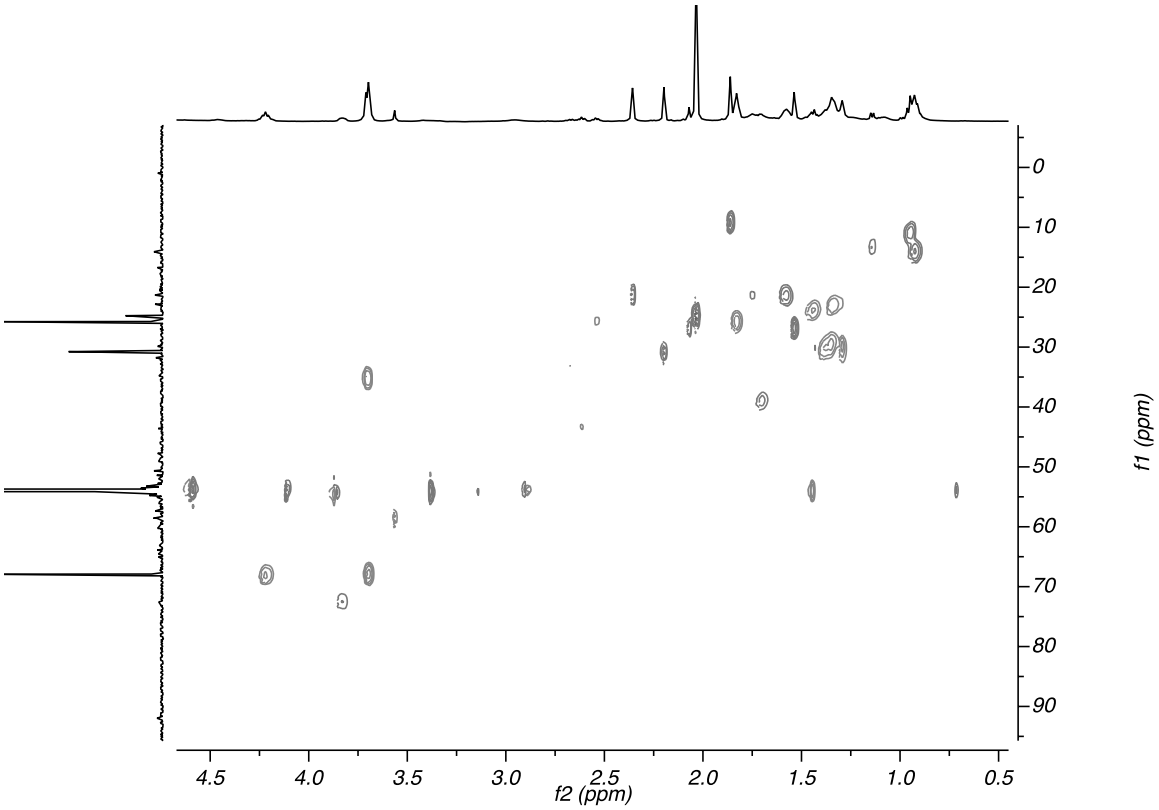

Figure A-37. ^{1}H-^{13}C gHSQC following the reaction of **1** with *trans*-1-phenyl-1,3-butadiene (1 atm CO, (f2,f1) = 500.02, 125.74 MHz; 0 °C; nt = 4, ni = 256).

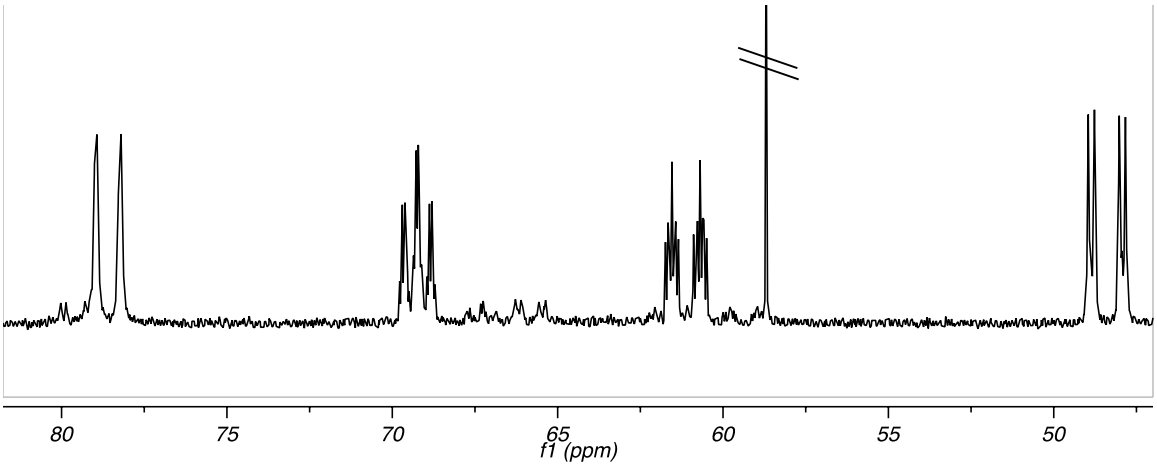

Figure A-38. $^{31}P\{^{1}H\}$ NMR spectrum taken following the reaction of $[Rh(H)(^{13}CO)_2(BDP)]$ with *trans*-1-phenyl-1,3-butadiene. (1 atm ^{13}CO, 202.5 MHz, 0 ° C, CH_2Cl_2).

A.1.2.5 1-Octene

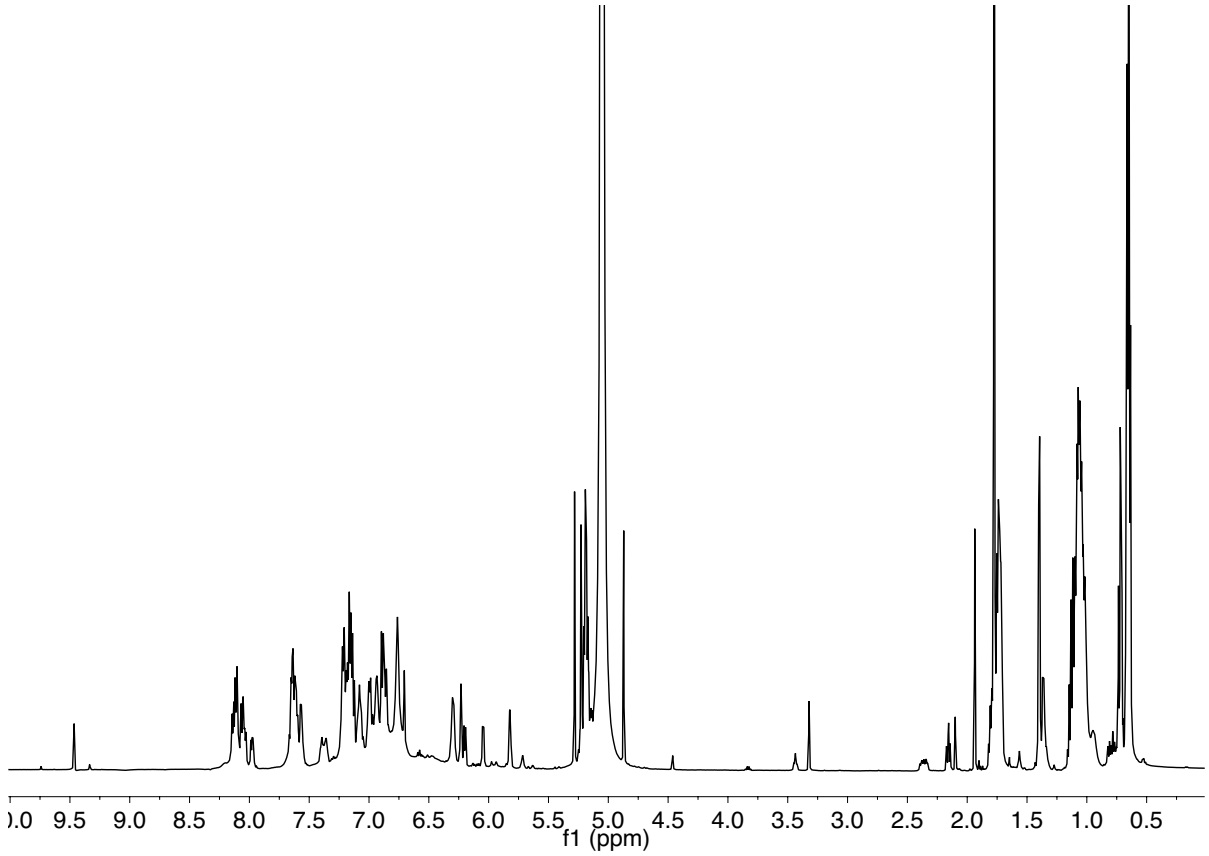

Figure A-39. ^{1}H NMR spectrum following the reaction of **1** with 1-octene (1 atm CO, 500.22 MHz, -10 °C, CH_2Cl_2).

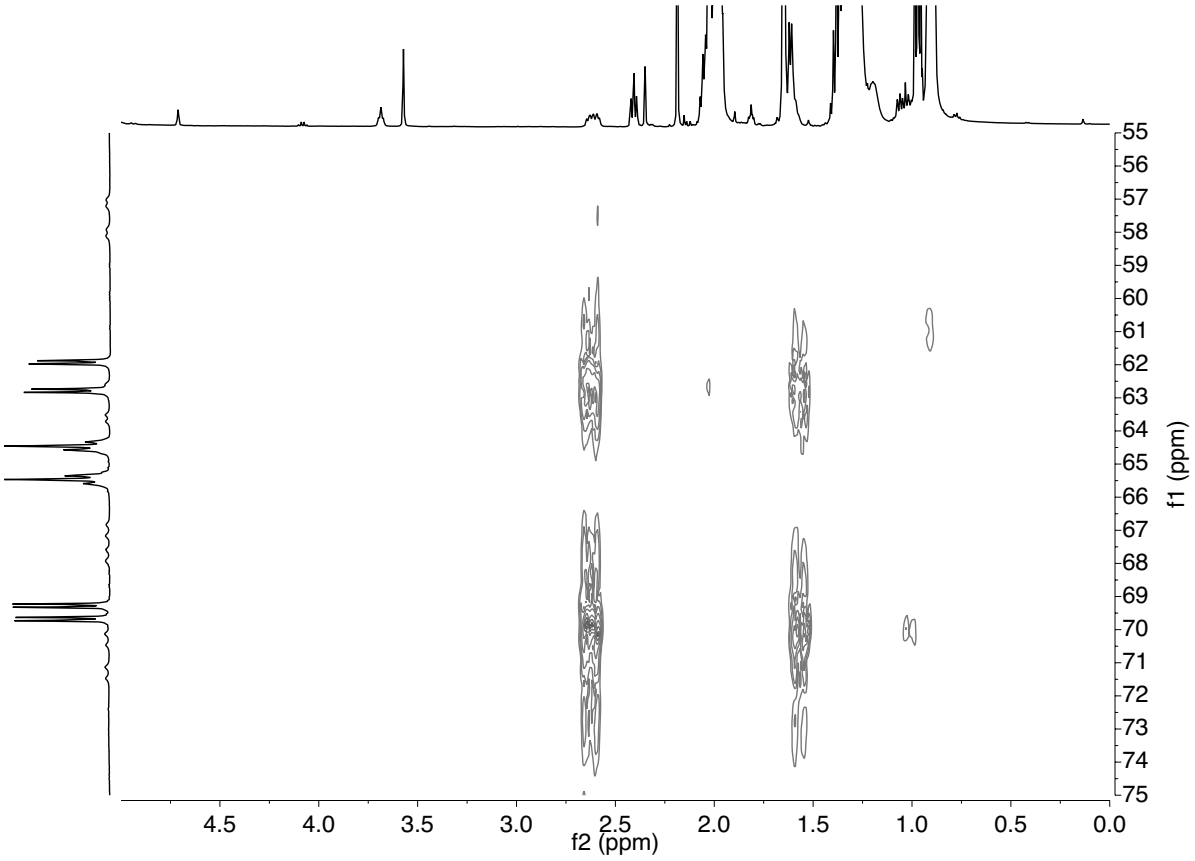

Figure A-40. ^{1}H-^{31}P gHMBC following the reaction of **1** with 1-octene (1 atm CO, (f2,f1) = 500.22, 202.5 MHz; -30 °C; nt = 16, ni = 256, jnxh = 3.0 Hz).

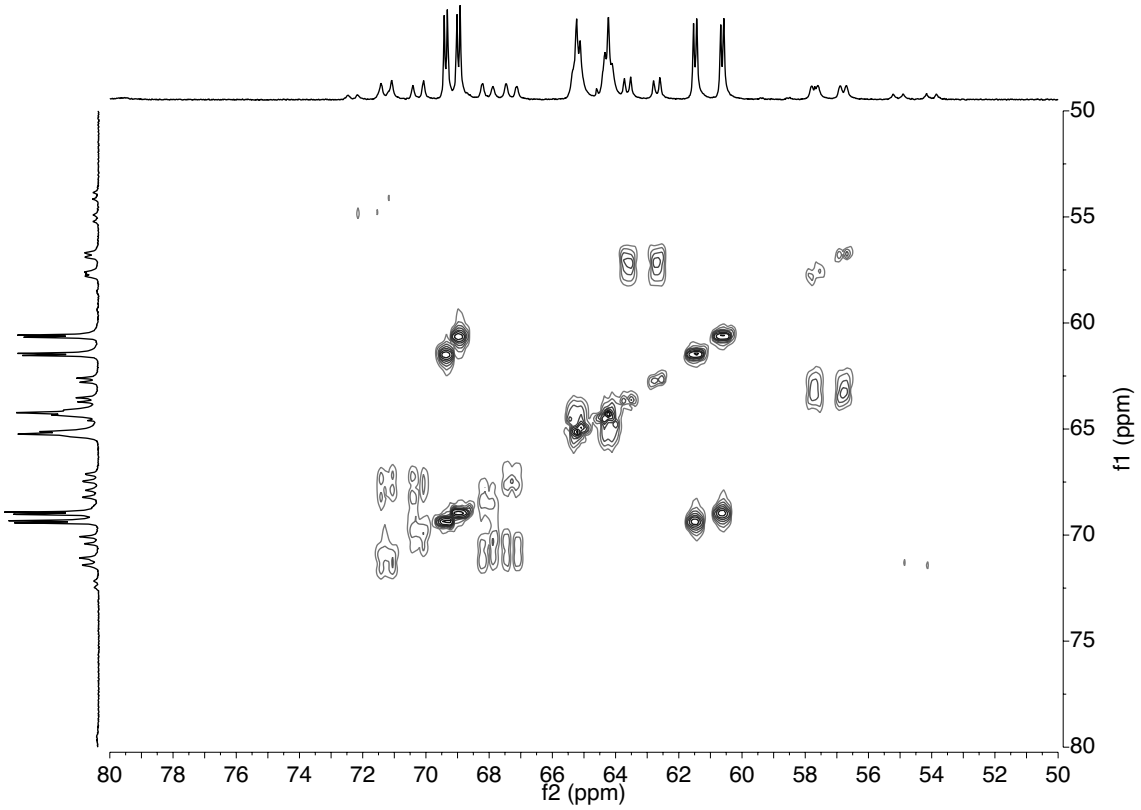

Figure A-41. ^{31}P-^{31}P gCOSY taken after the reaction of **1** with 1-octene (1 atm CO, 202.5 MHz, CH_2Cl_2, -80 °C; nt = 4, ni = 256).

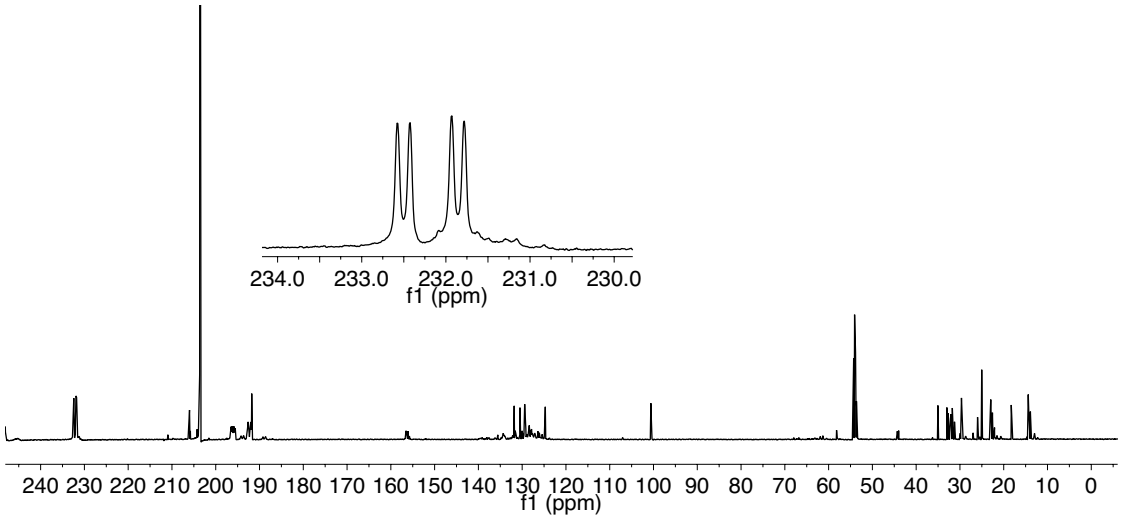

Figure A-42. $^{13}C\{^1H\}$ NMR spectrum taken after the reaction of [Rh(H)($^{13}CO)_2$(BDP)] with 1-octene; inset shows acyl carbonyl resonance of $\mathbf{7l_{oct}}$ (1 atm H_2, 125.79 MHz, -40 °C, CD_2Cl_2).

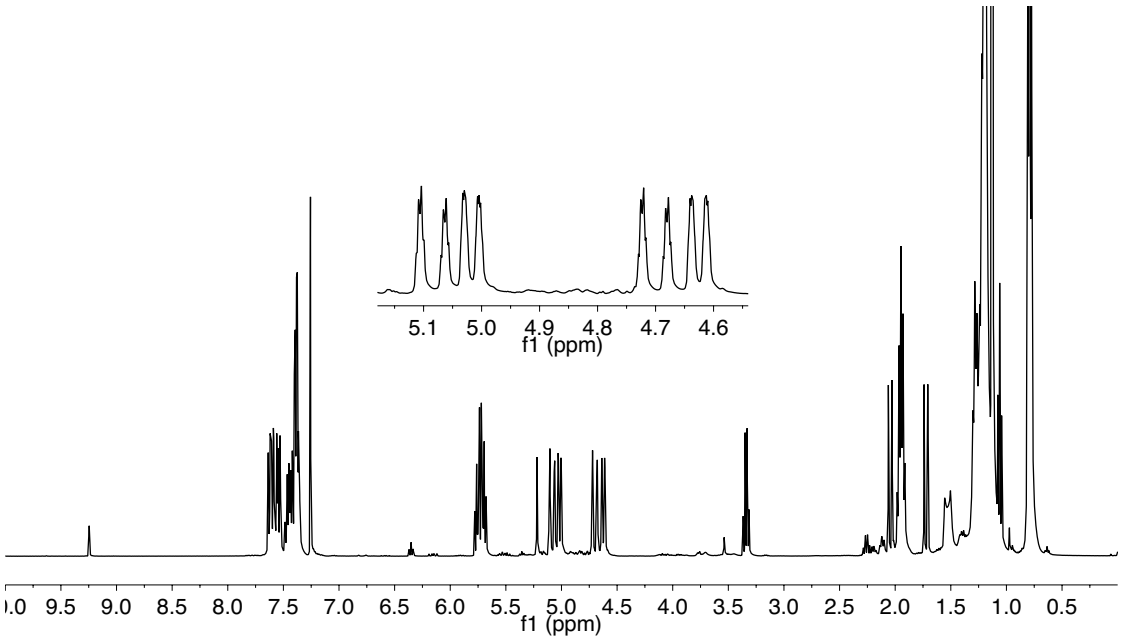

Figure A-43. ^{1}H NMR spectrum of 1-^{13}C-octene; inset shows overlapping *dddt* for terminal alkene protons (400 MHz, 24 °C, $CDCl_3$).

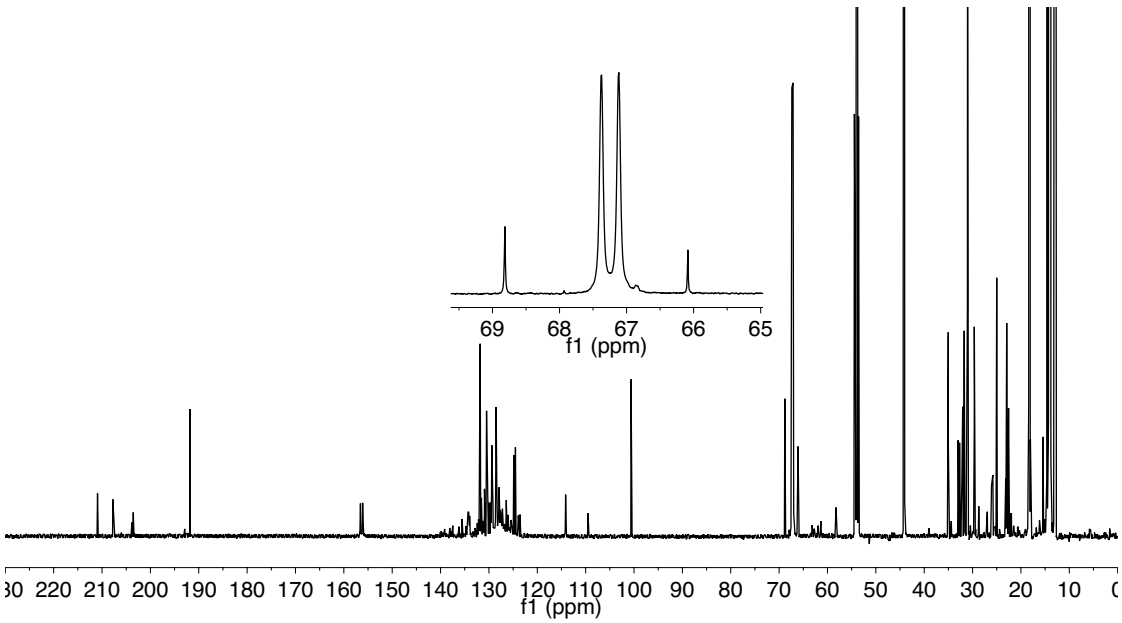

Figure A-44. ^{13}C NMR spectrum taken following the reaction of **1** with 1-13C-octene. Inset shows labeled methylene carbon of **7loct** (1 atm CO, 125.79 MHz, -40 °C, CD_2Cl_2).

A.1.3 COPASI Modeling

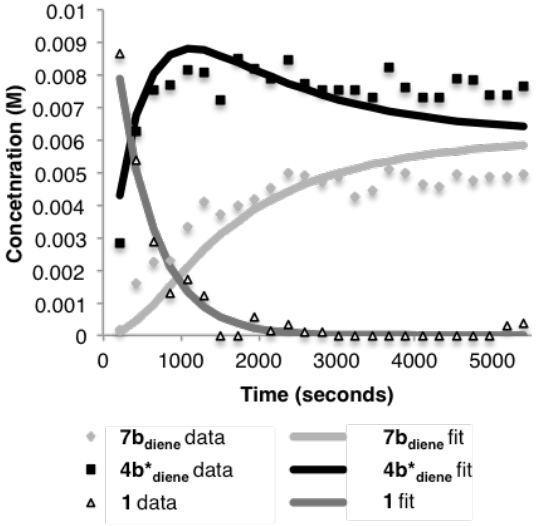

	Value	Standard Deviation
k_1	$2.06\times10^{-3}\ M^{-1}s^{-1}$	6.8×10^{-5}
k_{-1}	$2.22\times10^{-16}\ M^{-1}s^{-1}$	3.4×10^{-4}
k_2	$9.26\times10^{-1}\ M^{-2}\ s^{-1}$	8.1×10^{-2}
k_{-2}	$1.23\times10^{-2}\ s^{-1}$	2.0×10^{-4}

Figure A-45. Data and fit when 20 psia CO entered into the COPASI model (left). Rate constants and standard deviations computed for the left plot (right).

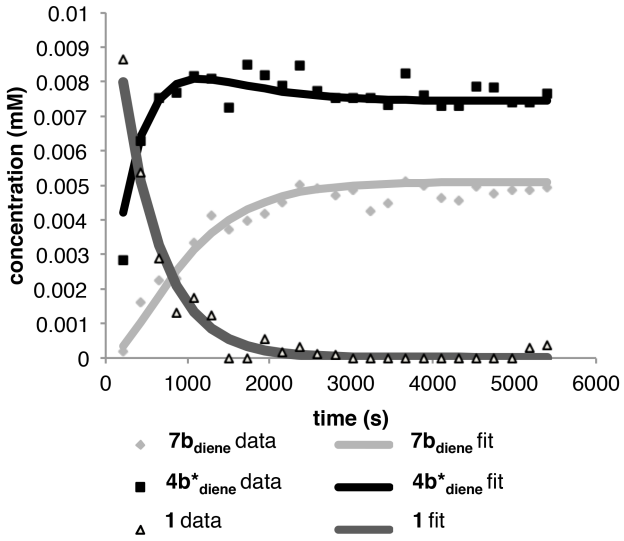

	Value	Standard Deviation
k_1	$2.09\times10^{-3}\ M^{-1}s^{-1}$	6×10^{-5}
k_{-1}	$1.8\times10^{-15}\ M^{-1}s^{-1}$	1×10^{-3}
k_2	$7.3\ M^{-2}\ s^{-1}$	7×10^{-1}
k_{-2}	$1.1\times10^{-3}\ s^{-1}$	1×10^{-4}

Figure A-46. Data and fit when 17 psia CO entered into the COPASI model (left). Rate constants and standard deviations computed for the left plot with reversible formation of **4b*$_{diene}$** (right).

A.2 Chapter 4: Unexpected CO Dependenices, Catalyst Speciation, and Single Turnover Hydrogenolysis Studies of Hydroformylation *via* High Pressure NMR Spectroscopy

A.2.1 Additional Time Course and Catalytic Data

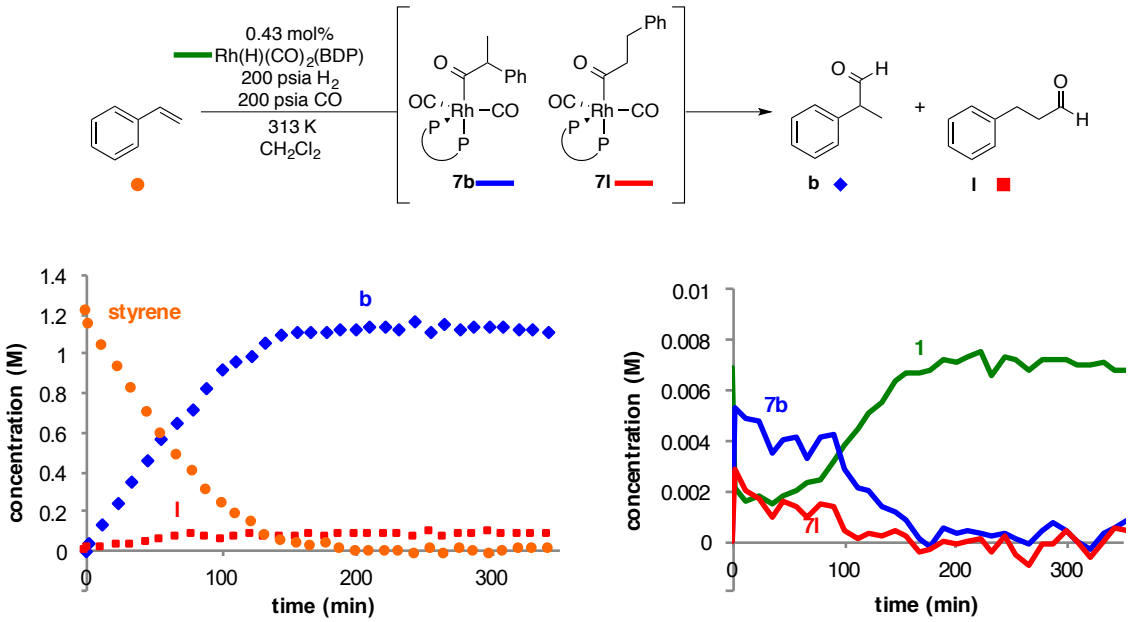

Figure A-47. Catalytic time course collected using the Wisconsin High Pressure NMR reactor (WiHP-NMRR) (1.3 M styrene, 6 mM $Rh(H)(CO)_2(BDP)$, 313 K, 200 psia H_2 and 200 psia CO. Rate approximately four times faster than reaction at 20 psia H_2 (Figure 2) due to higher concentration dihydrogen. Rate not first order in $[H_2]$ due to a change in resting state between these reactions.

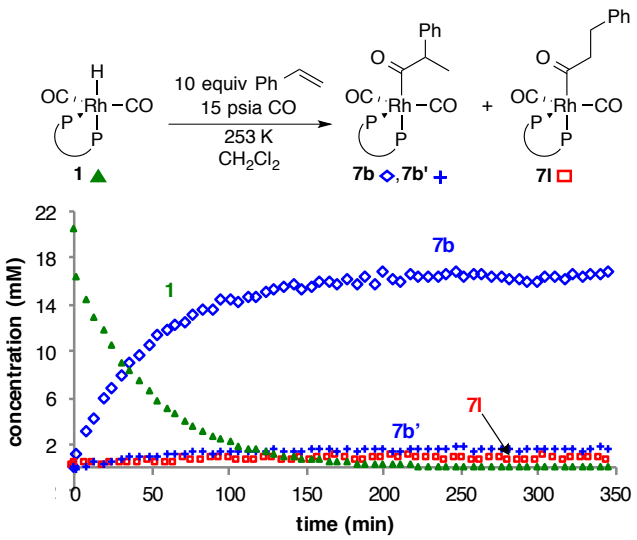

Figure A-48. Reaction of 1 with styrene leads to primarily the branched acyl dicarbonyl (7b:7l = 95:5) (253 K, 15 psia CO, 21 mM 1, 210 mM styrene, CH_2Cl_2). Because no isomerization is observed after 7 hours, this is interpreted as the intrinsic kinetic selectivity of the acyl dicarbonyls.

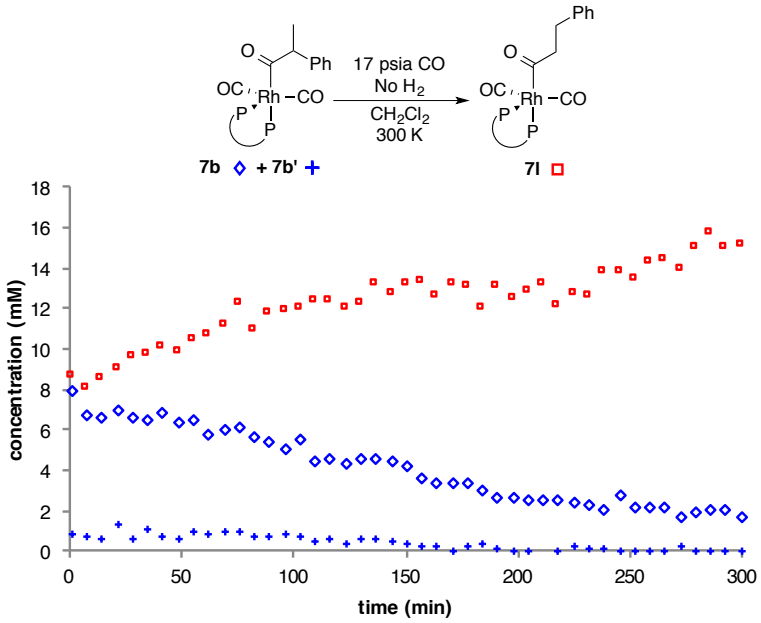

Figure A-49. A 1:1 mixture of acyl dicarbonyls isomerize to the thermodynamically favored species at warmer temperatures (300 K, 17 psia CO, 8 mM **7l**, 8 mM **7b**, 1 mM **7b'**, CH_2Cl_2).

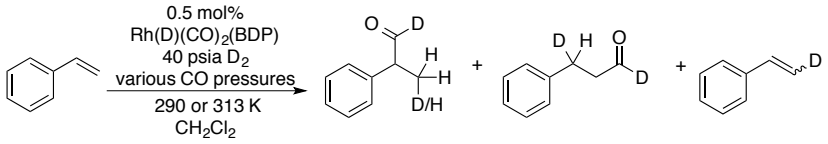

Temperatue (K)	Pressure CO (psia)	Aldehydes : Deuterated alkenes
290	40	1.5 : 1
290	80	6.3 : 1
313	40	0.75 : 1
313	80	4.2 : 1

Table A-1. Deuteroformylation of Styrene.

Reaction	Steady state range	Catalyst concentrations	[7b] : [7l]
Figure A-50	0 to 300 min	$[\mathbf{7l}]_{ss}$ = 4.4(4) mM $[\mathbf{7b}]_{ss}$ = 0.1(3) mM ≈ 0 mM	<1 : 10
Figure A-51	0 to 100 min	$[\mathbf{7l}]_{ss}$ = 1.4(3) mM $[\mathbf{7b}]_{ss}$ = 3.8 (3) mM	2.7(6) : 1
Figure A-52	0 to 300 min	$[\mathbf{7l}]_{ss}$ = 1.6(4) mM $[\mathbf{7b}]_{ss}$ = 4.6(5) mM	2.9(8) : 1
Figure A-53	0 to 3600 s	$[\mathbf{1}]_{ss}$ = 10.3(9) mM	--
Figure A-54	0 to 1300 s	$[\mathbf{7l}]_{ss}$ = 1.36(6) mM $[\mathbf{7b}]_{ss}$ = 4.8(5) mM	3.5(4) : 1
Figure A-55	0 to 30000 s	$[\mathbf{1}]_{ss}$ = 9.0(9) mM	--
Figure A-56	6000 to 23000 s	$[\mathbf{7l}]_{ss}$ = 0.2(7) mM ≈ 0 mM $[\mathbf{7b}]_{ss}$ = 6.2(7) mM	>6 : 1

Table A-2. Steady state catalyst concentrations and computed errors for catalytic reactions over the give time period encompassing the steady-state region.

A.2.2 Selected NMR Spectra

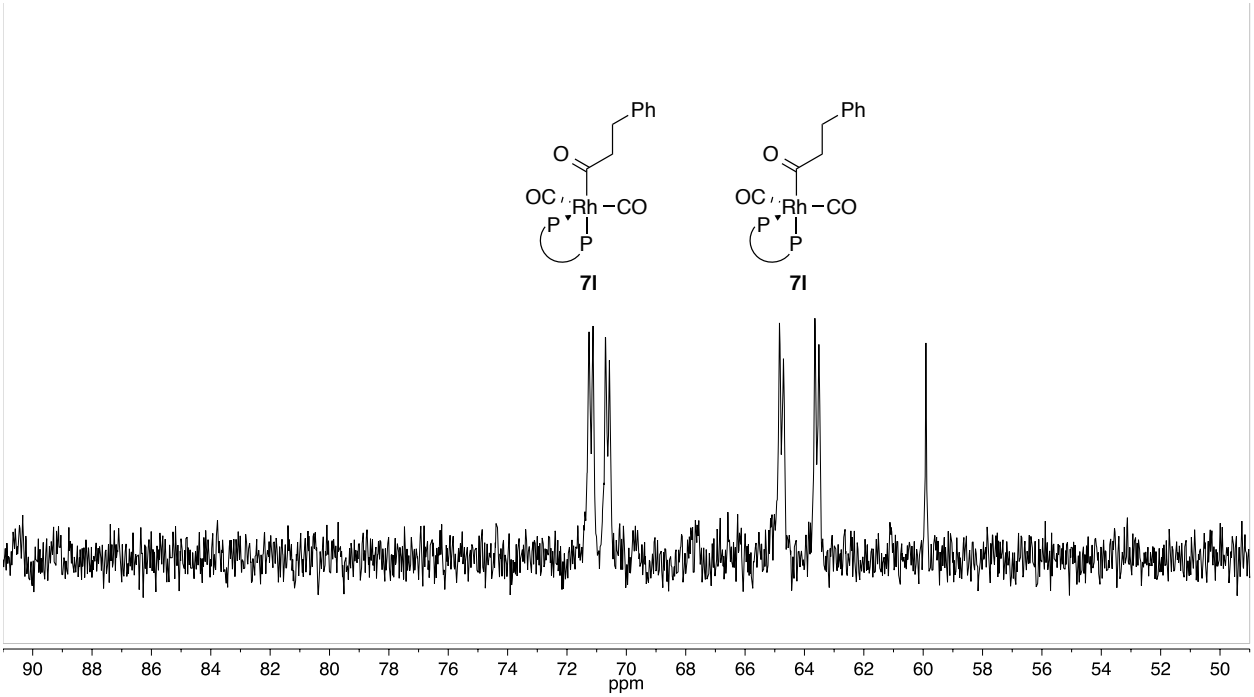

Figure A-50. $^{31}P\{^{1}H\}$ NMR spectrum acquired during catalytic reaction presented in Figures 4-1A and 4-2A. This sample spectrum is acquired at t = 78 minutes and thus is representative of the steady state distribution in the $[styrene]^0$ regime (1.4 M styrene, 6 mM $Rh(H)(CO)_2(BDP)$, 313 K, 20 psia H_2, and 20 psia CO).

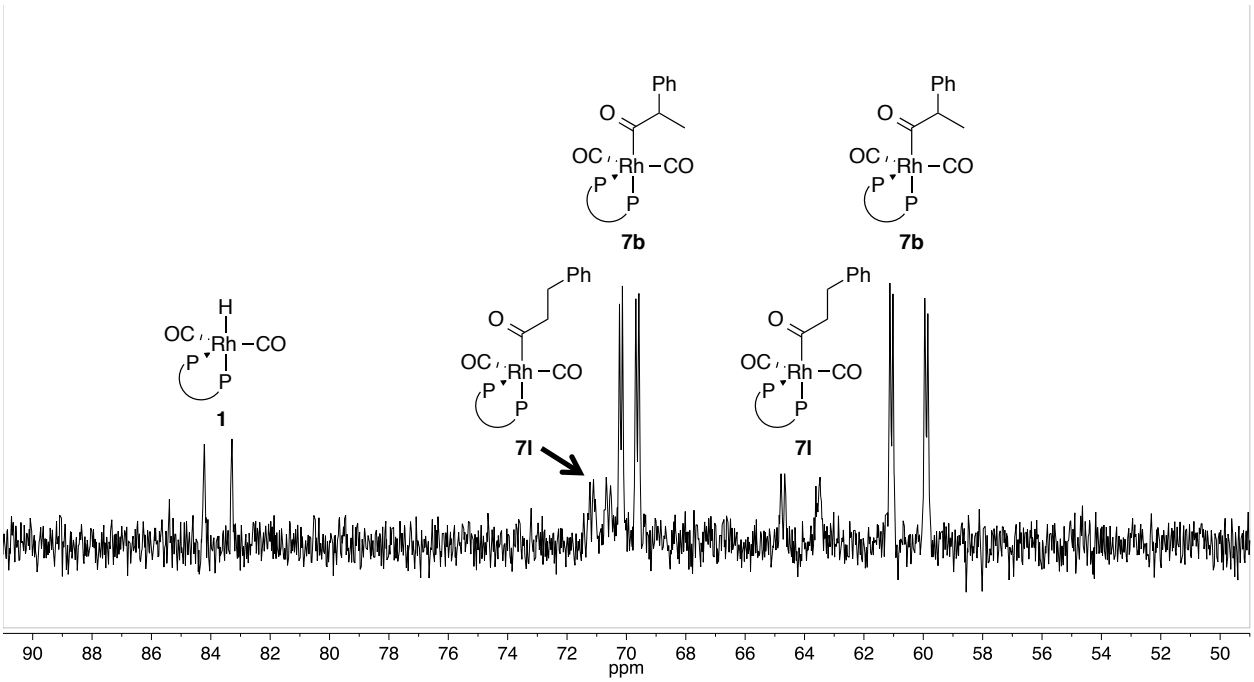

Figure A-51. $^{31}P\{^{1}H\}$ NMR spectrum acquired during catalytic reaction presented in Figures 4-1B and 4-2B. This sample spectrum is acquired at t = 78 minutes and thus is representative of the steady state distribution in the $[styrene]^0$ regime (1.4 M styrene, 6 mM $Rh(H)(CO)_2(BDP)$, 313 K, 20 psia H_2, and 115 psia CO).

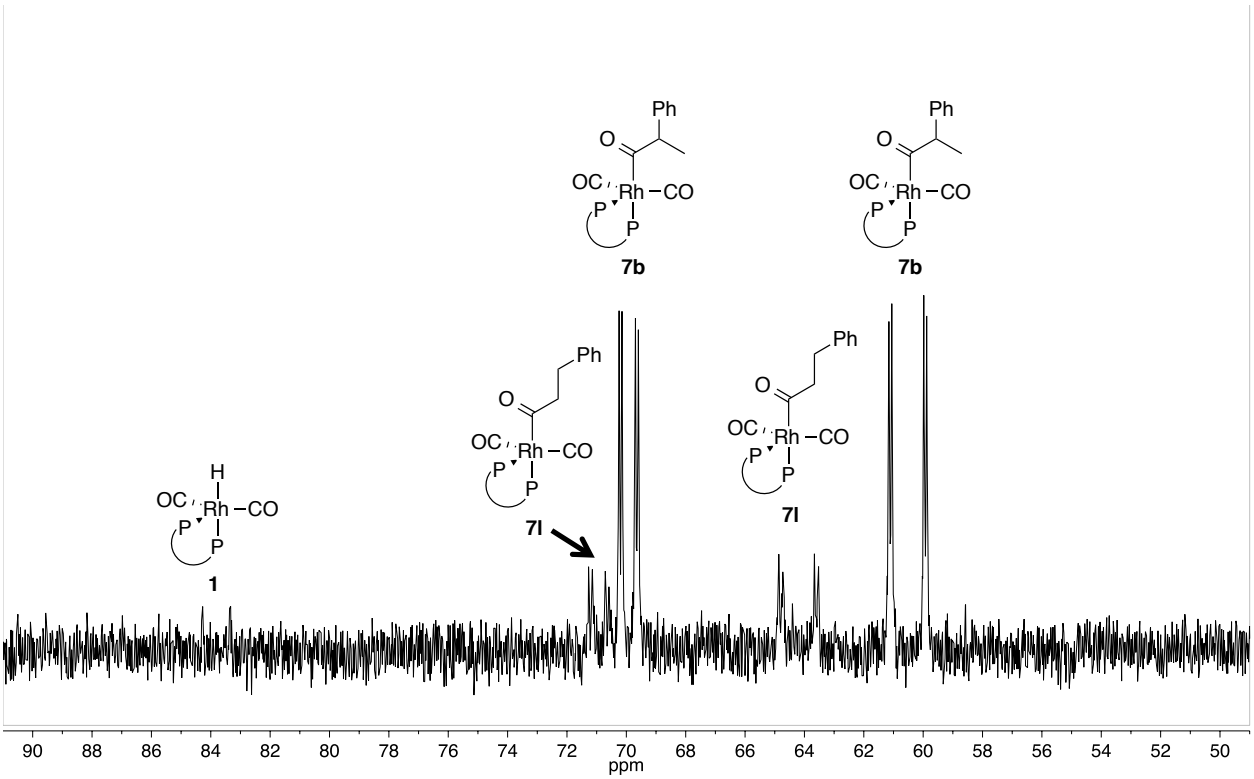

Figure A-52. $^{31}P\{^{1}H\}$ NMR spectrum acquired during catalytic reaction presented in Figures 4-1B and 4-2B. This sample spectrum is acquired at t = 78 minutes and thus is representative of the steady state distribution in the $[styrene]^0$ regime (1.4 M styrene, 6 mM $Rh(H)(CO)_2(BDP)$, 313 K, 20 psia H_2, and 200 psia CO).

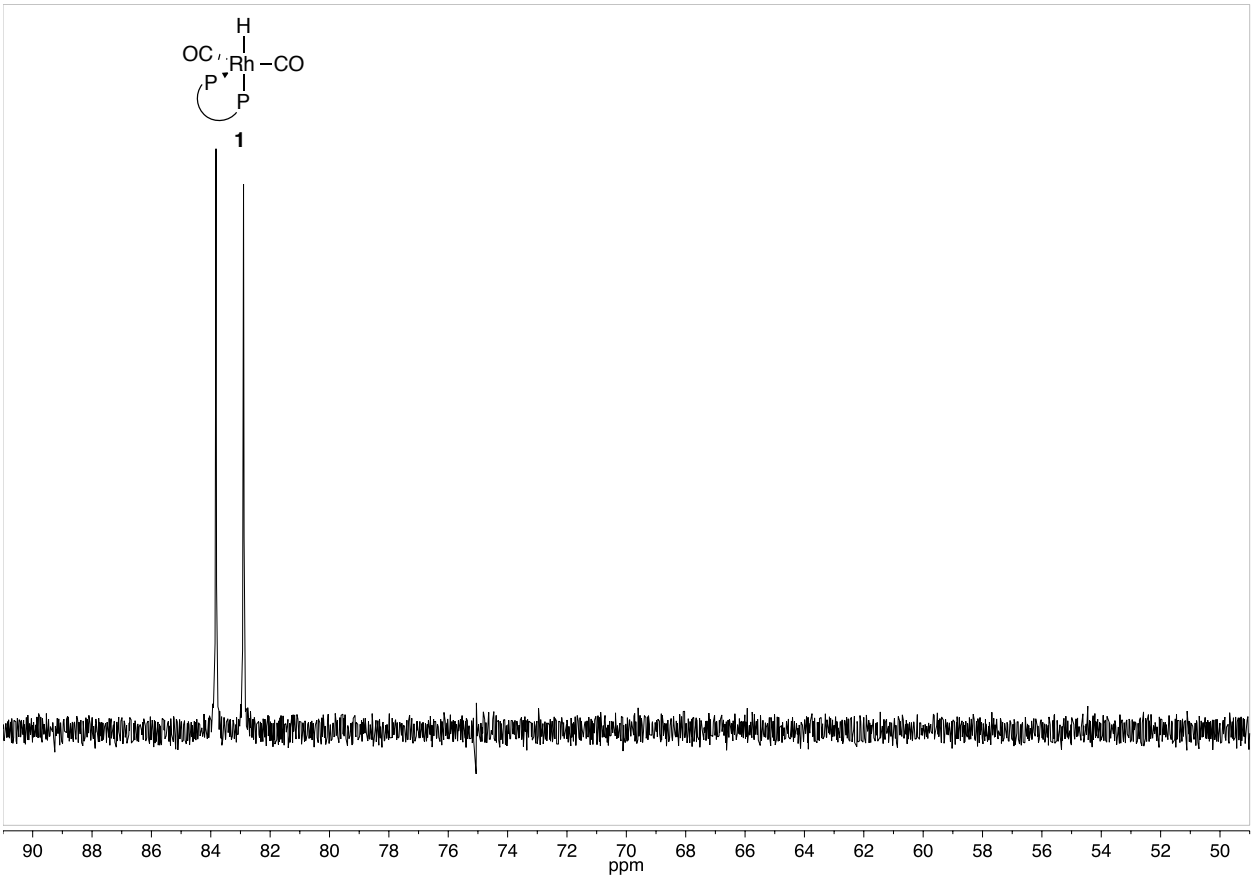

Figure A-53. $^{31}P\{^{1}H\}$ NMR spectrum acquired during catalytic reaction presented in Figure 4-6A. This sample spectrum is acquired at t = 575 seconds and thus is representative of the steady state regime (0.06 M styrene, 0.01M $Rh(H)(CO)_2(BDP)$, 290 K, 200 psia H_2, and 20 psia CO).

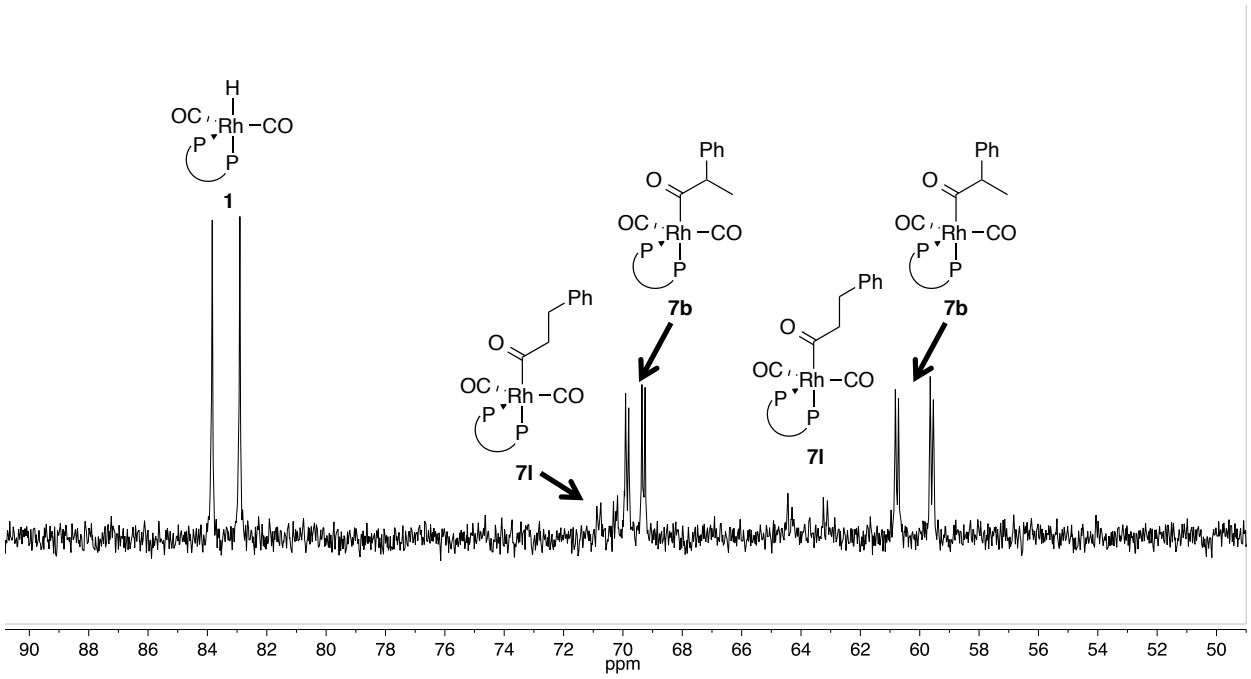

Figure A-54. $^{31}P\{^{1}H\}$ NMR spectrum acquired during catalytic reaction presented in Figure 4-6B. This sample spectrum is acquired at t = 550 seconds and thus is representative of the steady state regime (0.06 M styrene, 0.01M $Rh(H)(CO)_2(BDP)$, 290 K, 20 psia H_2, and 20 psia CO).

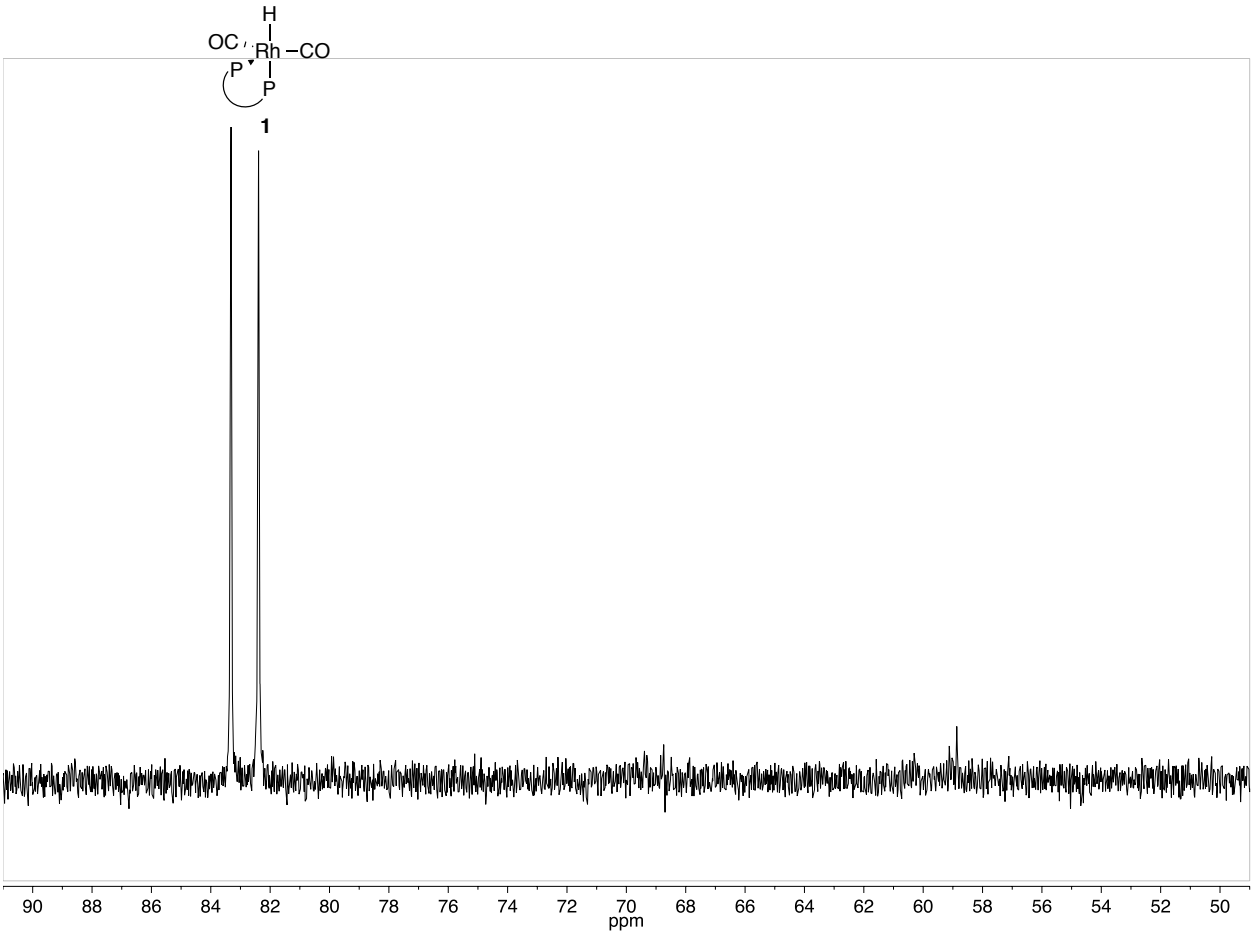

Figure A-55. $^{31}P\{^{1}H\}$ NMR spectrum acquired during catalytic reaction presented in Figure 7C. This sample spectrum is acquired at t = 3600 seconds and thus is representative of the steady state regime (0.06 M styrene, 0.01M $Rh(H)(CO)_2(BDP)$, 290 K, 200 psia H_2, and 200 psia CO).

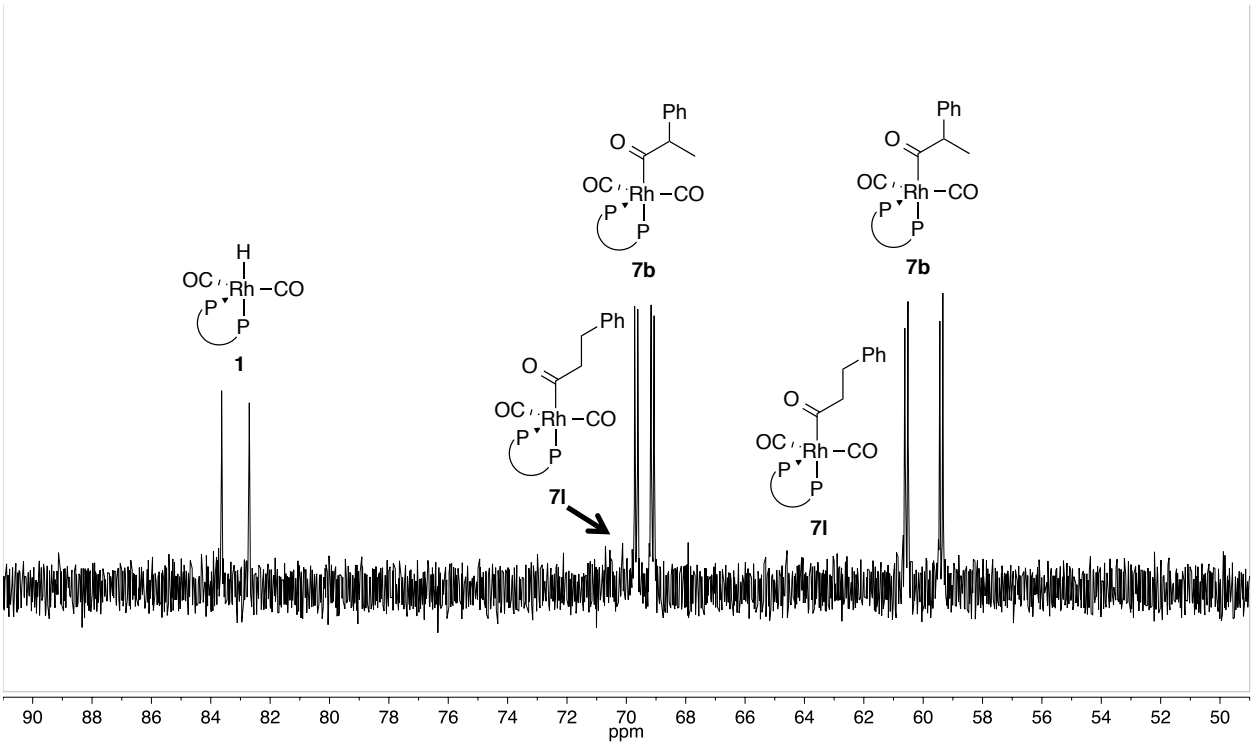

Figure A-56. $^{31}P\{^{1}H\}$ NMR spectrum acquired during catalytic reaction presented in Figure 4-6D. This sample spectrum is acquired at t = 12250 seconds and thus is representative of the steady state regime (0.06 M styrene, 0.01M $Rh(H)(CO)_2(BDP)$, 290 K, 20 psia H_2, and 200 psia CO).

A.2.3 Single Turnover Experiments

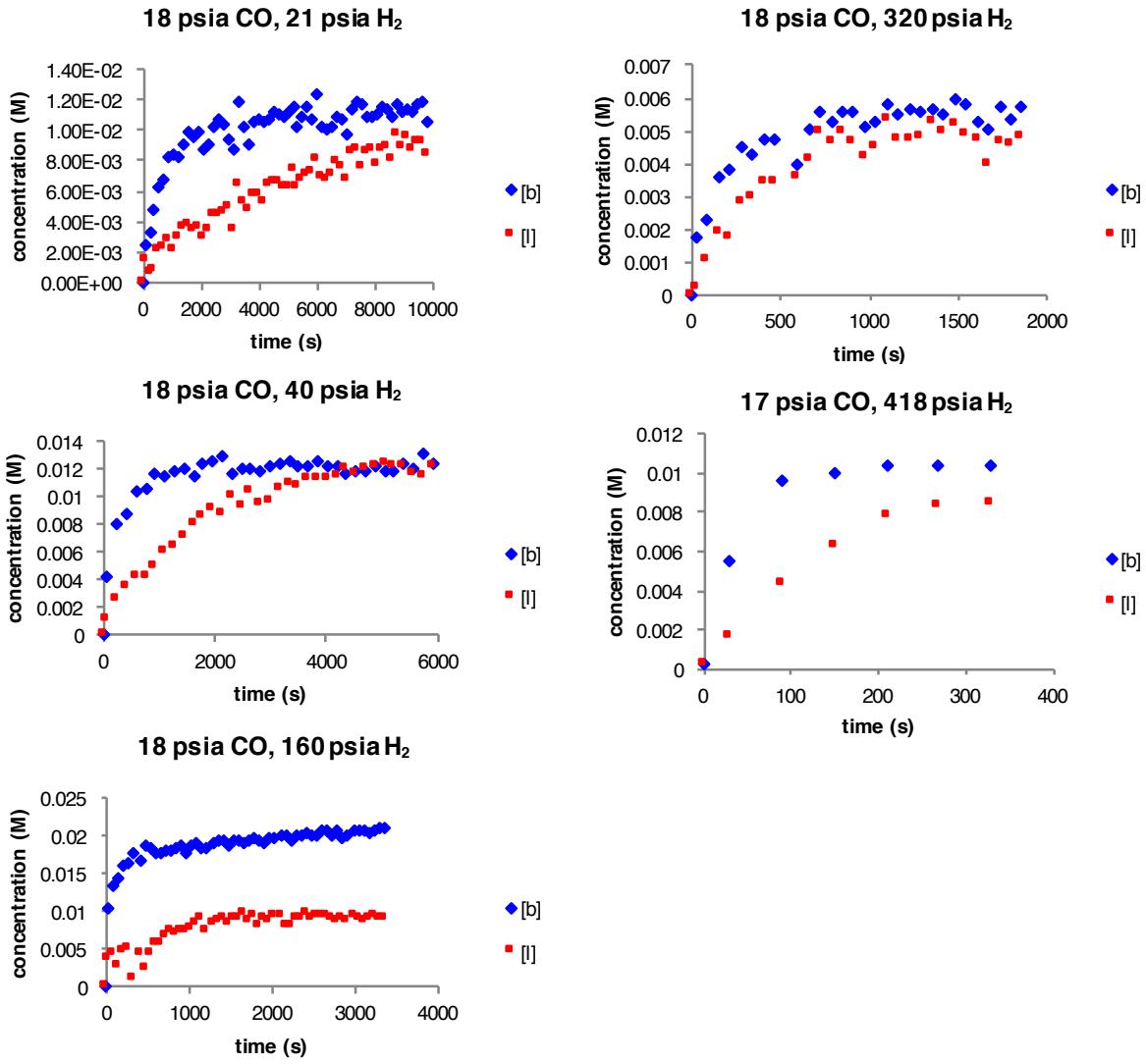

Figure A-57. Single turnover hydrogenolysis experiments in the WiHP-NMRR following formation of aldehydes by ^{1}H NMR spectroscopy. (~20 mM Rh(BDP) as ~1:1 mixture of acyls, 290 K, 17 psia CO, varied H_2 pressures, CH_2Cl_2).

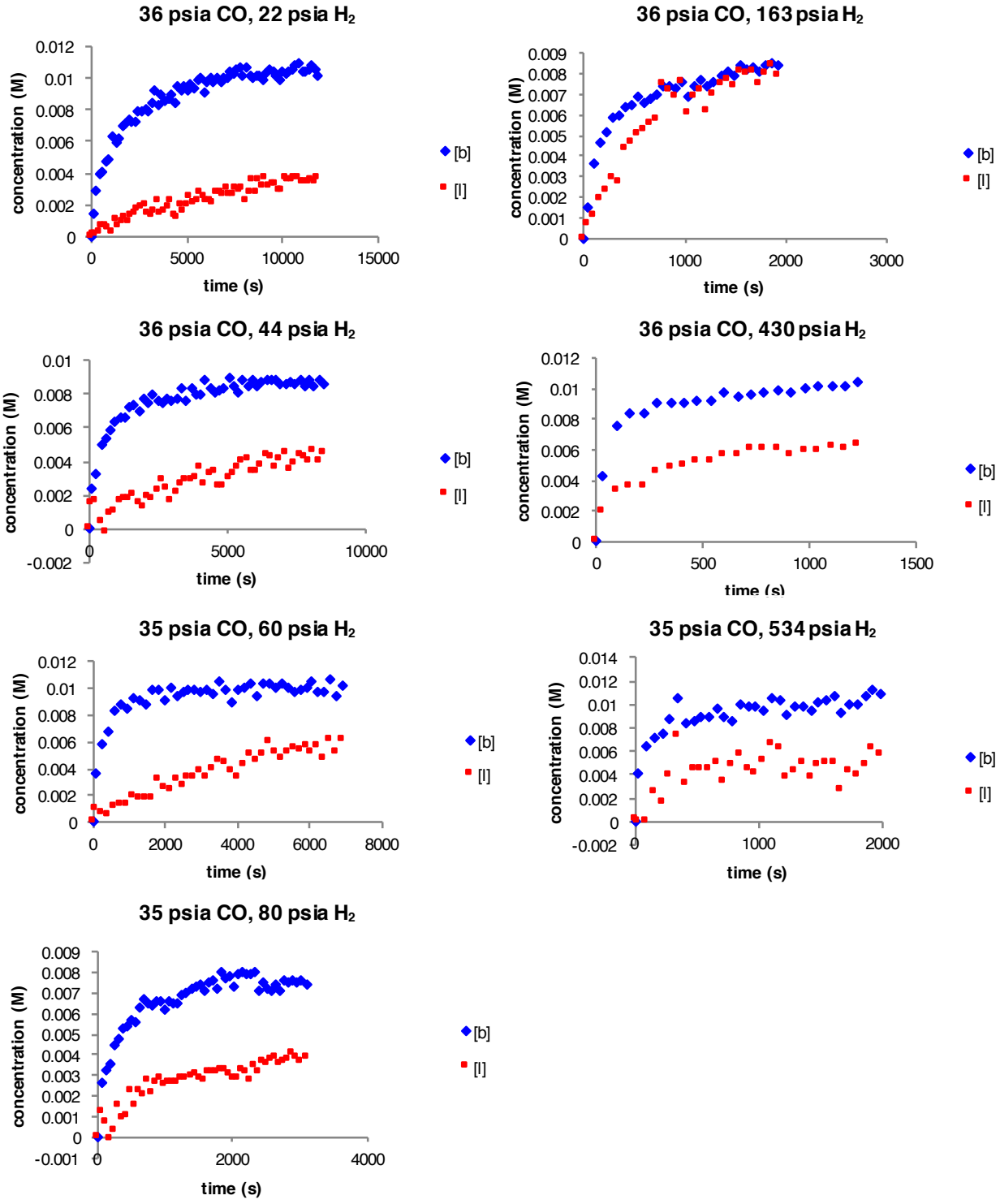

Figure A-58. Single turnover hydrogenolysis experiments in the WiHP-NMRR following formation of aldehydes by ^{1}H NMR spectroscopy. (~20 mM Rh(BDP) as ~1:1 mixture of acyls, 290 K, 35 psia CO, varied H_2 pressures, CH_2Cl_2).

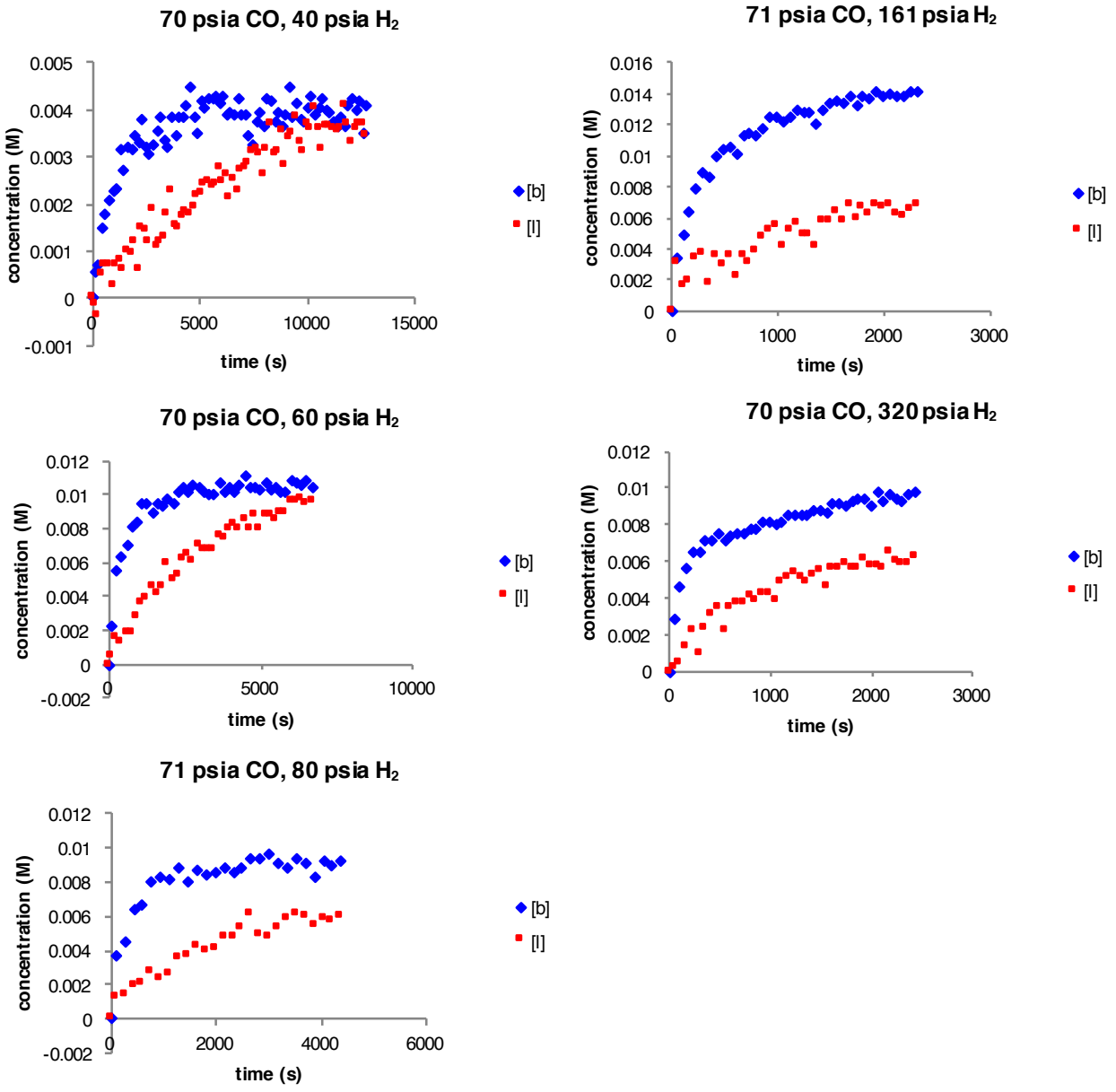

Figure A-59. Single turnover hydrogenolysis experiments in the WiHP-NMRR following formation of aldehydes by ^{1}H NMR spectroscopy. (~20 mM Rh(BDP) as ~1:1 mixture of acyls, 290 K, 70 psia CO, varied H_2 pressures, CH_2Cl_2).

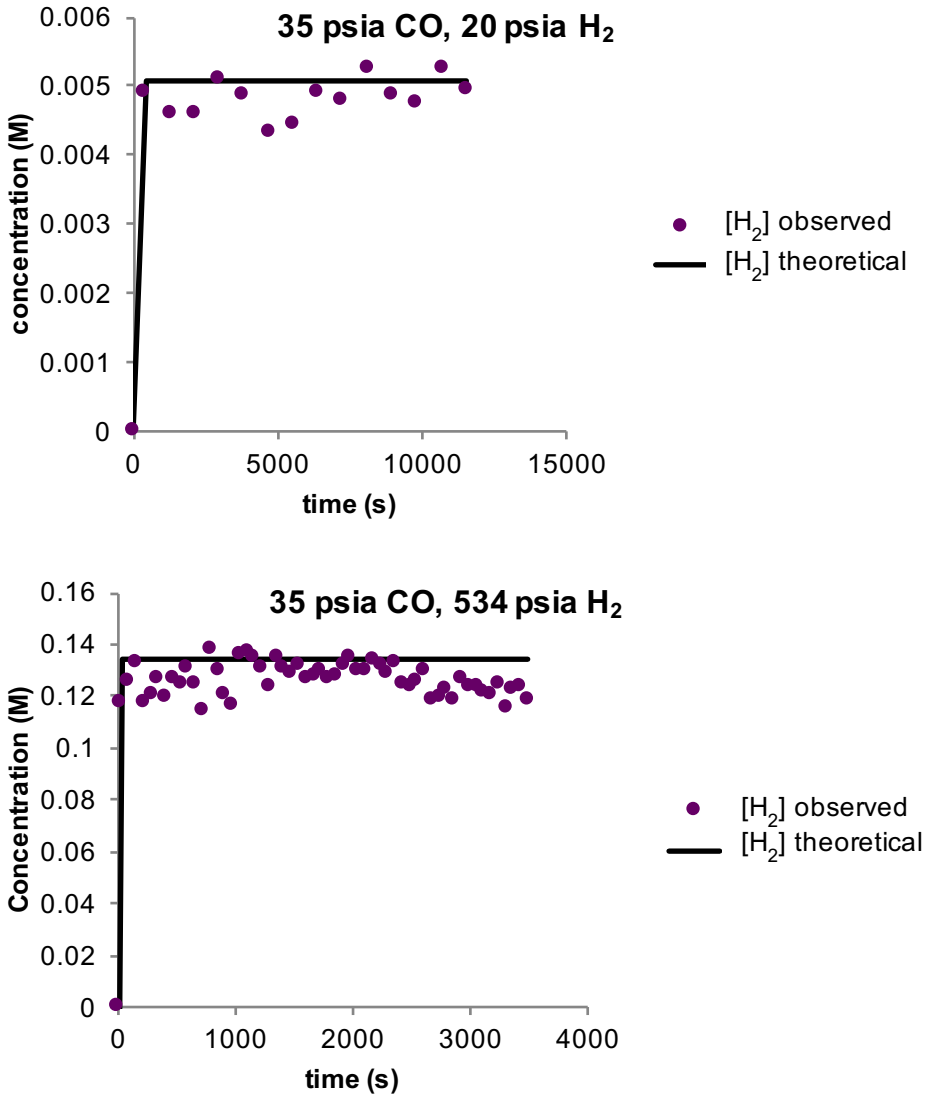

Figure A-60. Dihydrogen pressures maintain Henry's law throughout single turnover hydrogenolysis reactions. The constant [H_2] indicate that sufficient gas/liquid mixing occurs. Due to slight overlap between the dihydrogen and CH_2Cl_2 signals, line fitting analysis in Mestre Nova was used. Because CO is not consumed in this reaction and dihydrogen obeys Henry's law, [CO] can be assumed constant. (~20 mM Rh(BDP) as ~1:1 mixture of acyls, 290 K, 35 psia CO, various psia H_2, CH_2Cl_2).

A.2.4 Kinetic Modeling Fits

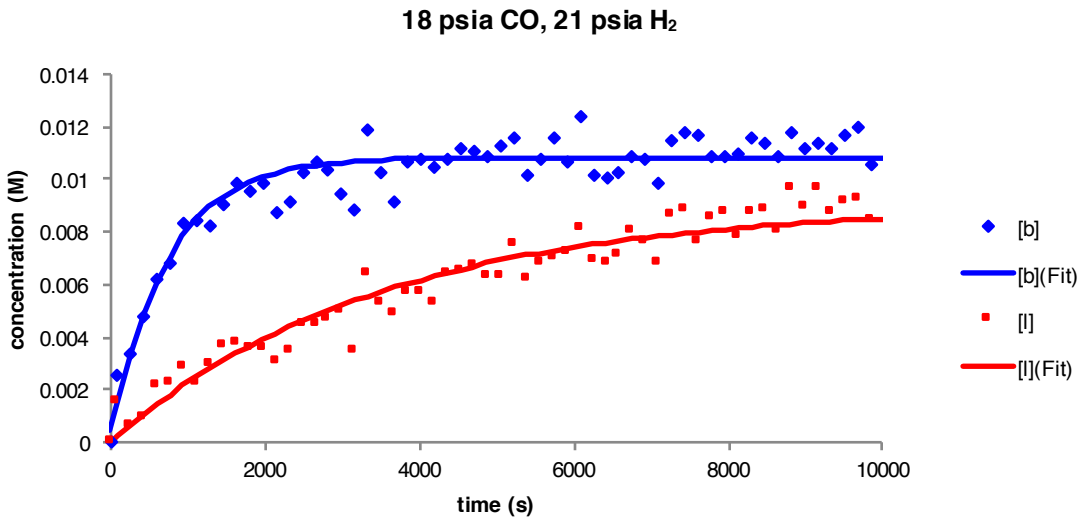

Figure A-61. Data and fits for simplified model of single turnover hydrogenolysis experiments (~20 mM Rh(BDP) as ~1:1 mixture of acyls, 290 K, 18 psia CO, 21 psia H_2, CH_2Cl_2).

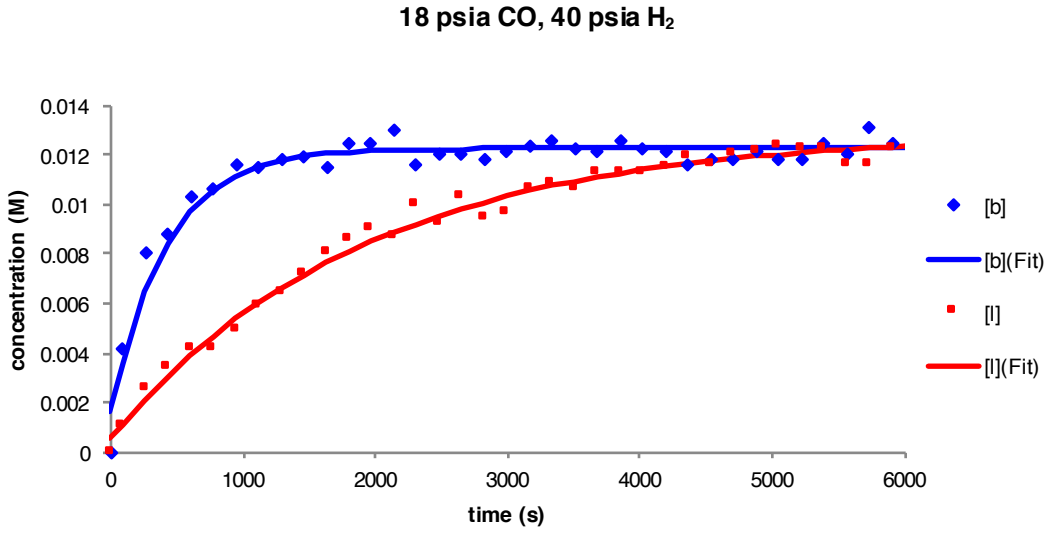

Figure A-62. Data and fits for simplified model of single turnover hydrogenolysis experiments (~20 mM Rh(BDP) as ~1:1 mixture of acyls, 290 K, 18 psia CO, 40 psia H_2, CH_2Cl_2).

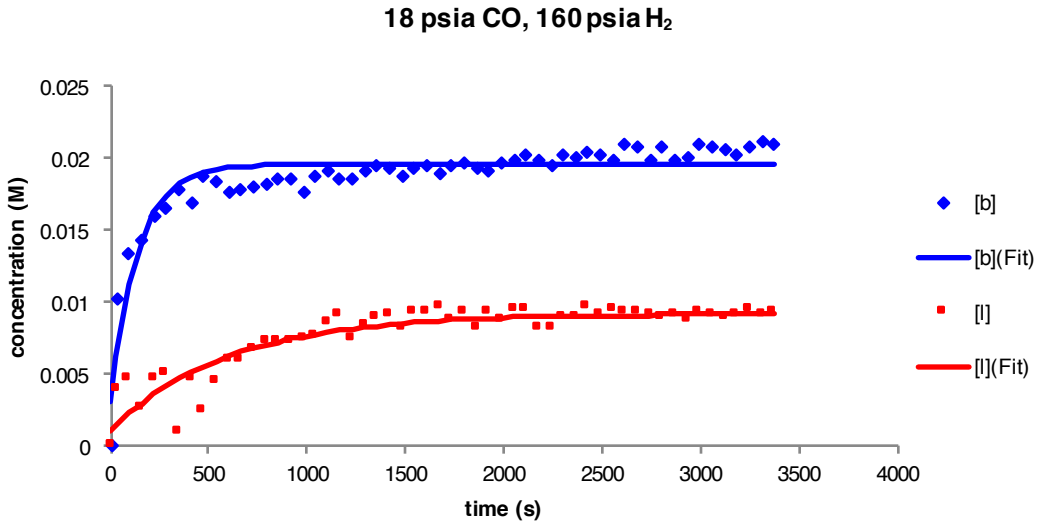

Figure A-63. Data and fits for simplified model of single turnover hydrogenolysis experiments (~20 mM Rh(BDP) as ~1:1 mixture of acyls, 290 K, 18 psia CO, 160 psia H_2, CH_2Cl_2).

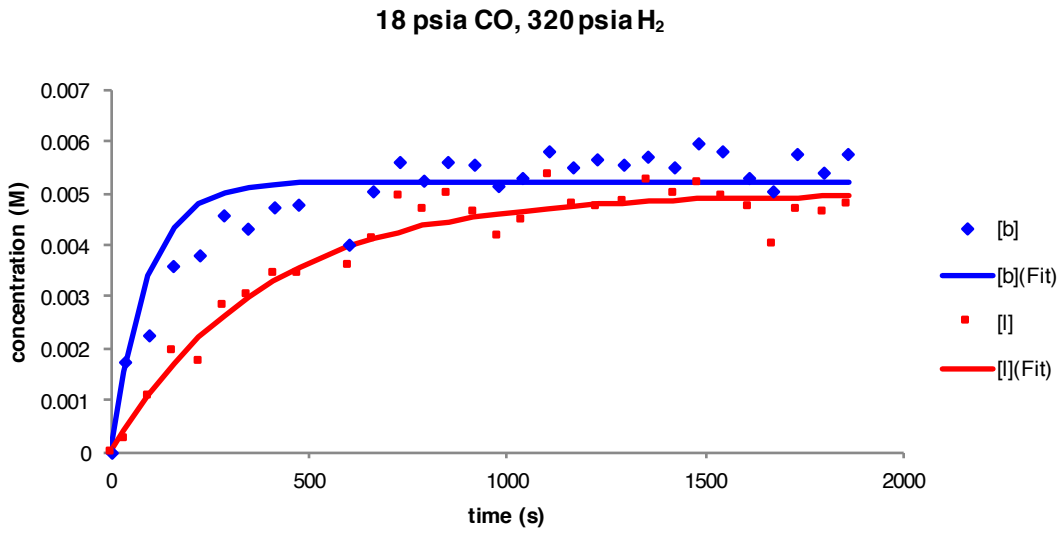

Figure A-64. Data and fits for simplified model of single turnover hydrogenolysis experiments (~20 mM Rh(BDP) as ~1:1 mixture of acyls, 290 K, 18 psia CO, 320 psia H_2, CH_2Cl_2).

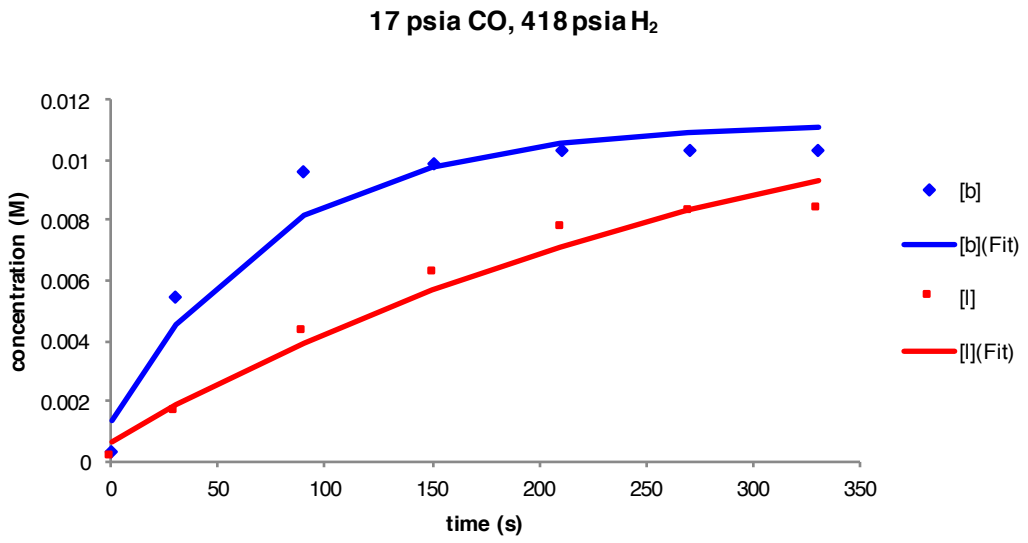

Figure A-65. Data and fits for simplified model of single turnover hydrogenolysis experiments (~20 mM Rh(BDP) as ~1:1 mixture of acyls, 290 K, 18 psia CO, 418 psia H_2, CH_2Cl_2).

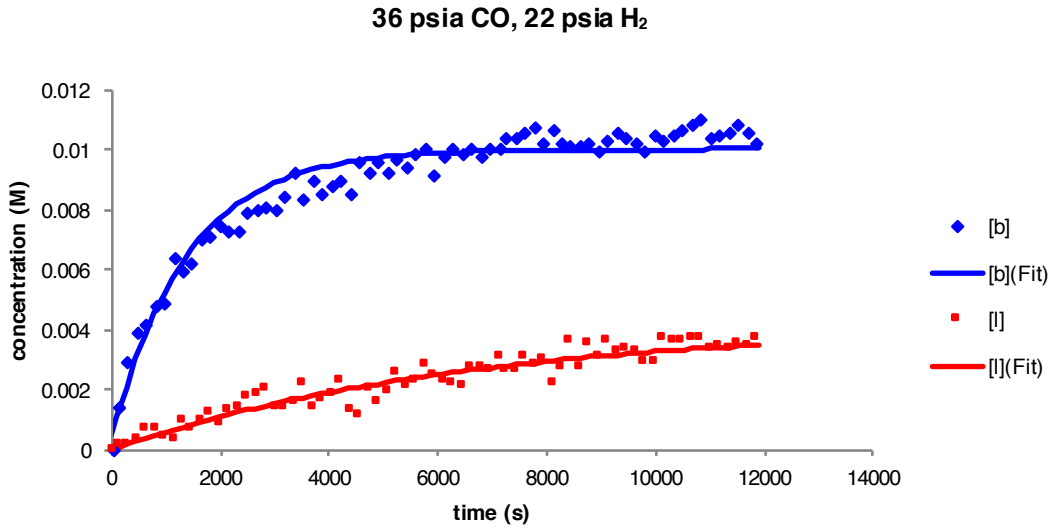

Figure A-66. Data and fits for simplified model of single turnover hydrogenolysis experiments (~20 mM Rh(BDP) as ~1:1 mixture of acyls, 290 K, 36 psia CO, 22 psia H_2, CH_2Cl_2).

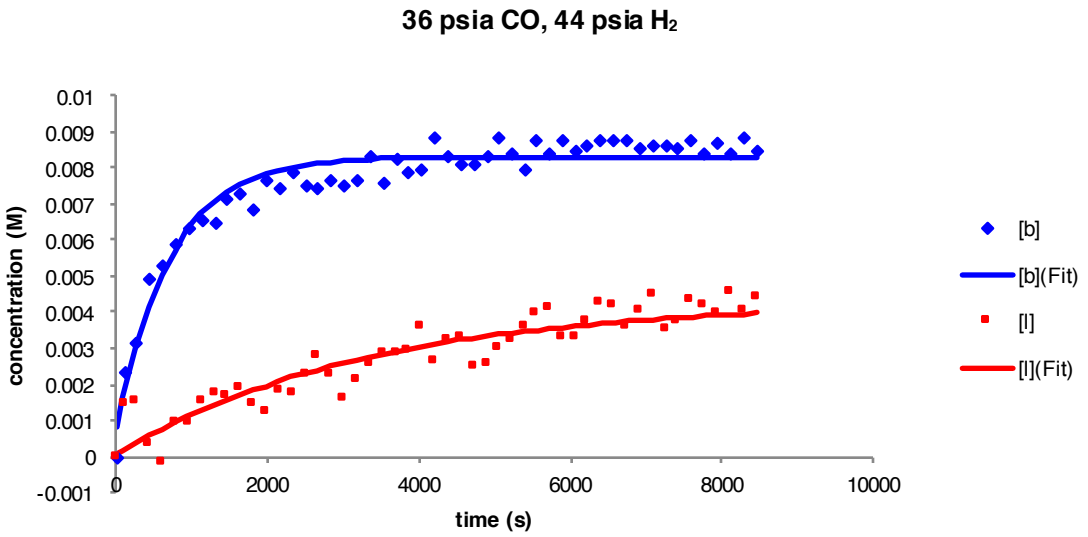

Figure A-67. Data and fits for simplified model of single turnover hydrogenolysis experiments (~20 mM Rh(BDP) as ~1:1 mixture of acyls, 290 K, 36 psia CO, 44 psia H_2, CH_2Cl_2).

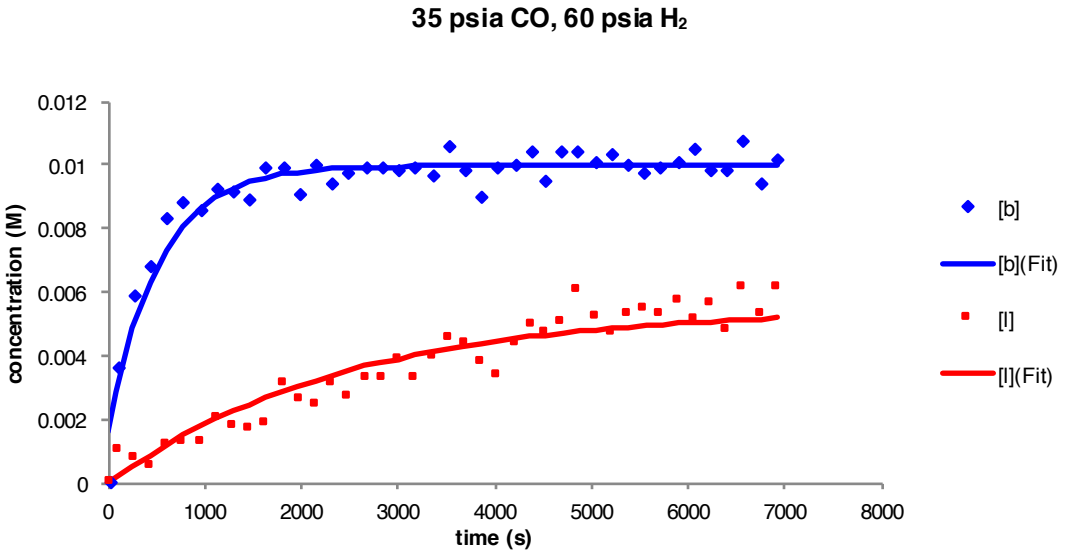

Figure A-68. Data and fits for simplified model of single turnover hydrogenolysis experiments (~20 mM Rh(BDP) as ~1:1 mixture of acyls, 290 K, 35 psia CO, 60 psia H_2, CH_2Cl_2).

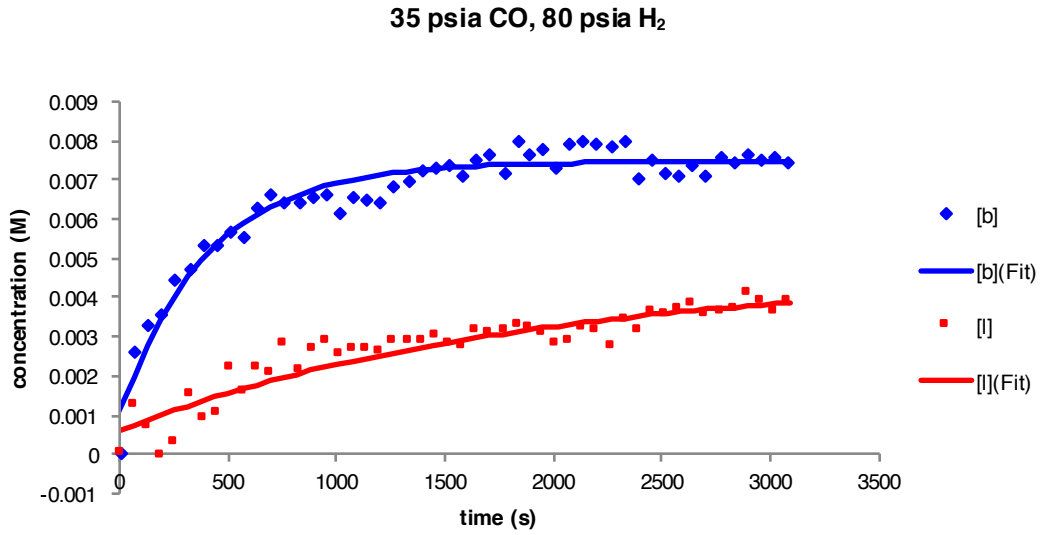

Figure A-69. Data and fits for simplified model of single turnover hydrogenolysis experiments (~20 mM Rh(BDP) as ~1:1 mixture of acyls, 290 K, 35 psia CO, 80 psia H_2, CH_2Cl_2).

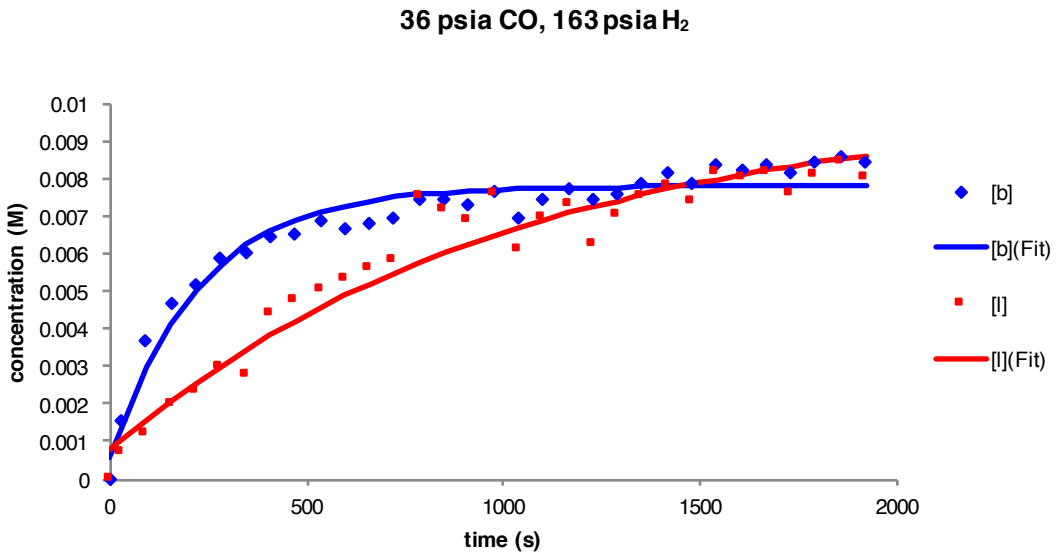

Figure A-70. Data and fits for simplified model of single turnover hydrogenolysis experiments (~20 mM Rh(BDP) as ~1:1 mixture of acyls, 290 K, 36 psia CO, 163 psia H_2, CH_2Cl_2).

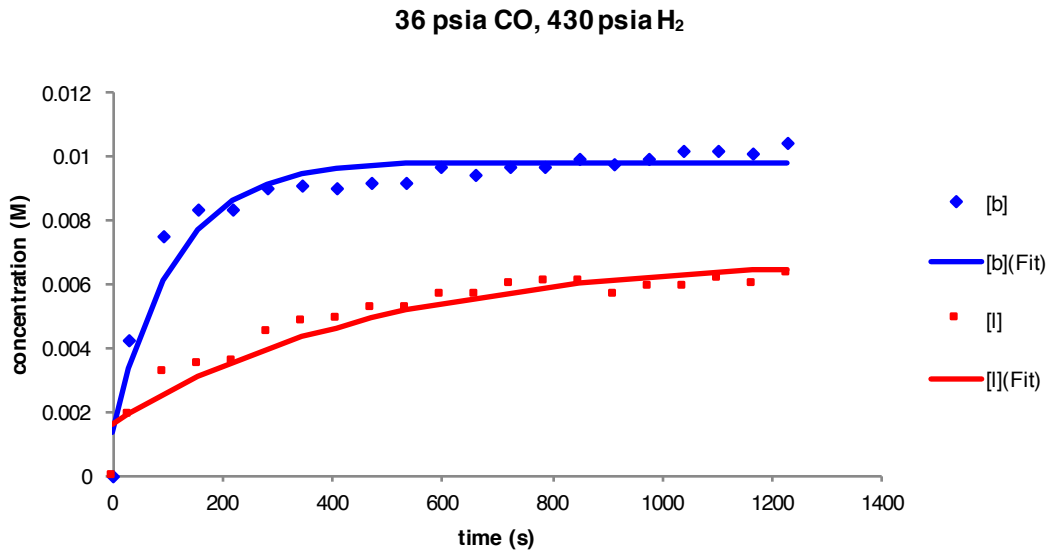

Figure A-71. Data and fits for simplified model of single turnover hydrogenolysis experiments (~20 mM Rh(BDP) as ~1:1 mixture of acyls, 290 K, 36 psia CO, 430 psia H_2, CH_2Cl_2).

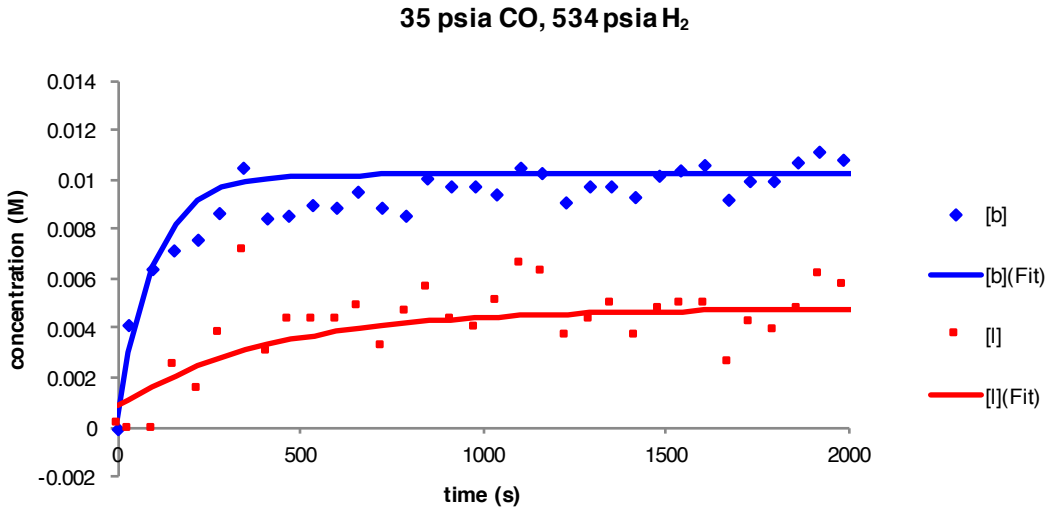

Figure A-72. Data and fits for simplified model of single turnover hydrogenolysis experiments (~20 mM Rh(BDP) as ~1:1 mixture of acyls, 290 K, 35 psia CO, 534 psia H_2, CH_2Cl_2).

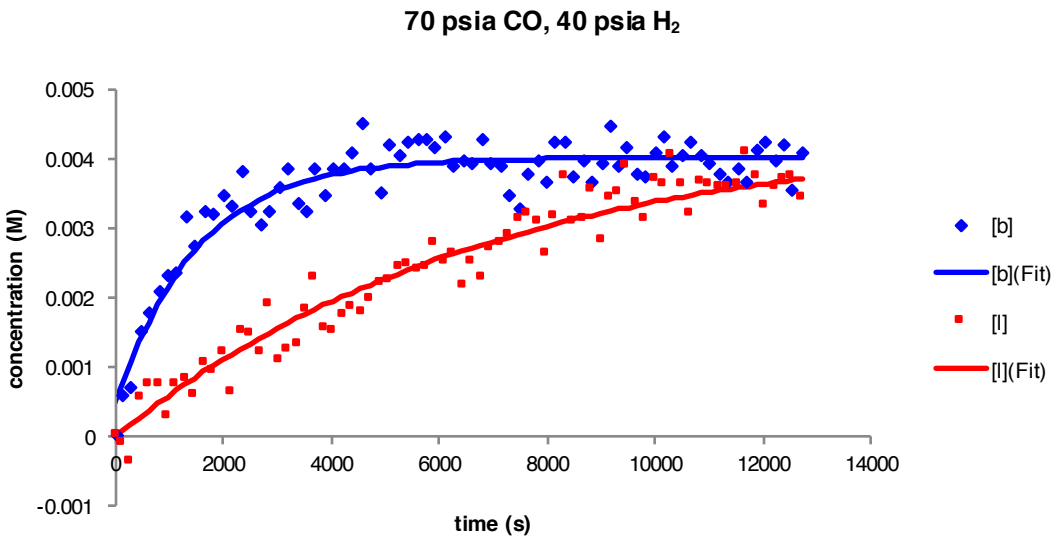

Figure A-73. Data and fits for simplified model of single turnover hydrogenolysis experiments (~20 mM Rh(BDP) as ~1:1 mixture of acyls, 290 K, 70 psia CO, 40 psia H_2, CH_2Cl_2).

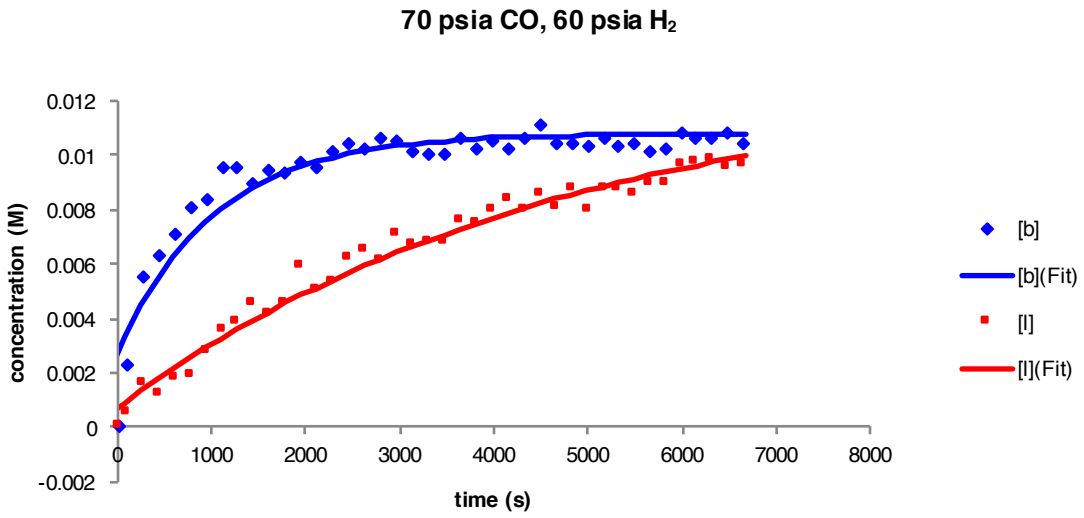

Figure A-74. Data and fits for simplified model of single turnover hydrogenolysis experiments (~20 mM Rh(BDP) as ~1:1 mixture of acyls, 290 K, 70 psia CO, 60 psia H_2, CH_2Cl_2).

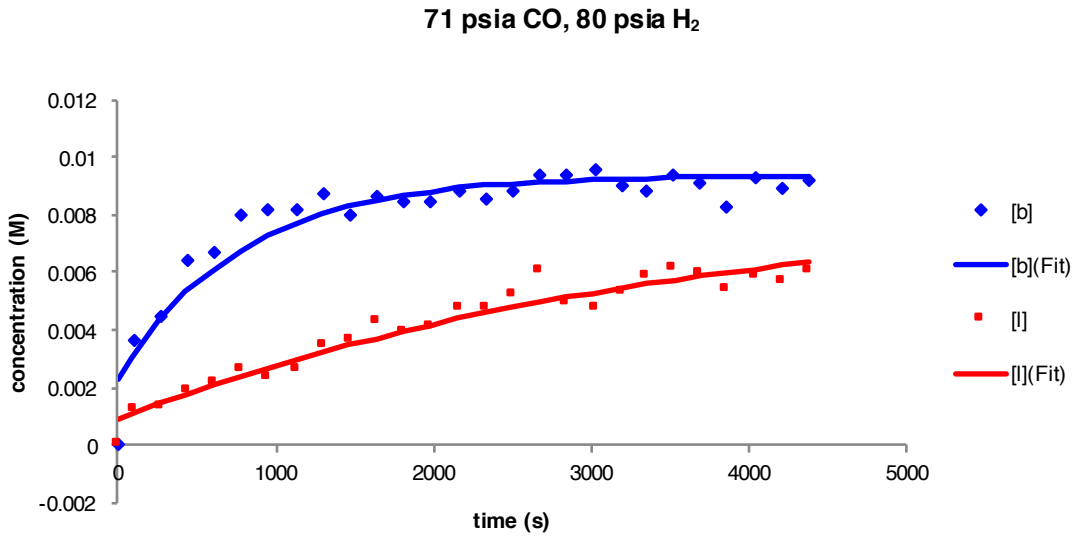

Figure A-75. Data and fits for simplified model of single turnover hydrogenolysis experiments (~20 mM Rh(BDP) as ~1:1 mixture of acyls, 290 K, 71 psia CO, 80 psia H_2, CH_2Cl_2).

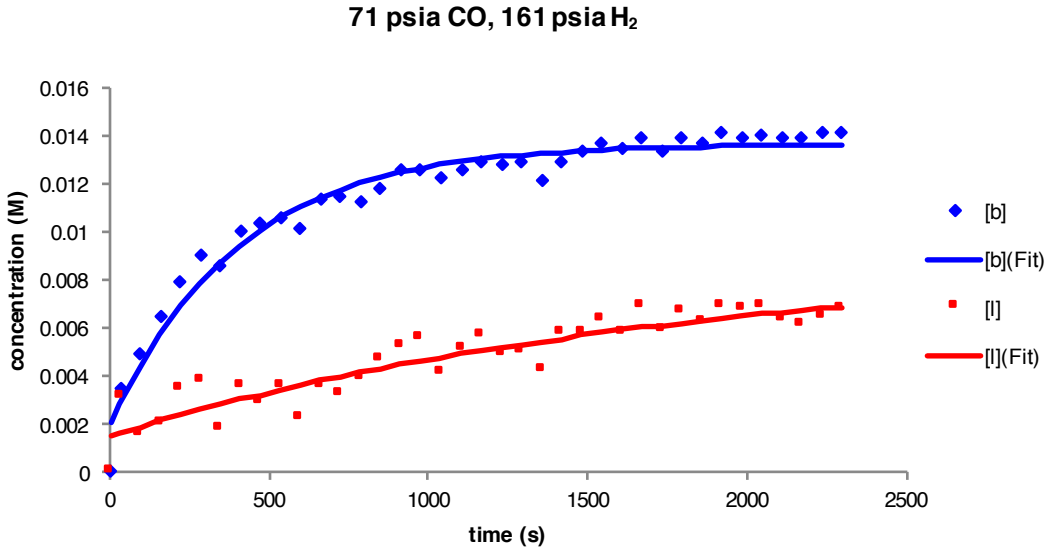

Figure A-76. Data and fits for simplified model of single turnover hydrogenolysis experiments (~20 mM Rh(BDP) as ~1:1 mixture of acyls, 290 K, 71 psia CO, 161 psia H_2, CH_2Cl_2).

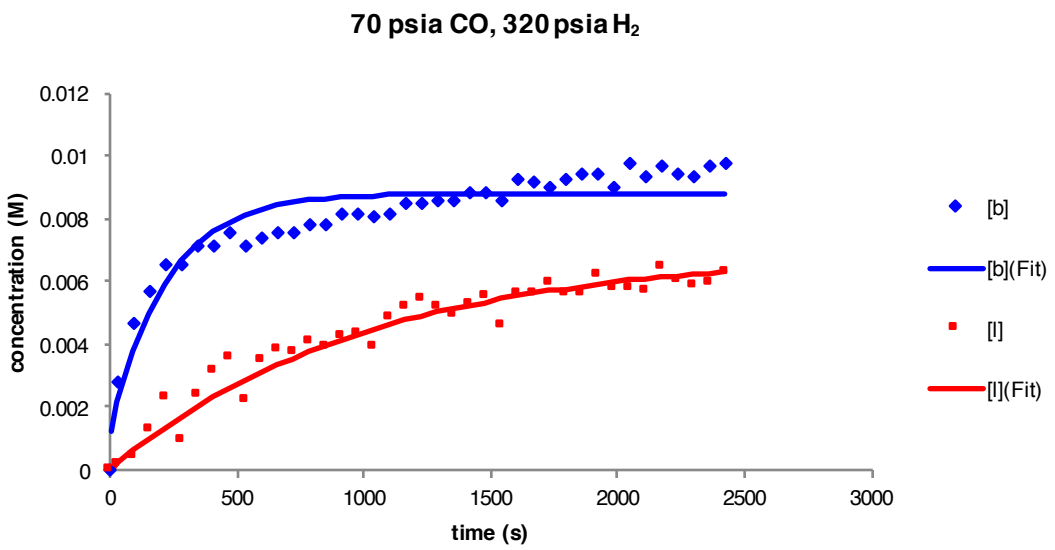

Figure A-77. Data and fits for simplified model of single turnover hydrogenolysis experiments (~20 mM Rh(BDP) as ~1:1 mixture of acyls, 290 K, 70 psia CO, 320 psia H_2, CH_2Cl_2).

A.3 Chapter 6: Backbone-Modified Bis(diazaphospholanes) for Regioselective Rhodium-Catalyzed Hydroformylation of Alkenes

A.3.1 Computed and Crystallographic Structures for BDP Ligands

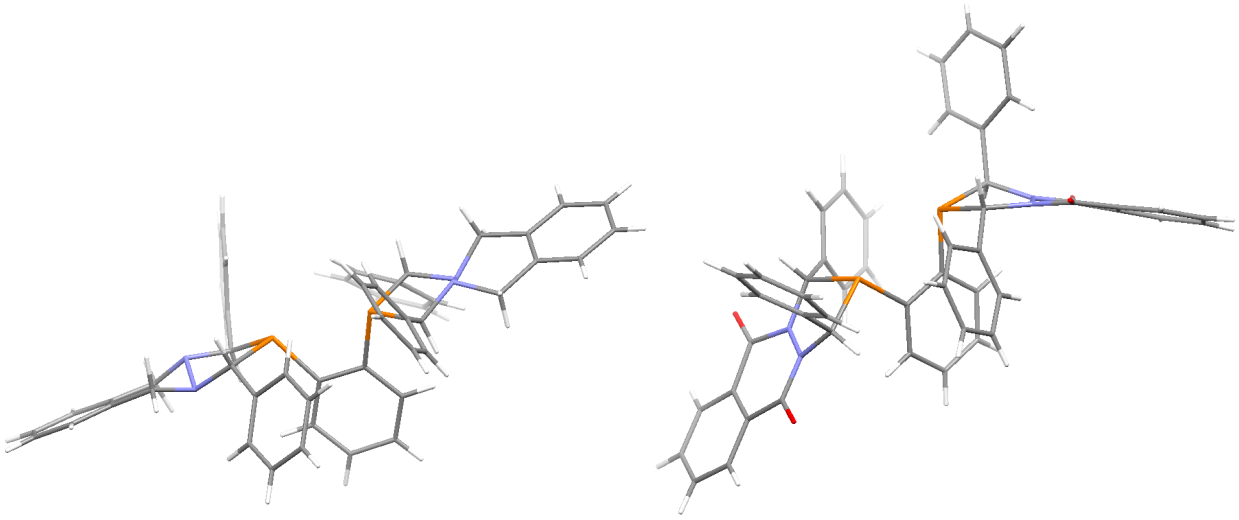

Figure A-78. Crystal structures of red-TPPB BDP **4** (left, θ = 56.0) and TPPB BDP **3** (right, θ = 10.4°), oriented along the N–N bond of one of the diazaphospholane rings (blue: nitrogen atoms, orange: phosphorous atoms, red: oxygen atoms).

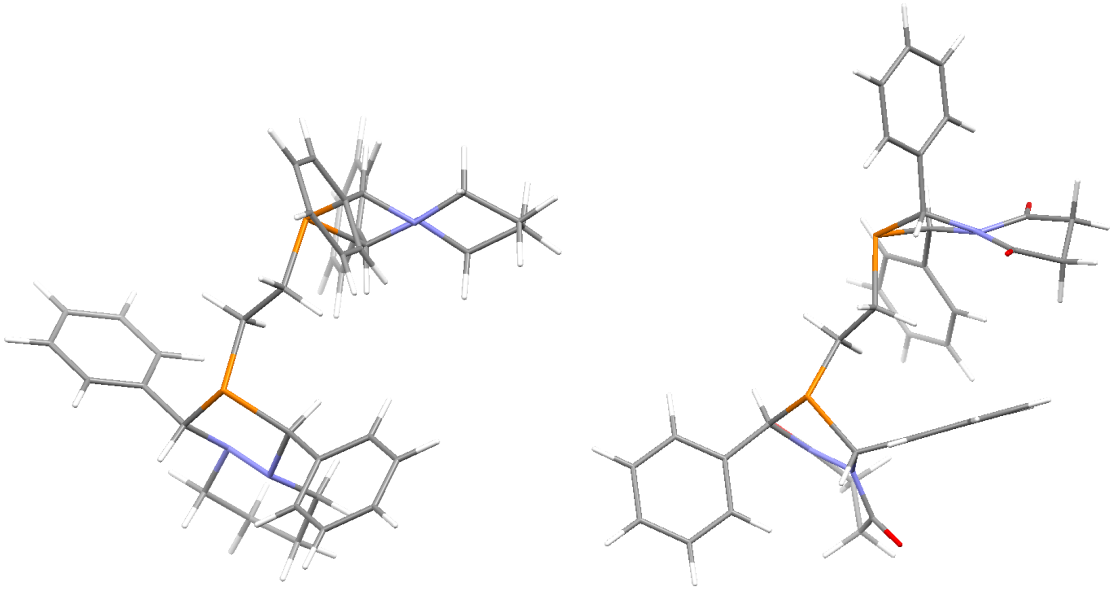

Figure A-79. Calculated structures of red-TPSB BDPE **6** (left, θ = 56.4) and TPSB BDPE **5** (right, θ = 14.0°), oriented along the N–N bond of one of the diazaphospholane rings (blue: nitrogen atoms, orange: phosphorous atoms, red: oxygen atoms).

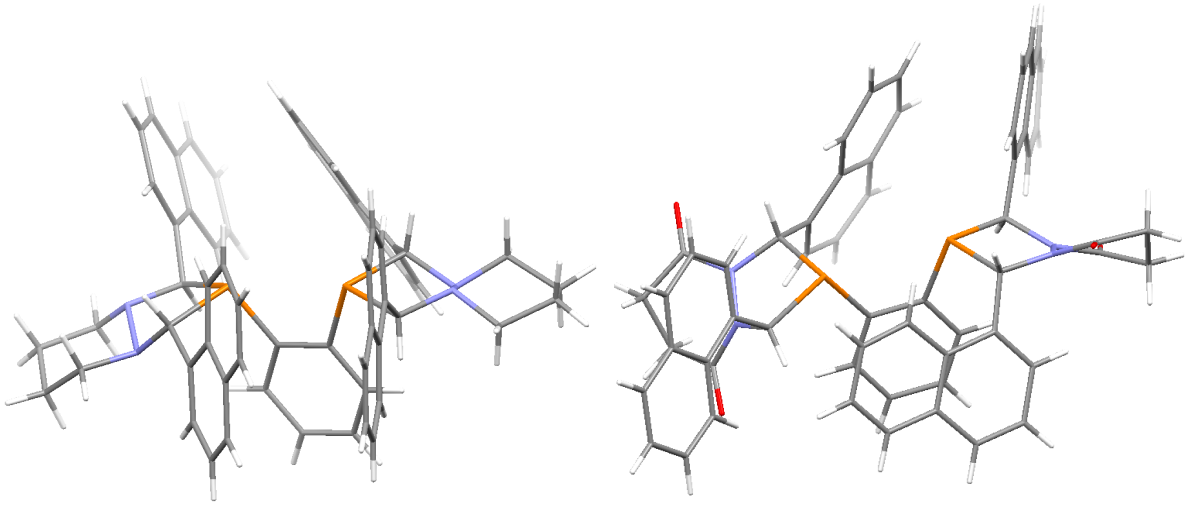

Figure A-80. Crystal structures of red-TNSB BDP **8** (left, θ = 58.9°) and TNSB BDP **7** (right, θ = 33.4°) oriented along the N–N bond of one of the diazaphospholane rings (blue: nitrogen atoms, orange: phosphorous atoms, red: oxygen atoms).

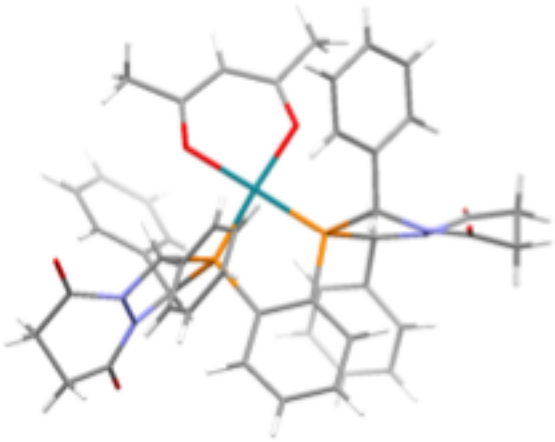

Figure A-81. Crystal structure of [Rh(acac)(**1**)] oriented along the N–N bond of one of the diazaphospholane rings with a torsion angle (θ) of 21.7°.

A.3.2 NMR Spectra for Ligands 1, 2, and 4-8.

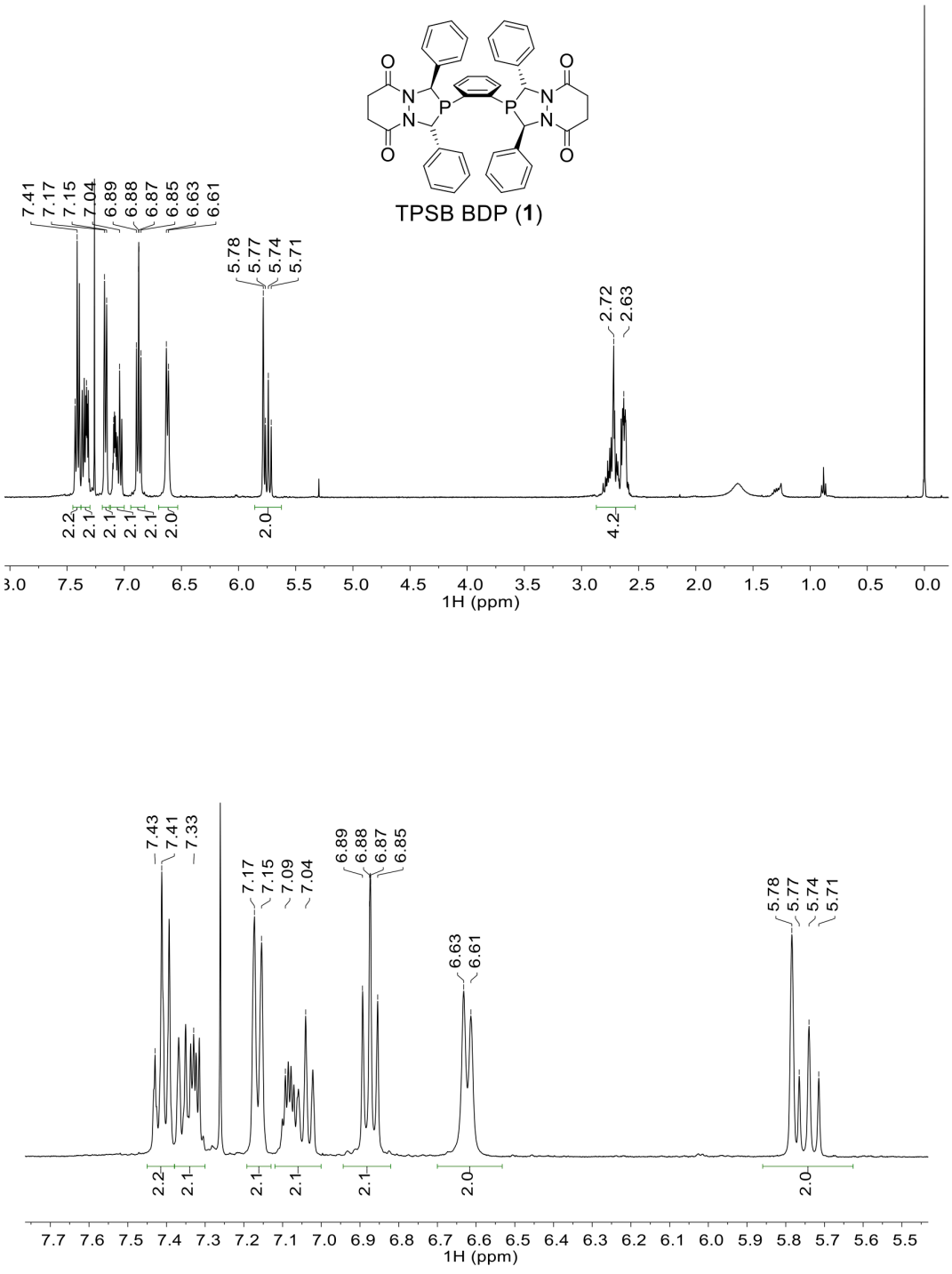

Figure A-82. ^{1}H NMR spectrum (400 MHz) of **1** in $CDCl_3$ (top: full spectrum, bottom: zoom).

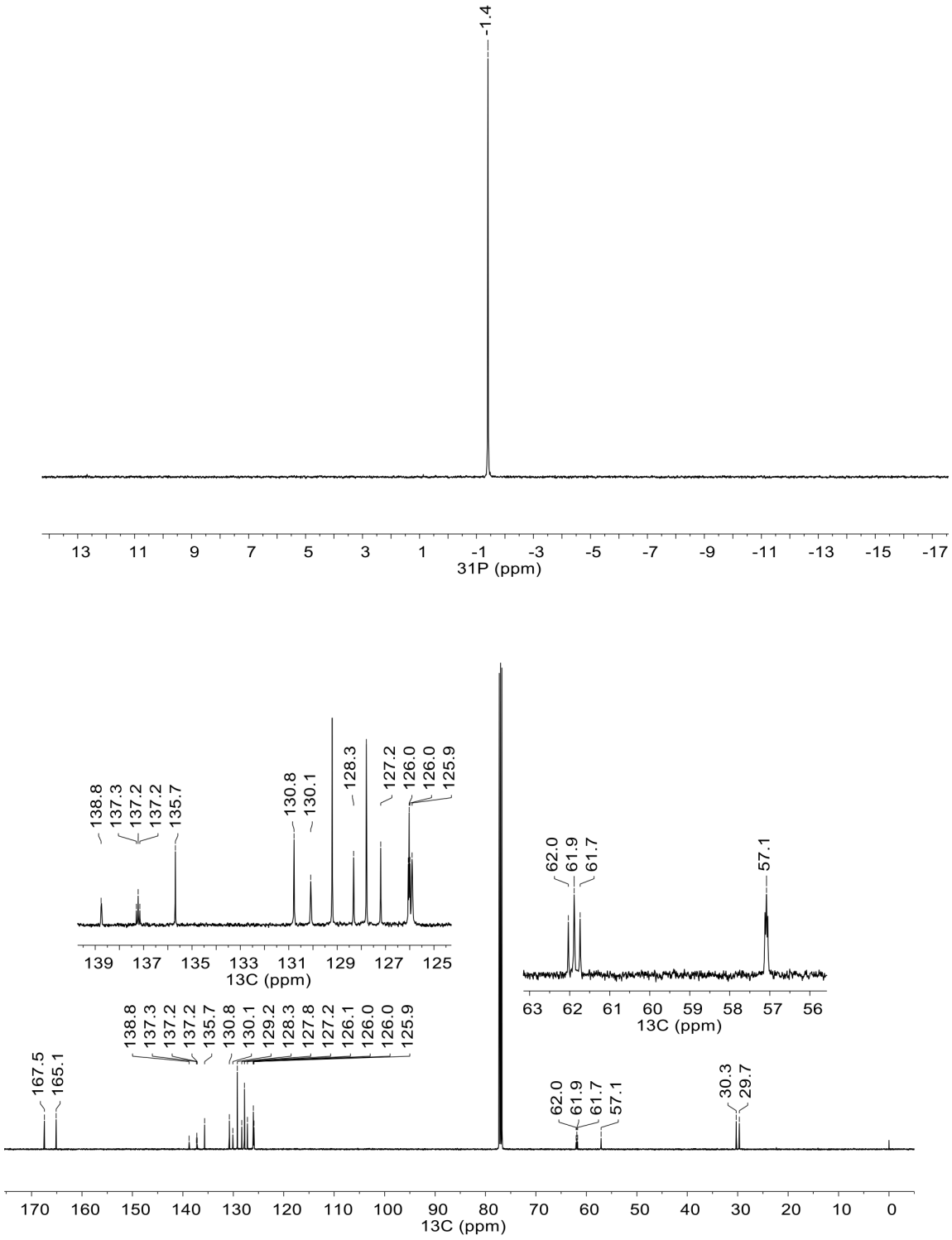

Figure A-83. NMR spectra of **1** in $CDCl_3$ (top: $^{31}P\{^1H\}$ (162 MHz), bottom: $^{13}C\{^1H\}$ (126 MHz)).

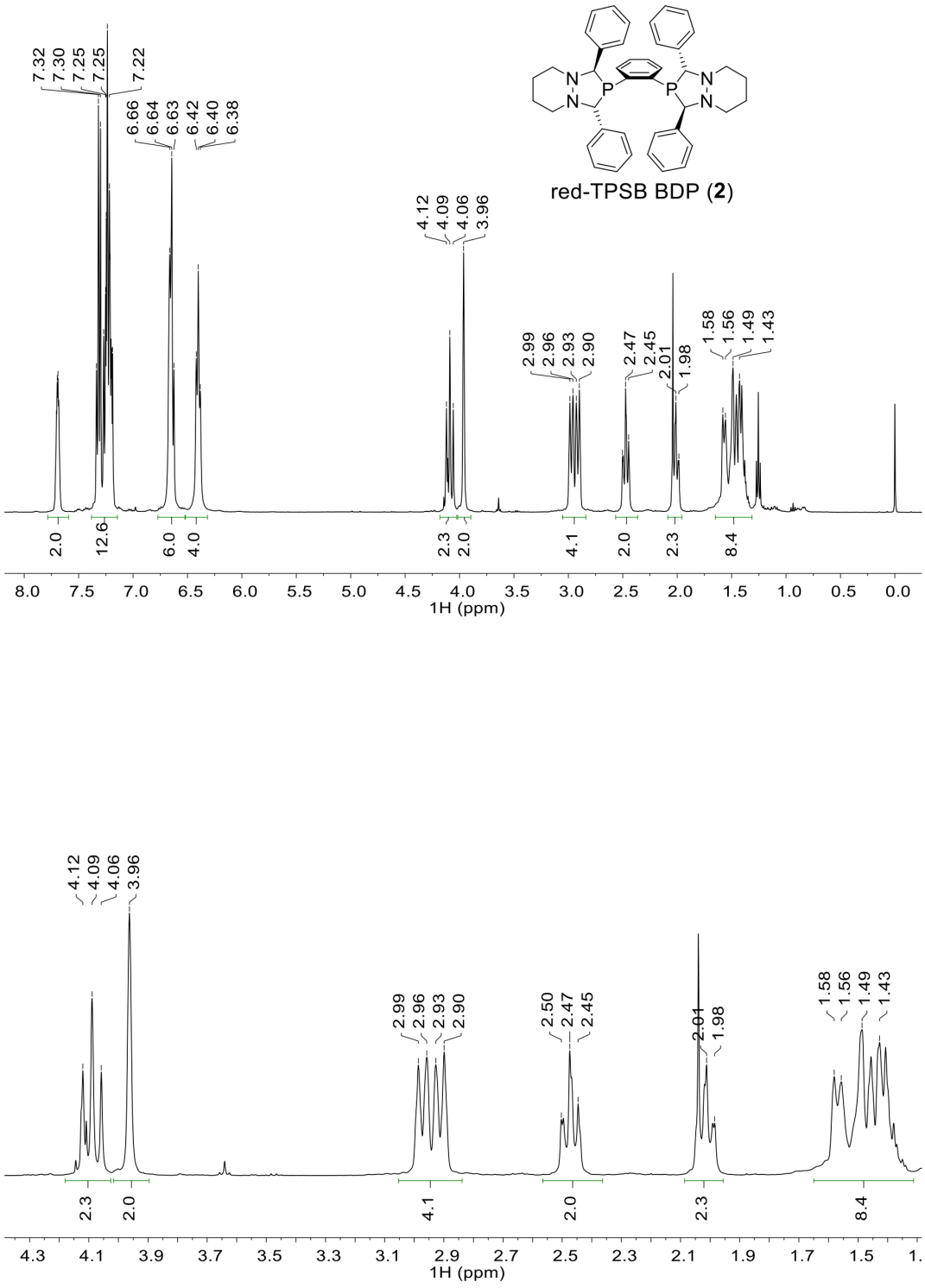

Figure A-84. ^{1}H NMR spectrum (400 MHz) of **2** in $CDCl_3$ (top: full spectrum, bottom: zoom).

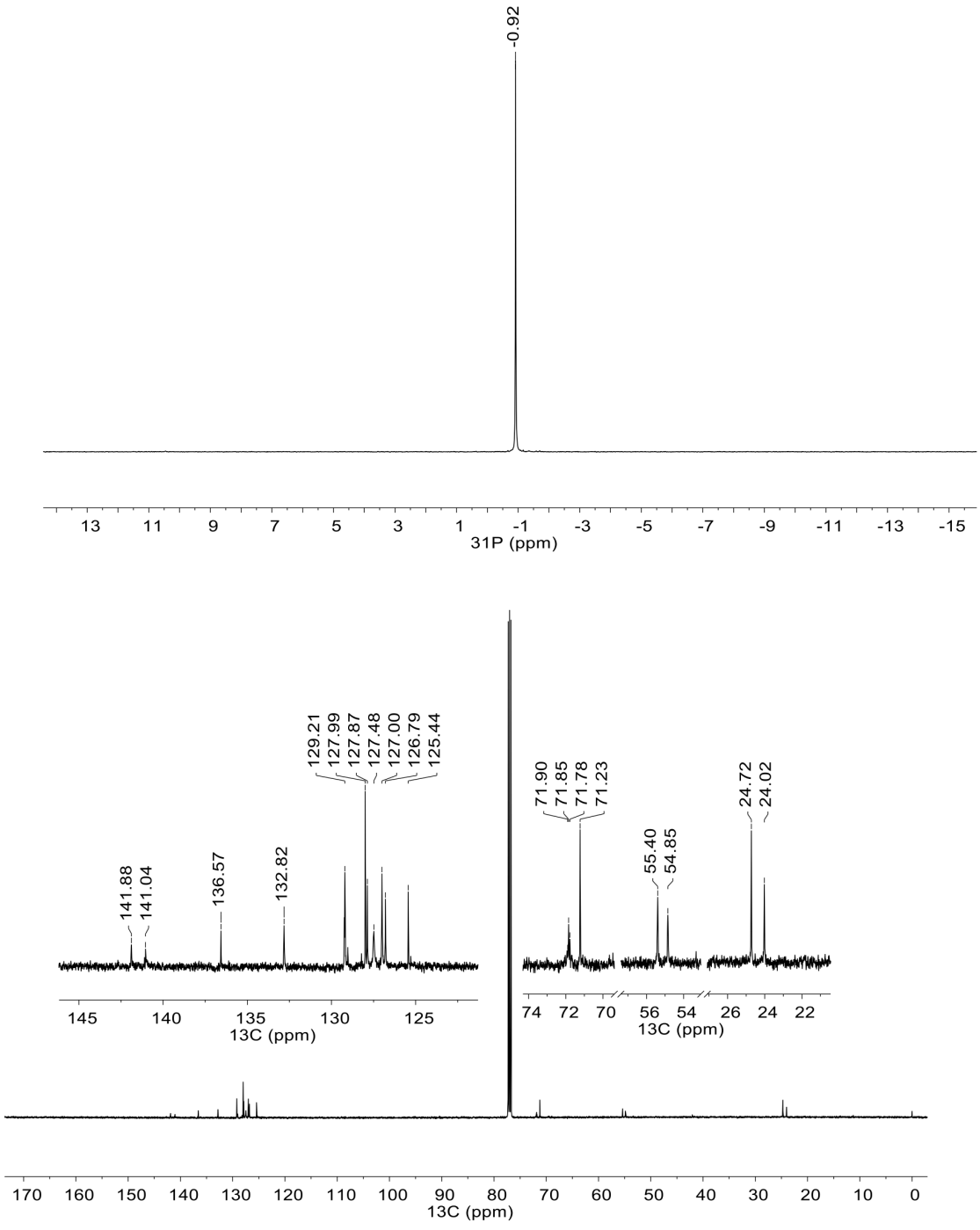

Figure A-85. NMR spectra of **2** in $CDCl_3$ (top: $^{31}P\{^1H\}$ (162 MHz), bottom: $^{13}C\{^1H\}$ (126 MHz)).

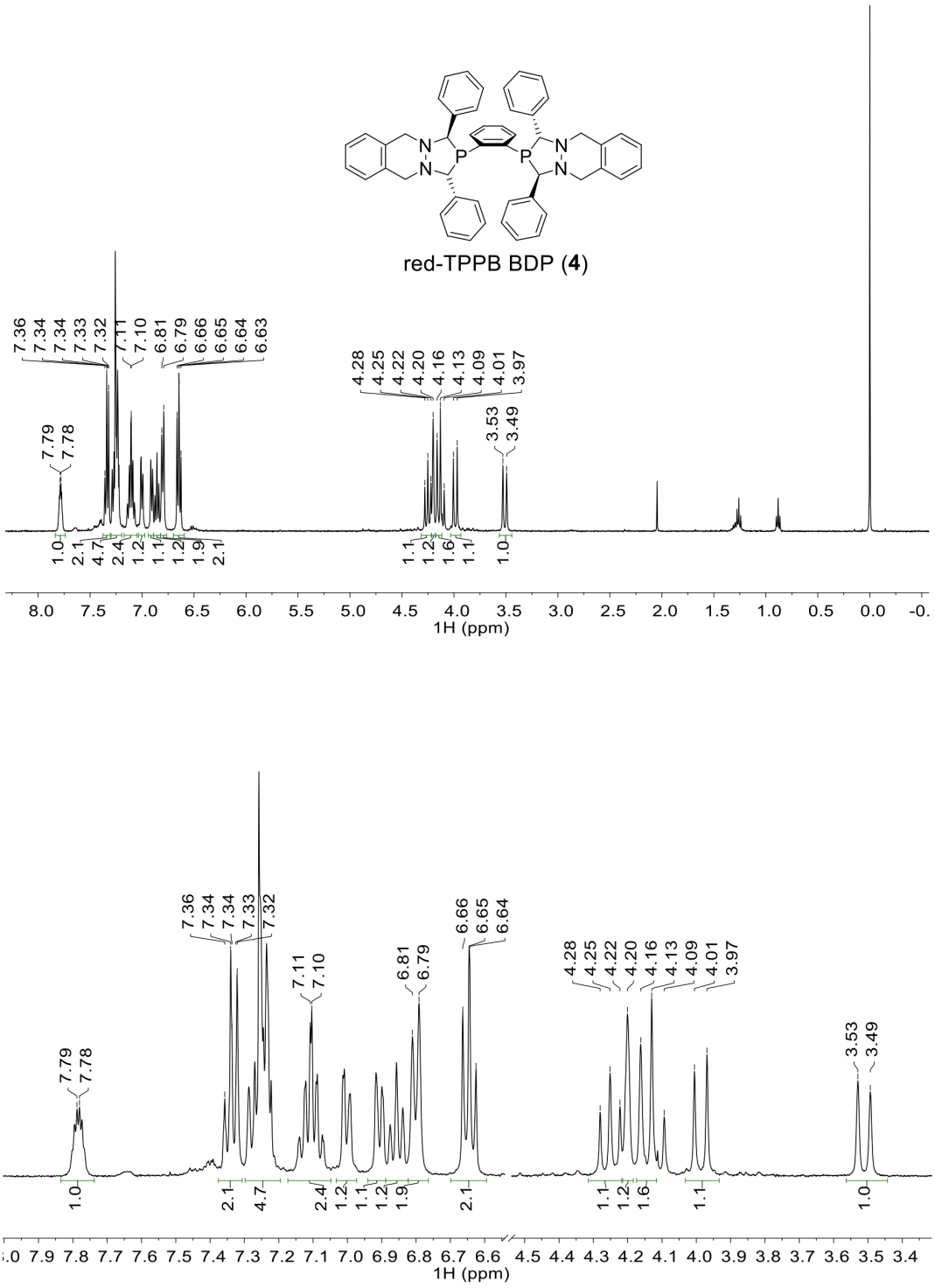

Figure A-86. ^{1}H NMR spectrum (400 MHz) of **4** in $CDCl_3$ (top: full spectrum, bottom: zoom).

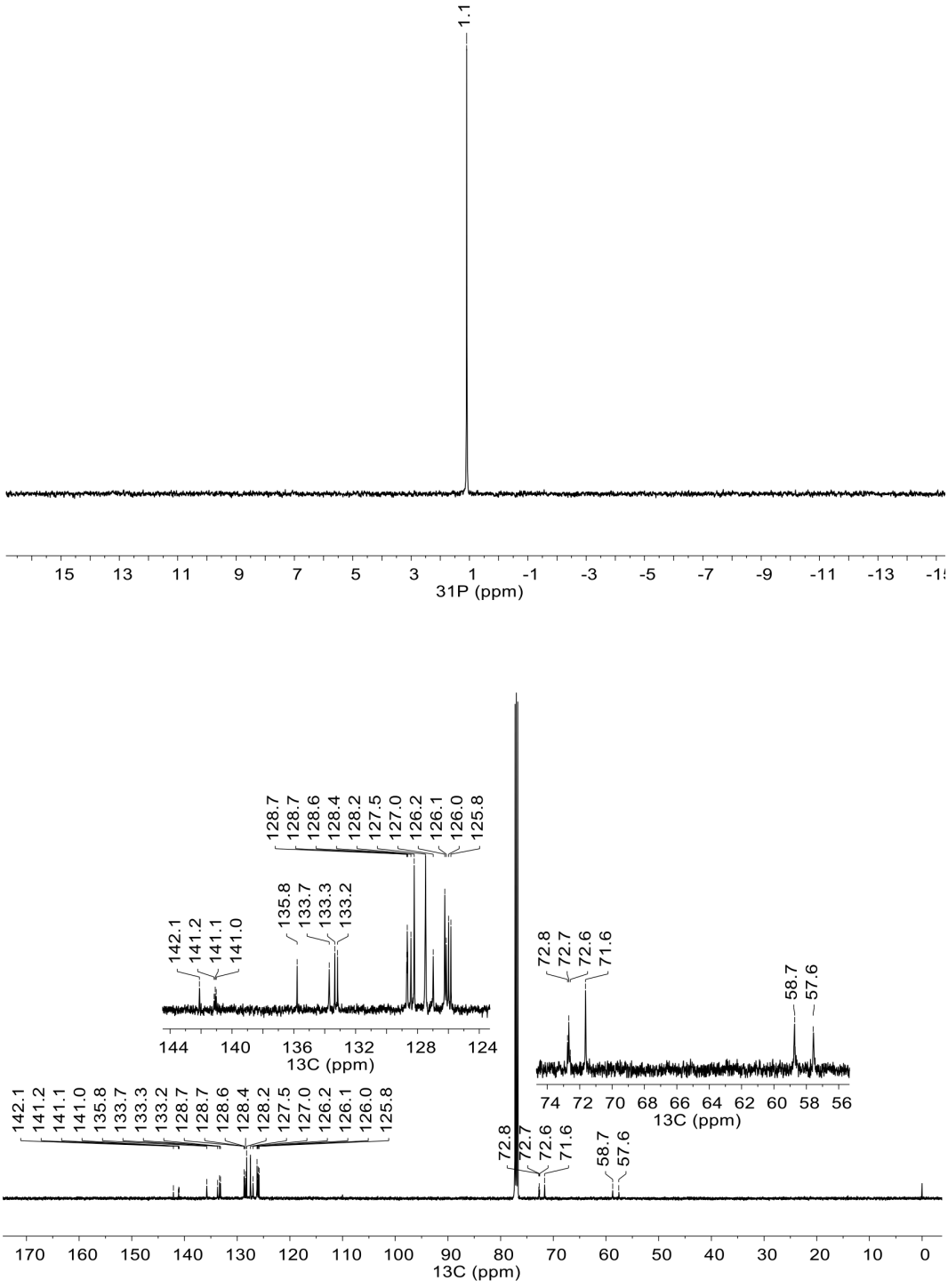

Figure A-87. NMR spectra of **4** in $CDCl_3$ (top: $^{31}P\{^1H\}$ (162 MHz), bottom:$^{13}C\{^1H\}$ (126 MHz)).

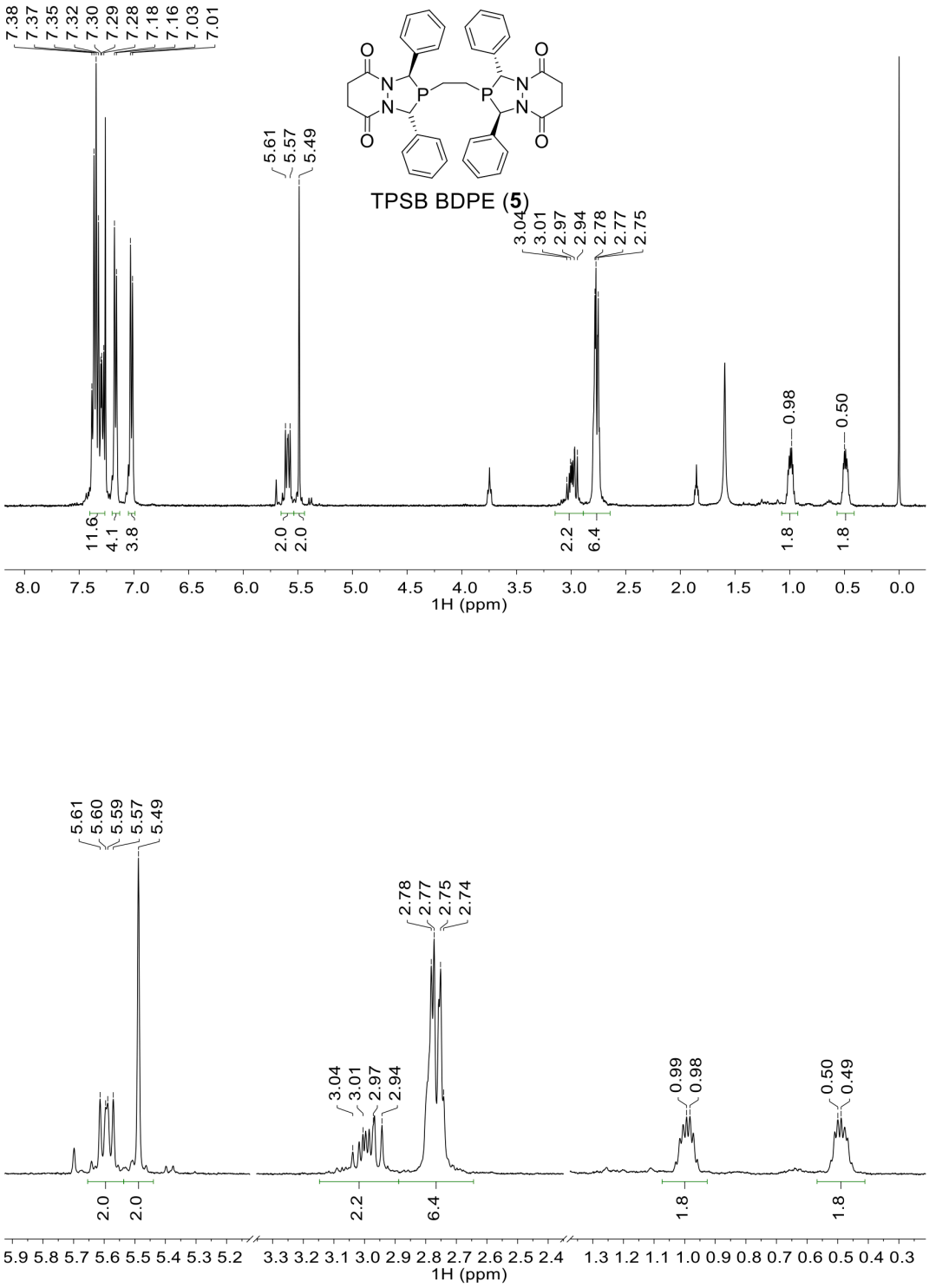

Figure A-88. ^{1}H NMR spectrum (400 MHz) of **5** in $CDCl_3$ (top: full spectrum, bottom: zoom).

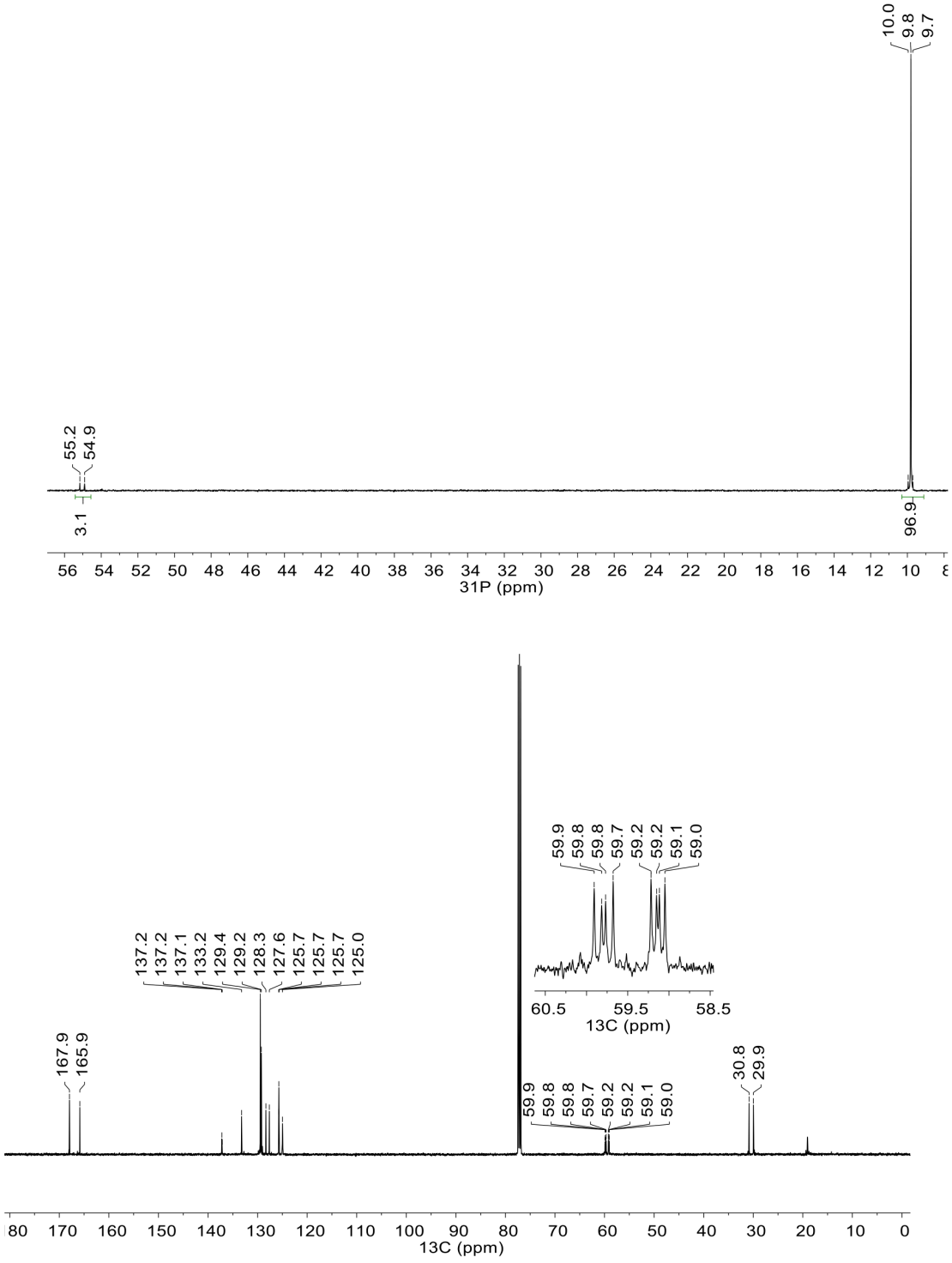

Figure A-89. NMR spectra of **5** in $CDCl_3$ (top: $^{31}P\{^1H\}$ (162 MHz), bottom: $^{13}C\{^1H\}$ (126 MHz)).

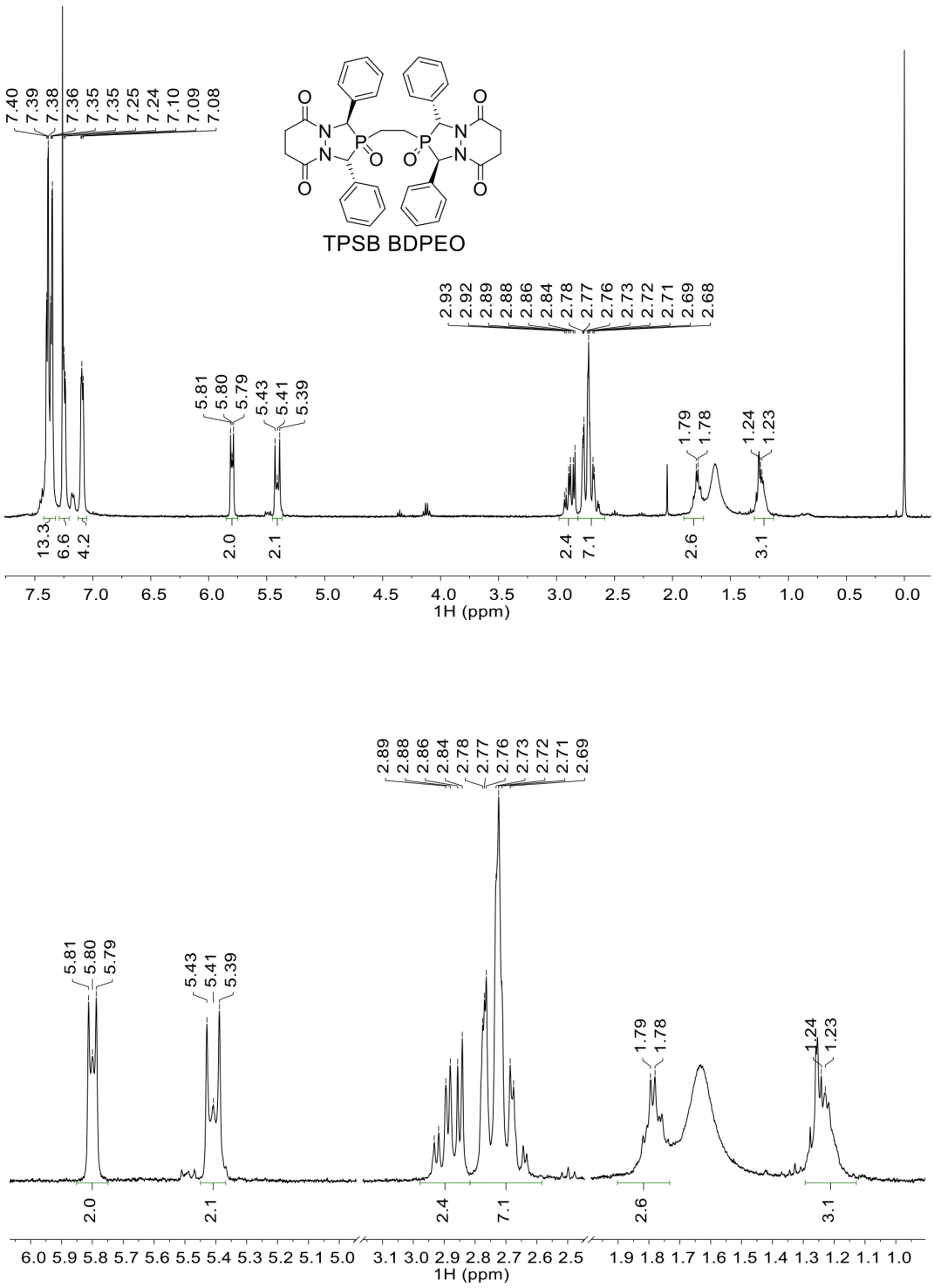

Figure A-90. ^{1}H NMR spectrum (400 MHz) of TPSB BDPEO in $CDCl_3$ (top: full spectrum, bottom: zoom).

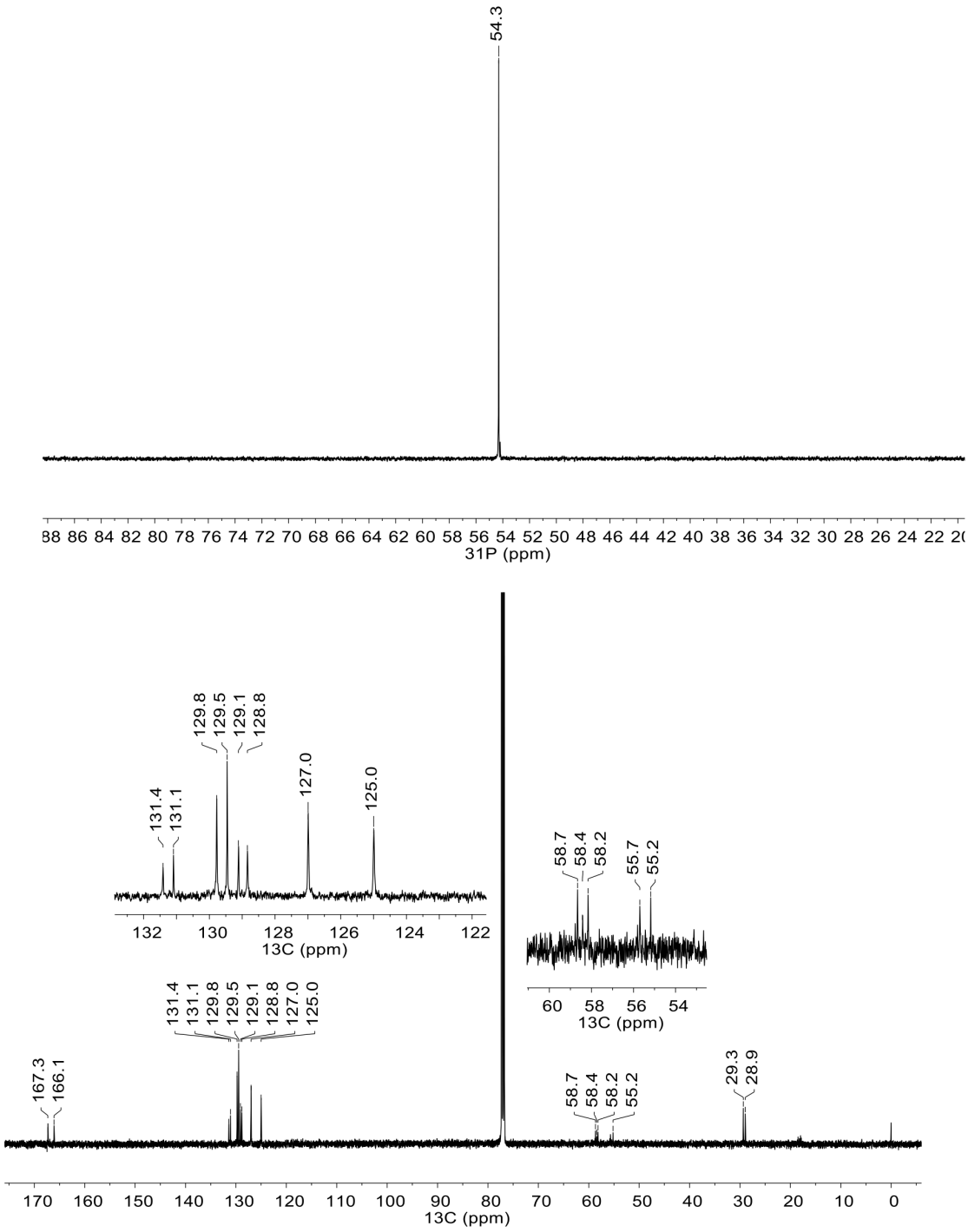

Figure A-91. NMR spectra of TPSB BDPEO in $CDCl_3$ (top: $^{31}P\{^1H\}$ (162 MHz), bottom: $^{13}C\{^1H\}$ (126 MHz)).

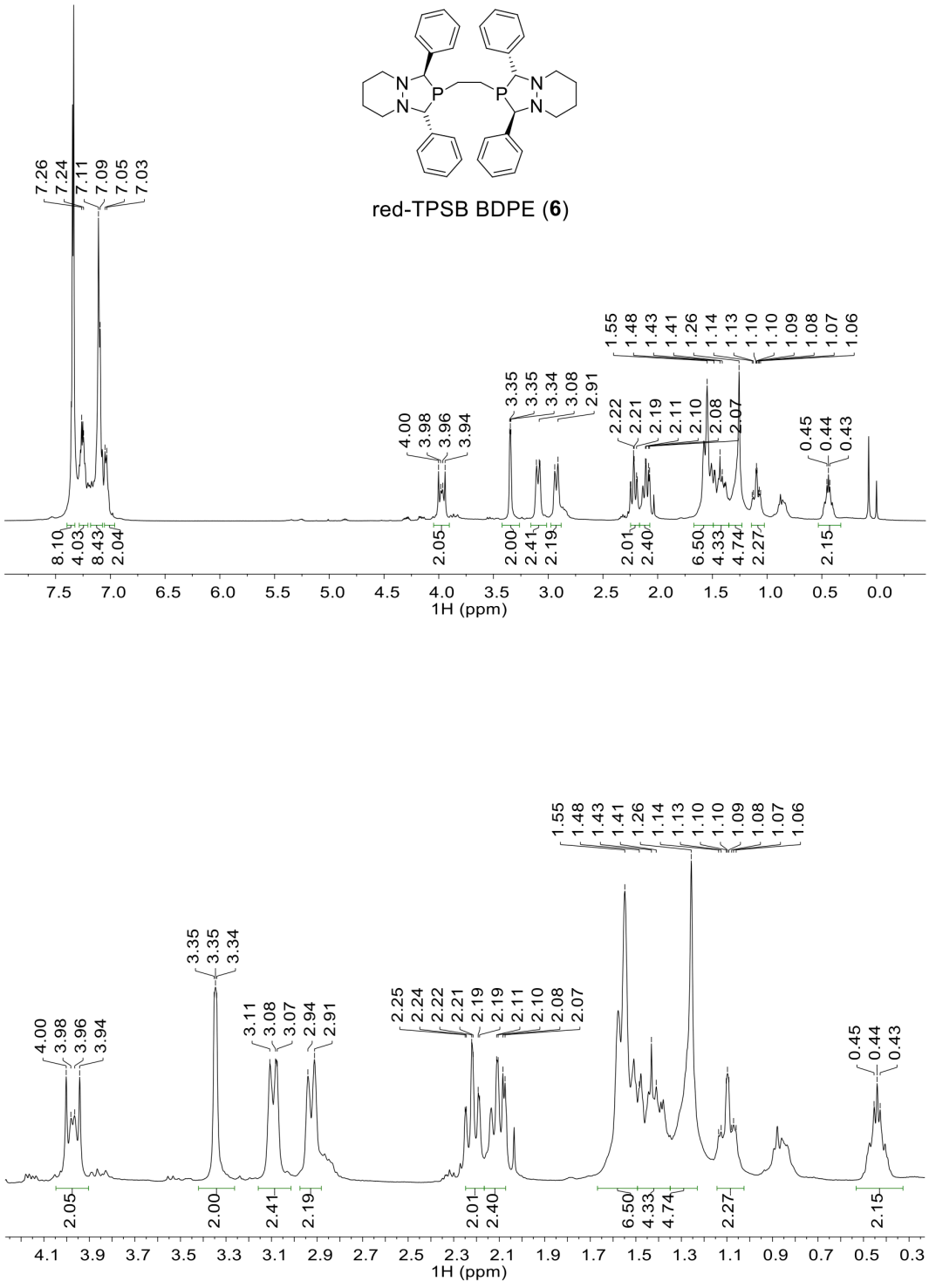

Figure A-92. ^{1}H NMR spectra (400 MHz) of red-TPSB BDPE **6** in $CDCl_3$ (top: full spectrum, bottom: zoom).

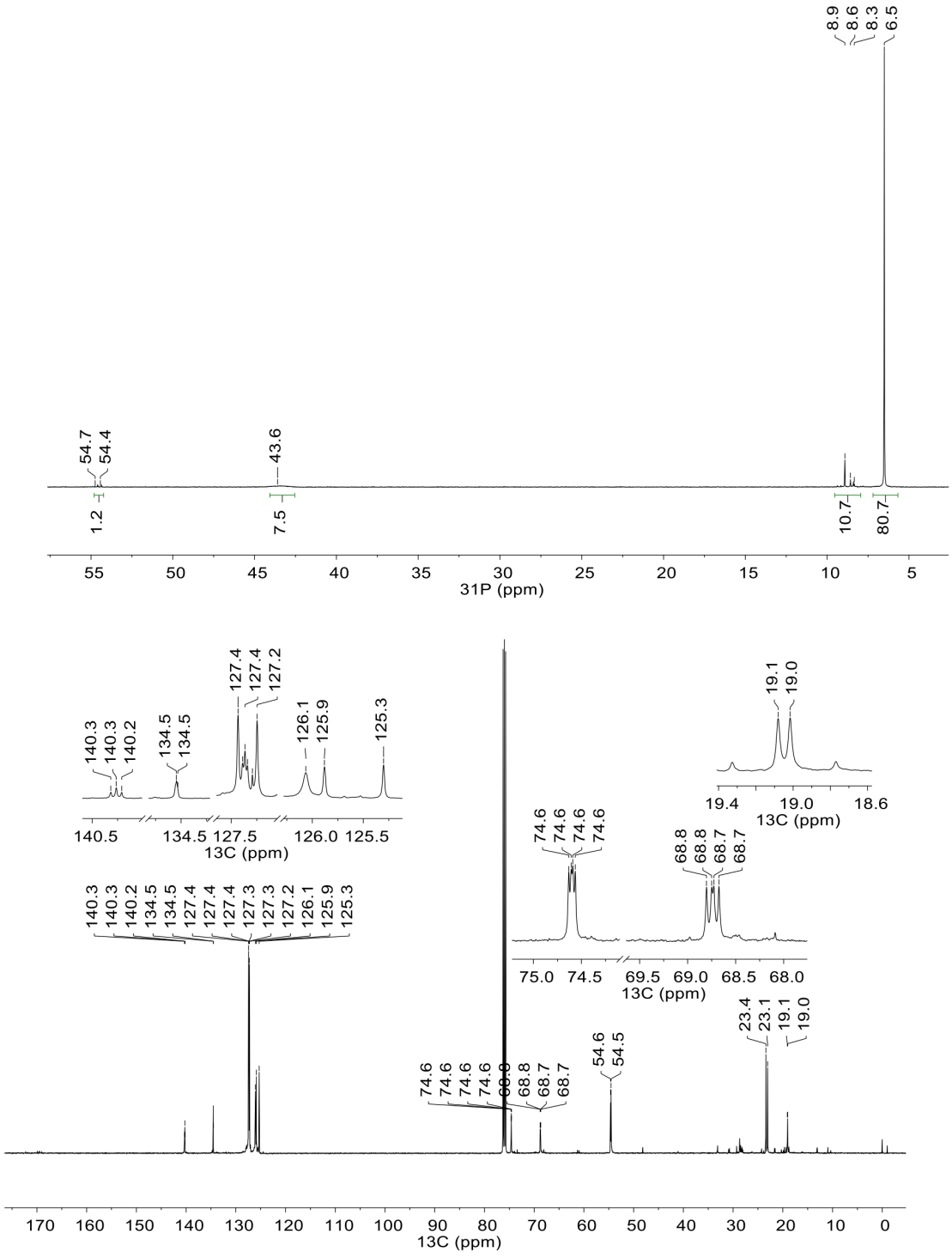

Figure A-93. NMR spectra of red-TPSB BDPE **6** in $CDCl_3$ (top: $^{31}P\{^1H\}$ (162 MHz), bottom: $^{13}C\{^1H\}$ (126 MHz)).

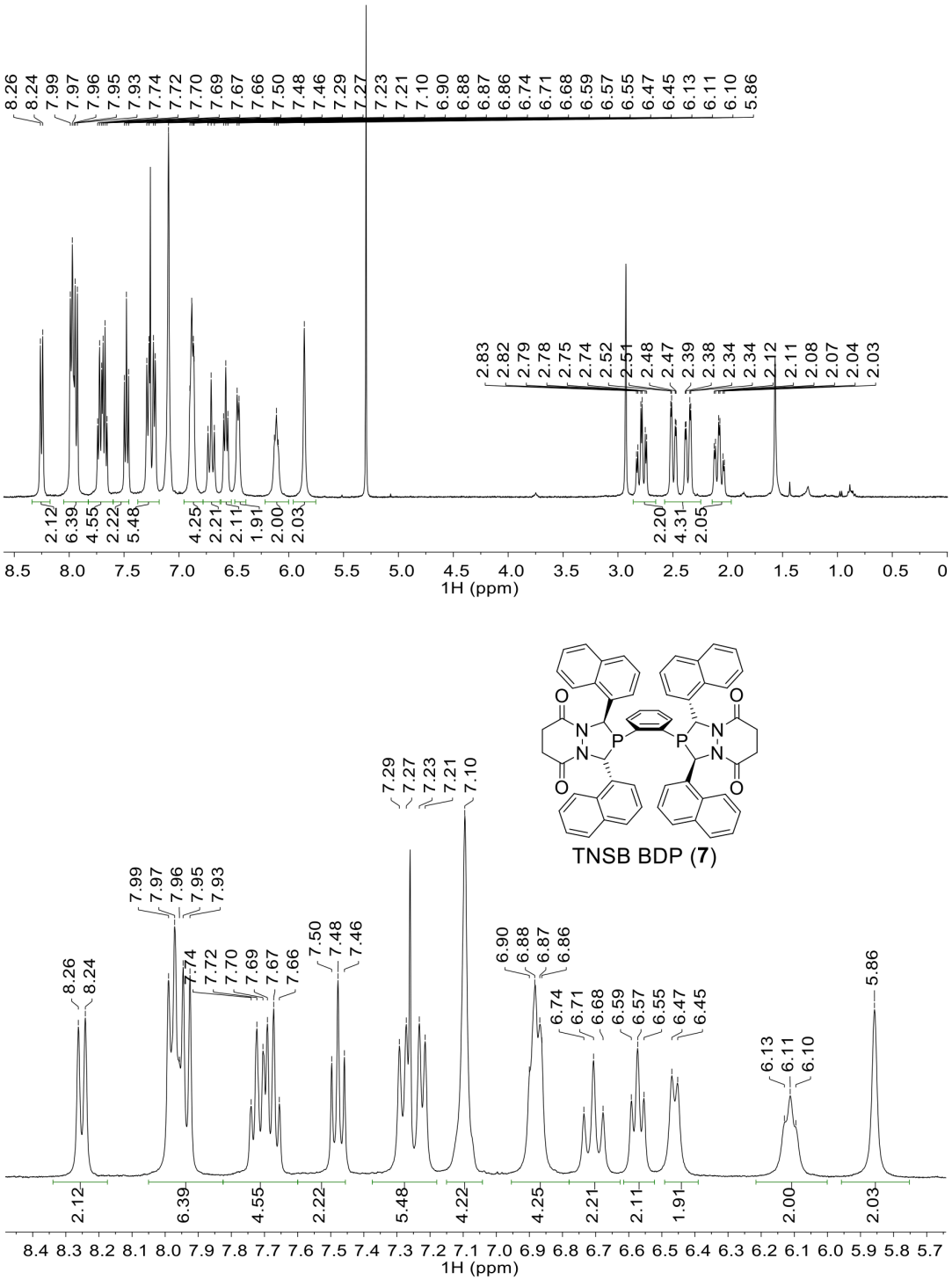

Figure A-94. ^{1}H NMR spectrum (400 MHz) of TNSB BDP **7** in $CDCl_3$ (top: full spectrum, bottom: zoom).

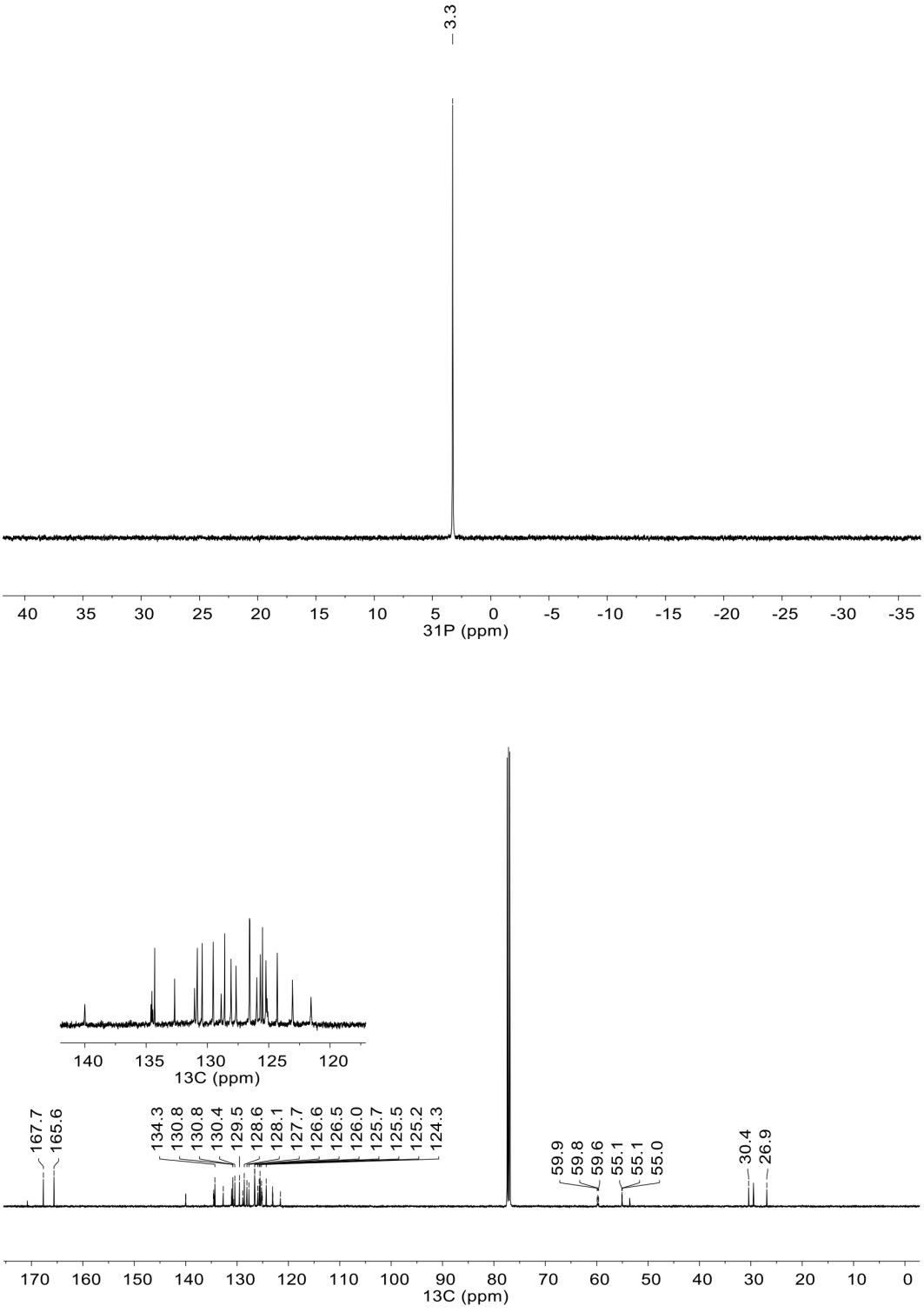

Figure A-95. NMR spectra of TNSB BDP **7** in $CDCl_3$ (top: $^{31}P\{^1H\}$ (162 MHz), bottom: $^{13}C\{^1H\}$ (126 MHz)).

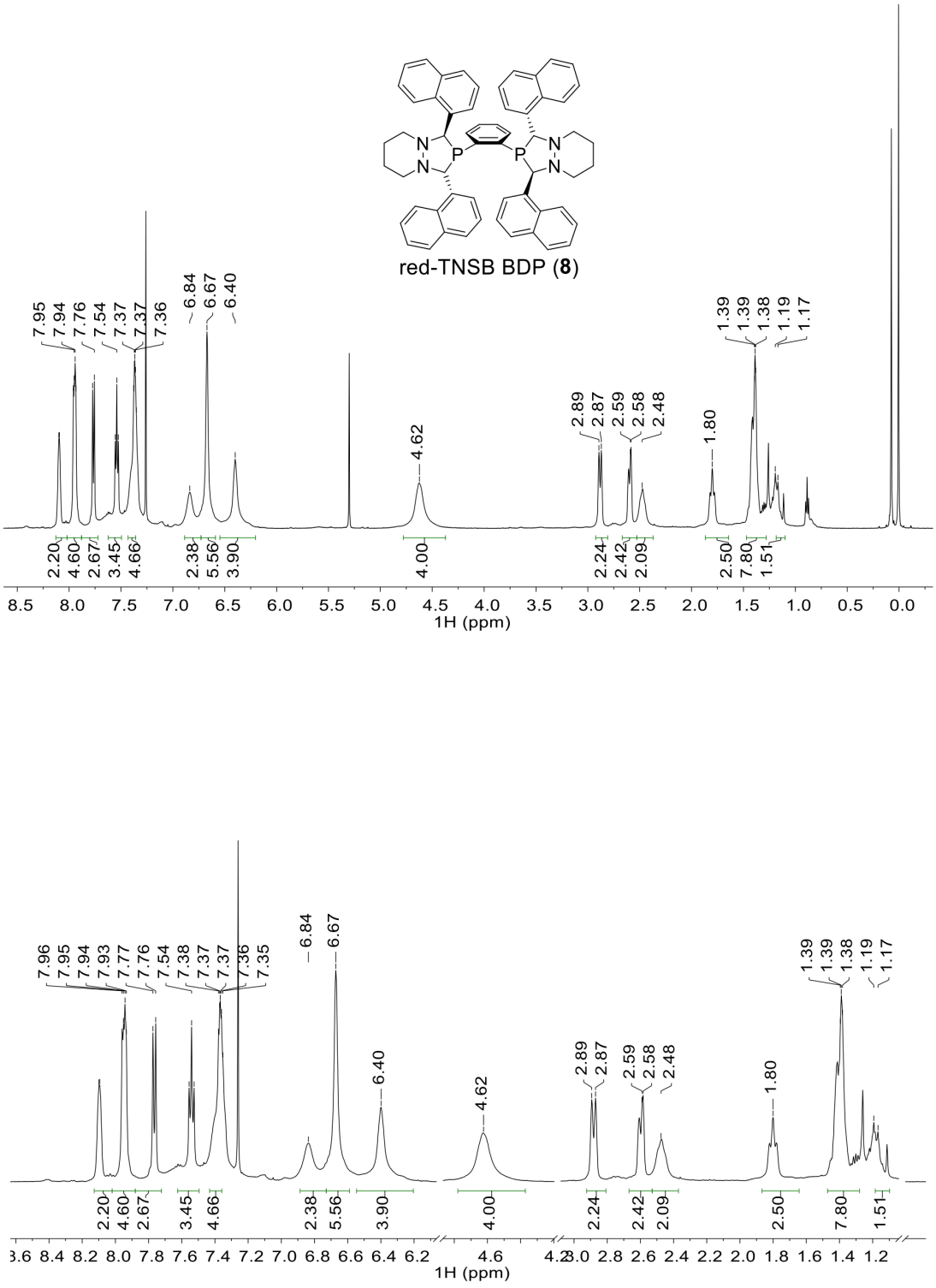

Figure A-96. ^{1}H NMR spectrum (400 MHz) of red-TNSB BDP **8** in $CDCl_3$ (top: full spectrum, bottom: zoom).

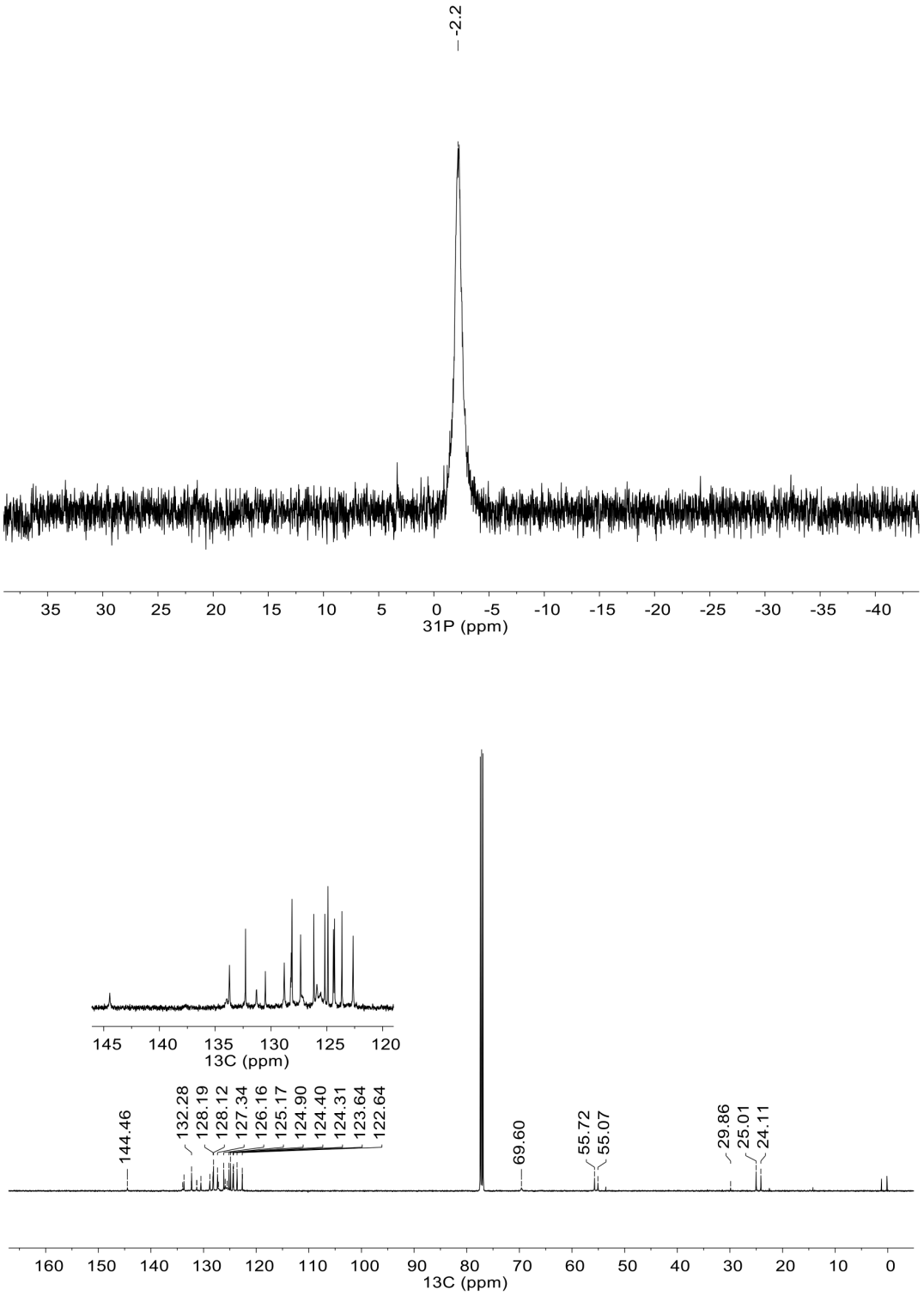

Figure A-97. NMR spectra of red-TNSB BDP **8** in $CDCl_3$ (top:$^{31}P\{^1H\}$ (162 MHz), bottom:$^{13}C\{^1H\}$ (126 MHz)).

Appendix B

Modeling Results for Chapter 5

B.1 Model For Approach 1: General Activation Parameters

B.1.1 Model Set Up

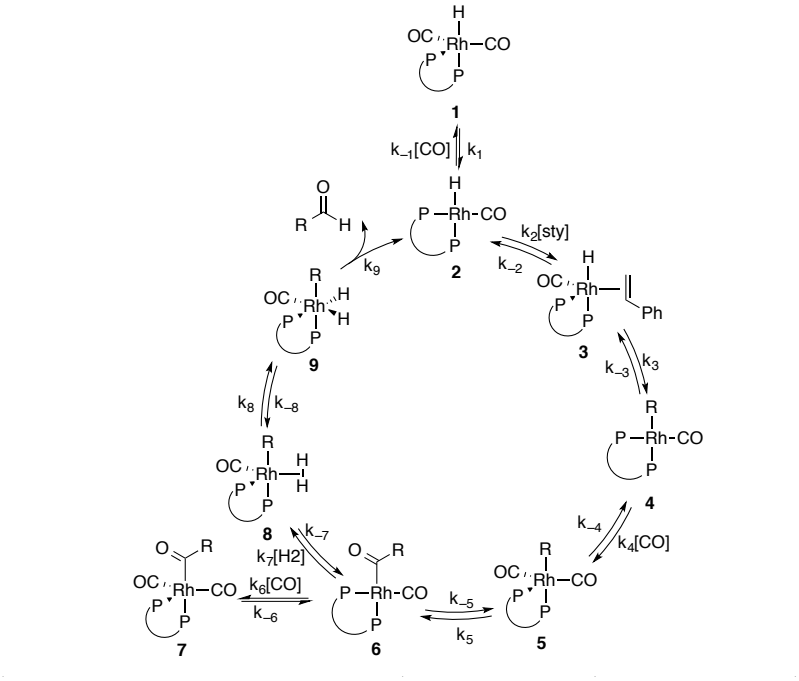

Figure B-1. Model for approach 1: general (non-isomeric) activation parameters.

$$k_1 = 2.0837\times10^{10}(T)e^{-\left(\frac{\text{thermo\_HCO}_2\text{\_COdiss}+\Delta H^{\ddagger}\text{\_barrierless}-(\Delta S^{\ddagger}\text{\_1\_for})(T)}{1.987(T)}\right)}$$

$$k_{-1} = 2.0837\times10^{10}(T)e^{-\left(\frac{\Delta H^{\ddagger}\text{\_barrierless}-(\Delta S^{\ddagger}\text{\_1\_back})(T)}{1.987(T)}\right)}$$

$$k_2 = 2.0837\times10^{10}(T)e^{-\left(\frac{\Delta H^{\ddagger}\text{\_barrierless}-(\Delta S^{\ddagger}\text{\_2\_for})(T)}{1.987(T)}\right)}$$

$$k_{-2} = 2.0837\times10^{10}(T)e^{-\left(\frac{\text{thermo\_sty\_addition}+\Delta H^{\ddagger}\text{\_barrierless}-(\Delta S^{\ddagger}\text{\_2\_back})(T)}{1.987(T)}\right)}$$

$$k_3 = 2.0837\times10^{10}(T)e^{-\left(\frac{\Delta H^{\ddagger}\text{\_insertion}-(\Delta S^{\ddagger}\text{\_3\_for})(T)}{1.987(T)}\right)}$$

$$k_{-3} = 2.0837\times10^{10}(T)e^{-\left(\frac{\text{thermo\_insertion}+\Delta H^{\ddagger}\text{\_insertion}-(\Delta S^{\ddagger}\text{\_3\_back})(T)}{1.987(T)}\right)}$$

$$k_4 = 2.0837\times10^{10}(T)e^{-\left(\frac{\Delta H^{\ddagger}\text{\_barrierless}-(\Delta S^{\ddagger}\text{\_4\_for})(T)}{1.987(T)}\right)}$$

$$k_{-4} = 2.0837\times10^{10}(T)e^{-\left(\frac{\text{thermo\_alkCOaddn}+\Delta H^{\ddagger}\text{\_barrierless}-(\Delta S^{\ddagger}\text{\_4\_back})(T)}{1.987(T)}\right)}$$

$$k_5 = 2.0837\times10^{10}(T)e^{-\left(\frac{\Delta H^{\ddagger}\text{\_COins}-(\Delta S^{\ddagger}\text{\_5\_for})(T)}{1.987(T)}\right)}$$

$$k_{-5} = 2.0837\times10^{10}(T)e^{-\left(\frac{\text{thermo\_COins}+\Delta H^{\ddagger}\text{\_ins}-(\Delta S^{\ddagger}\text{\_5\_back})(T)}{1.987(T)}\right)}$$

$$k_6 = 2.0837\times10^{10}(T)e^{-\left(\frac{\Delta H^{\ddagger}\text{\_barrierless}-(\Delta S^{\ddagger}\text{\_6\_for})(T)}{1.987(T)}\right)}$$

$$k_{-6} = 2.0837\times10^{10}(T)e^{-\left(\frac{\text{thermo\_acylCOaddn}+\Delta H^{\ddagger}\text{\_barrierless}-(\Delta S^{\ddagger}\text{\_6\_back})(T)}{1.987(T)}\right)}$$

$$k_7 = 2.0837\times10^{10}(T)e^{-\left(\frac{\Delta H^{\ddagger}\text{\_barrierless}-(\Delta S^{\ddagger}\text{\_7\_for})(T)}{1.987(T)}\right)}$$

$$k_{-7} = 2.0837\times10^{10}(T)e^{-\left(\frac{\text{thermo\_H2addn}+\Delta H^{\ddagger}\text{\_barrierless}-(\Delta S^{\ddagger}\text{\_7\_back})(T)}{1.987(T)}\right)}$$

$$k_8 = 2.0837\times10^{10}(T)e^{-\left(\frac{\Delta H^{\ddagger}\text{\_barrierless}-(\Delta S^{\ddagger}\text{\_8\_for})(T)}{1.987(T)}\right)}$$

$$k_{-8} = 2.0837\times10^{10}(T)e^{-\left(\frac{\text{thermo\_H2oxadd}+\Delta H^{\ddagger}\text{\_barrierless}-(\Delta S^{\ddagger}\text{\_8\_back})(T)}{1.987(T)}\right)}$$

$$k_9 = 2.0837\times10^{10}(T)e^{-\left(\frac{\Delta H^{\ddagger}\text{\_redelim}-(\Delta S^{\ddagger}\text{\_9\_for})(T)}{1.987(T)}\right)}$$

Figure B-2. List of equations to build general activation model.

Table B-1. Parameters for general activation model (optimized parameters bolded).

Parameter	Value
Enthalpic Barriers	
ΔH‡_barrierless	2000 cal/mol
ΔH‡_insertion	*11293 cal/mol*
ΔH‡_COins	*15028 cal/mol*
ΔH‡_redelim	*15289 cal/mol*
Enthalpic Thermodynamics	
thermo_HCO2_COdiss	16000 cal/mol
thermo_sty_addition	–6000 cal/mol
thermo_insertion	–4500 cal/mol
thermo_alkCOaddn	–10000 cal/mol
thermo_COins	7000 cal/mol
thermo_acylCOaddn	*–16856 cal/mol*
thermo_H2addn	–2000 cal/mol
thermo_H2oxadd	–6000 cal/mol
Entropic Barriers	
ΔS‡_1_for	15 cal·mol^{-1}K^{-1}
ΔS‡_1_back	–15 cal·mol^{-1}K^{-1}
ΔS‡_2for	–15 cal·mol^{-1}K^{-1}
ΔS‡_2back	15 cal·mol^{-1}K^{-1}
ΔS‡_3for	0 cal·mol^{-1}K^{-1}
ΔS‡_3back	0 cal·mol^{-1}K^{-1}
ΔS‡_4for	–15 cal·mol^{-1}K^{-1}
ΔS‡_4back	15 cal·mol^{-1}K^{-1}
ΔS‡_5for	0 cal·mol^{-1}K^{-1}
ΔS‡_5back	0 cal·mol^{-1}K^{-1}
ΔS‡_6for	–15 cal·mol^{-1}K^{-1}
ΔS‡_6back	15 cal·mol^{-1}K^{-1}
ΔS‡_7for	–15 cal·mol^{-1}K^{-1}
ΔS‡_7back	15 cal·mol^{-1}K^{-1}
ΔS‡_8for	0 cal·mol^{-1}K^{-1}
ΔS‡_8back	0 cal·mol^{-1}K^{-1}
ΔS‡_9for	15 cal·mol^{-1}K^{-1}

B.1.2 Fits of Catalytic Data

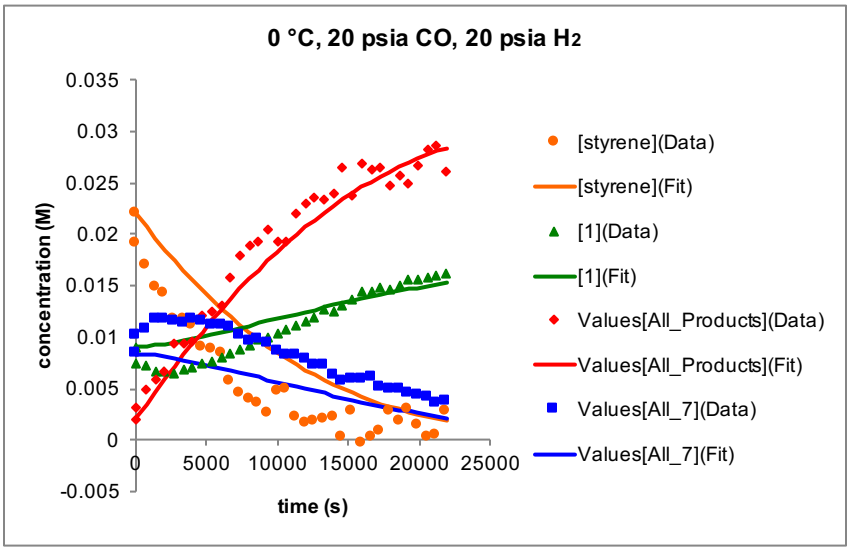

Figure B-3. Data and fit of catalytic reaction at 0 °C using general activation model (points indicate data, lines indicate fit). (25 mM styrene, 20 mM Rh(BDP), 20 psia CO, 20 psia H_2, 273K, CH_2Cl_2).

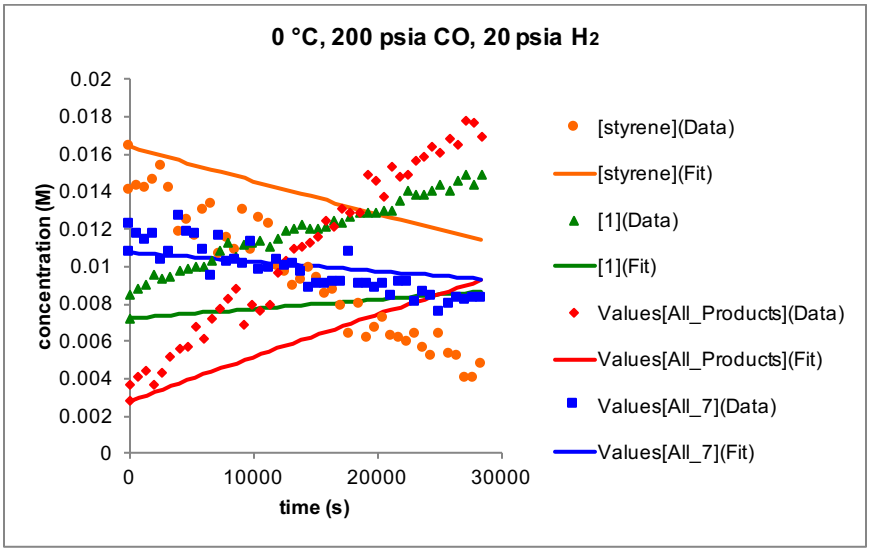

Figure B-4. Data and fit of catalytic reaction at 0 °C using general activation model (points indicate data, lines indicate fit). (16 mM styrene, 20 mM Rh(BDP), 200 psia CO, 20 psia H_2, 273K, CH_2Cl_2).

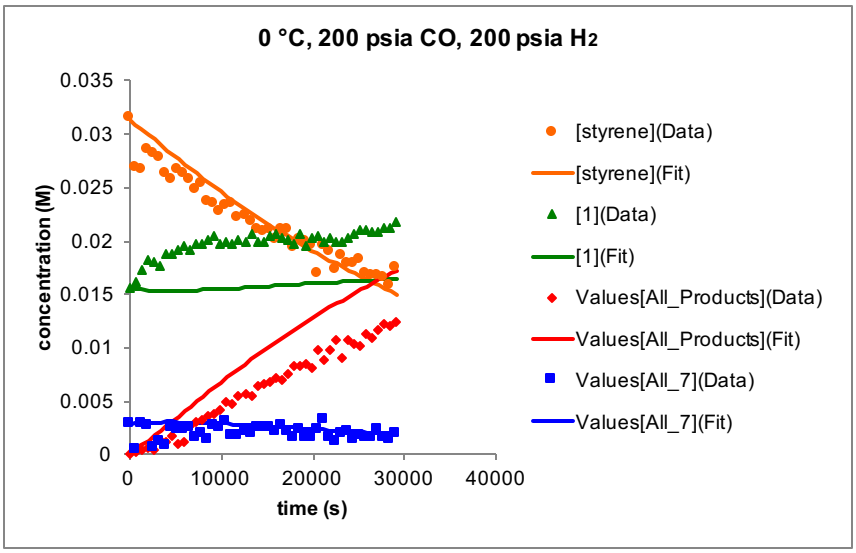

Figure B-5. Data and fit of catalytic reaction at 0 °C using general activation model (points indicate data, lines indicate fit). (30 mM styrene, 20 mM Rh(BDP), 200 psia CO, 200 psia H_2, 273K, CH_2Cl_2).

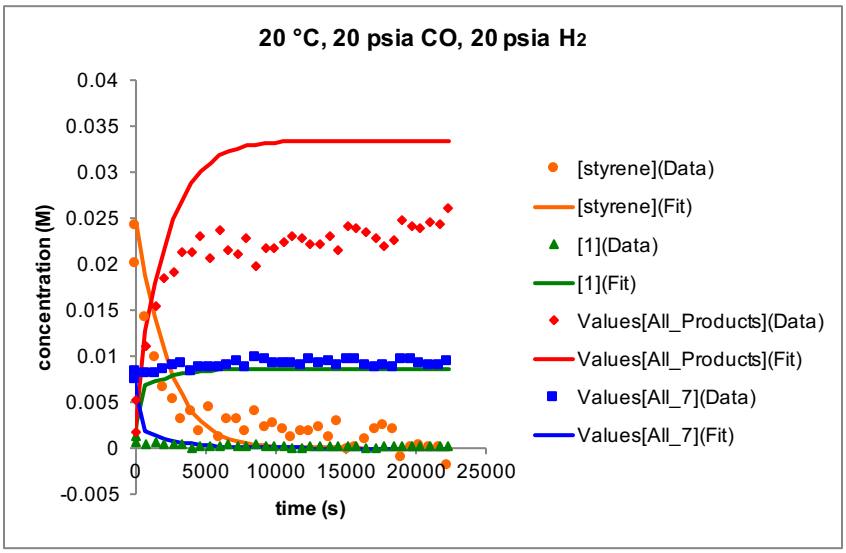

Figure B-6. Data and fit of catalytic reaction at 20 °C using general activation model (points indicate data, lines indicate fit). (25 mM styrene, 10 mM Rh(BDP), 20 psia CO, 20 psia H_2, 293K, CH_2Cl_2).

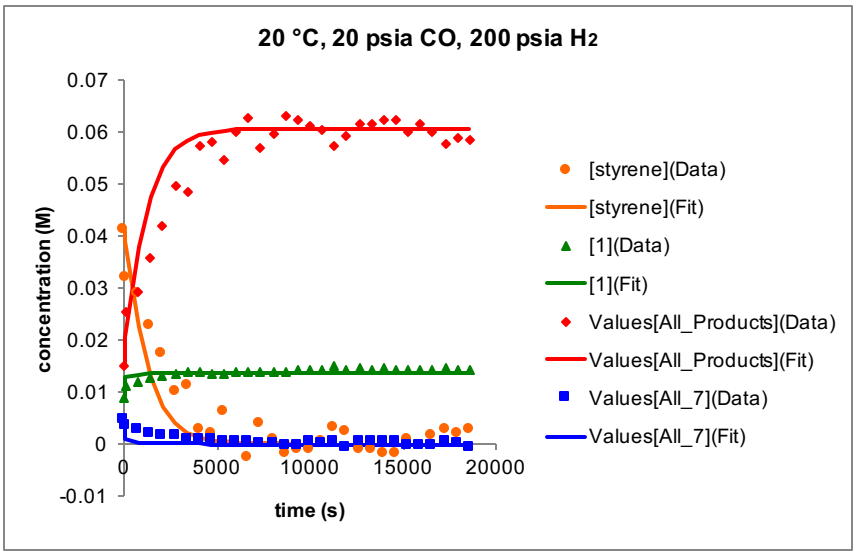

Figure B-7. Data and fit of catalytic reaction at 20 °C using general activation model (points indicate data, lines indicate fit). (40 mM styrene, 15 mM Rh(BDP), 20 psia CO, 200 psia H_2, 293K, CH_2Cl_2).

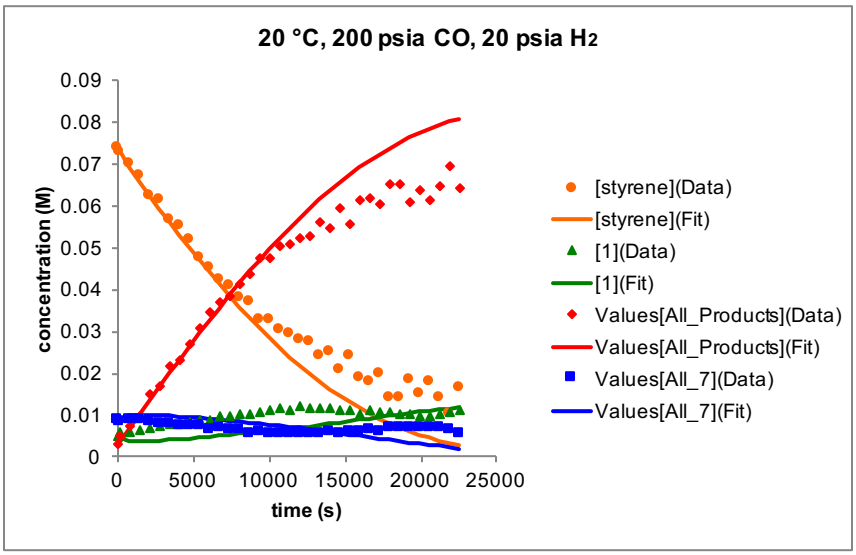

Figure B-8. Data and fit of catalytic reaction at 20 °C using general activation model (points indicate data, lines indicate fit). (75 mM styrene, 10 mM Rh(BDP), 200 psia CO, 20 psia H_2, 293K, CH_2Cl_2).

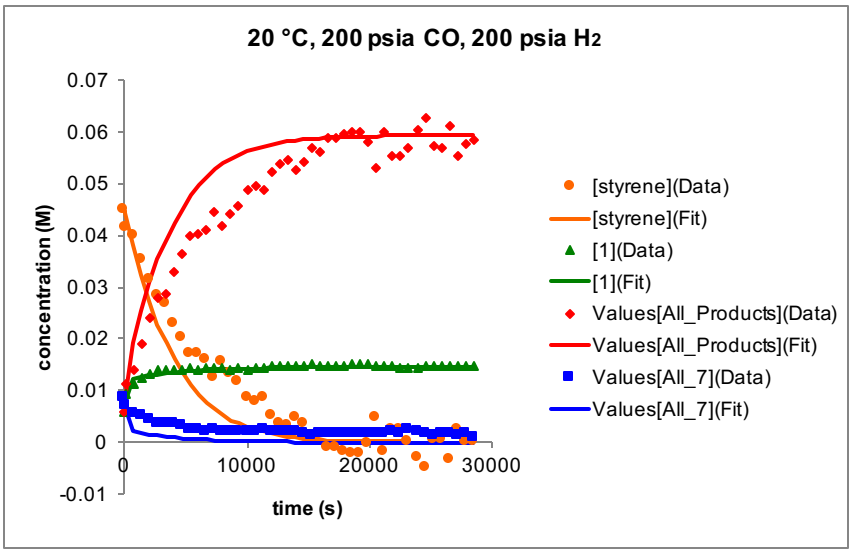

Figure B-9. Data and fit of catalytic reaction at 20 °C using general activation model (points indicate data, lines indicate fit). (45 mM styrene, 12 mM Rh(BDP), 200 psia CO, 200 psia H_2, 293K, CH_2Cl_2).

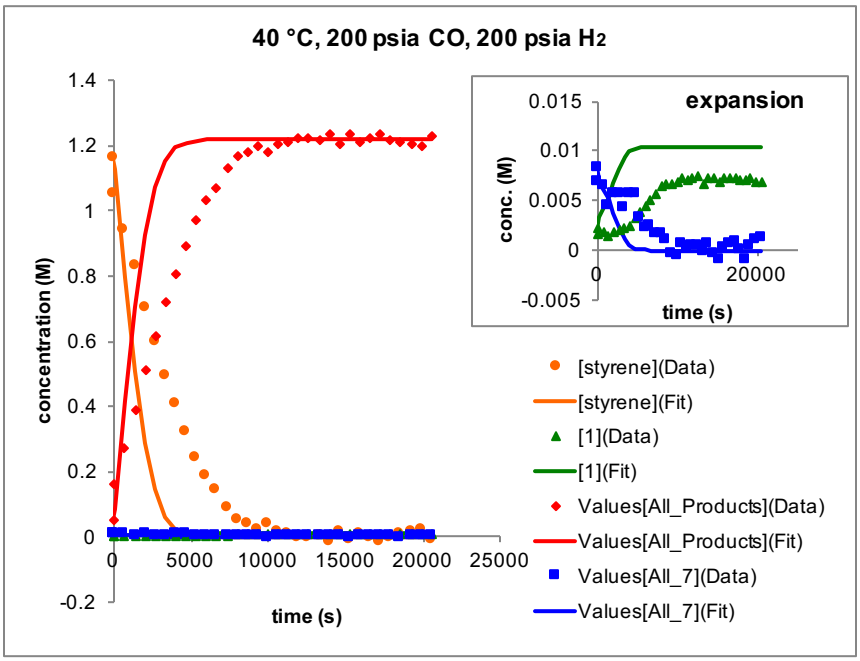

Figure B-10. Data and fit of catalytic reaction at 40 °C using general activation model (points indicate data, lines indicate fit). (1.2 M styrene, 10 mM Rh(BDP), 200 psia CO, 200 psia H_2, 313K, CH_2Cl_2).

B.2 Model for Approach 2: Reintroducing Three Isomeric Pathways

B.2.1 Model Set Up

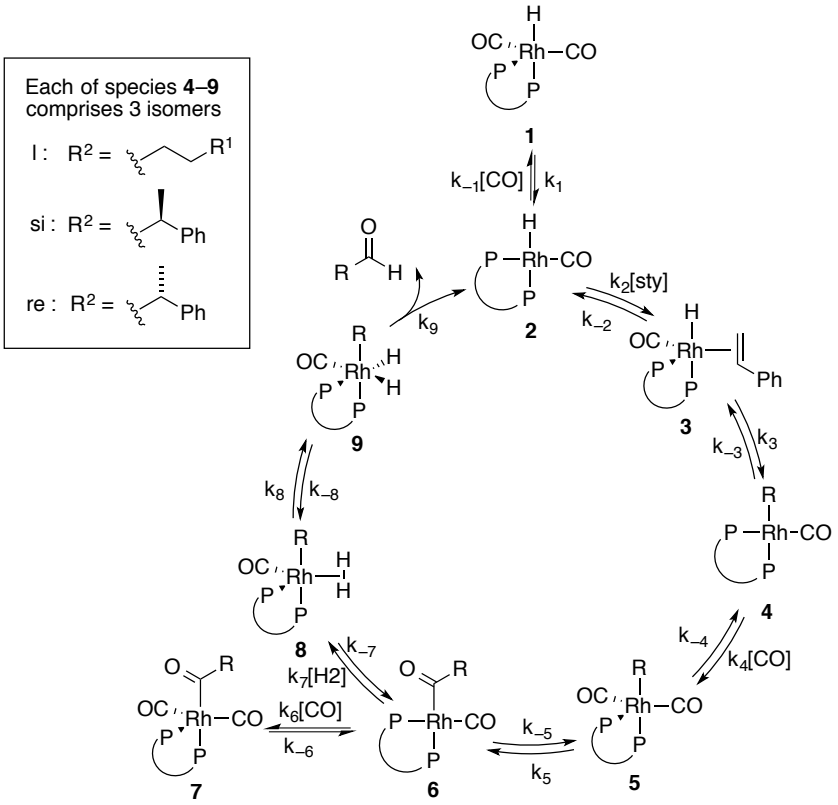

Figure B-11. Model for approach 2: reintroducing isomeric pathways.

$$k_1 = 2.0837 \times 10^{10}(T) e^{-\left(\frac{\text{thermo\_HCO}_2\text{\_COdiss} + \Delta H^{\ddagger}\text{\_barrierless} - (\Delta S^{\ddagger}\text{\_1\_for})(T)}{1.987(T)}\right)}$$

$$k_{-1} = 2.0837 \times 10^{10}(T) e^{-\left(\frac{\Delta H^{\ddagger}\text{\_barrierless} - (\Delta S^{\ddagger}\text{\_1\_back})(T)}{1.987(T)}\right)}$$

$$k_2^{si} = 2.0837 \times 10^{10}(T) e^{-\left(\frac{\Delta H\ddagger\text{\_barrierless} - (\Delta S\ddagger\text{\_2si\_for})(T)}{1.987(T)}\right)}$$

$$k_2^{re} = 2.0837 \times 10^{10}(T) e^{-\left(\frac{\Delta H\ddagger\text{\_barrierless} - (\Delta S\ddagger\text{\_2re\_for})(T)}{1.987(T)}\right)}$$

$$k_{-2}^{si} = 2.0837 \times 10^{10}(T) e^{-\left(\frac{\text{thermo\_sty\_addn\_si} + \Delta H\ddagger\text{\_barrierless} - (\Delta S\ddagger\text{\_2si\_back})(T)}{1.987(T)}\right)}$$

$$k_{-2}^{re} = 2.0837 \times 10^{10}(T) e^{-\left(\frac{\text{thermo\_sty\_addn\_re} + \Delta H\ddagger\text{\_barrierless} - (\Delta S\ddagger\text{\_2re\_back})(T)}{1.987(T)}\right)}$$

$$k_3^{si\_to\_si} = 2.0837 \times 10^{10}(T) e^{-\left(\frac{\Delta H\ddagger\text{\_insertion\_sisi} - (\Delta S\ddagger\text{\_3sisi\_for})(T)}{1.987(T)}\right)}$$

$$k_3^{si\_to\_l} = 2.0837 \times 10^{10}(T) e^{-\left(\frac{\Delta H\ddagger\text{\_insertion\_sil} - (\Delta S\ddagger\text{\_3sil\_for})(T)}{1.987(T)}\right)}$$

$$k_3^{re\_to\_re} = 2.0837 \times 10^{10}(T) e^{-\left(\frac{\Delta H\ddagger\text{\_insertion\_rere} - (\Delta S\ddagger\text{\_3rere\_for})(T)}{1.987(T)}\right)}$$

$$k_3^{re\_to\_l} = 2.0837 \times 10^{10}(T) e^{-\left(\frac{\Delta H\ddagger\text{\_insertion\_rel} - (\Delta S\ddagger\text{\_3rel\_for})(T)}{1.987(T)}\right)}$$

$$k_{-3}^{si\_to\_si} = 2.0837 \times 10^{10}(T) e^{-\left(\frac{\text{thermo\_insertion\_sisi} + \Delta H\ddagger\text{\_insertion\_sisi} - (\Delta S\ddagger\text{\_3sisi\_back})(T)}{1.987(T)}\right)}$$

$$k_{-3}^{si\_to\_l} = 2.0837 \times 10^{10}(T) e^{-\left(\frac{\text{thermo\_insertion\_sil} + \Delta H\ddagger\text{\_insertion\_sil} - (\Delta S\ddagger\text{\_3sil\_back})(T)}{1.987(T)}\right)}$$

$$k_{-3}^{re\_to\_re} = 2.0837 \times 10^{10}(T) e^{-\left(\frac{\text{thermo\_insertion\_rere} + \Delta H\ddagger\text{\_insertion\_rere} - (\Delta S\ddagger\text{\_3rere\_back})(T)}{1.987(T)}\right)}$$

$$k_{-3}^{re\_to\_l} = 2.0837 \times 10^{10}(T) e^{-\left(\frac{\text{thermo\_insertion\_rel} + \Delta H\ddagger\text{\_insertion\_rel} - (\Delta S\ddagger\text{\_3rel\_back})(T)}{1.987(T)}\right)}$$

Figure B-12. List of equations for k_1–k_3 to build kinetic model reintroducing isomeric pathways.

$$k_4^{si}=2.0837x10^{10}(T)e^{-\left(\frac{\Delta H‡\_barrierless-(\Delta S‡\_4si\_for)(T)}{1.987(T)}\right)}$$

$$k_4^{re}=2.0837x10^{10}(T)e^{-\left(\frac{\Delta H‡\_barrierless-(\Delta S‡\_4re\_for)(T)}{1.987(T)}\right)}$$

$$k_4^{I}=2.0837x10^{10}(T)e^{-\left(\frac{\Delta H‡\_barrierless-(\Delta S‡\_4I\_for)(T)}{1.987(T)}\right)}$$

$$k_{-4}^{si}=2.0837x10^{10}(T)e^{-\left(\frac{thermo\_alkCOaddn\_si+\Delta H‡\_barrierless-(\Delta S‡\_4si\_back)(T)}{1.987(T)}\right)}$$

$$k_{-4}^{re}=2.0837x10^{10}(T)e^{-\left(\frac{thermo\_alkCOaddn\_re+\Delta H‡\_barrierless-(\Delta S‡\_4re\_back)(T)}{1.987(T)}\right)}$$

$$k_{-4}^{I}=2.0837x10^{10}(T)e^{-\left(\frac{thermo\_alkCOaddn\_I+\Delta H‡\_barrierless-(\Delta S‡\_4I\_back)(T)}{1.987(T)}\right)}$$

$$k_5^{si}=2.0837x10^{10}(T)e^{-\left(\frac{\Delta H‡\_COins\_si-(\Delta S‡\_5si\_for)(T)}{1.987(T)}\right)}$$

$$k_5^{re}=2.0837x10^{10}(T)e^{-\left(\frac{\Delta H‡\_COins\_re-(\Delta S‡\_5re\_for)(T)}{1.987(T)}\right)}$$

$$k_5^{I}=2.0837x10^{10}(T)e^{-\left(\frac{\Delta H‡\_COins\_I-(\Delta S‡\_5I\_for)(T)}{1.987(T)}\right)}$$

$$k_{-5}^{si}=2.0837x10^{10}(T)e^{-\left(\frac{thermo\_COins\_si+\Delta H‡\_COins\_si-(\Delta S‡\_5si\_back)(T)}{1.987(T)}\right)}$$

$$k_{-5}^{re}=2.0837x10^{10}(T)e^{-\left(\frac{thermo\_COins\_re+\Delta H‡\_COins\_re-(\Delta S‡\_5re\_back)(T)}{1.987(T)}\right)}$$

$$k_{-5}^{I}=2.0837x10^{10}(T)e^{-\left(\frac{thermo\_COins\_I+\Delta H‡\_COins\_I-(\Delta S‡\_5I\_back)(T)}{1.987(T)}\right)}$$

$$k_6^{si}=2.0837x10^{10}(T)e^{-\left(\frac{\Delta H‡\_barrierless-(\Delta S‡\_6si\_for)(T)}{1.987(T)}\right)}$$

$$k_6^{re}=2.0837x10^{10}(T)e^{-\left(\frac{\Delta H‡\_barrierless-(\Delta S‡\_6re\_for)(T)}{1.987(T)}\right)}$$

$$k_6^{I}=2.0837x10^{10}(T)e^{-\left(\frac{\Delta H‡\_barrierless-(\Delta S‡\_6I\_for)(T)}{1.987(T)}\right)}$$

$$k_{-6}^{si}=2.0837x10^{10}(T)e^{-\left(\frac{thermo\_acylCOaddn\_si+\Delta H‡\_barrierless-(\Delta S‡\_6si\_back)(T)}{1.987(T)}\right)}$$

$$k_{-6}^{re}=2.0837x10^{10}(T)e^{-\left(\frac{thermo\_acylCOaddn\_re+\Delta H‡\_barrierless-(\Delta S‡\_6re\_back)(T)}{1.987(T)}\right)}$$

$$k_{-6}^{I}=2.0837x10^{10}(T)e^{-\left(\frac{thermo\_acylCOaddn\_I+\Delta H‡\_barrierless-(\Delta S‡\_6I\_back)(T)}{1.987(T)}\right)}$$

Figure B-13. List of equations for k_4–k_6 to build kinetic model reintroducing isomeric pathways.

$$k_{7}^{si}=2.0837x10^{10}(T)e^{-\left(\frac{\Delta H‡\_barrierless-(\Delta S‡\_7si\_for)(T)}{1.987(T)}\right)}$$

$$k_{7}^{re}=2.0837x10^{10}(T)e^{-\left(\frac{\Delta H‡\_barrierless-(\Delta S‡\_7re\_for)(T)}{1.987(T)}\right)}$$

$$k_{7}^{l}=2.0837x10^{10}(T)e^{-\left(\frac{\Delta H‡\_barrierless-(\Delta S‡\_7l\_for)(T)}{1.987(T)}\right)}$$

$$k_{-7}^{si}=2.0837x10^{10}(T)e^{-\left(\frac{thermo\_H2addn\_si+\Delta H‡\_barrierless-(\Delta S‡\_7si\_back)(T)}{1.987(T)}\right)}$$

$$k_{-7}^{re}=2.0837x10^{10}(T)e^{-\left(\frac{thermo\_H2addn\_re+\Delta H‡\_barrierless-(\Delta S‡\_7re\_back)(T)}{1.987(T)}\right)}$$

$$k_{-7}^{l}=2.0837x10^{10}(T)e^{-\left(\frac{thermo\_H2addn\_l+\Delta H‡\_barrierless-(\Delta S‡\_7l\_back)(T)}{1.987(T)}\right)}$$

$$k_{8}^{si}=2.0837x10^{10}(T)e^{-\left(\frac{\Delta H‡\_barrierless-(\Delta S‡\_8si\_for)(T)}{1.987(T)}\right)}$$

$$k_{8}^{re}=2.0837x10^{10}(T)e^{-\left(\frac{\Delta H‡\_barrierless-(\Delta S‡\_8re\_for)(T)}{1.987(T)}\right)}$$

$$k_{8}^{l}=2.0837x10^{10}(T)e^{-\left(\frac{\Delta H‡\_barrierless-(\Delta S‡\_8l\_for)(T)}{1.987(T)}\right)}$$

$$k_{-8}^{si}=2.0837x10^{10}(T)e^{-\left(\frac{thermo\_H2oxadd\_si+\Delta H‡\_barrierless-(\Delta S‡\_8si\_back)(T)}{1.987(T)}\right)}$$

$$k_{-8}^{re}=2.0837x10^{10}(T)e^{-\left(\frac{thermo\_H2oxadd\_re+\Delta H‡\_barrierless-(\Delta S‡\_8re\_back)(T)}{1.987(T)}\right)}$$

$$k_{-8}^{l}=2.0837x10^{10}(T)e^{-\left(\frac{thermo\_H2oxadd\_l+\Delta H‡\_barrierless-(\Delta S‡\_8l\_back)(T)}{1.987(T)}\right)}$$

$$k_{9}^{si}=2.0837x10^{10}(T)e^{-\left(\frac{\Delta H‡\_redelim\_si-(\Delta S‡\_9si\_for)(T)}{1.987(T)}\right)}$$

$$k_{9}^{re}=2.0837x10^{10}(T)e^{-\left(\frac{\Delta H‡\_redelim\_re-(\Delta S‡\_9re\_for)(T)}{1.987(T)}\right)}$$

$$k_{9}^{l}=2.0837x10^{10}(T)e^{-\left(\frac{\Delta H‡\_redelim\_l-(\Delta S‡\_9l\_for)(T)}{1.987(T)}\right)}$$

Figure B-14. List of equations for k_7–k_9 to build kinetic model reintroducing isomeric pathways.

B.3 Model for Approach 3: Simplifying the Kinetic Model

B.3.1 Model Set Up

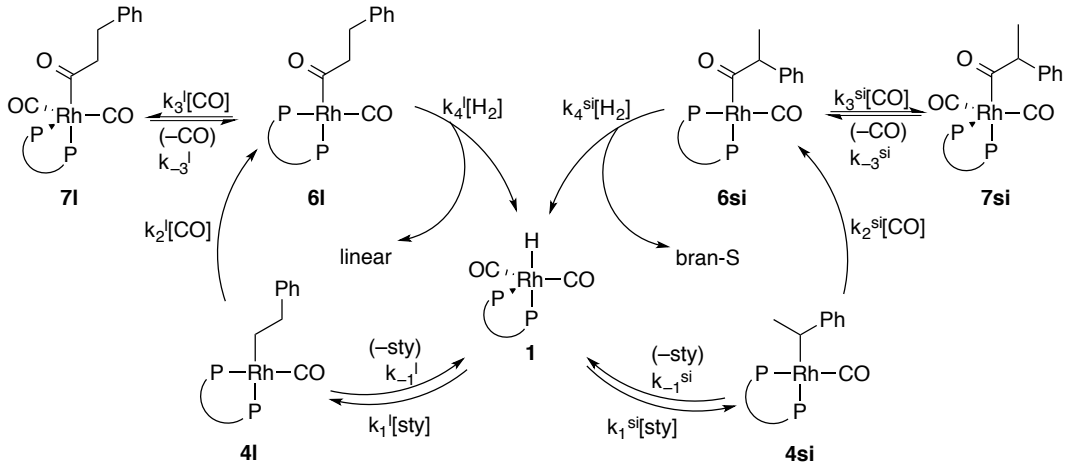

Figure B-15. Model for approach 3: simplifying the kinetic model.

Table B-2. Set and optimized parameters for simplified model at 17 °C.

Parameter	Value	Set or Optimized?
k_1^{si}	1.56(2) x10^{-3} M^{-1}s^{-1}	optimized
k_{-1}^{si}	6.4(6)x10^{-2} s^{-1}	optimized
k_1^l	3.7(1)x10^{-5} M^{-1}s^{-1}	optimized
k_{-1}^l	0 s^{-1}	optimized
k_2^{si}	16.25 s^{-1} M^{-1}s^{-1}	set (fast relative to **4si** formation)
k_2^l	2.022 s^{-1} M^{-1}s^{-1}	set (fast relative to **4l** formation)
k_3^{si}	3.0x10^7 M^{-1}s^{-1}	set relative k_4^{si}
k_{-3}^{si}	0.0188 s^{-1}	set from independent measure
k_3^l	7.2x10^7 M^{-1}s^{-1}	set relative k_4^l
k_{-3}^l	0.0079 s^{-1}	set from independent measure
k_4^{si}	8.5x10^6 M^{-1}s^{-1}	set (fast)
k_4^l	8.5x10^6 M^{-1}s^{-1}	set (fast)

Table 3. Set and optimized parameters for simplified model at 40 °C.

Parameter	Value	Set or Optimized?
k_1^{si}	$1.5(1)\times10^{-3}$ $M^{-1}s^{-1}$	optimized
k_{-1}^{si}	0.03 ± 0.1 s^{-1}	optimized
k_1^{I}	$1.7(2)\times10^{-4}$ $M^{-1}s^{-1}$	optimized
k_{-1}^{I}	0 s^{-1}	set
k_2^{si}	4 ± 15 $M^{-1}s^{-1}$	optimized
k_2^{I}	$0.13(5)$ s^{-1}	optimized
k_3^{si}	2.1×10^{4}	set based on k_4^{si} (assumed same ratio as measured at 17 °C)
k_{-3}^{si}	$2\times10^{5} \pm 1\times10^{7}$ s^{-1}	optimized
k_3^{I}	1.5×10^{5}	set based on k_4^{I} (assumed same ratio as measured at 17 °C)
k_{-3}^{I}	$1\times10^{5} \pm 7\times10^{6}$ s^{-1}	optimized
k_4^{si}	$6\times10^{3} \pm 3\times10^{5}$ $M^{-1}s^{-1}$	optimized
k_4^{I}	$2\times10^{4} \pm 8\times10^{5}$ $M^{-1}s^{-1}$	optimized

B.3.2 Fits of Catalytic Data

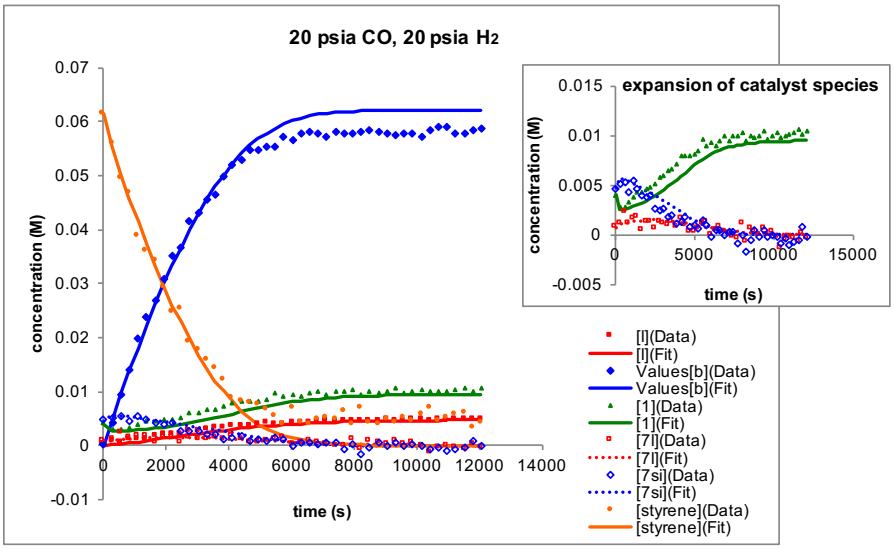

Figure B-16. Data and fit of catalytic reaction at 17 °C using simplified model (3) (points indicate data, lines indicate fit). (60 mM styrene, 10 mM Rh(BDP), 20 psia CO, 20 psia H_2, 290K, CH_2Cl_2).

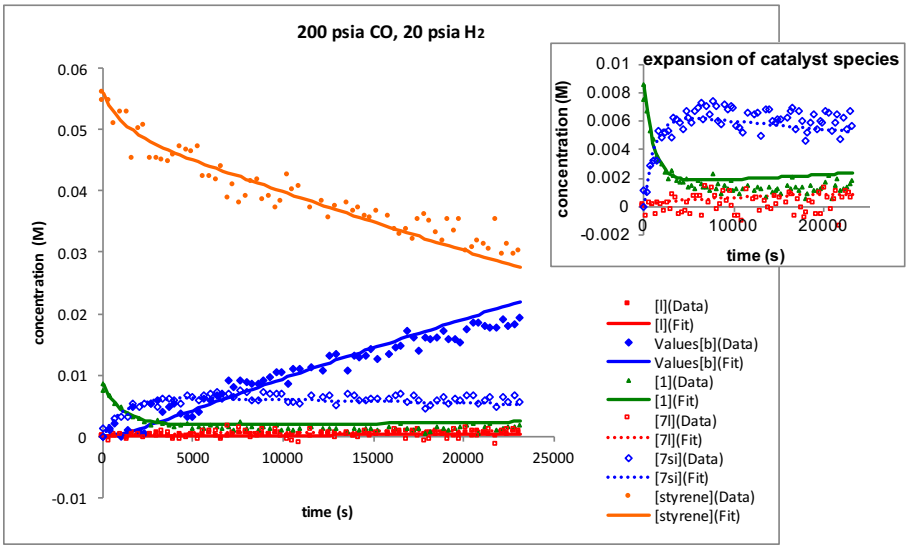

Figure B-17. Data and fit of catalytic reaction at 17 °C using simplified model (3) (points indicate data, lines indicate fit). (55 mM styrene, 10 mM Rh(BDP), 200 psia CO, 20 psia H_2, 290K, CH_2Cl_2).

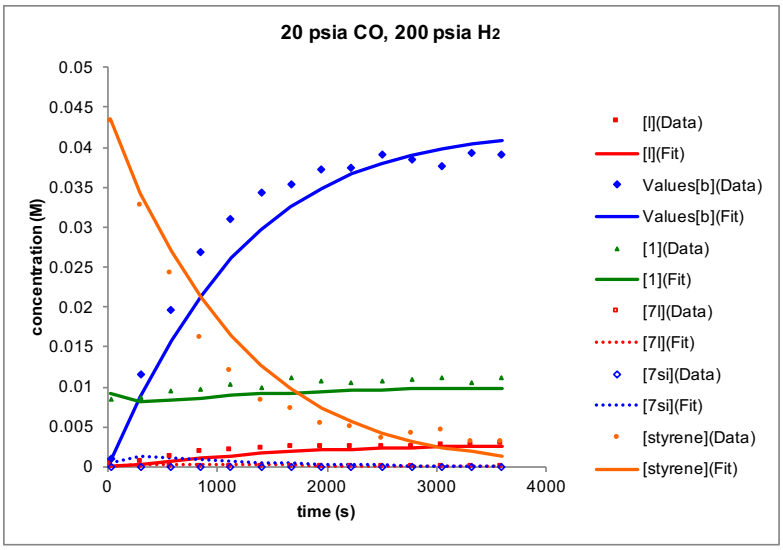

Figure B-18. Data and fit of catalytic reaction at 17 °C using simplified model (3) (points indicate data, lines indicate fit). (45 mM styrene, 10 mM Rh(BDP), 20 psia CO, 200 psia H_2, 290K, CH_2Cl_2).

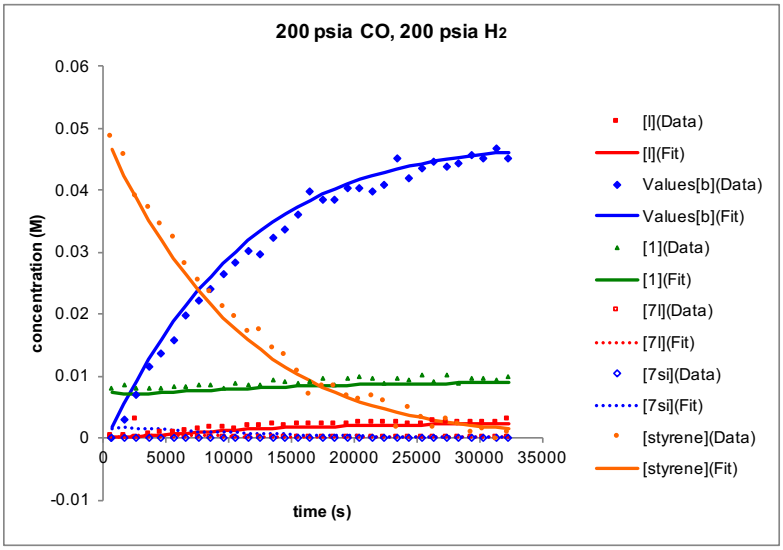

Figure B-19. Data and fit of catalytic reaction at 17 °C using simplified model (3) (points indicate data, lines indicate fit). (50 mM styrene, 10 mM Rh(BDP), 200 psia CO, 200 psia H_2, 290K, CH_2Cl_2).

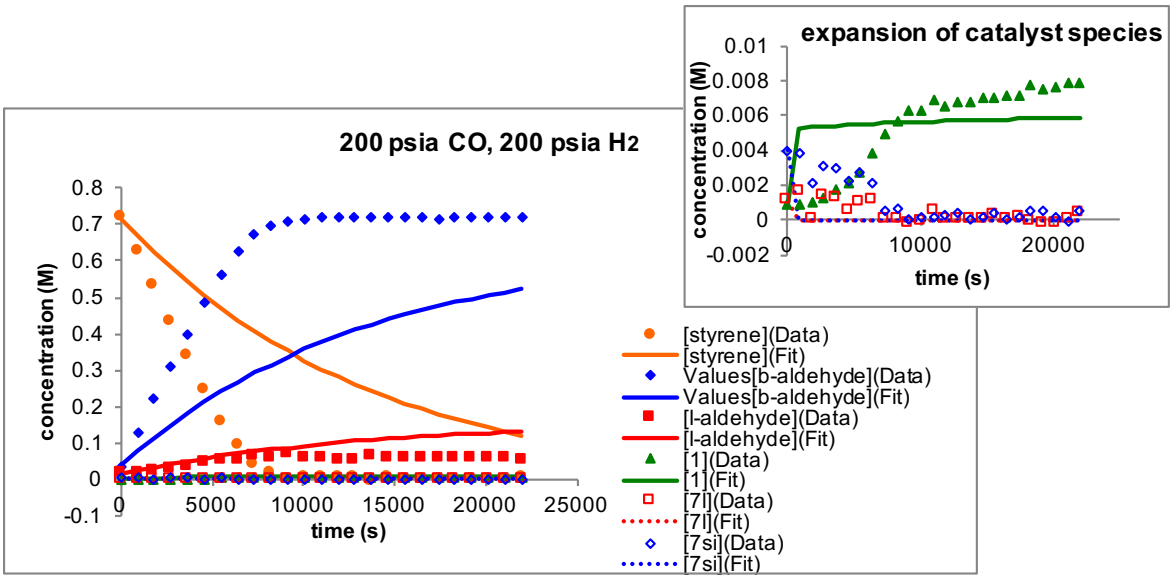

Figure B-20. Data and fit of catalytic reaction at 40 °C using simplified model (3) (points indicate data, lines indicate fit). (70 mM styrene, 9 mM Rh(BDP), 200 psia CO, 200 psia H_2, 313K, CH_2Cl_2).

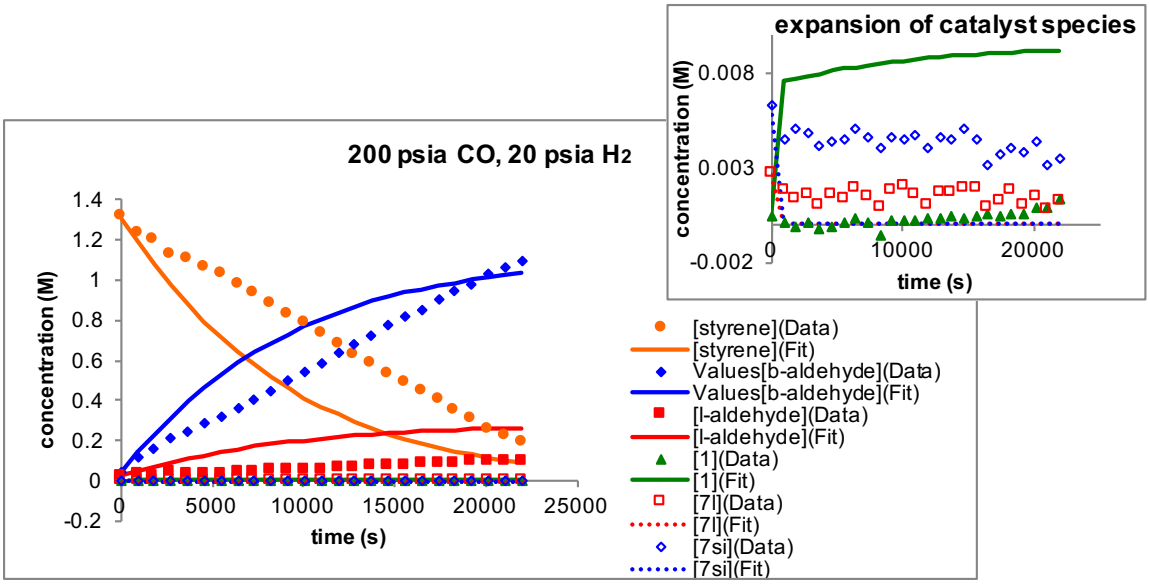

Figure B-21. Data and fit of catalytic reaction at 40 °C using simplified model (3) (points indicate data, lines indicate fit). (1.3 M styrene, 8 mM Rh(BDP), 200 psia CO, 20 psia H_2, 313K, CH_2Cl_2).

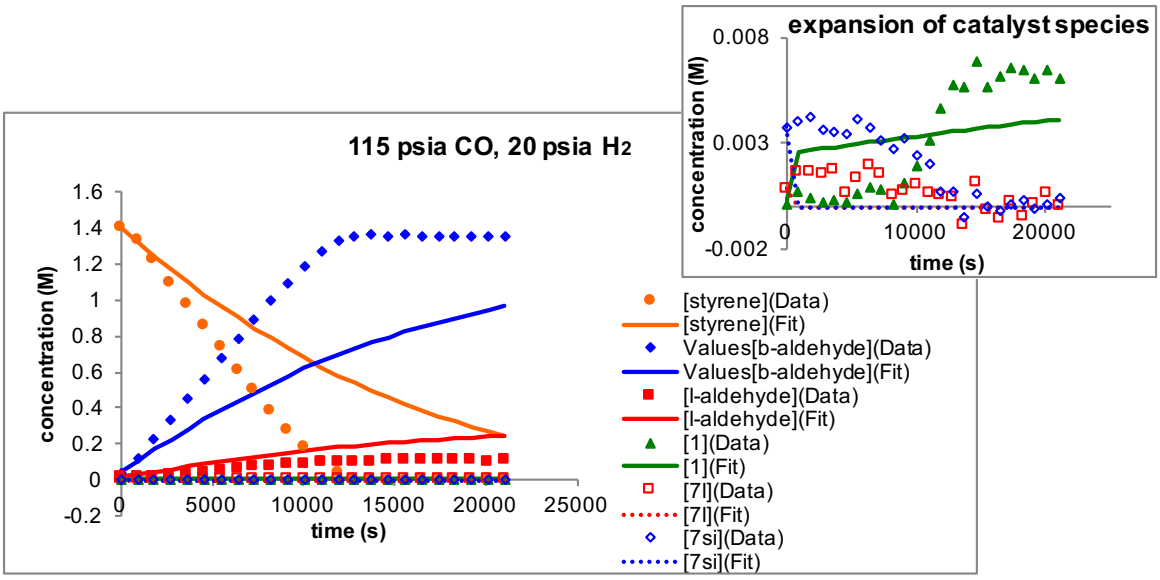

Figure B-22. Data and fit of catalytic reaction at 40 °C using simplified model (3) (points indicate data, lines indicate fit). (1.4 M styrene, 6 mM Rh(BDP), 115 psia CO, 20 psia H_2, 313K, CH_2Cl_2).

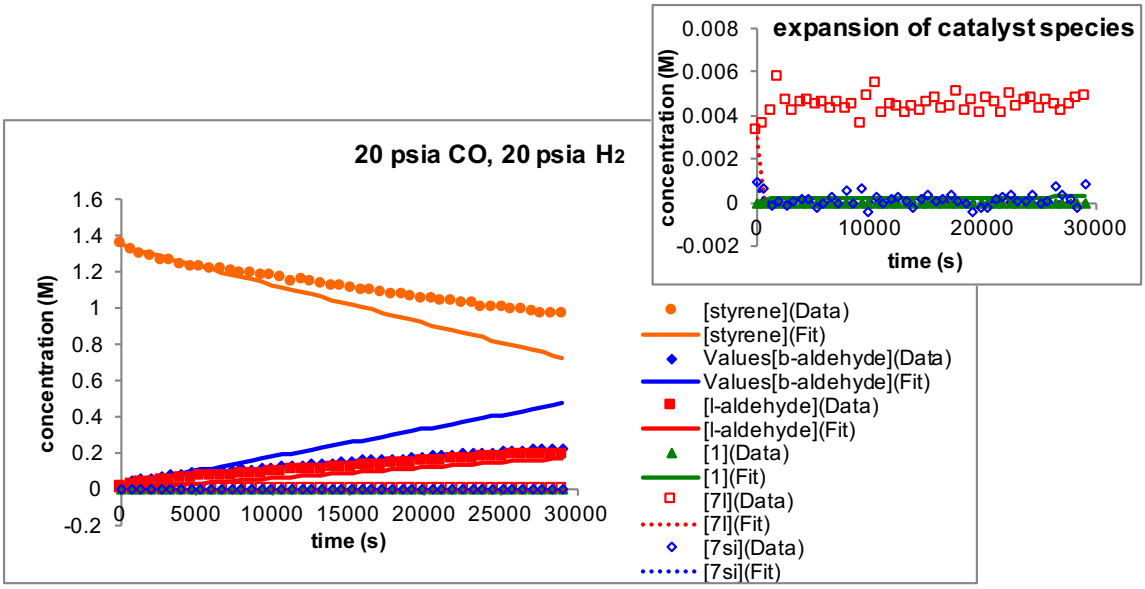

Figure B-23. Data and fit of catalytic reaction at 40 °C using simplified model (3) (points indicate data, lines indicate fit). (1.4 M styrene, 6 mM Rh(BDP), 20 psia CO, 20 psia H_2, 313K, CH_2Cl_2).

B.4 Model for Approach 4: Divide and Conquer Models

B.4.1 Modeling Non-catalytic Hydrogenolysis

B.4.1.1 Model Set Up

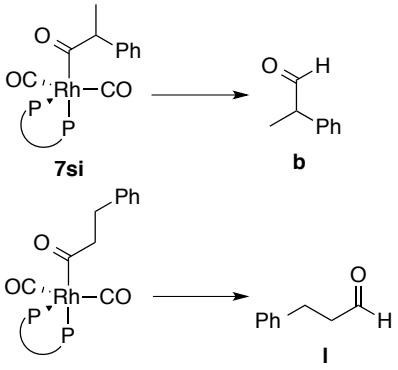

$$\frac{d[\mathbf{b}]}{dt} = \frac{k_{5b}k_{4b}[\mathbf{7b}][H_2]}{k_{5b}[H_2]+k_{-4b}[CO]}$$

$$\frac{d[\mathbf{l}]}{dt} = \frac{k_{5l}k_{4l}[\mathbf{7l}][H_2]}{k_{5l}[H_2]+k_{-4l}[CO]}$$

$$k^{b}_{-4} = 2.0837\text{x}10^{10}(T)e^{-\left(\frac{(\Delta H\ddagger\_4back\_b)-(\Delta S\ddagger\_4back\_b)(T)}{1.987(T)}\right)}$$

$$k^{l}_{-4} = 2.0837\text{x}10^{10}(T)e^{-\left(\frac{(\Delta H\ddagger\_4back\_l)-(\Delta S\ddagger\_4back\_l)(T)}{1.987(T)}\right)}$$

$$\frac{k^{b}_{4}}{k^{b}_{5}} = e^{\left(\frac{-[\Delta H\ddagger\_4for\_b]+[\Delta H\ddagger\_5for\_b]+([\Delta S\ddagger\_4for\_b]-[\Delta S\ddagger\_5for\_b](T)}{1.987(T)}\right)}$$

$$\frac{k^{l}_{4}}{k^{l}_{5}} = e^{\left(\frac{-[\Delta H\ddagger\_4for\_l]+[\Delta H\ddagger\_5for\_l]+([\Delta S\ddagger\_4for\_l]-[\Delta S\ddagger\_5for\_l](T)}{1.987(T)}\right)}$$

Figure B-24. Model for obtaining hydrogenolysis activation parameters.

Table B-4. Optimized parameters for non-catalytic hydrogenolysis model.

Parameter	Value	Set or Optimized?
ΔH‡_4back_b	2.29(2) kcal/mol	optimized
ΔS‡_4back_b	17.8(7) cal·mol^{-1}K^{-1}	optimized
ΔH‡_4back_l	2.38(1) kcal/mol	optimized
ΔS‡_4back_l	15.2(2) cal·mol^{-1}K^{-1}	optimized
–ΔH‡_4for_b+ΔH‡_5for_b	–6.4(2) kcal/mol	optimized
ΔS‡_4for_b–ΔS‡_5for_b	30.6(6) cal·mol^{-1}K^{-1}	optimized
–ΔH‡_4for_l+ΔH‡_5for_l	–6.1(5) kcal/mol	optimized
ΔS‡_4for_l–ΔS‡_5for_l	28(1) cal·mol^{-1}K^{-1}	optimized

B.4.1.2 Data and Fits of Non-catalytic Hydrogenolysis Experiments

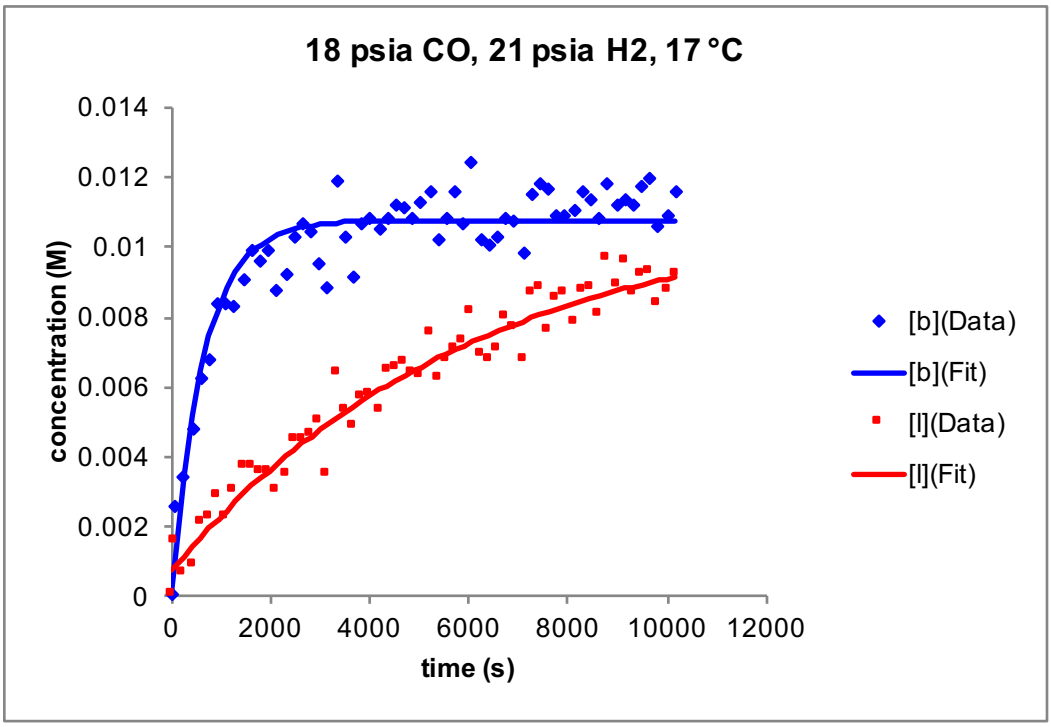

Figure B-25. Data and fits for simplified model of single turnover hydrogenolysis experiments (~20 mM Rh(BDP) as ~1:1 mixture of acyls, 290 K, 18 psia CO, 21 psia H_2, CH_2Cl_2).

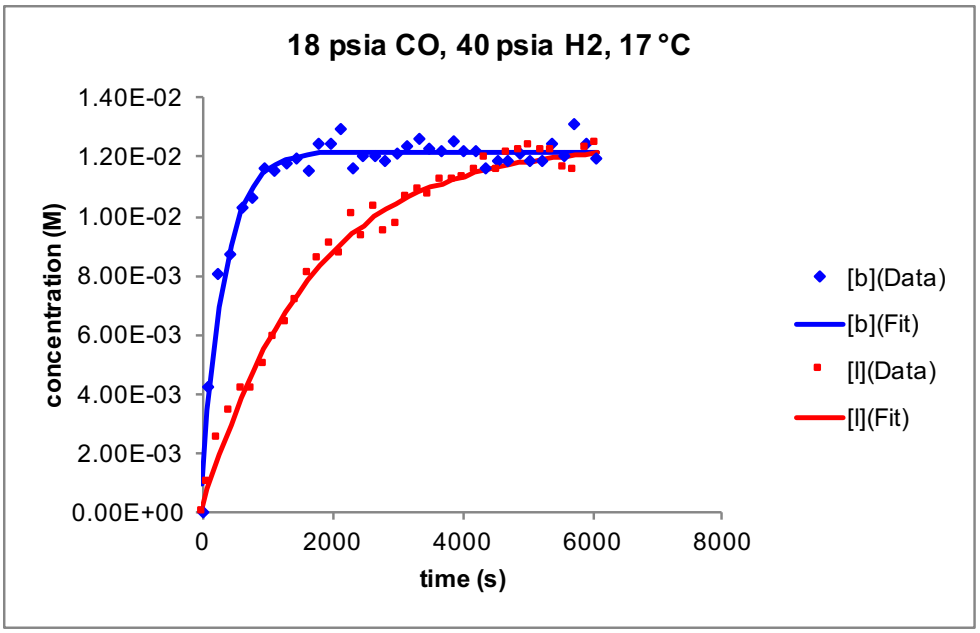

Figure B-26. Data and fits for simplified model of single turnover hydrogenolysis experiments (~20 mM Rh(BDP) as ~1:1 mixture of acyls, 290 K, 18 psia CO, 40 psia H_2, CH_2Cl_2).

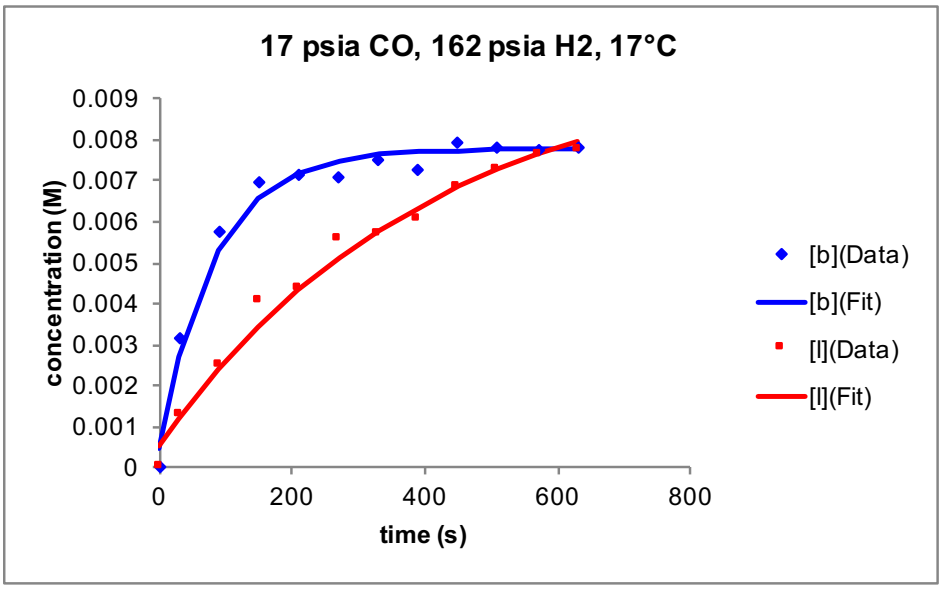

Figure B-27. Data and fits for simplified model of single turnover hydrogenolysis experiments (~20 mM Rh(BDP) as ~1:1 mixture of acyls, 290 K, 17 psia CO, 160 psia H_2, CH_2Cl_2).

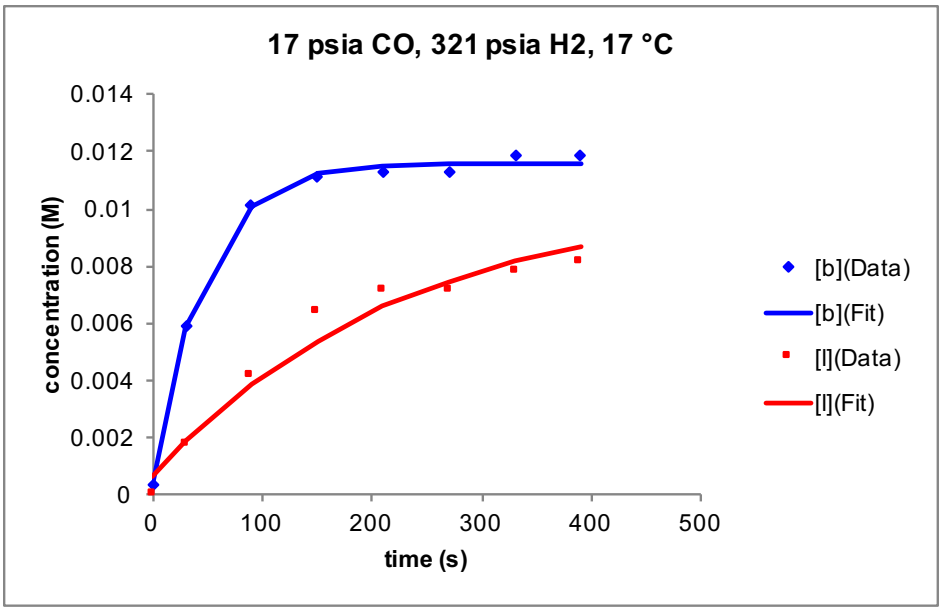

Figure B-28. Data and fits for simplified model of single turnover hydrogenolysis experiments (~20 mM Rh(BDP) as ~1:1 mixture of acyls, 290 K, 17 psia CO, 321 psia H_2, CH_2Cl_2).

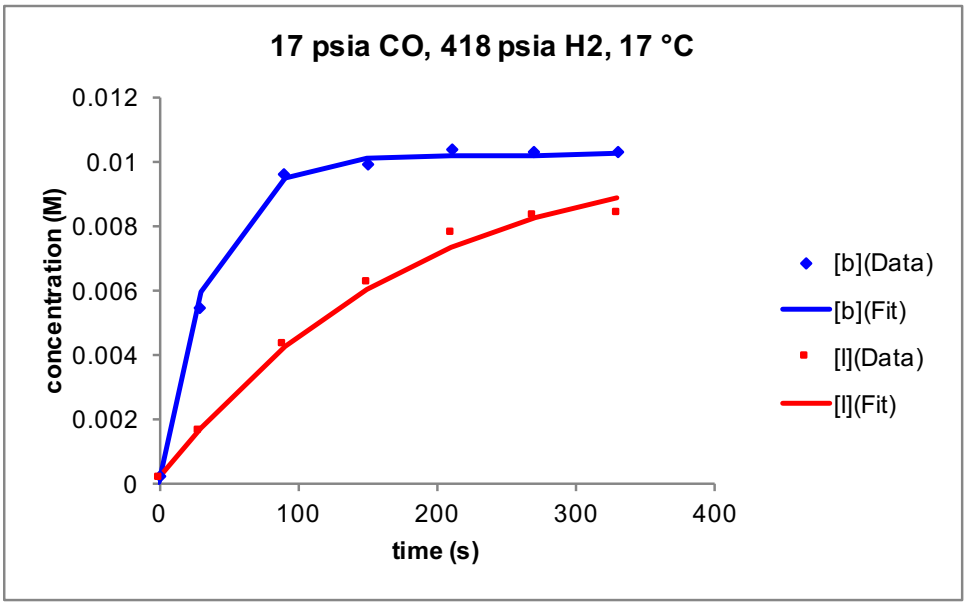

Figure B-29. Data and fits for simplified model of single turnover hydrogenolysis experiments (~20 mM Rh(BDP) as ~1:1 mixture of acyls, 290 K, 17 psia CO, 418 psia H_2, CH_2Cl_2).

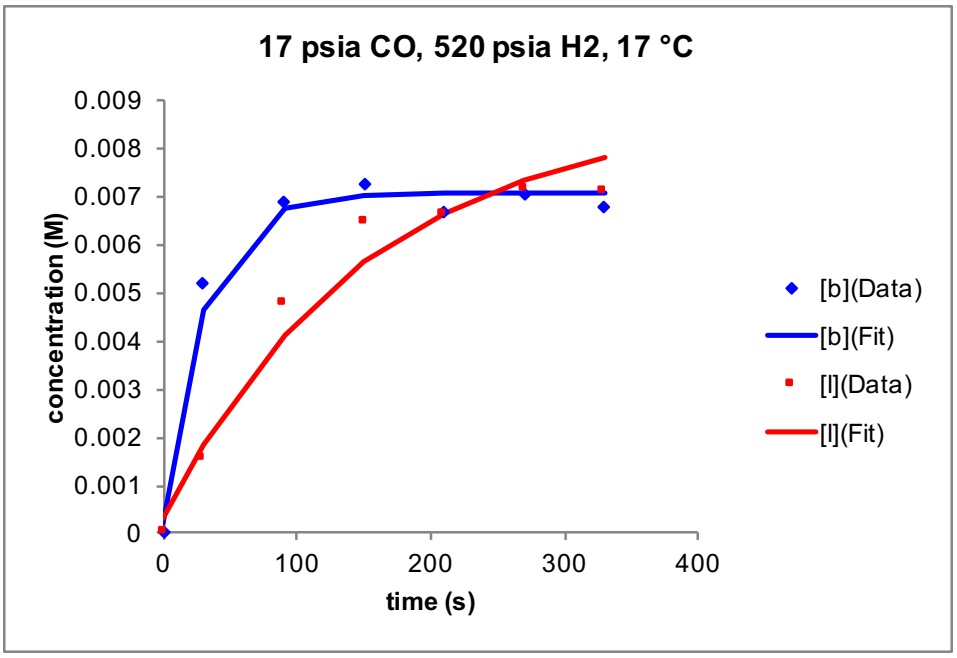

Figure B-30. Data and fits for simplified model of single turnover hydrogenolysis experiments (~20 mM Rh(BDP) as ~1:1 mixture of acyls, 290 K, 17 psia CO, 520 psia H_2, CH_2Cl_2).

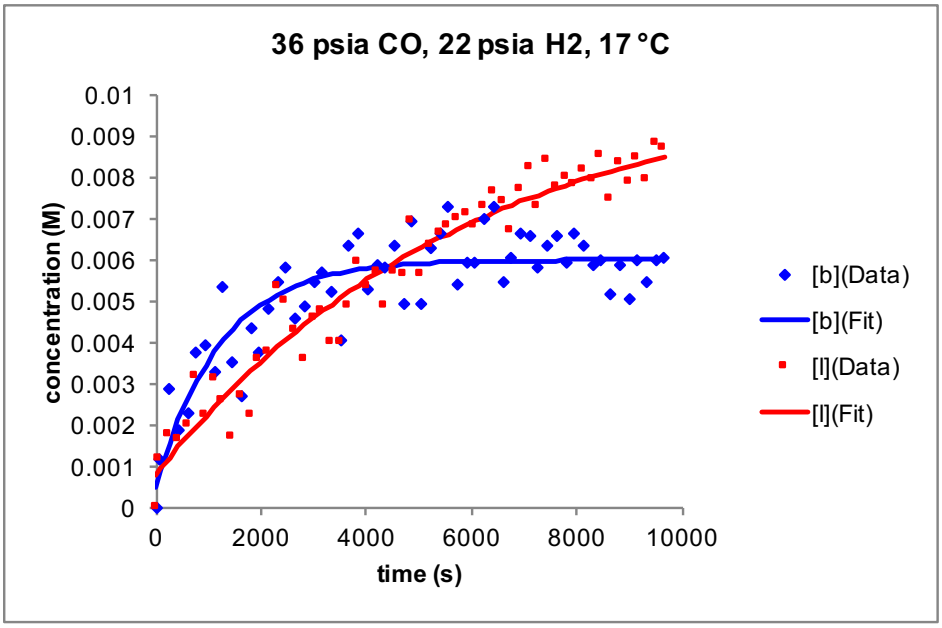

Figure B-31. Data and fits for simplified model of single turnover hydrogenolysis experiments (~20 mM Rh(BDP) as ~1:1 mixture of acyls, 290 K, 36 psia CO, 22 psia H_2, CH_2Cl_2).

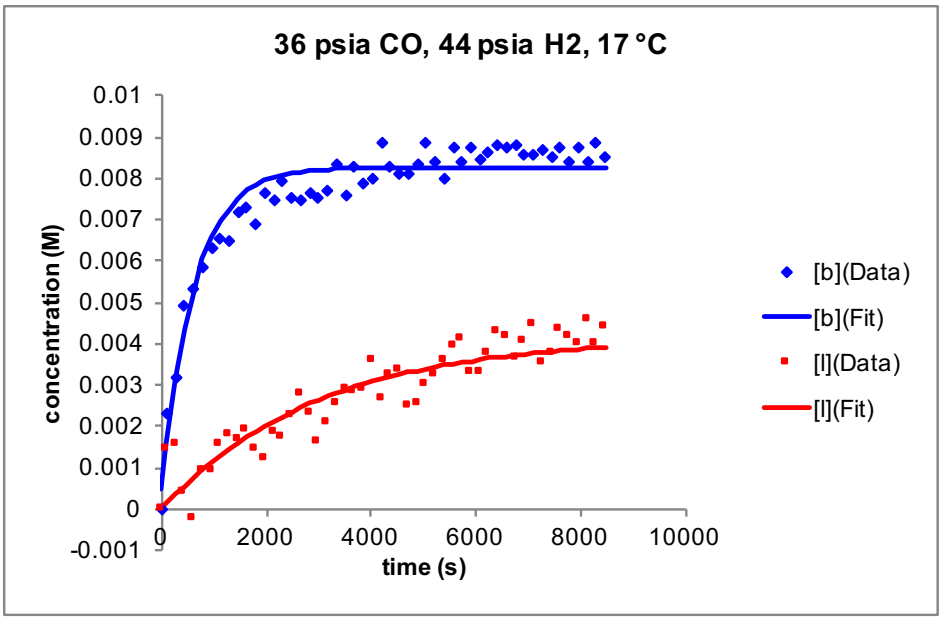

Figure B-32. Data and fits for simplified model of single turnover hydrogenolysis experiments (~20 mM Rh(BDP) as ~1:1 mixture of acyls, 290 K, 36 psia CO, 44 psia H_2, CH_2Cl_2).

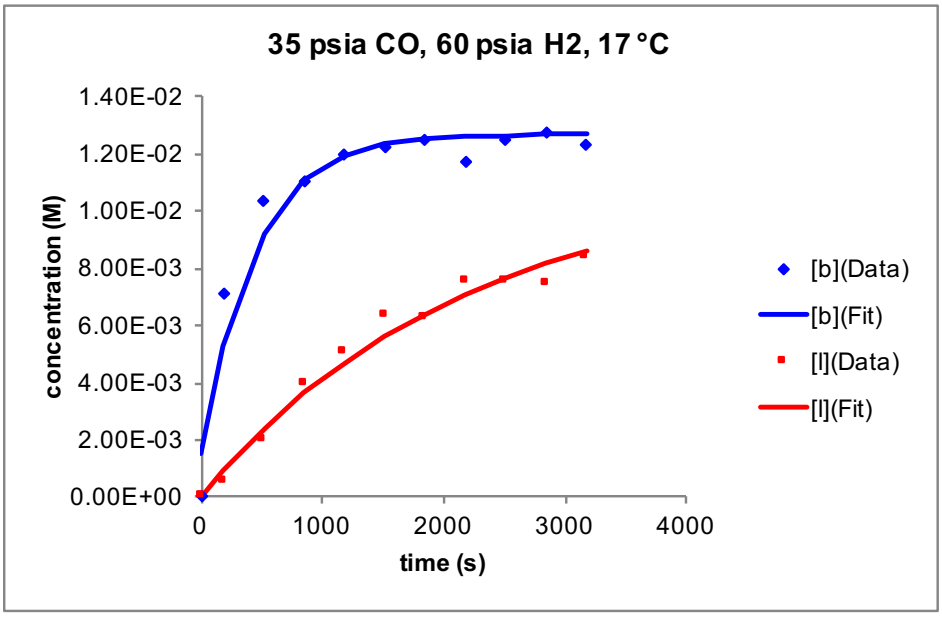

Figure B-33. Data and fits for simplified model of single turnover hydrogenolysis experiments (~20 mM Rh(BDP) as ~1:1 mixture of acyls, 290 K, 36 psia CO, 60 psia H_2, CH_2Cl_2).

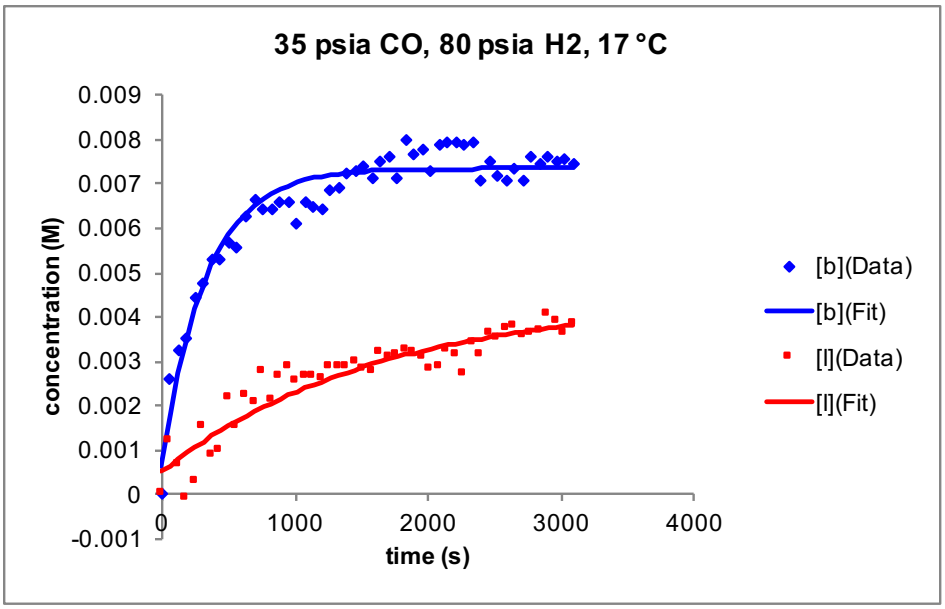

Figure B-34. Data and fits for simplified model of single turnover hydrogenolysis experiments (~20 mM Rh(BDP) as ~1:1 mixture of acyls, 290 K, 35 psia CO, 80 psia H_2, CH_2Cl_2).

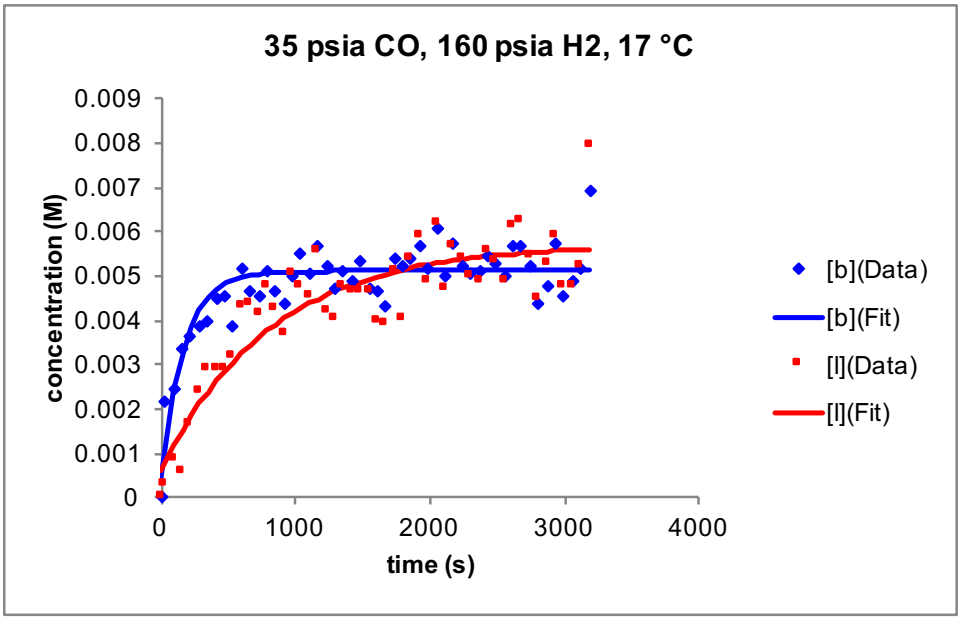

Figure B-35. Data and fits for simplified model of single turnover hydrogenolysis experiments (~20 mM Rh(BDP) as ~1:1 mixture of acyls, 290 K, 35 psia CO, 160 psia H_2, CH_2Cl_2).

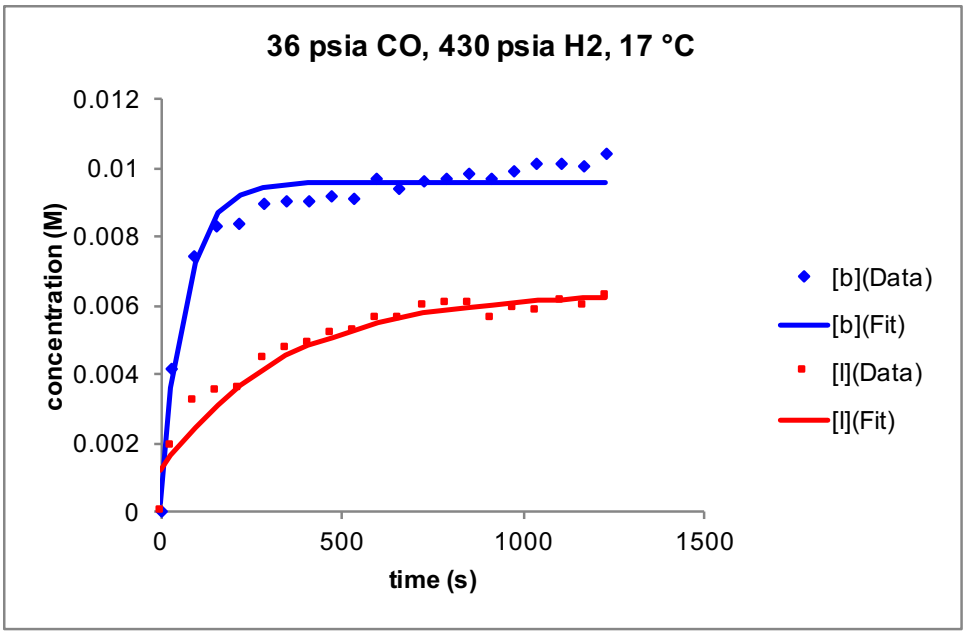

Figure B-36. Data and fits for simplified model of single turnover hydrogenolysis experiments (~20 mM Rh(BDP) as ~1:1 mixture of acyls, 290 K, 36 psia CO, 430 psia H_2, CH_2Cl_2).

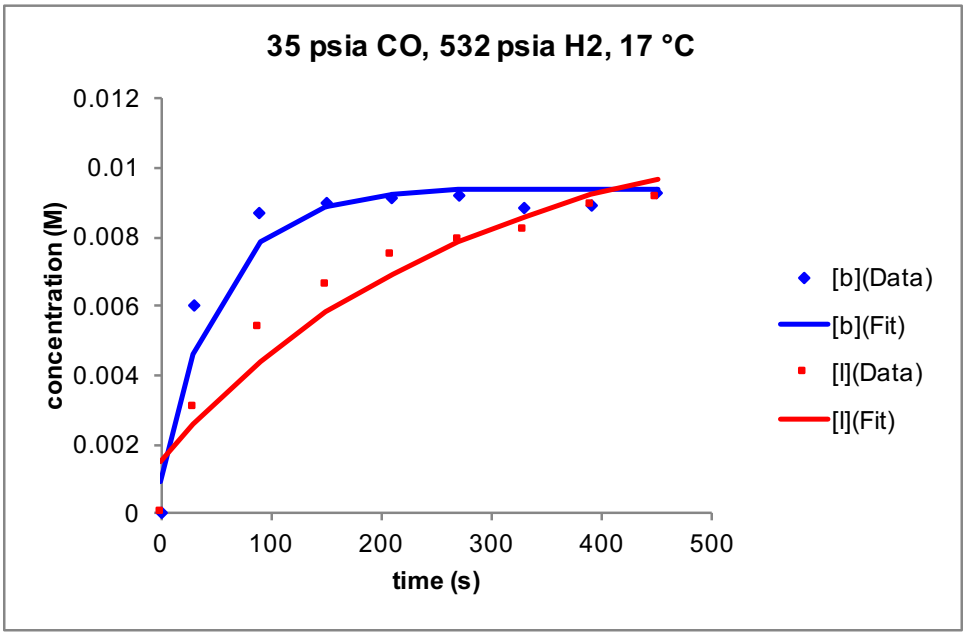

Figure B-37. Data and fits for simplified model of single turnover hydrogenolysis experiments (~20 mM Rh(BDP) as ~1:1 mixture of acyls, 290 K, 36 psia CO, 532 psia H_2, CH_2Cl_2).

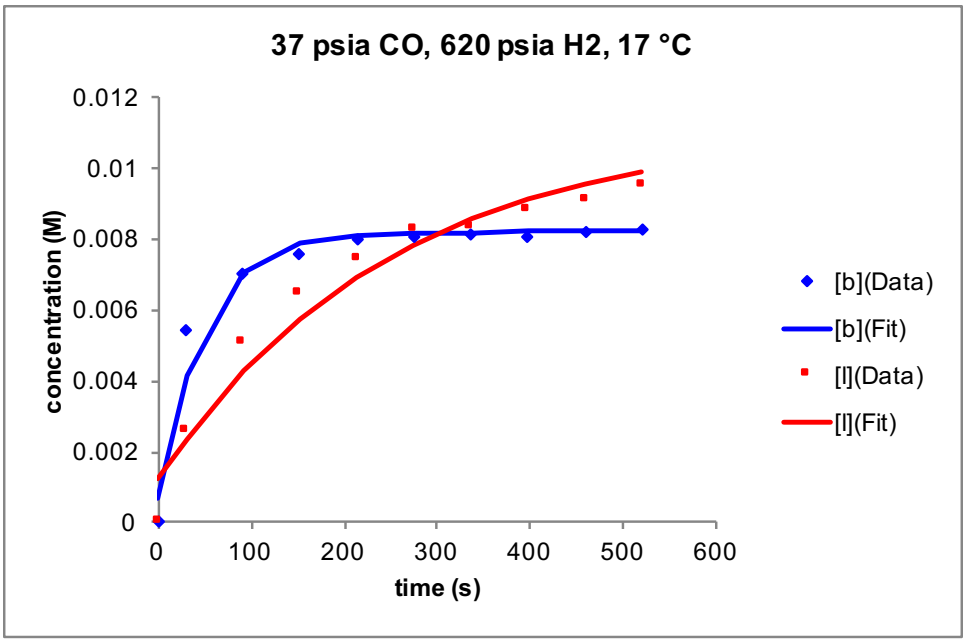

Figure B-38. Data and fits for simplified model of single turnover hydrogenolysis experiments (~20 mM Rh(BDP) as ~1:1 mixture of acyls, 290 K, 37 psia CO, 620 psia H_2, CH_2Cl_2).

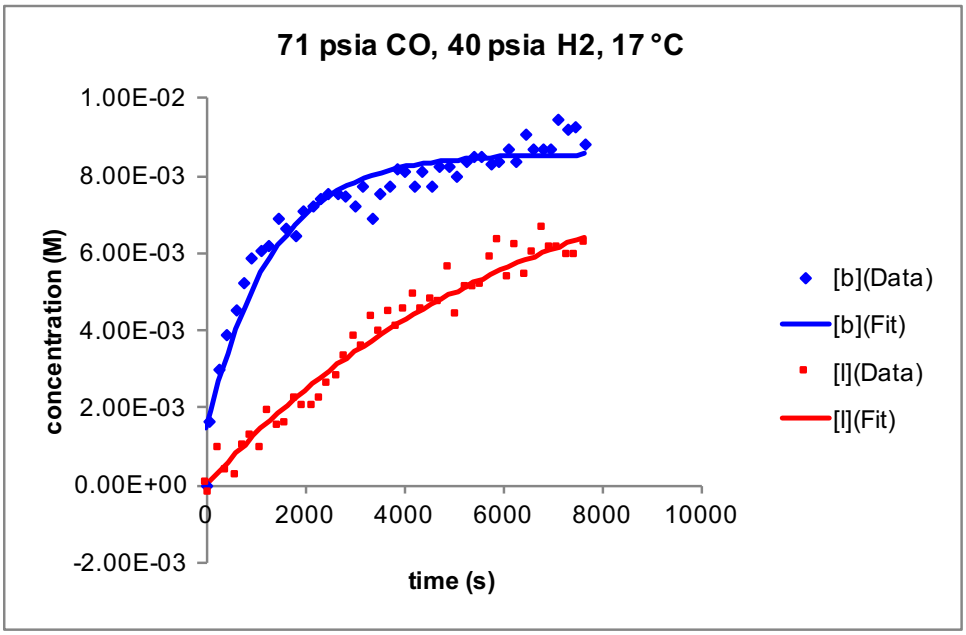

Figure B-39. Data and fits for simplified model of single turnover hydrogenolysis experiments (~20 mM Rh(BDP) as ~1:1 mixture of acyls, 290 K, 71 psia CO, 40 psia H_2, CH_2Cl_2).

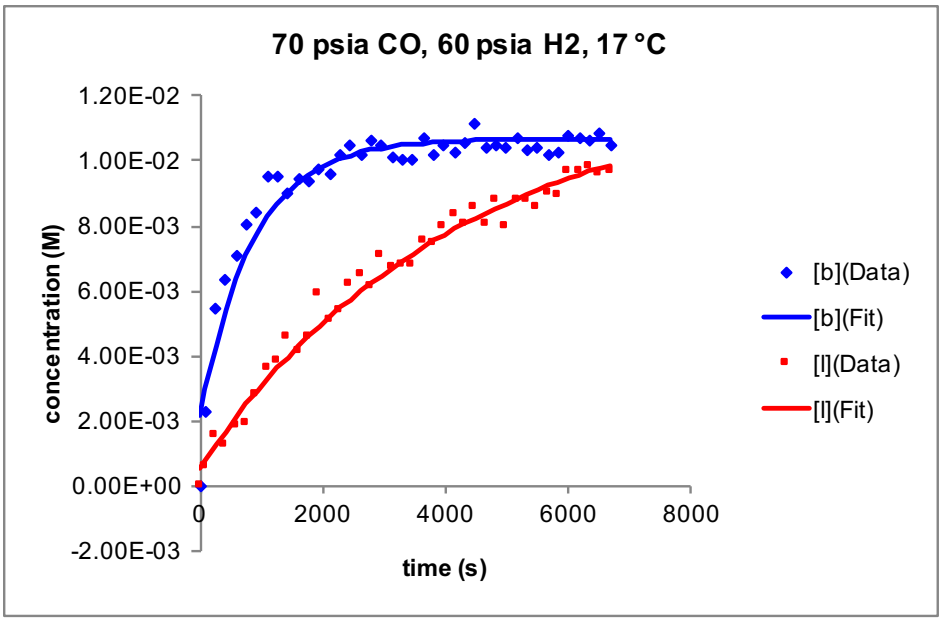

Figure B-40. Data and fits for simplified model of single turnover hydrogenolysis experiments (~20 mM Rh(BDP) as ~1:1 mixture of acyls, 290 K, 70 psia CO, 60 psia H_2, CH_2Cl_2).

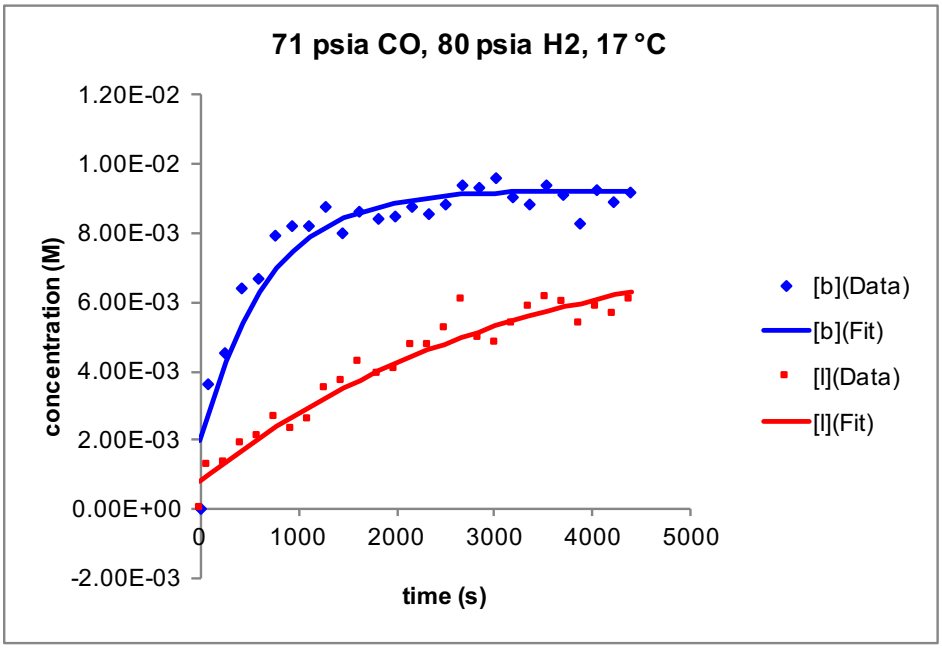

Figure B-41. Data and fits for simplified model of single turnover hydrogenolysis experiments (~20 mM Rh(BDP) as ~1:1 mixture of acyls, 290 K, 71 psia CO, 80 psia H_2, CH_2Cl_2).

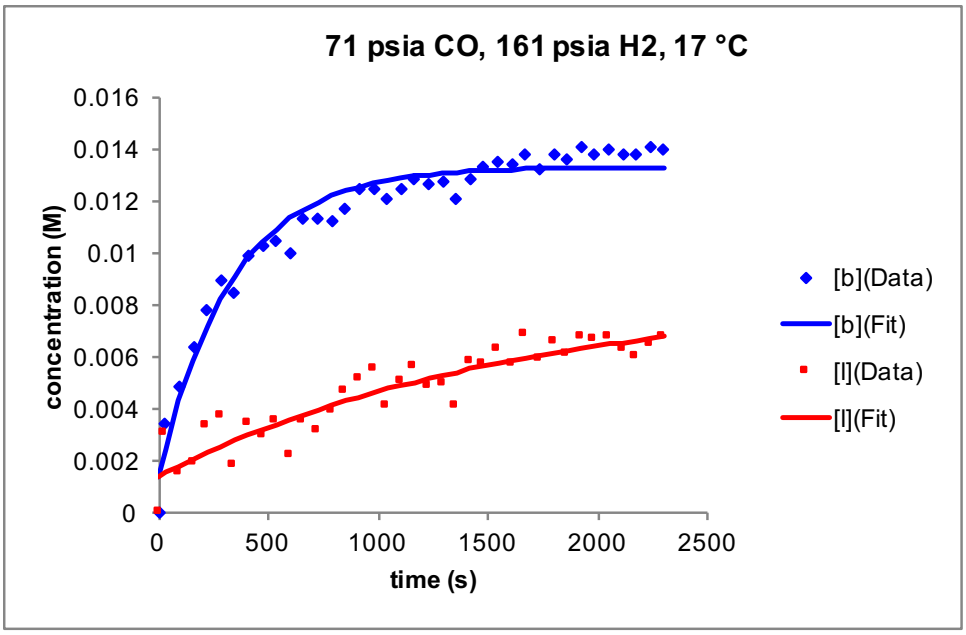

Figure B-42. Data and fits for simplified model of single turnover hydrogenolysis experiments (~20 mM Rh(BDP) as ~1:1 mixture of acyls, 290 K, 71 psia CO, 161 psia H_2, CH_2Cl_2).

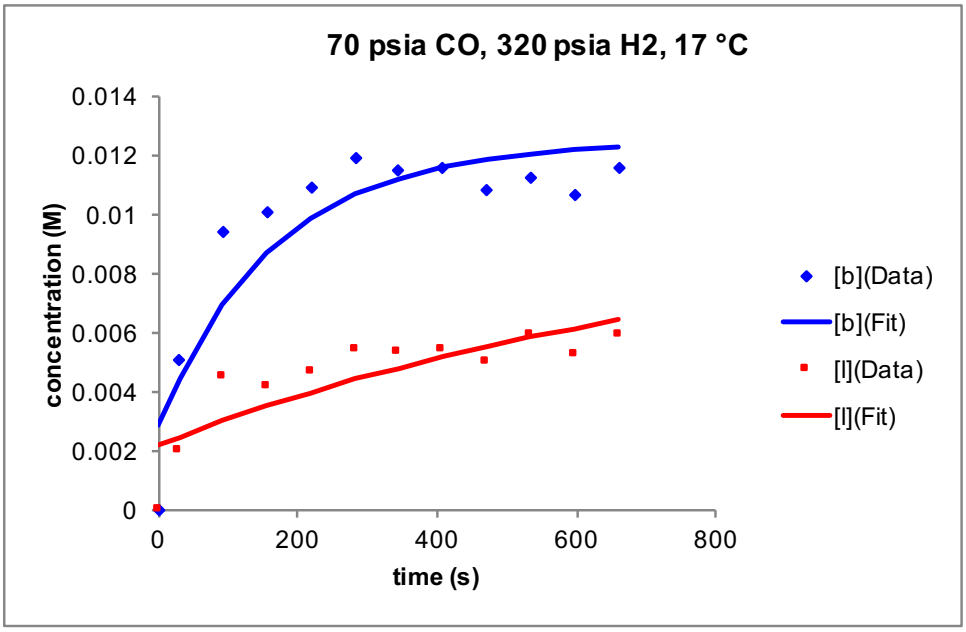

Figure B-43. Data and fits for simplified model of single turnover hydrogenolysis experiments (~20 mM Rh(BDP) as ~1:1 mixture of acyls, 290 K, 70 psia CO, 320 psia H_2, CH_2Cl_2).

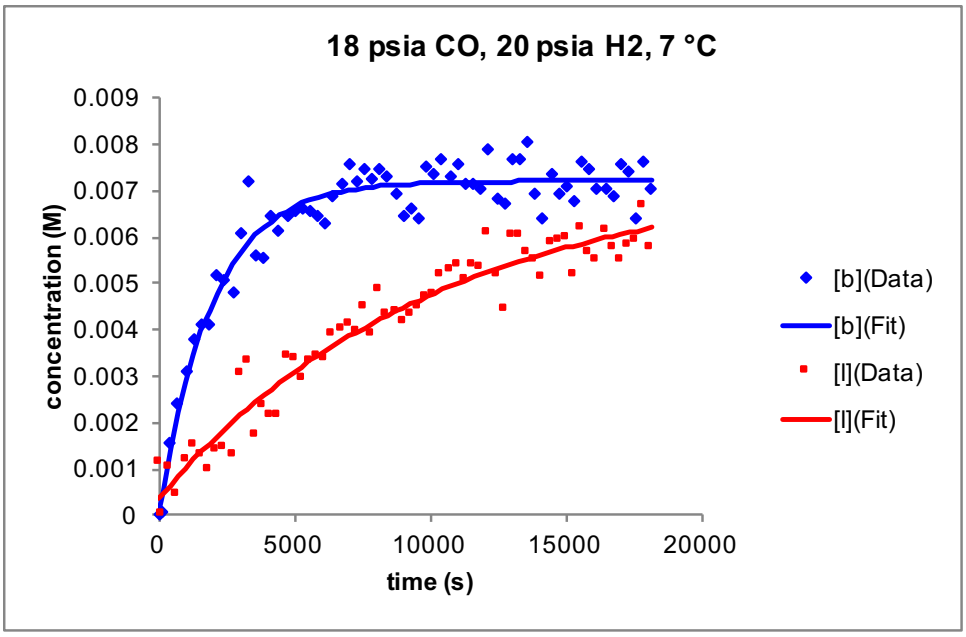

Figure B-44. Data and fits for simplified model of single turnover hydrogenolysis experiments (~20 mM Rh(BDP) as ~1:1 mixture of acyls, 280 K, 18 psia CO, 20 psia H_2, CH_2Cl_2).

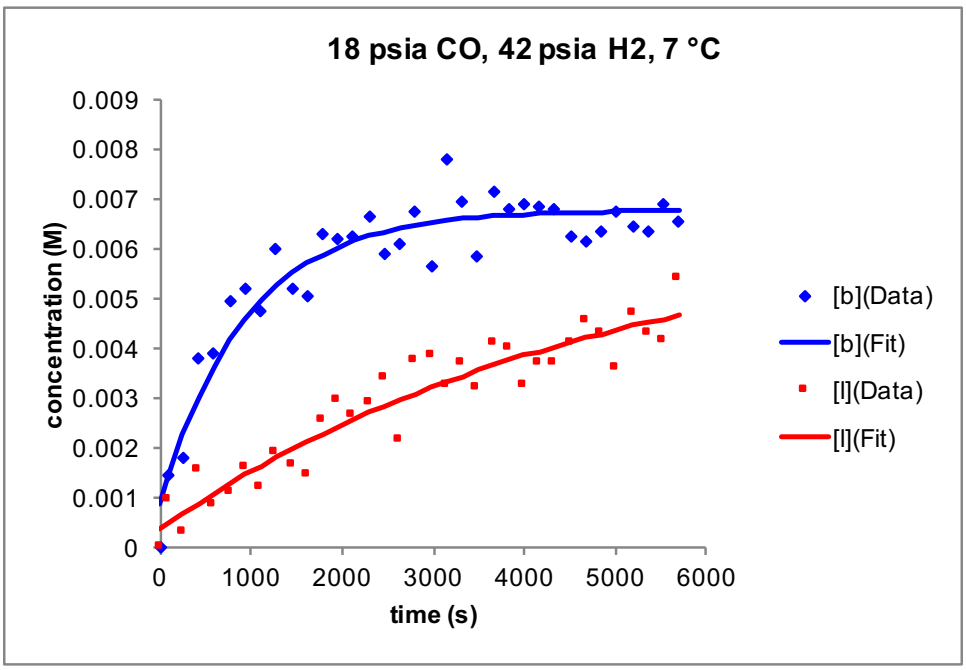

Figure B-45. Data and fits for simplified model of single turnover hydrogenolysis experiments (~20 mM Rh(BDP) as ~1:1 mixture of acyls, 280 K, 18 psia CO, 42 psia H_2, CH_2Cl_2).

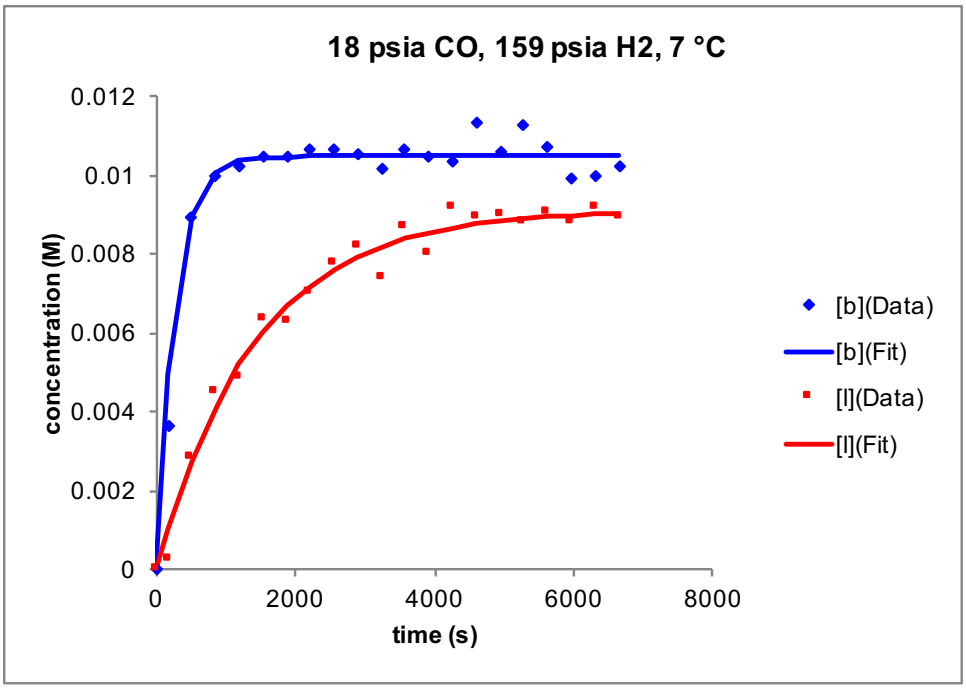

Figure B-46. Data and fits for simplified model of single turnover hydrogenolysis experiments (~20 mM Rh(BDP) as ~1:1 mixture of acyls, 280 K, 18 psia CO, 159 psia H_2, CH_2Cl_2).

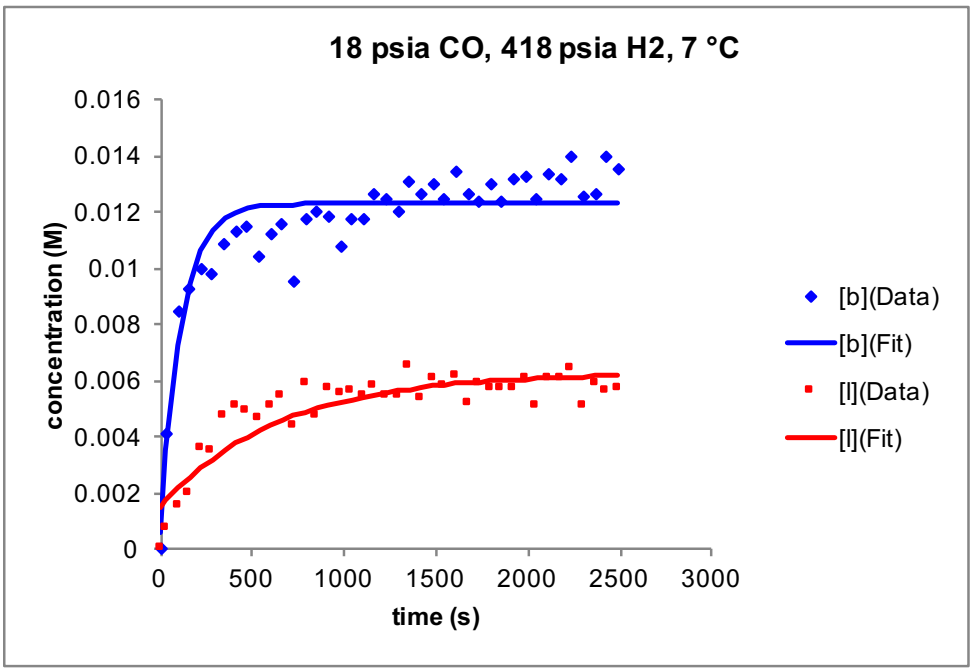

Figure B-47. Data and fits for simplified model of single turnover hydrogenolysis experiments (~20 mM Rh(BDP) as ~1:1 mixture of acyls, 280 K, 18 psia CO, 418 psia H_2, CH_2Cl_2).

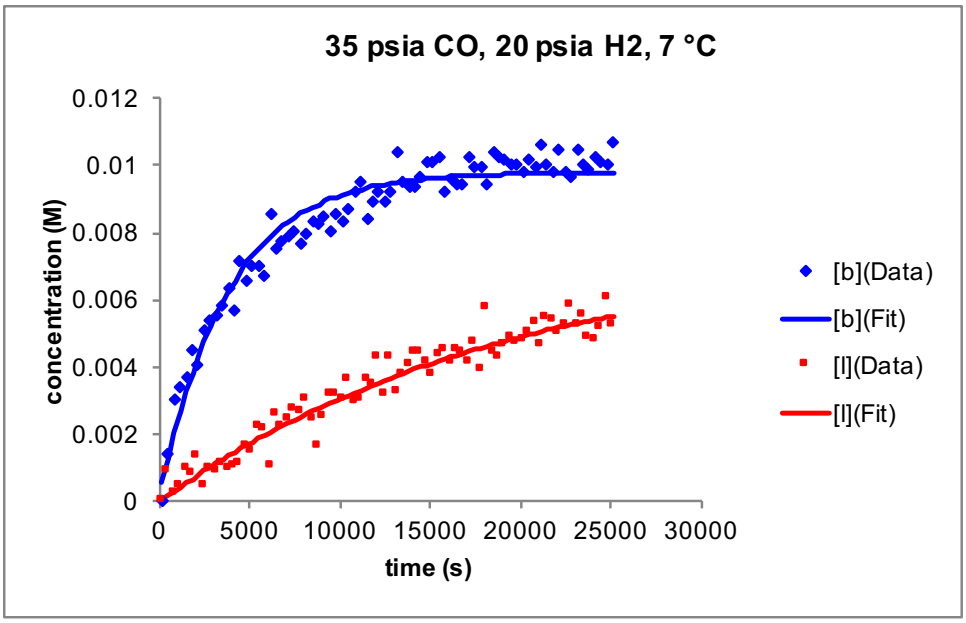

Figure B-48. Data and fits for simplified model of single turnover hydrogenolysis experiments (~20 mM Rh(BDP) as ~1:1 mixture of acyls, 280 K, 35 psia CO, 20 psia H_2, CH_2Cl_2).

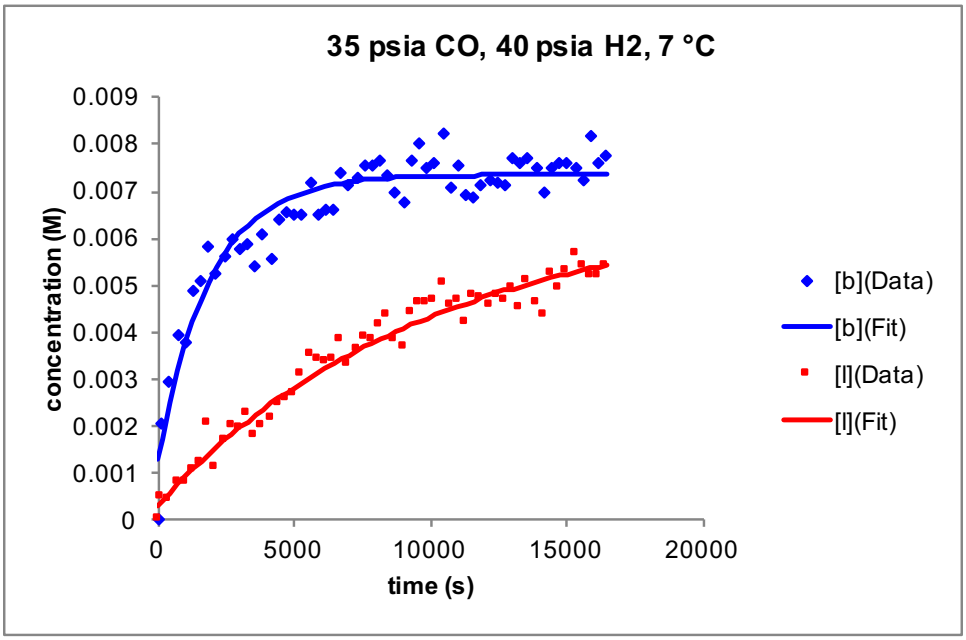

Figure B-49. Data and fits for simplified model of single turnover hydrogenolysis experiments (~20 mM Rh(BDP) as ~1:1 mixture of acyls, 280 K, 35 psia CO, 40 psia H_2, CH_2Cl_2).

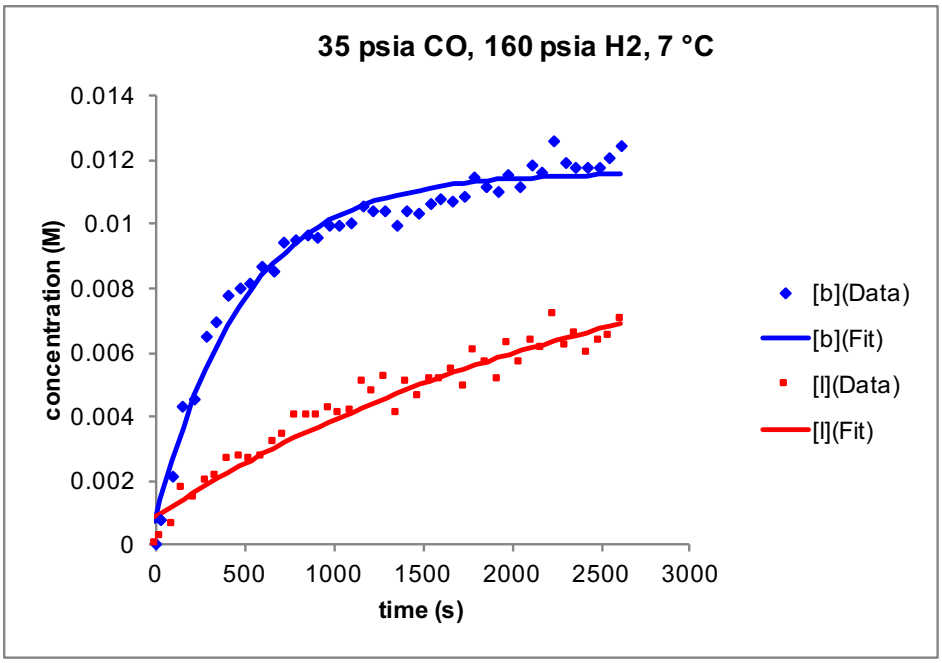

Figure B-50. Data and fits for simplified model of single turnover hydrogenolysis experiments (~20 mM Rh(BDP) as ~1:1 mixture of acyls, 280 K, 35 psia CO, 160 psia H_2, CH_2Cl_2).

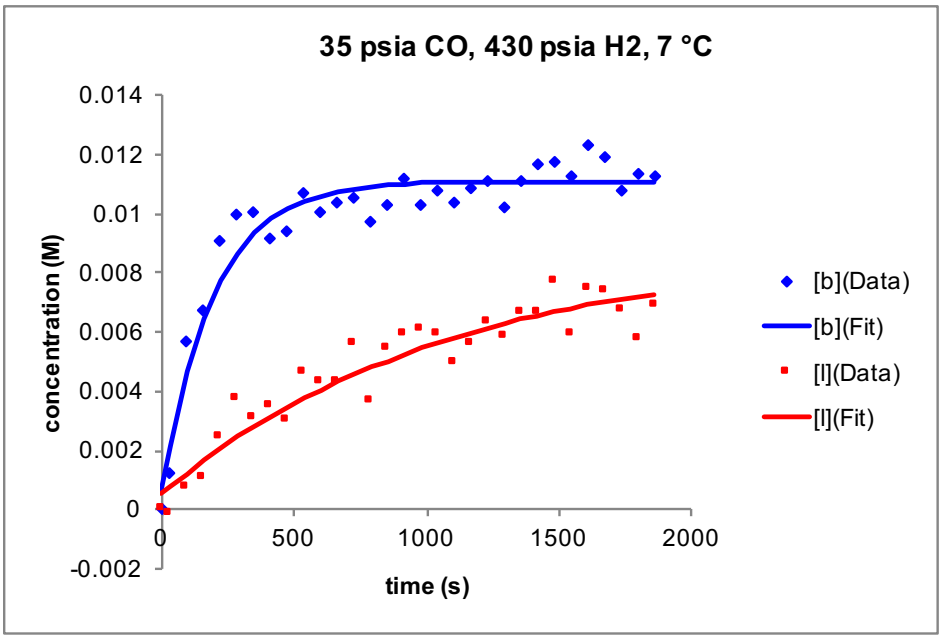

Figure B-51. Data and fits for simplified model of single turnover hydrogenolysis experiments (~20 mM Rh(BDP) as ~1:1 mixture of acyls, 280 K, 35 psia CO, 430 psia H_2, CH_2Cl_2).

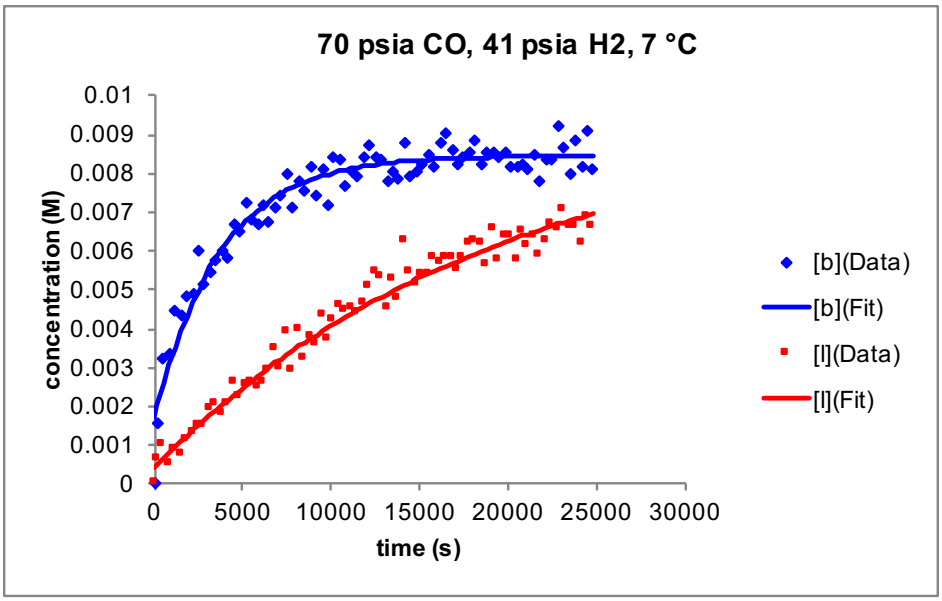

Figure B-52. Data and fits for simplified model of single turnover hydrogenolysis experiments (~20 mM Rh(BDP) as ~1:1 mixture of acyls, 280 K, 70 psia CO, 41 psia H_2, CH_2Cl_2).

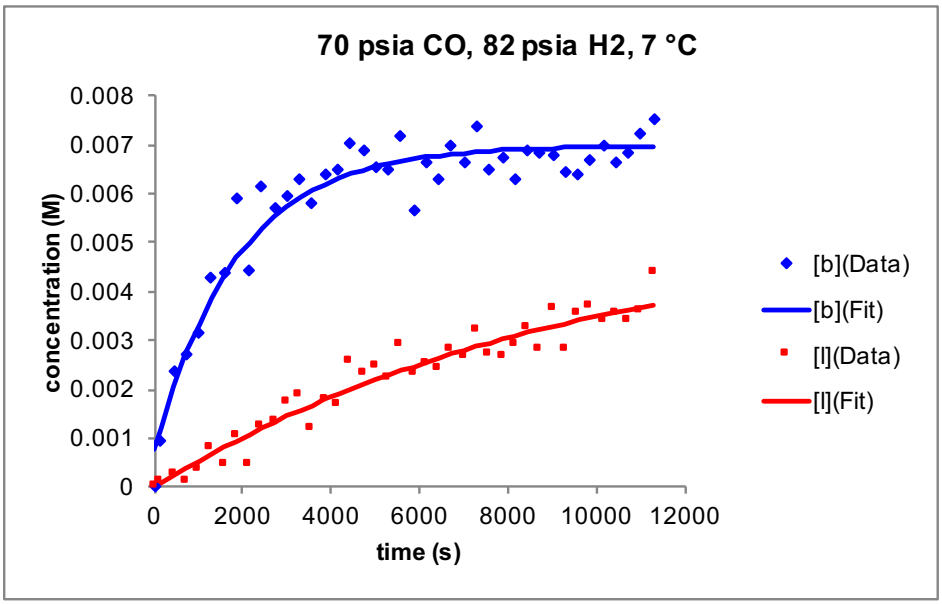

Figure B-53. Data and fits for simplified model of single turnover hydrogenolysis experiments (~20 mM Rh(BDP) as ~1:1 mixture of acyls, 280 K, 70 psia CO, 82 psia H_2, CH_2Cl_2).

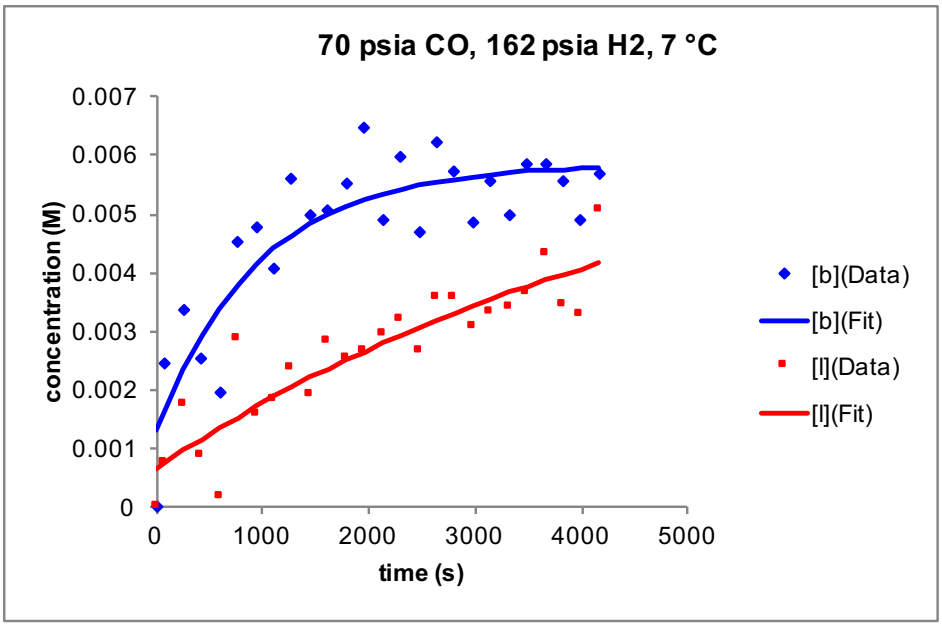

Figure B-54. Data and fits for simplified model of single turnover hydrogenolysis experiments (~20 mM Rh(BDP) as ~1:1 mixture of acyls, 280 K, 70 psia CO, 162 psia H_2, CH_2Cl_2).

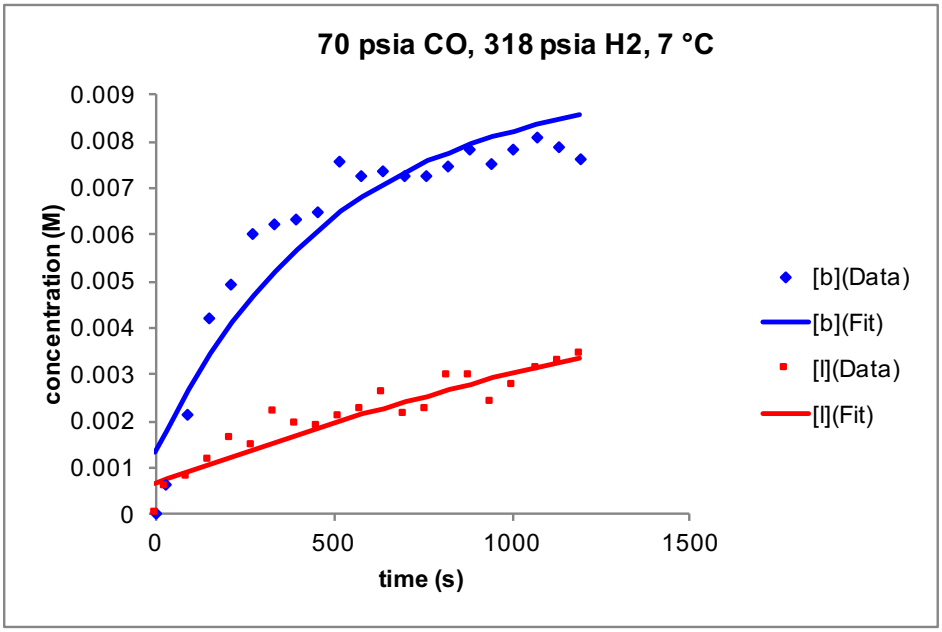

Figure B-55. Data and fits for simplified model of single turnover hydrogenolysis experiments (~20 mM Rh(BDP) as ~1:1 mixture of acyls, 280 K, 70 psia CO, 318 psia H_2, CH_2Cl_2).

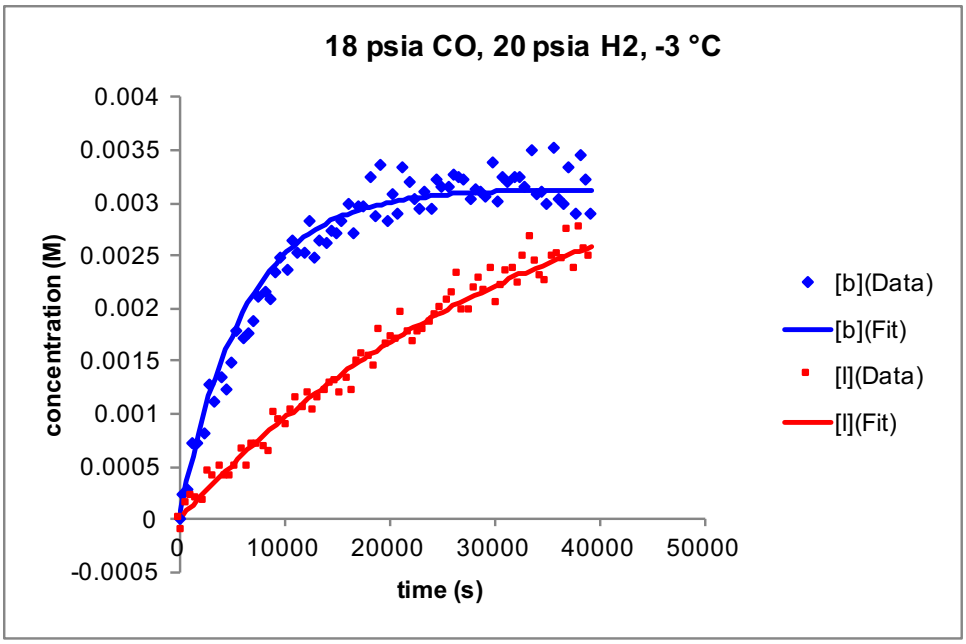

Figure B-56. Data and fits for simplified model of single turnover hydrogenolysis experiments (~20 mM Rh(BDP) as ~1:1 mixture of acyls, 270 K, 18 psia CO, 20 psia H_2, CH_2Cl_2).

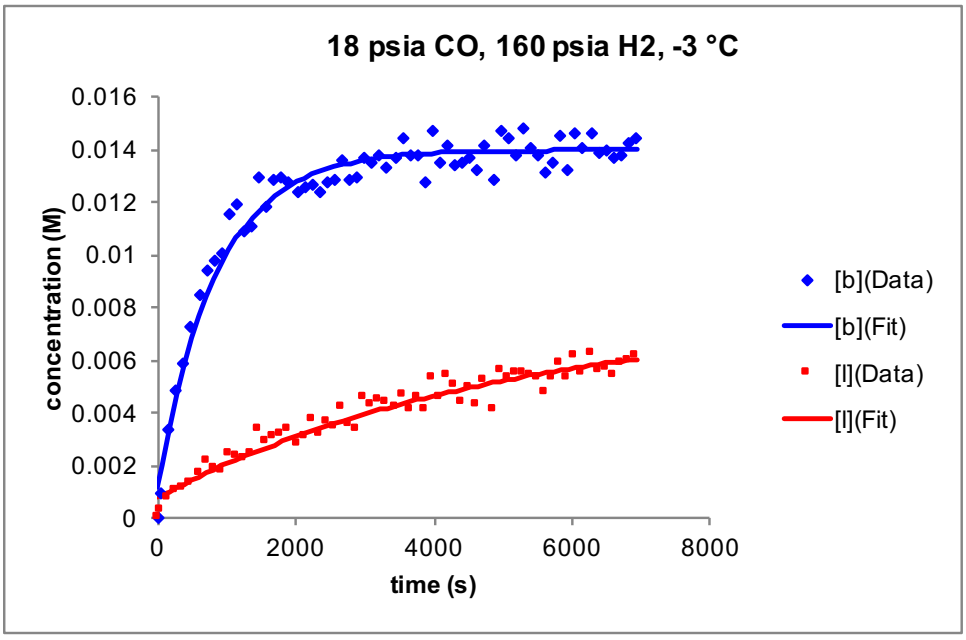

Figure B-57. Data and fits for simplified model of single turnover hydrogenolysis experiments (~20 mM Rh(BDP) as ~1:1 mixture of acyls, 270 K, 18 psia CO, 160 psia H_2, CH_2Cl_2).

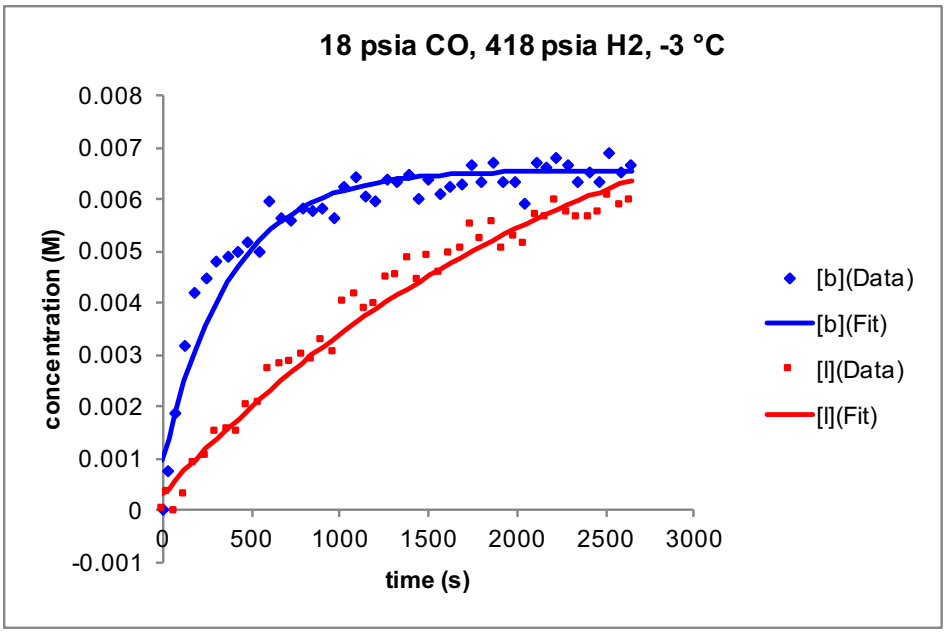

Figure B-58. Data and fits for simplified model of single turnover hydrogenolysis experiments (~20 mM Rh(BDP) as ~1:1 mixture of acyls, 270 K, 18 psia CO, 418 psia H_2, CH_2Cl_2).

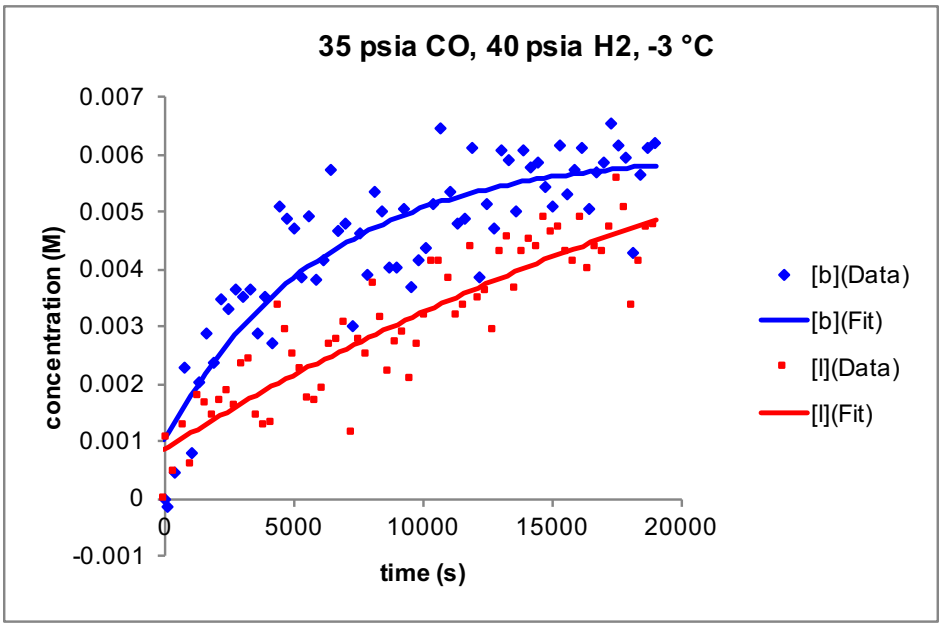

Figure B-59. Data and fits for simplified model of single turnover hydrogenolysis experiments (~20 mM Rh(BDP) as ~1:1 mixture of acyls, 270 K, 35 psia CO, 40 psia H_2, CH_2Cl_2).

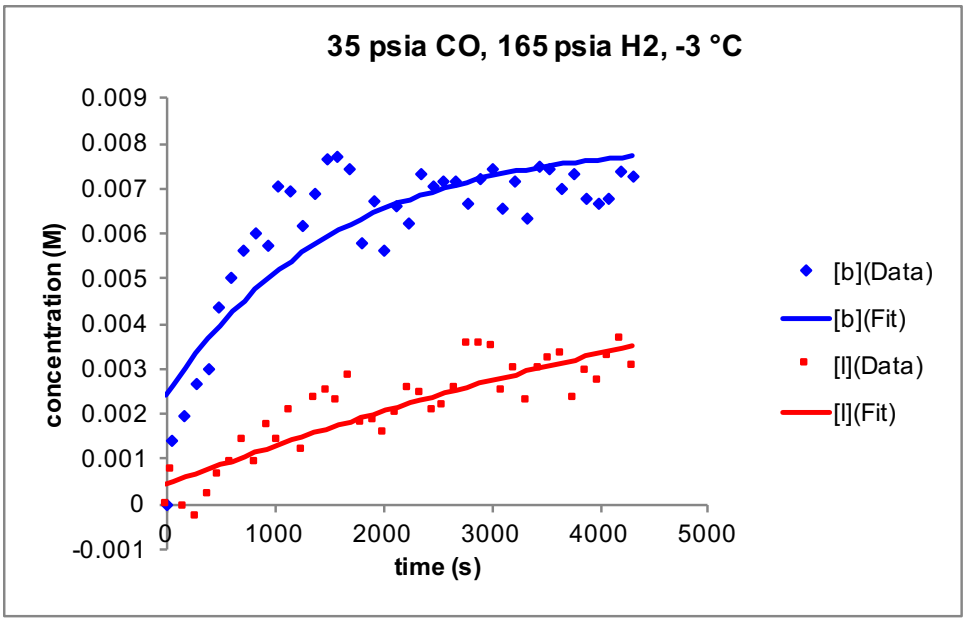

Figure B-60. Data and fits for simplified model of single turnover hydrogenolysis experiments (~20 mM Rh(BDP) as ~1:1 mixture of acyls, 270 K, 35 psia CO, 165 psia H_2, CH_2Cl_2).

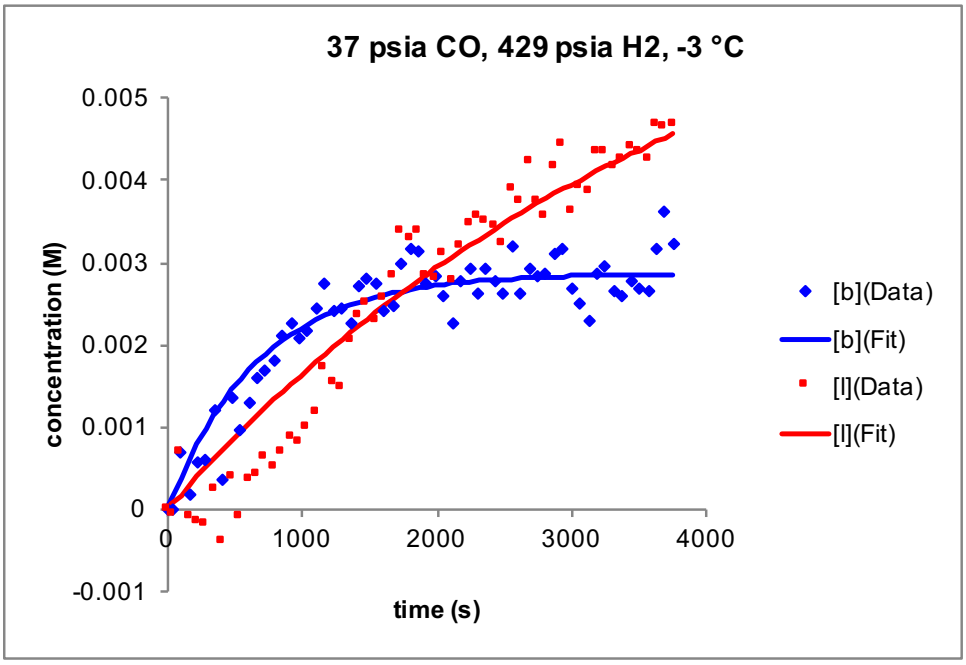

Figure B-61. Data and fits for simplified model of single turnover hydrogenolysis experiments (~20 mM Rh(BDP) as ~1:1 mixture of acyls, 270 K, 37 psia CO, 429 psia H_2, CH_2Cl_2).

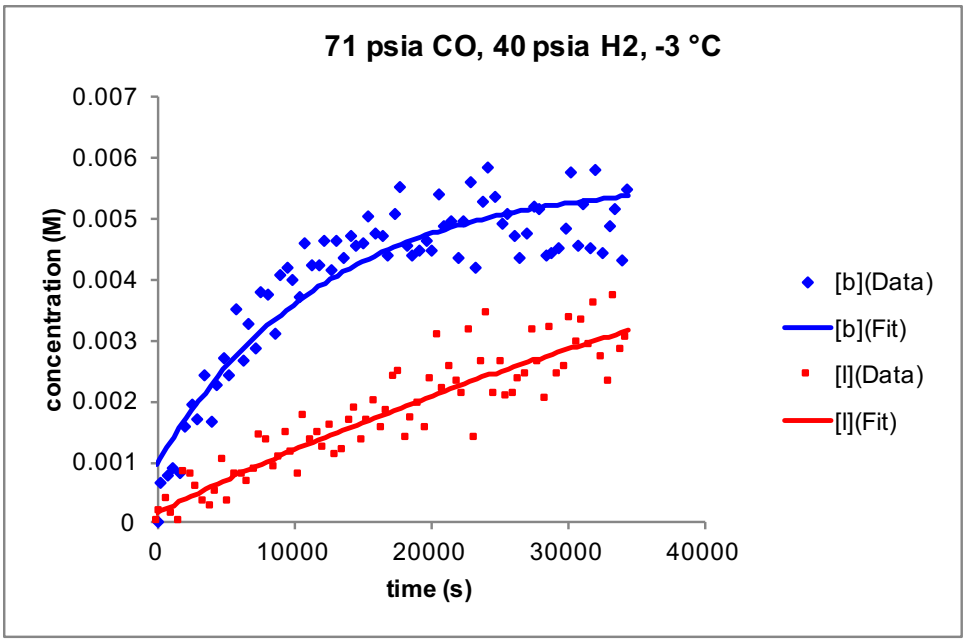

Figure B-62. Data and fits for simplified model of single turnover hydrogenolysis experiments (~20 mM Rh(BDP) as ~1:1 mixture of acyls, 270 K, 71 psia CO, 40 psia H_2, CH_2Cl_2).

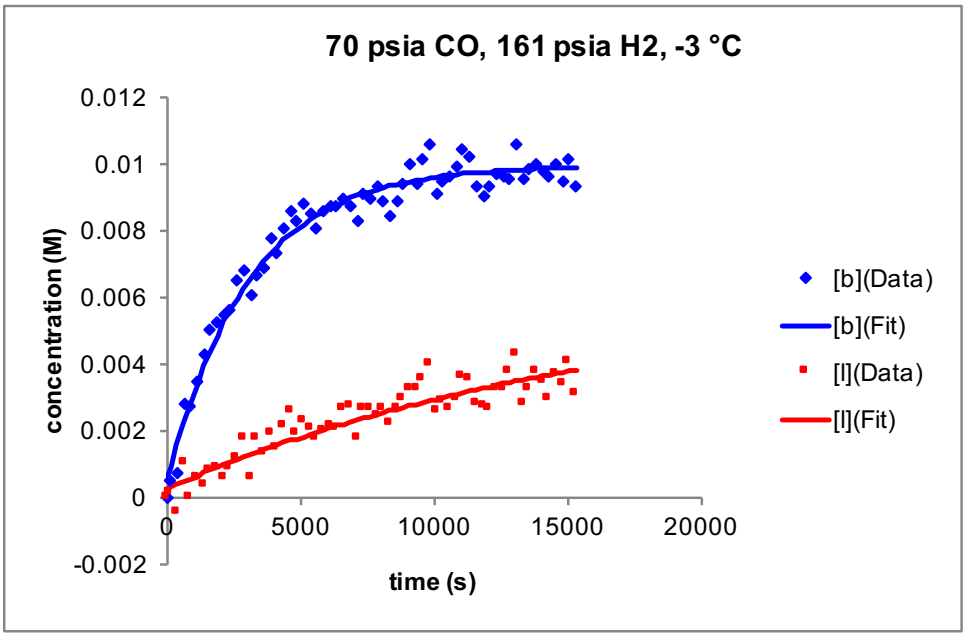

Figure B-63. Data and fits for simplified model of single turnover hydrogenolysis experiments (~20 mM Rh(BDP) as ~1:1 mixture of acyls, 270 K, 70 psia CO, 161 psia H_2, CH_2Cl_2).

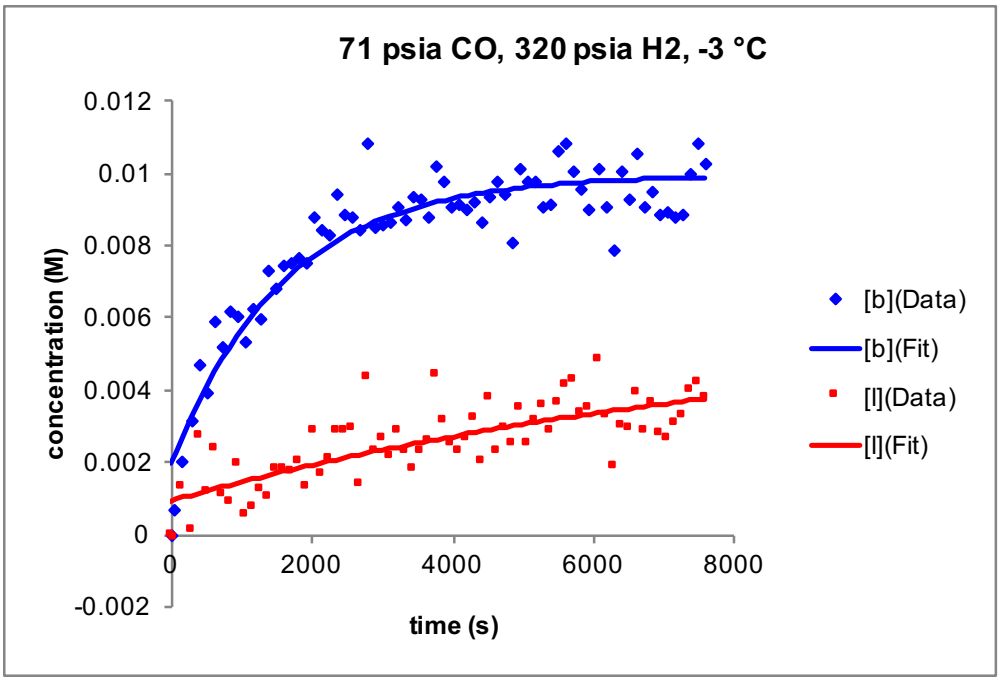

Figure B-64. Data and fits for simplified model of single turnover hydrogenolysis experiments (~20 mM Rh(BDP) as ~1:1 mixture of acyls, 270 K, 71 psia CO, 320 psia H_2, CH_2Cl_2).

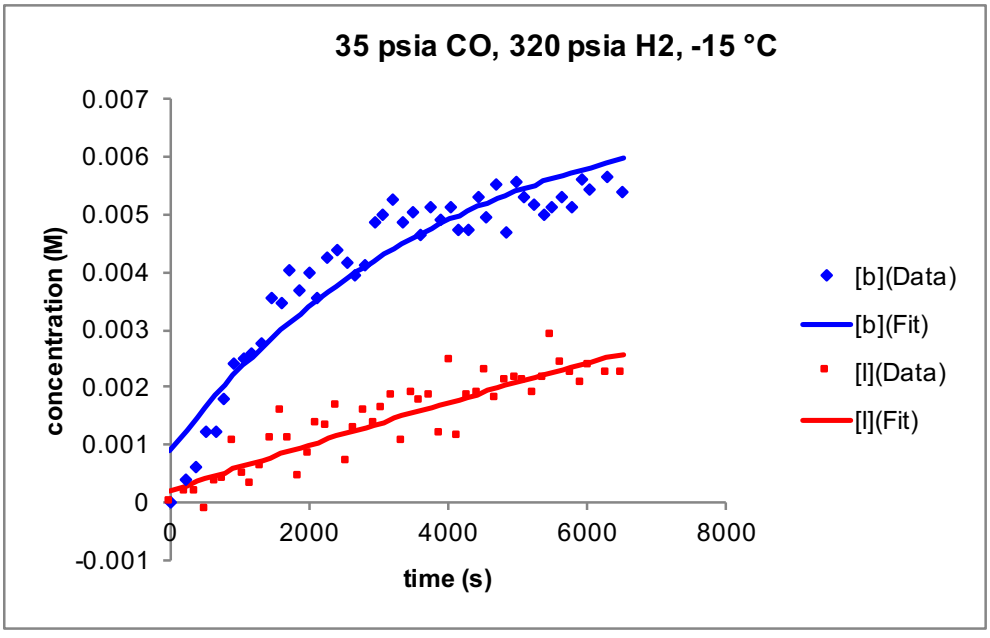

Figure B-65. Data and fits for simplified model of single turnover hydrogenolysis experiments (~20 mM Rh(BDP) as ~1:1 mixture of acyls, 258 K, 35 psia CO, 320 psia H_2, CH_2Cl_2).

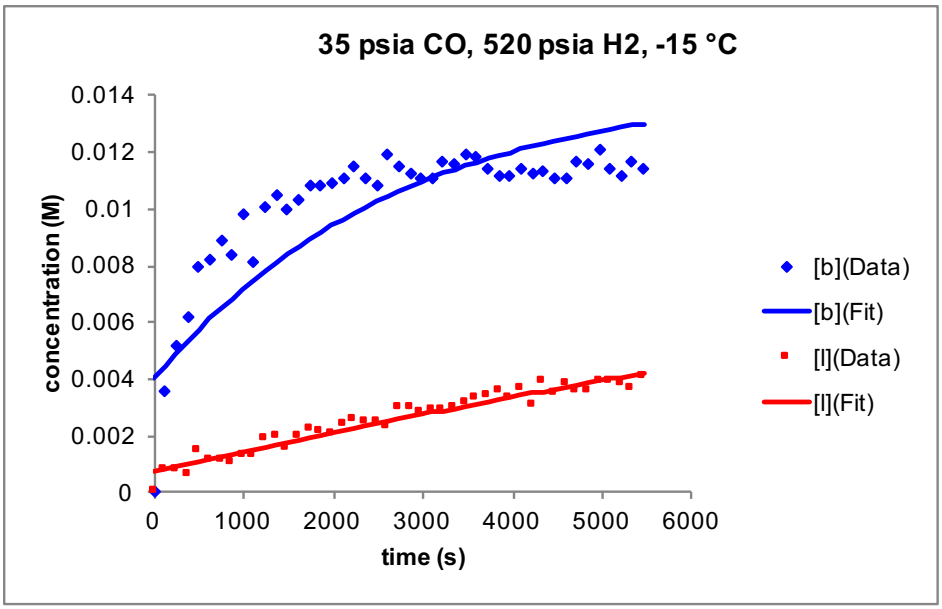

Figure B-66. Data and fits for simplified model of single turnover hydrogenolysis experiments (~20 mM Rh(BDP) as ~1:1 mixture of acyls, 258 K, 35 psia CO, 520 psia H_2, CH_2Cl_2).

B.4.2 Modeling CO Exchange from Hydrido Dicarbonyl Complex 1

B.4.2.1 Modeling Set Up

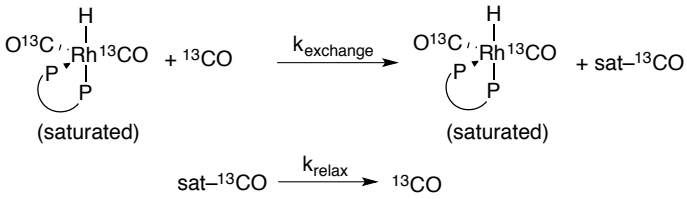

$$k_{exchange} = 2.0847 \times 10^{10}(T)e^{\frac{\Delta H\ddagger\_exchange - \Delta S\ddagger\_exchange(T)}{1.987(T)}}$$

Figure B-67. Model for optimizing activation parameters for CO loss from **1**.

Table B-5. Set and optimized parameters for CO exchange model.

Parameter	Value	Set or Optimized?
ΔH‡_exchange	24.04(3) kcal/mol	optimized
ΔS‡_exchange	16 cal·mol^{-1}K^{-1}	set
krelax (all temps)	0.11 s^{-1}	set based on independent T1 measurement

B.4.3 Modeling Formation of Non-catalytic Acyl Dicarbonyl Species (7)

B.4.3.1 Model Set Up

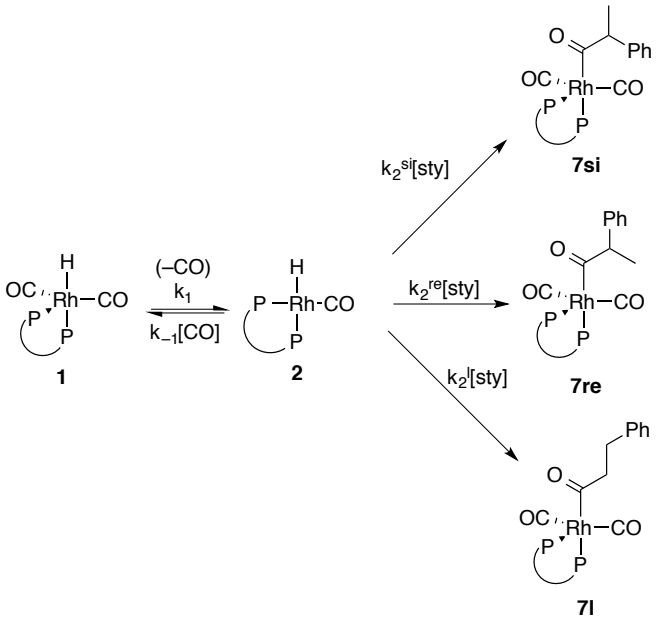

$$k_1 = 2.0837 \times 10^{10}(T)e^{\frac{\Delta H‡\_1for - \Delta S‡\_1for(T)}{1.987(T)}}$$

$$k_{-1} = 2.0837 \times 10^{10}(T)e^{\frac{\Delta H‡\_1back - \Delta S‡\_1back(T)}{1.987(T)}}$$

$$k_2^{si} = 2.0837 \times 10^{10}(T)e^{\frac{\Delta H‡\_2for\_si - \Delta S‡\_2for\_si(T)}{1.987(T)}}$$

$$k_2^{re} = 2.0837 \times 10^{10}(T)e^{\frac{\Delta H‡\_2for\_re - \Delta S‡\_2for\_re(T)}{1.987(T)}}$$

$$k_2^{l} = 2.0837 \times 10^{10}(T)e^{\frac{\Delta H‡\_2for\_l - \Delta S‡\_2for\_l(T)}{1.987(T)}}$$

Figure B-68. Model for determining activation parameters for formation of acyls **7**.

Table B-6. Set and optimized parameters for acyl 7 formation model.

Parameter	Value	Set or Optimized?
ΔH‡_1for	24.04 kcal/mol	set from CO exchange model
ΔS‡_1for	16 cal·mol^{-1}K^{-1}	set from CO exchange model
ΔH‡_1back	7 kcal/mol	set
ΔS‡_1back	–16 cal·mol^{-1}K^{-1}	set based on ΔS‡_1for
ΔH‡_2for_si	4.00(7) kcal/mol	optimized
ΔS‡_2for_si	-30.5(2) cal·mol^{-1}K^{-1}	optimized
ΔH‡_2for_re	5.45(7) kcal/mol	optimized
ΔS‡_2for_re	-30.5(2) cal·mol^{-1}K^{-1}	set based on ΔS‡_2for_si
ΔH‡_2for_l	5.49(7) kcal/mol	optimized
ΔS‡_2for_l	-30.5(2) cal·mol^{-1}K^{-1}	set based on ΔS‡_2for_si

B.4.3.2 Data and Fits of Non-catalytic Acyl 7 Formation Model

Note: 7l = 7n (normal)

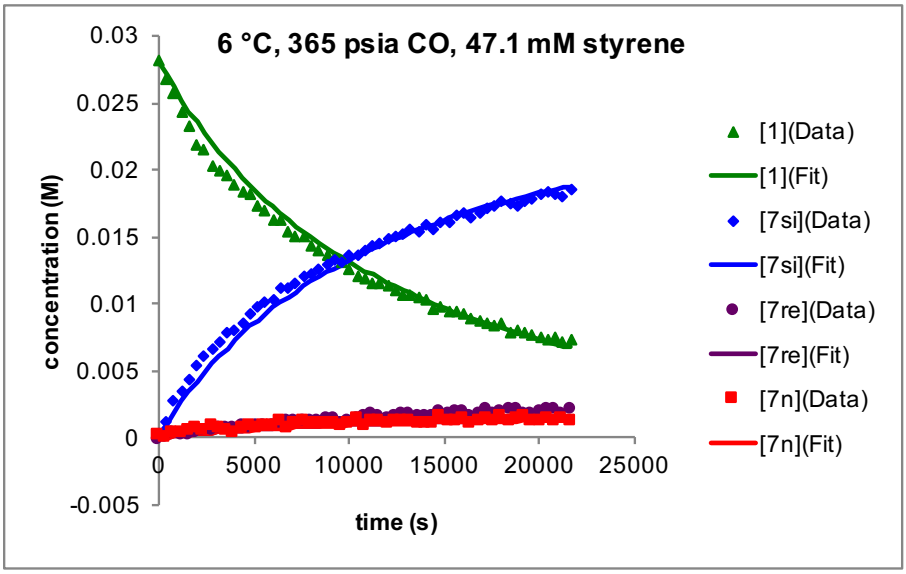

Figure B-69. Data and fits for simplified model of formation of acyl dicarbonyl species (~25 mM **1**, 47.1 mM styrene, 279 K, 365 psia CO, CH_2Cl_2).

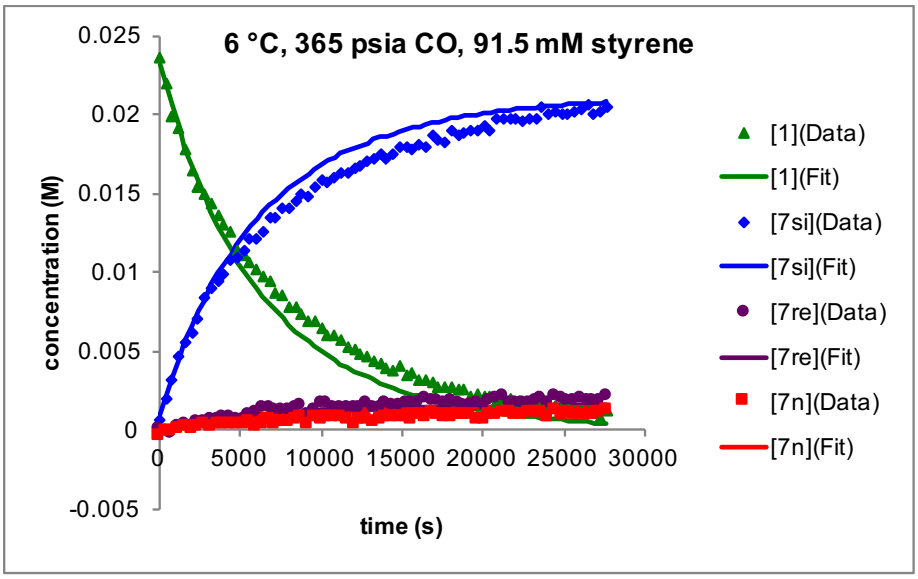

Figure B-70. Data and fits for simplified model of formation of acyl dicarbonyl species (~25 mM **1**, 91.5 mM styrene, 279 K, 365 psia CO, CH_2Cl_2).

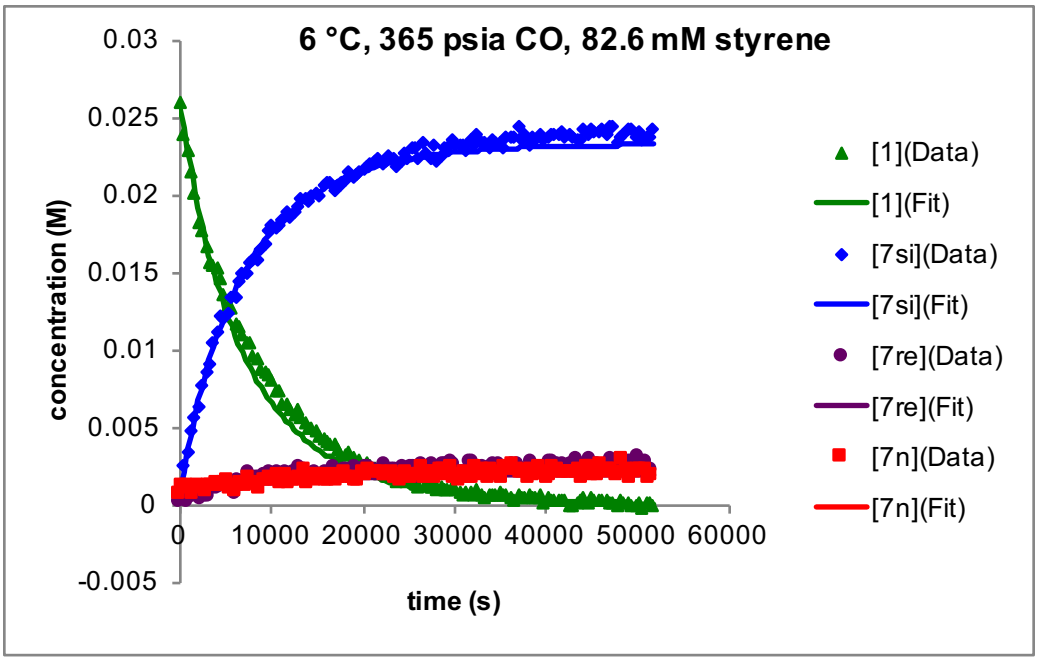

Figure B-71. Data and fits for simplified model of formation of acyl dicarbonyl species (~25 mM **1**, 82.6 mM styrene, 279 K, 365 psia CO, CH_2Cl_2).

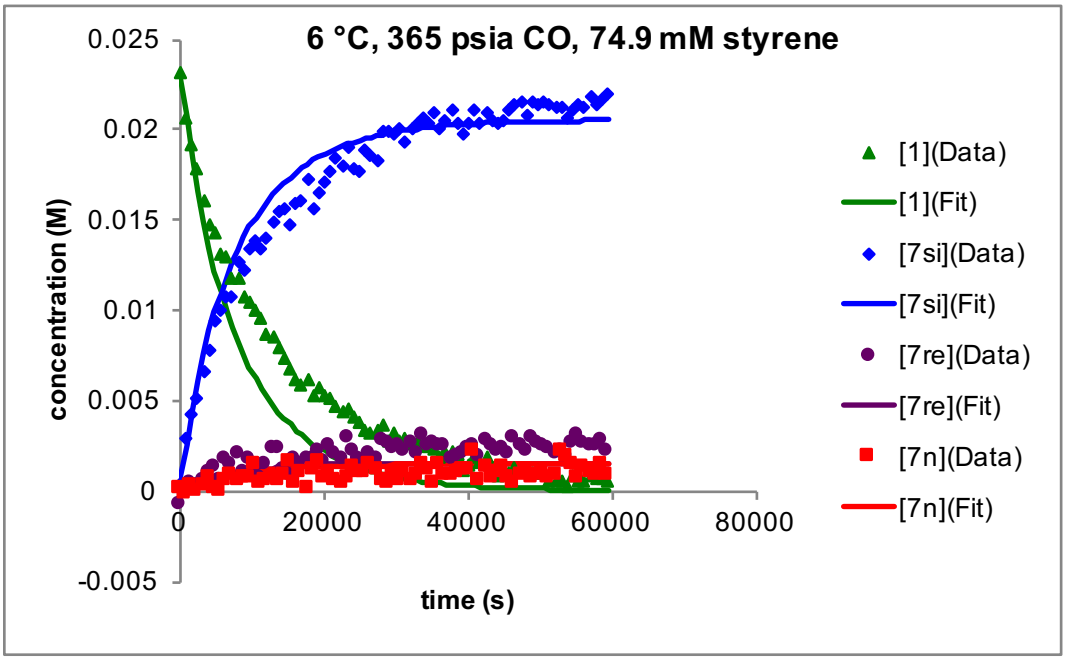

Figure B-72. Data and fits for simplified model of formation of acyl dicarbonyl species (~25 mM **1**, 74.9 mM styrene, 279 K, 365 psia CO, CH_2Cl_2).

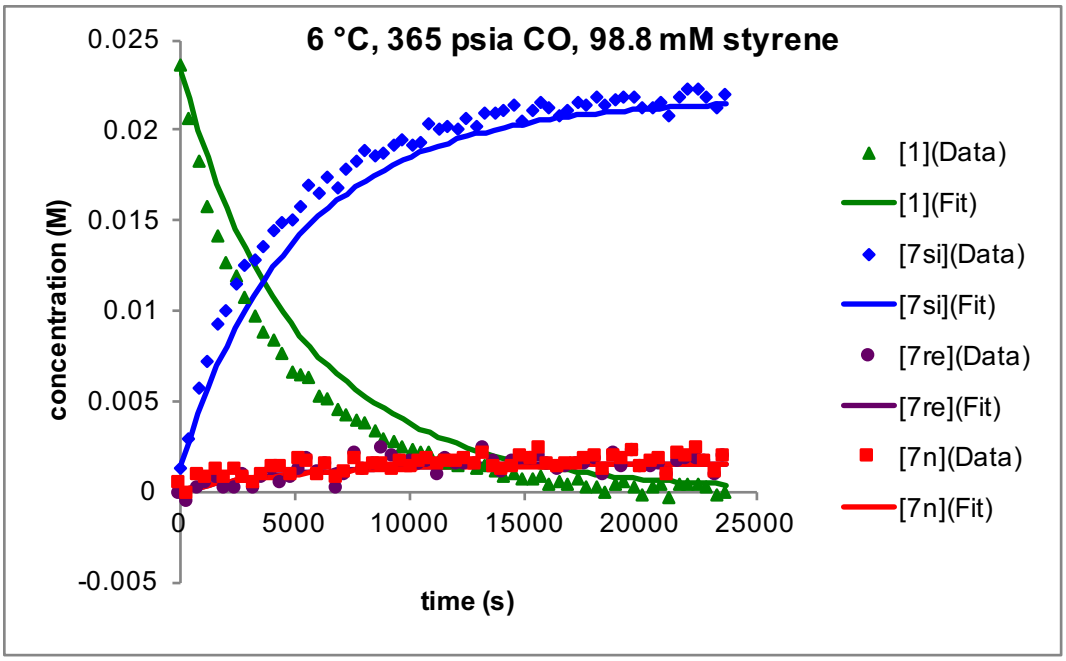

Figure B-73. Data and fits for simplified model of formation of acyl dicarbonyl species (~25 mM **1**, 98.8 mM styrene, 279 K, 365 psia CO, CH_2Cl_2).

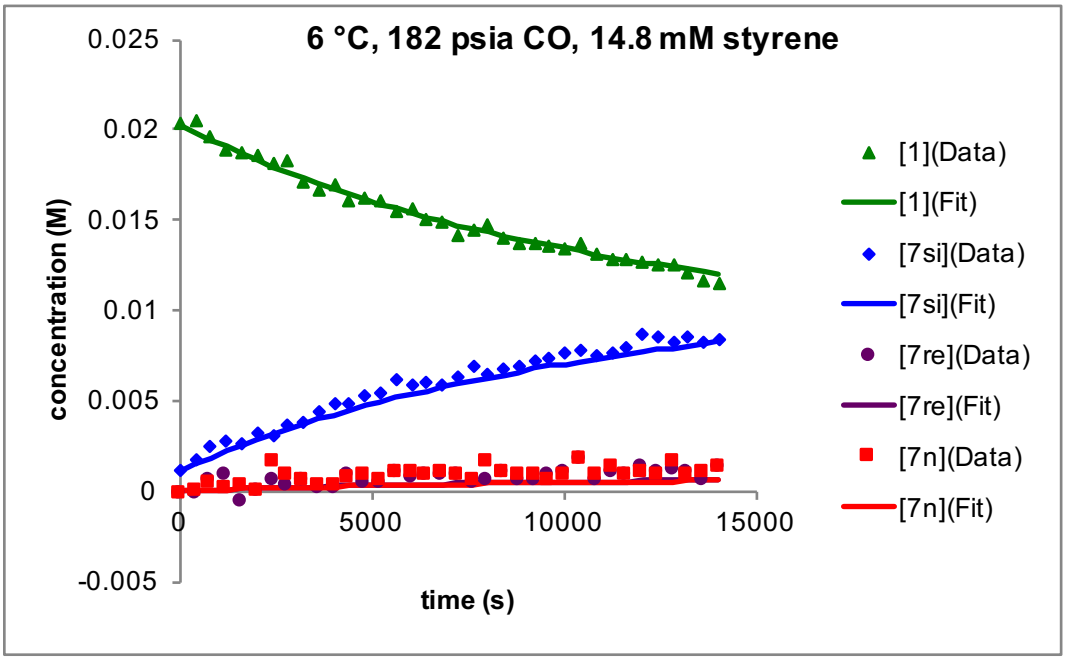

Figure B-74. Data and fits for simplified model of formation of acyl dicarbonyl species (~25 mM **1**, 14.8 mM styrene, 279 K, 182 psia CO, CH_2Cl_2).

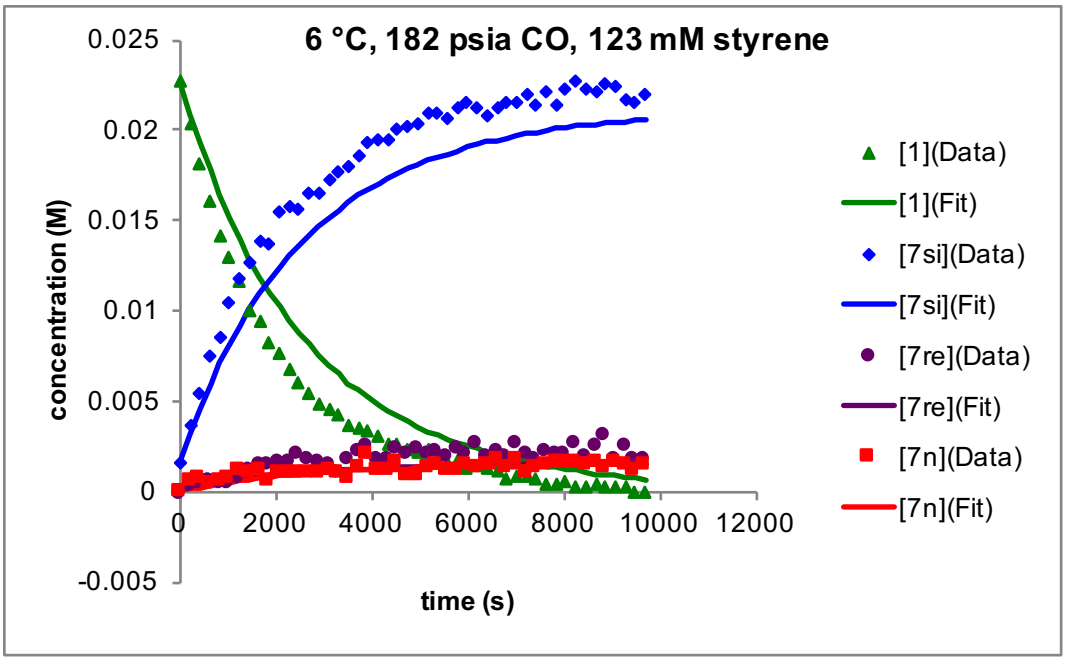

Figure 75. Data and fits for simplified model of formation of acyl dicarbonyl species (~25 mM **1**, 123 mM styrene, 279 K, 182 psia CO, CH_2Cl_2).

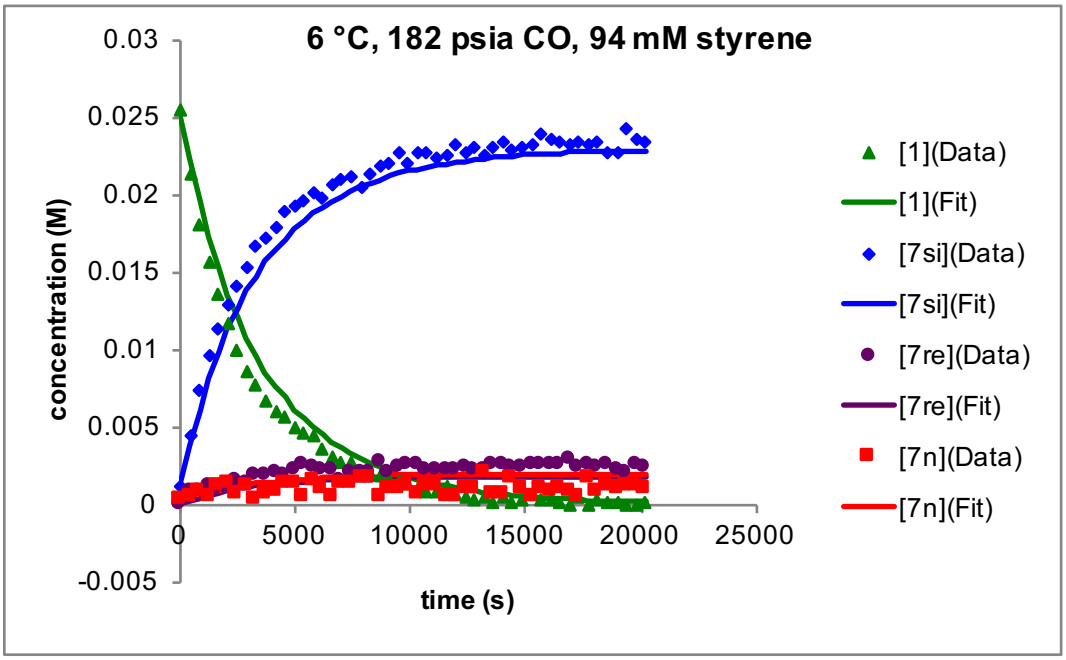

Figure B-76. Data and fits for simplified model of formation of acyl dicarbonyl species (~25 mM **1**, 94.0 mM styrene, 279 K, 182 psia CO, CH_2Cl_2).

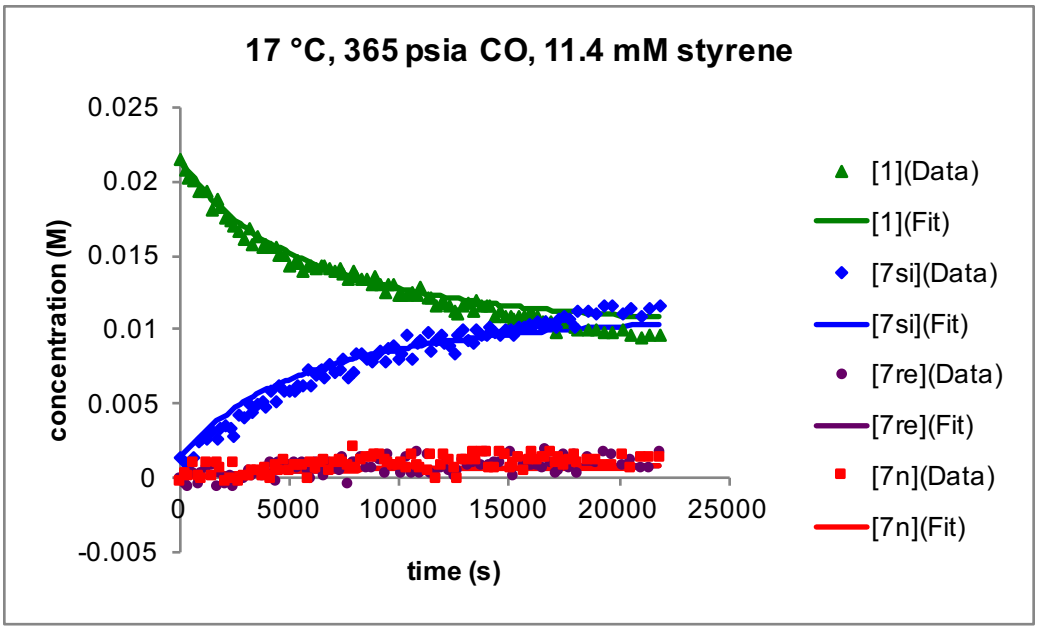

Figure B-77. Data and fits for simplified model of formation of acyl dicarbonyl species (~25 mM **1**, 11.4 mM styrene, 290 K, 365 psia CO, CH_2Cl_2).

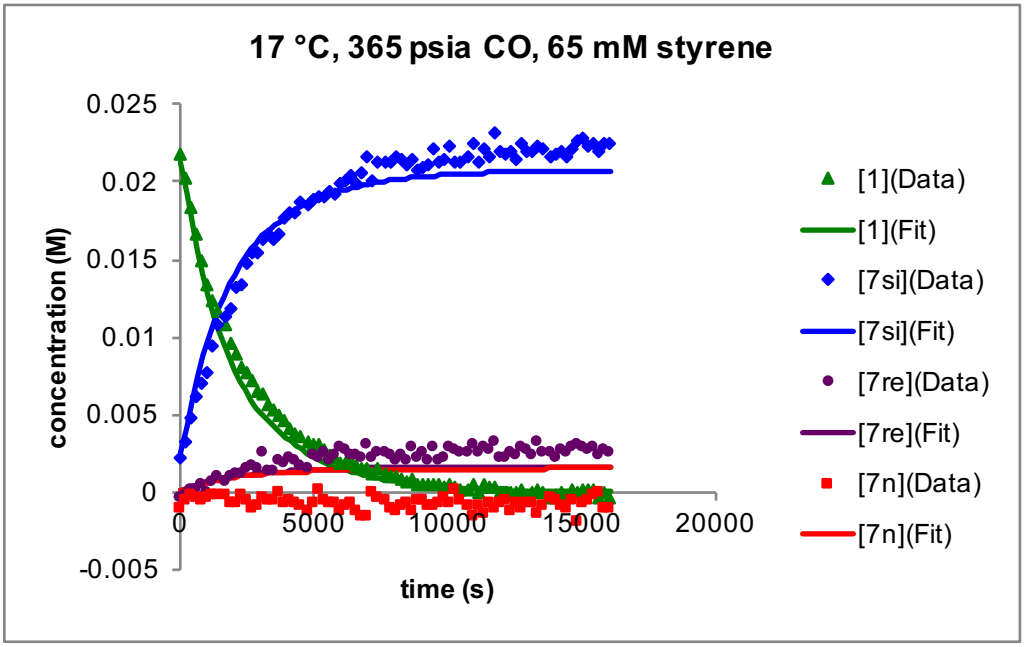

Figure B-78. Data and fits for simplified model of formation of acyl dicarbonyl species (~25 mM **1**, 65 mM styrene, 290 K, 365 psia CO, CH_2Cl_2).

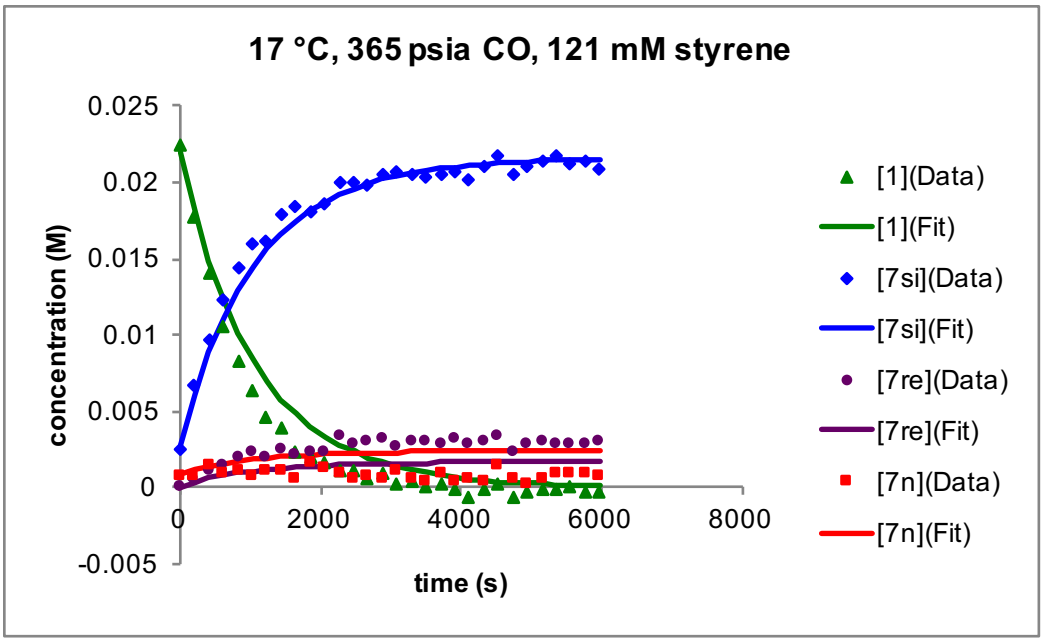

Figure B-79. Data and fits for simplified model of formation of acyl dicarbonyl species (~25 mM **1**, 121 mM styrene, 290 K, 365 psia CO, CH_2Cl_2).

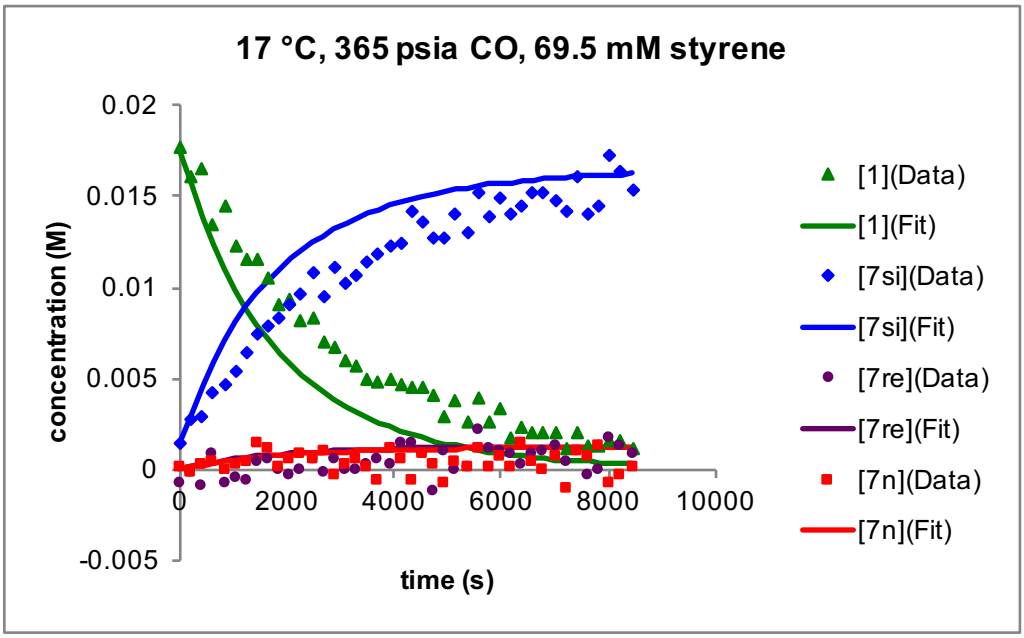

Figure B-80. Data and fits for simplified model of formation of acyl dicarbonyl species (~20 mM **1**, 69.5 mM styrene, 290 K, 365 psia CO, CH_2Cl_2).

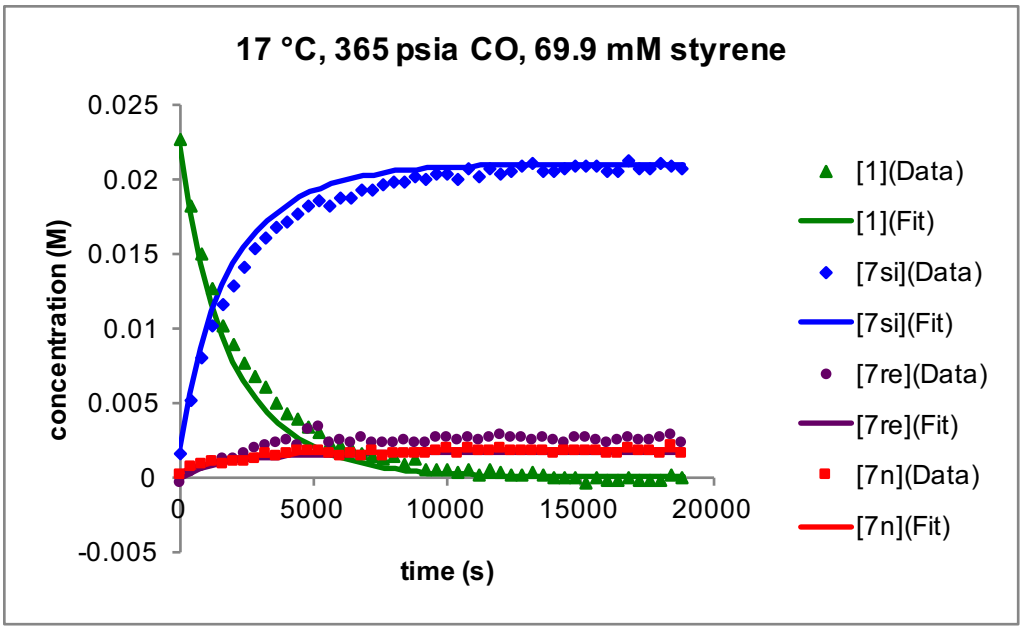

Figure B-81. Data and fits for simplified model of formation of acyl dicarbonyl species (~25 mM **1**, 69.9 mM styrene, 290 K, 365 psia CO, CH_2Cl_2).

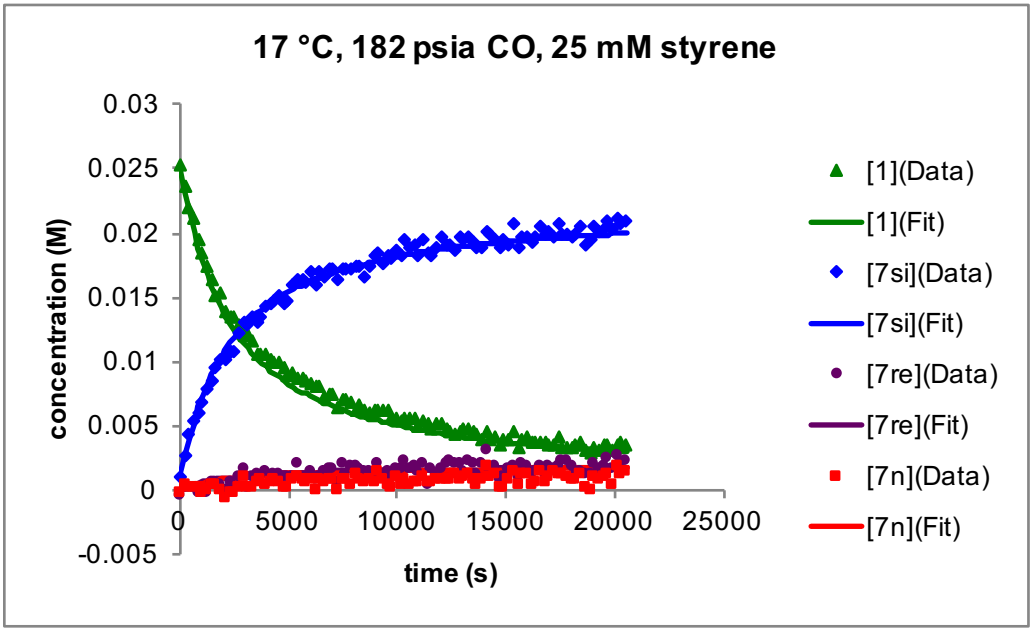

Figure B-82. Data and fits for simplified model of formation of acyl dicarbonyl species (~25 mM **1**, 25.0 mM styrene, 290 K, 182 psia CO, CH_2Cl_2).

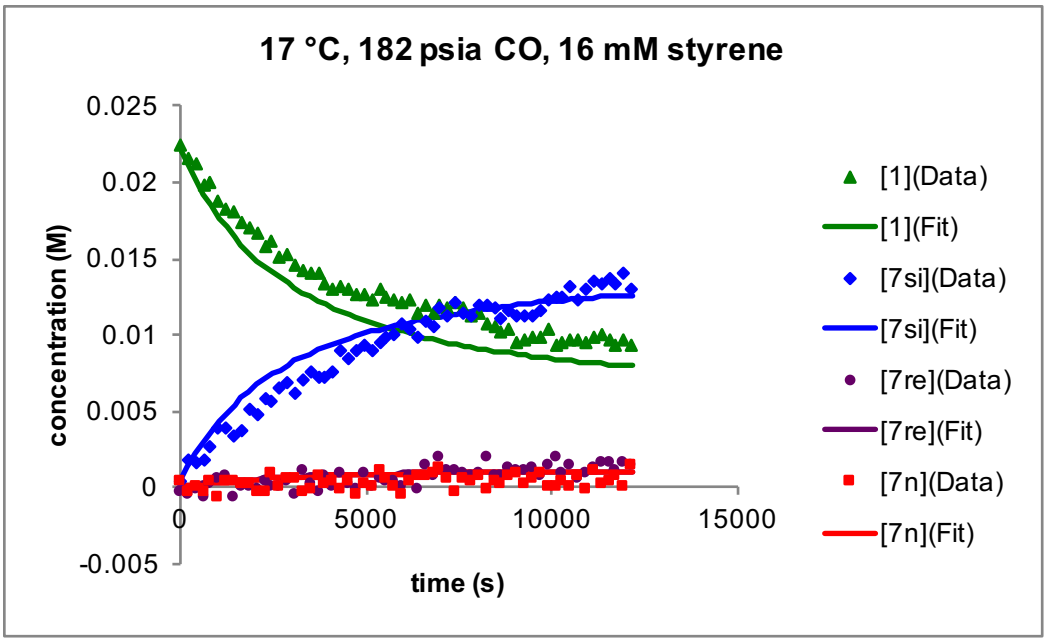

Figure B-83. Data and fits for simplified model of formation of acyl dicarbonyl species (~25 mM **1**, 16.0 mM styrene, 290 K, 182 psia CO, CH_2Cl_2).

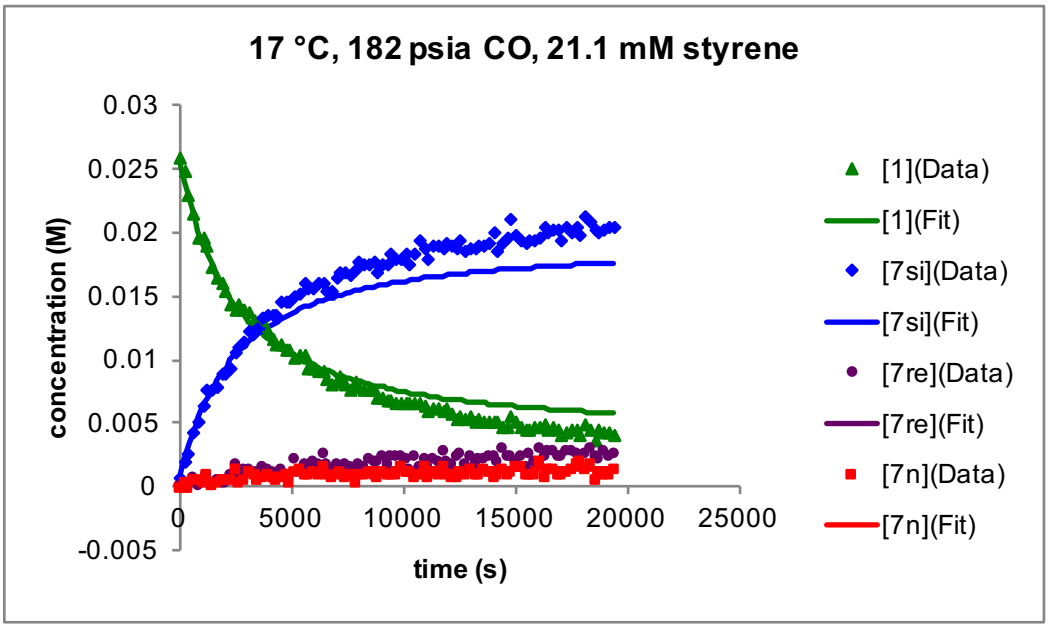

Figure B-84. Data and fits for simplified model of formation of acyl dicarbonyl species (~25 mM **1**, 21.1 mM styrene, 290 K, 182 psia CO, CH_2Cl_2).

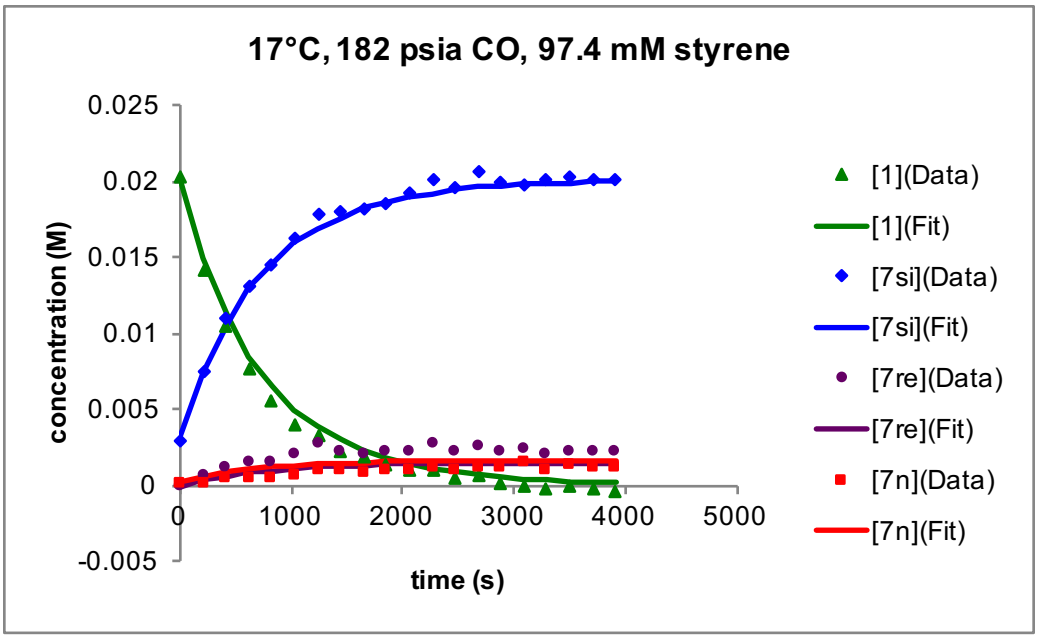

Figure B-85. Data and fits for simplified model of formation of acyl dicarbonyl species (~25 mM **1**, 97.4 mM styrene, 290 K, 182 psia CO, CH_2Cl_2).

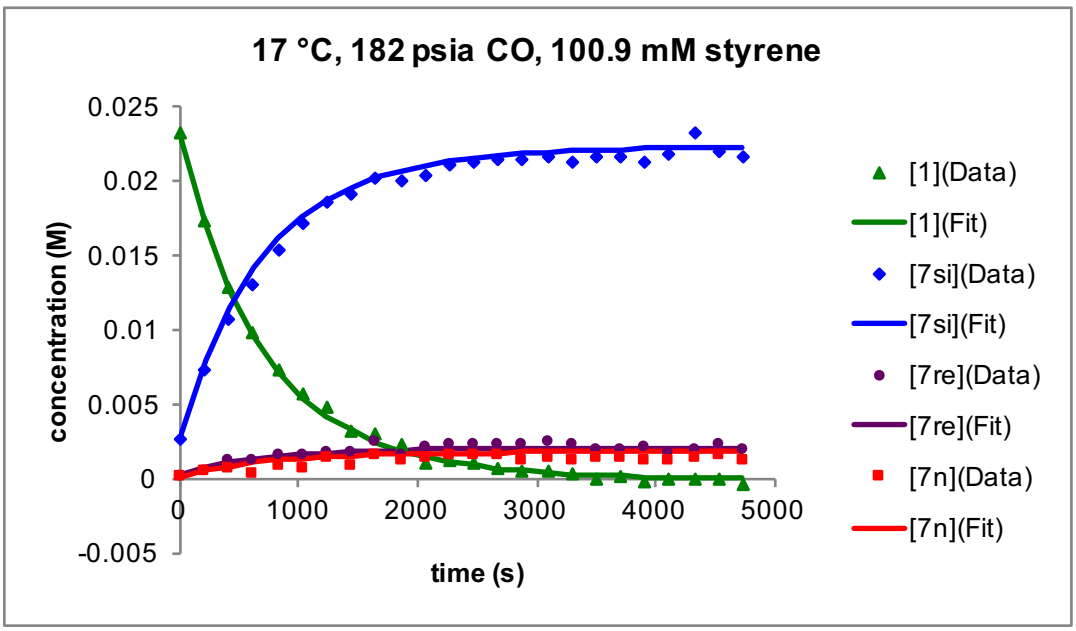

Figure B-86. Data and fits for simplified model of formation of acyl dicarbonyl species (~25 mM 1, 101 mM styrene, 290 K, 182 psia CO, CH_2Cl_2).

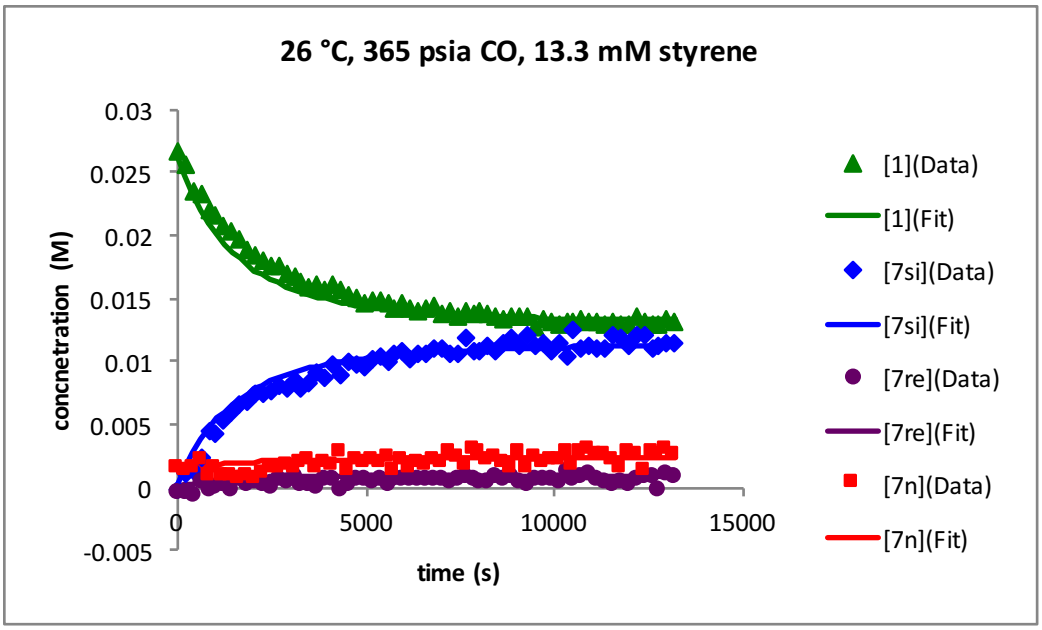

Figure B-87. Data and fits for simplified model of formation of acyl dicarbonyl species (~25 mM **1**, 13.3 mM styrene, 299 K, 365 psia CO, CH_2Cl_2).

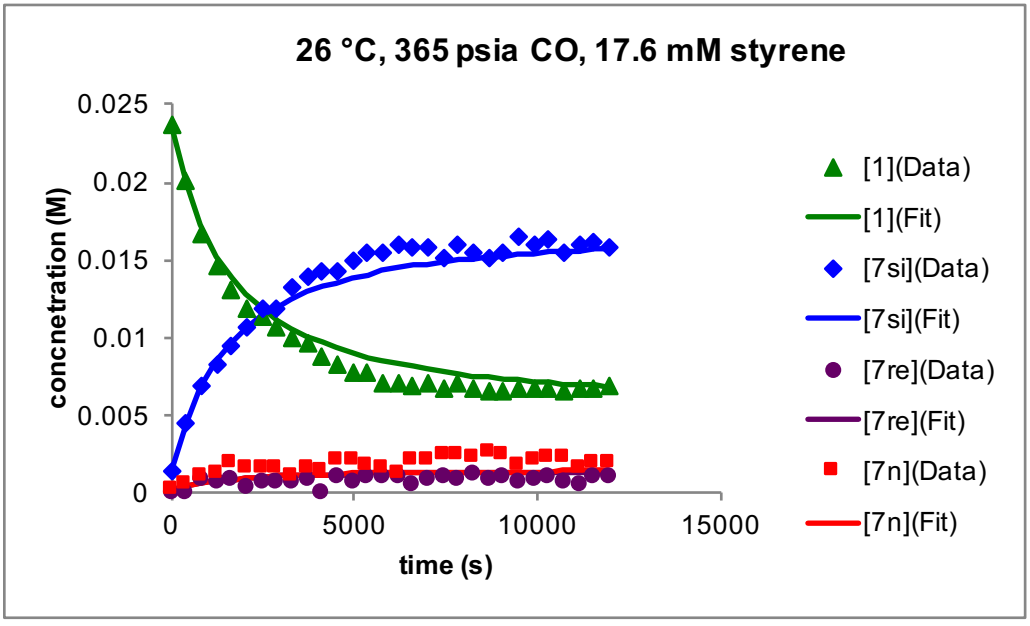

Figure B-88. Data and fits for simplified model of formation of acyl dicarbonyl species (~25 mM **1**, 17.6 mM styrene, 299 K, 365 psia CO, CH_2Cl_2).

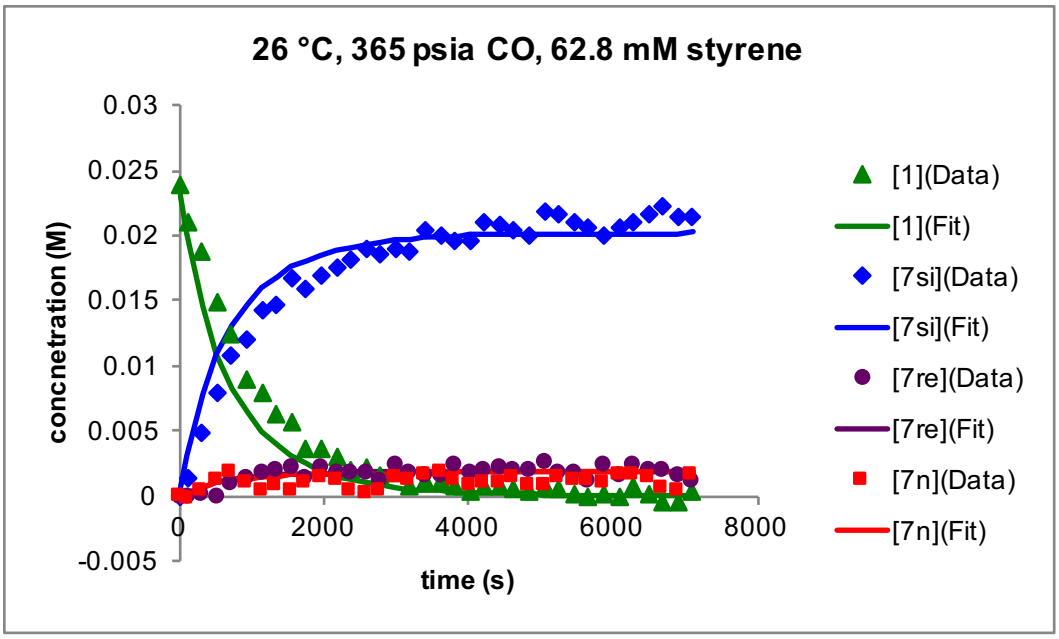

Figure B-89. Data and fits for simplified model of formation of acyl dicarbonyl species (~25 mM **1**, 62.8 mM styrene, 299 K, 365 psia CO, CH_2Cl_2).

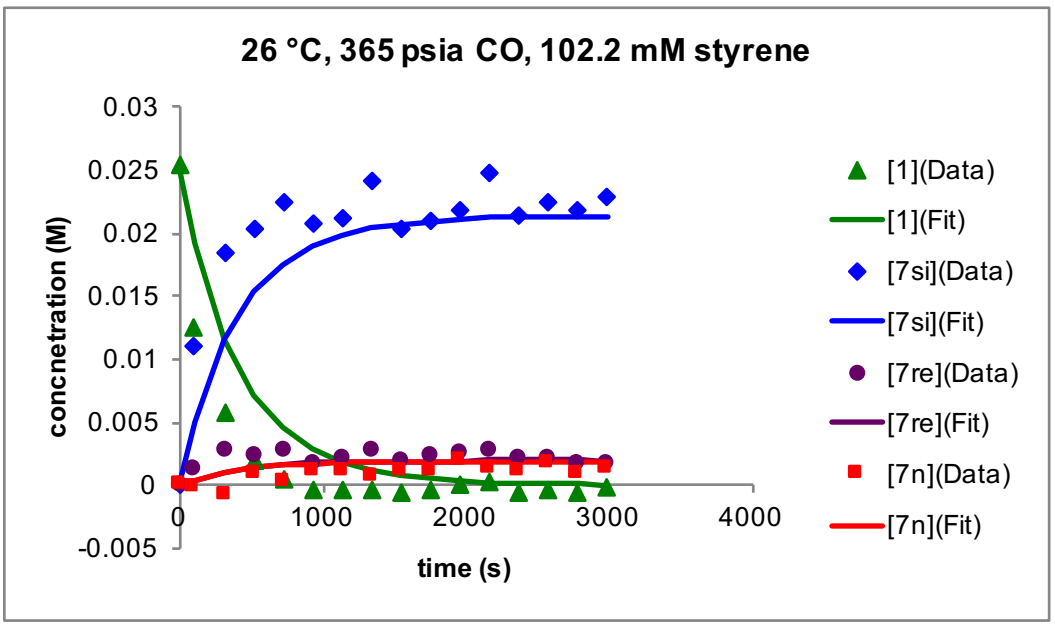

Figure B-90. Data and fits for simplified model of formation of acyl dicarbonyl species (~25 mM **1**, 102 mM styrene, 299 K, 365 psia CO, CH_2Cl_2).

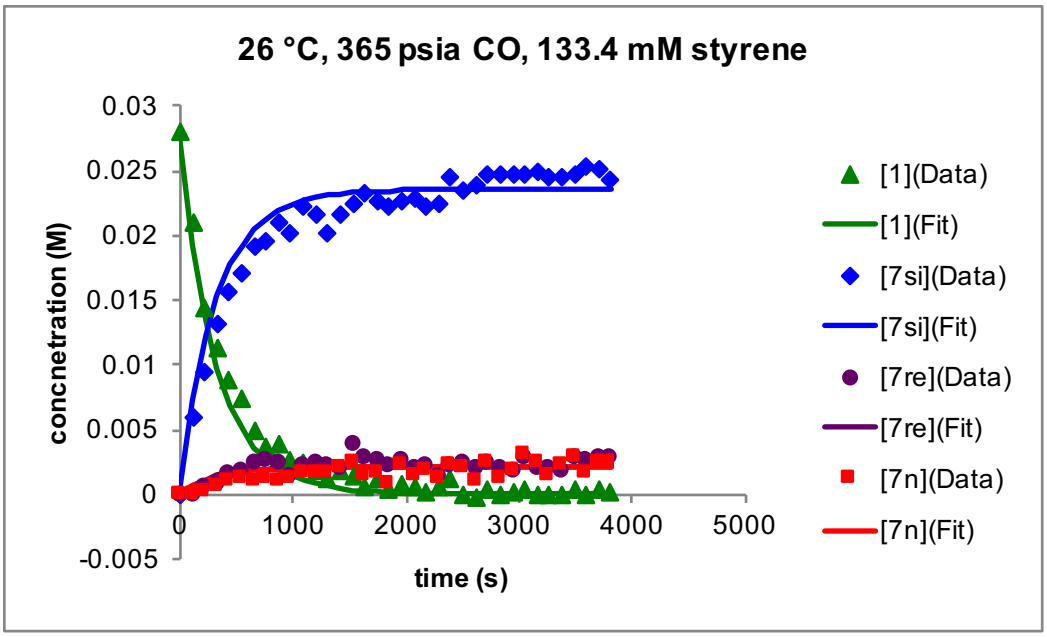

Figure B-91. Data and fits for simplified model of formation of acyl dicarbonyl species (~25 mM **1**, 133 mM styrene, 299 K, 365 psia CO, CH_2Cl_2).

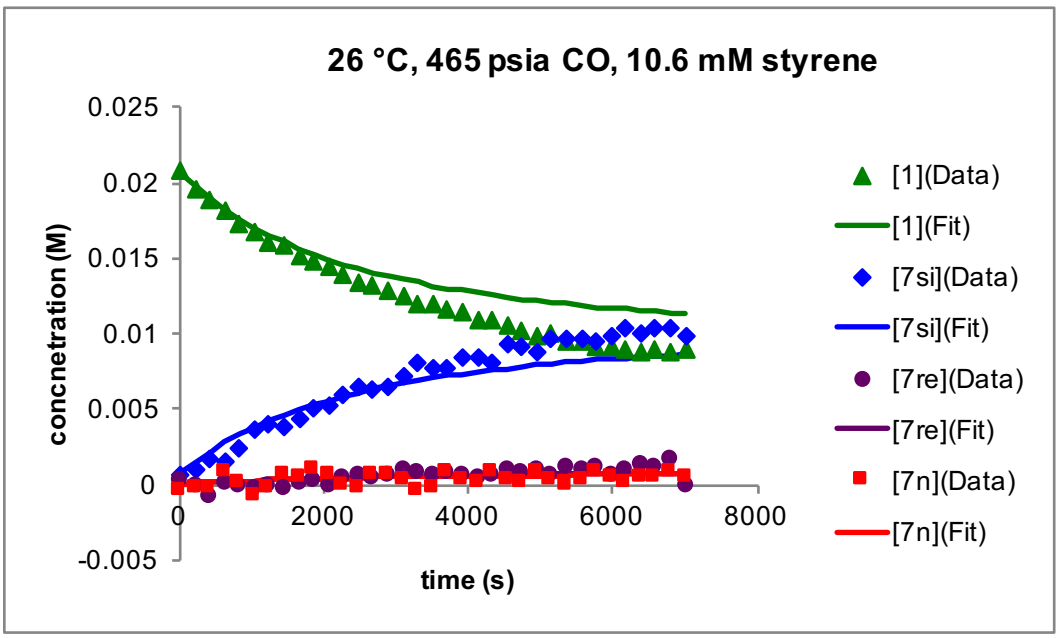

Figure B-92. Data and fits for simplified model of formation of acyl dicarbonyl species (~25 mM **1**, 10.6 mM styrene, 299 K, 465 psia CO, CH_2Cl_2).

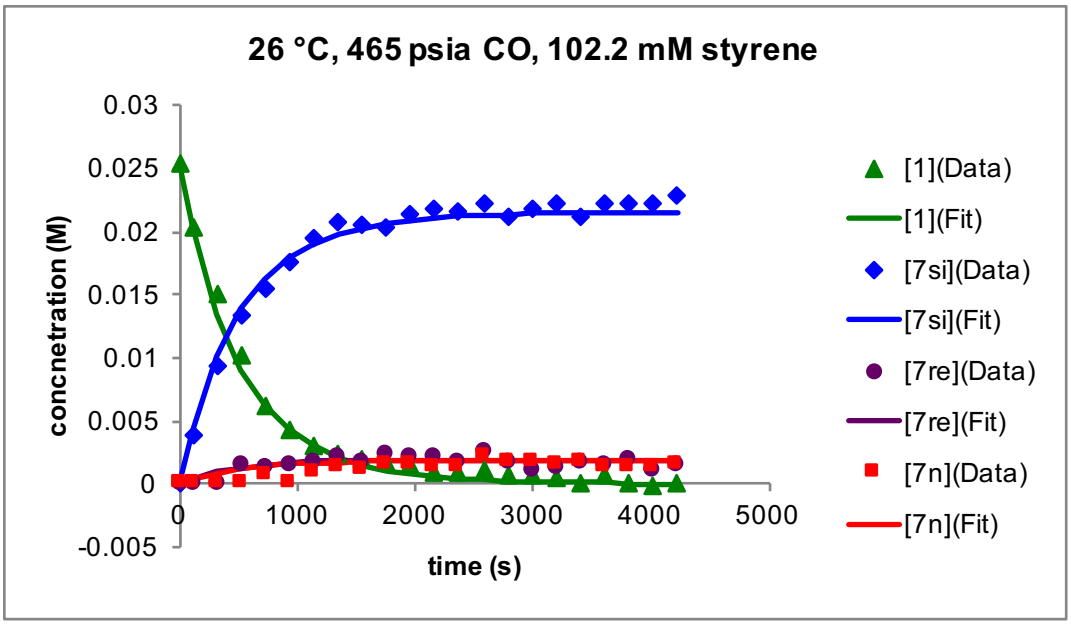

Figure B-93. Data and fits for simplified model of formation of acyl dicarbonyl species (~25 mM **1**, 102 mM styrene, 299 K, 465 psia CO, CH_2Cl_2).

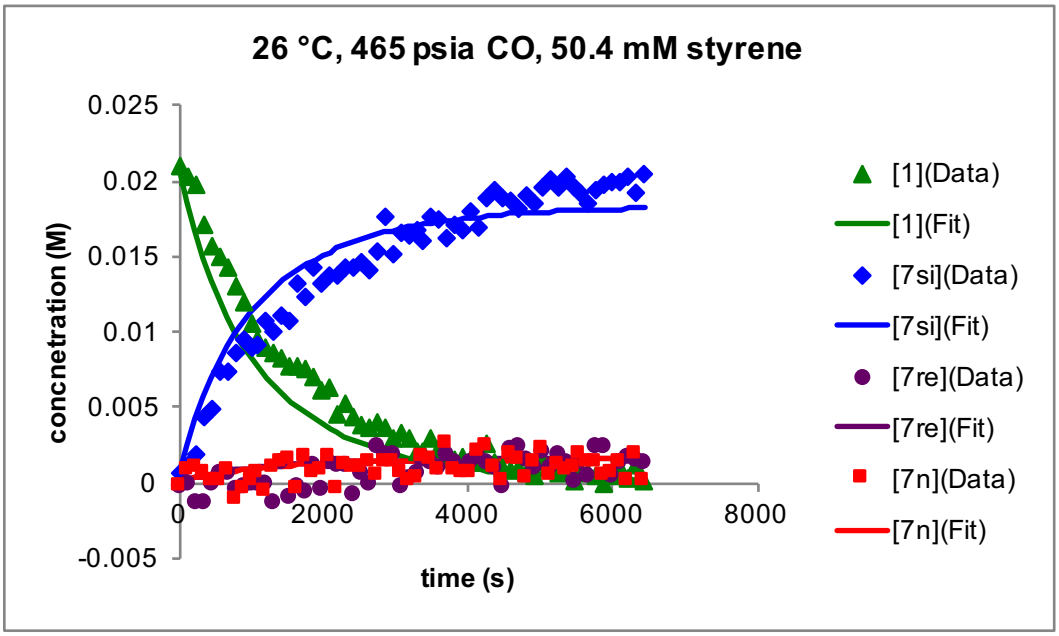

Figure B-94. Data and fits for simplified model of formation of acyl dicarbonyl species (~25 mM **1**, 50.4 mM styrene, 299 K, 465 psia CO, CH_2Cl_2).

B.4.4 Modeling Acyl 7 Isomerization

B.4.4.1 Model Set Up

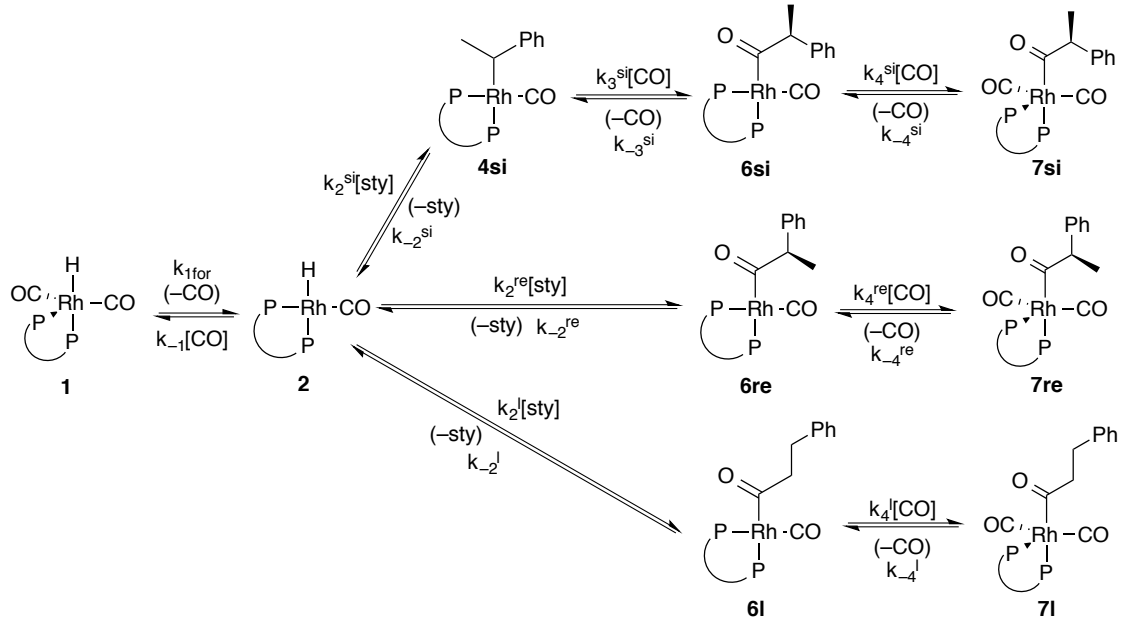

$$k_1 = 2.0837\times10^{10}(T)e^{\frac{\Delta H\ddagger\_1for - \Delta S\ddagger\_1for(T)}{1.987(T)}} \qquad k_3^{si} = 2.0837\times10^{10}(T)e^{\frac{\Delta H\ddagger\_3for\_si - \Delta S\ddagger\_3for\_si(T)}{1.987(T)}}$$

$$k_{-1} = 2.0837\times10^{10}(T)e^{\frac{\Delta H\ddagger\_1back - \Delta S\ddagger\_1back(T)}{1.987(T)}} \qquad k_{-3}^{si} = 2.0837\times10^{10}(T)e^{\frac{\Delta H\ddagger\_3back\_si - \Delta S\ddagger\_3back\_si(T)}{1.987(T)}}$$

$$k_2^{si} = 2.0837\times10^{10}(T)e^{\frac{\Delta H\ddagger\_2for\_si - \Delta S\ddagger\_2for\_si(T)}{1.987(T)}} \qquad k_4^{si} = 2.0837\times10^{10}(T)e^{\frac{\Delta H\ddagger\_4for\_si - \Delta S\ddagger\_4for\_si(T)}{1.987(T)}}$$

$$k_{-2}^{si} = 2.0837\times10^{10}(T)e^{\frac{\Delta H\ddagger\_2back\_si - \Delta S\ddagger\_2back\_si(T)}{1.987(T)}} \qquad k_{-4}^{si} = 2.0837\times10^{10}(T)e^{\frac{\Delta H\ddagger\_4back\_si - \Delta S\ddagger\_4back\_si(T)}{1.987(T)}}$$

$$k_2^{re} = 2.0837\times10^{10}(T)e^{\frac{\Delta H\ddagger\_2for\_re - \Delta S\ddagger\_2for\_re(T)}{1.987(T)}} \qquad k_4^{re} = 2.0837\times10^{10}(T)e^{\frac{\Delta H\ddagger\_4for\_re - \Delta S\ddagger\_4for\_re(T)}{1.987(T)}}$$

$$k_{-2}^{re} = 2.0837\times10^{10}(T)e^{\frac{\Delta H\ddagger\_2back\_re - \Delta S\ddagger\_2back\_re(T)}{1.987(T)}} \qquad k_{-4}^{re} = 2.0837\times10^{10}(T)e^{\frac{\Delta H\ddagger\_2back\_re - \Delta S\ddagger\_2back\_re(T)}{1.987(T)}}$$

$$k_2^{l} = 2.0837\times10^{10}(T)e^{\frac{\Delta H\ddagger\_2for\_l - \Delta S\ddagger\_2for\_l(T)}{1.987(T)}} \qquad k_4^{l} = 2.0837\times10^{10}(T)e^{\frac{\Delta H\ddagger\_4for\_l - \Delta S\ddagger\_4for\_l(T)}{1.987(T)}}$$

$$k_{-2}^{l} = 2.0837\times10^{10}(T)e^{\frac{\Delta H\ddagger\_2back\_l - \Delta S\ddagger\_2back\_l(T)}{1.987(T)}} \qquad k_{-4}^{l} = 2.0837\times10^{10}(T)e^{\frac{\Delta H\ddagger\_4back\_l - \Delta S\ddagger\_4back\_l(T)}{1.987(T)}}$$

Figure B-95. Model for determining activation parameters for isomerization of acyls **7**.

Table B-7. Set and optimized parameters for acyl 7 isomerization model.

Parameter	Value	Set or Optimized?
ΔH‡_1for	24.04 kcal/mol	set from CO exchange model
ΔS‡_1for	16 cal·mol^{-1}K^{-1}	set from CO exchange model
ΔH‡_1back	7 kcal/mol	set from acyl **7** formation model
ΔS‡_1back	–16 cal·mol^{-1}K^{-1}	set from acyl **7** formation model
ΔH‡_2for_si	4.00 kcal/mol	set from acyl **7** formation model
ΔS‡_2for_si	-30.5 cal·mol^{-1}K^{-1}	set from acyl **7** formation model
ΔH‡_2back_si	13.90 kcal/mol	set based on alkyl **4** isomerization model
ΔS‡_2back_si	–1.1 cal·mol^{-1}K^{-1}	set based on alkyl **4** isomerization model
ΔH‡_2for_re	5.45 kcal/mol	set from acyl **7** formation model
ΔS‡_2for_re	-30.5cal·mol^{-1}K^{-1}	set from acyl **7** formation model
ΔH‡_2back_re	20.063(8) kcal/mol	optimized
ΔS‡_2back_re	0 cal·mol^{-1}K^{-1}	set based on ΔS‡_2for_re
ΔH‡_2for_l	5.49 kcal/mol	set from acyl **7** formation model
ΔS‡_2for_l	-30.5 cal·mol^{-1}K^{-1}	set from acyl **7** formation model
ΔH‡_2back_l	22.49(3) kcal/mol	optimized
ΔS‡_2back_l	0 cal·mol^{-1}K^{-1}	set based on ΔS‡_2for_l
ΔH‡_3for_si	11.80 kcal/mol	set
ΔS‡_3for_si	0 cal·mol^{-1}K^{-1}	set
ΔH‡_3back_si	19.739(2) kcal/mol	optimized
ΔS‡_3back_si	0 cal·mol^{-1}K^{-1}	set
ΔH‡_4for_si	9 kcal/mol	set
ΔS‡_4for_si	–12.2 cal·mol^{-1}K^{-1}	set based on ΔS‡_4back_si
ΔH‡_4back_si	23.0(2) kcal/mol	set from hydrogenolysis model
ΔS‡_4back_si	17.8(7) cal·mol^{-1}K^{-1}	set from hydrogenolysis model
ΔH‡_4for_re	9 kcal/mol	set
ΔS‡_4for_re	–12.2 cal·mol^{-1}K^{-1}	set based on ΔS‡_4back_re
ΔH‡_4back_re	23.0(2) kcal/mol	set from hydrogenolysis model
ΔS‡_4back_re	17.8(7) cal·mol^{-1}K^{-1}	set from hydrogenolysis model
ΔH‡_4for_l	9 kcal/mol	set
ΔS‡_4for_l	–14.8 cal·mol^{-1}K^{-1}	set based on ΔS‡_4back_l
ΔH‡_4back_l	23.8(1) kcal/mol	set from hydrogenolysis model
ΔS‡_4back_l	15.5(2) cal·mol^{-1}K^{-1}	set from hydrogenolysis model

B.4.4.2 Data and fits of Non-catalytic Acyl 7 Isomerization Model

Note: **7l** = **7n** (normal)

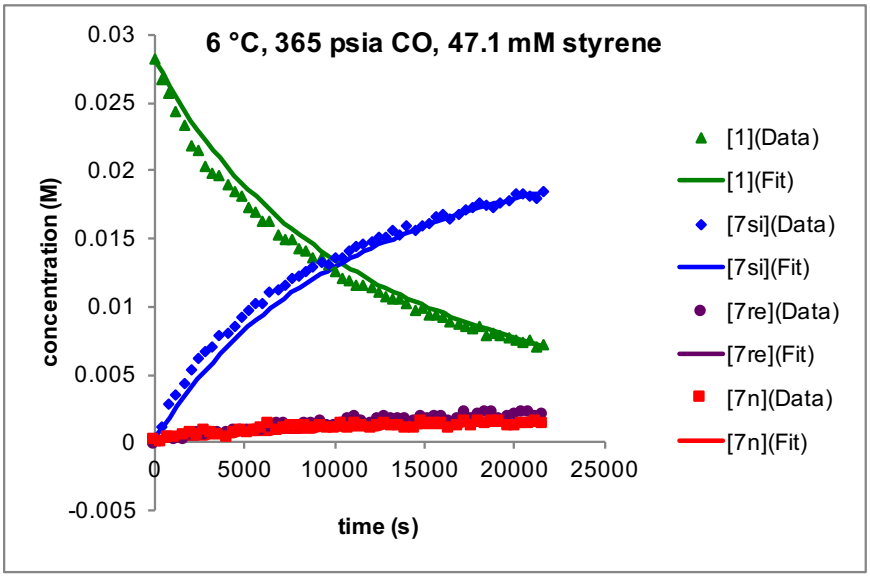

Figure B-96. Data and fits for model of formation and isomerization of acyl dicarbonyl species (~25 mM **1**, 47.1 mM styrene, 279 K, 365 psia CO, CH_2Cl_2).

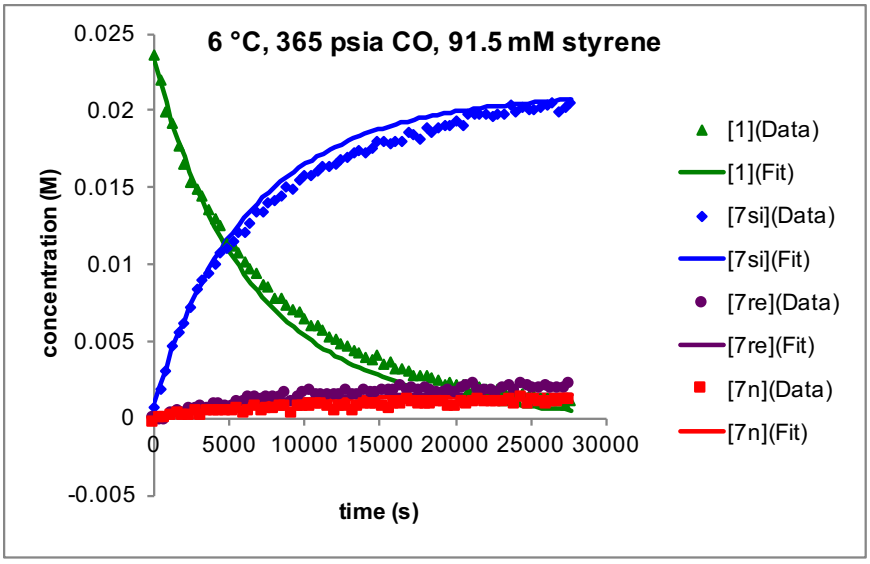

Figure B-97. Data and fits for model of formation and isomeriztion of acyl dicarbonyl species (~25 mM **1**, 91.5 mM styrene, 279 K, 365 psia CO, CH_2Cl_2).

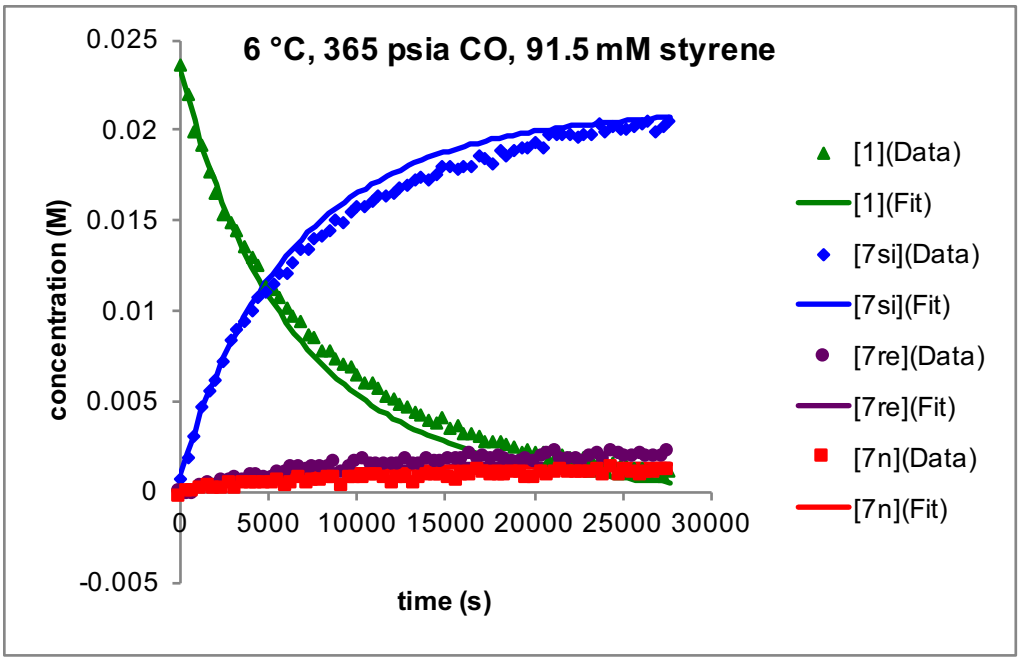

Figure B-98. Data and fits for model of formation and isomerization of acyl dicarbonyl species (~25 mM **1**, 82.6 mM styrene, 279 K, 365 psia CO, CH_2Cl_2).

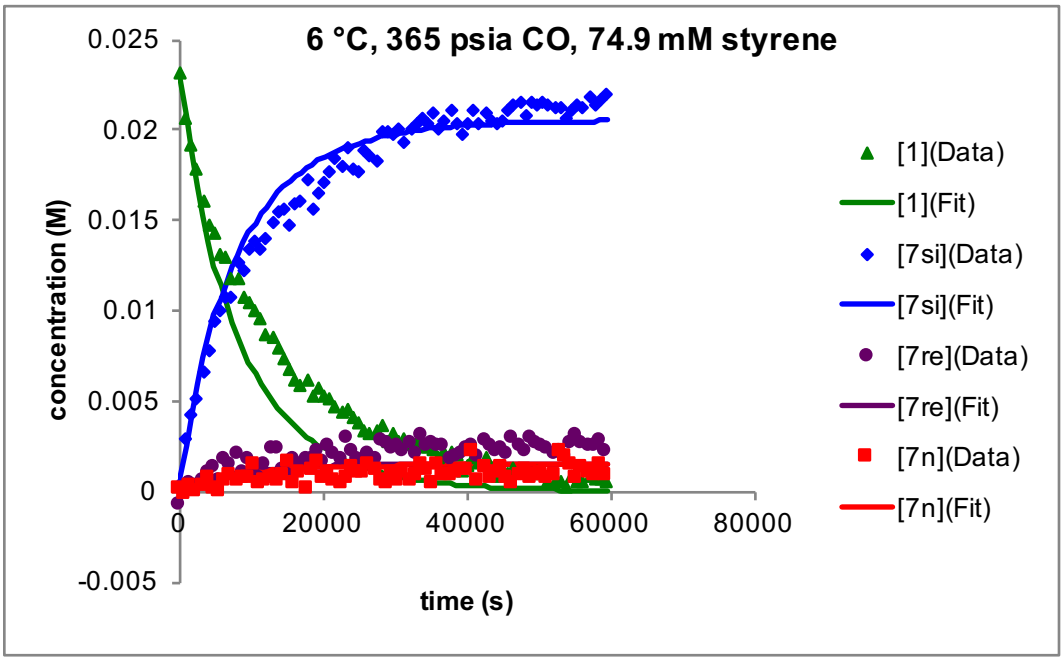

Figure B-99. Data and fits for model of formation and isomerization of acyl dicarbonyl species (~25 mM **1**, 74.9 mM styrene, 279 K, 365 psia CO, CH_2Cl_2).

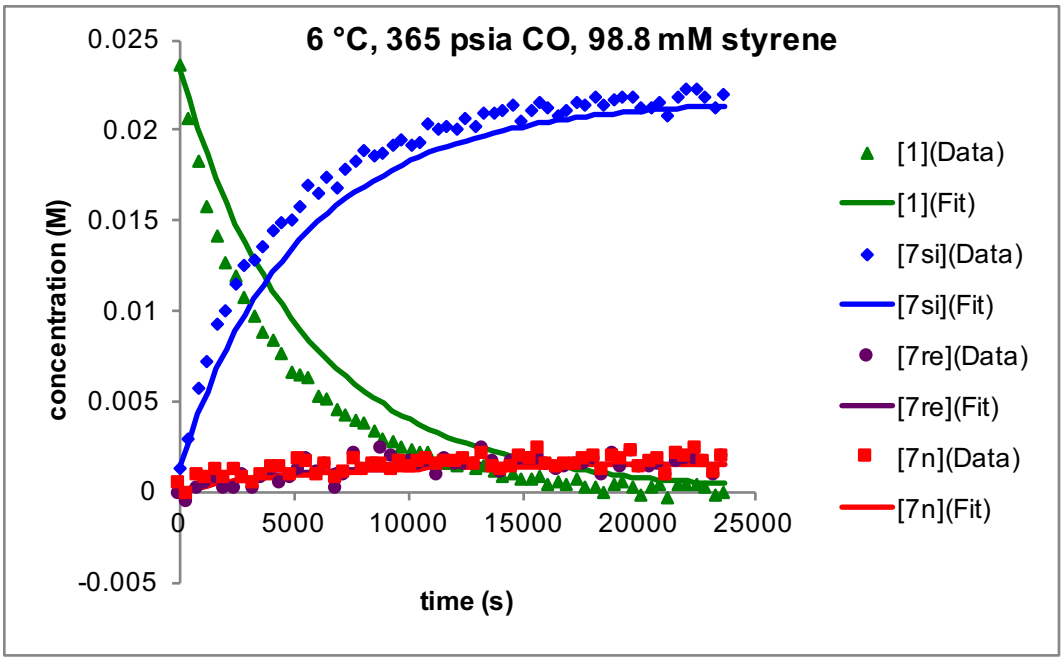

Figure B-100. Data and fits for model of formation and isomerization of acyl dicarbonyl species (~25 mM **1**, 98.8 mM styrene, 279 K, 365 psia CO, CH_2Cl_2).

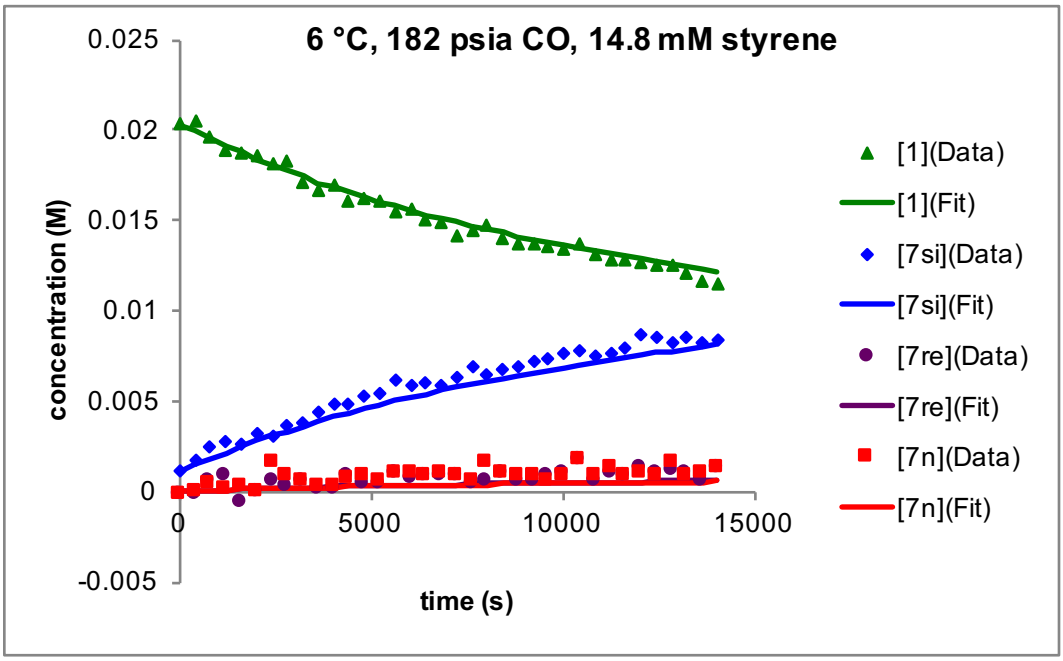

Figure B-101. Data and fits for simplified of formation and isomerization of acyl dicarbonyl species (~25 mM **1**, 14.8 mM styrene, 279 K, 182 psia CO, CH_2Cl_2).

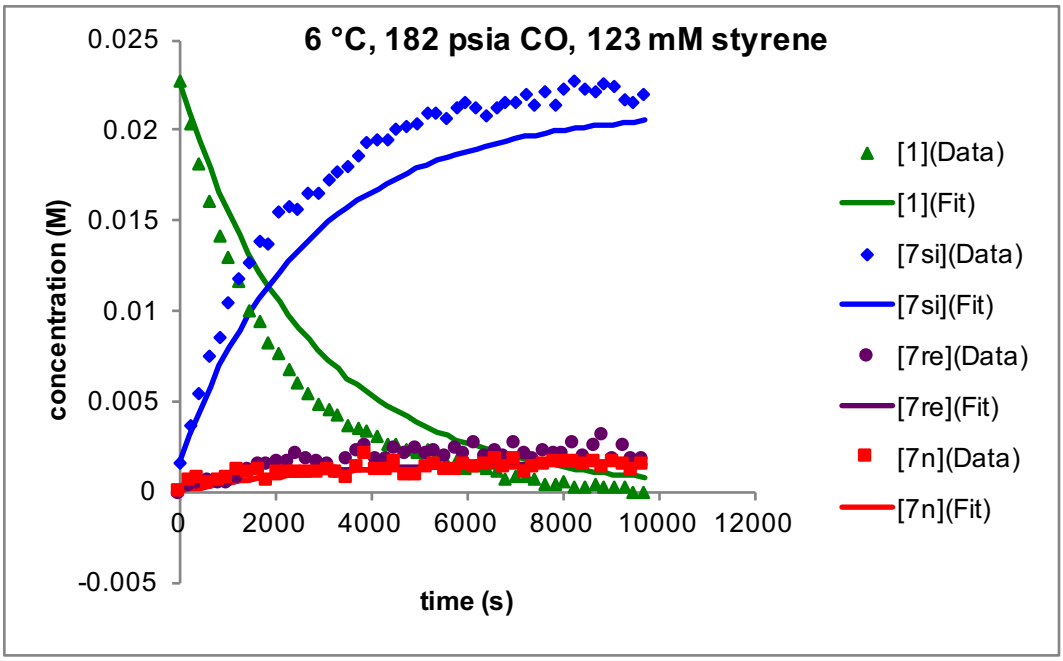

Figure B-102. Data and fits for model of formation and isomerization of acyl dicarbonyl species (~25 mM **1**, 123 mM styrene, 279 K, 182 psia CO, CH_2Cl_2).

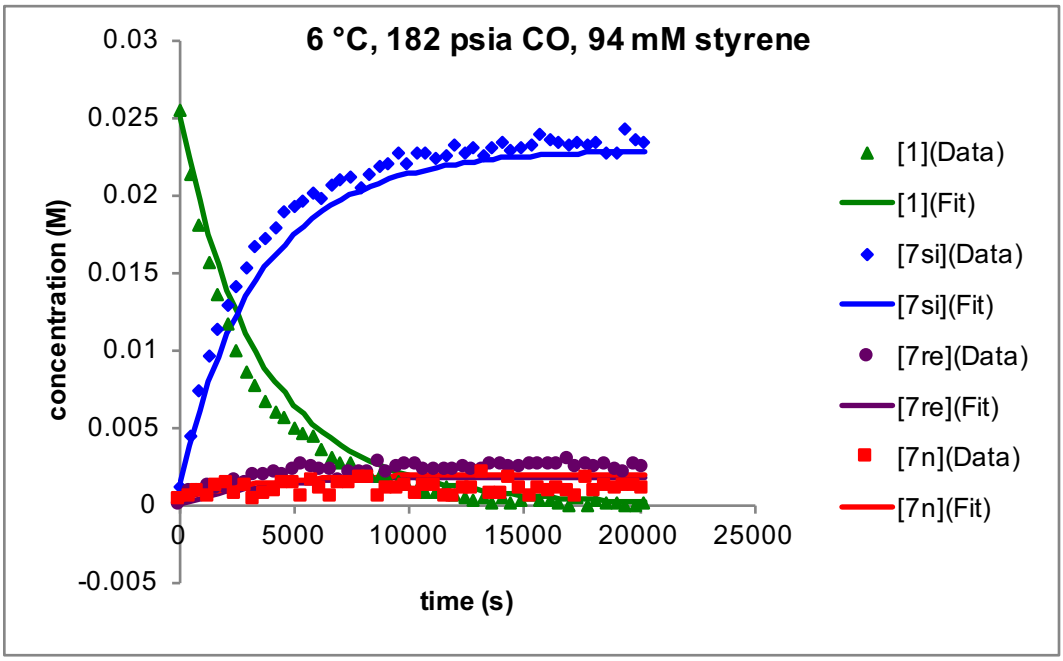

Figure B-103. Data and fits for model of formation and isomerizaiton of acyl dicarbonyl species (~25 mM **1**, 94.0 mM styrene, 279 K, 182 psia CO, CH_2Cl_2).

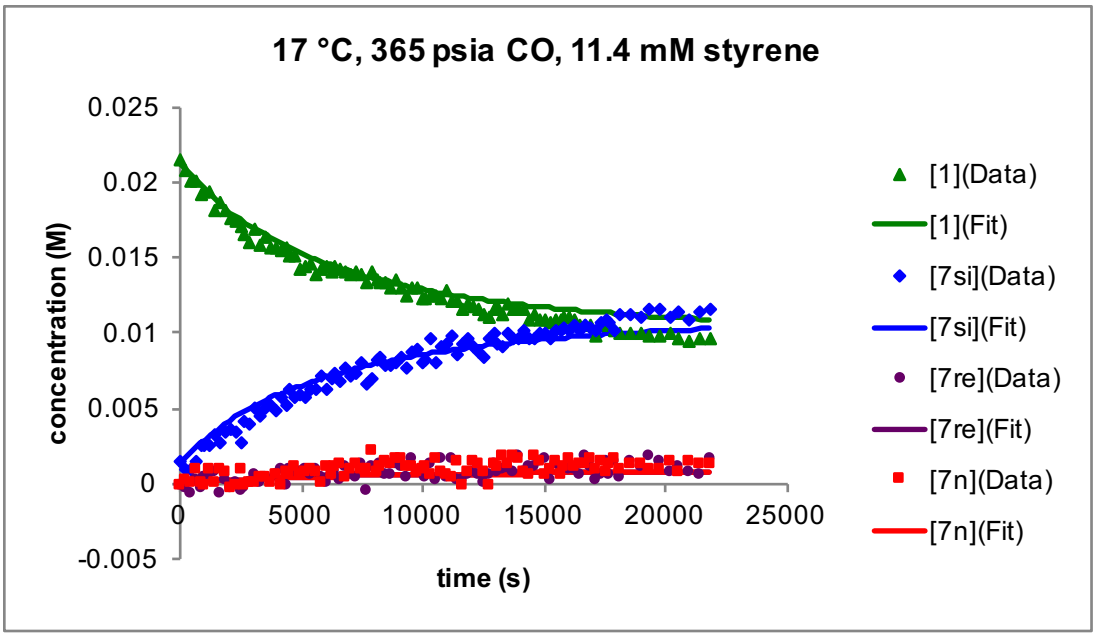

Figure B-104. Data and fits for model of formation and isomerization of acyl dicarbonyl species (~25 mM **1**, 11.4 mM styrene, 290 K, 365 psia CO, CH_2Cl_2).

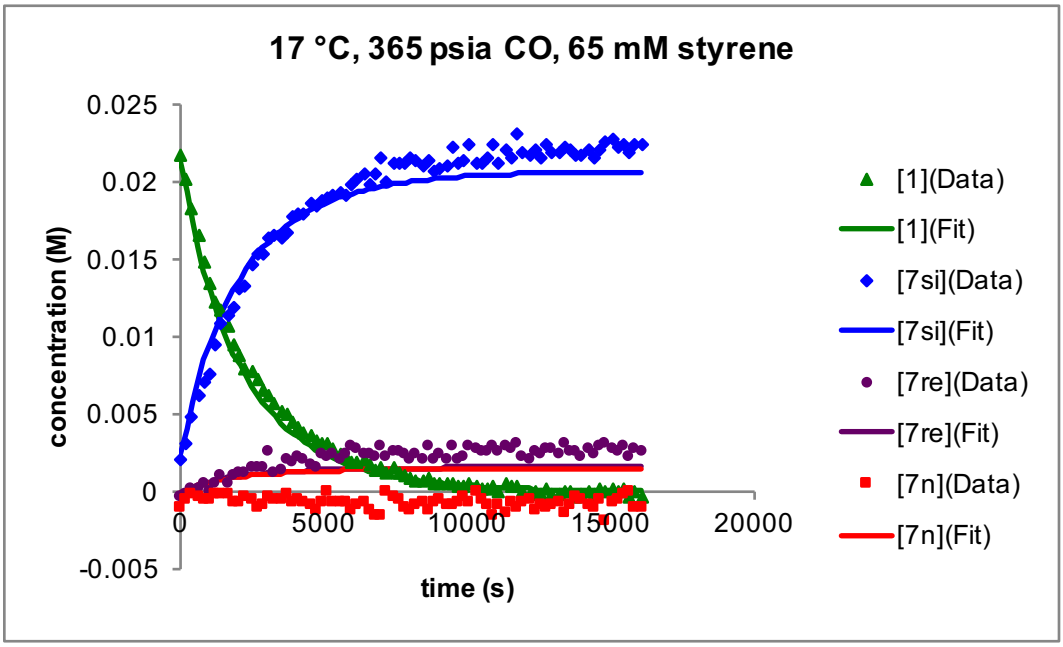

Figure B-105. Data and fits for model of formation and isomerization of acyl dicarbonyl species (~25 mM **1**, 65 mM styrene, 290 K, 365 psia CO, CH_2Cl_2).

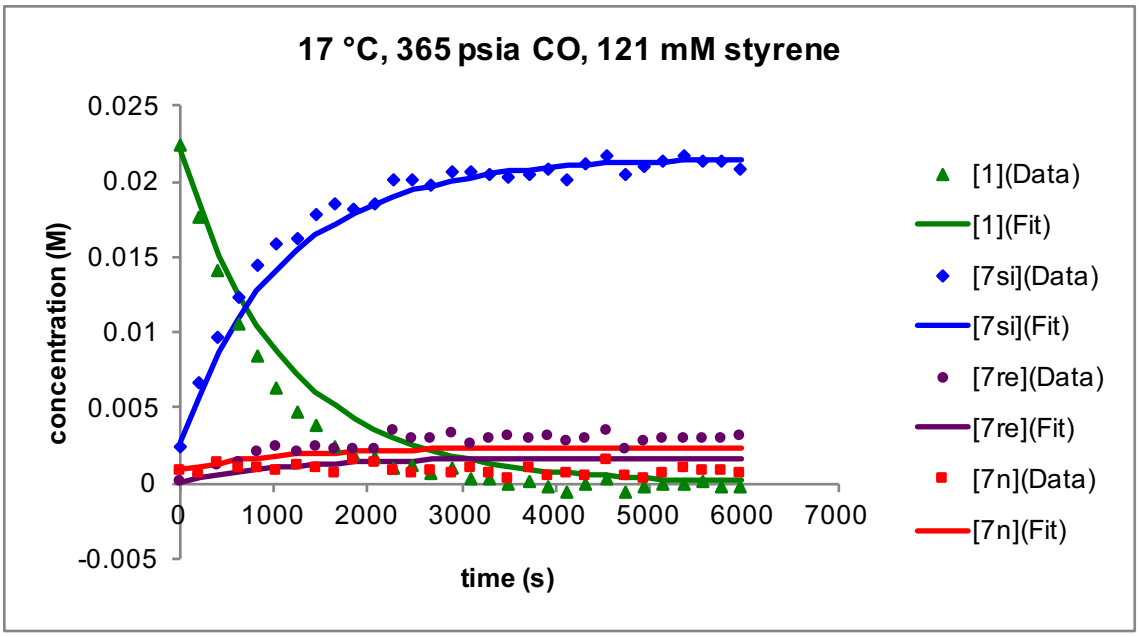

Figure B-106. Data and fits for model of formation and isomerization of acyl dicarbonyl species (~25 mM **1**, 121 mM styrene, 290 K, 365 psia CO, CH_2Cl_2).

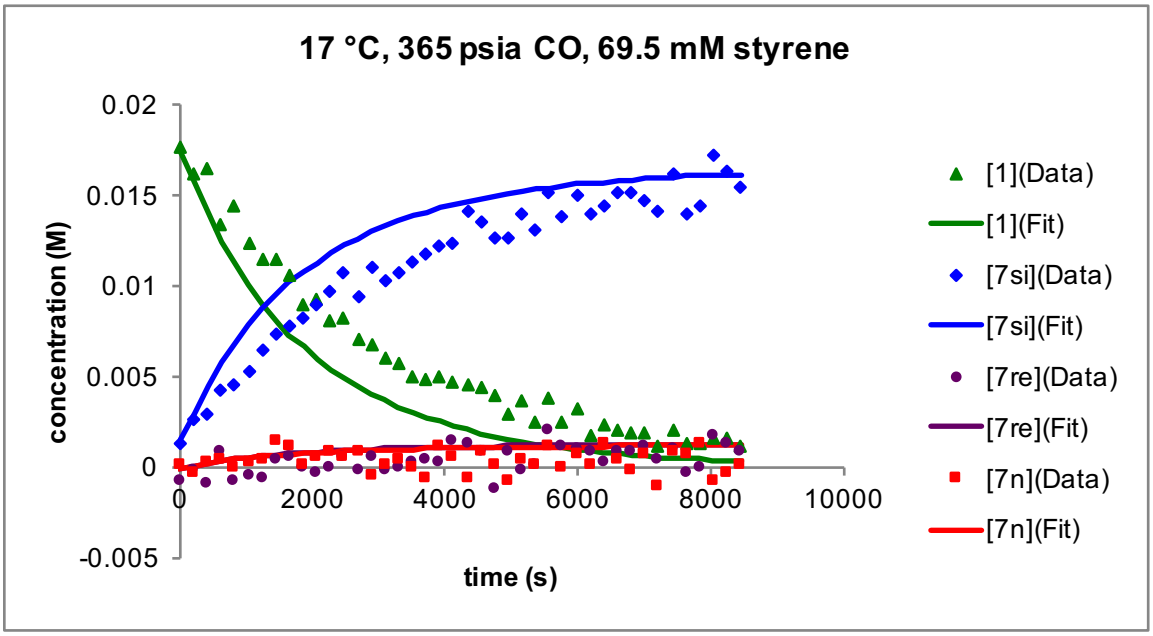

Figure B-107. Data and fits for model of formation and isomerization of acyl dicarbonyl species (~20 mM **1**, 69.5 mM styrene, 290 K, 365 psia CO, CH_2Cl_2).

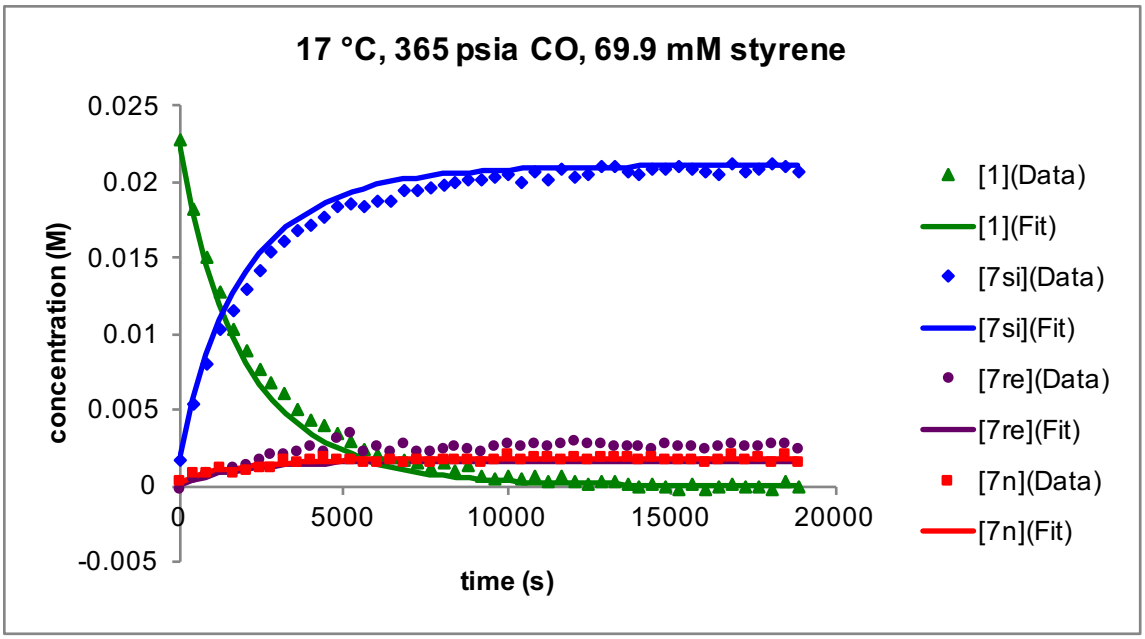

Figure B-108. Data and fits for model of formation and isomerization of acyl dicarbonyl species (~25 mM **1**, 69.9 mM styrene, 290 K, 365 psia CO, CH_2Cl_2).

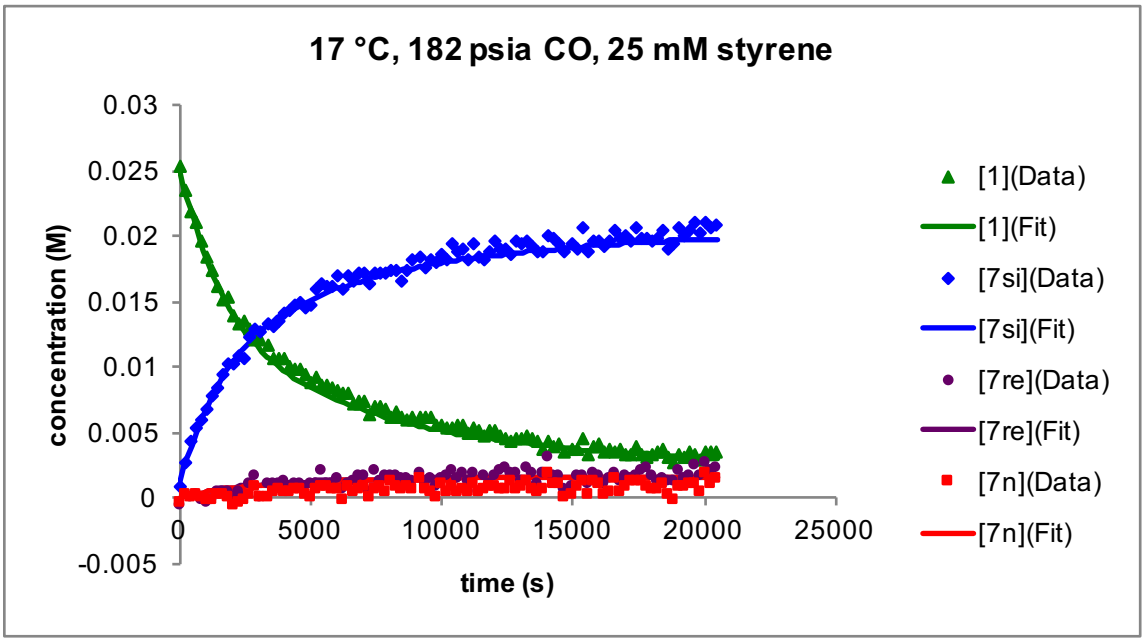

Figure B-109. Data and fits for model of formation and isomerization of acyl dicarbonyl species (~25 mM **1**, 25.0 mM styrene, 290 K, 182 psia CO, CH_2Cl_2).

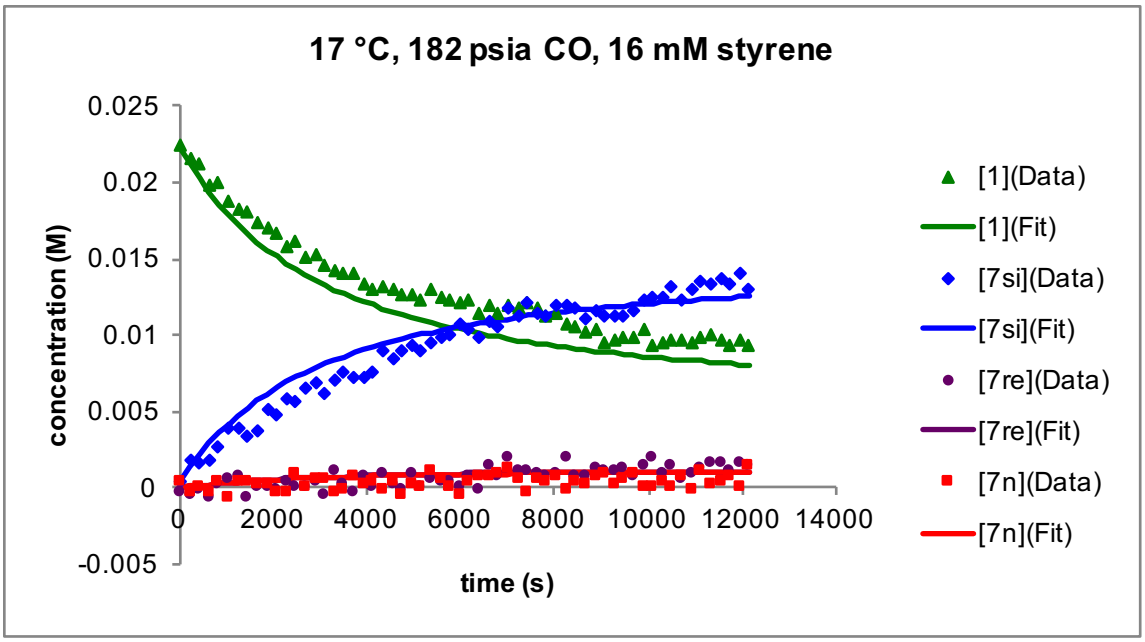

Figure B-110, Data and fits for model of formation and isomerization of acyl dicarbonyl species (~25 mM **1**, 16.0 mM styrene, 290 K, 182 psia CO, CH_2Cl_2).

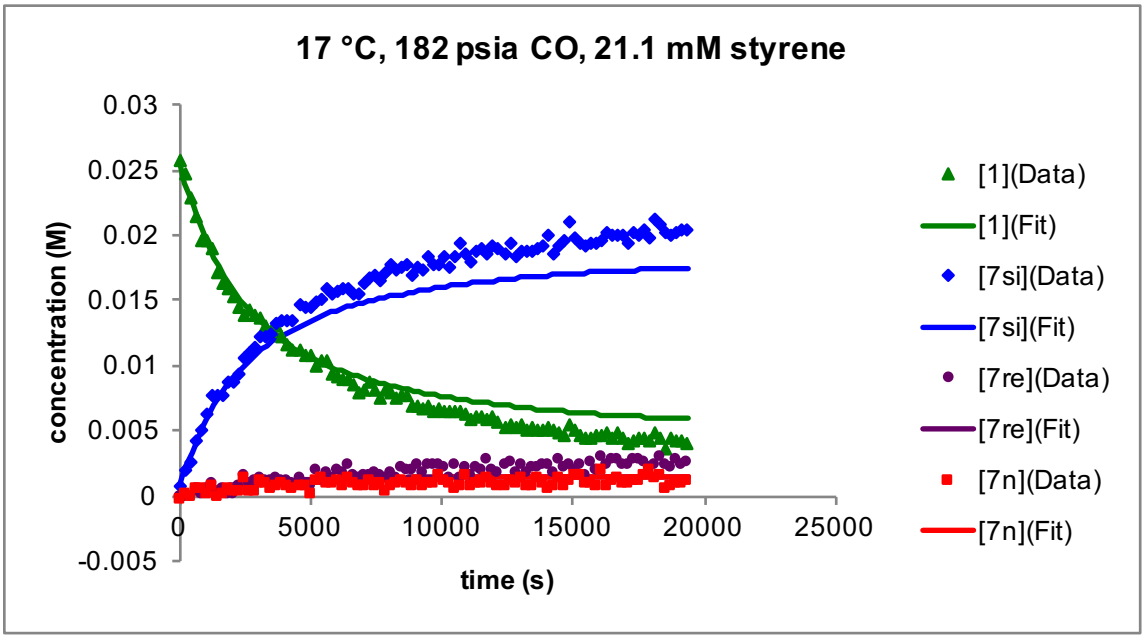

Figure B-111. Data and fits for model of formation and isomerization of acyl dicarbonyl species (~25 mM **1**, 21.1 mM styrene, 290 K, 182 psia CO, CH_2Cl_2).

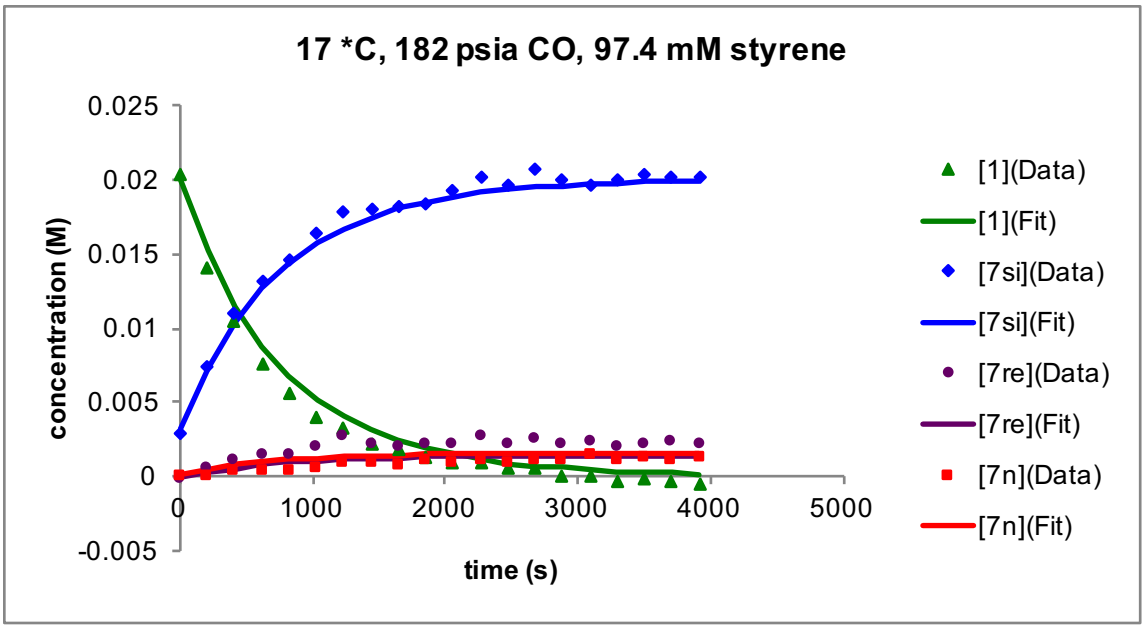

Figure B-112. Data and fits for model of formation and isomerization of acyl dicarbonyl species (~25 mM **1**, 97.4 mM styrene, 290 K, 182 psia CO, CH_2Cl_2).

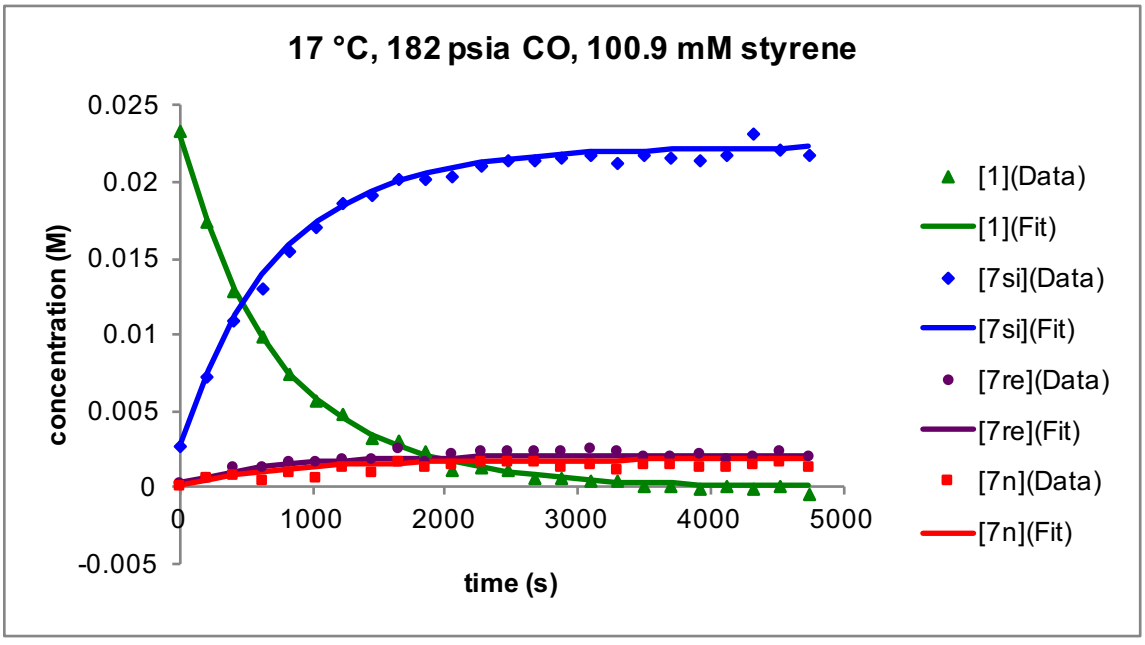

Figure B-113. Data and fits for model of formation and isomerization of acyl dicarbonyl species (~25 mM 1, 101 mM styrene, 290 K, 182 psia CO, CH_2Cl_2).

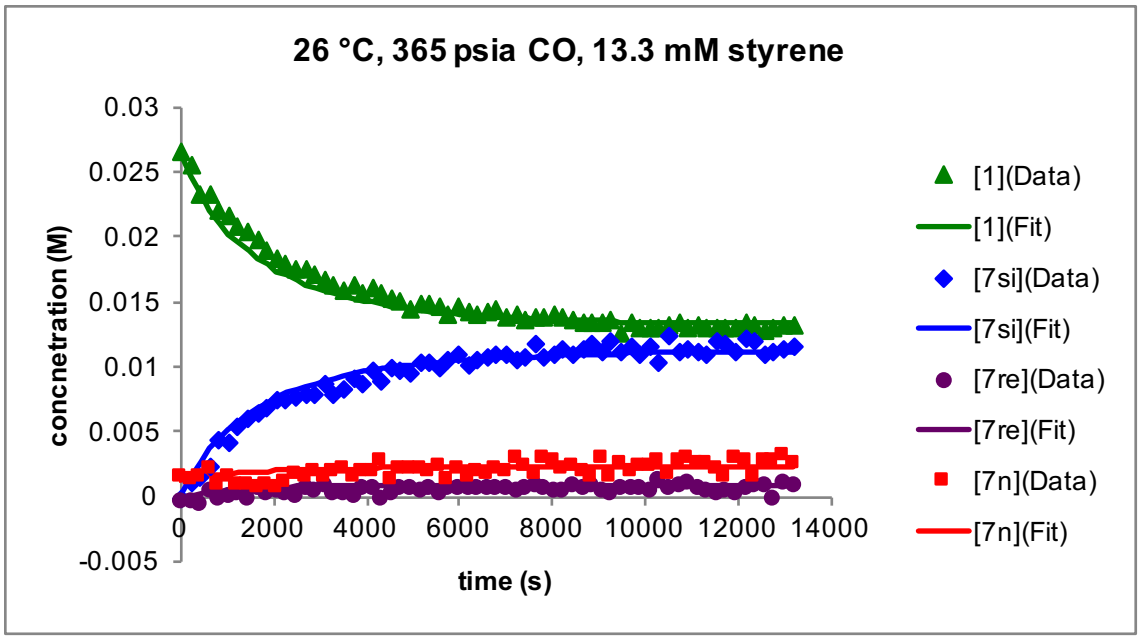

Figure B-114. Data and fits for model of formation and isomerization of acyl dicarbonyl species (~25 mM **1**, 13.3 mM styrene, 299 K, 365 psia CO, CH_2Cl_2).

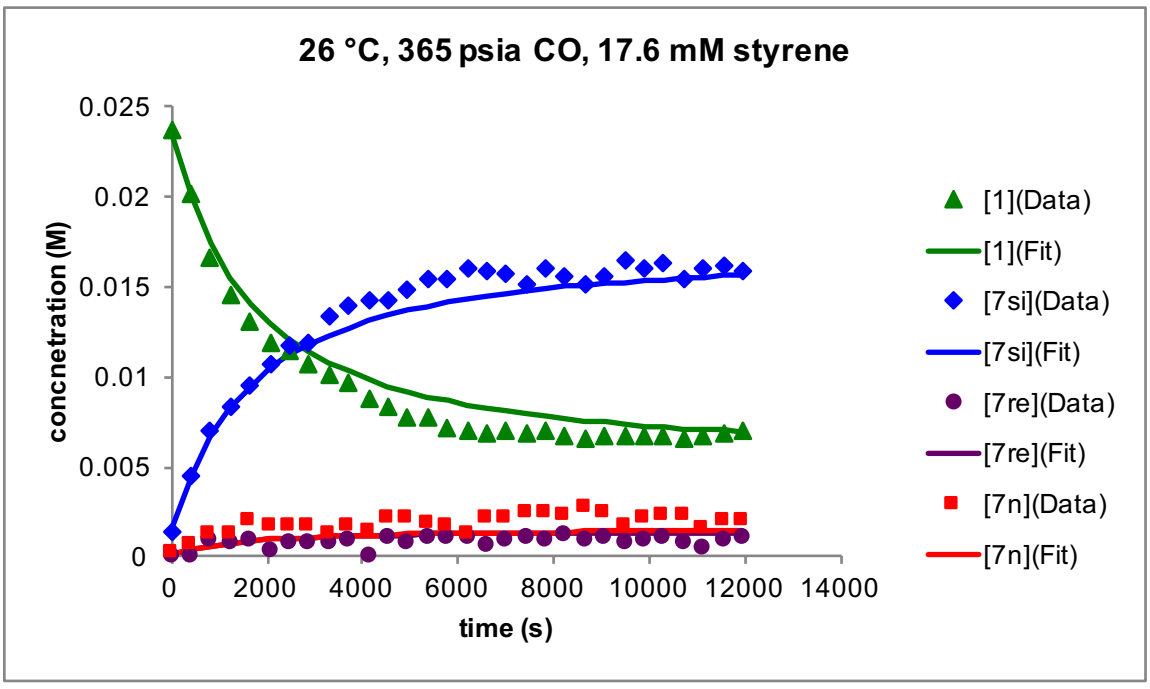

Figure B-115. Data and fits for model of formation and isomerization of acyl dicarbonyl species (~25 mM **1**, 17.6 mM styrene, 299 K, 365 psia CO, CH_2Cl_2).

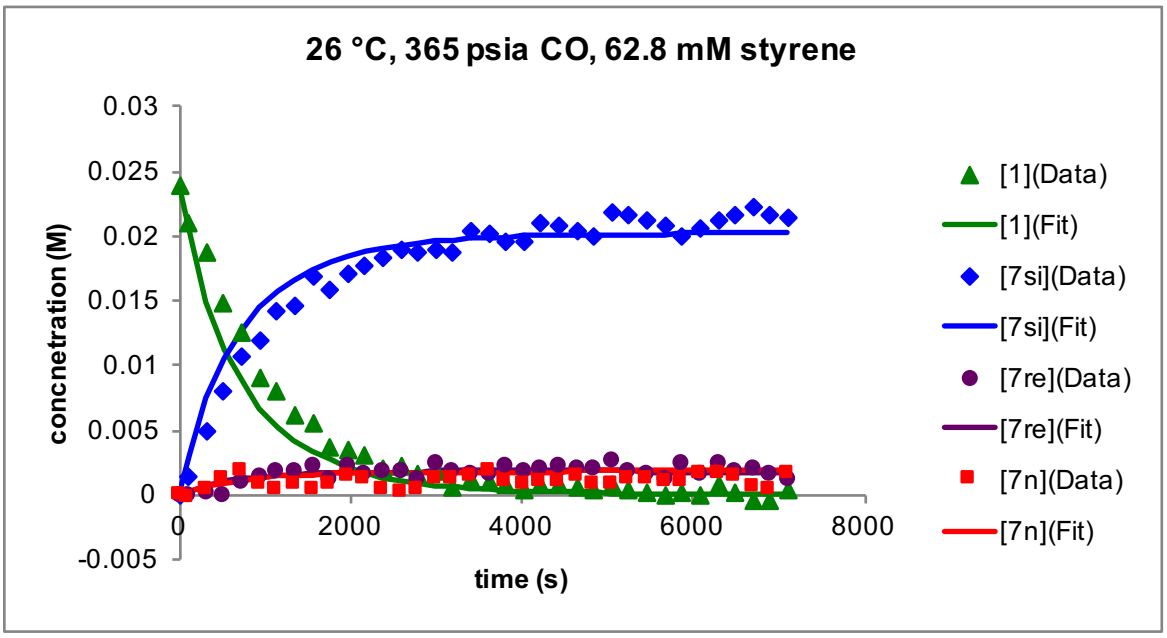

Figure B-116. Data and fits for model of formation and isomerization of acyl dicarbonyl species (~25 mM **1**, 62.8 mM styrene, 299 K, 365 psia CO, CH_2Cl_2).

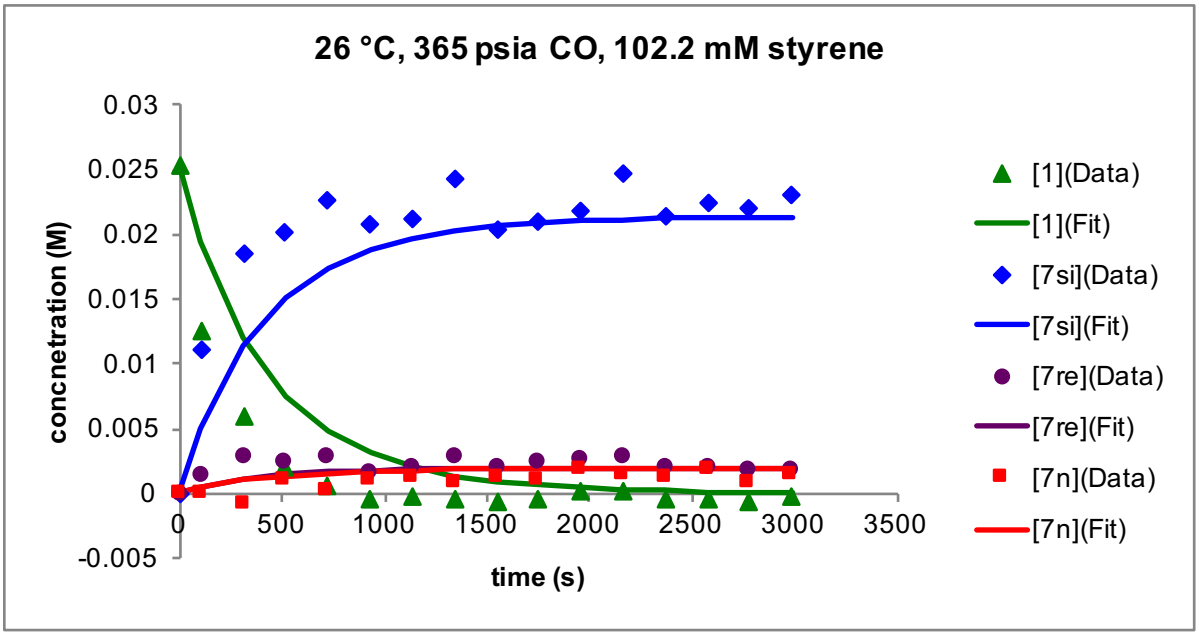

Figure B-117. Data and fits for model of formation and isomerization of acyl dicarbonyl species (~25 mM **1**, 102 mM styrene, 299 K, 365 psia CO, CH_2Cl_2).

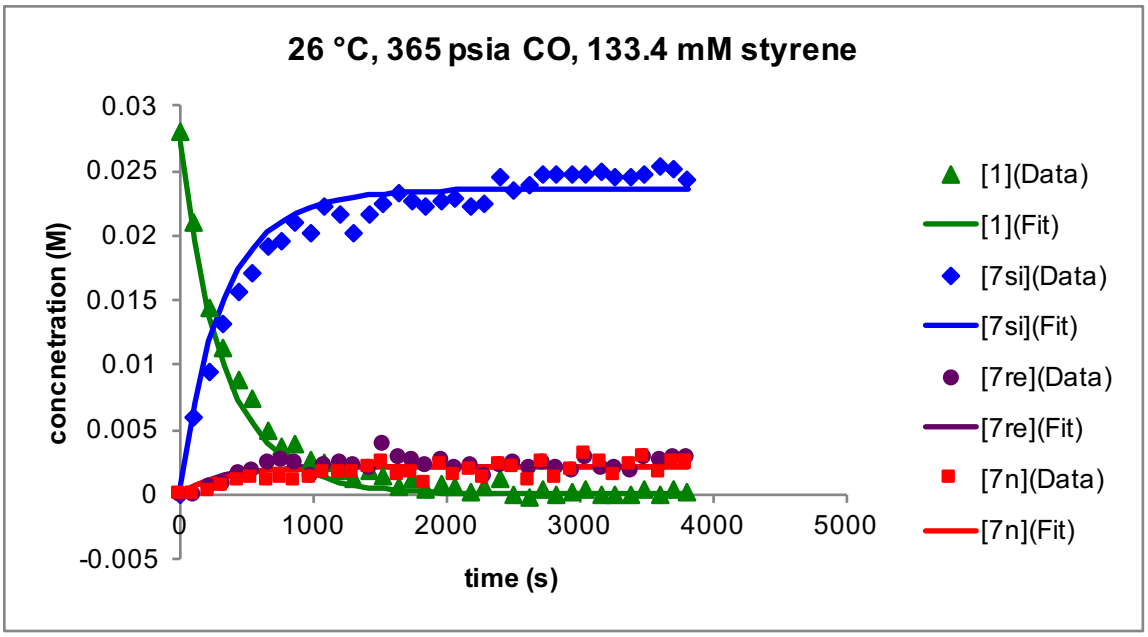

Figure B-118. Data and fits for model of formation and isomerization of acyl dicarbonyl species (~25 mM **1**, 133 mM styrene, 299 K, 365 psia CO, CH_2Cl_2).

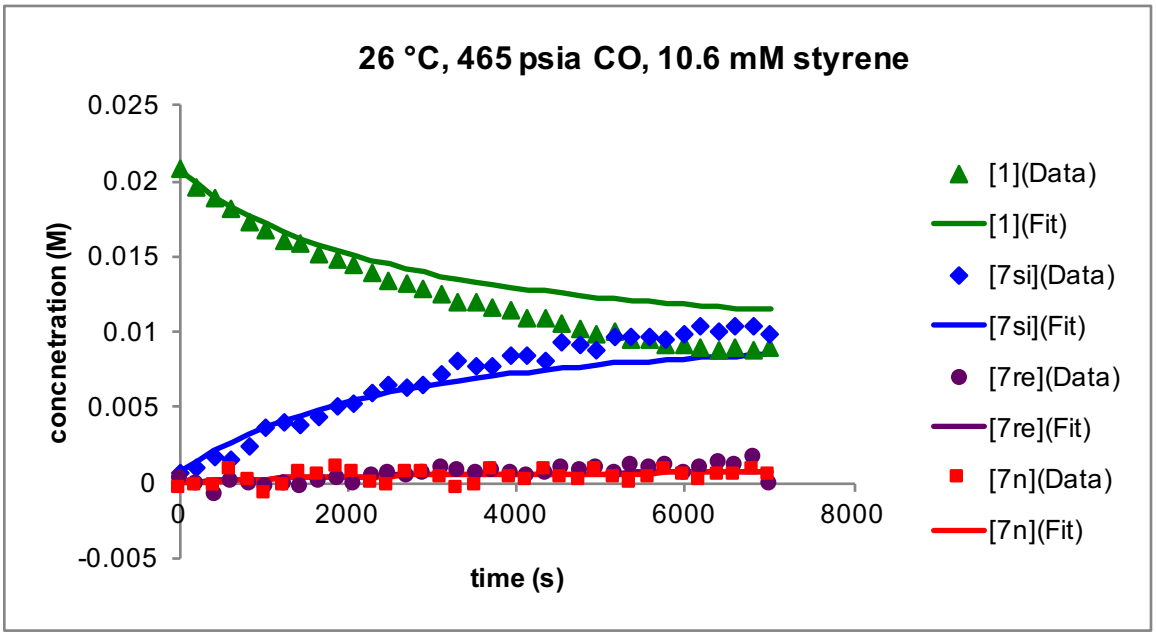

Figure B-119. Data and fits for model of formation and isomerization of acyl dicarbonyl species (~25 mM **1**, 10.6 mM styrene, 299 K, 465 psia CO, CH_2Cl_2).

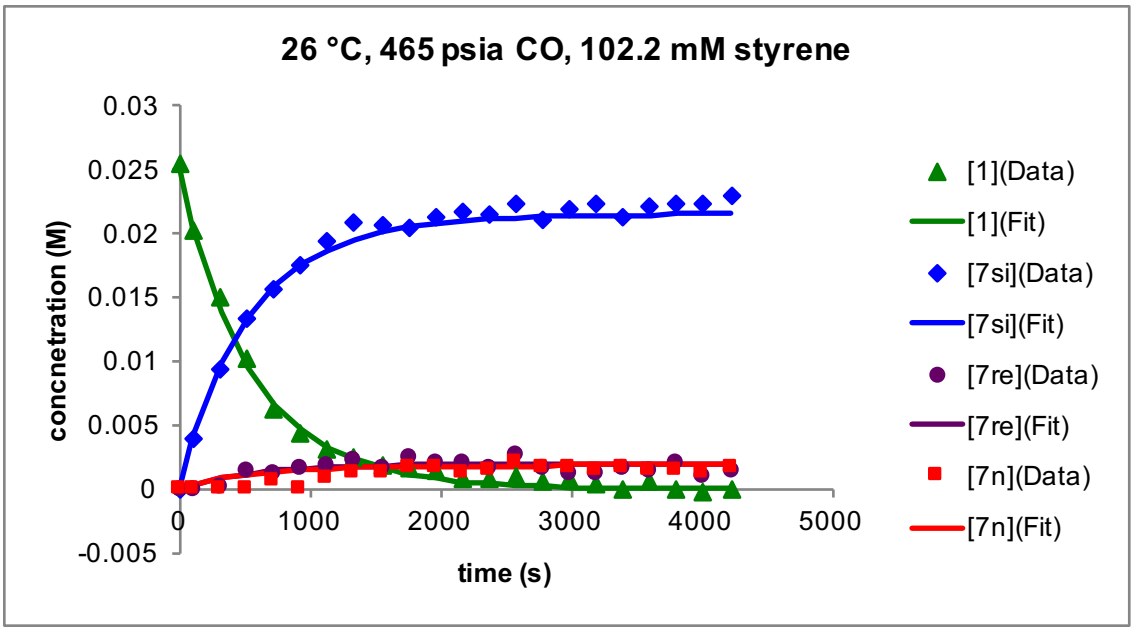

Figure B-120. Data and fits for model of formation and isomerization of acyl dicarbonyl species (~25 mM **1**, 102 mM styrene, 299 K, 465 psia CO, CH_2Cl_2).

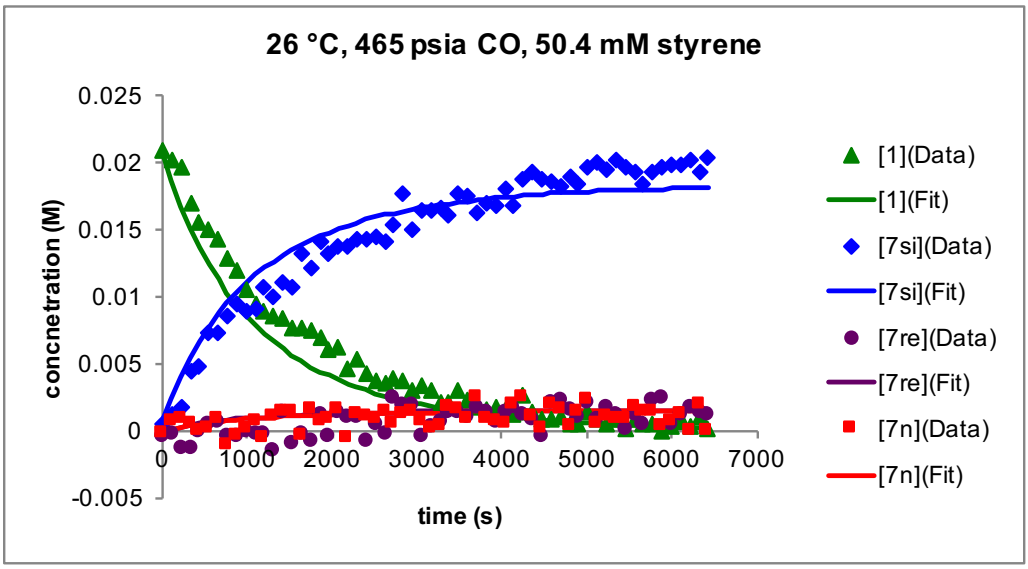

Figure B-121. Data and fits for model of formation and isomerization of acyl dicarbonyl species (~25 mM **1**, 50.4 mM styrene, 299 K, 465 psia CO, CH_2Cl_2).

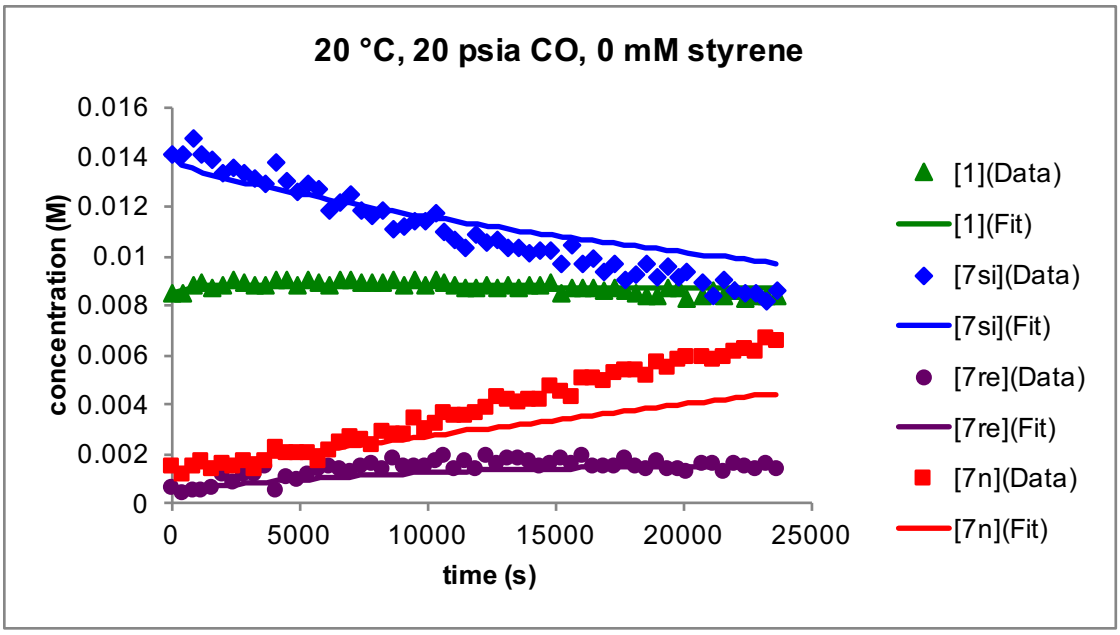

Figure B-122. Data and fits for model of formation and isomerization of acyl dicarbonyl species (15 mM **7si**, 0 mM styrene, 293 K, 20 psia CO, CH_2Cl_2).

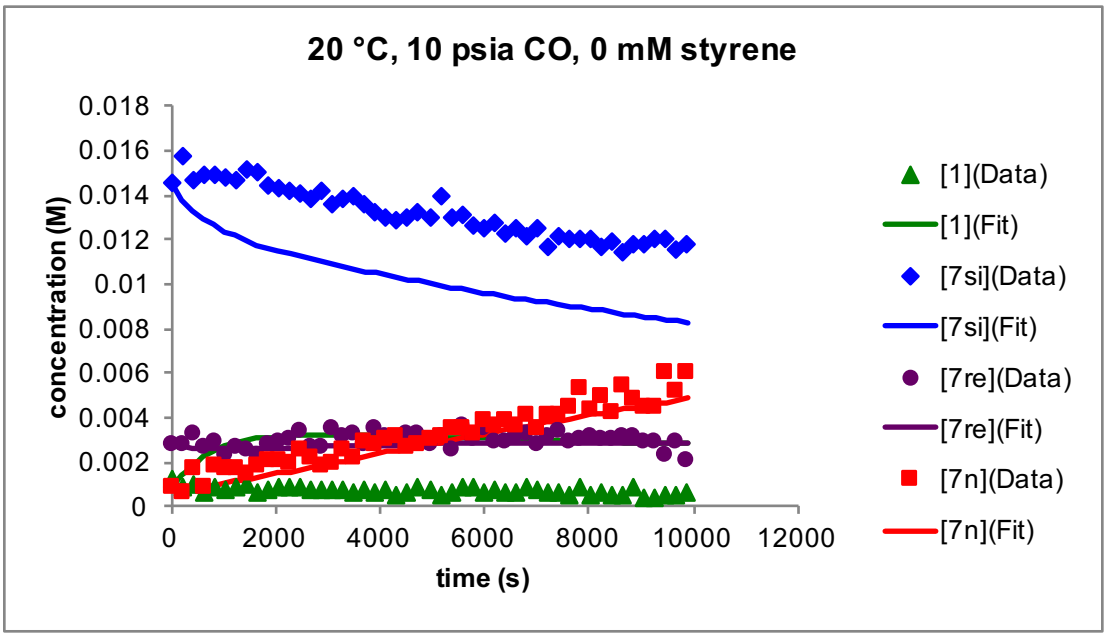

Figure B-123. Data and fits for model of formation and isomerization of acyl dicarbonyl species (15 mM **7si**, 0 mM styrene, 293 K, 10 psia CO, CH_2Cl_2).

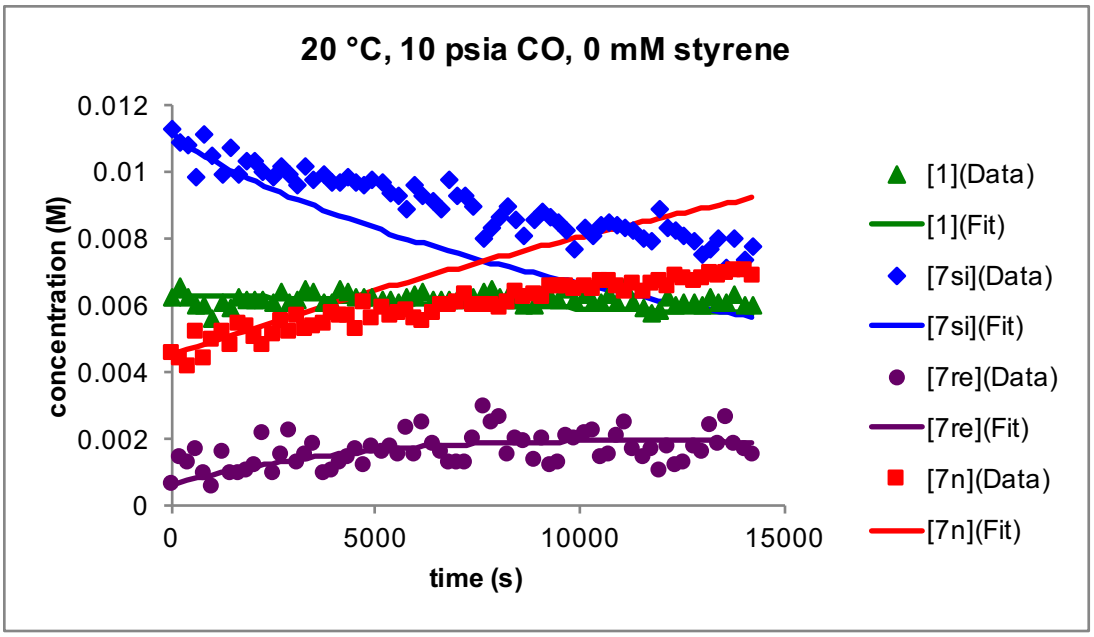

Figure B-124. Data and fits for model of formation and isomerization of acyl dicarbonyl species (12 mM **7si**, 0 mM styrene, 293 K, 10 psia CO, CH_2Cl_2).

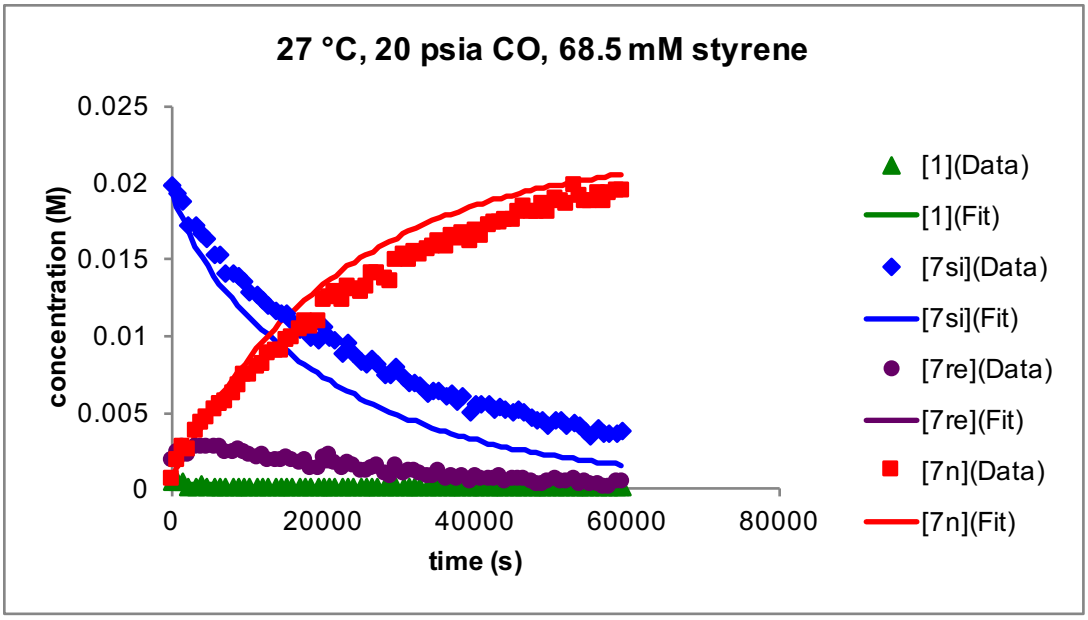

Figure B-125. Data and fits for model of formation and isomerization of acyl dicarbonyl species (20 mM **7si**, 68.5 mM styrene, 300 K, 20 psia CO, CH_2Cl_2).

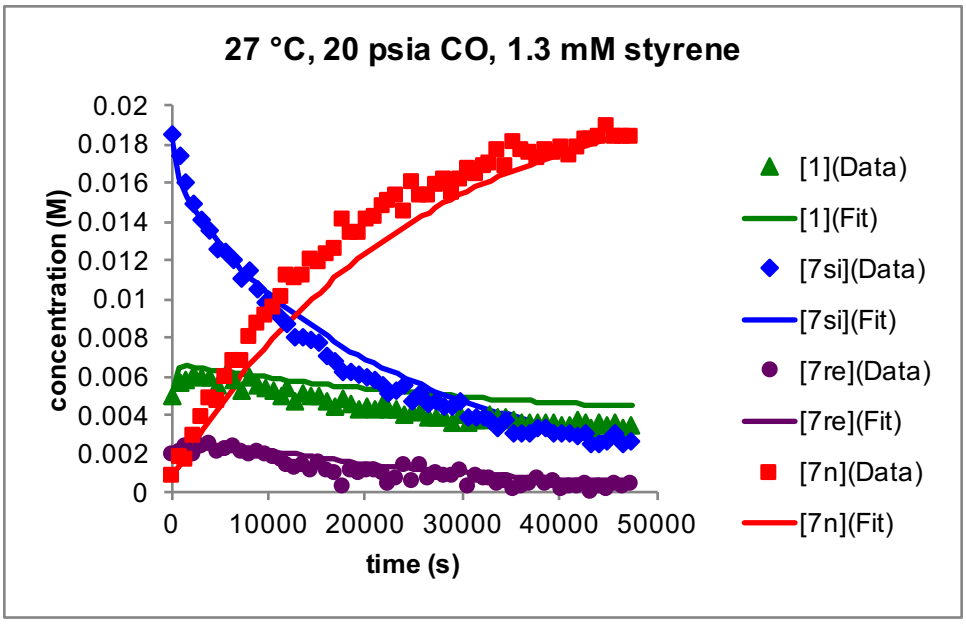

Figure B-126. Data and fits for model of formation and isomerization of acyl dicarbonyl species (19 mM **7si**, 1.3 mM styrene, 300 K, 20 psia CO, CH_2Cl_2).

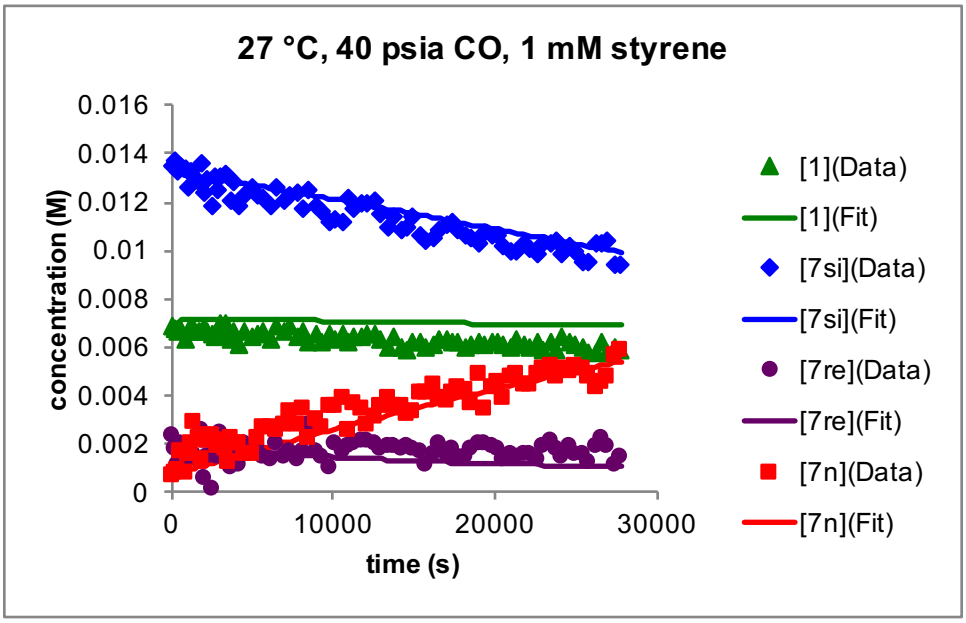

Figure B-127. Data and fits for model of formation and isomerization of acyl dicarbonyl species (14 mM **7si**, 1 mM styrene, 300 K, 40 psia CO, CH_2Cl_2).

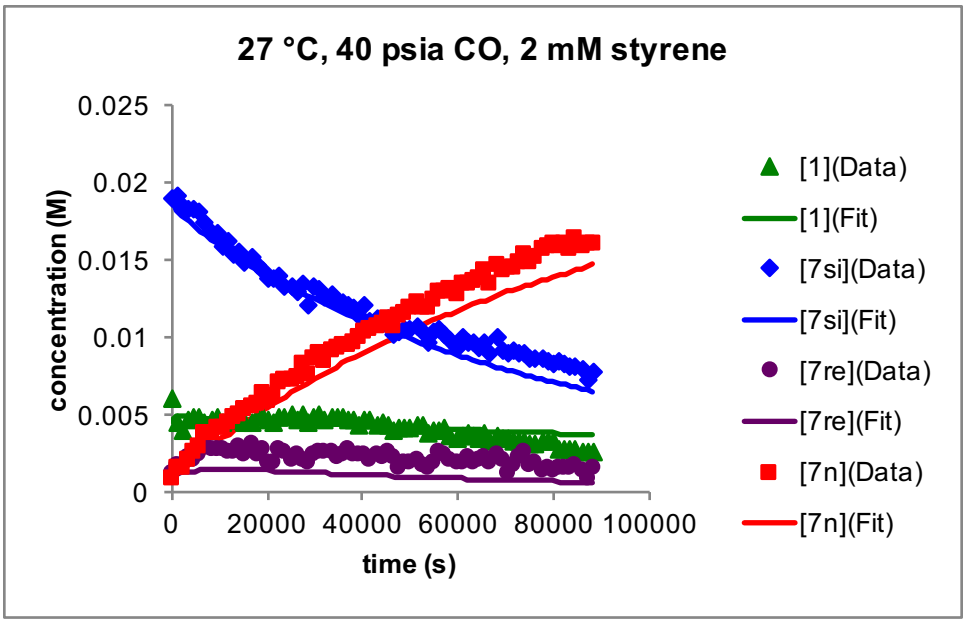

Figure B-128. Data and fits for model of formation and isomerization of acyl dicarbonyl species (20 mM **7si**, 2 mM styrene, 300 K, 40 psia CO, CH_2Cl_2).

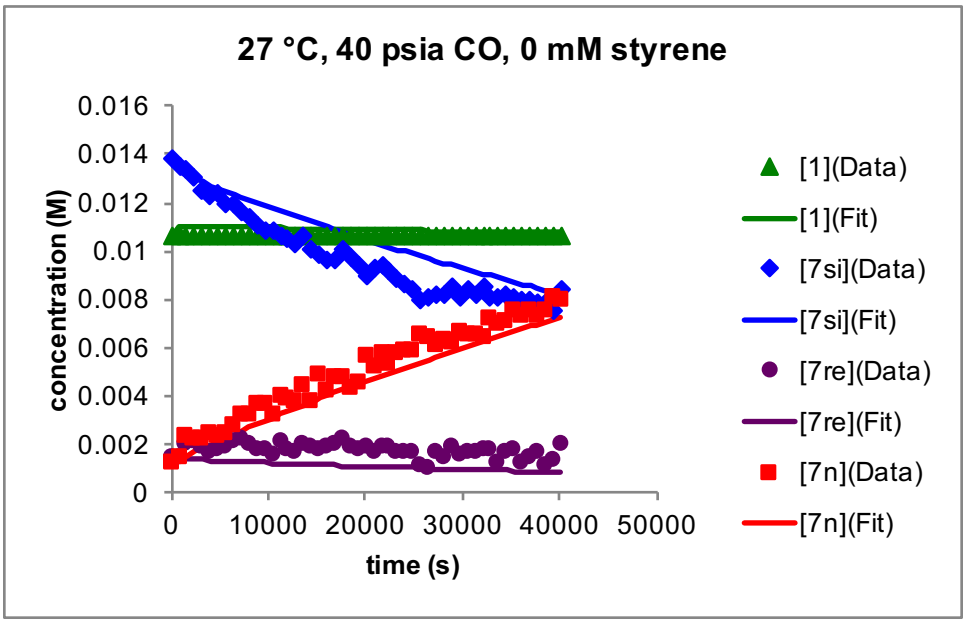

Figure B-129. Data and fits for model of formation and isomerization of acyl dicarbonyl species (14 mM **7si**, 0 mM styrene, 300 K, 40 psia CO, CH_2Cl_2).

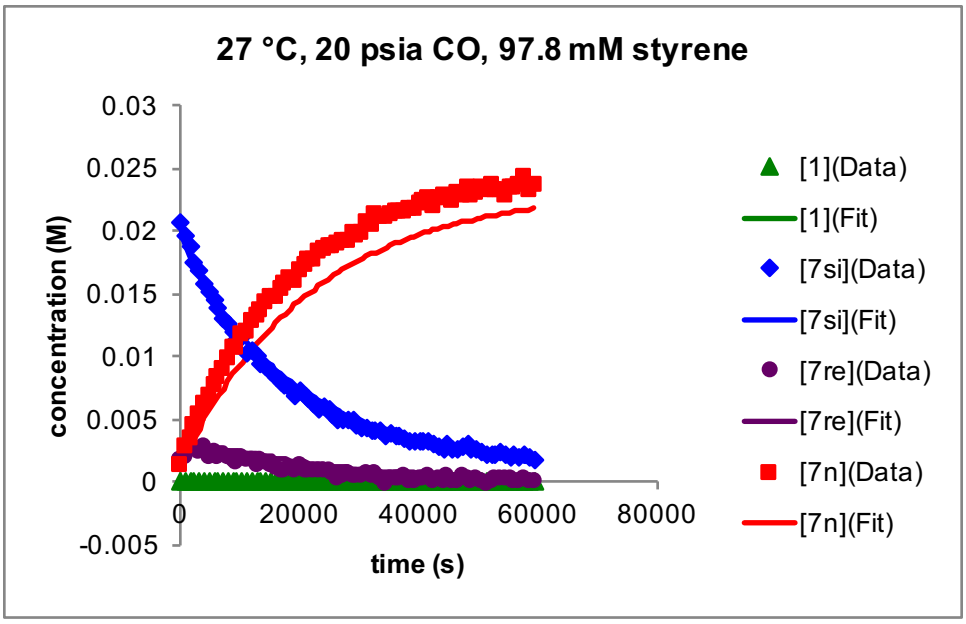

Figure B-130. Data and fits for model of formation and isomerization of acyl dicarbonyl species (21 mM **7si**, 97.8 mM styrene, 300 K, 20 psia CO, CH_2Cl_2).

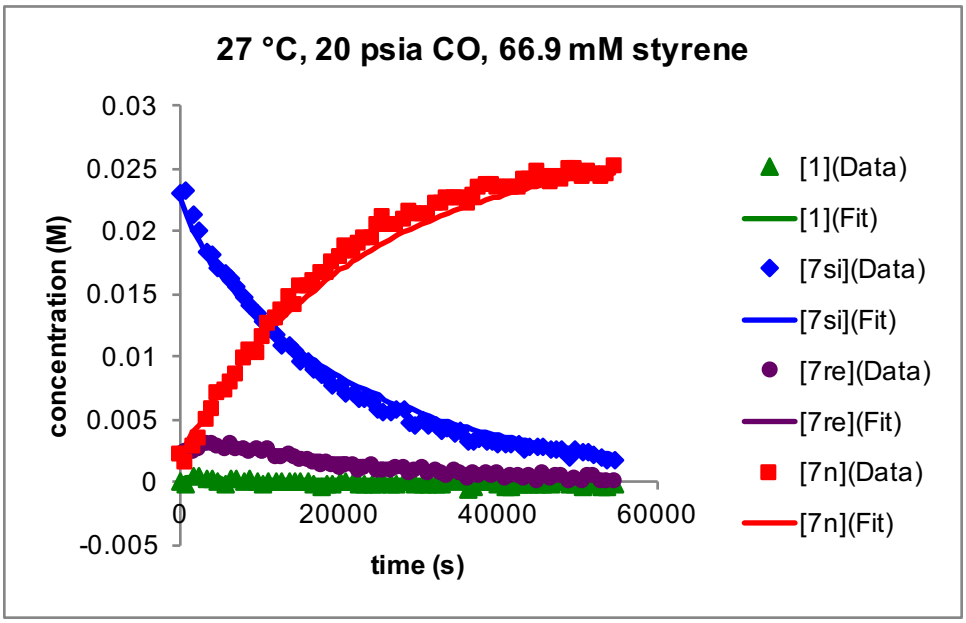

Figure B-131. Data and fits for model of formation and isomerization of acyl dicarbonyl species (24 mM **7si**, 66.9 mM styrene, 300 K, 20 psia CO, CH_2Cl_2).

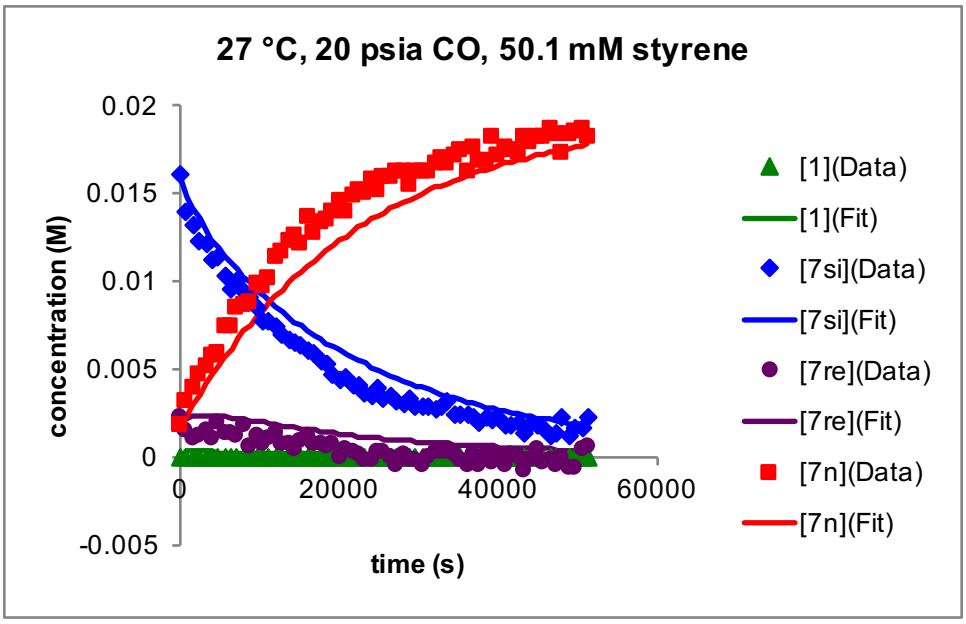

Figure B-132. Data and fits for model of formation and isomerization of acyl dicarbonyl species (15 mM **7si**, 50.1 mM styrene, 300 K, 20 psia CO, CH_2Cl_2).

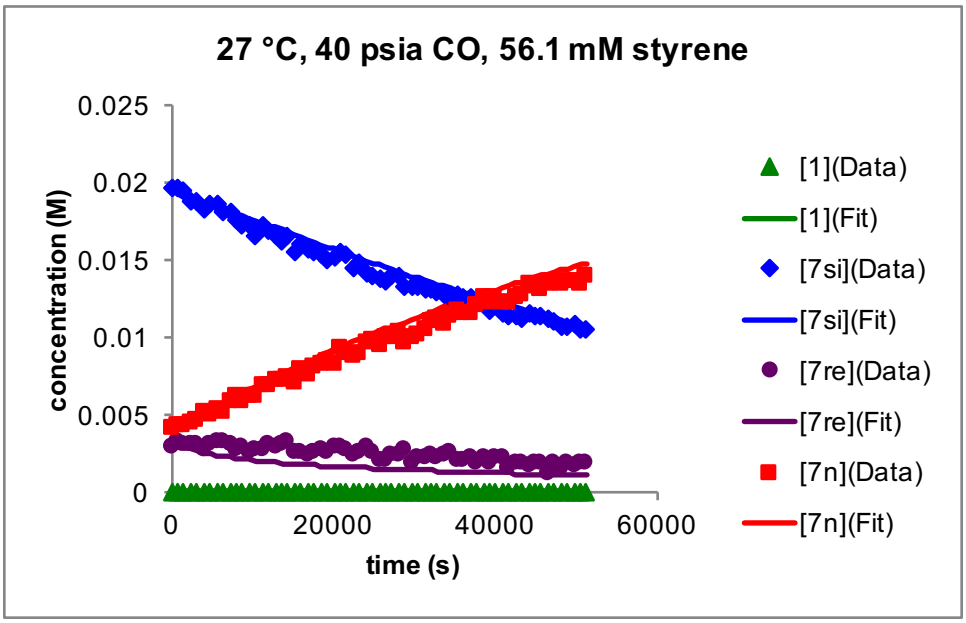

Figure B-133. Data and fits for model of formation and isomerization of acyl dicarbonyl species (20 mM **7si**, 56.1 mM styrene, 300 K, 40 psia CO, CH_2Cl_2).

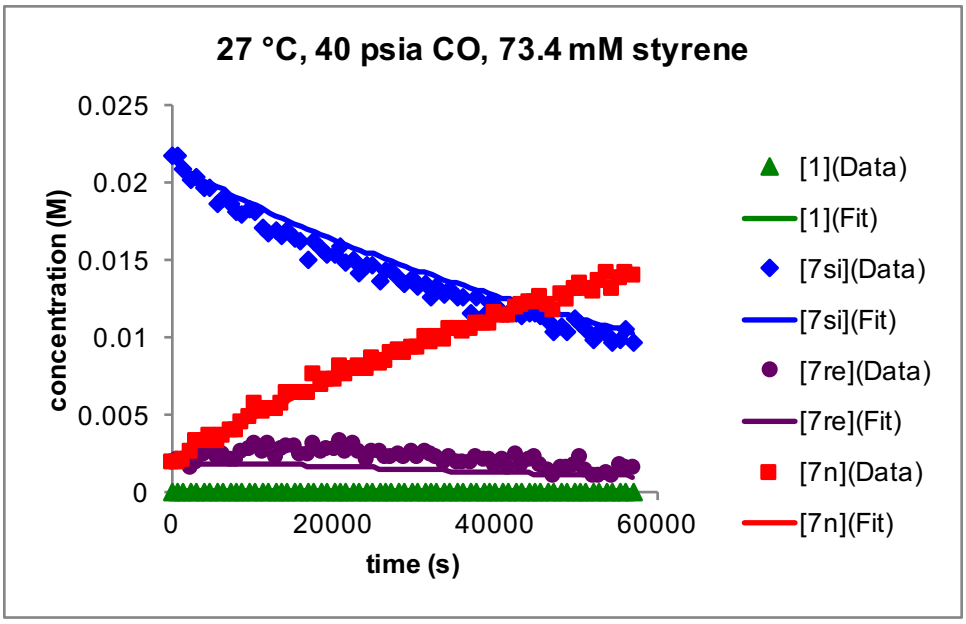

Figure B-134. Data and fits for model of formation and isomerization of acyl dicarbonyl species (22 mM **7si**, 73.4 mM styrene, 300 K, 40 psia CO, CH_2Cl_2).

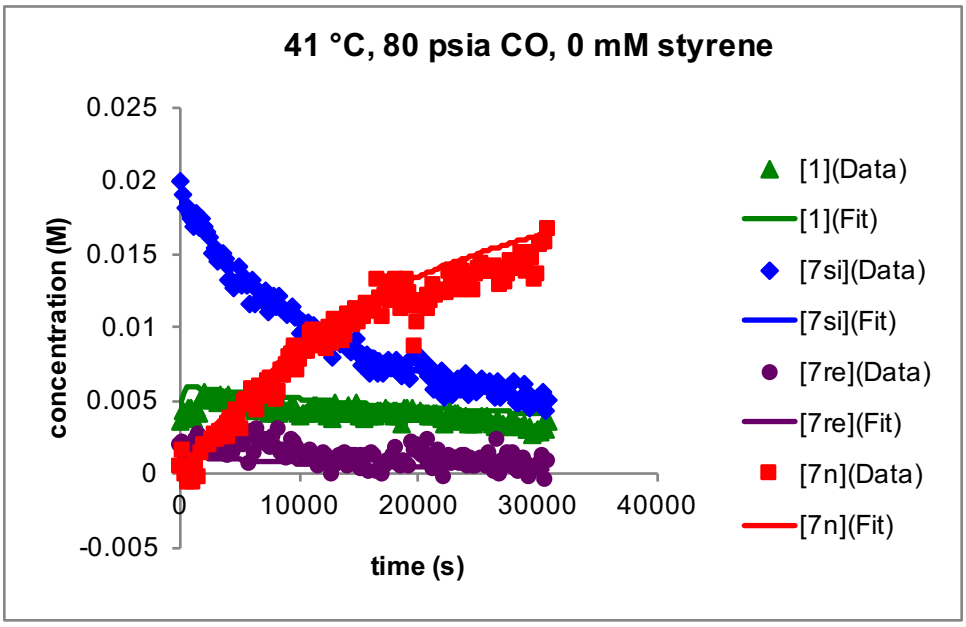

Figure B-135. Data and fits for model of formation and isomerization of acyl dicarbonyl species (20 mM **7si**, 0 mM styrene, 314 K, 80 psia CO, CH_2Cl_2).

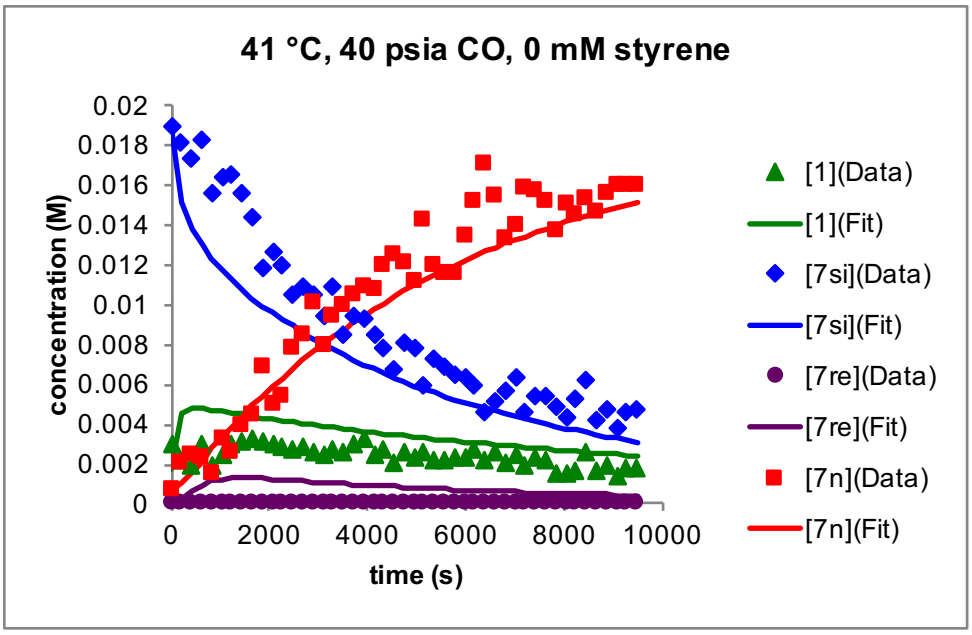

Figure B-136. Data and fits for model of formation and isomerization of acyl dicarbonyl species (20 mM **7si**, 0 mM styrene, 314 K, 40 psia CO, CH_2Cl_2).

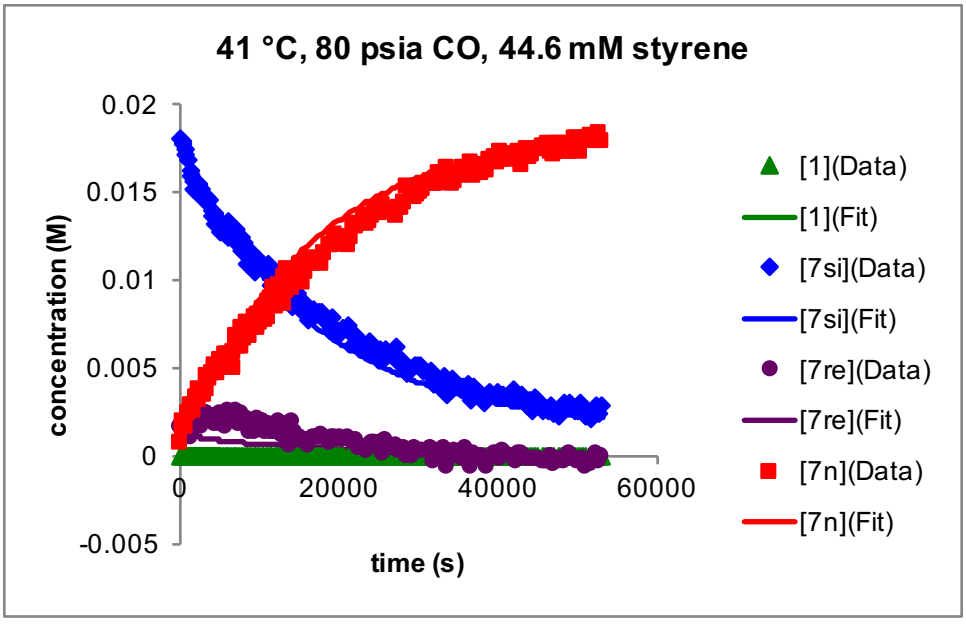

Figure B-137. Data and fits for model of formation and isomerization of acyl dicarbonyl species (18 mM **7si**, 44.6 mM styrene, 314 K, 80 psia CO, CH_2Cl_2).

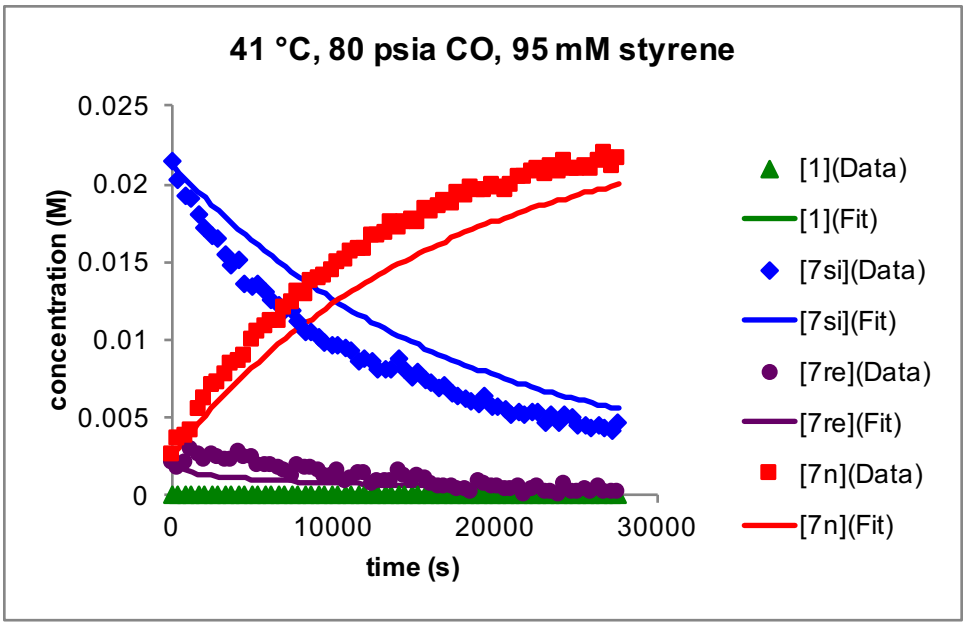

Figure B-138. Data and fits for model of formation and isomerization of acyl dicarbonyl species (22 mM **7si**, 95 mM styrene, 314 K, 80 psia CO, CH_2Cl_2).

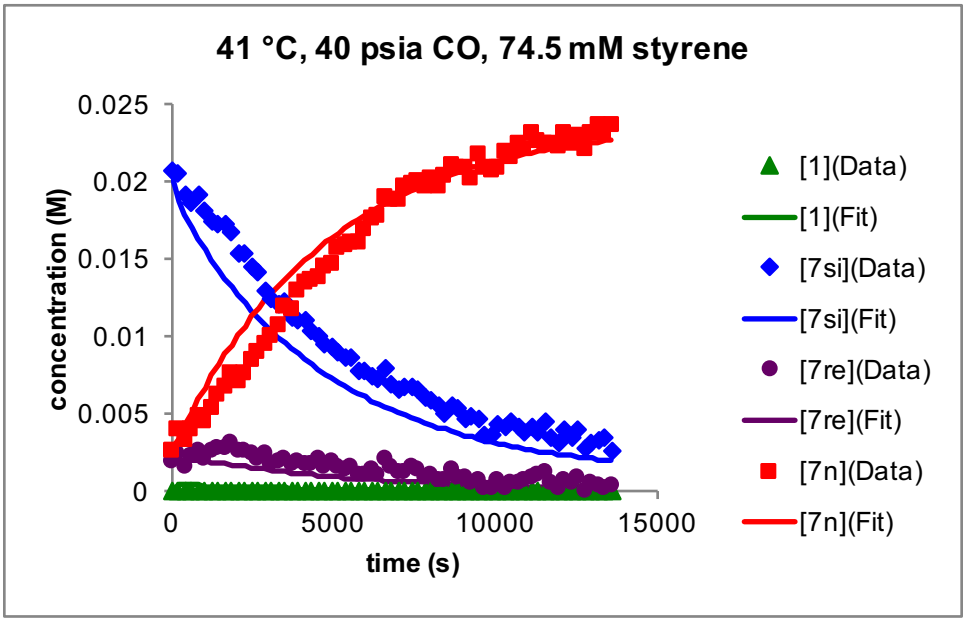

Figure B-139. Data and fits for model of formation and isomerization of acyl dicarbonyl species (20 mM **7si**, 74.5 mM styrene, 314 K, 40 psia CO, CH_2Cl_2).

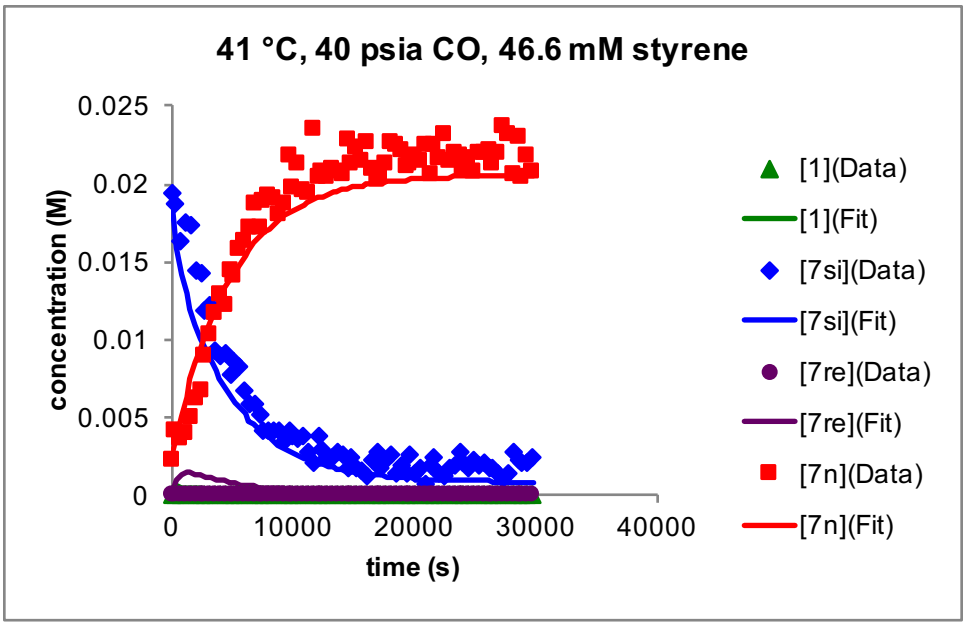

Figure B-140. Data and fits for model of formation and isomerization of acyl dicarbonyl species (20 mM **7si**, 46.6 mM styrene, 314 K, 40 psia CO, CH_2Cl_2).

B.4.5 Combining Acyl 7 Formation/Isomerization Model with Hydrogenolysis

The acyl **7** formation and isomerization model (B.4.4) was combined with the hydrogenolysis model (B.4.1) to make the full catalytic model.

B.4.5.1 Model Set Up

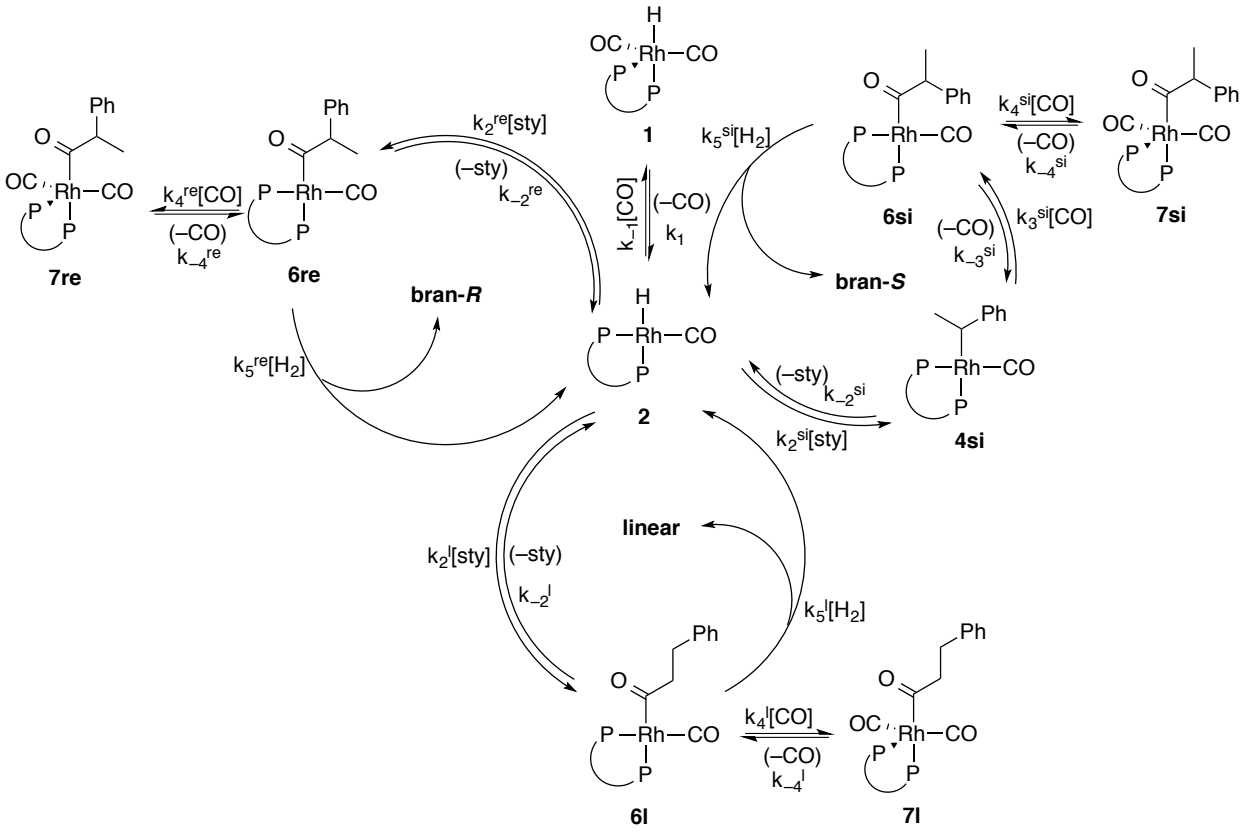

Figure B-141. Combined catalytic model comprised of activation parameters for formation and isomerization of acyls **7** as well as parameters for hydrogenolysis.

$$k_1 = 2.0837\times10^{10}(T)e^{\frac{\Delta H\ddagger\_1for - \Delta S\ddagger\_1for(T)}{1.987(T)}}$$

$$k_{-1} = 2.0837\times10^{10}(T)e^{\frac{\Delta H\ddagger\_1back - \Delta S\ddagger\_1back(T)}{1.987(T)}}$$

$$k_2^{si} = 2.0837\times10^{10}(T)e^{\frac{\Delta H\ddagger\_2for\_si - \Delta S\ddagger\_2for\_si(T)}{1.987(T)}}$$

$$k_{-2}^{si} = 2.0837\times10^{10}(T)e^{\frac{\Delta H\ddagger\_2back\_si - \Delta S\ddagger\_2back\_si(T)}{1.987(T)}}$$

$$k_2^{re} = 2.0837\times10^{10}(T)e^{\frac{\Delta H\ddagger\_2for\_re - \Delta S\ddagger\_2for\_re(T)}{1.987(T)}}$$

$$k_{-2}^{re} = 2.0837\times10^{10}(T)e^{\frac{\Delta H\ddagger\_2back\_re - \Delta S\ddagger\_2back\_re(T)}{1.987(T)}}$$

$$k_2^{I} = 2.0837\times10^{10}(T)e^{\frac{\Delta H\ddagger\_2for\_I - \Delta S\ddagger\_2for\_I(T)}{1.987(T)}}$$

$$k_{-2}^{I} = 2.0837\times10^{10}(T)e^{\frac{\Delta H\ddagger\_2back\_I - \Delta S\ddagger\_2back\_I(T)}{1.987(T)}}$$

$$k_3^{si} = 2.0837\times10^{10}(T)e^{\frac{\Delta H\ddagger\_3for\_si - \Delta S\ddagger\_3for\_si(T)}{1.987(T)}}$$

$$k_{-3}^{si} = 2.0837\times10^{10}(T)e^{\frac{\Delta H\ddagger\_3back\_si - \Delta S\ddagger\_3back\_si(T)}{1.987(T)}}$$

$$k_4^{si} = 2.0837\times10^{10}(T)e^{\frac{\Delta H\ddagger\_4for\_si - \Delta S\ddagger\_4for\_si(T)}{1.987(T)}}$$

$$k_{-4}^{si} = 2.0837\times10^{10}(T)e^{\frac{\Delta H\ddagger\_4back\_si - \Delta S\ddagger\_4back\_si(T)}{1.987(T)}}$$

$$k_4^{re} = 2.0837\times10^{10}(T)e^{\frac{\Delta H\ddagger\_4for\_re - \Delta S\ddagger\_4for\_re(T)}{1.987(T)}}$$

$$k_{-4}^{re} = 2.0837\times10^{10}(T)e^{\frac{\Delta H\ddagger\_2back\_re - \Delta S\ddagger\_2back\_re(T)}{1.987(T)}}$$

$$k_4^{I} = 2.0837\times10^{10}(T)e^{\frac{\Delta H\ddagger\_4for\_I - \Delta S\ddagger\_4for\_I(T)}{1.987(T)}}$$

$$k_{-4}^{I} = 2.0837\times10^{10}(T)e^{\frac{\Delta H\ddagger\_4back\_I - \Delta S\ddagger\_4back\_I(T)}{1.987(T)}}$$

$$k_5^{si} = 2.0837\times10^{10}(T)e^{\frac{\Delta H\ddagger\_5for\_si - \Delta S\ddagger\_5for\_si(T)}{1.987(T)}}$$

$$k_5^{re} = 2.0837\times10^{10}(T)e^{\frac{\Delta H\ddagger\_5for\_re - \Delta S\ddagger\_5for\_re(T)}{1.987(T)}}$$

$$k_5^{I} = 2.0837\times10^{10}(T)e^{\frac{\Delta H\ddagger\_5for\_I - \Delta S\ddagger\_5for\_I(T)}{1.987(T)}}$$

Figure B-142. Equations used for combined catalytic model.

Table B-8. Set and re-optimized parameters for combined full catalytic model.

Parameter	Value	Set or Optimized?
ΔH‡_1for	24.04 kcal/mol	set from CO exchange model
ΔS‡_1for	16 cal·mol^{-1}K^{-1}	set from CO exchange model
ΔH‡_1back	7 kcal/mol	set from acyl **7** formation model
ΔS‡_1back	–16 cal·mol^{-1}K^{-1}	set from acyl **7** formation model
ΔH‡_2for_si	4.00 kcal/mol	set from acyl **7** formation model
ΔS‡_2for_si	-30.5 cal·mol^{-1}K^{-1}	set from acyl **7** formation model
ΔH‡_2back_si	13.90 kcal/mol	set based on alkyl **4** isomerization model
ΔS‡_2back_si	–1.1 cal·mol^{-1}K^{-1}	set based on alkyl **4** isomerization model
ΔH‡_2for_re	5.45 kcal/mol	set from acyl **7** formation model
ΔS‡_2for_re	-30.5cal·mol^{-1}K^{-1}	set from acyl **7** formation model
ΔH‡_2back_re	20.063(8) kcal/mol	set based on acyl **7** isomerization model
ΔS‡_2back_re	0 cal·mol^{-1}K^{-1}	set based on ΔS‡_2for_re
ΔH‡_2for_l	5.49 kcal/mol	set from acyl **7** formation model
ΔS‡_2for_l	-30.5 cal·mol^{-1}K^{-1}	set from acyl **7** formation model
ΔH‡_2back_l	22.49(3) kcal/mol	set based on acyl **7** isomerization model
ΔS‡_2back_l	0 cal·mol^{-1}K^{-1}	set based on ΔS‡_2for_l
ΔH‡_3for_si	11.80 kcal/mol	set
ΔS‡_3for_si	0 cal·mol^{-1}K^{-1}	set
ΔH‡_3back_si	19.739(2) kcal/mol	set based on acyl **7** isomerization model
ΔS‡_3back_si	0 cal·mol^{-1}K^{-1}	set
ΔH‡_4for_si	9 kcal/mol	set
ΔS‡_4for_si	–12.2 cal·mol^{-1}K^{-1}	set based on ΔS‡_4back_si
ΔH‡_4back_si	23.0(2) kcal/mol	set from hydrogenolysis model
ΔS‡_4back_si	17.8(7) cal·mol^{-1}K^{-1}	set from hydrogenolysis model
ΔH‡_4for_re	9 kcal/mol	set
ΔS‡_4for_re	–12.2 cal·mol^{-1}K^{-1}	set based on ΔS‡_4back_re
ΔH‡_4back_re	23.0(2) kcal/mol	set from hydrogenolysis model
ΔS‡_4back_re	17.8(7) cal·mol^{-1}K^{-1}	set from hydrogenolysis model
ΔH‡_4for_l	9 kcal/mol	set
ΔS‡_4for_l	–14.8 cal·mol^{-1}K^{-1}	set based on ΔS‡_4back_l
ΔH‡_4back_l	23.8(1) kcal/mol	set from hydrogenolysis model
ΔS‡_4back_l	15.5(2) cal·mol^{-1}K^{-1}	set from hydrogenolysis model
ΔH‡_5for_si	2.5(2)x10^3 kcal/mol	re-optimized hydrogenolysis expts with full model, within error of simple hydrogenolysis model
ΔS‡_5for_si	–43.3(6) cal·mol^{-1}K^{-1}	re-optimized hydrogenolysis expts with full model, within error of simple hydrogenolysis model
ΔH‡_5for_re	2.5(2)x10^3 kcal/mol	set based on ΔH‡_5for_si
ΔS‡_5for_re	–43.3(6) cal·mol^{-1}K^{-1}	set based on ΔS‡_5for_si
ΔH‡_5for_l	2.5(5)x10^3 kcal/mol	re-optimized hydrogenolysis expts with full model, within error of simple hydrogenolysis model
ΔS‡_5for_l	–43(2) cal·mol^{-1}K^{-1}	re-optimized hydrogenolysis expts with full model, within error of simple hydrogenolysis model

B.4.4.2 Data and Model for Catalytic Reactions

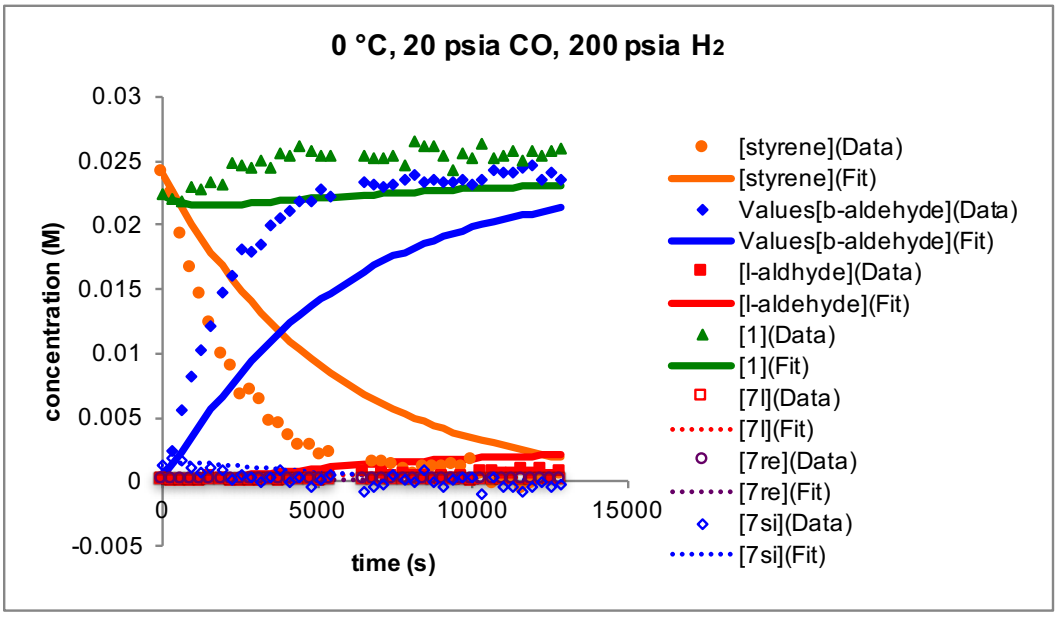

Figure B-143. Data and model for catalytic reaction at 0 °C using combined full model. (25 mM styrene, 25 mM Rh(BDP), 20 psia CO, 200 psia H_2, 273K, CH_2Cl_2).

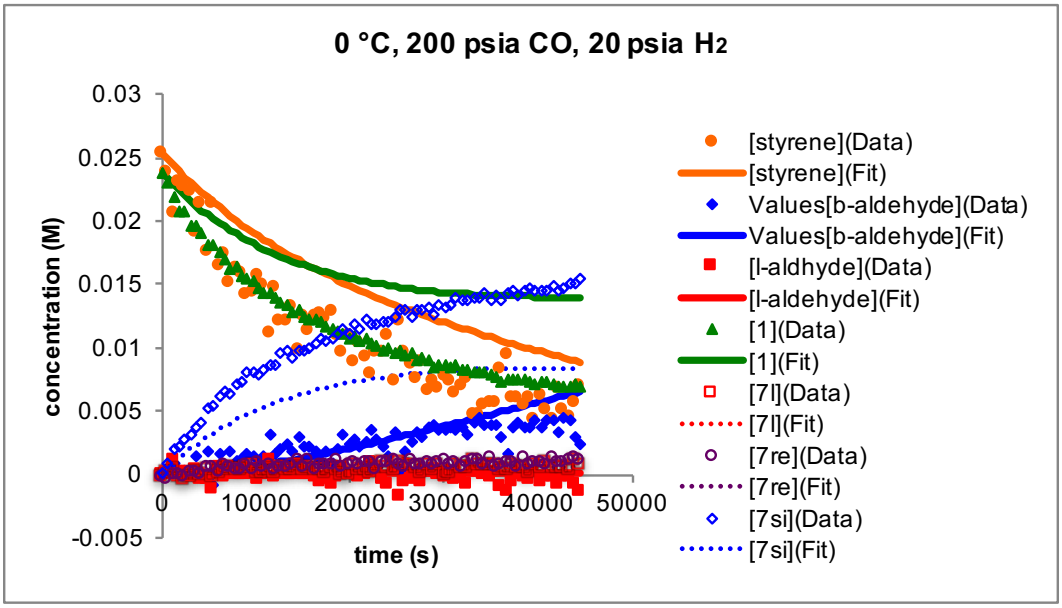

Figure B-144. Data and model for catalytic reaction at 0 °C using combined full model. (25 mM styrene, 25 mM Rh(BDP), 200 psia CO, 20 psia H_2, 273K, CH_2Cl_2).

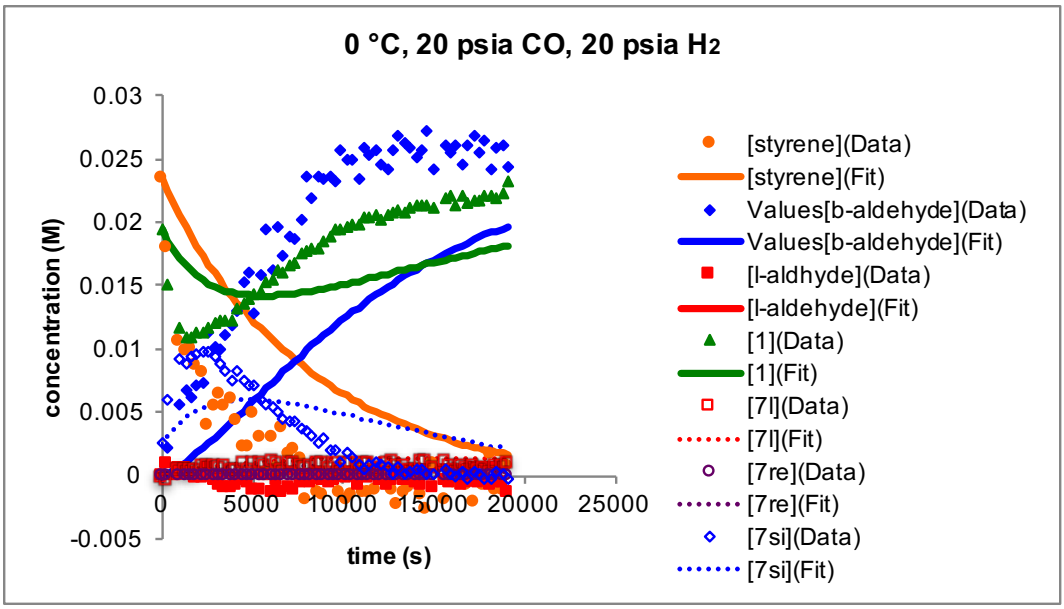

Figure B-145. Data and model for catalytic reaction at 0 °C using combined full model. (25 mM styrene, 20 mM Rh(BDP), 20 psia CO, 20 psia H_2, 273K, CH_2Cl_2).

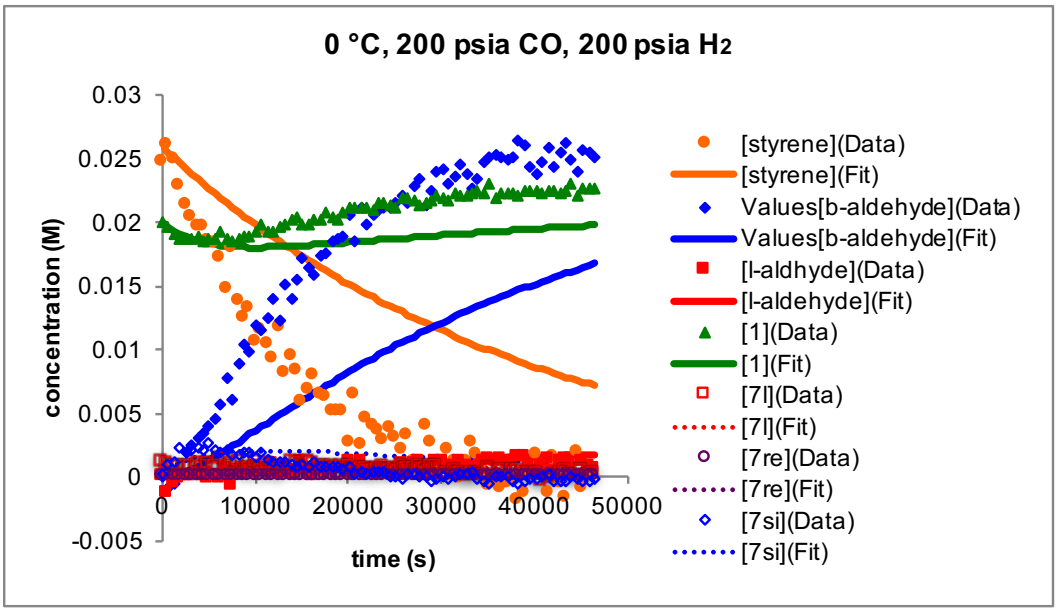

Figure B-146. Data and model for catalytic reaction at 0 °C using combined full model. (25 mM styrene, 20 mM Rh(BDP), 200 psia CO, 200 psia H_2, 273K, CH_2Cl_2).

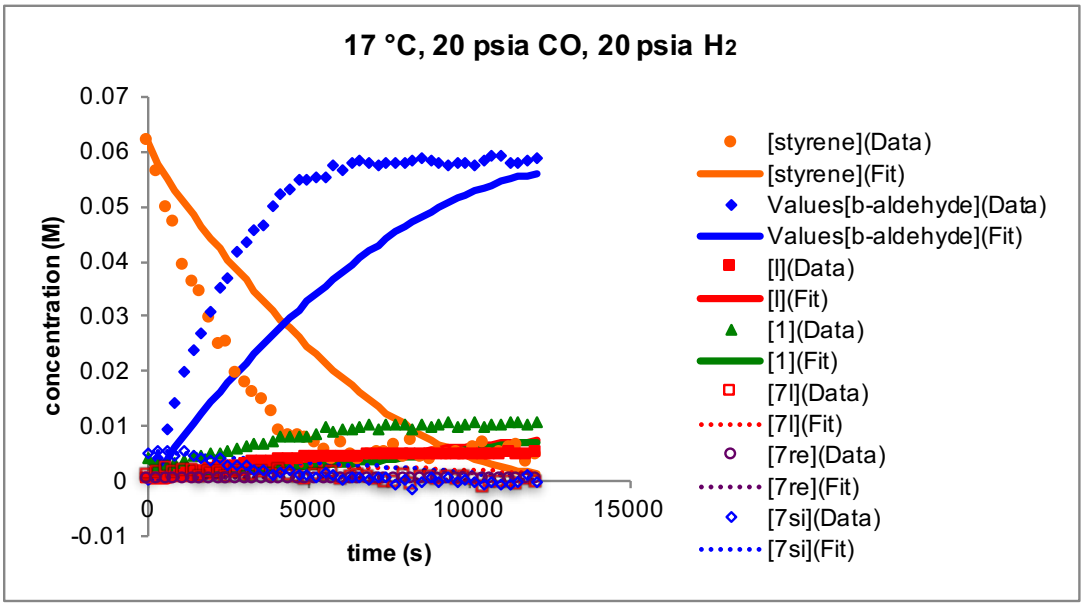

Figure B-147. Data and model for catalytic reaction at 17 °C using combined full model. (60 mM styrene, 10 mM Rh(BDP), 20 psia CO, 20 psia H_2, 290K, CH_2Cl_2).

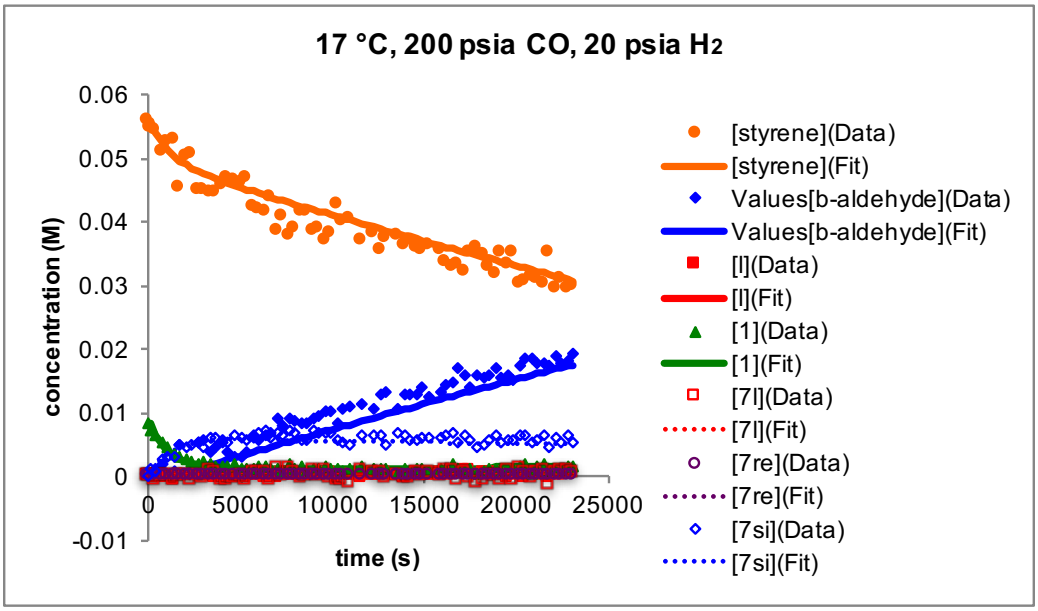

Figure B-148. Data and model for catalytic reaction at 17 °C using combined full model. (60 mM styrene, 10 mM Rh(BDP), 200 psia CO, 20 psia H_2, 290K, CH_2Cl_2).

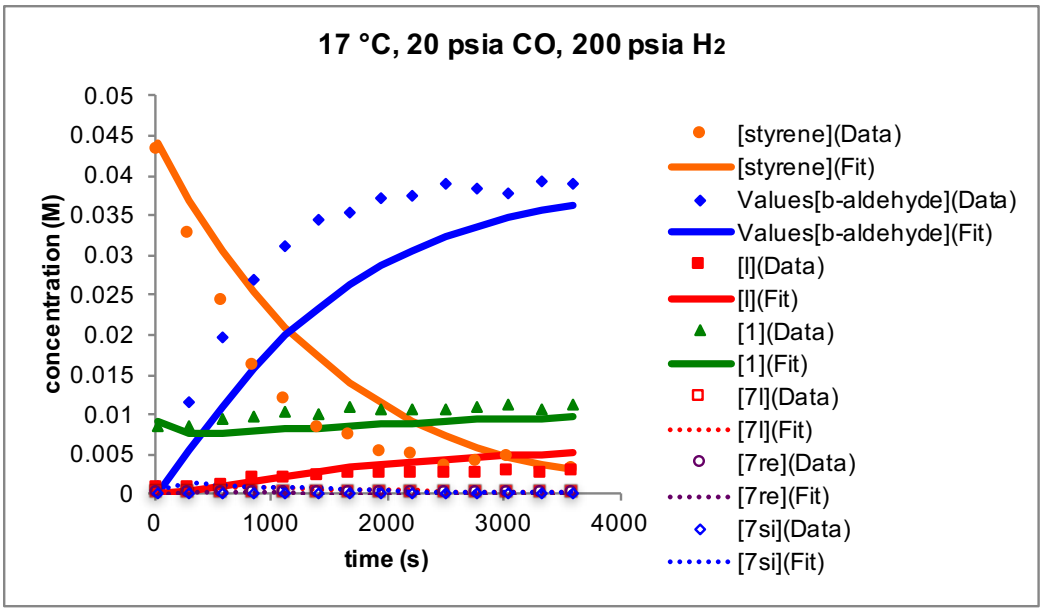

Figure B-149. Data and model for catalytic reaction at 17 °C using combined full model. (45 mM styrene, 10 mM Rh(BDP), 20 psia CO, 200 psia H_2, 290K, CH_2Cl_2).

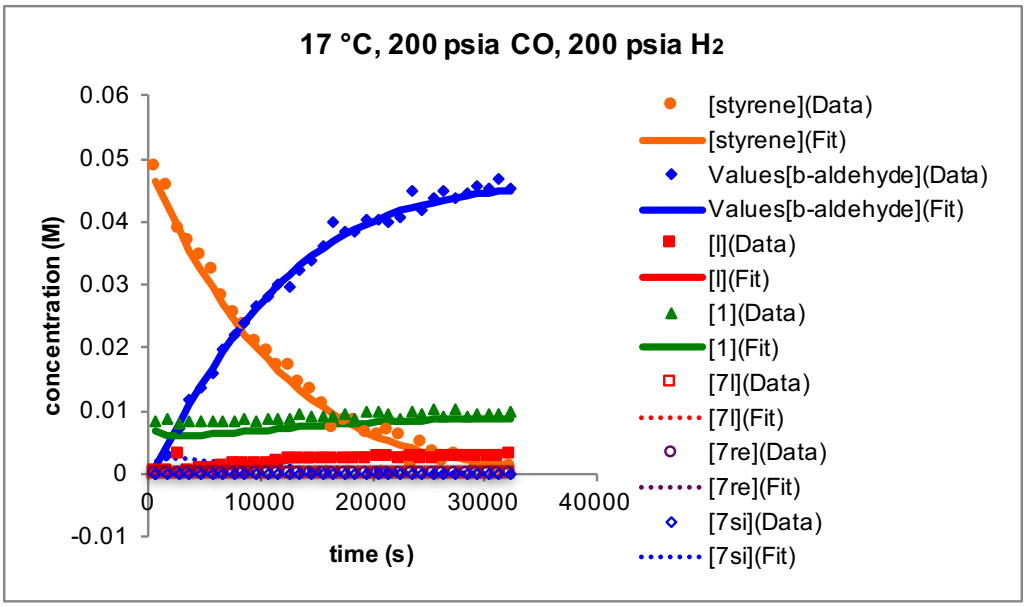

Figure B-150. Data and model for catalytic reaction at 17 °C using combined full model. (50 mM styrene, 10 mM Rh(BDP), 200 psia CO, 200 psia H_2, 290K, CH_2Cl_2).

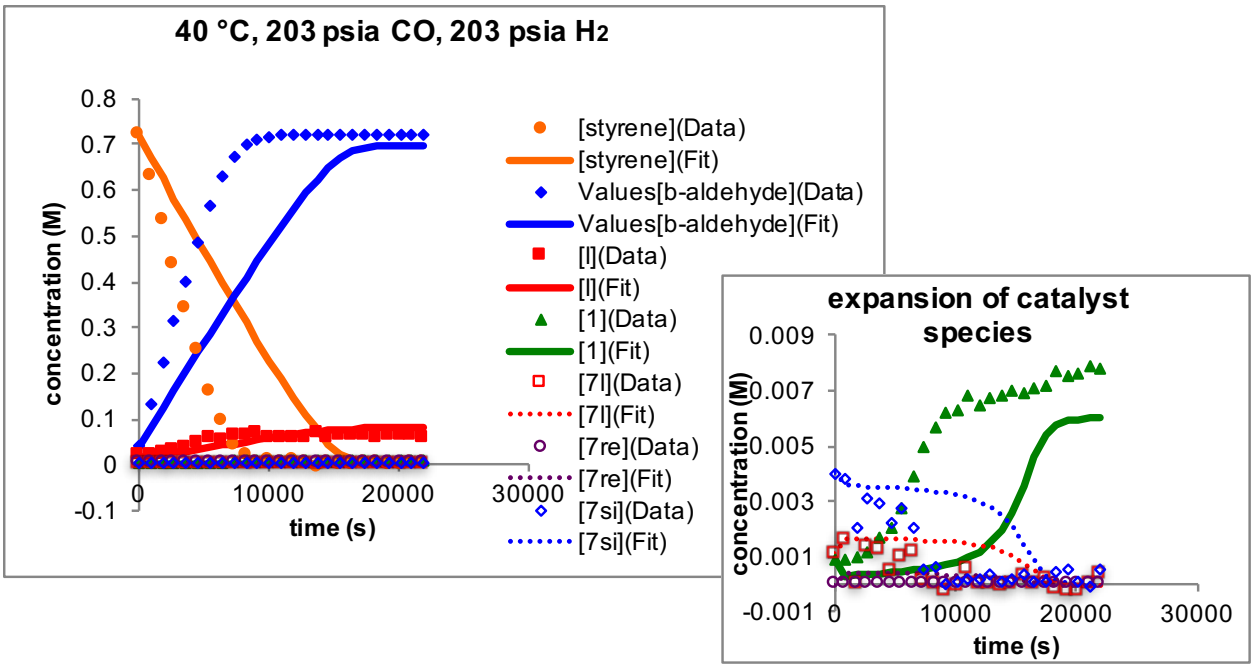

Figure B-151. Data and model for catalytic reaction at 40 °C using combined full model. (0.7 M styrene, 9 mM Rh(BDP), 203 psia CO, 203 psia H_2, 313K, CH_2Cl_2).

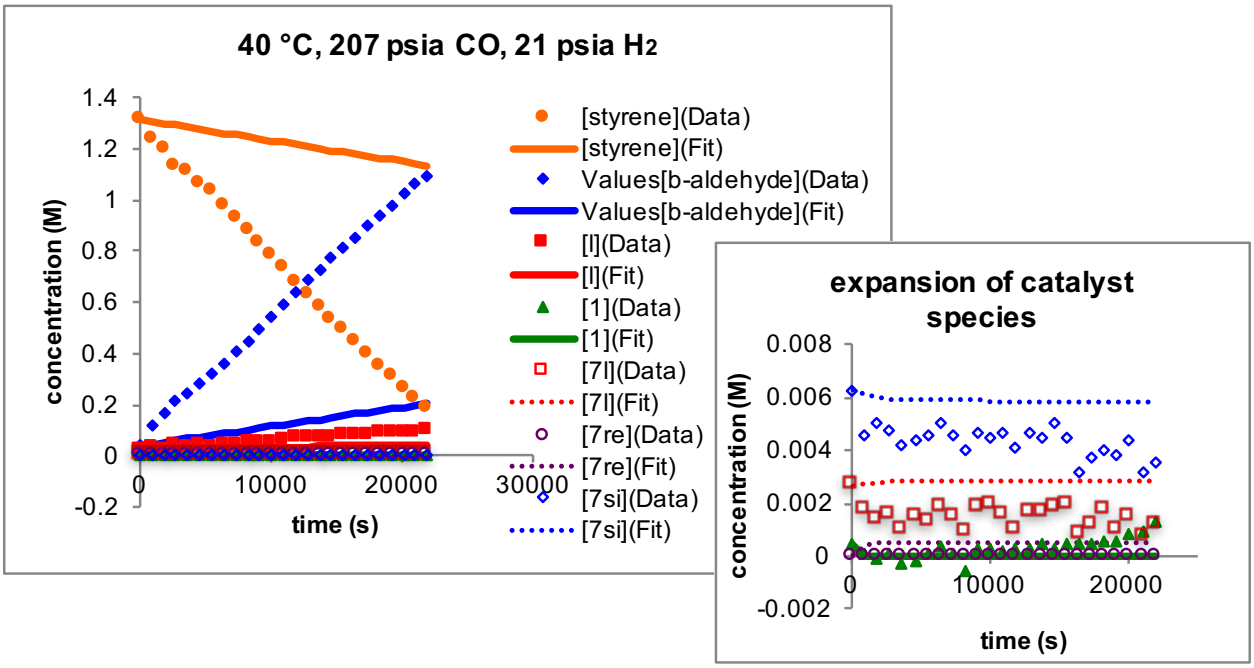

Figure B-152. Data and model for catalytic reaction at 40 °C using combined full model. (1.3 M styrene, 9 mM Rh(BDP), 207 psia CO, 21 psia H_2, 313K, CH_2Cl_2).

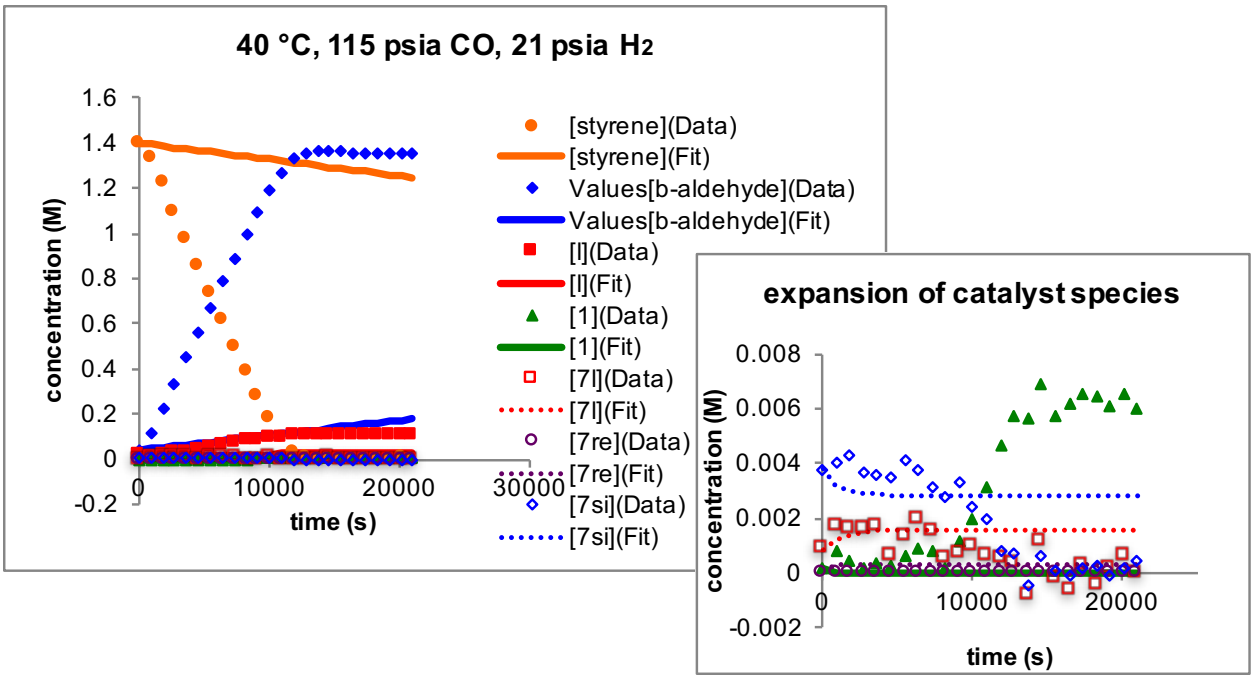

Figure **B-153.** Data and model for catalytic reaction at 40 °C using combined full model. (1.4 M styrene, 7 mM Rh(BDP), 115 psia CO, 21 psia H_2, 313K, CH_2Cl_2).

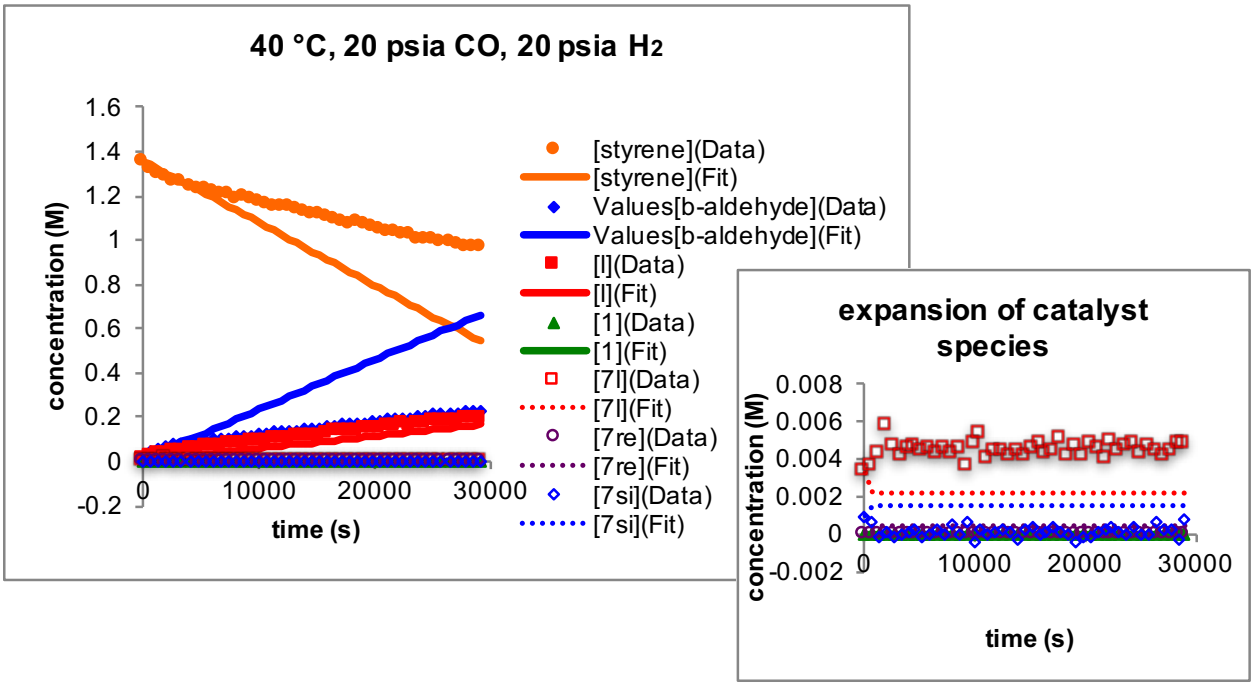

Figure B-154. Data and model for catalytic reaction at 40 °C using combined full model. (1.4 M styrene, 6 mM Rh(BDP), 20 psia CO, 20 psia H_2, 313K, CH_2Cl_2).

Appendix C

Crystallographic Data for Chapter 6

C.1 Crystallographic Data for TPSB BDP 1

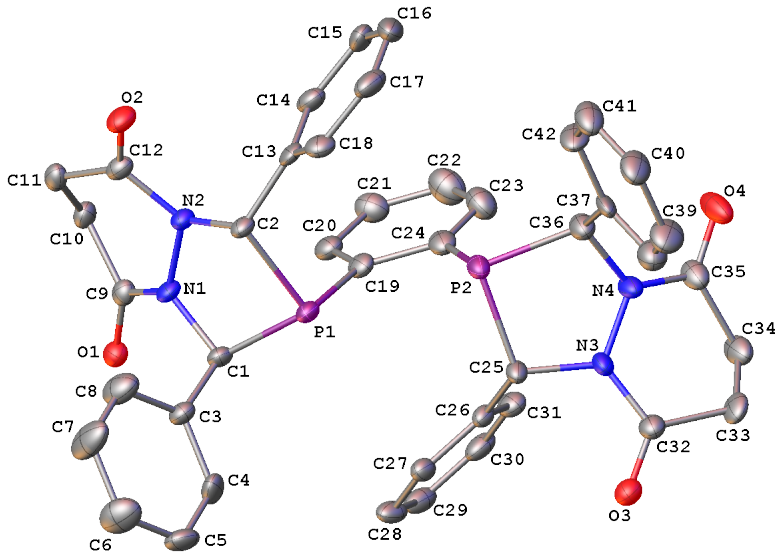

Figure C-1. A molecular drawing of the first diphosphine molecule in TPSB BDP **1** shown with 50% probability ellipsoids. All H atoms are omitted.

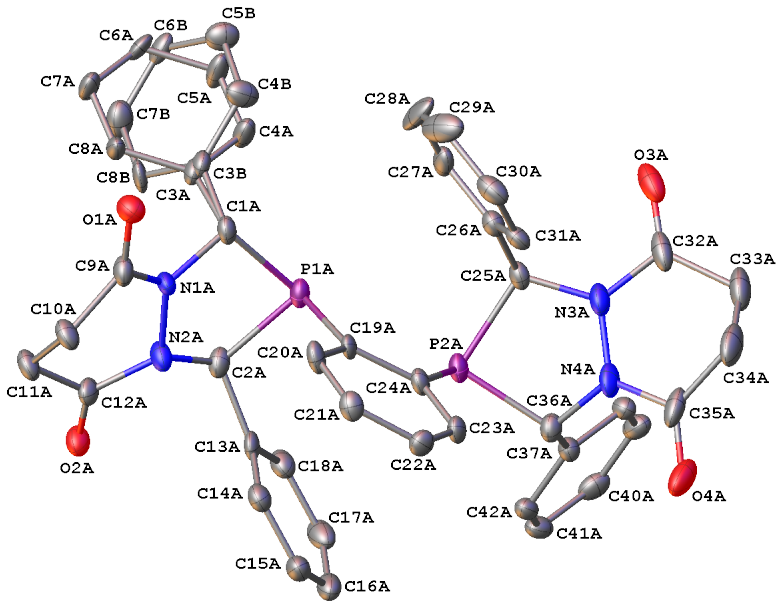

Figure C-2. A molecular drawing of the second diphosphine molecule in TPSB BDP **1** shown with 50% probability ellipsoids. All H atoms are omitted but both positions of the disordered Ph ring are shown.

C.1.1 Data Collection

A colorless crystal with approximate dimensions 0.37 × 0.05 × 0.046 mm^3 was selected under oil under ambient conditions and attached to the tip of a MiTeGen MicroMount©. The crystal was mounted in a stream of cold nitrogen at 100(1) K and centered in the X-ray beam by using a video camera.

The crystal evaluation and data collection were performed on a Bruker Quazar SMART APEXII diffractometer with Mo K_α (λ = 0.71073 Å) radiation and the diffractometer to crystal distance of 4.96 cm.[1]

The initial cell constants were obtained from three series of ω scans at different starting angles. Each series consisted of 12 frames collected at intervals of 0.5º in a 6º range about ω with the exposure time of 20 seconds per frame. The reflections were successfully indexed by an automated indexing routine built in the APEXII program suite. The final cell constants were calculated from a set of 9854 strong reflections from the actual data collection.

The data were collected by using the full sphere data collection routine to survey the reciprocal space to the extent of a full sphere to a resolution of 0.70 Å. A total of 107270 data were harvested by collecting 4 sets of frames with 0.6º scans in ω and φ with exposure times of 90/120 sec per frame. These highly redundant datasets were corrected for Lorentz and polarization effects. The absorption correction was based on fitting a function to the empirical transmission surface as sampled by multiple equivalent measurements.[2]

C.1.2 Structure Solution and Refinement

The systematic absences in the diffraction data were consistent for the space group $Pca2_1$ that yielded chemically reasonable and computationally stable results of refinement.[3–8]

A successful solution by the direct methods provided most non-hydrogen atoms from the *E*-map. The remaining non-hydrogen atoms were located in an alternating series of least-squares cycles and difference Fourier maps. All non-hydrogen atoms were refined with anisotropic displacement coefficients. All hydrogen atoms were included in the structure factor calculation at idealized positions and were allowed to ride on the neighboring atoms with relative isotropic displacement coefficients.

There are two symmetry-independent diphosphine molecules in the asymmetric unit. The phenyl ring at atom C1a is disordered over two positions with the major component contribution of 0.574(12).

The crystal appears to be a racemic twin with the minor component contribution of 0.40(6).

There were several partially occupied solvent molecules present in the asymmetric unit. A significant amount of time was invested in identifying and refining the disordered molecules. Bond length restraints were applied to model the molecules but the resulting isotropic displacement coefficients suggested the molecules were mobile. In addition, the refinement was computationally unstable. Option SQUEEZE of program PLATON[9] was used to correct the diffraction data for diffuse scattering effects and to identify the solvate molecule. PLATON calculated the upper limit of volume that can be occupied by the solvent to be 1494 $Å^3$, or 18% of the unit cell volume. The program calculated 539 electrons in the unit cell for the diffuse species. This approximately corresponds to 2.5 molecules of CH_2Cl_2 and ¾ molecules of THF per two diphosphines in the asymmetric unit (540 electrons). The solvent molecules are disordered over several positions. All derived results in the following tables are based on the known contents. No data are given for the diffusely scattering species.

The diphosphine molecules were refined with restraints and constraints.

The final least-squares refinement of 878 parameters against 16646 data resulted in residuals *R* (based on F^2 for $I \geq 2\sigma$) and *wR* (based on F^2 for all data) of 0.0685 and 0.1799, respectively.

C.1.3 Summary

Crystal data for $C_{42}H_{36}N_4O_4P_2$ (M =722.69 g/mol): orthorhombic, space group $Pca2_1$ (no. 29), a = 23.708(8) Å, b = 13.125(5) Å, c = 26.110(8) Å, V = 8125(5) Å^3, Z = 8, T = 100.02 K, μ(Mo Kα) = 0.151 mm^{-1}, *Dcalc* = 1.182 g/cm^3, 107270 reflections measured ($3.102° \leq 2\Theta \leq 52.82°$), 16646 unique ($R_{int}$ = 0.0821, R_{sigma} = 0.0611) which were used in all calculations. The final R_1 was 0.0685 ($I > 2\sigma(I)$) and wR_2 was 0.1799 (all data).

Table C-1. Crystal data and structure refinement for TPSB BDP 1.

Empirical formula	$C_{42}H_{36}N_4O_4P_2$
Formula weight	722.69
Temperature/K	100.02
Crystal system	orthorhombic
Space group	$Pca2_1$
a/Å	23.708(8)
b/Å	13.125(5)
c/Å	26.110(8)
α/°	90
β/°	90
γ/°	90

Volume/Å^3	8125(5)
Z	8
ϱ_{calc}g/cm^3	1.182
μ/mm^{-1}	0.151
F(000)	3024.0
Crystal size/mm^3	0.37 × 0.05 × 0.046
Radiation	Mo Kα (λ = 0.71073)
2Θ range for data collection/°	3.102 to 52.82
Index ranges	-29 ≤ h ≤ 25, -16 ≤ k ≤ 16, -32 ≤ l ≤ 32
Reflections collected	107270
Independent reflections	16646 [R_{int} = 0.0821, R_{sigma} = 0.0611]
Data/restraints/parameters	16646/947/878
Goodness-of-fit on F^2	1.040
Final R indexes [I>=2σ (I)]	R_1 = 0.0685, wR_2 = 0.1679
Final R indexes [all data]	R_1 = 0.0908, wR_2 = 0.1799
Largest diff. peak/hole / e Å^{-3}	1.34/-0.41
Flack parameter	0.40(6)

Table C-2. Fractional Atomic Coordinates (×10^4) and Equivalent Isotropic Displacement Parameters (Å^2×10^3) for TPSB BDP **1**. U_{eq} is defined as 1/3 of of the trace of the orthogonalised U_{IJ} tensor.

Atom	***x***	***y***	***z***	**U(eq)**
P1	5201.8(6)	1152.0(15)	5123.7(6)	27.1(4)
P2	5972.1(7)	1507.1(16)	4203.2(6)	30.7(4)

O1	4385.7(19)	-1046(4)	6207.4(17)	29.8(10)
O2	3292.8(19)	1227(4)	4836.3(19)	36.7(12)
O3	7785.4(19)	1976(4)	4775.9(19)	35.0(11)
O4	7149(3)	181(6)	3033(2)	56.0(18)
N1	4359(2)	176(5)	5609(2)	27.6(12)
N2	4108(2)	599(4)	5153(2)	25.5(11)
N3	7111(2)	1440(5)	4231(2)	31.8(13)
N4	6953(2)	1081(5)	3738(2)	34.2(14)
C1	4918(3)	601(5)	5730(2)	26.5(13)
C2	4448(2)	1402(5)	4919(2)	25.5(13)
C3	4904.8(18)	1434(3)	6131.0(17)	28.8(14)
C4	5396.8(14)	1666(4)	6396.0(19)	43.2(18)
C5	5403.2(17)	2469(4)	6743.4(19)	42.9(18)
C6	4918(2)	3039(4)	6826(2)	58(2)
C7	4425.6(18)	2807(4)	6561(2)	64(3)
C8	4419.2(15)	2004(4)	6213(2)	51(2)
C9	4148(3)	-665(5)	5833(2)	26.1(13)
C10	3605(3)	-1012(6)	5595(3)	30.2(14)
C11	3232(3)	-111(5)	5465(3)	30.4(15)
C12	3523(3)	632(5)	5128(3)	28.6(13)
C13	4403.9(19)	1509(3)	4344.9(11)	28.1(13)
C14	4327.4(18)	675(3)	4024.3(16)	34.4(15)
C15	4338(2)	804(4)	3496.0(15)	41.5(17)
C16	4425(2)	1766(4)	3288.2(12)	50.9(19)
C17	4502(2)	2600(3)	3608.8(17)	44.7(18)

C18	4491.0(19)	2472(3)	4137.2(16)	34.2(15)
C19	5361(3)	27(6)	4730(3)	29.5(15)
C20	5147(3)	-948(6)	4815(3)	34.4(15)
C21	5258(3)	-1734(7)	4474(3)	41.2(17)
C22	5592(4)	-1565(7)	4062(3)	54(2)
C23	5815(4)	-617(7)	3967(3)	44.3(18)
C24	5722(3)	188(6)	4284(3)	35.0(15)
C25	6645(3)	1522(6)	4604(2)	27.1(14)
C26	6683.4(18)	699(3)	5008.5(13)	25.5(13)
C27	6558.2(18)	953(3)	5512.6(15)	30.0(14)
C28	6595(2)	219(4)	5894.9(11)	37.4(16)
C29	6757(2)	-769(3)	5773.2(15)	38.3(16)
C30	6882.3(19)	-1024(3)	5269.1(17)	38.4(16)
C31	6845.4(19)	-290(3)	4886.7(12)	33.9(15)
C32	7655(3)	1636(6)	4359(3)	31.0(15)
C33	8072(3)	1317(7)	3951(3)	39.5(17)
C34	7882(3)	366(7)	3685(3)	44.6(19)
C35	7299(3)	498(6)	3451(3)	38.0(17)
C36	6396(3)	1435(6)	3592(3)	36.8(16)
C37	6394.1(19)	2480(3)	3334.6(17)	35.2(15)
C38	6839.6(16)	3162(4)	3378.5(18)	48.4(19)
C39	6793.4(19)	4135(4)	3172(2)	55(2)
C40	6302(2)	4424(3)	2921(2)	52(2)
C41	5856.1(17)	3741(4)	2877.1(19)	50(2)
C42	5902.3(17)	2769(4)	3083.9(18)	48(2)

P1A	7255.7(7)	6096.5(14)	5043.9(7)	28.3(4)
P2A	6464.7(7)	6542.9(15)	5951.5(7)	28.9(4)
O1A	8010(2)	3803(4)	3970.5(19)	36.8(12)
O2A	9167.3(19)	6054(4)	5305.7(18)	35.9(12)
O3A	4647(2)	7020(5)	5405(3)	49.0(14)
O4A	5290(3)	5400(6)	7178(2)	57.0(17)
N1A	8058(2)	5046(4)	4568(2)	26.4(12)
N2A	8336(2)	5471(5)	5007(2)	31.8(13)
N3A	5323(2)	6436(5)	5931(2)	35.7(13)
N4A	5496(2)	6138(5)	6426(2)	36.5(14)
C1A	7515(3)	5498(5)	4438(3)	28.2(13)
C2A	8007(3)	6289(6)	5242(3)	31.1(15)
C3A	7588(3)	6326(6)	4032(3)	28.4(15)
C4A	7163(3)	7046(7)	3974(3)	40(4)
C5A	7171(4)	7707(7)	3558(3)	46(4)
C6A	7604(4)	7648(7)	3201(3)	32(3)
C7A	8030(3)	6929(7)	3259(3)	40(4)
C8A	8022(3)	6268(6)	3675(3)	36(3)
C3B	7510(4)	6287(8)	4005(4)	28.4(15)
C4B	7030(4)	6427(8)	3708(5)	39(4)
C5B	7014(4)	7197(9)	3343(4)	39(4)
C6B	7479(5)	7828(8)	3275(4)	32(4)
C7B	7960(4)	7688(8)	3572(5)	45(5)
C8B	7975(4)	6917(9)	3937(4)	35(4)
C9A	8267(3)	4205(6)	4336(3)	31.8(15)

C10A	8817(3)	3833(6)	4543(3)	33.5(16)
C11A	9203(3)	4752(6)	4658(3)	34.6(16)
C12A	8923(3)	5488(6)	5015(3)	30.5(14)
C13A	8052.0(19)	6321(3)	5829.9(12)	29.5(14)
C14A	8127.6(19)	5450(3)	6124.6(16)	34.9(15)
C15A	8095(2)	5507(3)	6655.4(15)	40.7(17)
C16A	7988(2)	6437(4)	6891.4(12)	43.2(18)
C17A	7912(2)	7308(3)	6596.7(17)	46.4(18)
C18A	7944.2(19)	7250(3)	6066.0(16)	35.9(16)
C19A	7055(2)	5004(5)	5452(3)	24.7(14)
C20A	7262(3)	4023(6)	5380(3)	32.8(15)
C21A	7152(3)	3271(6)	5737(3)	30.4(15)
C22A	6815(3)	3477(6)	6161(3)	30.2(14)
C23A	6581(3)	4437(6)	6221(3)	29.6(14)
C24A	6705(2)	5216(5)	5868(3)	26.6(13)
C25A	5779(3)	6533(5)	5569(3)	27.6(14)
C26A	5756.2(18)	5729(3)	5149.9(14)	30.1(14)
C27A	5901(2)	5999(3)	4652.2(17)	37.9(17)
C28A	5890(2)	5272(4)	4265.2(13)	58(2)
C29A	5733(2)	4275(4)	4375.8(16)	61(2)
C30A	5588(2)	4006(3)	4873.4(19)	39.7(17)
C31A	5599.6(18)	4733(3)	5260.5(13)	29.5(14)
C32A	4775(3)	6684(7)	5828(4)	44.7(18)
C33A	4369(3)	6428(7)	6258(4)	54(2)
C34A	4560(3)	5466(8)	6527(4)	57(2)

C35A	5133(3)	5652(7)	6750(3)	45.8(19)
C36A	6042(3)	6532(6)	6565(3)	30.5(14)
C37A	6035.7(17)	7603(3)	6789.9(16)	28.1(13)
C38A	5572.7(14)	8240(3)	6726.5(16)	29.6(14)
C39A	5587.6(16)	9230(3)	6915.6(17)	36.7(15)
C40A	6065(2)	9582(3)	7168.2(17)	37.1(16)
C41A	6528.5(15)	8945(3)	7231.6(17)	35.3(15)
C42A	6513.5(14)	7955(3)	7042.4(17)	31.2(14)

Table C-3. Anisotropic Displacement Parameters ($Å^2 \times 10^3$) for TPSB BDP **1**. The Anisotropic displacement factor exponent takes the form: $-2\pi^2[h^2a^{*2}U_{11}+2hka^*b^*U_{12}+\ldots]$.

Atom	$\mathbf{U_{11}}$	$\mathbf{U_{22}}$	$\mathbf{U_{33}}$	$\mathbf{U_{23}}$	$\mathbf{U_{13}}$	$\mathbf{U_{12}}$
P1	16.7(7)	39.3(10)	25.3(8)	1.4(8)	-3.2(6)	-1.6(7)
P2	23.4(8)	48.3(12)	20.3(8)	3.9(8)	0.0(6)	9.2(8)
O1	24(2)	37(3)	28(2)	0(2)	0.5(18)	4(2)
O2	23(2)	47(3)	40(3)	6(2)	-7(2)	4(2)
O3	25(2)	46(3)	34(2)	2(2)	-2.4(19)	2(2)
O4	52(3)	88(5)	27(3)	-6(3)	-1(2)	35(3)
N1	15(2)	40(3)	29(3)	0(2)	-4(2)	3(2)
N2	17(2)	35(3)	24(3)	3(2)	-3.9(19)	1(2)
N3	24(2)	55(4)	16(2)	2(2)	2(2)	6(3)
N4	24(3)	58(4)	21(3)	-2(3)	-4(2)	13(3)
C1	19(3)	35(4)	25(3)	-2(3)	-5(2)	-4(3)
C2	16(3)	34(4)	27(3)	4(3)	-5(2)	2(2)

C3	19(3)	37(4)	31(3)	-1(3)	-5(2)	1(3)
C4	24(3)	66(5)	39(4)	-8(4)	9(3)	-15(3)
C5	34(4)	56(5)	38(4)	-2(3)	-15(3)	-11(3)
C6	53(5)	47(5)	72(6)	-19(5)	-11(4)	6(4)
C7	31(4)	69(6)	91(7)	-35(5)	-3(4)	15(4)
C8	34(4)	57(5)	62(5)	-12(4)	-10(4)	10(4)
C9	23(3)	27(3)	29(3)	-4(3)	3(2)	4(2)
C10	22(3)	38(4)	31(3)	-2(3)	4(3)	-4(3)
C11	25(3)	36(4)	30(3)	-9(3)	6(3)	-1(3)
C12	21(3)	32(4)	33(3)	-5(3)	-4(2)	2(2)
C13	11(3)	42(4)	32(3)	-2(3)	-3(2)	2(3)
C14	20(3)	44(4)	39(3)	-8(3)	-6(3)	0(3)
C15	20(3)	67(5)	37(3)	-8(3)	3(3)	-10(3)
C16	29(4)	101(6)	22(3)	2(3)	-1(3)	-3(4)
C17	24(3)	62(5)	47(4)	15(3)	-9(3)	-8(3)
C18	27(3)	44(4)	32(3)	5(3)	-10(3)	5(3)
C19	19(3)	37(4)	32(3)	-1(3)	-4(3)	9(3)
C20	22(3)	47(4)	34(4)	-3(3)	-6(3)	5(3)
C21	45(4)	39(4)	39(4)	-3(3)	-6(3)	10(3)
C22	66(6)	51(5)	45(4)	-2(4)	1(4)	14(4)
C23	49(5)	53(4)	31(4)	3(3)	3(3)	13(4)
C24	26(3)	51(4)	28(3)	5(3)	-5(3)	12(3)
C25	21(3)	42(4)	19(3)	7(3)	0(2)	6(3)
C26	17(3)	36(3)	23(3)	7(3)	-1(2)	-1(3)
C27	24(3)	41(4)	25(3)	4(3)	-3(3)	-6(3)

C28	34(4)	53(4)	25(3)	12(3)	-10(3)	-10(3)
C29	29(4)	45(4)	41(4)	17(3)	-11(3)	-10(3)
C30	21(3)	47(4)	48(4)	10(3)	-7(3)	-2(3)
C31	25(3)	43(4)	34(4)	-1(3)	-5(3)	7(3)
C32	25(3)	42(4)	27(3)	3(3)	-3(2)	7(3)
C33	21(3)	57(5)	41(4)	6(3)	3(3)	16(3)
C34	36(4)	66(5)	32(4)	-3(4)	-1(3)	25(4)
C35	37(4)	48(5)	29(3)	4(3)	1(3)	19(3)
C36	28(3)	56(5)	27(3)	3(3)	0(3)	12(3)
C37	26(3)	68(5)	12(3)	4(3)	3(2)	12(3)
C38	38(4)	71(5)	36(4)	7(4)	0(3)	8(3)
C39	50(4)	76(6)	40(4)	27(4)	-2(4)	6(4)
C40	44(4)	76(6)	35(4)	25(4)	3(3)	10(4)
C41	42(4)	75(6)	34(4)	19(4)	4(3)	19(4)
C42	30(4)	81(6)	33(4)	21(4)	-6(3)	14(4)
P1A	20.4(8)	31.6(10)	32.9(9)	2.5(8)	8.2(7)	0.6(7)
P2A	17.2(8)	34(1)	35.5(9)	1.0(8)	5.7(7)	-1.0(7)
O1A	31(3)	45(3)	35(3)	-3(2)	-3(2)	1(2)
O2A	24(2)	47(3)	36(3)	-7(2)	4(2)	-8(2)
O3A	23(3)	57(4)	67(3)	-25(3)	-1(2)	3(2)
O4A	47(3)	87(5)	36(3)	-10(3)	17(2)	-30(3)
N1A	13(2)	41(3)	24(3)	-4(2)	0(2)	1(2)
N2A	19(2)	39(3)	37(3)	-10(3)	3(2)	0(2)
N3A	18(2)	47(4)	41(3)	-8(3)	6(2)	-5(2)
N4A	20(3)	45(4)	45(3)	-8(3)	9(2)	-11(2)

C1A	17(3)	34(4)	34(3)	2(3)	6(2)	-1(3)
C2A	25(3)	34(4)	34(3)	-3(3)	9(3)	-4(3)
C3A	21(3)	41(4)	24(3)	-3(3)	8(3)	-1(3)
C4A	33(6)	57(9)	30(6)	16(6)	13(5)	14(6)
C5A	39(8)	59(10)	40(7)	24(7)	22(6)	18(7)
C6A	39(7)	42(8)	15(5)	4(5)	12(5)	-2(5)
C7A	30(6)	64(9)	27(6)	18(6)	13(5)	10(5)
C8A	18(5)	68(10)	23(5)	13(5)	4(4)	12(5)
C3B	21(3)	41(4)	24(3)	-3(3)	8(3)	-1(3)
C4B	37(7)	40(10)	39(9)	12(7)	-9(6)	-11(7)
C5B	47(9)	34(10)	36(9)	8(7)	-4(7)	-3(7)
C6B	40(8)	30(9)	27(9)	2(7)	18(6)	6(6)
C7B	35(8)	46(11)	53(11)	10(8)	12(7)	-1(7)
C8B	11(6)	47(10)	47(10)	9(7)	10(6)	4(5)
C9A	21(3)	39(4)	35(3)	-4(3)	8(2)	-1(3)
C10A	18(3)	39(4)	44(4)	-6(3)	-2(3)	-3(3)
C11A	16(3)	44(4)	44(4)	-6(3)	-1(3)	-2(3)
C12A	19(3)	43(4)	30(3)	0(3)	5(2)	-9(3)
C13A	13(3)	42(4)	33(3)	0(3)	8(2)	-4(3)
C14A	20(3)	49(4)	35(3)	-1(3)	-1(3)	-2(3)
C15A	24(3)	68(5)	30(3)	6(3)	0(3)	4(3)
C16A	25(4)	76(5)	28(3)	-11(3)	1(3)	0(3)
C17A	29(4)	72(5)	38(4)	-22(3)	-5(3)	7(4)
C18A	23(3)	49(4)	36(3)	-9(3)	-2(3)	-2(3)
C19A	11(3)	37(4)	26(3)	4(3)	4(2)	-3(2)

C20A	15(3)	37(4)	47(4)	3(3)	7(3)	-2(3)
C21A	25(3)	28(4)	39(4)	0(3)	3(3)	-1(3)
C22A	29(3)	35(4)	27(3)	8(3)	3(3)	-5(3)
C23A	16(3)	42(4)	31(3)	5(3)	5(2)	-3(3)
C24A	13(3)	33(3)	33(3)	3(3)	3(2)	-2(2)
C25A	17(3)	30(4)	36(3)	3(3)	3(2)	2(3)
C26A	20(3)	39(3)	32(3)	3(3)	0(3)	2(3)
C27A	22(3)	54(5)	37(3)	14(3)	8(3)	14(3)
C28A	69(6)	81(5)	25(4)	10(4)	23(4)	40(5)
C29A	74(6)	71(5)	37(4)	-15(4)	-10(4)	42(5)
C30A	29(4)	42(4)	49(4)	-4(3)	-11(3)	5(3)
C31A	18(3)	39(4)	32(3)	2(3)	-7(3)	1(3)
C32A	20(3)	52(5)	63(4)	-22(4)	10(3)	-2(3)
C33A	25(4)	71(6)	66(5)	-20(4)	18(3)	-10(4)
C34A	35(4)	80(6)	56(5)	-16(4)	22(3)	-26(4)
C35A	38(4)	56(5)	43(4)	-15(3)	24(3)	-14(3)
C36A	23(3)	37(4)	32(3)	0(3)	6(2)	-4(3)
C37A	19(3)	38(4)	27(3)	2(3)	1(2)	0(2)
C38A	23(3)	42(4)	23(3)	0(3)	-2(2)	3(3)
C39A	39(4)	48(4)	24(3)	2(3)	2(3)	11(3)
C40A	50(4)	37(4)	24(3)	7(3)	4(3)	-5(3)
C41A	28(3)	52(4)	26(3)	6(3)	-6(3)	-10(3)
C42A	21(3)	49(4)	23(3)	8(3)	-3(2)	-2(3)

Table C-4. Bond Lengths for TPSB BDP **1.**

Atom	Atom	Length/Å	Atom	Atom	Length/Å
P1	C1	1.867(7)	P2A	C25A	1.907(7)
P1	C2	1.893(6)	P2A	C36A	1.890(7)
P1	C19	1.839(8)	O1A	C9A	1.250(9)
P2	C24	1.843(9)	O2A	C12A	1.210(8)
P2	C25	1.909(6)	O3A	C32A	1.227(11)
P2	C36	1.889(7)	O4A	C35A	1.226(11)
O1	C9	1.234(8)	N1A	N2A	1.433(8)
O2	C12	1.221(8)	N1A	C1A	1.460(8)
O3	C32	1.216(8)	N1A	C9A	1.353(9)
O4	C35	1.223(9)	N2A	C2A	1.463(9)
N1	N2	1.442(8)	N2A	C12A	1.391(8)
N1	C1	1.474(8)	N3A	N4A	1.411(9)
N1	C9	1.345(9)	N3A	C25A	1.443(8)
N2	C2	1.461(8)	N3A	C32A	1.365(9)
N2	C12	1.389(8)	N4A	C35A	1.364(9)
N3	N4	1.420(8)	N4A	C36A	1.442(9)
N3	C25	1.476(8)	C1A	C3A	1.528(8)
N3	C32	1.359(9)	C1A	C3B	1.532(8)
N4	C35	1.350(9)	C2A	C13A	1.540(7)
N4	C36	1.450(8)	C3A	C4A	1.3900
C1	C3	1.514(7)	C3A	C8A	1.3900
C2	C13	1.510(7)	C4A	C5A	1.3900
C3	C4	1.3900	C5A	C6A	1.3900
C3	C8	1.3900	C6A	C7A	1.3900

C4	C5	1.3900	C7A	C8A	1.3900
C5	C6	1.3900	C3B	C4B	1.3900
C6	C7	1.3900	C3B	C8B	1.3900
C7	C8	1.3900	C4B	C5B	1.3900
C9	C10	1.501(9)	C5B	C6B	1.3900
C10	C11	1.516(10)	C6B	C7B	1.3900
C11	C12	1.482(10)	C7B	C8B	1.3900
C13	C14	1.3900	C9A	C10A	1.494(10)
C13	C18	1.3900	C10A	C11A	1.543(10)
C14	C15	1.3900	C11A	C12A	1.498(10)
C15	C16	1.3900	C13A	C14A	1.3900
C16	C17	1.3900	C13A	C18A	1.3900
C17	C18	1.3900	C14A	C15A	1.3900
C19	C20	1.394(11)	C15A	C16A	1.3900
C19	C24	1.459(11)	C16A	C17A	1.3900
C20	C21	1.387(11)	C17A	C18A	1.3900
C21	C22	1.354(12)	C19A	C20A	1.391(10)
C22	C23	1.375(13)	C19A	C24A	1.395(9)
C23	C24	1.360(11)	C20A	C21A	1.382(10)
C25	C26	1.514(7)	C21A	C22A	1.392(9)
C26	C27	1.3900	C22A	C23A	1.386(10)
C26	C31	1.3900	C23A	C24A	1.407(9)
C27	C28	1.3900	C25A	C26A	1.521(8)
C28	C29	1.3900	C26A	C27A	1.3900
C29	C30	1.3900	C26A	C31A	1.3900

C30	C31	1.3900	C27A	C28A	1.3900
C32	C33	1.513(10)	C28A	C29A	1.3900
C33	C34	1.497(12)	C29A	C30A	1.3900
C34	C35	1.520(10)	C30A	C31A	1.3900
C36	C37	1.527(9)	C32A	C33A	1.518(11)
C37	C38	1.3900	C33A	C34A	1.514(14)
C37	C42	1.3900	C34A	C35A	1.498(12)
C38	C39	1.3900	C36A	C37A	1.523(8)
C39	C40	1.3900	C37A	C38A	1.3900
C40	C41	1.3900	C37A	C42A	1.3900
C41	C42	1.3900	C38A	C39A	1.3900
P1A	C1A	1.870(7)	C39A	C40A	1.3900
P1A	C2A	1.872(7)	C40A	C41A	1.3900
P1A	C19A	1.849(7)	C41A	C42A	1.3900
P2A	C24A	1.846(7)			

Table C-5. Bond Angles for TPSB BDP **1.**

Atom	**Atom**	**Atom**	**Angle/°**	**Atom**	**Atom**	**Atom**	**Angle/°**
C1	P1	C2	88.1(3)	C36A	P2A	C25A	89.6(3)
C19	P1	C1	103.7(3)	N2A	N1A	C1A	115.7(5)
C19	P1	C2	100.1(3)	C9A	N1A	N2A	120.5(5)
C24	P2	C25	102.5(3)	C9A	N1A	C1A	123.4(6)
C24	P2	C36	102.8(4)	N1A	N2A	C2A	112.1(5)
C36	P2	C25	91.0(3)	C12A	N2A	N1A	118.6(5)
N2	N1	C1	113.8(5)	C12A	N2A	C2A	121.0(6)

C9	N1	N2	121.5(5)	N4A	N3A	C25A	114.0(5)
C9	N1	C1	123.4(5)	C32A	N3A	N4A	121.6(6)
N1	N2	C2	113.3(5)	C32A	N3A	C25A	124.2(7)
C12	N2	N1	117.5(5)	N3A	N4A	C36A	113.1(5)
C12	N2	C2	120.7(5)	C35A	N4A	N3A	120.9(6)
N4	N3	C25	115.2(5)	C35A	N4A	C36A	125.4(7)
C32	N3	N4	122.5(5)	N1A	C1A	P1A	105.3(4)
C32	N3	C25	122.2(5)	N1A	C1A	C3A	110.5(5)
N3	N4	C36	111.8(5)	N1A	C1A	C3B	116.9(6)
C35	N4	N3	122.0(6)	C3A	C1A	P1A	109.0(5)
C35	N4	C36	126.1(6)	C3B	C1A	P1A	109.7(6)
N1	C1	P1	106.7(4)	N2A	C2A	P1A	107.0(5)
N1	C1	C3	113.8(5)	N2A	C2A	C13A	113.7(6)
C3	C1	P1	108.3(4)	C13A	C2A	P1A	110.2(4)
N2	C2	P1	106.2(4)	C4A	C3A	C1A	118.5(5)
N2	C2	C13	116.4(5)	C4A	C3A	C8A	120.0
C13	C2	P1	111.2(4)	C8A	C3A	C1A	120.7(5)
C4	C3	C1	119.0(4)	C5A	C4A	C3A	120.0
C4	C3	C8	120.0	C6A	C5A	C4A	120.0
C8	C3	C1	120.9(4)	C5A	C6A	C7A	120.0
C5	C4	C3	120.0	C6A	C7A	C8A	120.0
C4	C5	C6	120.0	C7A	C8A	C3A	120.0
C7	C6	C5	120.0	C4B	C3B	C1A	120.4(7)
C6	C7	C8	120.0	C4B	C3B	C8B	120.0
C7	C8	C3	120.0	C8B	C3B	C1A	119.4(7)

O1	C9	N1	120.5(6)	C3B	C4B	C5B	120.0
O1	C9	C10	126.6(6)	C6B	C5B	C4B	120.0
N1	C9	C10	112.8(6)	C5B	C6B	C7B	120.0
C9	C10	C11	110.9(6)	C8B	C7B	C6B	120.0
C12	C11	C10	111.9(5)	C7B	C8B	C3B	120.0
O2	C12	N2	119.7(6)	O1A	C9A	N1A	120.6(6)
O2	C12	C11	125.6(6)	O1A	C9A	C10A	124.4(6)
N2	C12	C11	114.7(6)	N1A	C9A	C10A	115.1(6)
C14	C13	C2	122.2(4)	C9A	C10A	C11A	109.4(6)
C14	C13	C18	120.0	C12A	C11A	C10A	111.3(6)
C18	C13	C2	117.5(4)	O2A	C12A	N2A	120.0(6)
C13	C14	C15	120.0	O2A	C12A	C11A	125.1(6)
C16	C15	C14	120.0	N2A	C12A	C11A	115.0(6)
C15	C16	C17	120.0	C14A	C13A	C2A	122.6(4)
C18	C17	C16	120.0	C14A	C13A	C18A	120.0
C17	C18	C13	120.0	C18A	C13A	C2A	116.9(4)
C20	C19	P1	125.0(6)	C13A	C14A	C15A	120.0
C20	C19	C24	118.2(7)	C16A	C15A	C14A	120.0
C24	C19	P1	116.8(6)	C17A	C16A	C15A	120.0
C21	C20	C19	120.8(7)	C16A	C17A	C18A	120.0
C22	C21	C20	119.9(8)	C17A	C18A	C13A	120.0
C21	C22	C23	121.0(8)	C20A	C19A	P1A	123.3(5)
C24	C23	C22	122.1(8)	C20A	C19A	C24A	120.0(6)
C19	C24	P2	114.6(6)	C24A	C19A	P1A	116.6(5)
C23	C24	P2	127.4(6)	C21A	C20A	C19A	120.2(7)

C23	C24	C19	117.9(7)	C20A	C21A	C22A	120.4(7)
N3	C25	P2	105.2(4)	C23A	C22A	C21A	119.8(6)
N3	C25	C26	111.3(5)	C22A	C23A	C24A	120.2(6)
C26	C25	P2	115.1(4)	C19A	C24A	P2A	117.6(5)
C27	C26	C25	118.4(4)	C19A	C24A	C23A	119.3(6)
C27	C26	C31	120.0	C23A	C24A	P2A	123.0(5)
C31	C26	C25	121.6(4)	N3A	C25A	P2A	107.3(5)
C28	C27	C26	120.0	N3A	C25A	C26A	112.6(5)
C29	C28	C27	120.0	C26A	C25A	P2A	114.4(4)
C28	C29	C30	120.0	C27A	C26A	C25A	119.2(4)
C31	C30	C29	120.0	C27A	C26A	C31A	120.0
C30	C31	C26	120.0	C31A	C26A	C25A	120.8(4)
O3	C32	N3	122.1(6)	C28A	C27A	C26A	120.0
O3	C32	C33	124.5(6)	C27A	C28A	C29A	120.0
N3	C32	C33	113.2(6)	C28A	C29A	C30A	120.0
C34	C33	C32	111.2(6)	C29A	C30A	C31A	120.0
C33	C34	C35	111.3(6)	C30A	C31A	C26A	120.0
O4	C35	N4	120.8(7)	O3A	C32A	N3A	120.0(7)
O4	C35	C34	125.8(7)	O3A	C32A	C33A	126.0(7)
N4	C35	C34	113.3(6)	N3A	C32A	C33A	113.9(8)
N4	C36	P2	106.2(4)	C34A	C33A	C32A	109.7(7)
N4	C36	C37	114.0(6)	C35A	C34A	C33A	108.4(7)
C37	C36	P2	109.0(5)	O4A	C35A	N4A	119.9(7)
C38	C37	C36	122.7(4)	O4A	C35A	C34A	126.0(7)
C38	C37	C42	120.0	N4A	C35A	C34A	114.1(8)

C42	C37	C36	117.1(4)	N4A	C36A	P2A	105.4(5)
C37	C38	C39	120.0	N4A	C36A	C37A	114.7(5)
C38	C39	C40	120.0	C37A	C36A	P2A	108.9(4)
C41	C40	C39	120.0	C38A	C37A	C36A	121.2(4)
C42	C41	C40	120.0	C38A	C37A	C42A	120.0
C41	C42	C37	120.0	C42A	C37A	C36A	118.7(4)
C1A	P1A	C2A	88.7(3)	C39A	C38A	C37A	120.0
C19A	P1A	C1A	104.3(3)	C40A	C39A	C38A	120.0
C19A	P1A	C2A	101.0(3)	C41A	C40A	C39A	120.0
C24A	P2A	C25A	101.2(3)	C40A	C41A	C42A	120.0
C24A	P2A	C36A	104.8(3)	C41A	C42A	C37A	120.0

Table C-6. Torsion Angles for TPSB BDP **1.**

A	**B**	**C**	**D**	**Angle/˚**	**A**	**B**	**C**	**D**	**Angle/˚**
P1	C1	C3	C4	-81.9(5)	P1A	C19A	C24A	C23A	-173.9(5)
P1	C1	C3	C8	94.2(4)	P2A	C25A	C26A	C27A	-95.5(4)
P1	C2	C13	C14	87.4(5)	P2A	C25A	C26A	C31A	83.7(5)
P1	C2	C13	C18	-87.2(4)	P2A	C36A	C37A	C38A	100.3(4)
P1	C19	C20	C21	175.2(5)	P2A	C36A	C37A	C42A	-76.9(5)
P1	C19	C24	P2	1.4(7)	O1A	C9A	C10A	C11A	138.2(7)
P1	C19	C24	C23	-175.6(5)	O3A	C32A	C33A	C34A	141.1(9)
P2	C25	C26	C27	-100.2(4)	N1A	N2A	C2A	P1A	22.3(7)
P2	C25	C26	C31	80.6(5)	N1A	N2A	C2A	C13A	144.1(5)
P2	C36	C37	C38	99.2(4)	N1A	N2A	C12A	O2A	161.3(6)
P2	C36	C37	C42	-75.5(5)	N1A	N2A	C12A	C11A	-20.3(9)

O1	C9	C10	C11	137.0(7)	N1A	C1A	C3A	C4A	-160.4(6)
O3	C32	C33	C34	140.3(8)	N1A	C1A	C3A	C8A	30.0(9)
N1	N2	C2	P1	25.1(6)	N1A	C1A	C3B	C4B	151.9(7)
N1	N2	C2	C13	149.5(5)	N1A	C1A	C3B	C8B	-33.0(11)
N1	N2	C12	O2	158.7(6)	N1A	C9A	C10A	C11A	-40.5(8)
N1	N2	C12	C11	-22.8(8)	N2A	N1A	C1A	P1A	-22.6(6)
N1	C1	C3	C4	159.6(5)	N2A	N1A	C1A	C3A	95.0(7)
N1	C1	C3	C8	-24.3(7)	N2A	N1A	C1A	C3B	99.5(8)
N1	C9	C10	C11	-40.2(7)	N2A	N1A	C9A	O1A	176.3(6)
N2	N1	C1	P1	-21.1(6)	N2A	N1A	C9A	C10A	-5.0(9)
N2	N1	C1	C3	98.3(6)	N2A	C2A	C13A	C14A	-31.6(7)
N2	N1	C9	O1	176.2(6)	N2A	C2A	C13A	C18A	156.1(4)
N2	N1	C9	C10	-6.5(8)	N3A	N4A	C35A	O4A	-179.9(7)
N2	C2	C13	C14	-34.4(7)	N3A	N4A	C35A	C34A	0.8(11)
N2	C2	C13	C18	151.1(4)	N3A	N4A	C36A	P2A	-34.7(7)
N3	N4	C35	O4	178.5(7)	N3A	N4A	C36A	C37A	85.1(7)
N3	N4	C35	C34	-5.8(11)	N3A	C25A	C26A	C27A	141.8(5)
N3	N4	C36	P2	-33.3(7)	N3A	C25A	C26A	C31A	-39.1(6)
N3	N4	C36	C37	86.7(7)	N3A	C32A	C33A	C34A	-34.2(10)
N3	C25	C26	C27	140.2(4)	N4A	N3A	C25A	P2A	-14.3(7)
N3	C25	C26	C31	-39.0(6)	N4A	N3A	C25A	C26A	112.3(6)
N3	C32	C33	C34	-35.2(9)	N4A	N3A	C32A	O3A	174.0(7)
N4	N3	C25	P2	-17.7(7)	N4A	N3A	C32A	C33A	-10.3(11)
N4	N3	C25	C26	107.6(6)	N4A	C36A	C37A	C38A	-17.5(7)
N4	N3	C32	O3	177.5(7)	N4A	C36A	C37A	C42A	165.3(5)

N4	N3	C32	C33	-6.8(10)	C1A	P1A	C2A	N2A	-29.5(5)
N4	C36	C37	C38	-19.2(7)	C1A	P1A	C2A	C13A	-153.5(5)
N4	C36	C37	C42	166.1(5)	C1A	P1A	C19A	C20A	21.4(6)
C1	P1	C2	N2	-30.9(5)	C1A	P1A	C19A	C24A	-162.7(5)
C1	P1	C2	C13	-158.4(5)	C1A	N1A	N2A	C2A	0.3(8)
C1	P1	C19	C20	17.8(7)	C1A	N1A	N2A	C12A	-148.3(6)
C1	P1	C19	C24	-164.7(5)	C1A	N1A	C9A	O1A	4.2(10)
C1	N1	N2	C2	-3.0(7)	C1A	N1A	C9A	C10A	-177.0(6)
C1	N1	N2	C12	-151.1(6)	C1A	C3A	C4A	C5A	-169.7(9)
C1	N1	C9	O1	10.0(10)	C1A	C3A	C8A	C7A	169.5(9)
C1	N1	C9	C10	-172.6(6)	C1A	C3B	C4B	C5B	175.0(11)
C1	C3	C4	C5	176.2(5)	C1A	C3B	C8B	C7B	-175.1(11)
C1	C3	C8	C7	-176.1(5)	C2A	P1A	C1A	N1A	28.9(5)
C2	P1	C1	N1	29.2(5)	C2A	P1A	C1A	C3A	-89.6(5)
C2	P1	C1	C3	-93.6(4)	C2A	P1A	C1A	C3B	-97.7(6)
C2	P1	C19	C20	-72.7(6)	C2A	P1A	C19A	C20A	-70.1(6)
C2	P1	C19	C24	104.8(5)	C2A	P1A	C19A	C24A	105.8(5)
C2	N2	C12	O2	13.0(10)	C2A	N2A	C12A	O2A	15.6(10)
C2	N2	C12	C11	-168.6(6)	C2A	N2A	C12A	C11A	-166.0(6)
C2	C13	C14	C15	-174.4(5)	C2A	C13A	C14A	C15A	-172.0(5)
C2	C13	C18	C17	174.7(4)	C2A	C13A	C18A	C17A	172.5(5)
C3	C4	C5	C6	0.0	C3A	C4A	C5A	C6A	0.0
C4	C3	C8	C7	0.0	C4A	C3A	C8A	C7A	0.0
C4	C5	C6	C7	0.0	C4A	C5A	C6A	C7A	0.0
C5	C6	C7	C8	0.0	C5A	C6A	C7A	C8A	0.0

C6	C7	C8	C3	0.0	C6A	C7A	C8A	C3A	0.0
C8	C3	C4	C5	0.0	C8A	C3A	C4A	C5A	0.0
C9	N1	N2	C2	-170.3(6)	C3B	C4B	C5B	C6B	0.0
C9	N1	N2	C12	41.5(8)	C4B	C3B	C8B	C7B	0.0
C9	N1	C1	P1	146.0(5)	C4B	C5B	C6B	C7B	0.0
C9	N1	C1	C3	-94.6(8)	C5B	C6B	C7B	C8B	0.0
C9	C10	C11	C12	55.8(8)	C6B	C7B	C8B	C3B	0.0
C10	C11	C12	O2	154.9(7)	C8B	C3B	C4B	C5B	0.0
C10	C11	C12	N2	-23.4(8)	C9A	N1A	N2A	C2A	-172.3(6)
C12	N2	C2	P1	172.2(5)	C9A	N1A	N2A	C12A	39.1(9)
C12	N2	C2	C13	-63.4(8)	C9A	N1A	C1A	P1A	149.8(6)
C13	C14	C15	C16	0.0	C9A	N1A	C1A	C3A	-92.6(8)
C14	C13	C18	C17	0.0	C9A	N1A	C1A	C3B	-88.1(9)
C14	C15	C16	C17	0.0	C9A	C10A	C11A	C12A	55.9(8)
C15	C16	C17	C18	0.0	C10A	C11A	C12A	O2A	152.7(7)
C16	C17	C18	C13	0.0	C10A	C11A	C12A	N2A	-25.7(9)
C18	C13	C14	C15	0.0	C12A	N2A	C2A	P1A	170.0(5)
C19	P1	C1	N1	-70.7(5)	C12A	N2A	C2A	C13A	-68.1(8)
C19	P1	C1	C3	166.5(4)	C13A	C14A	C15A	C16A	0.0
C19	P1	C2	N2	72.7(5)	C14A	C13A	C18A	C17A	0.0
C19	P1	C2	C13	-54.8(5)	C14A	C15A	C16A	C17A	0.0
C19	C20	C21	C22	1.9(11)	C15A	C16A	C17A	C18A	0.0
C20	C19	C24	P2	179.1(5)	C16A	C17A	C18A	C13A	0.0
C20	C19	C24	C23	2.1(10)	C18A	C13A	C14A	C15A	0.0
C20	C21	C22	C23	-1.3(13)	C19A	P1A	C1A	N1A	-72.1(5)

C21	C22	C23	C24	1.3(13)	C19A	P1A	C1A	C3A	169.3(5)
C22	C23	C24	P2	-178.2(6)	C19A	P1A	C1A	C3B	161.3(5)
C22	C23	C24	C19	-1.6(12)	C19A	P1A	C2A	N2A	74.8(5)
C24	P2	C36	N4	-83.8(6)	C19A	P1A	C2A	C13A	-49.2(5)
C24	P2	C36	C37	152.9(4)	C19A	C20A	C21A	C22A	2.4(10)
C24	C19	C20	C21	-2.2(10)	C20A	C19A	C24A	P2A	178.0(5)
C25	P2	C24	C19	87.7(5)	C20A	C19A	C24A	C23A	2.1(10)
C25	P2	C24	C23	-95.6(7)	C20A	C21A	C22A	C23A	1.1(10)
C25	P2	C36	N4	19.2(6)	C21A	C22A	C23A	C24A	-3.0(10)
C25	P2	C36	C37	-104.0(5)	C22A	C23A	C24A	P2A	-174.3(5)
C25	N3	N4	C35	-146.1(7)	C22A	C23A	C24A	C19A	1.4(10)
C25	N3	N4	C36	35.0(8)	C24A	P2A	C36A	N4A	-80.2(5)
C25	N3	C32	O3	-6.5(11)	C24A	P2A	C36A	C37A	156.2(4)
C25	N3	C32	C33	169.2(6)	C24A	C19A	C20A	C21A	-4.0(10)
C25	C26	C27	C28	-179.2(4)	C25A	P2A	C24A	C19A	90.5(5)
C25	C26	C31	C30	179.2(5)	C25A	P2A	C24A	C23A	-93.8(6)
C26	C27	C28	C29	0.0	C25A	P2A	C36A	N4A	21.3(5)
C27	C26	C31	C30	0.0	C25A	P2A	C36A	C37A	-102.3(5)
C27	C28	C29	C30	0.0	C25A	N3A	N4A	C35A	-155.1(7)
C28	C29	C30	C31	0.0	C25A	N3A	N4A	C36A	33.6(8)
C29	C30	C31	C26	0.0	C25A	N3A	C32A	O3A	-0.6(12)
C31	C26	C27	C28	0.0	C25A	N3A	C32A	C33A	175.1(7)
C32	N3	N4	C35	30.1(11)	C25A	C26A	C27A	C28A	179.2(5)
C32	N3	N4	C36	-148.7(7)	C25A	C26A	C31A	C30A	-179.2(5)
C32	N3	C25	P2	166.0(6)	C26A	C27A	C28A	C29A	0.0

C32	N3	C25	C26	-68.6(8)	C27A	C26A	C31A	C30A	0.0
C32	C33	C34	C35	57.0(8)	C27A	C28A	C29A	C30A	0.0
C33	C34	C35	O4	139.3(9)	C28A	C29A	C30A	C31A	0.0
C33	C34	C35	N4	-36.2(10)	C29A	C30A	C31A	C26A	0.0
C35	N4	C36	P2	147.9(7)	C31A	C26A	C27A	C28A	0.0
C35	N4	C36	C37	-92.1(9)	C32A	N3A	N4A	C35A	29.7(11)
C36	P2	C24	C19	-178.3(5)	C32A	N3A	N4A	C36A	-141.6(7)
C36	P2	C24	C23	-1.6(7)	C32A	N3A	C25A	P2A	160.7(6)
C36	N4	C35	O4	-2.8(13)	C32A	N3A	C25A	C26A	-72.6(9)
C36	N4	C35	C34	172.8(7)	C32A	C33A	C34A	C35A	61.1(9)
C36	C37	C38	C39	-174.6(5)	C33A	C34A	C35A	O4A	136.2(9)
C36	C37	C42	C41	174.8(5)	C33A	C34A	C35A	N4A	-44.5(10)
C37	C38	C39	C40	0.0	C35A	N4A	C36A	P2A	154.5(7)
C38	C37	C42	C41	0.0	C35A	N4A	C36A	C37A	-85.7(9)
C38	C39	C40	C41	0.0	C36A	P2A	C24A	C19A	-177.0(5)
C39	C40	C41	C42	0.0	C36A	P2A	C24A	C23A	-1.2(6)
C40	C41	C42	C37	0.0	C36A	N4A	C35A	O4A	-9.7(13)
C42	C37	C38	C39	0.0	C36A	N4A	C35A	C34A	171.0(7)
P1A	C1A	C3A	C4A	-45.2(7)	C36A	C37A	C38A	C39A	-177.1(5)
P1A	C1A	C3A	C8A	145.2(5)	C36A	C37A	C42A	C41A	177.2(5)
P1A	C1A	C3B	C4B	-88.3(8)	C37A	C38A	C39A	C40A	0.0
P1A	C1A	C3B	C8B	86.7(8)	C38A	C37A	C42A	C41A	0.0
P1A	C2A	C13A	C14A	88.4(5)	C38A	C39A	C40A	C41A	0.0
P1A	C2A	C13A	C18A	-83.8(5)	C39A	C40A	C41A	C42A	0.0
P1A	C19A	C20A	C21A	171.7(5)	C40A	C41A	C42A	C37A	0.0

P1A	C19A	C24A	P2A	2.0(7)	C42A	C37A	C38A	C39A	0.0

Table C-7. Hydrogen Atom Coordinates (Å×10^4) and Isotropic Displacement Parameters (Å^2×10^3) for TPSB BDP **1.**

Atom	***x***	***y***	***z***	**U(eq)**
H1	5172.58	40.1	5848.94	32
H2	4329.42	2064.03	5074.74	31
H4	5728.73	1276.67	6339.7	52
H5	5739.42	2627.43	6924.53	51
H6	4921.88	3587.38	7063.27	69
H7	4093.65	3196.58	6617.16	76
H8	4082.96	1845.83	6032.32	61
H10C	3404.26	-1468.74	5835.25	36
H10D	3687.92	-1403.07	5279.2	36
H11C	2886.8	-358.22	5290.84	36
H11D	3115.82	233.71	5784.98	36
H14	4267.81	17.73	4166.33	41
H15	4285.78	233.5	3276.87	50
H16	4432.52	1853.41	2927.12	61
H17	4561.29	3257.56	3466.83	54
H18	4543.31	3041.81	4356.3	41
H20	4921.92	-1075.06	5109	41
H21	5100.76	-2390.24	4530.6	49
H22	5672.65	-2111.1	3834.24	64

H23	6040.6	-520.35	3670.29	53
H25	6673.72	2199.56	4777.73	33
H27	6447.46	1628.77	5595.81	36
H28	6509.55	393.26	6239.45	45
H29	6782.35	-1270.88	6034.47	46
H30	6993.06	-1699.53	5185.86	46
H31	6930.97	-464.03	4542.22	41
H33C	8112.07	1871.84	3696.49	47
H33D	8445.16	1199.13	4109.52	47
H34C	7873.67	-203.55	3933.98	54
H34D	8154.99	189.43	3412.37	54
H36	6219.61	925.65	3357.03	44
H38	7175.71	2964.58	3549.79	58
H39	7097.91	4601.31	3201.59	66
H40	6270.05	5088.59	2779.56	62
H41	5519.99	3939.13	2705.73	60
H42	5597.78	2302.39	3053.93	57
H1A	7245.29	4963.65	4316.79	34
H1AA	7249.68	4935.95	4343.44	34
H2A	8140.95	6955.78	5101.45	37
H4A	6866.64	7085.61	4217.84	48
H5A	6880.28	8198.53	3517.81	55
H6A	7609.9	8100.08	2916.31	38
H7A	8325.89	6888.72	3014.83	48
H8A	8312.26	5775.79	3714.85	43

H4B	6711.74	5996.38	3755.19	47
H5B	6685.8	7293.06	3140.58	47
H6B	7468.81	8354.03	3025.56	39
H7B	8277.76	8118.31	3525.14	54
H8B	8303.7	6821.64	4139.76	42
H10A	9000.67	3380.14	4289.72	40
H10B	8752.17	3437.48	4860.51	40
H11A	9558.69	4507.62	4813.35	42
H11B	9296.74	5103.76	4333.77	42
H14A	8201.24	4814.71	5963.32	42
H15A	8147	4911.95	6856.82	49
H16A	7965.56	6475.99	7254.18	52
H17A	7838.35	7942.78	6758.04	56
H18A	7892.58	7845.56	5864.53	43
H20A	7480.69	3869.26	5084.66	39
H21A	7306.67	2609.13	5692.07	36
H22A	6745.8	2961.03	6408.24	36
H23A	6336.71	4569.69	6501.58	36
H25A	5741.89	7213.41	5400.64	33
H27A	6008.31	6679.9	4576.63	46
H28A	5988.78	5456.39	3925.03	70
H29A	5725.1	3778.78	4111.23	73
H30A	5480.95	3324.66	4949.03	48
H31A	5500.48	4548.15	5600.64	35
H33A	4354.61	6998.88	6505.81	65

H33B	3984.89	6328.83	6116.98	65
H34A	4290.21	5287.18	6802.64	69
H34B	4574.78	4893.79	6280.83	69
H36A	6224.54	6056.66	6815.18	37
H38A	5246.08	7999.6	6553.88	35
H39A	5271.19	9665.48	6872.31	44
H40A	6075.67	10258.33	7297.45	45
H41A	6855.06	9185.3	7404.18	42
H42A	6829.96	7519.41	7085.76	37

Table C-8. Atomic Occupancy for TPSB BDP **1.**

Atom	**Occupancy**	**Atom**	**Occupancy**	**Atom**	**Occupancy**
H1A	0.574(12)	H1AA	0.426(12)	C3A	0.574(12)
C4A	0.574(12)	H4A	0.574(12)	C5A	0.574(12)
H5A	0.574(12)	C6A	0.574(12)	H6A	0.574(12)
C7A	0.574(12)	H7A	0.574(12)	C8A	0.574(12)
H8A	0.574(12)	C3B	0.426(12)	C4B	0.426(12)
H4B	0.426(12)	C5B	0.426(12)	H5B	0.426(12)
C6B	0.426(12)	H6B	0.426(12)	C7B	0.426(12)
H7B	0.426(12)	C8B	0.426(12)	H8B	0.426(12)

C.2 Crystallographic Data for red-TPSB BDP 2

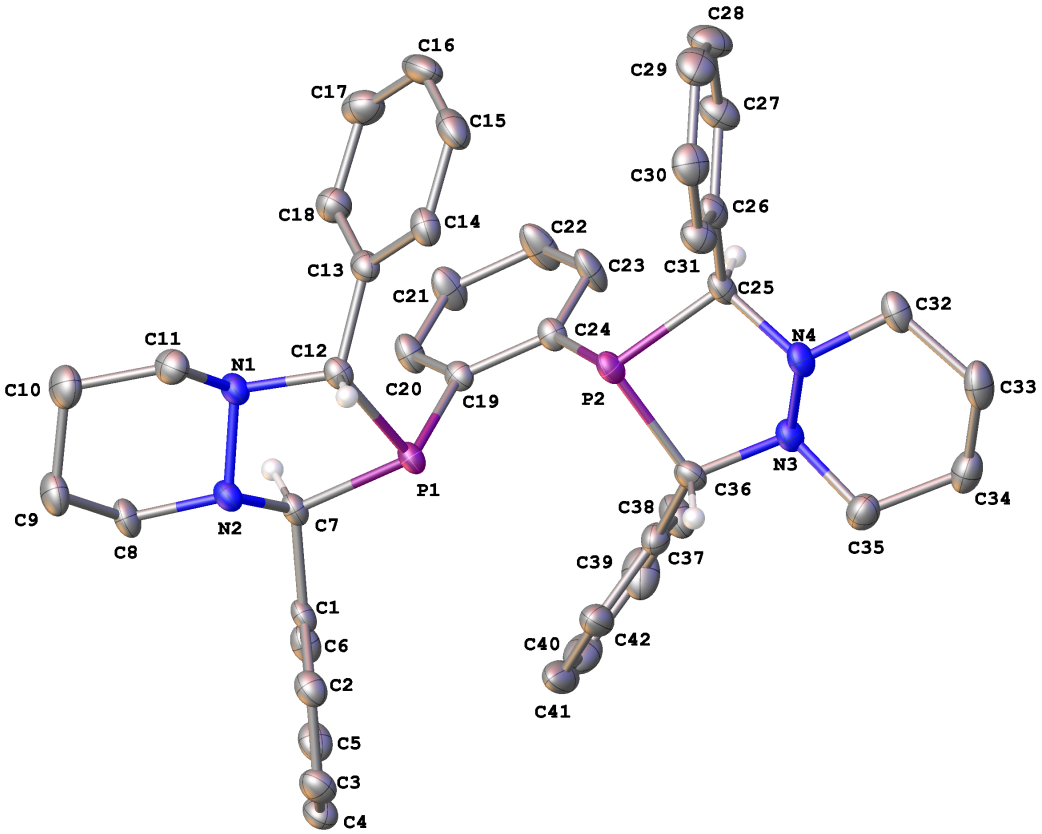

Figure C-3. A molecular drawing red-TPSB BDP 2. All atoms are drawn as 50% thermal probability ellipsoids. All H atoms except those on chiral carbons are omitted for clarity.

C.2.1 Data Collection

A colorless crystal with approximate dimensions 0.096 x 0.080 x 0.051 mm^3 was selected under oil under ambient conditions and attached to the tip of a MiTeGen MicroMount©. The crystal was mounted in a stream of cold nitrogen at 100(1) K and centered in the X-ray beam by using a video camera.

The crystal evaluation and data collection were performed on a Bruker Quazar SMART APEXII diffractometer with Mo K_α (λ = 0.71073 Å) radiation and the diffractometer to crystal distance of 4.96 cm.

The initial cell constants were obtained from three series of ω scans at different starting angles. Each series consisted of 12 frames collected at intervals of 0.5º in a 6º range about ω with the exposure time of 20 seconds per frame. The reflections were successfully indexed by an automated indexing routine built in the APEXII program suite. The final cell constants were calculated from a set of 3193 strong reflections from the actual data collection.

The data were collected by using the full sphere data collection routine to survey the reciprocal space to the extent of a full sphere to a resolution of 0.70 Å. A total of 22928 data were harvested by collecting 4 sets of frames with 0.5º scans in ω and φ with exposure times of 40 sec per frame. These highly redundant datasets were corrected for Lorentz and polarization effects. The absorption correction was based on fitting a function to the empirical transmission surface as sampled by multiple equivalent measurements.[10]

C.2.2 Structure Solution and Refinement

The systematic absences in the diffraction data were consistent for the space groups *P*1 and $P\bar{1}$. The *E*-statistics strongly suggested the centrosymmetric space group $P\bar{1}$ that yielded chemically reasonable and computationally stable results of refinement.[7,8,11]

A successful solution by the direct methods provided most non-hydrogen atoms from the *E*-map. The remaining non-hydrogen atoms were located in an alternating series of least-squares cycles and difference Fourier maps. All non-hydrogen atoms were refined with anisotropic displacement coefficients. All hydrogen atoms were included in the structure factor calculation at idealized positions and were allowed to ride on the neighboring atoms with relative isotropic displacement coefficients.

The structure contains stereocenters at carbons C7, C12, C25, and C36. The relative configuration of these stereocenters is *S*, *S*, *S*, *S*. Since this is a centrosymmetric spacegroup, the crystals are racemic.

The final least-squares refinement of 433 parameters against 7224 data resulted in residuals *R* (based on F^2 for $I \geq 2\sigma$) and *wR* (based on F^2 for all data) of 0.0492 and 0.1256, respectively. The final difference Fourier map was featureless.

C.2.3 Summary

Crystal Data for $C_{42}H_{44}N_4P_2$ (M =666.75 g/mol): triclinic, space group $P\bar{1}$ (no. 2), a = 10.340(3) Å, b = 11.392(4) Å, c = 15.662(5) Å, α = 75.80(2)°, β = 82.291(19)°, γ = 86.231(16)°, V = 1771.5(11) Å3, Z = 2, T = 100.0 K, μ(MoKα) = 0.159 mm-1, Dcalc = 1.250 g/cm3, 22997 reflections measured (2.702° ≤ 2Θ ≤ 52.812°), 7245 unique (R_{int} = 0.0580, R_{sigma} = 0.0674) which were used in all calculations. The final R1 was 0.0492 (I > 2σ(I)) and wR2 was 0.1256 (all data).

Table C-9. Crystal Data and Structure Refinement for red-TPSB BDP **2.**

Empirical formula	$C_{42}H_{44}N_4P_2$
Formula weight	666.75
Temperature/K	100.0
Crystal system	triclinic
Space group	$P\bar{1}$
a/Å	10.340(3)
b/Å	11.392(4)
c/Å	15.662(5)
α/°	75.80(2)
β/°	82.291(19)
γ/°	86.231(16)
Volume/Å^3	1771.5(11)
Z	2
ϱ_{calc}g/cm^3	1.250
μ/mm^{-1}	0.159
F(000)	708.0
Crystal size/mm^3	0.096 × 0.08 × 0.051
Radiation	MoKα (λ = 0.71073)
2Θ range for data collection/°	2.702 to 52.812
Index ranges	$-12 \le h \le 12, -14 \le k \le 14, -19 \le l \le 19$
Reflections collected	22928
Independent reflections	7224 [$R_{int} = 0.0578$, $R_{sigma} = 0.0669$]

Data/restraints/parameters	7224/0/433
Goodness-of-fit on F^2	1.017
Final R indexes [I>=2σ (I)]	$R_1 = 0.0492$, $wR_2 = 0.1099$
Final R indexes [all data]	$R_1 = 0.0826$, $wR_2 = 0.1256$
Largest diff. peak/hole / e $Å^{-3}$	0.82/-0.33

Table C-10. Fractional Atomic Coordinates ($\times 10^4$) and Equivalent Isotropic Displacement Parameters ($Å^2 \times 10^3$) for red-TPSB BDP **2**. U_{eq} is defined as 1/3 of of the trace of the orthogonalised U_{IJ} tensor.

Atom	*x*	*y*	*z*	U(eq)
P(1)	792.5(6)	6825.0(6)	3365.8(4)	17.57(15)
P(2)	-1519.1(6)	7670.9(6)	2348.2(4)	18.43(16)
N(1)	1901.8(19)	4590.0(17)	3759.9(12)	19.8(4)
N(2)	2246.4(18)	5291.1(17)	4375.2(12)	19.2(4)
N(3)	-2711.9(18)	9877.0(17)	1972.5(12)	19.9(4)
N(4)	-3602.4(18)	8979.5(18)	1854.9(12)	20.5(4)
C(1)	2686(2)	7415(2)	4317.2(14)	17.7(5)
C(2)	2015(2)	7379(2)	5157.0(15)	23.3(5)
C(3)	2267(2)	8182(2)	5639.5(16)	26.7(6)
C(4)	3182(2)	9061(2)	5278.1(16)	26.2(6)
C(5)	3836(2)	9122(2)	4444.3(16)	25.9(6)
C(6)	3602(2)	8297(2)	3971.7(15)	22.7(5)
C(7)	2409(2)	6526(2)	3801.4(14)	18.2(5)
C(8)	3501(2)	4805(2)	4677.6(16)	24.1(6)
C(9)	3404(3)	3487(2)	5185.2(17)	28.4(6)
C(10)	2947(3)	2756(2)	4601.6(17)	31.0(6)
C(11)	1692(2)	3335(2)	4265.6(16)	24.5(6)
C(12)	650(2)	5155(2)	3478.3(14)	18.1(5)
C(13)	329(2)	4772(2)	2678.6(15)	19.9(5)

C(14)	-953(2)	4519(2)	2621.0(16)	24.4(6)
C(15)	-1274(3)	4201(2)	1876.9(17)	32.5(6)
C(16)	-331(3)	4148(2)	1181.5(17)	34.8(7)
C(17)	943(3)	4408(2)	1225.5(17)	32.6(6)
C(18)	1278(3)	4705(2)	1973.0(16)	26.5(6)
C(19)	1176(2)	7439(2)	2159.6(14)	17.0(5)
C(20)	2421(2)	7527(2)	1703.1(15)	23.9(6)
C(21)	2628(2)	7963(2)	791.0(16)	28.4(6)
C(22)	1581(2)	8347(3)	321.7(16)	33.2(7)
C(23)	328(2)	8290(2)	770.6(15)	28.2(6)
C(24)	100(2)	7847(2)	1682.2(14)	18.7(5)
C(25)	-2715(2)	8079(2)	1515.2(15)	19.7(5)
C(26)	-3431(2)	6999(2)	1460.3(15)	21.4(5)
C(27)	-3341(2)	6653(2)	664.6(16)	28.5(6)
C(28)	-3982(3)	5650(3)	609.1(18)	35.1(7)
C(29)	-4725(3)	4994(3)	1336.6(18)	33.3(6)
C(30)	-4829(2)	5324(2)	2135.5(17)	29.1(6)
C(31)	-4181(2)	6317(2)	2197.1(16)	25.0(6)
C(32)	-4413(2)	9594(2)	1164.0(16)	25.4(6)
C(33)	-5274(2)	10583(2)	1466.0(17)	31.4(6)
C(34)	-4442(3)	11473(2)	1705.0(17)	30.3(6)
C(35)	-3519(2)	10782(2)	2346.7(16)	26.1(6)
C(36)	-1891(2)	9172(2)	2639.2(14)	20.4(5)
C(37)	-726(2)	9853(2)	2713.7(16)	21.4(5)

C(38)	-43(3)	10594(2)	1978.8(18)	31.5(6)
C(39)	1053(3)	11168(2)	2063(2)	37.8(7)
C(40)	1481(3)	11008(3)	2878(2)	39.0(7)
C(41)	817(3)	10275(3)	3616.1(19)	35.1(7)
C(42)	-282(2)	9698(2)	3538.0(17)	27.7(6)

Table C-11. Anisotropic Displacement Parameters ($Å^2 \times 10^3$) for red-TPSB BDP **2.** The Anisotropic displacement factor exponent takes the form: $-2\pi^2[h^2a^{*2}U_{11}+2hka^*b^*U_{12}+\ldots]$.

Atom	U_{11}	U_{22}	U_{33}	U_{23}	U_{13}	U_{12}
P(1)	15.2(3)	20.4(3)	16.4(3)	-0.7(2)	-5.6(2)	-2.3(2)
P(2)	12.9(3)	24.5(4)	17.5(3)	-2.8(2)	-4.0(2)	-2.2(2)
N(1)	20.3(11)	19.5(11)	20.1(10)	-2.8(8)	-7.3(8)	-0.8(8)
N(2)	19.9(10)	19.2(11)	18.9(10)	-2.5(8)	-7.3(8)	-1.3(8)
N(3)	15.9(10)	22.5(11)	21.5(10)	-4.3(8)	-5.3(8)	0.6(8)
N(4)	13.9(10)	24.5(11)	22.8(10)	-3.6(8)	-5.8(8)	0.3(8)
C(1)	14.4(11)	20.1(13)	18.5(11)	-1.4(9)	-7.8(9)	-0.5(9)
C(2)	22.2(13)	23.4(13)	23.9(12)	-1.7(10)	-7(1)	-3.7(10)
C(3)	27.4(14)	32.8(15)	20.1(12)	-5.6(11)	-4.9(11)	-1.5(12)
C(4)	27.2(14)	25.6(14)	29.6(14)	-8.9(11)	-11.6(11)	-2.5(11)
C(5)	19.5(13)	24.3(14)	34.1(14)	-3.8(11)	-7.7(11)	-5.2(10)
C(6)	17.8(12)	26.9(14)	21.4(12)	-0.6(10)	-4.2(10)	-1.1(10)
C(7)	15.8(12)	21.6(13)	16.2(11)	-1.0(9)	-5.1(9)	-0.5(10)
C(8)	17.6(12)	28.3(14)	25.7(13)	-1.8(11)	-9.4(10)	1.7(10)

C(9)	25.9(14)	24.4(14)	31.7(14)	2.3(11)	-10.6(11)	2.2(11)
C(10)	33.5(15)	23.1(14)	33.1(14)	1.0(11)	-8.1(12)	3.0(12)
C(11)	28.8(14)	18.9(13)	25.0(12)	-2.5(10)	-4.9(11)	-2.2(11)
C(12)	15.3(12)	20.7(13)	16.9(11)	-1.1(9)	-2.5(9)	-3(1)
C(13)	21.5(13)	16.8(12)	21.7(12)	-3(1)	-6.6(10)	-1(1)
C(14)	21.6(13)	22.9(14)	27.2(13)	-0.8(10)	-7.9(11)	-0.8(10)
C(15)	32.0(15)	29.6(15)	38.1(15)	-4.0(12)	-19.6(13)	-2.0(12)
C(16)	52.6(19)	31.8(16)	25.5(14)	-10.8(12)	-18.9(13)	2.1(14)
C(17)	42.6(17)	31.9(16)	23.5(13)	-8.8(11)	-1.3(12)	-0.5(13)
C(18)	26.3(14)	27.9(15)	25.7(13)	-7.0(11)	-4.0(11)	0.4(11)
C(19)	18.4(12)	14.9(12)	17.2(11)	-1.3(9)	-4.0(9)	-2.5(9)
C(20)	16.7(12)	29.8(14)	23.4(12)	-0.1(10)	-7.1(10)	-1.8(10)
C(21)	14.6(12)	43.4(17)	23.3(13)	-0.4(11)	-1.2(10)	-3.2(11)
C(22)	21.1(14)	56.7(19)	16.0(12)	3.3(12)	-1.9(10)	-5.3(13)
C(23)	15.7(12)	45.5(17)	19.8(12)	1.6(11)	-7.4(10)	-1.4(11)
C(24)	16.7(12)	18.9(13)	19.4(11)	-1.1(9)	-4.1(10)	-2.8(10)
C(25)	13.9(12)	28.4(14)	16.7(11)	-3.7(10)	-4.3(9)	-1.1(10)
C(26)	12.3(11)	27.4(14)	25.2(12)	-5.8(10)	-6.4(10)	0.6(10)
C(27)	24.6(14)	37.8(16)	24.9(13)	-8.4(11)	-5.2(11)	-6.6(12)
C(28)	33.2(16)	46.4(18)	33.3(15)	-19.8(13)	-10.4(13)	-4.3(13)
C(29)	27.9(15)	34.4(16)	42.4(16)	-13.5(13)	-12.0(13)	-4.4(12)
C(30)	19.5(13)	32.4(16)	34.0(14)	-5.2(12)	-1.8(11)	-3.8(11)
C(31)	19.5(13)	31.4(15)	25.4(13)	-8.2(11)	-3.5(10)	-3.7(11)
C(32)	18.0(12)	30.5(15)	24.9(13)	0.8(11)	-6.5(10)	-1.6(11)

C(33)	17.9(13)	37.7(16)	32.8(14)	1.6(12)	-3.7(11)	4.5(11)
C(34)	27.5(14)	26.6(15)	33.7(14)	-4.5(12)	-1.4(12)	7.0(12)
C(35)	25.4(14)	26.4(14)	25.9(13)	-6.9(11)	-1.5(11)	2.4(11)
C(36)	19.9(12)	26.9(14)	14.7(11)	-4.8(10)	-3.5(10)	-1(1)
C(37)	18.0(12)	20.3(13)	27.5(13)	-8.1(10)	-6(1)	2.2(10)
C(38)	29.2(15)	29.1(15)	35.0(15)	0.9(12)	-13.2(12)	-5.6(12)
C(39)	27.6(15)	26.6(16)	56.0(19)	-0.9(13)	-8.3(14)	-4.8(12)
C(40)	26.5(15)	33.4(17)	68(2)	-27.1(15)	-17.2(15)	1.7(13)
C(41)	24.3(14)	47.5(18)	44.5(17)	-28.1(15)	-15.4(13)	8.3(13)
C(42)	24.2(14)	34.9(16)	28.3(13)	-15.0(12)	-7.6(11)	5.7(12)

Table C-12. Bond Lengths for red-TPSB BDP **2.**

Atom	**Atom**	**Length/Å**	**Atom**	**Atom**	**Length/Å**
P(1)	C(7)	1.869(2)	C(13)	C(18)	1.389(3)
P(1)	C(12)	1.881(3)	C(14)	C(15)	1.388(3)
P(1)	C(19)	1.845(2)	C(15)	C(16)	1.371(4)
P(2)	C(24)	1.845(2)	C(16)	C(17)	1.383(4)
P(2)	C(25)	1.873(2)	C(17)	C(18)	1.387(3)
P(2)	C(36)	1.879(3)	C(19)	C(20)	1.383(3)
N(1)	N(2)	1.484(3)	C(19)	C(24)	1.413(3)
N(1)	C(11)	1.469(3)	C(20)	C(21)	1.385(3)
N(1)	C(12)	1.479(3)	C(21)	C(22)	1.377(3)
N(2)	C(7)	1.478(3)	C(22)	C(23)	1.387(3)

N(2)	C(8)	1.468(3)	C(23)	C(24)	1.386(3)
N(3)	N(4)	1.479(3)	C(25)	C(26)	1.502(3)
N(3)	C(35)	1.468(3)	C(26)	C(27)	1.387(3)
N(3)	C(36)	1.481(3)	C(26)	C(31)	1.392(3)
N(4)	C(25)	1.480(3)	C(27)	C(28)	1.384(4)
N(4)	C(32)	1.469(3)	C(28)	C(29)	1.368(4)
C(1)	C(2)	1.395(3)	C(29)	C(30)	1.381(4)
C(1)	C(6)	1.386(3)	C(30)	C(31)	1.381(4)
C(1)	C(7)	1.505(3)	C(32)	C(33)	1.518(4)
C(2)	C(3)	1.378(3)	C(33)	C(34)	1.515(4)
C(3)	C(4)	1.386(4)	C(34)	C(35)	1.520(3)
C(4)	C(5)	1.376(4)	C(36)	C(37)	1.508(3)
C(5)	C(6)	1.381(3)	C(37)	C(38)	1.386(3)
C(8)	C(9)	1.519(3)	C(37)	C(42)	1.395(3)
C(9)	C(10)	1.515(4)	C(38)	C(39)	1.382(4)
C(10)	C(11)	1.516(3)	C(39)	C(40)	1.374(4)
C(12)	C(13)	1.506(3)	C(40)	C(41)	1.376(4)
C(13)	C(14)	1.393(3)	C(41)	C(42)	1.383(4)

Table C-13. Bond Angles for red-TPSB BDP **2.**

Atom	**Atom**	**Atom**	**Angle/°**	**Atom**	**Atom**	**Atom**	**Angle/°**
C(7)	P(1)	C(12)	89.83(10)	C(16)	C(15)	C(14)	120.2(3)
C(19)	P(1)	C(7)	105.28(10)	C(15)	C(16)	C(17)	119.8(2)

C(19)	P(1)	C(12)	103.67(10)	C(16)	C(17)	C(18)	120.5(3)
C(24)	P(2)	C(25)	104.83(10)	C(17)	C(18)	C(13)	120.3(2)
C(24)	P(2)	C(36)	104.24(11)	C(20)	C(19)	P(1)	124.91(17)
C(25)	P(2)	C(36)	89.65(10)	C(20)	C(19)	C(24)	118.8(2)
C(11)	N(1)	N(2)	108.01(17)	C(24)	C(19)	P(1)	116.32(17)
C(11)	N(1)	C(12)	109.37(18)	C(19)	C(20)	C(21)	121.5(2)
C(12)	N(1)	N(2)	104.46(17)	C(22)	C(21)	C(20)	119.9(2)
C(7)	N(2)	N(1)	103.01(16)	C(21)	C(22)	C(23)	119.4(2)
C(8)	N(2)	N(1)	108.28(18)	C(24)	C(23)	C(22)	121.5(2)
C(8)	N(2)	C(7)	109.77(17)	C(19)	C(24)	P(2)	115.46(16)
N(4)	N(3)	C(36)	104.17(17)	C(23)	C(24)	P(2)	125.64(17)
C(35)	N(3)	N(4)	107.30(18)	C(23)	C(24)	C(19)	118.8(2)
C(35)	N(3)	C(36)	109.46(18)	N(4)	C(25)	P(2)	102.72(14)
N(3)	N(4)	C(25)	103.89(17)	N(4)	C(25)	C(26)	111.87(19)
C(32)	N(4)	N(3)	107.76(18)	C(26)	C(25)	P(2)	112.17(16)
C(32)	N(4)	C(25)	108.93(18)	C(27)	C(26)	C(25)	120.0(2)
C(2)	C(1)	C(7)	120.6(2)	C(27)	C(26)	C(31)	118.4(2)
C(6)	C(1)	C(2)	118.1(2)	C(31)	C(26)	C(25)	121.6(2)
C(6)	C(1)	C(7)	121.2(2)	C(28)	C(27)	C(26)	120.5(2)
C(3)	C(2)	C(1)	121.2(2)	C(29)	C(28)	C(27)	120.4(3)
C(2)	C(3)	C(4)	119.6(2)	C(28)	C(29)	C(30)	120.0(3)
C(5)	C(4)	C(3)	119.9(2)	C(29)	C(30)	C(31)	119.9(3)
C(4)	C(5)	C(6)	120.3(2)	C(30)	C(31)	C(26)	120.8(2)
C(5)	C(6)	C(1)	120.8(2)	N(4)	C(32)	C(33)	110.5(2)

N(2)	C(7)	P(1)	101.21(14)	C(34)	C(33)	C(32)	110.0(2)
N(2)	C(7)	C(1)	111.74(18)	C(33)	C(34)	C(35)	109.3(2)
C(1)	C(7)	P(1)	113.01(15)	N(3)	C(35)	C(34)	111.2(2)
N(2)	C(8)	C(9)	111.1(2)	N(3)	C(36)	P(2)	105.90(15)
C(10)	C(9)	C(8)	109.3(2)	N(3)	C(36)	C(37)	112.64(19)
C(9)	C(10)	C(11)	109.0(2)	C(37)	C(36)	P(2)	115.84(16)
N(1)	C(11)	C(10)	110.4(2)	C(38)	C(37)	C(36)	121.9(2)
N(1)	C(12)	P(1)	105.51(15)	C(38)	C(37)	C(42)	118.6(2)
N(1)	C(12)	C(13)	111.35(19)	C(42)	C(37)	C(36)	119.4(2)
C(13)	C(12)	P(1)	117.02(15)	C(39)	C(38)	C(37)	120.6(2)
C(14)	C(13)	C(12)	119.9(2)	C(40)	C(39)	C(38)	120.3(3)
C(18)	C(13)	C(12)	121.4(2)	C(39)	C(40)	C(41)	120.0(3)
C(18)	C(13)	C(14)	118.6(2)	C(40)	C(41)	C(42)	120.1(2)
C(15)	C(14)	C(13)	120.7(2)	C(41)	C(42)	C(37)	120.4(3)

Table C-14. Torsion Angles for red-TPSB BDP **2.**

A	**B**	**C**	**D**	**Angle/˚**	**A**	**B**	**C**	**D**	**Angle/˚**
P(1)	C(12)	C(13)	C(14)	-98.5(2)	C(12)	C(13)	C(14)	C(15)	178.0(2)
P(1)	C(12)	C(13)	C(18)	79.0(3)	C(12)	C(13)	C(18)	C(17)	-176.8(2)
P(1)	C(19)	C(20)	C(21)	177.9(2)	C(13)	C(14)	C(15)	C(16)	-0.9(4)
P(1)	C(19)	C(24)	P(2)	-1.0(2)	C(14)	C(13)	C(18)	C(17)	0.8(4)
P(1)	C(19)	C(24)	C(23)	-178.48(19)	C(14)	C(15)	C(16)	C(17)	0.3(4)
P(2)	C(25)	C(26)	C(27)	-120.2(2)	C(15)	C(16)	C(17)	C(18)	0.9(4)

P(2)	C(25)	C(26)	C(31)	59.0(3)	C(16)	C(17)	C(18)	C(13)	-1.5(4)
P(2)	C(36)	C(37)	C(38)	84.8(3)	C(18)	C(13)	C(14)	C(15)	0.4(3)
P(2)	C(36)	C(37)	C(42)	-92.5(2)	C(19)	P(1)	C(7)	N(2)	-132.92(14)
N(1)	N(2)	C(7)	P(1)	55.95(17)	C(19)	P(1)	C(7)	C(1)	107.45(17)
N(1)	N(2)	C(7)	C(1)	176.48(17)	C(19)	P(1)	C(12)	N(1)	100.95(15)
N(1)	N(2)	C(8)	C(9)	-62.0(2)	C(19)	P(1)	C(12)	C(13)	-23.5(2)
N(1)	C(12)	C(13)	C(14)	140.0(2)	C(19)	C(20)	C(21)	C(22)	1.5(4)
N(1)	C(12)	C(13)	C(18)	-42.4(3)	C(20)	C(19)	C(24)	P(2)	179.17(18)
N(2)	N(1)	C(11)	C(10)	-64.0(2)	C(20)	C(19)	C(24)	C(23)	1.7(3)
N(2)	N(1)	C(12)	P(1)	37.46(18)	C(20)	C(21)	C(22)	C(23)	-0.1(4)
N(2)	N(1)	C(12)	C(13)	165.39(18)	C(21)	C(22)	C(23)	C(24)	-0.5(4)
N(2)	C(8)	C(9)	C(10)	57.1(3)	C(22)	C(23)	C(24)	P(2)	-177.5(2)
N(3)	N(4)	C(25)	P(2)	52.33(17)	C(22)	C(23)	C(24)	C(19)	-0.3(4)
N(3)	N(4)	C(25)	C(26)	172.83(17)	C(24)	P(2)	C(25)	N(4)	-128.96(15)
N(3)	N(4)	C(32)	C(33)	-64.2(2)	C(24)	P(2)	C(25)	C(26)	110.76(17)
N(3)	C(36)	C(37)	C(38)	-37.3(3)	C(24)	P(2)	C(36)	N(3)	96.35(16)
N(3)	C(36)	C(37)	C(42)	145.4(2)	C(24)	P(2)	C(36)	C(37)	-29.30(19)
N(4)	N(3)	C(35)	C(34)	-63.9(2)	C(24)	C(19)	C(20)	C(21)	-2.3(4)
N(4)	N(3)	C(36)	P(2)	40.16(19)	C(25)	P(2)	C(24)	C(19)	-172.25(18)
N(4)	N(3)	C(36)	C(37)	167.74(18)	C(25)	P(2)	C(24)	C(23)	5.0(3)
N(4)	C(25)	C(26)	C(27)	125.0(2)	C(25)	P(2)	C(36)	N(3)	-8.87(16)
N(4)	C(25)	C(26)	C(31)	-55.8(3)	C(25)	P(2)	C(36)	C(37)	-134.52(18)
N(4)	C(32)	C(33)	C(34)	56.9(3)	C(25)	N(4)	C(32)	C(33)	-176.29(19)
C(1)	C(2)	C(3)	C(4)	1.4(4)	C(25)	C(26)	C(27)	C(28)	179.1(2)

C(2)	C(1)	C(6)	C(5)	-0.5(3)	C(25)	C(26)	C(31)	C(30)	-179.7(2)
C(2)	C(1)	C(7)	P(1)	71.9(2)	C(26)	C(27)	C(28)	C(29)	0.7(4)
C(2)	C(1)	C(7)	N(2)	-41.5(3)	C(27)	C(26)	C(31)	C(30)	-0.5(3)
C(2)	C(3)	C(4)	C(5)	-0.3(4)	C(27)	C(28)	C(29)	C(30)	-0.7(4)
C(3)	C(4)	C(5)	C(6)	-1.2(4)	C(28)	C(29)	C(30)	C(31)	0.0(4)
C(4)	C(5)	C(6)	C(1)	1.6(4)	C(29)	C(30)	C(31)	C(26)	0.6(4)
C(6)	C(1)	C(2)	C(3)	-1.1(3)	C(31)	C(26)	C(27)	C(28)	-0.1(4)
C(6)	C(1)	C(7)	P(1)	-107.5(2)	C(32)	N(4)	C(25)	P(2)	166.97(16)
C(6)	C(1)	C(7)	N(2)	139.1(2)	C(32)	N(4)	C(25)	C(26)	-72.5(2)
C(7)	P(1)	C(12)	N(1)	-4.75(15)	C(32)	C(33)	C(34)	C(35)	-51.3(3)
C(7)	P(1)	C(12)	C(13)	-129.19(18)	C(33)	C(34)	C(35)	N(3)	56.5(3)
C(7)	P(1)	C(19)	C(20)	5.5(2)	C(35)	N(3)	N(4)	C(25)	-177.64(16)
C(7)	P(1)	C(19)	C(24)	-174.36(17)	C(35)	N(3)	N(4)	C(32)	66.9(2)
C(7)	N(2)	C(8)	C(9)	-173.7(2)	C(35)	N(3)	C(36)	P(2)	154.65(16)
C(7)	C(1)	C(2)	C(3)	179.5(2)	C(35)	N(3)	C(36)	C(37)	-77.8(2)
C(7)	C(1)	C(6)	C(5)	179.0(2)	C(36)	P(2)	C(24)	C(19)	94.28(19)
C(8)	N(2)	C(7)	P(1)	171.11(15)	C(36)	P(2)	C(24)	C(23)	-88.4(2)
C(8)	N(2)	C(7)	C(1)	-68.4(2)	C(36)	P(2)	C(25)	N(4)	-24.31(15)
C(8)	C(9)	C(10)	C(11)	-53.9(3)	C(36)	P(2)	C(25)	C(26)	-144.59(18)
C(9)	C(10)	C(11)	N(1)	59.1(3)	C(36)	N(3)	N(4)	C(25)	-61.6(2)
C(11)	N(1)	N(2)	C(7)	-179.05(17)	C(36)	N(3)	N(4)	C(32)	-177.10(18)
C(11)	N(1)	N(2)	C(8)	64.7(2)	C(36)	N(3)	C(35)	C(34)	-176.3(2)
C(11)	N(1)	C(12)	P(1)	152.87(16)	C(36)	C(37)	C(38)	C(39)	-177.4(2)
C(11)	N(1)	C(12)	C(13)	-79.2(2)	C(36)	C(37)	C(42)	C(41)	177.4(2)

C(12)	P(1)	C(7)	N(2)	-28.79(15)	C(37)	C(38)	C(39)	C(40)	0.2(4)
C(12)	P(1)	C(7)	C(1)	-148.42(17)	C(38)	C(37)	C(42)	C(41)	0.0(4)
C(12)	P(1)	C(19)	C(20)	-88.2(2)	C(38)	C(39)	C(40)	C(41)	-0.2(4)
C(12)	P(1)	C(19)	C(24)	92.01(19)	C(39)	C(40)	C(41)	C(42)	0.1(4)
C(12)	N(1)	N(2)	C(7)	-62.7(2)	C(40)	C(41)	C(42)	C(37)	0.0(4)
C(12)	N(1)	N(2)	C(8)	-178.91(17)	C(42)	C(37)	C(38)	C(39)	-0.1(4)
C(12)	N(1)	C(11)	C(10)	-177.2(2)					

Table C-15. Hydrogen Atom Coordinates ($Å \times 10^4$) and Isotropic Displacement Parameters ($Å^2 \times 10^3$) for red-TPSB BDP **2**.

Atom	*x*	*y*	*z*	U(eq)
H(2)	1373	6790	5401	28
H(3)	1815	8134	6216	32
H(4)	3358	9620	5606	31
H(5)	4451	9734	4192	31
H(6)	4075	8335	3403	27
H(7)	3123	6520	3304	22
H(8A)	3769	5289	5065	29
H(8B)	4177	4871	4158	29
H(9A)	4268	3167	5361	34
H(9B)	2779	3422	5731	34
H(10A)	2795	1913	4946	37
H(10B)	3624	2734	4094	37

H(11A)	1387	2864	3882	29
H(11B)	1008	3326	4774	29
H(12)	-53	4860	3976	22
H(14)	-1614	4566	3096	29
H(15)	-2148	4019	1849	39
H(16)	-552	3935	671	42
H(17)	1594	4382	740	39
H(18)	2159	4863	2003	32
H(20)	3150	7282	2023	29
H(21)	3491	7997	490	34
H(22)	1717	8648	-304	40
H(23)	-392	8562	446	34
H(25)	-2255	8465	918	24
H(27)	-2836	7107	153	34
H(28)	-3905	5416	62	42
H(29)	-5170	4311	1292	40
H(30)	-5344	4869	2641	35
H(31)	-4249	6537	2749	30
H(32A)	-4965	8998	1033	30
H(32B)	-3844	9953	613	30
H(33A)	-5787	11014	985	38
H(33B)	-5893	10218	1989	38
H(34A)	-5008	12047	1983	36
H(34B)	-3934	11944	1162	36

H(35A)	-2946	11359	2482	31
H(35B)	-4032	10373	2909	31
H(36)	-2442	9015	3229	24
H(38)	-331	10708	1412	38
H(39)	1512	11676	1554	45
H(40)	2237	11402	2933	47
H(41)	1113	10165	4180	42
H(42)	-738	9194	4049	33

C.3 Crystallographic Data for red-TPPB BDP 4

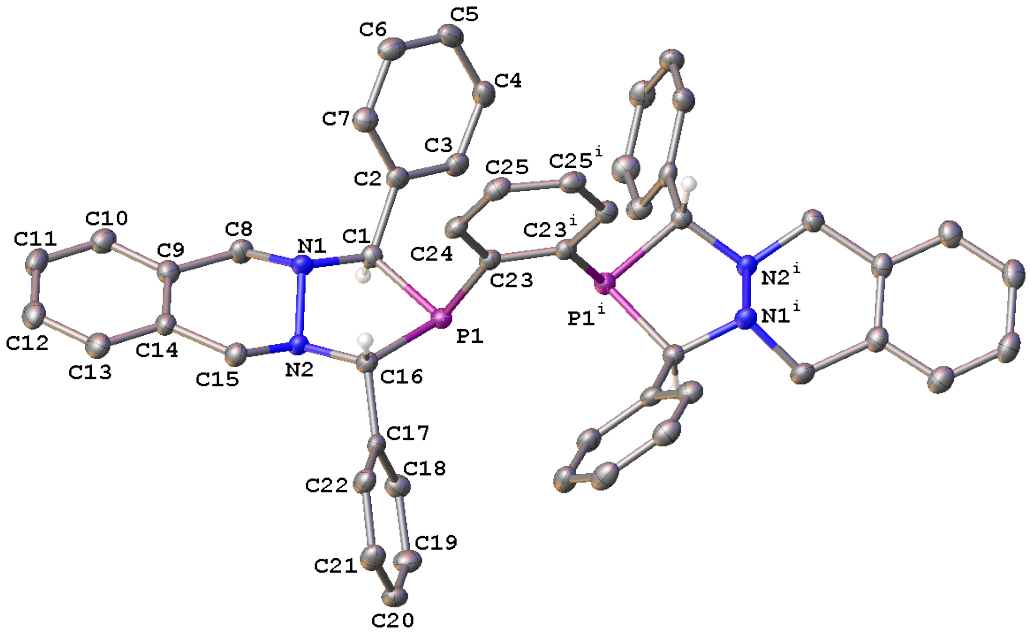

Figure C-4. A molecular drawing of red-TPPB BDP 4 shown with 50% probability ellipsoids. All H atoms except those on anomeric C atoms are omitted. Symmetry code: i = 1-x, 1-y, z.

C.3.1 Data Collection

A colorless crystal with approximate dimensions 0.55 × 0.243 × 0.03 mm^3 was selected under oil under ambient conditions and attached to the tip of a MiTeGen MicroMount©. The crystal was mounted in a stream of cold nitrogen at 100(1) K and centered in the X-ray beam by using a video camera.

The crystal evaluation and data collection were performed on a Bruker Quazar SMART APEXII diffractometer with Mo K_α (λ = 0.71073 Å) radiation and the diffractometer to crystal distance of 7.00 cm.[1]

The initial cell constants were obtained from three series of ω scans at different starting angles. Each series consisted of 12 frames collected at intervals of 0.5º in a 6º range about ω with the exposure time of 3 seconds per frame. The reflections were successfully indexed by an automated indexing routine built in the APEXII program suite. The final cell constants were calculated from a set of 9893 strong reflections from the actual data collection.

The data were collected by using the full sphere data collection routine to survey the reciprocal space to the extent of a full sphere to a resolution of 0.80 Å. A total of 22130 data were harvested by collecting 9 sets of frames with 0.6º scans in ω with exposure times of 15 sec per frame. These highly redundant datasets were corrected for Lorentz and polarization effects. The absorption correction was based on fitting a function to the empirical transmission surface as sampled by multiple equivalent measurements.[2]

C.3.2 Structure Solution and Refinement

The systematic absences in the diffraction data were uniquely consistent for the space group *Fdd*2 that yielded chemically reasonable and computationally stable results of refinement.[3-8]

A successful solution by the direct methods provided most non-hydrogen atoms from the *E*-map. The remaining non-hydrogen atoms were located in an alternating series of least-squares cycles and difference Fourier maps. All non-hydrogen atoms were refined with anisotropic displacement coefficients. All hydrogen atoms were included in the structure factor calculation at idealized positions and were allowed to ride on the neighboring atoms with relative isotropic displacement coefficients.

The diphosphine resides on a crystallographic twofold axis and only one half of it is symmetry-independent. Both unique anomeric carbons C1 and C16 have the same configuration, arbitrarily shown as R. In the lattice there are two stereoisomers; in one all chiral carbons are *R*, whereas in the other *S*.

The final least-squares refinement of 253 parameters against 47953 data resulted in residuals *R* (based on F^2 for $I \geq 2\sigma$) and *wR* (based on F^2 for all data) of 0.0339 and 0.0940, respectively. The final difference Fourier map was featureless.

C.3.3 Summary

Crystal data for $C_{50}H_{44}N_4P_2$ (M =762.83 g/mol): orthorhombic, space group Fdd2 (no. 43), a = 12.554(6) Å, b = 54.22(2) Å, c = 11.598(6) Å, V = 7894(6) Å^3, Z = 8, T = 100.0 K, μ(MoKα) = 0.152 mm^{-1}, *Dcalc* = 1.284 g/cm^3, 47953 reflections measured (3.004° ≤ 2Θ ≤ 52.774°), 4043 unique (R_{int} = 0.0592, R_{sigma} = 0.0289) which were used in all calculations. The final R_1 was 0.0339 (I > 2σ(I)) and wR_2 was 0.0940 (all data).

Table C-16. Crystal Data and Structure Refinement for red-TPPB BDP 4.

Empirical formula	$C_{50}H_{44}N_4P_2$
Formula weight	762.83
Temperature/K	100.0
Crystal system	orthorhombic
Space group	Fdd2
a/Å	12.554(6)
b/Å	54.22(2)
c/Å	11.598(6)
α/°	90
β/°	90
γ/°	90
Volume/Å^3	7894(6)
Z	8
ϱ_{calc}g/cm^3	1.284
μ/mm^{-1}	0.152
F(000)	3216.0
Crystal size/mm^3	0.55 × 0.243 × 0.03
Radiation	MoKα (λ = 0.71073)
2Θ range for data collection/°	3.004 to 52.774
Index ranges	$-15 \le h \le 15$, $-67 \le k \le 67$, $-14 \le l \le 14$
Reflections collected	47953
Independent reflections	4043 [R_{int} = 0.0592, R_{sigma} = 0.0289]
Data/restraints/parameters	4043/1/253
Goodness-of-fit on F^2	1.000

Final R indexes [I>=2σ (I)]	$R_1 = 0.0339$, $wR_2 = 0.0930$
Final R indexes [all data]	$R_1 = 0.0355$, $wR_2 = 0.0940$
Largest diff. peak/hole / e Å^{-3}	0.34/-0.17
Flack parameter	-0.09(5)

Table C-17. Fractional Atomic Coordinates ($\times 10^4$) and Equivalent Isotropic Displacement Parameters (Å$^2 \times 10^3$) for red-TPPB BDP **4**. U_{eq} is defined as 1/3 of the trace of the orthogonalised U_{IJ} tensor.

Atom	***x***	***y***	***z***	**U(eq)**
P1	5557.6(4)	5255.3(2)	1718.9(5)	18.02(17)
N1	7437.2(14)	5495.5(3)	1997.1(18)	19.6(4)
N2	6631.7(14)	5677.7(3)	1585.0(18)	18.3(4)
C1	7046.5(17)	5254.3(4)	1579(2)	18.7(5)
C2	7568.1(17)	5034.2(4)	2134(2)	19.2(5)
C3	7350.0(17)	4802.2(4)	1672(2)	23.2(5)
C4	7796.9(18)	4591.6(5)	2147(3)	27.9(6)
C5	8485.0(18)	4611.9(5)	3086(3)	28.4(6)
C6	8703.1(19)	4841.3(5)	3540(2)	26.4(6)
C7	8243.3(19)	5052.5(5)	3077(2)	23.0(5)
C8	8426.7(18)	5553.7(4)	1369(2)	22.8(5)
C9	8782.9(18)	5815.1(4)	1577(2)	21.8(5)
C10	9839.1(19)	5884.5(5)	1432(2)	26.6(6)
C11	10145.9(19)	6126.7(5)	1602(2)	28.1(5)
C12	9394.4(18)	6304.3(5)	1904(2)	26.8(6)

C13	8349.8(19)	6236.1(5)	2053(2)	25.7(5)
C14	8034.3(17)	5991.4(5)	1895(2)	20.7(5)
C15	6900.5(17)	5915.1(4)	2118(2)	20.8(5)
C16	5589.5(15)	5593.4(4)	2043(2)	18.8(5)
C17	4691.6(17)	5731.1(4)	1449(2)	19.5(5)
C18	4410.9(17)	5676.8(5)	312(2)	22.9(5)
C19	3583.1(19)	5799.7(5)	-226(2)	27.2(6)
C20	3035.7(18)	5983.1(5)	358(3)	26.9(6)
C21	3310.0(19)	6041.8(5)	1477(2)	26.3(6)
C22	4129.5(18)	5913.4(4)	2026(2)	24.1(5)
C23	5294.6(16)	5110.6(4)	3125(2)	18.0(5)
C24	5617.7(17)	5212.2(4)	4181(2)	20.5(5)
C25	5314.8(17)	5105.4(5)	5213(2)	22.5(5)

Table C-18. Anisotropic Displacement Parameters ($Å^2 \times 10^3$) for red-TPPB BDP **4**. The Anisotropic Displacement Factor Exponent Takes the Form: $-2\pi^2[h^2a^{*2}U_{11}+2hka^*b^*U_{12}+\ldots]$.

Atom	$\mathbf{U_{11}}$	$\mathbf{U_{22}}$	$\mathbf{U_{33}}$	$\mathbf{U_{23}}$	$\mathbf{U_{13}}$	$\mathbf{U_{12}}$
P1	16.8(3)	17.4(3)	19.8(3)	0.8(2)	-1.3(2)	0.5(2)
N1	15.6(9)	17.2(9)	26.0(11)	1.9(8)	0.3(8)	2.2(7)
N2	13.4(9)	16.6(9)	25.0(11)	0.5(8)	-0.6(8)	0.8(7)
C1	16.8(10)	18.4(11)	20.8(12)	-0.7(9)	2.3(9)	0.5(8)
C2	14.7(10)	20.7(11)	22.3(11)	1.4(9)	4.2(9)	2.0(8)
C3	15.0(11)	25.2(12)	29.5(13)	1.3(11)	0.5(10)	1.7(8)
C4	19.8(11)	20.2(12)	43.6(16)	2.1(11)	2.2(11)	0.0(9)

C5	21.1(12)	26.9(13)	37.0(16)	12.3(12)	3.7(11)	3.3(10)
C6	20.3(12)	33.9(14)	25.1(14)	6.2(11)	0.5(10)	2.8(10)
C7	21.4(11)	25.4(13)	22.2(12)	0.4(10)	3.2(10)	1.6(9)
C8	16.7(11)	21.9(12)	29.9(13)	0.2(10)	3.5(9)	2.4(9)
C9	20.5(11)	22.3(12)	22.7(13)	3.6(10)	0.4(9)	-1.7(8)
C10	20.6(12)	30.9(13)	28.4(14)	3.8(11)	0(1)	0.3(10)
C11	19.7(11)	34.0(13)	30.5(14)	4.8(11)	-2(1)	-7.3(10)
C12	27.3(13)	27.3(13)	25.7(14)	-0.9(11)	-4.5(10)	-6.9(9)
C13	26.0(12)	24.5(12)	26.6(14)	-1.5(10)	-4.5(10)	-2.3(10)
C14	18.6(11)	20.5(12)	22.9(13)	2.6(10)	-3.2(9)	-2.5(8)
C15	18.9(11)	19.7(12)	23.8(13)	-2.6(10)	-1.0(9)	-0.3(8)
C16	16.7(11)	18.2(11)	21.6(13)	-0.9(9)	-0.9(9)	0.3(8)
C17	13.9(10)	18.1(11)	26.4(13)	3.6(9)	-0.7(9)	-3.1(8)
C18	20.6(12)	23.3(13)	24.8(13)	2.4(10)	2.7(10)	3.0(9)
C19	25.2(12)	30.4(13)	25.9(14)	3.9(11)	-3.9(10)	2.7(10)
C20	20.6(11)	24.0(13)	36.2(14)	6.2(11)	-5.9(10)	3.4(9)
C21	18.9(11)	21.9(12)	38.1(16)	-4.1(11)	0.6(10)	3.5(9)
C22	19.2(10)	21.2(12)	31.9(14)	-3.5(10)	-3.9(10)	-0.4(9)
C23	13.8(10)	19.1(12)	21.2(12)	-0.1(9)	0.1(9)	1.5(8)
C24	15.5(11)	23.4(11)	22.7(13)	-2.8(10)	-3.1(9)	0.7(8)
C25	17.1(11)	30.2(14)	20.3(12)	-4(1)	-1.8(10)	3.5(9)

Table C19. Bond Lengths for red-TPPB BDP **4**.

Atom	**Atom**	**Length/Å**	**Atom**	**Atom**	**Length/Å**
P1	C1	1.876(2)	C9	C14	1.390(3)

P1	C16	1.872(3)	C10	C11	1.383(4)
P1	C23	1.839(3)	C11	C12	1.393(4)
N1	N2	1.492(3)	C12	C13	1.373(3)
N1	C1	1.479(3)	C13	C14	1.397(4)
N1	C8	1.474(3)	C14	C15	1.505(3)
N2	C15	1.467(3)	C16	C17	1.518(3)
N2	C16	1.484(3)	C17	C18	1.396(4)
C1	C2	1.506(3)	C17	C22	1.387(3)
C2	C3	1.395(4)	C18	C19	1.383(3)
C2	C7	1.387(4)	C19	C20	1.386(4)
C3	C4	1.387(3)	C20	C21	1.380(4)
C4	C5	1.394(4)	C21	C22	1.396(4)
C5	C6	1.378(4)	C23	C23[1]	1.409(4)
C6	C7	1.390(4)	C23	C24	1.403(3)
C8	C9	1.505(3)	C24	C25	1.383(4)
C9	C10	1.389(3)	C25	C25[1]	1.390(5)

Table C-20. Bond Angles for red-TPPB BDP **4**.

Atom	**Atom**	**Atom**	**Angle/°**	**Atom**	**Atom**	**Atom**	**Angle/°**
C16	P1	C1	89.94(10)	C11	C10	C9	120.4(2)
C23	P1	C1	104.74(11)	C10	C11	C12	120.2(2)
C23	P1	C16	104.10(11)	C13	C12	C11	119.5(2)
C1	N1	N2	104.82(17)	C12	C13	C14	120.7(2)
C8	N1	N2	105.71(17)	C9	C14	C13	119.7(2)
C8	N1	C1	107.86(18)	C9	C14	C15	119.7(2)

C15	N2	N1	106.86(17)	C13	C14	C15	120.5(2)
C15	N2	C16	108.81(18)	N2	C15	C14	112.75(19)
C16	N2	N1	106.19(16)	N2	C16	P1	104.40(14)
N1	C1	P1	107.42(14)	N2	C16	C17	109.92(18)
N1	C1	C2	114.6(2)	C17	C16	P1	112.01(15)
C2	C1	P1	113.48(16)	C18	C17	C16	120.8(2)
C3	C2	C1	117.7(2)	C22	C17	C16	120.6(2)
C7	C2	C1	123.1(2)	C22	C17	C18	118.6(2)
C7	C2	C3	119.2(2)	C19	C18	C17	120.9(2)
C4	C3	C2	120.7(2)	C18	C19	C20	119.8(3)
C3	C4	C5	119.8(2)	C21	C20	C19	120.1(2)
C6	C5	C4	119.5(2)	C20	C21	C22	119.9(2)
C5	C6	C7	120.9(3)	C17	C22	C21	120.6(2)
C2	C7	C6	120.0(2)	C23[1]	C23	P1	117.21(7)
N1	C8	C9	111.87(19)	C24	C23	P1	123.67(18)
C10	C9	C8	121.3(2)	C24	C23	C23[1]	119.08(14)
C10	C9	C14	119.4(2)	C25	C24	C23	120.8(2)
C14	C9	C8	119.3(2)	C24	C25	C25[1]	120.06(14)

Table C-21. Torsion Angles for red-TPPB BDP **4**.

A	**B**	**C**	**D**	**Angle/°**	**A**	**B**	**C**	**D**	**Angle/°**
P1	C1	C2	C3	64.9(3)	C8	N1	C1	C2	82.5(2)
P1	C1	C2	C7	-114.8(2)	C8	C9	C10	C11	178.5(2)
P1	C16	C17	C18	-41.8(3)	C8	C9	C14	C13	-177.8(2)
P1	C16	C17	C22	138.02(19)	C8	C9	C14	C15	4.8(4)

P1	C23	C24	C25	174.32(18)	C9	C10	C11	C12	-0.9(4)
N1	N2	C15	C14	54.2(2)	C9	C14	C15	N2	-20.3(3)
N1	N2	C16	P1	-46.61(19)	C10	C9	C14	C13	0.7(4)
N1	N2	C16	C17	-166.92(18)	C10	C9	C14	C15	-176.7(2)
N1	C1	C2	C3	-171.2(2)	C10	C11	C12	C13	1.2(4)
N1	C1	C2	C7	9.1(3)	C11	C12	C13	C14	-0.5(4)
N1	C8	C9	C10	156.8(2)	C12	C13	C14	C9	-0.4(4)
N1	C8	C9	C14	-24.7(3)	C12	C13	C14	C15	176.9(2)
N2	N1	C1	P1	-38.1(2)	C13	C14	C15	N2	162.4(2)
N2	N1	C1	C2	-165.18(17)	C14	C9	C10	C11	0.0(4)
N2	N1	C8	C9	58.2(2)	C15	N2	C16	P1	-161.32(15)
N2	C16	C17	C18	73.8(3)	C15	N2	C16	C17	78.4(2)
N2	C16	C17	C22	-106.4(2)	C16	P1	C1	N1	10.24(17)
C1	P1	C16	N2	20.36(16)	C16	P1	C1	C2	137.96(19)
C1	P1	C16	C17	139.25(17)	C16	P1	C23	$C23^{1}$	148.3(2)
C1	P1	C23	$C23^{1}$	-118.0(2)	C16	P1	C23	C24	-29.7(2)
C1	P1	C23	C24	64.0(2)	C16	N2	C15	C14	168.47(19)
C1	N1	N2	C15	172.05(18)	C16	C17	C18	C19	179.1(2)
C1	N1	N2	C16	56.0(2)	C16	C17	C22	C21	179.4(2)
C1	N1	C8	C9	169.9(2)	C17	C18	C19	C20	1.4(4)
C1	C2	C3	C4	-179.5(2)	C18	C17	C22	C21	-0.8(4)
C1	C2	C7	C6	-179.5(2)	C18	C19	C20	C21	-0.5(4)
C2	C3	C4	C5	-1.1(4)	C19	C20	C21	C22	-1.0(4)
C3	C2	C7	C6	0.8(4)	C20	C21	C22	C17	1.7(4)
C3	C4	C5	C6	0.8(4)	C22	C17	C18	C19	-0.7(4)

C4	C5	C6	C7	0.2(4)	C23	P1	C1	N1	-94.33(17)
C5	C6	C7	C2	-1.0(4)	C23	P1	C1	C2	33.4(2)
C7	C2	C3	C4	0.3(4)	C23	P1	C16	N2	125.55(15)
C8	N1	N2	C15	-74.1(2)	C23	P1	C16	C17	-115.55(16)
C8	N1	N2	C16	169.86(17)	$C23^{1}$	C23	C24	C25	-3.6(4)
C8	N1	C1	P1	-150.41(16)	C23	C24	C25	$C25^{1}$	0.1(4)

Table C-22. Hydrogen Atom Coordinates ($Å \times 10^4$) and Isotropic Displacement Parameters ($Å^2 \times 10^3$) for red-TPPB BDP **4**.

Atom	***x***	***y***	***z***	**U(eq)**
H1	7212.09	5245.9	736.26	22
H3	6890.66	4788.37	1023.8	28
H4	7634.55	4434.03	1834.96	33
H5	8801.49	4468.59	3409.58	34
H6	9173.77	4855.2	4178.53	32
H7	8391.4	5209.19	3406.79	28
H8A	8309.36	5528.86	532.79	27
H8B	8995.92	5439.09	1617.84	27
H10	10354.15	5764.82	1215.02	32
H11	10872.03	6172.19	1511.73	34
H12	9602.67	6471.38	2005.48	32
H13	7836.68	6356.6	2265.27	31
H15A	6784.16	5903.49	2960.26	25
H15B	6416.18	6043.62	1813.45	25

H16	5556.26	5620.99	2894.66	23
H18	4793.93	5553.65	-97.88	28
H19	3390.33	5758.41	-994.77	33
H20	2470.59	6068.54	-12.48	32
H21	2941.85	6169.35	1872.32	32
H22	4303.8	5951.28	2803.5	29
H24	6049.5	5356.14	4187.27	25
H25	5537.39	5176.19	5922.32	27

C.4 Crystallographic Data for TNSB BDP 7

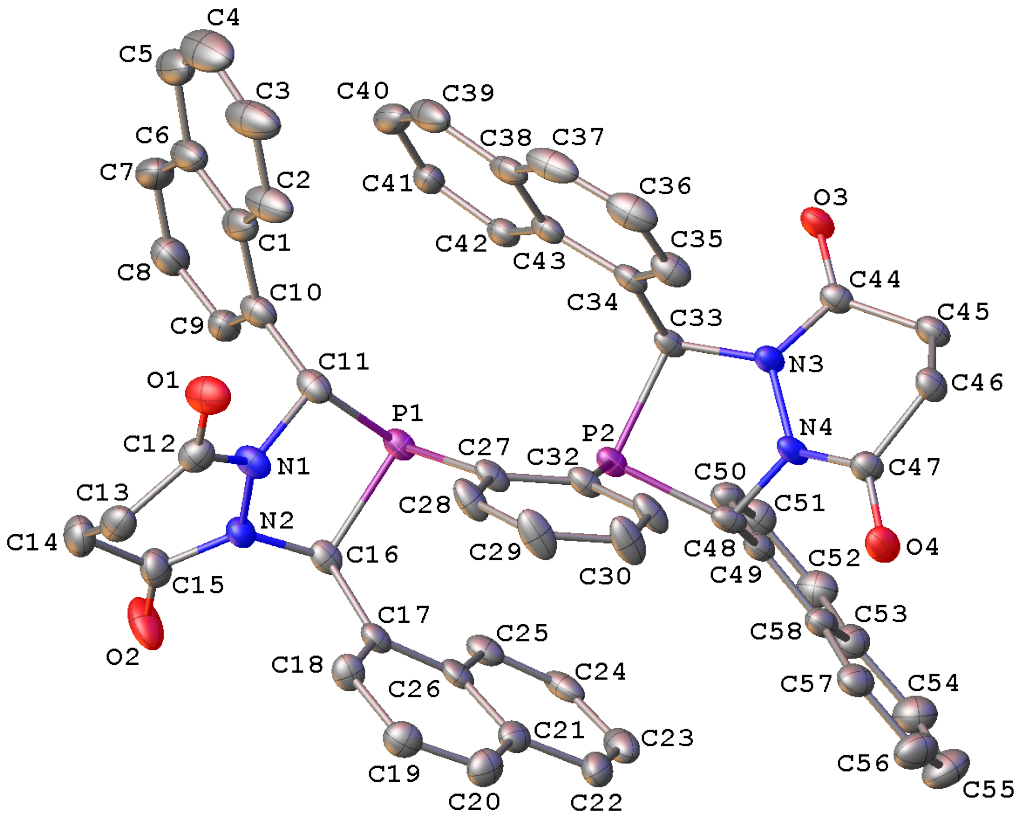

Figure C-5. A molecular drawing of the first diphosphine in TNSB BDP **7** shown with 40% probability ellipsoids. All H atoms are omitted.

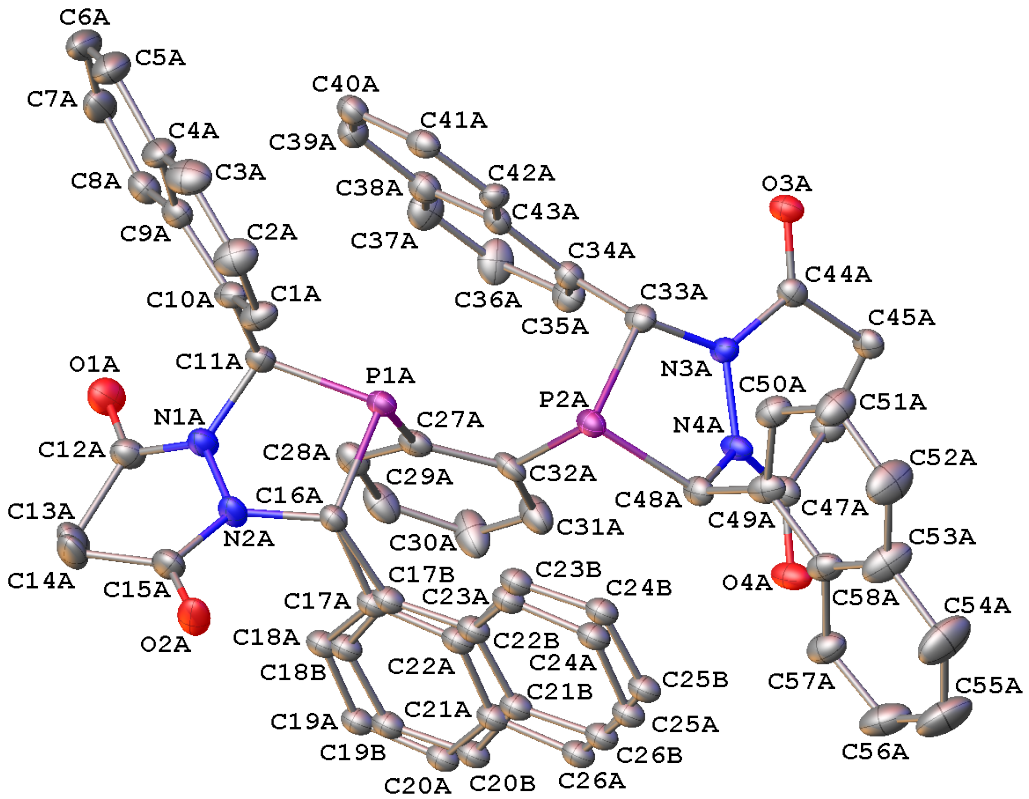

Figure C-6. A molecular drawing of the second diphosphine in TNSB BDP **7** shown with 40% probability ellipsoids. All H atoms are omitted. Both disordered positions of the disordered naphthalenyl group are shown.

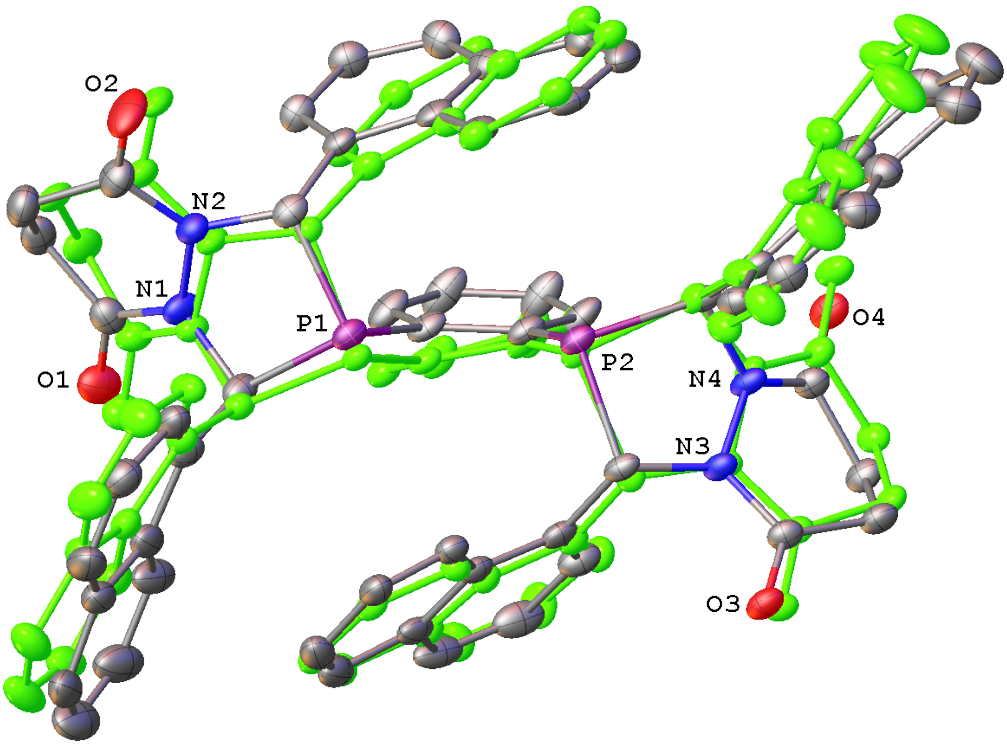

Figure C-7. A superposition of the two symmetry-independent disphosphines. All H atoms are omitted.

C.4.1 Data Collection

A colorless crystal with approximate dimensions 0.248 × 0.018 × 0.016 mm^3 was selected under oil under ambient conditions and attached to the tip of a MiTeGen MicroMount©. The crystal was mounted in a stream of cold nitrogen at 100(1) K and centered in the X-ray beam by using a video camera.

The crystal evaluation and data collection were performed on a Bruker Quazar SMART APEXII diffractometer with Mo K_α (λ = 0.71073 Å) radiation and the diffractometer to crystal distance of 4.96 cm.[1]

The initial cell constants were obtained from three series of ω scans at different starting angles. Each series consisted of 12 frames collected at intervals of 0.5º in a 6º range about ω with

the exposure time of 10 seconds per frame. The reflections were successfully indexed by an automated indexing routine built in the APEXII program suite. The final cell constants were calculated from a set of 9945 strong reflections from the actual data collection.

The data were collected by using the full sphere data collection routine to survey the reciprocal space to the extent of a full sphere to a resolution of 0.82 Å. A total of 155176 data were harvested by collecting 4 sets of frames with 0.5º scans in ω and φ with exposure times of 180 sec per frame. These highly redundant datasets were corrected for Lorentz and polarization effects. The absorption correction was based on fitting a function to the empirical transmission surface as sampled by multiple equivalent measurements.[2]

C.4.2 Structure Solution and Refinement

The systematic absences in the diffraction data were uniquely consistent for the space group $P2_1/c$ that yielded chemically reasonable and computationally stable results of refinement.[3-8]

A successful solution by the direct methods provided most non-hydrogen atoms from the *E*-map. The remaining non-hydrogen atoms were located in an alternating series of least-squares cycles and difference Fourier maps. All non-hydrogen atoms were refined with anisotropic displacement coefficients. All hydrogen atoms were included in the structure factor calculation at idealized positions and were allowed to ride on the neighboring atoms with relative isotropic displacement coefficients.

There are two symmetry independent diphosphines in the asymmetric unit with identical composition but different conformations.

The C17a naphthalenyl group, equally disordered over two positions, was refined with constraints.

There were five or more fully or partially occupied molecules of CH_2Cl_2, pentane, and unidentifiable solvents present in the asymmetric unit. A significant amount of time was invested in identifying and refining the disordered molecules. Bond length restraints were applied to model the molecules but the resulting isotropic displacement coefficients suggested the molecules were mobile. In addition, the refinement was computationally unstable. Option SQUEEZE of program PLATON[9] was used to correct the diffraction data for diffuse scattering effects and to identify the solvent molecules. PLATON calculated the upper limit of volume that can be occupied by the solvent to be 2564 $Å^3$, or 23% of the unit cell volume. The program calculated 762 electrons in the unit cell for the diffuse species. This approximately corresponds to two molecules of CH_2Cl_2 and 2.5 molecules of pentane in the asymmetric unit (756 electrons). However, this is an approximation because the diphosphine of interest has also been exposed to chloroform, ethyl acetate, and THF, and these solvents may also be present. Please note that all derived results in the following tables are based on the known contents. No data are given for the diffusely scattering species.

The final least-squares refinement of 1153 parameters against 20864 data resulted in residuals R (based on F^2 for $I \geq 2\sigma$) and wR (based on F^2 for all data) of 0.0874 and 0.2219, respectively. The final difference Fourier map was featureless.

C.4.3 Summary

Crystal data for $C_{58}H_{44}N_4O_4P_2$ (M =922.91 g/mol): monoclinic, space group $P2_1/c$ (no. 14), a = 18.883(5) Å, b = 35.438(9) Å, c = 16.404(4) Å, β = 90.815(10)°, V = 10976(5) $Å^3$, Z = 8, T = 100.0 K, μ(MoKα) = 0.126 mm^{-1}, $Dcalc$ = 1.117 g/cm^3, 155176 reflections measured (2.156° ≤ 2Θ ≤ 51.436°), 20864 unique (R_{int} = 0.1053, R_{sigma} = 0.0734) which were used in all calculations. The final R_1 was 0.0874 (I > 2σ(I)) and wR_2 was 0.2219 (all data).

Table C-23. Crystal Data and Structure Refinement for TNSB BDP **7**.

Empirical formula	$C_{58}H_{44}N_4O_4P_2$ x solvents
Formula weight	922.91
Temperature/K	100.0
Crystal system	monoclinic
Space group	$P2_1/c$
a/Å	18.883(5)
b/Å	35.438(9)
c/Å	16.404(4)
α/°	90
β/°	90.815(10)
γ/°	90
Volume/Å^3	10976(5)
Z	8
ϱ_{calc}g/cm^3	1.117
μ/mm^{-1}	0.126
F(000)	3856.0
Crystal size/mm^3	0.248 × 0.018 × 0.016
Radiation	MoKα (λ = 0.71073)
2Θ range for data collection/°	2.156 to 51.436
Index ranges	$-23 \le h \le 23$, $-43 \le k \le 43$, $-20 \le l \le 20$
Reflections collected	155176
Independent reflections	20864 [R_{int} = 0.1053, R_{sigma} = 0.0734]
Data/restraints/parameters	20864/2/1153
Goodness-of-fit on F^2	1.060

Final R indexes [I>=2σ (I)]	$R_1 = 0.0874$, $wR_2 = 0.2071$
Final R indexes [all data]	$R_1 = 0.1219$, $wR_2 = 0.2219$
Largest diff. peak/hole / e Å^{-3}	0.77/-0.60

Table C-24. Fractional Atomic Coordinates ($\times 10^4$) and Equivalent Isotropic Displacement Parameters (Å$^2 \times 10^3$) for TNSB BDP **7**. U_{eq} is defined as 1/3 of the trace of the orthogonalised U_{IJ} tensor.

Atom	***x***	***y***	***z***	**U(eq)**
P1	8842.4(6)	6684.2(4)	6988.5(7)	26.7(3)
P2	9561.5(6)	7429.4(4)	6195.1(7)	25.6(3)
O1	7564.4(19)	5611.4(11)	6513(3)	46.9(10)
O2	7390(2)	6504.7(12)	9122(2)	57.0(12)
O3	11650.4(16)	7487(1)	4769.7(19)	32.4(8)
O4	9183.4(17)	8160.6(10)	4029.8(19)	35.2(8)
N1	7887(2)	6131.7(12)	7206(2)	32.0(9)
N2	7761(2)	6391.3(11)	7844(2)	28.9(9)
N3	10484.9(19)	7590.0(11)	4986(2)	26.5(8)
N4	9903.4(19)	7834.4(12)	4890(2)	27.4(9)
C1	9349(3)	5561.2(15)	6947(4)	43.4(14)
C2	9132(3)	5431.8(16)	6181(4)	54.0(17)
C3	9394(4)	5107(2)	5843(5)	70(2)
C4	9905(4)	4898.5(19)	6267(6)	76(2)
C5	10126(3)	5002.9(17)	7021(5)	63(2)
C6	9838(3)	5332.5(16)	7387(4)	49.0(15)

C7	10063(3)	5441.2(18)	8185(5)	59.5(17)
C8	9818(3)	5762.6(18)	8533(4)	51.0(15)
C9	9346(3)	6003.4(16)	8089(3)	40.4(13)
C10	9113(3)	5908.9(15)	7319(3)	35.5(12)
C11	8613(3)	6166.9(14)	6875(3)	32.2(11)
C12	7459(3)	5831.9(15)	7073(3)	35.6(12)
C13	6885(3)	5790.1(16)	7695(3)	40.3(13)
C14	7161(3)	5885.3(16)	8542(3)	45.0(14)
C15	7451(3)	6284.2(16)	8556(3)	37.9(12)
C16	8028(2)	6765.8(14)	7672(3)	27.9(10)
C17	7485(2)	7025.6(14)	7286(3)	27.3(10)
C18	6839(2)	6888.2(15)	7006(3)	31.4(11)
C19	6373(3)	7120.3(15)	6543(3)	37.8(12)
C20	6562(3)	7474.7(15)	6331(3)	38.1(12)
C21	7208(3)	7633.2(14)	6631(3)	32.3(11)
C22	7397(3)	8009.1(15)	6455(3)	38.0(12)
C23	7986(3)	8170.8(16)	6794(3)	42.9(14)
C24	8418(3)	7956.9(15)	7318(3)	37.4(13)
C25	8272(3)	7586.2(15)	7480(3)	33.5(11)
C26	7660(2)	7410.6(14)	7138(3)	30.2(11)
C27	8508(2)	6868.9(15)	5996(3)	29.4(11)
C28	7912(3)	6713.8(17)	5624(3)	38.3(13)
C29	7598(3)	6873.7(19)	4938(3)	47.0(15)
C30	7911(3)	7187.6(18)	4594(3)	45.9(15)
C31	8519(2)	7336.4(17)	4934(3)	36.4(12)

C32	8827(2)	7190.3(14)	5644(3)	28.8(11)
C33	10389(2)	7296.1(14)	5604(3)	25.8(10)
C34	10338(2)	6903.5(14)	5255(3)	29.0(11)
C35	10106(3)	6841.2(16)	4475(3)	37.4(12)
C36	10031(3)	6473.0(19)	4163(4)	49.1(15)
C37	10192(3)	6171.5(18)	4644(4)	50.3(17)
C38	10454(3)	6219.1(15)	5448(3)	37.4(13)
C39	10686(3)	5910.1(16)	5936(4)	50.3(16)
C40	10971(3)	5965.5(16)	6700(4)	47.7(15)
C41	11019(3)	6331.7(15)	7026(3)	38.1(12)
C42	10795(2)	6633.0(14)	6577(3)	30.8(11)
C43	10524(2)	6591.8(14)	5769(3)	29.1(11)
C44	11108(2)	7666.3(14)	4612(3)	27.5(10)
C45	11036(2)	7966.7(15)	3962(3)	33.1(11)
C46	10319(2)	7937.4(15)	3533(3)	31.0(11)
C47	9741(2)	7981.7(14)	4151(3)	28.4(10)
C48	9535(2)	7901.8(14)	5663(3)	28.4(11)
C49	9886(2)	8219.6(14)	6133(3)	28.7(11)
C50	10437(2)	8141.4(15)	6669(3)	31.6(11)
C51	10788(3)	8429.7(15)	7093(3)	37.5(12)
C52	10597(3)	8798.2(16)	6989(3)	42.1(13)
C53	10045(3)	8893.2(15)	6449(3)	38.3(12)
C54	9848(3)	9275.7(18)	6329(4)	50.5(15)
C55	9286(4)	9369.2(18)	5824(4)	57.5(17)
C56	8911(3)	9084.6(17)	5409(4)	49.7(15)

C57	9089(3)	8713.2(16)	5498(3)	38.7(13)
C58	9666(3)	8602.9(15)	6019(3)	32.7(11)
P1A	4021.2(6)	6488.1(3)	4571.3(7)	23.8(3)
P2A	3652.5(6)	7234.3(3)	3675.7(7)	24.5(3)
O1A	4613.6(19)	5290.7(10)	4120(2)	40.2(9)
O2A	6039.8(19)	6233.9(10)	6075(2)	40.4(9)
O3A	1604.1(16)	7527.7(9)	2233.7(18)	28.2(7)
O4A	4249.6(17)	7930.4(10)	1524.5(19)	35.5(8)
N1A	4731.4(19)	5845.3(11)	4783(2)	27.9(9)
N2A	5168(2)	6114.2(11)	5157(2)	28.5(9)
N3A	2783.1(19)	7497.1(10)	2458(2)	23.9(8)
N4A	3461.3(18)	7662.9(11)	2359(2)	25.2(8)
C1A	3704(3)	6117.2(15)	6209(3)	33.4(11)
C2A	3346(3)	6055.9(17)	6950(3)	44.5(14)
C3A	2876(3)	5765.5(18)	7007(3)	46.6(14)
C4A	2757(3)	5515.5(15)	6361(3)	39.2(13)
C5A	2256(3)	5216.6(16)	6414(4)	50.5(15)
C6A	2140(3)	4980.5(16)	5786(4)	51.9(16)
C7A	2533(3)	5018.4(15)	5062(4)	45.8(14)
C8A	3021(3)	5298.5(15)	4992(3)	36.6(12)
C9A	3139(2)	5560.4(14)	5623(3)	31.1(11)
C10A	3607(2)	5878.2(14)	5559(3)	28.6(10)
C11A	3987(2)	5964.2(13)	4756(3)	26.8(10)
C12A	4986(3)	5511.6(14)	4503(3)	32.9(11)
C13A	5744(3)	5444.2(15)	4771(4)	42.6(13)

C14A	5851(3)	5586.3(15)	5643(4)	41.0(13)
C15A	5713(3)	6000.9(15)	5681(3)	35.2(12)
C16A	4977(2)	6509.5(12)	5000(3)	23.2(9)
C17A	5491(4)	6696.4(15)	4416(5)	26.5(7)
C18A	5896(4)	6469.9(12)	3911(5)	26.5(7)
C19A	6365(4)	6633.8(12)	3370(4)	26.5(7)
C20A	6429(3)	7024.1(12)	3334(3)	26.5(7)
C21A	6025(2)	7250.6(12)	3839(3)	26.5(7)
C22A	5556(3)	7086.8(15)	4380(3)	26.5(7)
C23A	5151(3)	7313.3(18)	4885(4)	26.5(7)
C24A	5216(3)	7703.6(18)	4849(4)	26.5(7)
C25A	5685(3)	7867.4(14)	4308(4)	26.5(7)
C26A	6089(3)	7641.0(12)	3803(3)	26.5(7)
C27A	4211(2)	6514.1(13)	3470(3)	25.6(10)
C28A	4464(3)	6212.4(15)	3011(3)	32.1(11)
C29A	4701(3)	6270.6(16)	2229(3)	38.7(13)
C30A	4705(3)	6629.2(17)	1898(3)	48.6(15)
C31A	4422(3)	6928.6(16)	2324(3)	40.3(13)
C32A	4152(2)	6876.7(14)	3103(3)	28(1)
C33A	2763(2)	7210.2(13)	3105(3)	26.5(10)
C34A	2615(2)	6816.0(13)	2792(3)	25.8(10)
C35A	2743(3)	6719.9(14)	1997(3)	32.0(11)
C36A	2671(3)	6339.4(15)	1740(3)	39.8(13)
C37A	2471(3)	6065.2(15)	2265(3)	38.3(12)
C38A	2323(2)	6153.0(14)	3085(3)	30.7(11)

C39A	2100(2)	5871.5(14)	3637(3)	31.3(11)
C40A	1956(2)	5959.2(14)	4427(3)	30.4(11)
C41A	2037(2)	6332.7(14)	4704(3)	28.4(10)
C42A	2239(2)	6613.1(13)	4188(3)	24(1)
C43A	2392(2)	6534.0(13)	3360(3)	24.2(10)
C44A	2199(2)	7638.7(13)	2069(3)	24.2(10)
C45A	2377(2)	7915.7(13)	1397(3)	26.9(10)
C46A	3075(2)	7800.7(14)	991(3)	27.4(10)
C47A	3652(2)	7803.6(13)	1625(3)	27(1)
C48A	3880(2)	7679.1(13)	3123(3)	25.9(10)
C49A	3712(2)	8026.6(14)	3614(3)	29.4(11)
C50A	3144(3)	8030.0(14)	4133(3)	32.0(11)
C51A	2973(3)	8347.0(15)	4604(3)	40.2(13)
C52A	3391(3)	8659.0(17)	4560(4)	53.0(16)
C53A	3971(3)	8677.4(17)	4036(3)	48.7(15)
C54A	4398(4)	9006.5(18)	3984(4)	64(2)
C55A	4944(4)	9027(2)	3446(4)	68(2)
C56A	5098(3)	8718.9(19)	2962(4)	54.5(17)
C57A	4715(3)	8392.9(16)	3015(3)	39.0(13)
C58A	4141(2)	8360.6(14)	3557(3)	31.3(11)
C17B	5429(4)	6759.0(14)	4447(5)	26.5(7)
C18B	5867(4)	6568.3(12)	3912(5)	26.5(7)
C19B	6319(3)	6769.4(12)	3410(4)	26.5(7)
C20B	6333(3)	7161.3(12)	3444(3)	26.5(7)
C21B	5895(2)	7352.0(12)	3979(3)	26.5(7)

C22B	5443(3)	7150.8(15)	4481(3)	26.5(7)
C23B	5005(3)	7341.5(19)	5016(4)	26.5(7)
C24B	5019(3)	7733.4(19)	5050(4)	26.5(7)
C25B	5471(3)	7934.5(15)	4548(4)	26.5(7)
C26B	5909(3)	7743.8(12)	4013(3)	26.5(7)

Table C-25. Anisotropic Displacement Parameters ($Å^2 \times 10^3$) for TNSB BDP **7**. The Anisotropic displacement factor exponent takes the form: $-2\pi^2[h^2a^{*2}U_{11}+2hka^*b^*U_{12}+\ldots]$.

Atom	$\mathbf{U_{11}}$	$\mathbf{U_{22}}$	$\mathbf{U_{33}}$	$\mathbf{U_{23}}$	$\mathbf{U_{13}}$	$\mathbf{U_{12}}$
P1	20.5(6)	38.1(7)	21.5(6)	-3.1(5)	-0.4(5)	-3.5(5)
P2	18.8(6)	40.7(7)	17.2(6)	0.2(5)	-0.8(4)	1.3(5)
O1	32(2)	46(2)	62(3)	-12(2)	-0.5(18)	-7.2(17)
O2	80(3)	62(3)	30(2)	-7(2)	21(2)	-22(2)
O3	21.9(17)	49(2)	26.9(17)	3.1(15)	2.7(13)	2.5(15)
O4	28.7(18)	52(2)	24.5(17)	5.9(16)	-5.3(14)	3.6(16)
N1	21(2)	41(2)	34(2)	-6.1(19)	3.0(17)	-5.8(18)
N2	29(2)	35(2)	22(2)	2.0(17)	3.7(16)	2.1(18)
N3	20.1(19)	38(2)	21.1(19)	4.3(17)	0.9(15)	6.1(17)
N4	18.8(19)	47(2)	16.8(19)	2.8(17)	1.0(15)	6.5(17)
C1	30(3)	33(3)	67(4)	1(3)	16(3)	-5(2)
C2	39(3)	40(3)	84(5)	-24(3)	20(3)	-14(3)
C3	45(4)	55(4)	112(6)	-27(4)	27(4)	-12(3)
C4	70(5)	39(4)	120(7)	-29(4)	35(5)	-15(4)
C5	49(4)	36(3)	104(6)	11(4)	34(4)	0(3)

C6	40(3)	35(3)	72(4)	2(3)	25(3)	1(3)
C7	45(4)	52(4)	83(5)	21(3)	24(3)	19(3)
C8	44(3)	60(4)	49(4)	7(3)	11(3)	4(3)
C9	32(3)	43(3)	46(3)	11(3)	10(2)	7(2)
C10	26(3)	40(3)	41(3)	-7(2)	8(2)	-6(2)
C11	31(3)	36(3)	29(3)	-9(2)	6(2)	-7(2)
C12	30(3)	35(3)	41(3)	1(2)	-7(2)	0(2)
C13	24(3)	40(3)	57(4)	7(3)	-2(2)	-3(2)
C14	44(3)	45(3)	46(3)	11(3)	6(3)	-5(3)
C15	39(3)	46(3)	29(3)	7(2)	0(2)	-1(2)
C16	26(2)	41(3)	17(2)	-3(2)	-2.7(18)	-3(2)
C17	24(2)	40(3)	19(2)	-1(2)	5.3(18)	1(2)
C18	28(3)	41(3)	24(2)	1(2)	-7(2)	-4(2)
C19	31(3)	47(3)	35(3)	-3(2)	-6(2)	0(2)
C20	43(3)	43(3)	28(3)	2(2)	-7(2)	3(2)
C21	37(3)	39(3)	21(2)	0(2)	4(2)	6(2)
C22	45(3)	39(3)	30(3)	4(2)	9(2)	3(2)
C23	48(3)	35(3)	47(3)	-7(3)	19(3)	-4(3)
C24	28(3)	44(3)	41(3)	-18(3)	15(2)	-7(2)
C25	30(3)	43(3)	27(3)	-11(2)	7(2)	1(2)
C26	27(2)	43(3)	21(2)	-5(2)	10.2(19)	1(2)
C27	23(2)	50(3)	15(2)	-5(2)	2.3(18)	0(2)
C28	33(3)	64(4)	18(2)	-4(2)	3(2)	-13(3)
C29	31(3)	87(5)	22(3)	2(3)	-7(2)	-20(3)
C30	31(3)	85(4)	22(3)	11(3)	-7(2)	-14(3)

C31	25(2)	66(4)	18(2)	-1(2)	2.4(19)	-8(2)
C32	21(2)	45(3)	20(2)	-4(2)	2.9(18)	0(2)
C33	19(2)	43(3)	16(2)	0(2)	-0.1(17)	4(2)
C34	18(2)	40(3)	29(3)	-4(2)	7.3(19)	-2(2)
C35	29(3)	54(3)	29(3)	-9(2)	1(2)	-1(2)
C36	31(3)	67(4)	50(4)	-27(3)	1(3)	-9(3)
C37	30(3)	51(4)	70(4)	-37(3)	14(3)	-14(3)
C38	23(2)	35(3)	55(3)	-10(3)	16(2)	-6(2)
C39	39(3)	31(3)	82(5)	-8(3)	28(3)	-8(2)
C40	32(3)	35(3)	77(5)	10(3)	16(3)	5(2)
C41	31(3)	40(3)	44(3)	10(2)	13(2)	7(2)
C42	24(2)	34(3)	35(3)	-1(2)	7(2)	1(2)
C43	20(2)	35(3)	32(3)	-5(2)	8.8(19)	-3(2)
C44	20(2)	37(3)	25(2)	-3(2)	-1.9(18)	1(2)
C45	22(2)	45(3)	32(3)	0(2)	5(2)	2(2)
C46	29(3)	45(3)	19(2)	2(2)	-0.6(19)	1(2)
C47	23(2)	38(3)	24(2)	1(2)	-2.9(19)	3(2)
C48	20(2)	45(3)	20(2)	-2(2)	-1.0(18)	8(2)
C49	24(2)	39(3)	23(2)	2(2)	3.9(19)	5(2)
C50	28(3)	41(3)	26(2)	1(2)	0(2)	9(2)
C51	31(3)	48(3)	33(3)	-2(2)	-6(2)	-1(2)
C52	39(3)	43(3)	44(3)	-8(3)	-2(2)	-1(3)
C53	42(3)	40(3)	33(3)	-2(2)	2(2)	5(2)
C54	49(4)	50(4)	53(4)	-5(3)	1(3)	7(3)
C55	71(4)	41(4)	60(4)	-4(3)	-6(3)	16(3)

C56	54(4)	53(4)	42(3)	2(3)	-7(3)	20(3)
C57	42(3)	48(3)	26(3)	-2(2)	5(2)	10(3)
C58	29(3)	43(3)	27(3)	3(2)	5(2)	9(2)
P1A	18.1(5)	31.1(6)	22.2(6)	2.8(5)	-1.7(4)	0.8(5)
P2A	20.6(6)	32.2(7)	20.6(6)	4.8(5)	-0.1(5)	2.8(5)
O1A	39(2)	37(2)	45(2)	-10.6(17)	-2.1(17)	0.4(17)
O2A	38(2)	33(2)	50(2)	0.4(17)	-24.8(17)	-2.3(16)
O3A	21.3(16)	38.2(19)	25.0(17)	0.8(14)	-1.0(13)	-1.2(14)
O4A	22.5(17)	56(2)	27.8(18)	8.0(16)	1.5(14)	-3.2(16)
N1A	23(2)	28(2)	33(2)	-3.1(17)	-5.0(17)	0.3(16)
N2A	24(2)	29(2)	33(2)	-1.2(17)	-11.6(17)	1.7(17)
N3A	20.2(19)	28(2)	23.7(19)	5.6(16)	-1.9(15)	-3.1(16)
N4A	17.4(18)	38(2)	20.0(19)	6.3(17)	-2.2(15)	-0.2(16)
C1A	32(3)	41(3)	27(3)	6(2)	-3(2)	-11(2)
C2A	48(3)	56(4)	30(3)	2(3)	1(2)	-10(3)
C3A	40(3)	68(4)	32(3)	8(3)	5(2)	-7(3)
C4A	30(3)	40(3)	48(3)	15(3)	6(2)	-4(2)
C5A	38(3)	41(3)	73(4)	10(3)	11(3)	-7(3)
C6A	33(3)	30(3)	93(5)	3(3)	12(3)	-4(2)
C7A	34(3)	28(3)	75(4)	-6(3)	-9(3)	-1(2)
C8A	27(3)	38(3)	45(3)	3(2)	-1(2)	5(2)
C9A	25(2)	34(3)	34(3)	6(2)	-4(2)	1(2)
C10A	21(2)	37(3)	27(2)	8(2)	-1.1(19)	-3(2)
C11A	20(2)	30(3)	30(3)	1(2)	-3.5(19)	-1.0(19)
C12A	26(2)	36(3)	37(3)	-3(2)	-4(2)	-1(2)

C13A	28(3)	35(3)	65(4)	-5(3)	-5(3)	11(2)
C14A	27(3)	35(3)	60(4)	2(3)	-21(3)	4(2)
C15A	24(2)	39(3)	42(3)	7(2)	-8(2)	0(2)
C16A	20(2)	27(2)	23(2)	0.4(19)	-1.7(17)	2.0(18)
C17A	20.2(13)	35.4(17)	24.0(12)	0.5(13)	1.0(7)	1.9(14)
C18A	20.2(13)	35.4(17)	24.0(12)	0.5(13)	1.0(7)	1.9(14)
C19A	20.2(13)	35.4(17)	24.0(12)	0.5(13)	1.0(7)	1.9(14)
C20A	20.2(13)	35.4(17)	24.0(12)	0.5(13)	1.0(7)	1.9(14)
C21A	20.2(13)	35.4(17)	24.0(12)	0.5(13)	1.0(7)	1.9(14)
C22A	20.2(13)	35.4(17)	24.0(12)	0.5(13)	1.0(7)	1.9(14)
C23A	20.2(13)	35.4(17)	24.0(12)	0.5(13)	1.0(7)	1.9(14)
C24A	20.2(13)	35.4(17)	24.0(12)	0.5(13)	1.0(7)	1.9(14)
C25A	20.2(13)	35.4(17)	24.0(12)	0.5(13)	1.0(7)	1.9(14)
C26A	20.2(13)	35.4(17)	24.0(12)	0.5(13)	1.0(7)	1.9(14)
C27A	19(2)	38(3)	20(2)	0(2)	-3.3(17)	1(2)
C28A	29(3)	39(3)	28(3)	-1(2)	-6(2)	5(2)
C29A	39(3)	51(3)	26(3)	-4(2)	1(2)	16(3)
C30A	59(4)	59(4)	28(3)	11(3)	12(3)	24(3)
C31A	37(3)	51(3)	33(3)	10(2)	6(2)	16(3)
C32A	18(2)	42(3)	24(2)	3(2)	-1.0(18)	10(2)
C33A	26(2)	33(3)	20(2)	5.7(19)	2.3(19)	-2(2)
C34A	23(2)	29(2)	26(2)	0.3(19)	-1.2(19)	2.4(19)
C35A	35(3)	38(3)	23(2)	6(2)	1(2)	1(2)
C36A	62(4)	38(3)	20(3)	-7(2)	4(2)	7(3)
C37A	48(3)	33(3)	34(3)	-8(2)	2(2)	-1(2)

C38A	27(2)	36(3)	28(3)	1(2)	-2(2)	3(2)
C39A	29(3)	29(3)	37(3)	1(2)	1(2)	2(2)
C40A	24(2)	34(3)	32(3)	2(2)	-1(2)	4(2)
C41A	22(2)	40(3)	23(2)	5(2)	-1.8(18)	0(2)
C42A	20(2)	26(2)	26(2)	1.0(19)	-1.3(18)	-2.9(18)
C43A	22(2)	27(2)	24(2)	0.7(19)	-2.8(18)	3.3(19)
C44A	24(2)	27(2)	22(2)	-3.2(19)	-3.1(18)	-0.6(19)
C45A	24(2)	34(3)	22(2)	3(2)	-5.9(19)	0(2)
C46A	28(2)	36(3)	19(2)	0(2)	0.3(19)	-4(2)
C47A	25(2)	36(3)	20(2)	2(2)	-0.9(18)	2(2)
C48A	24(2)	34(3)	19(2)	6.2(19)	-2.0(18)	1(2)
C49A	27(2)	43(3)	18(2)	4(2)	-5.0(19)	-8(2)
C50A	35(3)	36(3)	25(2)	2(2)	1(2)	-7(2)
C51A	51(3)	38(3)	32(3)	-3(2)	13(2)	-8(3)
C52A	69(4)	44(3)	46(4)	-17(3)	19(3)	-9(3)
C53A	66(4)	53(4)	27(3)	-8(3)	5(3)	-26(3)
C54A	93(5)	48(4)	53(4)	-14(3)	16(4)	-30(4)
C55A	72(5)	64(4)	68(5)	-4(4)	10(4)	-40(4)
C56A	46(4)	71(4)	47(4)	5(3)	4(3)	-26(3)
C57A	37(3)	47(3)	33(3)	9(2)	-3(2)	-11(2)
C58A	26(2)	41(3)	27(2)	4(2)	-6(2)	-9(2)
C17B	20.2(13)	35.4(17)	24.0(12)	0.5(13)	1.0(7)	1.9(14)
C18B	20.2(13)	35.4(17)	24.0(12)	0.5(13)	1.0(7)	1.9(14)
C19B	20.2(13)	35.4(17)	24.0(12)	0.5(13)	1.0(7)	1.9(14)
C20B	20.2(13)	35.4(17)	24.0(12)	0.5(13)	1.0(7)	1.9(14)

C21B	20.2(13)	35.4(17)	24.0(12)	0.5(13)	1.0(7)	1.9(14)
C22B	20.2(13)	35.4(17)	24.0(12)	0.5(13)	1.0(7)	1.9(14)
C23B	20.2(13)	35.4(17)	24.0(12)	0.5(13)	1.0(7)	1.9(14)
C24B	20.2(13)	35.4(17)	24.0(12)	0.5(13)	1.0(7)	1.9(14)
C25B	20.2(13)	35.4(17)	24.0(12)	0.5(13)	1.0(7)	1.9(14)
C26B	20.2(13)	35.4(17)	24.0(12)	0.5(13)	1.0(7)	1.9(14)

Table C-26. Bond Lengths for TNSB BDP **7**.

Atom	**Atom**	**Length/Å**	**Atom**	**Atom**	**Length/Å**
P1	C11	1.892(5)	O1A	C12A	1.221(6)
P1	C16	1.938(5)	O2A	C15A	1.212(6)
P1	C27	1.856(5)	O3A	C44A	1.223(5)
P2	C32	1.850(5)	O4A	C47A	1.228(5)
P2	C33	1.910(4)	N1A	N2A	1.396(5)
P2	C48	1.888(5)	N1A	C11A	1.467(6)
O1	C12	1.225(6)	N1A	C12A	1.359(6)
O2	C15	1.220(6)	N2A	C15A	1.390(6)
O3	C44	1.230(5)	N2A	C16A	1.469(6)
O4	C47	1.242(5)	N3A	N4A	1.420(5)
N1	N2	1.416(5)	N3A	C33A	1.470(6)
N1	C11	1.488(6)	N3A	C44A	1.362(6)
N1	C12	1.350(6)	N4A	C47A	1.357(6)
N2	C15	1.368(6)	N4A	C48A	1.473(6)
N2	C16	1.449(6)	C1A	C2A	1.417(7)
N3	N4	1.406(5)	C1A	C10A	1.371(7)

N3	C33	1.467(6)	C2A	C3A	1.364(8)
N3	C44	1.361(6)	C3A	C4A	1.397(8)
N4	C47	1.350(6)	C4A	C5A	1.424(7)
N4	C48	1.475(5)	C4A	C9A	1.427(7)
C1	C2	1.394(9)	C5A	C6A	1.343(9)
C1	C6	1.419(8)	C6A	C7A	1.414(9)
C1	C10	1.448(7)	C7A	C8A	1.360(7)
C2	C3	1.373(8)	C8A	C9A	1.405(7)
C3	C4	1.394(11)	C9A	C10A	1.436(7)
C4	C5	1.352(11)	C10A	C11A	1.540(6)
C5	C6	1.424(8)	C12A	C13A	1.510(7)
C6	C7	1.424(9)	C13A	C14A	1.528(8)
C7	C8	1.358(9)	C14A	C15A	1.494(7)
C8	C9	1.427(8)	C16A	C17A	1.525(5)
C9	C10	1.374(7)	C16A	C17B	1.535(5)
C10	C11	1.496(7)	C17A	C18A	1.3900
C12	C13	1.505(7)	C17A	C22A	1.3900
C13	C14	1.515(8)	C18A	C19A	1.3900
C14	C15	1.516(8)	C19A	C20A	1.3900
C16	C17	1.511(7)	C20A	C21A	1.3900
C17	C18	1.385(6)	C21A	C22A	1.3900
C17	C26	1.425(7)	C21A	C26A	1.3900
C18	C19	1.417(7)	C22A	C23A	1.3900
C19	C20	1.353(7)	C23A	C24A	1.3900
C20	C21	1.424(7)	C24A	C25A	1.3900

C21	C22	1.410(7)	C25A	C26A	1.3900
C21	C26	1.423(7)	C27A	C28A	1.396(7)
C22	C23	1.362(8)	C27A	C32A	1.423(7)
C23	C24	1.400(8)	C28A	C29A	1.379(7)
C24	C25	1.369(7)	C29A	C30A	1.382(8)
C25	C26	1.421(7)	C30A	C31A	1.383(8)
C27	C28	1.386(7)	C31A	C32A	1.393(7)
C27	C32	1.416(7)	C33A	C34A	1.513(6)
C28	C29	1.387(7)	C34A	C35A	1.372(6)
C29	C30	1.384(8)	C34A	C43A	1.434(6)
C30	C31	1.375(7)	C35A	C36A	1.418(7)
C31	C32	1.393(7)	C36A	C37A	1.356(7)
C33	C34	1.508(7)	C37A	C38A	1.412(7)
C34	C35	1.363(7)	C38A	C39A	1.416(7)
C34	C43	1.431(7)	C38A	C43A	1.429(7)
C35	C36	1.408(8)	C39A	C40A	1.363(7)
C36	C37	1.360(9)	C40A	C41A	1.408(7)
C37	C38	1.412(8)	C41A	C42A	1.364(6)
C38	C39	1.422(8)	C42A	C43A	1.421(6)
C38	C43	1.428(7)	C44A	C45A	1.518(6)
C39	C40	1.371(9)	C45A	C46A	1.539(6)
C40	C41	1.406(8)	C46A	C47A	1.496(6)
C41	C42	1.361(7)	C48A	C49A	1.507(7)
C42	C43	1.420(7)	C49A	C50A	1.380(6)
C44	C45	1.512(7)	C49A	C58A	1.438(7)

C45	C46	1.521(7)	C50A	C51A	1.404(7)
C46	C47	1.509(6)	C51A	C52A	1.361(8)
C48	C49	1.513(7)	C52A	C53A	1.403(8)
C49	C50	1.381(7)	C53A	C54A	1.422(8)
C49	C58	1.432(7)	C53A	C58A	1.411(8)
C50	C51	1.398(7)	C54A	C55A	1.369(9)
C51	C52	1.365(8)	C55A	C56A	1.384(9)
C52	C53	1.399(8)	C56A	C57A	1.367(8)
C53	C54	1.419(8)	C57A	C58A	1.416(7)
C53	C58	1.433(7)	C17B	C18B	1.3900
C54	C55	1.376(9)	C17B	C22B	1.3900
C55	C56	1.404(9)	C18B	C19B	1.3900
C56	C57	1.366(8)	C19B	C20B	1.3900
C57	C58	1.431(7)	C20B	C21B	1.3900
P1A	C11A	1.882(5)	C21B	C22B	1.3900
P1A	C16A	1.929(4)	C21B	C26B	1.3900
P1A	C27A	1.849(4)	C22B	C23B	1.3900
P2A	C32A	1.845(5)	C23B	C24B	1.3900
P2A	C33A	1.913(5)	C24B	C25B	1.3900
P2A	C48A	1.872(5)	C25B	C26B	1.3900

Table C-27. Bond Angles for TNSB BDP **7**.

Atom	**Atom**	**Atom**	**Angle/°**	**Atom**	**Atom**	**Atom**	**Angle/°**
C11	P1	C16	91.1(2)	N1A	N2A	C16A	115.5(3)
C27	P1	C11	100.4(2)	C15A	N2A	N1A	120.1(4)

C27	P1	C16	101.1(2)	C15A	N2A	C16A	124.2(4)
C32	P2	C33	104.6(2)	N4A	N3A	C33A	113.6(3)
C32	P2	C48	99.5(2)	C44A	N3A	N4A	121.4(3)
C48	P2	C33	90.1(2)	C44A	N3A	C33A	124.3(4)
N2	N1	C11	112.4(4)	N3A	N4A	C48A	113.2(3)
C12	N1	N2	121.6(4)	C47A	N4A	N3A	120.3(4)
C12	N1	C11	124.1(4)	C47A	N4A	C48A	126.5(4)
N1	N2	C16	112.9(3)	C10A	C1A	C2A	120.8(5)
C15	N2	N1	122.0(4)	C3A	C2A	C1A	119.6(5)
C15	N2	C16	125.1(4)	C2A	C3A	C4A	121.6(5)
N4	N3	C33	114.3(3)	C3A	C4A	C5A	121.6(5)
C44	N3	N4	120.4(4)	C3A	C4A	C9A	119.7(5)
C44	N3	C33	124.6(4)	C5A	C4A	C9A	118.6(5)
N3	N4	C48	112.4(3)	C6A	C5A	C4A	121.2(6)
C47	N4	N3	120.4(4)	C5A	C6A	C7A	120.2(5)
C47	N4	C48	127.2(4)	C8A	C7A	C6A	120.3(6)
C2	C1	C6	116.9(5)	C7A	C8A	C9A	121.4(5)
C2	C1	C10	124.9(6)	C4A	C9A	C10A	117.9(5)
C6	C1	C10	118.3(6)	C8A	C9A	C4A	118.3(5)
C3	C2	C1	122.5(7)	C8A	C9A	C10A	123.8(5)
C2	C3	C4	119.6(8)	C1A	C10A	C9A	120.3(4)
C5	C4	C3	121.0(7)	C1A	C10A	C11A	118.9(4)
C4	C5	C6	119.7(7)	C9A	C10A	C11A	120.8(4)
C1	C6	C5	120.3(7)	N1A	C11A	P1A	104.7(3)
C1	C6	C7	119.8(5)	N1A	C11A	C10A	112.0(4)

C7	C6	C5	119.9(6)	C10A	C11A	P1A	110.5(3)
C8	C7	C6	121.0(6)	O1A	C12A	N1A	121.9(4)
C7	C8	C9	120.1(6)	O1A	C12A	C13A	125.8(5)
C10	C9	C8	120.9(5)	N1A	C12A	C13A	112.2(4)
C1	C10	C11	120.7(5)	C12A	C13A	C14A	109.4(4)
C9	C10	C1	119.9(5)	C15A	C14A	C13A	110.0(4)
C9	C10	C11	119.4(5)	O2A	C15A	N2A	120.0(5)
N1	C11	P1	104.8(3)	O2A	C15A	C14A	127.2(4)
N1	C11	C10	110.5(4)	N2A	C15A	C14A	112.7(4)
C10	C11	P1	113.8(3)	N2A	C16A	P1A	104.7(3)
O1	C12	N1	121.3(5)	N2A	C16A	C17A	111.5(4)
O1	C12	C13	124.9(5)	N2A	C16A	C17B	121.0(4)
N1	C12	C13	113.8(5)	C17A	C16A	P1A	112.9(5)
C12	C13	C14	111.0(4)	C17B	C16A	P1A	109.5(4)
C13	C14	C15	109.9(4)	C18A	C17A	C16A	118.9(3)
O2	C15	N2	121.2(5)	C18A	C17A	C22A	120.0
O2	C15	C14	124.8(5)	C22A	C17A	C16A	121.1(3)
N2	C15	C14	113.8(5)	C17A	C18A	C19A	120.0
N2	C16	P1	104.9(3)	C20A	C19A	C18A	120.0
N2	C16	C17	113.8(4)	C19A	C20A	C21A	120.0
C17	C16	P1	112.8(3)	C20A	C21A	C26A	120.0
C18	C17	C16	120.9(4)	C22A	C21A	C20A	120.0
C18	C17	C26	119.1(4)	C22A	C21A	C26A	120.0
C26	C17	C16	119.8(4)	C21A	C22A	C17A	120.0
C17	C18	C19	120.7(5)	C21A	C22A	C23A	120.0

C20	C19	C18	120.8(5)	C23A	C22A	C17A	120.0
C19	C20	C21	120.4(5)	C24A	C23A	C22A	120.0
C22	C21	C20	121.3(5)	C25A	C24A	C23A	120.0
C22	C21	C26	119.5(5)	C26A	C25A	C24A	120.0
C26	C21	C20	119.1(5)	C25A	C26A	C21A	120.0
C23	C22	C21	121.4(5)	C28A	C27A	P1A	124.1(4)
C22	C23	C24	119.2(5)	C28A	C27A	C32A	119.2(4)
C25	C24	C23	121.5(5)	C32A	C27A	P1A	116.3(3)
C24	C25	C26	120.5(5)	C29A	C28A	C27A	120.3(5)
C21	C26	C17	119.4(4)	C28A	C29A	C30A	120.4(5)
C25	C26	C17	122.8(5)	C29A	C30A	C31A	120.2(5)
C25	C26	C21	117.8(5)	C30A	C31A	C32A	120.7(5)
C28	C27	P1	120.7(4)	C27A	C32A	P2A	116.2(3)
C28	C27	C32	119.1(4)	C31A	C32A	P2A	124.9(4)
C32	C27	P1	120.0(3)	C31A	C32A	C27A	118.7(4)
C27	C28	C29	122.1(5)	N3A	C33A	P2A	106.9(3)
C30	C29	C28	118.6(5)	N3A	C33A	C34A	113.6(4)
C31	C30	C29	120.1(5)	C34A	C33A	P2A	111.3(3)
C30	C31	C32	122.3(5)	C35A	C34A	C33A	121.2(4)
C27	C32	P2	119.2(3)	C35A	C34A	C43A	120.1(4)
C31	C32	P2	122.7(4)	C43A	C34A	C33A	118.5(4)
C31	C32	C27	117.7(4)	C34A	C35A	C36A	120.0(4)
N3	C33	P2	106.6(3)	C37A	C36A	C35A	121.3(5)
N3	C33	C34	113.6(4)	C36A	C37A	C38A	120.5(5)
C34	C33	P2	111.9(3)	C37A	C38A	C39A	121.2(5)

C35	C34	C33	121.6(5)	C37A	C38A	C43A	119.4(4)
C35	C34	C43	120.1(5)	C39A	C38A	C43A	119.4(4)
C43	C34	C33	118.3(4)	C40A	C39A	C38A	120.8(5)
C34	C35	C36	121.4(6)	C39A	C40A	C41A	120.0(5)
C37	C36	C35	119.8(5)	C42A	C41A	C40A	120.9(4)
C36	C37	C38	121.4(5)	C41A	C42A	C43A	120.9(4)
C37	C38	C39	122.3(5)	C38A	C43A	C34A	118.7(4)
C37	C38	C43	119.0(5)	C42A	C43A	C34A	123.3(4)
C39	C38	C43	118.5(5)	C42A	C43A	C38A	118.0(4)
C40	C39	C38	121.2(5)	O3A	C44A	N3A	121.2(4)
C39	C40	C41	120.1(5)	O3A	C44A	C45A	125.6(4)
C42	C41	C40	120.0(6)	N3A	C44A	C45A	113.1(4)
C41	C42	C43	121.9(5)	C44A	C45A	C46A	110.1(4)
C38	C43	C34	118.4(5)	C47A	C46A	C45A	108.5(4)
C42	C43	C34	123.6(4)	O4A	C47A	N4A	120.6(4)
C42	C43	C38	118.0(5)	O4A	C47A	C46A	124.8(4)
O3	C44	N3	121.7(4)	N4A	C47A	C46A	114.5(4)
O3	C44	C45	125.4(4)	N4A	C48A	P2A	104.8(3)
N3	C44	C45	112.8(4)	N4A	C48A	C49A	111.8(4)
C44	C45	C46	110.4(4)	C49A	C48A	P2A	112.2(3)
C47	C46	C45	109.3(4)	C50A	C49A	C48A	120.5(4)
O4	C47	N4	121.5(4)	C50A	C49A	C58A	118.5(5)
O4	C47	C46	124.4(4)	C58A	C49A	C48A	121.0(4)
N4	C47	C46	113.9(4)	C49A	C50A	C51A	122.2(5)
N4	C48	P2	104.2(3)	C52A	C51A	C50A	118.9(5)

N4	C48	C49	110.5(4)	C51A	C52A	C53A	121.9(5)
C49	C48	P2	114.6(3)	C52A	C53A	C54A	121.6(6)
C50	C49	C48	119.7(4)	C52A	C53A	C58A	119.4(5)
C50	C49	C58	119.2(5)	C58A	C53A	C54A	119.0(5)
C58	C49	C48	121.0(4)	C55A	C54A	C53A	121.1(6)
C49	C50	C51	121.2(5)	C54A	C55A	C56A	119.5(6)
C52	C51	C50	120.9(5)	C57A	C56A	C55A	121.1(6)
C51	C52	C53	120.2(5)	C56A	C57A	C58A	121.2(6)
C52	C53	C54	120.6(5)	C53A	C58A	C49A	119.0(4)
C52	C53	C58	120.1(5)	C53A	C58A	C57A	118.0(5)
C54	C53	C58	119.3(5)	C57A	C58A	C49A	123.0(5)
C55	C54	C53	120.8(6)	C18B	C17B	C16A	115.7(4)
C54	C55	C56	119.9(6)	C18B	C17B	C22B	120.0
C57	C56	C55	121.2(6)	C22B	C17B	C16A	124.2(4)
C56	C57	C58	120.8(5)	C19B	C18B	C17B	120.0
C49	C58	C53	118.4(4)	C18B	C19B	C20B	120.0
C57	C58	C49	123.7(5)	C21B	C20B	C19B	120.0
C57	C58	C53	118.0(5)	C20B	C21B	C26B	120.0
C11A	P1A	C16A	90.8(2)	C22B	C21B	C20B	120.0
C27A	P1A	C11A	102.4(2)	C22B	C21B	C26B	120.0
C27A	P1A	C16A	99.26(19)	C21B	C22B	C17B	120.0
C32A	P2A	C33A	99.9(2)	C23B	C22B	C17B	120.0
C32A	P2A	C48A	102.1(2)	C23B	C22B	C21B	120.0
C48A	P2A	C33A	90.4(2)	C22B	C23B	C24B	120.0
N2A	N1A	C11A	112.2(3)	C25B	C24B	C23B	120.0

C12A	N1A	N2A	122.2(4)	C24B	C25B	C26B	120.0
C12A	N1A	C11A	125.7(4)	C25B	C26B	C21B	120.0

Table C-28. Torsion Angles for TNSB BDP **7**.

A	**B**	**C**	**D**	**Angle/˚**	**A**	**B**	**C**	**D**	**Angle/˚**
P1	C16	C17	C18	109.1(4)	N1A	N2A	C15A	C14A	11.8(6)
P1	C16	C17	C26	-65.2(5)	N1A	N2A	C16A	P1A	15.8(4)
P1	C27	C28	C29	171.9(4)	N1A	N2A	C16A	C17A	-106.6(5)
P1	C27	C32	P2	-1.6(5)	N1A	N2A	C16A	C17B	-108.2(6)
P1	C27	C32	C31	-174.7(4)	N1A	C12A	C13A	C14A	38.2(6)
P2	C33	C34	C35	94.8(5)	N2A	N1A	C11A	P1A	36.6(4)
P2	C33	C34	C43	-83.8(4)	N2A	N1A	C11A	C10A	-83.1(5)
P2	C48	C49	C50	28.6(5)	N2A	N1A	C12A	O1A	-174.1(4)
P2	C48	C49	C58	-152.7(4)	N2A	N1A	C12A	C13A	9.7(7)
O1	C12	C13	C14	137.9(5)	N2A	C16A	C17A	C18A	21.1(5)
O3	C44	C45	C46	141.0(5)	N2A	C16A	C17A	C22A	-159.4(3)
N1	N2	C15	O2	174.9(5)	N2A	C16A	C17B	C18B	20.3(6)
N1	N2	C15	C14	-8.8(7)	N2A	C16A	C17B	C22B	-156.9(4)
N1	N2	C16	P1	-30.5(4)	N3A	N4A	C47A	O4A	-176.4(4)
N1	N2	C16	C17	93.3(4)	N3A	N4A	C47A	C46A	5.7(6)
N1	C12	C13	C14	-39.0(6)	N3A	N4A	C48A	P2A	36.2(4)
N2	N1	C11	P1	-31.9(4)	N3A	N4A	C48A	C49A	-85.6(4)
N2	N1	C11	C10	91.0(5)	N3A	C33A	C34A	C35A	21.9(6)
N2	N1	C12	O1	178.9(4)	N3A	C33A	C34A	C43A	-163.2(4)
N2	N1	C12	C13	-4.1(7)	N3A	C44A	C45A	C46A	33.3(5)

N2	C16	C17	C18	-10.3(6)	N4A	N3A	C33A	P2A	9.0(4)
N2	C16	C17	C26	175.4(4)	N4A	N3A	C33A	C34A	-114.3(4)
N3	N4	C47	O4	171.2(4)	N4A	N3A	C44A	O3A	-170.5(4)
N3	N4	C47	C46	-13.9(6)	N4A	N3A	C44A	C45A	13.7(6)
N3	N4	C48	P2	-38.0(4)	N4A	C48A	C49A	C50A	84.5(5)
N3	N4	C48	C49	85.5(5)	N4A	C48A	C49A	C58A	-95.9(5)
N3	C33	C34	C35	-25.9(6)	C1A	C2A	C3A	C4A	2.7(9)
N3	C33	C34	C43	155.6(4)	C1A	C10A	C11A	P1A	-36.6(5)
N3	C44	C45	C46	-34.7(6)	C1A	C10A	C11A	N1A	79.7(5)
N4	N3	C33	P2	-11.4(4)	C2A	C1A	C10A	C9A	-0.1(8)
N4	N3	C33	C34	112.2(4)	C2A	C1A	C10A	C11A	177.9(5)
N4	N3	C44	O3	170.1(4)	C2A	C3A	C4A	C5A	-178.8(6)
N4	N3	C44	C45	-14.0(6)	C2A	C3A	C4A	C9A	0.5(9)
N4	C48	C49	C50	-88.7(5)	C3A	C4A	C5A	C6A	179.2(6)
N4	C48	C49	C58	90.0(5)	C3A	C4A	C9A	C8A	178.4(5)
C1	C2	C3	C4	-1.0(9)	C3A	C4A	C9A	C10A	-3.4(7)
C1	C6	C7	C8	-0.3(9)	C4A	C5A	C6A	C7A	1.9(9)
C1	C10	C11	P1	-138.4(4)	C4A	C9A	C10A	C1A	3.2(7)
C1	C10	C11	N1	104.0(5)	C4A	C9A	C10A	C11A	-174.7(4)
C2	C1	C6	C5	4.6(8)	C5A	C4A	C9A	C8A	-2.3(7)
C2	C1	C6	C7	-177.8(5)	C5A	C4A	C9A	C10A	175.9(5)
C2	C1	C10	C9	178.1(5)	C5A	C6A	C7A	C8A	-1.2(9)
C2	C1	C10	C11	-1.6(8)	C6A	C7A	C8A	C9A	-1.3(8)
C2	C3	C4	C5	2.6(10)	C7A	C8A	C9A	C4A	3.0(7)
C3	C4	C5	C6	-0.5(10)	C7A	C8A	C9A	C10A	-175.1(5)

C4	C5	C6	C1	-3.2(9)	C8A	C9A	C10A	C1A	-178.7(5)
C4	C5	C6	C7	179.2(6)	C8A	C9A	C10A	C11A	3.3(7)
C5	C6	C7	C8	177.3(5)	C9A	C4A	C5A	C6A	-0.1(8)
C6	C1	C2	C3	-2.6(8)	C9A	C10A	C11A	P1A	141.3(4)
C6	C1	C10	C9	-2.0(7)	C9A	C10A	C11A	N1A	-102.4(5)
C6	C1	C10	C11	178.3(4)	C10A	C1A	C2A	C3A	-2.9(8)
C6	C7	C8	C9	-2.0(9)	C11A	P1A	C27A	C28A	-16.3(4)
C7	C8	C9	C10	2.3(8)	C11A	P1A	C27A	C32A	169.7(3)
C8	C9	C10	C1	-0.2(8)	C11A	N1A	N2A	C15A	139.8(4)
C8	C9	C10	C11	179.5(5)	C11A	N1A	N2A	C16A	-36.1(5)
C9	C10	C11	P1	41.9(6)	C11A	N1A	C12A	O1A	7.7(8)
C9	C10	C11	N1	-75.7(6)	C11A	N1A	C12A	C13A	-168.6(4)
C10	C1	C2	C3	177.4(5)	C12A	N1A	N2A	C15A	-38.7(6)
C10	C1	C6	C5	-175.3(5)	C12A	N1A	N2A	C16A	145.4(4)
C10	C1	C6	C7	2.3(8)	C12A	N1A	C11A	P1A	-144.9(4)
C11	P1	C27	C28	33.8(4)	C12A	N1A	C11A	C10A	95.3(5)
C11	P1	C27	C32	-151.3(4)	C12A	C13A	C14A	C15A	-61.5(6)
C11	N1	N2	C15	-133.6(5)	C13A	C14A	C15A	O2A	-140.4(6)
C11	N1	N2	C16	43.2(5)	C13A	C14A	C15A	N2A	35.7(6)
C11	N1	C12	O1	-18.4(8)	C15A	N2A	C16A	P1A	-160.0(4)
C11	N1	C12	C13	158.5(4)	C15A	N2A	C16A	C17A	77.6(6)
C12	N1	N2	C15	30.9(7)	C15A	N2A	C16A	C17B	76.0(7)
C12	N1	N2	C16	-152.3(4)	C16A	P1A	C11A	N1A	-22.4(3)
C12	N1	C11	P1	164.0(4)	C16A	P1A	C11A	C10A	98.4(3)
C12	N1	C11	C10	-73.0(6)	C16A	P1A	C27A	C28A	76.6(4)

C12	C13	C14	C15	57.8(6)	C16A	P1A	C27A	C32A	-97.4(4)
C13	C14	C15	O2	142.3(6)	C16A	N2A	C15A	O2A	3.9(7)
C13	C14	C15	N2	-33.8(6)	C16A	N2A	C15A	C14A	-172.6(4)
C15	N2	C16	P1	146.3(4)	C16A	C17A	C18A	C19A	179.6(7)
C15	N2	C16	C17	-89.9(5)	C16A	C17A	C22A	C21A	-179.6(7)
C16	P1	C11	N1	11.5(3)	C16A	C17A	C22A	C23A	0.4(7)
C16	P1	C11	C10	-109.3(4)	C16A	C17B	C18B	C19B	-177.3(6)
C16	P1	C27	C28	-59.4(4)	C16A	C17B	C22B	C21B	177.0(7)
C16	P1	C27	C32	115.6(4)	C16A	C17B	C22B	C23B	-3.0(7)
C16	N2	C15	O2	-1.5(8)	C17A	C18A	C19A	C20A	0.0
C16	N2	C15	C14	174.8(4)	C17A	C22A	C23A	C24A	180.0
C16	C17	C18	C19	-171.1(4)	C18A	C17A	C22A	C21A	0.0
C16	C17	C26	C21	167.3(4)	C18A	C17A	C22A	C23A	180.0
C16	C17	C26	C25	-12.9(6)	C18A	C19A	C20A	C21A	0.0
C17	C18	C19	C20	3.2(8)	C19A	C20A	C21A	C22A	0.0
C18	C17	C26	C21	-7.1(6)	C19A	C20A	C21A	C26A	180.0
C18	C17	C26	C25	172.7(4)	C20A	C21A	C22A	C17A	0.0
C18	C19	C20	C21	-5.7(8)	C20A	C21A	C22A	C23A	180.0
C19	C20	C21	C22	-176.4(5)	C20A	C21A	C26A	C25A	180.0
C19	C20	C21	C26	1.6(7)	C21A	C22A	C23A	C24A	0.0
C20	C21	C22	C23	174.6(5)	C22A	C17A	C18A	C19A	0.0
C20	C21	C26	C17	4.8(6)	C22A	C21A	C26A	C25A	0.0
C20	C21	C26	C25	-175.1(4)	C22A	C23A	C24A	C25A	0.0
C21	C22	C23	C24	1.0(7)	C23A	C24A	C25A	C26A	0.0
C22	C21	C26	C17	-177.2(4)	C24A	C25A	C26A	C21A	0.0

C22	C21	C26	C25	3.0(6)	C26A	C21A	C22A	C17A	180.0
C22	C23	C24	C25	1.7(7)	C26A	C21A	C22A	C23A	0.0
C23	C24	C25	C26	-2.0(7)	C27A	P1A	C11A	N1A	77.2(3)
C24	C25	C26	C17	179.8(4)	C27A	P1A	C11A	C10A	-162.0(3)
C24	C25	C26	C21	-0.3(6)	C27A	C28A	C29A	C30A	1.5(8)
C26	C17	C18	C19	3.2(7)	C28A	C27A	C32A	P2A	168.3(3)
C26	C21	C22	C23	-3.4(7)	C28A	C27A	C32A	C31A	-6.9(7)
C27	P1	C11	N1	-89.9(3)	C28A	C29A	C30A	C31A	-4.9(9)
C27	P1	C11	C10	149.3(3)	C29A	C30A	C31A	C32A	2.3(9)
C27	C28	C29	C30	3.1(9)	C30A	C31A	C32A	P2A	-171.2(4)
C28	C27	C32	P2	173.4(4)	C30A	C31A	C32A	C27A	3.6(8)
C28	C27	C32	C31	0.3(7)	C32A	P2A	C48A	N4A	75.2(3)
C28	C29	C30	C31	-0.4(9)	C32A	P2A	C48A	C49A	-163.3(3)
C29	C30	C31	C32	-2.4(9)	C32A	C27A	C28A	C29A	4.5(7)
C30	C31	C32	P2	-170.4(4)	C33A	P2A	C32A	C27A	-100.0(4)
C30	C31	C32	C27	2.4(8)	C33A	P2A	C32A	C31A	74.8(5)
C32	P2	C48	N4	-79.4(3)	C33A	P2A	C48A	N4A	-25.0(3)
C32	P2	C48	C49	159.7(3)	C33A	P2A	C48A	C49A	96.5(3)
C32	C27	C28	C29	-3.1(8)	C33A	N3A	N4A	C47A	152.6(4)
C33	P2	C32	C27	106.6(4)	C33A	N3A	N4A	C48A	-30.6(5)
C33	P2	C32	C31	-80.6(4)	C33A	N3A	C44A	O3A	-1.1(7)
C33	P2	C48	N4	25.4(3)	C33A	N3A	C44A	C45A	-176.9(4)
C33	P2	C48	C49	-95.5(3)	C33A	C34A	C35A	C36A	173.4(5)
C33	N3	N4	C47	-146.8(4)	C33A	C34A	C43A	C38A	-173.6(4)
C33	N3	N4	C48	33.7(5)	C33A	C34A	C43A	C42A	6.1(6)

C33	N3	C44	O3	0.4(7)	C34A	C35A	C36A	C37A	0.6(8)
C33	N3	C44	C45	176.2(4)	C35A	C34A	C43A	C38A	1.4(7)
C33	C34	C35	C36	-177.4(4)	C35A	C34A	C43A	C42A	-178.9(4)
C33	C34	C43	C38	178.0(4)	C35A	C36A	C37A	C38A	0.6(8)
C33	C34	C43	C42	-3.8(6)	C36A	C37A	C38A	C39A	178.7(5)
C34	C35	C36	C37	0.1(8)	C36A	C37A	C38A	C43A	-0.7(8)
C35	C34	C43	C38	-0.6(6)	C37A	C38A	C39A	C40A	-179.8(5)
C35	C34	C43	C42	177.6(4)	C37A	C38A	C43A	C34A	-0.3(7)
C35	C36	C37	C38	-1.9(8)	C37A	C38A	C43A	C42A	180.0(4)
C36	C37	C38	C39	-174.2(5)	C38A	C39A	C40A	C41A	-0.9(7)
C36	C37	C38	C43	2.4(7)	C39A	C38A	C43A	C34A	-179.7(4)
C37	C38	C39	C40	176.7(5)	C39A	C38A	C43A	C42A	0.5(6)
C37	C38	C43	C34	-1.1(6)	C39A	C40A	C41A	C42A	2.0(7)
C37	C38	C43	C42	-179.4(4)	C40A	C41A	C42A	C43A	-1.8(7)
C38	C39	C40	C41	1.9(8)	C41A	C42A	C43A	C34A	-179.2(4)
C39	C38	C43	C34	175.6(4)	C41A	C42A	C43A	C38A	0.5(6)
C39	C38	C43	C42	-2.7(6)	C43A	C34A	C35A	C36A	-1.5(7)
C39	C40	C41	C42	-1.3(8)	C43A	C38A	C39A	C40A	-0.4(7)
C40	C41	C42	C43	-1.4(7)	C44A	N3A	N4A	C47A	-37.0(6)
C41	C42	C43	C34	-174.8(4)	C44A	N3A	N4A	C48A	139.9(4)
C41	C42	C43	C38	3.4(7)	C44A	N3A	C33A	P2A	-161.2(3)
C43	C34	C35	C36	1.1(7)	C44A	N3A	C33A	C34A	75.6(5)
C43	C38	C39	C40	0.1(7)	C44A	C45A	C46A	C47A	-60.2(5)
C44	N3	N4	C47	42.4(6)	C45A	C46A	C47A	O4A	-137.5(5)
C44	N3	N4	C48	-137.0(4)	C45A	C46A	C47A	N4A	40.4(5)

C44	N3	C33	P2	158.9(4)	C47A	N4A	C48A	P2A	-147.2(4)
C44	N3	C33	C34	-77.5(5)	C47A	N4A	C48A	C49A	91.0(5)
C44	C45	C46	C47	58.9(5)	C48A	P2A	C32A	C27A	167.5(3)
C45	C46	C47	O4	140.3(5)	C48A	P2A	C32A	C31A	-17.7(5)
C45	C46	C47	N4	-34.4(6)	C48A	N4A	C47A	O4A	7.2(7)
C47	N4	C48	P2	142.6(4)	C48A	N4A	C47A	C46A	-170.7(4)
C47	N4	C48	C49	-93.8(5)	C48A	C49A	C50A	C51A	179.5(5)
C48	P2	C32	C27	-160.8(4)	C48A	C49A	C58A	C53A	-179.0(5)
C48	P2	C32	C31	11.9(4)	C48A	C49A	C58A	C57A	3.5(7)
C48	N4	C47	O4	-9.5(8)	C49A	C50A	C51A	C52A	-1.3(8)
C48	N4	C47	C46	165.4(4)	C50A	C49A	C58A	C53A	0.5(7)
C48	C49	C50	C51	177.9(4)	C50A	C49A	C58A	C57A	-176.9(5)
C48	C49	C58	C53	-176.6(4)	C50A	C51A	C52A	C53A	2.3(10)
C48	C49	C58	C57	3.2(7)	C51A	C52A	C53A	C54A	179.0(6)
C49	C50	C51	C52	0.0(8)	C51A	C52A	C53A	C58A	-1.9(10)
C50	C49	C58	C53	2.1(7)	C52A	C53A	C54A	C55A	-177.2(7)
C50	C49	C58	C57	-178.0(4)	C52A	C53A	C58A	C49A	0.4(8)
C50	C51	C52	C53	-0.4(8)	C52A	C53A	C58A	C57A	177.9(5)
C51	C52	C53	C54	-179.2(5)	C53A	C54A	C55A	C56A	-2.1(12)
C51	C52	C53	C58	1.7(8)	C54A	C53A	C58A	C49A	179.5(5)
C52	C53	C54	C55	-177.2(6)	C54A	C53A	C58A	C57A	-2.9(8)
C52	C53	C58	C49	-2.6(7)	C54A	C55A	C56A	C57A	-0.2(11)
C52	C53	C58	C57	177.6(5)	C55A	C56A	C57A	C58A	0.9(9)
C53	C54	C55	C56	-1.3(10)	C56A	C57A	C58A	C49A	178.1(5)
C54	C53	C58	C49	178.4(5)	C56A	C57A	C58A	C53A	0.7(8)

C54	C53	C58	C57	-1.5(7)	C58A	C49A	C50A	C51A	-0.1(7)
C54	C55	C56	C57	0.4(10)	C58A	C53A	C54A	C55A	3.7(11)
C55	C56	C57	C58	0.0(9)	C17B	C18B	C19B	C20B	0.0
C56	C57	C58	C49	-179.2(5)	C17B	C22B	C23B	C24B	180.0
C56	C57	C58	C53	0.6(7)	C18B	C17B	C22B	C21B	0.0
C58	C49	C50	C51	-0.9(7)	C18B	C17B	C22B	C23B	180.0
C58	C53	C54	C55	1.9(8)	C18B	C19B	C20B	C21B	0.0
P1A	C16A	C17A	C18A	-96.5(4)	C19B	C20B	C21B	C22B	0.0
P1A	C16A	C17A	C22A	83.1(5)	C19B	C20B	C21B	C26B	180.0
P1A	C16A	C17B	C18B	-101.4(3)	C20B	C21B	C22B	C17B	0.0
P1A	C16A	C17B	C22B	81.4(5)	C20B	C21B	C22B	C23B	180.0
P1A	C27A	C28A	C29A	-169.4(4)	C20B	C21B	C26B	C25B	180.0
P1A	C27A	C32A	P2A	-17.4(5)	C21B	C22B	C23B	C24B	0.0
P1A	C27A	C32A	C31A	167.4(4)	C22B	C17B	C18B	C19B	0.0
P2A	C33A	C34A	C35A	-98.9(5)	C22B	C21B	C26B	C25B	0.0
P2A	C33A	C34A	C43A	76.1(4)	C22B	C23B	C24B	C25B	0.0
P2A	C48A	C49A	C50A	-32.9(5)	C23B	C24B	C25B	C26B	0.0
P2A	C48A	C49A	C58A	146.7(4)	C24B	C25B	C26B	C21B	0.0
O1A	C12A	C13A	C14A	-137.9(5)	C26B	C21B	C22B	C17B	180.0
O3A	C44A	C45A	C46A	-142.3(4)	C26B	C21B	C22B	C23B	0.0
N1A	N2A	C15A	O2A	-171.7(4)					

Table C-29. Hydrogen Atom Coordinates ($Å \times 10^4$) and Isotropic Displacement Parameters ($Å^2 \times 10^3$) for TNSB BDP **7**.

Atom	*x*	*y*	*z*	U(eq)
H2	8789.8	5573.7	5881.36	65
H3	9228.33	5025.23	5322.5	85
H4	10100.15	4679.6	6023.22	91
H5	10471.3	4857.05	7306.33	76
H7	10389.22	5286.61	8478.52	71
H8	9961.74	5827.1	9072.97	61
H9	9191.03	6232.3	8329.7	48
H11	8603.2	6099.22	6283.42	39
H13C	6706.9	5527.4	7687.42	48
H13D	6485.9	5959.6	7551.55	48
H14C	7539.22	5705.54	8701.99	54
H14D	6772.56	5862.49	8938.44	54
H16	8195.08	6881.61	8196.25	33
H18	6707.36	6635.67	7125.65	38
H19	5921.79	7025.89	6380.45	45
H20	6262.39	7618.61	5980.15	46
H22	7107.56	8152.71	6091.78	46
H23	8101.38	8425.74	6676.02	51
H24	8820.91	8071.52	7565.87	45
H25	8582.94	7445.38	7824.43	40
H28	7713.11	6490.92	5846.59	46
H29	7176.28	6769.83	4708.37	56
H30	7705.37	7300.52	4121.29	55
H31	8736.37	7545.89	4677.55	44

H33	10804.65	7304.34	5989.06	31
H35	9991.59	7050.47	4136.39	45
H36	9869.62	6435.36	3617.74	59
H37	10127.5	5923.74	4434.23	60
H39	10643.04	5660.72	5728.65	60
H40	11136.47	5755.99	7010.01	57
H41	11206.78	6368.91	7560.09	46
H42	10820.75	6878.07	6810.09	37
H45C	11417.06	7936.16	3558.95	40
H45D	11086.58	8219.28	4213.93	40
H46C	10274.27	8136.9	3112.88	37
H46D	10274.05	7689.28	3259.98	37
H48	9031.34	7970.93	5541.98	34
H50	10579.85	7887.07	6752	38
H51	11165.41	8368.36	7458.77	45
H52	10839.03	8990.7	7283.77	50
H54	10106.97	9469.64	6599.42	61
H55	9153.21	9625.94	5757.61	69
H56	8525.34	9151.7	5059.03	60
H57	8825.95	8525.85	5210.2	46
H1A	4015.44	6326.42	6160.63	40
H2A	3433.66	6216.06	7405.13	53
H3A	2621.79	5732.4	7497.66	56
H5A	1999.32	5183.62	6902.2	61
H6A	1793.53	4787.49	5827.02	62

H7A	2455.74	4847.62	4623.8	55
H8A	3287.73	5317.33	4507.34	44
H11A	3734.84	5836.88	4291.9	32
H13A	6068.23	5578.8	4401.71	51
H13B	5852.55	5171.24	4744.05	51
H14A	5524.42	5452.21	6010.26	49
H14B	6342.36	5533.53	5828	49
H16A	4980.01	6651.29	5526.72	28
H16B	4955.45	6638.29	5541.11	28
H18A	5851.77	6203.13	3935.83	32
H19A	6641.49	6478.95	3024.91	32
H20A	6750.11	7136.07	2964.02	32
H23A	4830.61	7201.27	5254.66	32
H24A	4939.22	7858.4	5193.8	32
H25A	5728.93	8134.23	4282.88	32
H26A	6410.03	7752.94	3432.83	32
H28A	4473.71	5965.83	3238.03	39
H29A	4862.19	6062.84	1916.49	46
H30A	4903.23	6670.04	1376.55	58
H31A	4410.69	7172.45	2083.94	48
H33A	2381.07	7280.18	3492.38	32
H35A	2879.14	6908.28	1618.37	38
H36A	2764.3	6275.61	1189.66	48
H37A	2430.67	5811.96	2080.18	46
H39A	2050.42	5618.22	3455.04	38

H40A	1800.19	5768.24	4789.04	36
H41A	1949.36	6390.26	5259.67	34
H42A	2277.07	6864.58	4384.26	29
H45A	2424.17	8172.69	1627.72	32
H45B	1989.56	7919.25	983.88	32
H46A	3028.08	7545.3	751.54	33
H46B	3187.85	7980.02	548.86	33
H48A	4395.79	7677.89	2993.12	31
H50A	2857.65	7810.35	4172.15	38
H51A	2572.68	8343.77	4948.11	48
H52A	3286.83	8870.42	4893.83	64
H54A	4303.86	9215.35	4329.12	77
H55A	5215.89	9252.11	3404.48	82
H56A	5475.89	8734.06	2587.09	65
H57A	4835.66	8183.96	2681.42	47
H18B	5857.6	6300.46	3888.42	32
H19B	6618.21	6639.08	3044.6	32
H20B	6641.51	7298.74	3101.67	32
H23B	4696.13	7204.06	5358.36	32
H24B	4719.4	7863.73	5415.46	32
H25B	5480	8202.36	4571.66	32
H26B	6217.34	7881.33	3670.75	32

Table C-30. Atomic Occupancy for TNSB BDP **7**.

Atom	Occupancy	Atom	Occupancy	Atom	Occupancy
H16A	0.5	H16B	0.5	C17A	0.5
C18A	0.5	H18A	0.5	C19A	0.5
H19A	0.5	C20A	0.5	H20A	0.5
C21A	0.5	C22A	0.5	C23A	0.5
H23A	0.5	C24A	0.5	H24A	0.5
C25A	0.5	H25A	0.5	C26A	0.5
H26A	0.5	C17B	0.5	C18B	0.5
H18B	0.5	C19B	0.5	H19B	0.5
C20B	0.5	H20B	0.5	C21B	0.5
C22B	0.5	C23B	0.5	H23B	0.5
C24B	0.5	H24B	0.5	C25B	0.5
H25B	0.5	C26B	0.5	H26B	0.5

C.5 Crystallographic Data for red-TNSB BDP 8

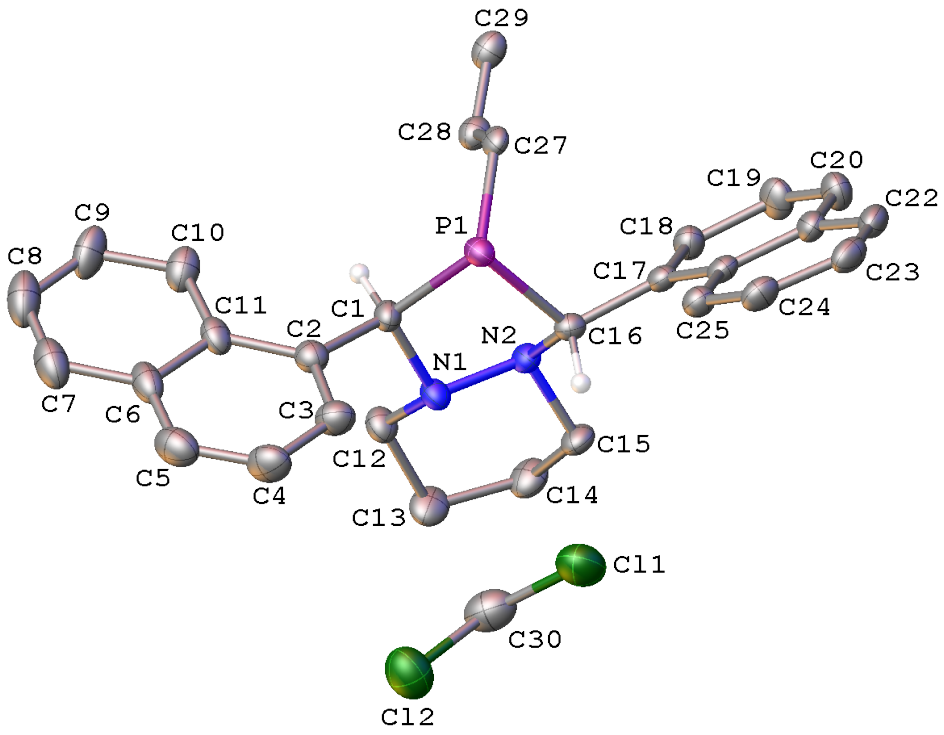

Figure C-8. A molecular drawing of the content of the asymmetric unit of red-TNSB BDP **8** – half of the diphosphine and one dichloromethane – shown with 50% probability ellipsoids. All H atoms are omitted except the ones on anomeric carbons.

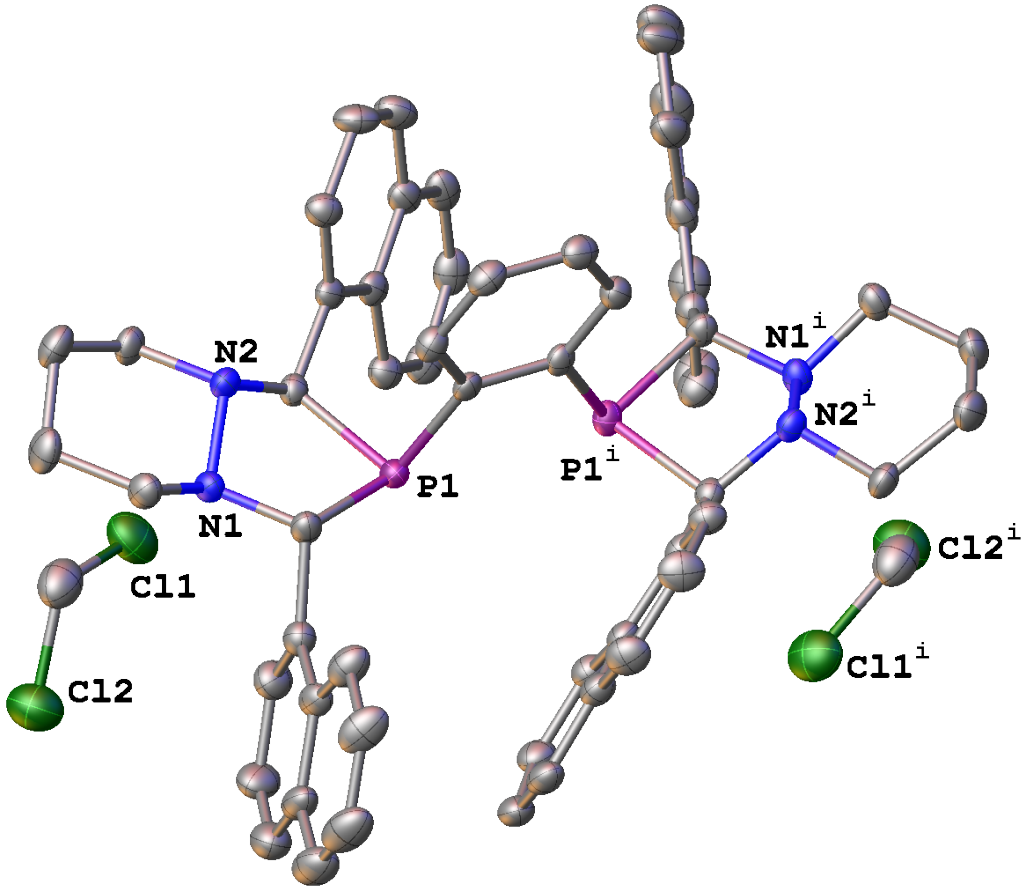

Figure C-9. A molecular drawing of red-TNSB BDP **8** shown with 50% probability ellipsoids. All H atoms are omitted. Symmetry code: i = ½ - x, ½ - y, z.

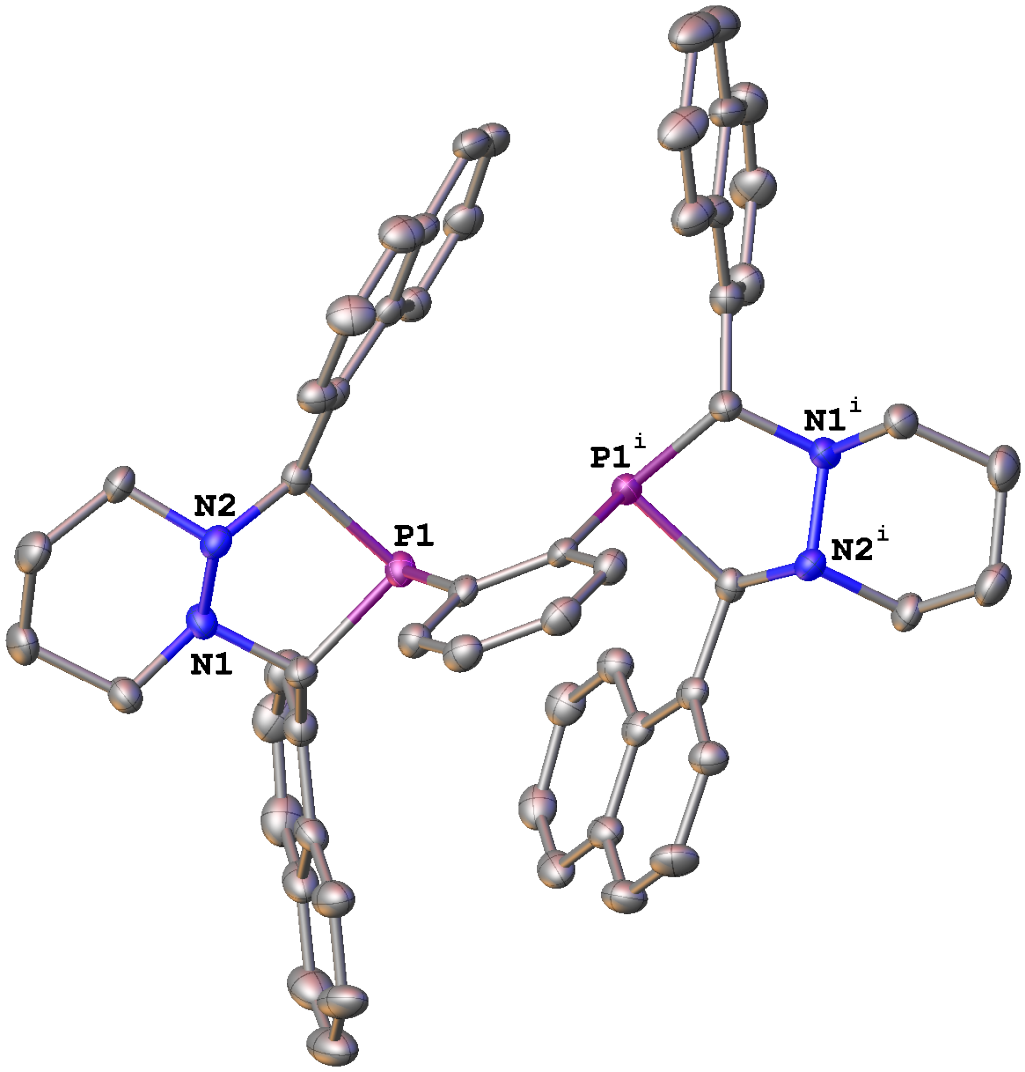

Figure C-10. A molecular drawing of the diphosphine in red-TNSB BDP **8** shown with 50% probability ellipsoids. All H atoms are omitted. Symmetry code: i = ½ - x, ½ - y, z.

C.5.1 Data Collection

A colorless crystal with approximate dimensions 0.281 × 0.107 × 0.01 mm^3 was selected under oil under ambient conditions and attached to the tip of a MiTeGen MicroMount©. The crystal was mounted in a stream of cold nitrogen at 100(1) K and centered in the X-ray beam by using a video camera.

The crystal evaluation and data collection were performed on a Bruker Quazar SMART APEXII diffractometer with Mo K_α (λ = 0.71073 Å) radiation and the diffractometer to crystal distance of 4.96 cm.[1]

The initial cell constants were obtained from three series of ω scans at different starting angles. Each series consisted of 12 frames collected at intervals of 0.5º in a 6º range about ω with the exposure time of 10 seconds per frame. The reflections were successfully indexed by an automated indexing routine built in the APEX3 program suite. The final cell constants were calculated from a set of 9870 strong reflections from the actual data collection.

The data were collected by using the full sphere data collection routine to survey the reciprocal space to the extent of a full sphere to a resolution of 0.80 Å. A total of 162027 data were harvested by collecting 4 sets of frames with 0.5º scans in ω and φ with exposure times of 90 sec per frame. These highly redundant datasets were corrected for Lorentz and polarization effects. The absorption correction was based on fitting a function to the empirical transmission surface as sampled by multiple equivalent measurements.[2]

C.5.2 Structure Solution and Refinement

The systematic absences in the diffraction data were uniquely consistent for the space group *Pccn* that yielded chemically reasonable and computationally stable results of refinement.[3-8]

A successful solution by the direct methods provided most non-hydrogen atoms from the *E*-map. The remaining non-hydrogen atoms were located in an alternating series of least-squares cycles and difference Fourier maps. All non-hydrogen atoms were refined with anisotropic displacement coefficients. All hydrogen atoms were included in the structure factor calculation at idealized positions and were allowed to ride on the neighboring atoms with relative isotropic displacement coefficients.

The diphosphine molecule resides on a crystallographic two-fold axis.

There are also two molecules of solvent dichloromethane per one diphosphine in the lattice.

The only crystal large enough for the single-crystal X-ray diffraction experiment proved to be a three-component non-merohedral twin with an approximate 66:28:6 component ratio. The reported structure is based on the major component data only.

The final least-squares refinement of 316 parameters against 4514 data resulted in residuals *R* (based on F^2 for $I \geq 2\sigma$) and *wR* (based on F^2 for all data) of 0.0606 and 0.1754, respectively. The final difference Fourier map was featureless.

C.5.3 Summary

Crystal data for $C_{60}H_{56}Cl_4N_4P_2$ (M =1036.82 g/mol): orthorhombic, space group Pccn (no. 56), a = 21.860(6) Å, b = 14.301(5) Å, c = 16.479(5) Å, V = 5152(3) Å^3, Z = 4, T = 100.0 K, μ(MoKα) = 0.337 mm^{-1}, *Dcalc* = 1.337 g/cm^3, 4514 reflections measured ($3.404° \leq 2\Theta \leq$

49.996°), 4514 unique (R_{int} = 0.0725, R_{sigma} = 0.0303) which were used in all calculations. The final R_1 was 0.0606 (I > 2σ(I)) and wR_2 was 0.1754 (all data).

Table C-31. Crystal Data and Structure Refinement for red-TNSB BDP **8**.

Empirical formula	$C_{60}H_{56}Cl_4N_4P_2$
Formula weight	1036.82
Temperature/K	100.0
Crystal system	orthorhombic
Space group	Pccn
a/Å	21.860(6)
b/Å	14.301(5)
c/Å	16.479(5)
α/°	90
β/°	90
γ/°	90
Volume/Å^3	5152(3)
Z	4
ϱ_{calc}g/cm^3	1.337
μ/mm^{-1}	0.337
F(000)	2168.0
Crystal size/mm^3	0.281 × 0.107 × 0.01
Radiation	MoKα (λ = 0.71073)
2Θ range for data collection/°	3.404 to 49.996
Index ranges	-25 ≤ h ≤ 25, -16 ≤ k ≤ 16, -19 ≤ l ≤ 19

Reflections collected	162027
Independent reflections	4514 [R_{int} = 0.0725, R_{sigma} = 0.0303]
Data/restraints/parameters	4514/0/316
Goodness-of-fit on F^2	1.036
Final R indexes [I>=2σ (I)]	R_1 = 0.0606, wR_2 = 0.1682
Final R indexes [all data]	R_1 = 0.0694, wR_2 = 0.1754
Largest diff. peak/hole / e $Å^{-3}$	0.75/-0.60

Table C-32. Fractional Atomic Coordinates ($\times 10^4$) and Equivalent Isotropic Displacement Parameters ($Å^2 \times 10^3$) for red-TNSB BDP **8**. U_{eq} is defined as 1/3 of of the trace of the orthogonalised U_{IJ} tensor.

Atom	***x***	***y***	***z***	**U(eq)**
Cl1	1132.7(5)	5078.4(7)	8908.6(6)	55.9(3)
Cl2	1815.1(5)	6757.8(7)	9314.3(6)	57.0(3)
C30	1391.3(18)	6185(3)	8570(2)	49.0(9)
P1	2384.9(3)	3595.8(5)	6852.7(4)	21.6(2)
N1	2038.7(11)	5392.1(15)	6658.7(14)	23.2(5)
N2	1553.7(10)	4815.4(16)	6284.6(14)	21.9(5)
C1	2606.2(12)	4836.2(19)	6620.5(18)	23.7(6)
C2	3053.2(13)	5238(2)	7239.0(18)	26.8(6)
C3	2890.2(15)	5267(2)	8041.5(19)	33.8(7)
C4	3255.4(16)	5684(2)	8639(2)	39.0(8)
C5	3795.1(16)	6083(2)	8425(2)	41.4(8)
C6	3998.1(14)	6067(2)	7603(2)	34.2(7)

C7	4567.8(16)	6452(2)	7394(2)	44.8(9)
C8	4770.6(17)	6400(3)	6613(3)	48.2(9)
C9	4413.1(15)	5973(3)	6017(2)	41.5(8)
C10	3858.2(14)	5591(2)	6197(2)	35.5(7)
C11	3622.4(14)	5621.9(19)	7006.0(19)	27.8(6)
C12	2103.7(14)	6256(2)	6175.6(19)	27.7(6)
C13	1525.9(15)	6836(2)	6223(2)	35.1(7)
C14	984.0(14)	6250(2)	5937(2)	34.2(7)
C15	973.9(13)	5333(2)	6406.2(19)	27.4(6)
C16	1557.1(12)	3968.8(18)	6798.6(16)	20.9(6)
C17	1138.1(12)	3206.1(19)	6513.8(17)	21.6(6)
C18	914.7(13)	3185(2)	5736.1(18)	26.7(6)
C19	510.3(14)	2470(2)	5481.1(19)	33.8(7)
C20	333.5(15)	1784(2)	6008(2)	33.9(7)
C21	558.1(13)	1773(2)	6815.7(18)	26.0(6)
C22	366.3(13)	1081(2)	7373.2(19)	30.7(7)
C23	582.8(14)	1070(2)	8152(2)	32.4(7)
C24	1011.3(14)	1739(2)	8401.8(19)	30.5(7)
C25	1197.8(13)	2432(2)	7879.9(17)	25.4(6)
C26	971.5(12)	2478(2)	7073.8(17)	22.6(6)
C27	2458.6(12)	2988.4(19)	5860.8(16)	20.6(6)
C28	2413.0(12)	3458(2)	5116.2(17)	25.0(6)
C29	2456.2(13)	2982(2)	4389.3(17)	28.3(6)

Table C-33. Anisotropic Displacement Parameters ($Å^2×10^3$) for red-TNSB BDP **8**. The Anisotropic displacement factor exponent takes the form: $-2\pi^2[h^2a^{*2}U_{11}+2hka^*b^*U_{12}+\ldots]$.

Atom	$\mathbf{U_{11}}$	$\mathbf{U_{22}}$	$\mathbf{U_{33}}$	$\mathbf{U_{23}}$	$\mathbf{U_{13}}$	$\mathbf{U_{12}}$
Cl1	62.2(7)	52.3(6)	53.2(6)	-14.5(4)	7.8(5)	-3.6(5)
Cl2	62.6(7)	56.4(6)	51.9(6)	-3.6(4)	-4.7(5)	-10.2(5)
C30	49(2)	58(2)	40.7(19)	-3.2(17)	-0.2(17)	12.9(18)
P1	20.5(4)	19.2(4)	25.1(4)	-2.1(3)	-4.5(3)	1.6(3)
N1	22.5(12)	17.7(11)	29.4(12)	-0.3(9)	-3.9(10)	-0.3(9)
N2	17.2(12)	22.5(12)	26.1(12)	-1.4(9)	-1.2(9)	2.0(9)
C1	17.9(14)	20.8(14)	32.4(15)	-1.2(12)	-0.3(11)	-0.8(11)
C2	25.8(15)	23.6(14)	30.9(15)	-0.8(12)	-1.9(12)	1.8(12)
C3	33.4(18)	36.8(17)	31.3(16)	-5.5(13)	0.1(13)	3.6(14)
C4	39.3(19)	47(2)	30.4(16)	-10.8(15)	-5.9(14)	3.6(16)
C5	42(2)	37.9(19)	44(2)	-8.9(15)	-11.8(16)	3.4(15)
C6	25.3(16)	24.2(15)	53(2)	1.0(14)	-12.1(14)	-2.0(12)
C7	36.5(19)	35.2(18)	63(2)	5.7(17)	-14.2(17)	-9.0(15)
C8	30.7(18)	45(2)	69(3)	18.8(19)	-7.6(18)	-10.0(16)
C9	27.7(17)	51(2)	46(2)	21.1(16)	3.1(14)	-5.9(15)
C10	26.4(17)	36.9(18)	43.0(18)	11.6(14)	-1.1(14)	-1.7(13)
C11	26.3(15)	18.8(14)	38.2(16)	3.3(12)	-6.9(13)	-2.9(11)
C12	26.6(15)	20.9(14)	35.6(16)	3.1(12)	-3.0(13)	-1.4(12)
C13	34.4(18)	23.4(15)	47.6(19)	10.1(13)	0.7(15)	5.9(13)
C14	25.1(16)	35.2(17)	42.1(18)	7.3(14)	-1.1(13)	8.4(13)
C15	19.6(14)	26.9(15)	35.6(16)	-0.7(12)	3.1(12)	5.9(12)

C16	21.2(14)	20.3(13)	21.1(13)	-1(1)	0.9(11)	2.9(11)
C17	17.1(13)	24.2(14)	23.5(14)	-4.7(11)	2.1(11)	2.5(11)
C18	24.0(15)	29.3(16)	26.9(15)	-2.2(12)	1.1(12)	-3.0(12)
C19	30.1(16)	42.8(18)	28.4(15)	-4.9(13)	-7.2(13)	-8.1(14)
C20	28.9(17)	35.0(17)	37.8(17)	-7.3(14)	-1.3(13)	-8.4(14)
C21	18.0(14)	27.4(15)	32.6(16)	-4.5(12)	2.9(11)	-0.5(11)
C22	21.4(15)	27.5(15)	43.2(18)	-2.9(13)	8.7(13)	-1.8(12)
C23	27.7(16)	30.4(16)	39.2(18)	5.5(13)	12.5(13)	1.8(13)
C24	28.2(16)	36.8(17)	26.6(15)	1.0(13)	7.5(12)	3.2(13)
C25	23.1(14)	27.8(15)	25.3(14)	-2.5(12)	2.6(11)	0.6(12)
C26	17.6(13)	25.3(14)	24.9(14)	-2.5(11)	4.4(11)	3.4(11)
C27	13.2(12)	21.7(14)	26.8(14)	-0.6(11)	-2.2(11)	1.9(10)
C28	21.9(15)	24.9(14)	28.3(15)	3.3(12)	0.5(11)	2.1(12)
C29	23.6(15)	35.8(16)	25.6(15)	5.2(12)	-0.9(12)	1.9(12)

Table C-34. Bond Lengths for red-TNSB BDP **8**.

Atom	**Atom**	**Length/Å**	**Atom**	**Atom**	**Length/Å**
Cl1	C30	1.771(4)	C10	C11	1.431(5)
Cl2	C30	1.741(4)	C12	C13	1.513(4)
P1	C1	1.878(3)	C13	C14	1.526(5)
P1	C16	1.889(3)	C14	C15	1.522(4)
P1	C27	1.858(3)	C16	C17	1.500(4)
N1	N2	1.478(3)	C17	C18	1.372(4)
N1	C1	1.475(4)	C17	C26	1.438(4)
N1	C12	1.476(4)	C18	C19	1.415(4)

N2	C15	1.481(3)	C19	C20	1.367(5)
N2	C16	1.478(3)	C20	C21	1.418(4)
C1	C2	1.524(4)	C21	C22	1.414(4)
C2	C3	1.370(4)	C21	C26	1.419(4)
C2	C11	1.413(4)	C22	C23	1.368(5)
C3	C4	1.401(5)	C23	C24	1.401(5)
C4	C5	1.357(5)	C24	C25	1.374(4)
C5	C6	1.425(5)	C25	C26	1.419(4)
C6	C7	1.405(5)	C27	C27[1]	1.409(6)
C6	C11	1.432(4)	C27	C28	1.402(4)
C7	C8	1.363(6)	C28	C29	1.381(4)
C8	C9	1.396(5)	C29	C29[1]	1.391(6)
C9	C10	1.363(5)			

Table C-35. Bond Angles for red-TNSB BDP **8**.

Atom	**Atom**	**Atom**	**Angle/°**	**Atom**	**Atom**	**Atom**	**Angle/°**
Cl2	C30	Cl1	111.6(2)	N1	C12	C13	110.5(2)
C1	P1	C16	88.30(12)	C12	C13	C14	109.3(3)
C27	P1	C1	103.89(13)	C15	C14	C13	109.1(3)
C27	P1	C16	100.00(12)	N2	C15	C14	110.4(2)
C1	N1	N2	106.5(2)	N2	C16	P1	105.26(17)
C1	N1	C12	110.3(2)	N2	C16	C17	114.4(2)
C12	N1	N2	108.1(2)	C17	C16	P1	113.23(18)
N1	N2	C15	106.2(2)	C18	C17	C16	121.7(3)
C16	N2	N1	102.39(19)	C18	C17	C26	119.5(3)

C16	N2	C15	109.6(2)	C26	C17	C16	118.7(2)
N1	C1	P1	106.49(18)	C17	C18	C19	121.1(3)
N1	C1	C2	107.9(2)	C20	C19	C18	120.4(3)
C2	C1	P1	112.6(2)	C19	C20	C21	120.4(3)
C3	C2	C1	119.3(3)	C20	C21	C26	119.6(3)
C3	C2	C11	118.6(3)	C22	C21	C20	120.9(3)
C11	C2	C1	122.0(3)	C22	C21	C26	119.4(3)
C2	C3	C4	122.9(3)	C23	C22	C21	121.0(3)
C5	C4	C3	119.4(3)	C22	C23	C24	119.9(3)
C4	C5	C6	120.7(3)	C25	C24	C23	120.5(3)
C5	C6	C11	118.8(3)	C24	C25	C26	121.1(3)
C7	C6	C5	120.2(3)	C21	C26	C17	118.9(3)
C7	C6	C11	120.9(3)	C21	C26	C25	118.0(3)
C8	C7	C6	119.9(3)	C25	C26	C17	123.1(3)
C7	C8	C9	120.4(3)	C27[1]	C27	P1	118.34(9)
C10	C9	C8	121.3(3)	C28	C27	P1	122.7(2)
C9	C10	C11	120.8(3)	C28	C27	C27[1]	118.96(16)
C2	C11	C6	119.4(3)	C29	C28	C27	121.2(3)
C2	C11	C10	124.0(3)	C28	C29	C29[1]	119.87(17)
C10	C11	C6	116.6(3)				

Table C-36. Torsion Angles for red-TNSB BDP **8**.

A	**B**	**C**	**D**	**Angle/°**	**A**	**B**	**C**	**D**	**Angle/°**
P1	C1	C2	C3	-58.3(3)	C11	C2	C3	C4	1.8(5)
P1	C1	C2	C11	124.7(3)	C11	C6	C7	C8	-0.4(5)

P1	C16	C17	C18	-102.7(3)	C12	N1	N2	C15	-67.5(3)
P1	C16	C17	C26	77.0(3)	C12	N1	N2	C16	177.6(2)
P1	C27	C28	C29	-178.5(2)	C12	N1	C1	P1	-156.78(19)
N1	N2	C15	C14	65.3(3)	C12	N1	C1	C2	82.1(3)
N1	N2	C16	P1	-50.0(2)	C12	C13	C14	C15	52.6(3)
N1	N2	C16	C17	-174.9(2)	C13	C14	C15	N2	-58.5(3)
N1	C1	C2	C3	59.0(3)	C15	N2	C16	P1	-162.39(18)
N1	C1	C2	C11	-118.1(3)	C15	N2	C16	C17	72.7(3)
N1	C12	C13	C14	-56.8(3)	C16	P1	C1	N1	8.55(19)
N2	N1	C1	P1	-39.7(2)	C16	P1	C1	C2	126.7(2)
N2	N1	C1	C2	-160.8(2)	C16	P1	C27	C27[1]	-111.7(3)
N2	N1	C12	C13	64.7(3)	C16	P1	C27	C28	65.9(2)
N2	C16	C17	C18	18.0(4)	C16	N2	C15	C14	175.2(2)
N2	C16	C17	C26	-162.4(2)	C16	C17	C18	C19	-178.8(3)
C1	P1	C16	N2	23.90(18)	C16	C17	C26	C21	177.8(2)
C1	P1	C16	C17	149.6(2)	C16	C17	C26	C25	-1.7(4)
C1	P1	C27	C27[1]	157.6(3)	C17	C18	C19	C20	0.0(5)
C1	P1	C27	C28	-24.8(3)	C18	C17	C26	C21	-2.6(4)
C1	N1	N2	C15	173.9(2)	C18	C17	C26	C25	177.9(3)
C1	N1	N2	C16	59.0(2)	C18	C19	C20	C21	-0.6(5)
C1	N1	C12	C13	-179.1(2)	C19	C20	C21	C22	178.3(3)
C1	C2	C3	C4	-175.4(3)	C19	C20	C21	C26	-0.4(5)
C1	C2	C11	C6	174.2(3)	C20	C21	C22	C23	179.9(3)
C1	C2	C11	C10	-6.3(4)	C20	C21	C26	C17	2.0(4)

C2	C3	C4	C5	0.2(5)	C20	C21	C26	C25	-178.5(3)
C3	C2	C11	C6	-2.9(4)	C21	C22	C23	C24	-1.4(4)
C3	C2	C11	C10	176.6(3)	C22	C21	C26	C17	-176.8(2)
C3	C4	C5	C6	-1.1(5)	C22	C21	C26	C25	2.8(4)
C4	C5	C6	C7	-177.7(3)	C22	C23	C24	C25	2.6(5)
C4	C5	C6	C11	0.0(5)	C23	C24	C25	C26	-1.1(4)
C5	C6	C7	C8	177.3(3)	C24	C25	C26	C17	178.0(3)
C5	C6	C11	C2	2.0(4)	C24	C25	C26	C21	-1.6(4)
C5	C6	C11	C10	-177.5(3)	C26	C17	C18	C19	1.6(4)
C6	C7	C8	C9	0.6(5)	C26	C21	C22	C23	-1.4(4)
C7	C6	C11	C2	179.7(3)	C27	P1	C1	N1	108.43(19)
C7	C6	C11	C10	0.1(4)	C27	P1	C1	C2	-133.5(2)
C7	C8	C9	C10	-0.6(6)	C27	P1	C16	N2	-79.90(18)
C8	C9	C10	C11	0.4(5)	C27	P1	C16	C17	45.8(2)
C9	C10	C11	C2	-179.7(3)	$C27^{1}$	C27	C28	C29	-0.9(5)
C9	C10	C11	C6	-0.1(5)	C27	C28	C29	$C29^{1}$	0.3(5)

Table C-37. Hydrogen Atom Coordinates ($Å \times 10^4$) and Isotropic Displacement Parameters ($Å^2 \times 10^3$) for red-TNSB BDP **8**.

Atom	***x***	***y***	***z***	**U(eq)**
H30A	1647	6102	8080	59
H30B	1034	6575	8420	59
H1	2786	4875	6064	28
H3	2513	4992	8200	41

H4	3126	5687	9190	47
H5	4040	6376	8827	50
H7	4811	6749	7796	54
H8	5158	6656	6474	58
H9	4560	5948	5474	50
H10	3625	5302	5780	43
H12A	2188	6092	5603	33
H12B	2454	6625	6383	33
H13A	1567	7398	5877	42
H13B	1458	7044	6789	42
H14A	598	6596	6030	41
H14B	1022	6122	5349	41
H15A	916	5463	6991	33
H15B	626	4945	6219	33
H16	1426	4156	7357	25
H18	1033	3657	5363	32
H19	361	2467	4940	41
H20	59	1310	5833	41
H22	83	617	7204	37
H23	443	608	8523	39
H24	1174	1714	8936	37
H25	1483	2887	8061	31
H28	2351	4116	5112	30
H29	2426	3311	3890	34

C.6 Crystallographic Data for [Rh(acac)TPSB BDP 1]

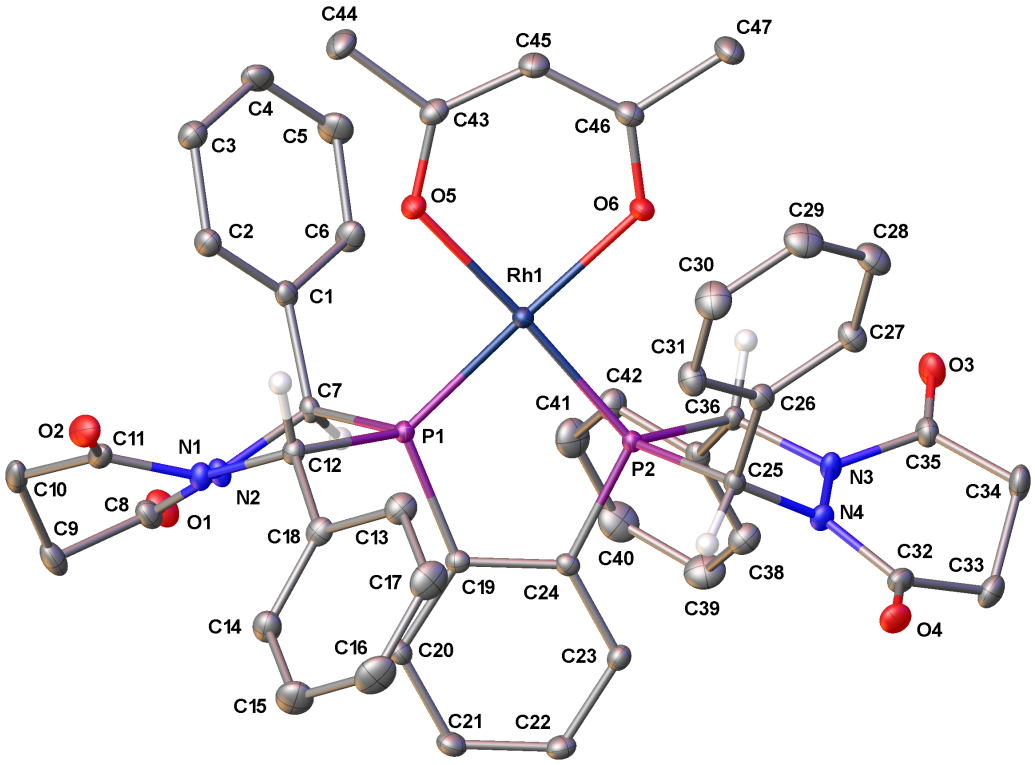

Figure C-11. A molecular drawing of [Rh(acac)TPSB BDP **1**] shown with 40% probability ellipsoids. All non stereoactive H atoms are omitted. All dichloromethane molecules are omitted.

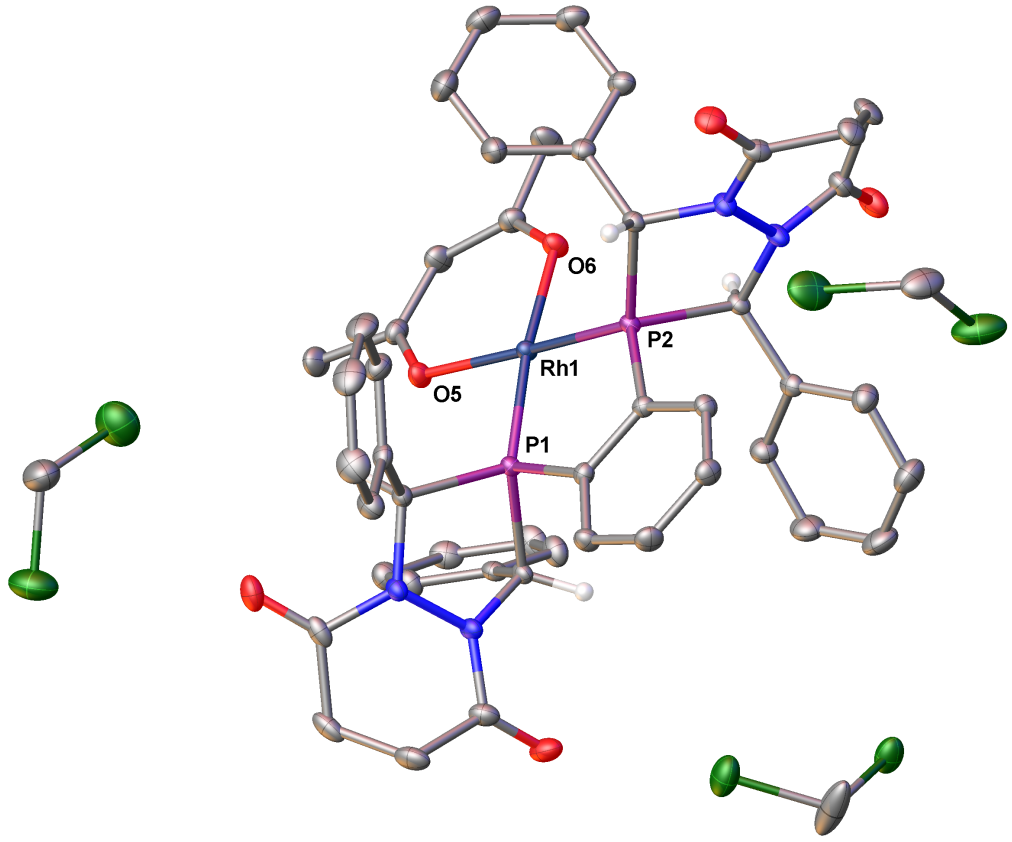

Figure C-12. A molecular drawing of [Rh(acac)TPSB BDP **1**] shown with 50% probability ellipsoids. All non stereoactive H atoms are omitted.

C.6.1 Data Collection

An orange crystal with approximate dimensions 0.204 x 0.172 x 0.124 mm^3 was selected under oil under ambient conditions and attached to the tip of a MiTeGen MicroMount©. The crystal was mounted in a stream of cold nitrogen at 100(1) K and centered in the X-ray beam by using a video camera.

The crystal evaluation and data collection were performed on a Bruker Quazar SMART APEXII diffractometer with Mo K_α (λ = 0.71073 Å) radiation and the diffractometer to crystal distance of 4.96 cm.[12]

The initial cell constants were obtained from three series of ω scans at different starting angles. Each series consisted of 12 frames collected at intervals of 0.5º in a 6º range about ω with the exposure time of 5 seconds per frame. The reflections were successfully indexed by an automated indexing routine built in the APEX3 program suite. The final cell constants were calculated from a set of 9703 strong reflections from the actual data collection.

The data were collected by using the full sphere data collection routine to survey the reciprocal space to the extent of a full sphere to a resolution of 0.70 Å. A total of 72109 data were harvested by collecting 6 sets of frames with 0.5º scans in ω and φ with exposure times of 25 sec per frame. These highly redundant datasets were corrected for Lorentz and polarization effects. The absorption correction was based on fitting a function to the empirical transmission surface as sampled by multiple equivalent measurements.[2]

C.6.2 Structure Solution and Refinement

The systematic absences in the diffraction data were consistent for the space groups $P\bar{1}$ and $P1$. The *E*-statistics strongly suggested the centrosymmetric space group $P\bar{1}$ that yielded chemically reasonable and computationally stable results of refinement.[2-4]

A successful solution by the direct methods provided most non-hydrogen atoms from the *E*-map. The remaining non-hydrogen atoms were located in an alternating series of least-squares cycles and difference Fourier maps. All non-hydrogen atoms were refined with anisotropic displacement coefficients. All hydrogen atoms were included in the structure factor calculation at idealized positions and were allowed to ride on the neighboring atoms with relative isotropic displacement coefficients.

The chiral centers are C7-*R*, C12-*R*, C25-*R*, and C36-*R*. Both enantiomers are present in the crystal structure.

There are also three molecule of solvate dichloromethane in the asymmetric unit. Atom Cl6 is disordered over two positions with major component contribution equal to 61.3(1.9)%

The final least-squares refinement of 634 parameters against 14629 data resulted in residuals *R* (based on F^2 for $I \geq 2\sigma$) and *wR* (based on F^2 for all data) of 0.0251 and 0.0675, respectively. The final difference Fourier map was featureless.

C.6.3 Summary

Crystal data for $C_{50}H_{49}Cl_6N_4O_6P_2Rh$ (M =1179.48 g/mol): triclinic, space group $P\bar{1}$ (no. 2), a = 12.305(3) Å, b = 13.540(4) Å, c = 17.593(6) Å, α = 111.943(5)°, β = 100.152(10)°, γ = 94.594(14)°, V = 2641.8(13) Å^3, Z = 2, T = 100.0 K, μ(MoKα) = 0.739 mm^{-1}, *Dcalc* = 1.483 g/cm^3, 72109 reflections measured (2.56° ≤ 2Θ ≤ 58.976°), 14629 unique (R_{int} = 0.0232, R_{sigma} = 0.0189) which were used in all calculations. The final R_1 was 0.0251 (I > 2σ(I)) and wR_2 was 0.0675 (all data).

Table C-38. Crystal Data and Structure Refinement for [Rh(acac)TPSB BDP **1**].

Empirical formula	$C_{50}H_{49}Cl_6N_4O_6P_2Rh$
Formula weight	1179.48
Temperature/K	100.0
Crystal system	triclinic
Space group	$P\bar{1}$
a/Å	12.305(3)
b/Å	13.540(4)
c/Å	17.593(6)
α/°	111.943(5)
β/°	100.152(10)
γ/°	94.594(14)
Volume/Å^3	2641.8(13)
Z	2
ϱ_{calc}g/cm^3	1.483
μ/mm^{-1}	0.739
F(000)	1204.0
Crystal size/mm^3	0.204 × 0.172 × 0.124
Radiation	MoKα (λ = 0.71073)
2Θ range for data collection/°	2.56 to 58.976
Index ranges	$-17 \le h \le 17$, $-18 \le k \le 18$, $-24 \le l \le 24$
Reflections collected	72109
Independent reflections	14629 [R_{int} = 0.0232, R_{sigma} = 0.0189]

Data/restraints/parameters	14629/0/634
Goodness-of-fit on F^2	1.089
Final R indexes [I>=2σ (I)]	$R_1 = 0.0251$, $wR_2 = 0.0663$
Final R indexes [all data]	$R_1 = 0.0286$, $wR_2 = 0.0675$
Largest diff. peak/hole / e $Å^{-3}$	0.62/-0.45

Table C-39. Fractional Atomic Coordinates ($\times 10^4$) and Equivalent Isotropic Displacement Parameters ($Å^2 \times 10^3$) for [Rh(acac)TPSB BDP **1**]. U_{eq} is defined as 1/3 of of the trace of the orthogonalised U_{IJ} tensor.

Atom	***x***	***y***	***z***	**U(eq)**
Rh1	7459.6(2)	4691.6(2)	6609.4(2)	11.41(3)
P1	7485.6(3)	6000.9(2)	7777.0(2)	11.19(6)
P2	6780.7(3)	3688.9(2)	7167.5(2)	10.88(6)
O1	5781.8(9)	8837.3(8)	8850.4(7)	24.6(2)
O2	10083.0(9)	9024.3(9)	8863.8(6)	24.3(2)
O3	4057.2(9)	856.9(8)	5590.8(6)	23.0(2)
O4	7576.3(9)	872.3(8)	7824.2(6)	21.1(2)
O5	8250.3(8)	5688.4(7)	6158.6(6)	16.30(18)
O6	7240.2(8)	3412.4(7)	5470.5(5)	16.21(18)
N1	7256.9(9)	8008.0(8)	8560.3(7)	14.2(2)
N2	8439.2(9)	8046.2(9)	8741.7(7)	14.3(2)
N3	5485.8(9)	1775.6(8)	6699.6(7)	14.5(2)
N4	6528.5(9)	1748.5(9)	7189.6(7)	14.3(2)

C1	6567.7(11)	7312.2(10)	7002.5(8)	14.4(2)
C2	7373.5(12)	8008.5(11)	6907.2(8)	18.8(3)
C3	7288.9(12)	8129.6(11)	6148.7(9)	20.9(3)
C4	6407.2(13)	7541.5(12)	5475.4(9)	22.0(3)
C5	5593.6(13)	6850.3(13)	5566.2(9)	26.0(3)
C6	5669.3(12)	6736.7(11)	6326.6(9)	20.5(3)
C7	6656.5(10)	7106.6(10)	7798.1(7)	12.8(2)
C8	6788.5(12)	8841.7(11)	9018.4(8)	18.7(3)
C9	7643.1(13)	9753.1(11)	9676.5(9)	23.1(3)
C10	8554.8(13)	9980.8(11)	9252.7(9)	22.5(3)
C11	9110.5(12)	9008.2(11)	8921.8(8)	17.9(2)
C12	8787.8(10)	7001.5(10)	8336.2(8)	13.5(2)
C13	9568.9(10)	6655.8(11)	8923.2(8)	15.8(2)
C14	9833.1(12)	7218.4(11)	9788.0(9)	20.1(3)
C15	10556.2(13)	6860.7(13)	10300.5(10)	28.2(3)
C16	11000.2(13)	5932.9(14)	9952.0(11)	30.2(3)
C17	10731.5(13)	5359.8(13)	9086.9(11)	27.6(3)
C18	10026.3(12)	5720.0(12)	8572.1(9)	21.1(3)
C19	7025.8(10)	5558.8(10)	8546.7(7)	12.6(2)
C20	6985.4(11)	6222(1)	9365.6(8)	16.5(2)
C21	6565.7(12)	5772.6(11)	9868.8(8)	18.7(3)
C22	6190.4(11)	4669.0(11)	9563.5(8)	17.7(2)
C23	6225.5(11)	4006(1)	8748.4(8)	14.8(2)
C24	6648.2(10)	4449(1)	8239.4(7)	12.3(2)

C25	7456.7(10)	2527.9(10)	7249.3(7)	13.1(2)
C26	8165.8(11)	2103.2(10)	6611.0(8)	15.3(2)
C27	7790.3(12)	1167.3(11)	5886.2(8)	19.2(3)
C28	8472.7(13)	813.5(13)	5315.0(9)	25.5(3)
C29	9522.0(13)	1396.2(13)	5460.3(10)	28.4(3)
C30	9894.3(13)	2328.9(13)	6178.5(10)	28.1(3)
C31	9222.1(12)	2683.0(11)	6755.4(9)	21.3(3)
C32	6660.1(12)	925.8(11)	7451.0(8)	17.1(2)
C33	5609.3(12)	119.2(11)	7196.5(9)	21.6(3)
C34	5071.4(13)	-158.4(11)	6272.2(9)	22.5(3)
C35	4819.0(11)	833.5(10)	6127.8(8)	18.0(2)
C36	5408(1)	2793.1(10)	6601.8(7)	12.9(2)
C37	4432.7(10)	3326.9(10)	6886.9(8)	14.5(2)
C38	3759.2(12)	2966.8(12)	7317.8(9)	21.4(3)
C39	2904.4(13)	3521.1(14)	7593.3(10)	29.0(3)
C40	2720.6(14)	4436.2(14)	7444.1(11)	31.0(3)
C41	3383.1(13)	4793.5(13)	7010(1)	27.8(3)
C42	4230.5(12)	4239.1(11)	6728.1(9)	20.1(3)
C43	8403.9(11)	5405.4(11)	5417.4(8)	16.9(2)
C44	8996.5(13)	6274.1(12)	5224.0(9)	23.2(3)
C45	8082.4(12)	4369.7(11)	4775.2(8)	20.5(3)
C46	7550.0(11)	3457.4(11)	4828.6(8)	17.8(2)
C47	7289.9(14)	2405.9(12)	4067.3(9)	25.7(3)
Cl1	1140.0(3)	6750.6(3)	7318.5(2)	28.21(8)

Cl2	3337.5(3)	7991.6(4)	8299.1(3)	34.61(9)
C48	1938.8(15)	7638(2)	8313.7(12)	58.6(7)
Cl3	3803.6(5)	1359.4(4)	8943.5(3)	47.34(12)
Cl4	6238.3(5)	2000.6(4)	9525.1(3)	43.62(11)
C49	5045.0(16)	1188.3(15)	9533.4(12)	35.7(4)
Cl5	8988.9(5)	8467.6(4)	1784.6(3)	50.25(12)
Cl6	9515(2)	10718.2(16)	3029.0(16)	45.0(8)
Cl6A	9241(13)	10529(11)	3102(4)	101(2)
C50	9941.3(16)	9483.8(15)	2638.7(13)	42.0(4)

Table C-40. Anisotropic Displacement Parameters ($Å^2 \times 10^3$) for [Rh(acac)TPSB BDP **1**]. The Anisotropic displacement factor exponent takes the form: $-2\pi^2[h^2a^{*2}U_{11}+2hka^*b^*U_{12}+\ldots]$.

Atom	$\mathbf{U_{11}}$	$\mathbf{U_{22}}$	$\mathbf{U_{33}}$	$\mathbf{U_{23}}$	$\mathbf{U_{13}}$	$\mathbf{U_{12}}$
Rh1	13.35(5)	10.46(5)	10.29(5)	3.94(3)	2.85(3)	1.53(3)
P1	12.29(14)	9.71(14)	10.84(13)	3.74(11)	1.85(10)	0.95(11)
P2	12.45(14)	9.30(14)	10.22(13)	3.60(11)	1.51(10)	1.52(11)
O1	21.1(5)	22.4(5)	24.7(5)	2.6(4)	3.8(4)	9.0(4)
O2	20.6(5)	25.3(5)	22.6(5)	9.3(4)	-0.3(4)	-7.3(4)
O3	22.9(5)	17.2(5)	21.9(5)	5.6(4)	-5.3(4)	-1.3(4)
O4	24.2(5)	21.1(5)	21.6(5)	12.9(4)	2.2(4)	7.7(4)
O5	19.2(5)	14.8(4)	15.5(4)	6.3(3)	5.8(3)	0.2(3)
O6	21.4(5)	14.1(4)	11.6(4)	3.6(3)	4.2(3)	0.9(4)
N1	12.1(5)	11.9(5)	14.4(5)	2.2(4)	-0.5(4)	1.3(4)

N2	12.7(5)	12.0(5)	16.4(5)	5.2(4)	-0.1(4)	0.6(4)
N3	14.3(5)	10.8(5)	16.6(5)	5.8(4)	-2.0(4)	1.2(4)
N4	13.9(5)	13.3(5)	16.1(5)	7.6(4)	-0.1(4)	2.3(4)
C1	15.8(6)	11.3(5)	14.7(5)	4.3(4)	1.1(4)	4.0(4)
C2	20.2(6)	17.3(6)	16.0(6)	6.0(5)	-0.1(5)	-0.6(5)
C3	24.1(7)	19.7(6)	20.1(6)	9.7(5)	4.1(5)	2.3(5)
C4	28.1(7)	22.8(7)	16.2(6)	10.0(5)	1.0(5)	8.0(6)
C5	24.1(7)	29.7(8)	19.7(6)	10.6(6)	-6.7(5)	0.5(6)
C6	17.4(6)	21.0(7)	21.2(6)	10.0(5)	-2.8(5)	-1.0(5)
C7	11.7(5)	10.0(5)	13.7(5)	2.9(4)	0.2(4)	0.5(4)
C8	23.1(7)	15.1(6)	15.0(6)	3.4(5)	1.4(5)	5.5(5)
C9	27.9(7)	15.4(6)	17.3(6)	-0.2(5)	-3.1(5)	5.9(5)
C10	29.4(7)	11.8(6)	19.2(6)	5.2(5)	-7.3(5)	-2.4(5)
C11	21.7(6)	15.5(6)	12.9(5)	6.7(5)	-3.9(5)	-5.1(5)
C12	12.4(5)	12.3(5)	15.3(5)	5.5(4)	2.0(4)	0.8(4)
C13	10.5(5)	17.6(6)	19.8(6)	9.3(5)	1.1(4)	0.4(5)
C14	18.6(6)	19.0(6)	20.5(6)	8.1(5)	-1.3(5)	1.2(5)
C15	26.1(8)	33.0(8)	23.1(7)	13.4(6)	-4.8(6)	3.0(6)
C16	20.7(7)	39.5(9)	36.6(8)	24.4(7)	-0.5(6)	8.6(6)
C17	21.6(7)	30.3(8)	38.1(8)	19.1(7)	8.2(6)	12.8(6)
C18	17.6(6)	23.4(7)	24.6(7)	11.1(6)	5.6(5)	5.5(5)
C19	11.2(5)	14.4(6)	11.9(5)	5.4(4)	1.9(4)	1.7(4)
C20	19.4(6)	13.9(6)	13.7(5)	3.0(4)	3.3(5)	1.9(5)
C21	22.7(7)	19.9(6)	13.3(5)	4.9(5)	6.3(5)	5.0(5)

C22	19.7(6)	20.5(6)	16.1(6)	9.5(5)	6.7(5)	4.2(5)
C23	16.1(6)	13.4(6)	16.0(5)	7.2(5)	3.3(4)	1.8(5)
C24	11.8(5)	13.4(6)	11.0(5)	4.4(4)	1.3(4)	2.7(4)
C25	13.8(6)	11.2(5)	13.2(5)	4.5(4)	0.8(4)	2.2(4)
C26	16.2(6)	14.1(6)	16.4(6)	6.8(5)	2.7(4)	5.1(5)
C27	18.5(6)	18.1(6)	18.2(6)	4.2(5)	2.7(5)	4.2(5)
C28	28.1(8)	25.1(7)	19.3(6)	3.1(5)	6.4(6)	8.8(6)
C29	27.3(8)	33.0(8)	27.6(7)	9.9(6)	13.7(6)	12.6(6)
C30	19.8(7)	30.6(8)	34.9(8)	11.8(7)	10.6(6)	4.2(6)
C31	17.7(6)	18.5(6)	24.3(7)	5.3(5)	3.9(5)	2.0(5)
C32	23.7(7)	15.0(6)	15.9(6)	8.4(5)	5.8(5)	6.4(5)
C33	24.7(7)	16.7(6)	27.7(7)	13.4(5)	6.0(5)	2.9(5)
C34	26.2(7)	10.9(6)	27.7(7)	7.3(5)	1.1(6)	-0.1(5)
C35	19.3(6)	13.0(6)	18.6(6)	4.5(5)	2.4(5)	-0.8(5)
C36	14.9(6)	10.4(5)	12.9(5)	5.3(4)	0.5(4)	1.4(4)
C37	13.1(6)	13.8(6)	14.0(5)	4.2(4)	-0.6(4)	1.9(4)
C38	18.6(6)	23.8(7)	24.8(7)	12.6(6)	4.9(5)	4.2(5)
C39	21.4(7)	38.8(9)	31.8(8)	16.4(7)	11.5(6)	8.4(6)
C40	23.2(8)	35.1(9)	35.0(8)	10.9(7)	9.6(6)	15.0(7)
C41	26.2(8)	23.9(7)	34.8(8)	12.3(6)	5.9(6)	11.9(6)
C42	19.7(6)	18.6(6)	23.1(6)	9.5(5)	3.6(5)	5.1(5)
C43	15.7(6)	19.7(6)	19.5(6)	10.7(5)	6.9(5)	4.2(5)
C44	27.4(7)	21.4(7)	26.1(7)	12.7(6)	12.4(6)	2.0(6)
C45	25.3(7)	21.8(7)	16.5(6)	7.8(5)	9.0(5)	4.0(5)

C46	19.8(6)	18.9(6)	13.6(5)	4.7(5)	4.5(5)	4.0(5)
C47	37.4(8)	20.1(7)	16.2(6)	2.1(5)	10.9(6)	0.3(6)
Cl1	22.68(17)	38.4(2)	19.89(15)	7.25(14)	7.14(13)	0.41(15)
Cl2	21.17(18)	47.0(2)	31.06(19)	12.22(17)	4.43(14)	-1.03(16)
C48	20.8(8)	97.3(18)	24.6(8)	-9.3(10)	6.4(7)	-9.1(10)
Cl3	61.7(3)	48.0(3)	36.4(2)	15.7(2)	11.8(2)	34.5(2)
Cl4	65.3(3)	37.8(2)	45.3(2)	30.3(2)	22.3(2)	14.0(2)
C49	48.1(10)	35.5(9)	39.2(9)	24.9(8)	19.0(8)	22.5(8)
Cl5	53.7(3)	48.0(3)	38.6(2)	10.4(2)	2.7(2)	0.2(2)
Cl6	57.1(11)	30.6(9)	42.7(7)	9.6(4)	5.3(7)	18.3(8)
Cl6A	128(4)	99(4)	64.9(16)	2(2)	32(2)	77(3)
C50	33.0(9)	33.8(10)	53.0(11)	8.0(8)	13.2(8)	9.4(8)

Table C-41. Bond Lengths for [Rh(acac)TPSB BDP **1**].

Atom	**Atom**	**Length/Å**	**Atom**	**Atom**	**Length/Å**
Rh1	P1	2.1470(6)	C14	C15	1.3972(19)
Rh1	P2	2.1469(5)	C15	C16	1.380(2)
Rh1	O5	2.0635(10)	C16	C17	1.388(2)
Rh1	O6	2.0562(10)	C17	C18	1.390(2)
P1	C7	1.8707(13)	C19	C20	1.3964(17)
P1	C12	1.8631(14)	C19	C24	1.3994(18)
P1	C19	1.8259(13)	C20	C21	1.3906(18)
P2	C24	1.8238(13)	C21	C22	1.392(2)

P2	C25	1.8762(13)	C22	C23	1.3891(18)
P2	C36	1.8686(14)	C23	C24	1.3957(17)
O1	C8	1.2209(18)	C25	C26	1.5153(17)
O2	C11	1.2180(18)	C26	C27	1.3914(18)
O3	C35	1.2195(17)	C26	C31	1.3934(19)
O4	C32	1.2227(17)	C27	C28	1.3953(19)
O5	C43	1.2680(16)	C28	C29	1.387(2)
O6	C46	1.2743(16)	C29	C30	1.383(2)
N1	N2	1.4258(15)	C30	C31	1.393(2)
N1	C7	1.4548(16)	C32	C33	1.506(2)
N1	C8	1.3579(17)	C33	C34	1.532(2)
N2	C11	1.3808(17)	C34	C35	1.5029(19)
N2	C12	1.4645(16)	C36	C37	1.5148(18)
N3	N4	1.4255(15)	C37	C38	1.3901(18)
N3	C35	1.3765(17)	C37	C42	1.3956(18)
N3	C36	1.4592(16)	C38	C39	1.392(2)
N4	C25	1.4530(16)	C39	C40	1.386(2)
N4	C32	1.3652(16)	C40	C41	1.384(2)
C1	C2	1.3881(19)	C41	C42	1.388(2)
C1	C6	1.3961(18)	C43	C44	1.5099(18)
C1	C7	1.5136(17)	C43	C45	1.403(2)
C2	C3	1.3914(19)	C45	C46	1.3938(19)
C3	C4	1.385(2)	C46	C47	1.5080(19)
C4	C5	1.386(2)	Cl1	C48	1.7627(19)

C5	C6	1.391(2)	Cl2	C48	1.7565(19)
C8	C9	1.5047(19)	Cl3	C49	1.7725(19)
C9	C10	1.524(2)	Cl4	C49	1.768(2)
C10	C11	1.501(2)	Cl5	C50	1.761(2)
C12	C13	1.5143(17)	Cl6	C50	1.717(3)
C13	C14	1.3858(19)	Cl6A	C50	1.730(5)
C13	C18	1.3984(19)			

Table C-42. Bond Angles for [Rh(acac)TPSB BDP **1**].

Atom	**Atom**	**Atom**	**Angle/°**	**Atom**	**Atom**	**Atom**	**Angle/°**
P2	Rh1	P1	85.09(3)	C13	C14	C15	120.37(14)
O5	Rh1	P1	92.66(4)	C16	C15	C14	120.34(14)
O5	Rh1	P2	174.56(3)	C15	C16	C17	119.61(14)
O6	Rh1	P1	173.49(3)	C16	C17	C18	120.36(15)
O6	Rh1	P2	92.14(4)	C17	C18	C13	120.20(14)
O6	Rh1	O5	90.60(4)	C20	C19	P1	126.12(10)
C7	P1	Rh1	120.43(4)	C20	C19	C24	119.90(11)
C12	P1	Rh1	119.43(4)	C24	C19	P1	113.93(9)
C12	P1	C7	90.89(6)	C21	C20	C19	119.59(12)
C19	P1	Rh1	113.19(5)	C20	C21	C22	120.53(12)
C19	P1	C7	102.71(6)	C23	C22	C21	120.12(12)
C19	P1	C12	107.04(6)	C22	C23	C24	119.78(12)
C24	P2	Rh1	112.95(5)	C19	C24	P2	114.68(9)

C24	P2	C25	103.37(6)	C23	C24	P2	125.22(10)
C24	P2	C36	106.29(6)	C23	C24	C19	120.09(11)
C25	P2	Rh1	121.31(4)	N4	C25	P2	104.00(8)
C36	P2	Rh1	118.29(4)	N4	C25	C26	114.87(10)
C36	P2	C25	91.70(6)	C26	C25	P2	113.42(8)
C43	O5	Rh1	125.09(9)	C27	C26	C25	122.20(12)
C46	O6	Rh1	125.02(9)	C27	C26	C31	119.38(12)
N2	N1	C7	114.61(10)	C31	C26	C25	118.42(12)
C8	N1	N2	120.29(11)	C26	C27	C28	120.00(13)
C8	N1	C7	124.54(11)	C29	C28	C27	120.38(14)
N1	N2	C12	113.35(10)	C30	C29	C28	119.68(14)
C11	N2	N1	118.05(11)	C29	C30	C31	120.31(14)
C11	N2	C12	121.97(11)	C30	C31	C26	120.25(14)
N4	N3	C36	114.31(10)	O4	C32	N4	120.31(12)
C35	N3	N4	120.48(11)	O4	C32	C33	126.17(12)
C35	N3	C36	120.88(10)	N4	C32	C33	113.46(12)
N3	N4	C25	115.04(10)	C32	C33	C34	108.92(11)
C32	N4	N3	120.80(11)	C35	C34	C33	111.33(11)
C32	N4	C25	123.23(11)	O3	C35	N3	120.19(12)
C2	C1	C6	119.05(12)	O3	C35	C34	125.29(12)
C2	C1	C7	122.43(11)	N3	C35	C34	114.39(12)
C6	C1	C7	118.44(12)	N3	C36	P2	106.94(8)
C1	C2	C3	120.51(13)	N3	C36	C37	114.66(10)
C4	C3	C2	120.19(13)	C37	C36	P2	112.16(9)

C3	C4	C5	119.72(13)	C38	C37	C36	122.91(12)
C4	C5	C6	120.19(13)	C38	C37	C42	119.11(12)
C5	C6	C1	120.32(13)	C42	C37	C36	117.95(11)
N1	C7	P1	102.81(8)	C37	C38	C39	120.05(14)
N1	C7	C1	114.60(10)	C40	C39	C38	120.45(14)
C1	C7	P1	111.55(8)	C41	C40	C39	119.75(14)
O1	C8	N1	120.98(12)	C40	C41	C42	120.04(14)
O1	C8	C9	126.11(12)	C41	C42	C37	120.60(13)
N1	C8	C9	112.75(12)	O5	C43	C44	115.98(12)
C8	C9	C10	107.25(11)	O5	C43	C45	126.02(12)
C11	C10	C9	110.52(11)	C45	C43	C44	117.99(12)
O2	C11	N2	120.50(13)	C46	C45	C43	126.97(12)
O2	C11	C10	125.59(12)	O6	C46	C45	126.26(12)
N2	C11	C10	113.71(12)	O6	C46	C47	114.76(12)
N2	C12	P1	106.78(8)	C45	C46	C47	118.98(12)
N2	C12	C13	114.69(10)	Cl2	C48	Cl1	112.61(10)
C13	C12	P1	112.26(9)	Cl4	C49	Cl3	111.99(9)
C14	C13	C12	122.77(12)	Cl6	C50	Cl5	115.96(13)
C14	C13	C18	119.11(12)	Cl6A	C50	Cl5	108.6(4)
C18	C13	C12	118.12(12)				

Table C-43. Torsion Angles for [Rh(acac)TPSB BDP **1**].

A	**B**	**C**	**D**	**Angle/˚**	**A**	**B**	**C**	**D**	**Angle/˚**

Rh1	P1	C7	N1	-155.12(6)	C9	C10	C11	O2	-148.94(13)
Rh1	P1	C7	C1	-31.84(10)	C9	C10	C11	N2	25.82(15)
Rh1	P1	C12	N2	145.61(6)	C11	N2	C12	P1	-154.01(10)
Rh1	P1	C12	C13	-87.88(9)	C11	N2	C12	C13	80.95(14)
Rh1	P1	C19	C20	178.04(10)	C12	P1	C7	N1	-29.73(8)
Rh1	P1	C19	C24	-4.57(10)	C12	P1	C7	C1	93.55(9)
Rh1	P2	C24	C19	-1.32(10)	C12	P1	C19	C20	44.38(13)
Rh1	P2	C24	C23	179.49(9)	C12	P1	C19	C24	-138.23(9)
Rh1	P2	C25	N4	-148.84(6)	C12	N2	C11	O2	-11.07(18)
Rh1	P2	C25	C26	-23.36(10)	C12	N2	C11	C10	173.88(11)
Rh1	P2	C36	N3	140.86(7)	C12	C13	C14	C15	179.77(13)
Rh1	P2	C36	C37	-92.62(9)	C12	C13	C18	C17	-178.82(13)
Rh1	O5	C43	C44	179.56(9)	C13	C14	C15	C16	-1.1(2)
Rh1	O5	C43	C45	-0.92(19)	C14	C13	C18	C17	0.3(2)
Rh1	O6	C46	C45	-0.4(2)	C14	C15	C16	C17	0.5(2)
Rh1	O6	C46	C47	-179.89(9)	C15	C16	C17	C18	0.5(2)
P1	C12	C13	C14	-115.06(12)	C16	C17	C18	C13	-0.9(2)
P1	C12	C13	C18	64.05(14)	C18	C13	C14	C15	0.7(2)
P1	C19	C20	C21	177.05(10)	C19	P1	C7	N1	77.96(9)
P1	C19	C24	P2	3.58(12)	C19	P1	C7	C1	-158.76(9)
P1	C19	C24	C23	-177.18(9)	C19	P1	C12	N2	-84.16(9)
P2	C25	C26	C27	-101.83(13)	C19	P1	C12	C13	42.35(10)
P2	C25	C26	C31	77.34(13)	C19	C20	C21	C22	0.2(2)
P2	C36	C37	C38	-113.35(13)	C20	C19	C24	P2	-178.85(10)

P2	C36	C37	C42	64.69(13)	C20	C19	C24	C23	0.39(18)
O1	C8	C9	C10	-128.18(15)	C20	C21	C22	C23	-0.4(2)
O4	C32	C33	C34	-131.61(14)	C21	C22	C23	C24	0.6(2)
O5	C43	C45	C46	-0.8(2)	C22	C23	C24	P2	178.56(10)
N1	N2	C11	O2	-160.61(11)	C22	C23	C24	C19	-0.59(19)
N1	N2	C11	C10	24.33(15)	C24	P2	C25	N4	83.32(9)
N1	N2	C12	P1	-3.17(12)	C24	P2	C25	C26	-151.21(9)
N1	N2	C12	C13	-128.21(11)	C24	P2	C36	N3	-90.93(9)
N1	C8	C9	C10	47.22(15)	C24	P2	C36	C37	35.59(10)
N2	N1	C7	P1	34.74(11)	C24	C19	C20	C21	-0.20(19)
N2	N1	C7	C1	-86.48(13)	C25	P2	C24	C19	131.57(9)
N2	N1	C8	O1	177.31(12)	C25	P2	C24	C23	-47.62(12)
N2	N1	C8	C9	1.64(17)	C25	P2	C36	N3	13.53(9)
N2	C12	C13	C14	7.05(17)	C25	P2	C36	C37	140.05(9)
N2	C12	C13	C18	-173.84(11)	C25	N4	C32	O4	6.84(19)
N3	N4	C25	P2	29.99(12)	C25	N4	C32	C33	-170.44(11)
N3	N4	C25	C26	-94.56(13)	C25	C26	C27	C28	179.58(12)
N3	N4	C32	O4	175.27(11)	C25	C26	C31	C30	-179.10(13)
N3	N4	C32	C33	-2.02(17)	C26	C27	C28	C29	-0.7(2)
N3	C36	C37	C38	8.88(17)	C27	C26	C31	C30	0.1(2)
N3	C36	C37	C42	-173.08(11)	C27	C28	C29	C30	0.4(2)
N4	N3	C35	O3	-164.52(12)	C28	C29	C30	C31	0.1(2)
N4	N3	C35	C34	19.43(17)	C29	C30	C31	C26	-0.4(2)
N4	N3	C36	P2	1.09(12)	C31	C26	C27	C28	0.4(2)

N4	N3	C36	C37	-123.93(11)	C32	N4	C25	P2	-160.98(10)
N4	C25	C26	C27	17.61(17)	C32	N4	C25	C26	74.48(15)
N4	C25	C26	C31	-163.23(11)	C32	C33	C34	C35	-57.64(16)
N4	C32	C33	C34	45.49(15)	C33	C34	C35	O3	-150.24(14)
C1	C2	C3	C4	-1.1(2)	C33	C34	C35	N3	25.58(17)
C2	C1	C6	C5	0.9(2)	C35	N3	N4	C25	135.26(12)
C2	C1	C7	P1	-86.74(13)	C35	N3	N4	C32	-34.07(17)
C2	C1	C7	N1	29.56(17)	C35	N3	C36	P2	-155.63(10)
C2	C3	C4	C5	1.6(2)	C35	N3	C36	C37	79.36(15)
C3	C4	C5	C6	-0.8(2)	C36	P2	C24	C19	-132.61(9)
C4	C5	C6	C1	-0.4(2)	C36	P2	C24	C23	48.20(12)
C6	C1	C2	C3	-0.1(2)	C36	P2	C25	N4	-23.87(8)
C6	C1	C7	P1	89.96(13)	C36	P2	C25	C26	101.61(10)
C6	C1	C7	N1	-153.74(12)	C36	N3	N4	C25	-21.57(14)
C7	P1	C12	N2	19.43(8)	C36	N3	N4	C32	169.11(11)
C7	P1	C12	C13	145.94(9)	C36	N3	C35	O3	-9.23(19)
C7	P1	C19	C20	-50.55(12)	C36	N3	C35	C34	174.72(11)
C7	P1	C19	C24	126.85(9)	C36	C37	C38	C39	177.30(13)
C7	N1	N2	C11	130.19(12)	C36	C37	C42	C41	-176.88(13)
C7	N1	N2	C12	-21.88(14)	C37	C38	C39	C40	-0.3(2)
C7	N1	C8	O1	6.4(2)	C38	C37	C42	C41	1.2(2)
C7	N1	C8	C9	-169.29(12)	C38	C39	C40	C41	0.7(3)
C7	C1	C2	C3	176.53(12)	C39	C40	C41	C42	-0.2(3)
C7	C1	C6	C5	-175.94(13)	C40	C41	C42	C37	-0.8(2)

C8	N1	N2	C11	-41.59(16)	C42	C37	C38	C39	-0.7(2)
C8	N1	N2	C12	166.33(11)	C43	C45	C46	O6	1.6(2)
C8	N1	C7	P1	-153.87(11)	C43	C45	C46	C47	-178.94(14)
C8	N1	C7	C1	84.91(15)	C44	C43	C45	C46	178.68(14)
C8	C9	C10	C11	-61.47(14)					

Table C-44. Hydrogen Atom Coordinates (Å×10^4) and Isotropic Displacement Parameters (Å^2×10^3) for [Rh(acac)TPSB BDP **1**].

Atom	***x***	***y***	***z***	**U(eq)**
H2	7987	8405	7363	23
H3	7838	8617	6092	25
H4	6360	7611	4953	26
H5	4983	6453	5108	31
H6	5107	6265	6387	25
H7	5889	6904	7862	15
H9A	7964	9548	10143	28
H9B	7293	10403	9907	28
H10A	8224	10177	8784	27
H10B	9119	10598	9663	27
H12	9188	7055	7902	16
H14	9521	7851	10034	24
H15	10743	7258	10892	34
H16	11487	5688	10302	36

H17	11031	4718	8845	33
H18	9854	5329	7980	25
H20	7243	6975	9578	20
H21	6535	6223	10425	22
H22	5910	4368	9913	21
H23	5963	3254	8538	18
H25	7951	2779	7824	16
H27	7069	769	5780	23
H28	8217	170	4824	31
H29	9983	1156	5068	34
H30	10612	2730	6279	34
H31	9485	3322	7249	26
H33A	5082	427	7553	26
H33B	5791	-541	7273	26
H34A	5584	-510	5917	27
H34B	4370	-675	6104	27
H36	5318	2641	5990	15
H38	3882	2342	7424	26
H39	2444	3271	7886	35
H40	2142	4816	7639	37
H41	3258	5419	6905	33
H42	4677	4483	6424	24
H44A	8459	6496	4862	35
H44B	9587	5993	4935	35

H44C	9328	6896	5749	35
H45	8245	4281	4247	25
H47A	7477	1819	4239	39
H47B	7732	2450	3666	39
H47C	6492	2265	3802	39
H48A	1599	8301	8511	70
H48B	1918	7293	8719	70
H49A	4975	1376	10121	43
H49B	5142	421	9297	43
H50A	10106	9229	3100	50
H50B	10649	9582	2462	50
H50C	10259	9191	3053	50
H50D	10563	9749	2440	50

Table C-45. Atomic Occupancy for [Rh(acac)TPSB BDP **1**]

Atom	**Occupancy**	**Atom**	**Occupancy**	**Atom**	**Occupancy**
Cl6	0.613(19)	Cl6A	0.387(19)	H50A	0.613(19)
H50B	0.613(19)	H50C	0.387(19)	H50D	0.387(19)

C.7 References

[1] Bruker-AXS (2016). *APEX3.* Version 2016.5-0. Madison, Wisconsin, USA.

[2] Krause, L., Herbst-Irmer, R., Sheldrick, G. M. & Stalke, D. (2015). *J. Appl. Cryst.* 48. 3-10.

[3] Sheldrick, G. M. (2013b). *XPREP*. Version 2013/1. Georg-August-Universität Göttingen, Göttingen, Germany.

[4] Sheldrick, G. M. (2013a). The *SHELX* homepage, http://shelx.uni-ac.gwdg.de/SHELX/.

[5] Sheldrick, G. M. (2015a). *Acta Cryst. A*, 71, 3-8.

[6] Sheldrick, G. M. (2015b). *Acta Cryst. C*, 71, 3-8.

[7] Dolomanov, O. V., Bourhis, L. J., Gildea, R. J., Howard, J. A. K. & Puschmann, H. (2009). *J. Appl. Crystallogr.* 42, 339-341.

[8] Guzei, I. A. (2007-2013). Programs *Gn*. University of Wisconsin-Madison, Madison, Wisconsin, USA.

[9] Spek, A. L. (2015). *Acta Cryst. C*, 71, 9-18.

[10] Bruker-AXS. (**2007-2014**) APEX2 (Ver. 2014.1-1), SADABS (2014-3), and SAINT+ (Ver. 8.32A) Software Reference Manuals. Bruker-AXS, Madison, Wisconsin, USA.

[11] Sheldrick, G. M. (**2008**) SHELXL. *Acta Cryst.* **A64**, 112-122.

[12] Bruker-AXS (2014). *APEX2.* Version 2014.11-0. Madison, Wisconsin, USA.

Appendix D

Calculated Optimized XYX Coordinates for Compounds in Chapter 6

Table D-1. Optimized XYZ Coordinates of TPSB BDP **1**.

C	0.00000000	0.00000000	0.00000000
P	-1.70467900	0.68293800	0.49057300
C	-0.89833800	2.40609100	0.75880200
N	0.37952900	2.39762800	0.03138700
N	0.74759700	1.13740900	-0.52098900
C	1.61810000	1.06865100	-1.58250500
O	1.81204500	0.02582500	-2.19400700
C	2.33483000	2.38515400	-1.84480900
H	1.69778200	3.01739000	-2.47874200
H	3.24122200	2.15918600	-2.41073900
C	2.63737400	3.10347700	-0.52112000
H	3.32925900	2.50155300	0.08426200
H	3.10825500	4.07721800	-0.67650800
C	1.36626700	3.33596200	0.28630300
O	1.17717700	4.28080200	1.03422000
H	-0.67682800	2.44004700	1.83279500
C	-1.77398200	3.59668300	0.42394300
C	-1.87941000	4.09975200	-0.87870100
H	-1.30643400	3.64276900	-1.67907300
C	-2.70557800	5.18924200	-1.15274500
H	-2.77079000	5.57130000	-2.16805700
C	-3.44218600	5.79003600	-0.12982200
H	-4.07750300	6.64560500	-0.34341800
C	-3.34448000	5.29271500	1.17120700
H	-3.90461700	5.75624300	1.97863700

C -2.51416000 4.20579400 1.44434400

H -2.43351600 3.83203400 2.46195000

C -2.56119400 0.84776600 -1.16148500

C -1.89412800 0.72037800 -2.39027000

H -0.82707800 0.53380600 -2.42422300

C -2.57898300 0.82683600 -3.60057000

H -2.03637700 0.72546600 -4.53661300

C -3.94914500 1.07411500 -3.60042500

H -4.49166600 1.17704000 -4.53634600

C -4.63410700 1.17860000 -2.39001200

H -5.70113900 1.36527600 -2.42376300

C -3.96713800 1.04918500 -1.16137200

P -4.82383200 1.21152300 0.49080200

C -6.52864500 1.89459000 0.00115700

N -7.27584100 0.75793200 -0.52205900

N -6.90697500 -0.50345200 0.02746900

C -7.89411100 -1.44180500 0.28163400

O -7.70564100 -2.38688200 1.02933900

C -9.16471200 -1.20865400 -0.52639800

C -8.86157800 -0.48831500 -1.84886600

C -8.14553400 0.82809400 -1.58414700

O -8.33942000 1.87178200 -2.19418700

H -8.22388100 -1.11940200 -2.48328300

H -9.76771500 -0.26190000 -2.41503500

H -9.85722200 -0.60788400 0.07941600

H -9.63515500 -2.18233100 -0.68351800

C -5.63005200 -0.51205800 0.75662100

H	-5.85290000	-0.54667100	1.83034000
C	-4.75414500	-1.70251200	0.42211100
C	-4.64624800	-2.20394100	-0.88098100
H	-5.21717700	-1.74552300	-1.68198900
C	-3.82027200	-3.29367700	-1.15465700
H	-3.75312000	-3.67444000	-2.17033100
C	-3.08637300	-3.89639300	-0.13091700
H	-2.45128900	-4.75221000	-0.34424100
C	-3.18650200	-3.40067100	1.17054600
H	-2.62848800	-3.86569900	1.97857500
C	-4.01654700	-2.31345200	1.44328700
H	-4.09912900	-1.94094800	2.46119900
H	-6.41512400	2.60912800	-0.81632500
C	-7.19695800	2.59334300	1.17601000
C	-7.97107400	1.90362900	2.11739600
H	-8.13574400	0.83523900	2.01329900
C	-8.54855600	2.57992300	3.19359300
H	-9.14901800	2.02921700	3.91271700
C	-8.35777600	3.95336800	3.34567100
H	-8.80996900	4.47943900	4.18190400
C	-7.58503800	4.64781100	2.41268100
H	-7.43686100	5.71945600	2.51697500
C	-7.00988400	3.97251500	1.33722800
H	-6.40731400	4.51871800	0.61561200
C	0.66784800	-0.70138900	1.17353000
C	1.44542800	-0.01459900	2.11415400
H	1.61304000	1.05335900	2.01043200

C	2.02258800	-0.69331100	3.18901100
H	2.62577200	-0.14485800	3.90757800
C	1.82804100	-2.06629100	3.34043900
H	2.27997700	-2.59426700	4.17561100
C	1.05180200	-2.75781700	2.40817500
H	0.90062200	-3.82909100	2.51197600
C	0.47693200	-2.08010600	1.33410700
H	-0.12844600	-2.62402400	0.61312300
H	-0.11379200	-0.71285100	-0.81891300

Table D-2. Optimized XYZ Coordinates of red-TPSB BDP **2**.

C	0.00000000	0.00000000	0.00000000
P	1.60164700	-0.94926700	-0.44902400
C	0.60761500	-2.57609700	-0.32139500
N	-0.56863000	-2.27781100	0.50877900
N	-1.08910500	-0.99527600	-0.01031900
C	-2.20518100	-0.55468800	0.83820100
H	-2.51490600	0.42915600	0.47244600
H	-1.87187900	-0.43911000	1.88639800
C	-3.36326500	-1.55088700	0.76718400
H	-4.16858300	-1.23005800	1.43918400
H	-3.76744300	-1.55404600	-0.25322600
C	-2.86190500	-2.95114400	1.13068500
H	-3.63790700	-3.70659600	0.95733400
H	-2.59965200	-2.98876100	2.19625100
C	-1.62260400	-3.28922800	0.30166500

H -1.20866500 -4.25712400 0.59665700

H -1.88934000 -3.33998600 -0.76950400

H 0.29030200 -2.74373100 -1.36714600

C 1.40323500 -3.77694500 0.13285500

C 2.17554100 -4.47510000 -0.80728000

H 2.17776700 -4.14870600 -1.84479800

C 2.94156900 -5.57689900 -0.42909900

H 3.53445600 -6.09869700 -1.17517600

C 2.94051800 -6.00946900 0.89892900

H 3.52802800 -6.87491100 1.19444000

C 2.17173100 -5.32536300 1.84154800

H 2.16043600 -5.65454300 2.87758900

C 1.41360200 -4.21589600 1.46439100

H 0.81576200 -3.68856600 2.19916100

C 2.53645200 -0.87394500 1.16971200

C 1.86868300 -0.97933100 2.40547300

H 0.79898400 -1.16005500 2.41389400

C 2.54999200 -0.88420300 3.61503700

H 2.00645600 -0.97502600 4.55231900

C 3.92891500 -0.67286400 3.61502100

H 4.47246900 -0.58202900 4.55229200

C 4.61020400 -0.57777000 2.40544400

H 5.67990400 -0.39705300 2.41382700

C 3.94240900 -0.68318400 1.16969500

P 4.87723200 -0.60796300 -0.44903900

C 6.47879600 -1.55735400 0.00000000

N 7.56799700 -0.56218100 -0.01042700

N	7.04768000	0.72042900	0.50865000
C	8.10173600	1.73173700	0.30142300
C	9.34105500	1.39356300	1.13037900
C	9.84225700	-0.00675800	0.76690600
C	8.68408500	-1.00284400	0.83804400
H	8.99368900	-1.98673100	0.47230400
H	8.35083600	-1.11835000	1.88626400
H	10.6475900	-0.32762500	1.43886900
H	10.2463680	-0.00368400	-0.25353000
H	10.1171240	2.14893000	0.95695000
H	9.07887200	1.43124800	2.19595900
H	7.68790900	2.69968400	0.59640400
H	8.36840900	1.78242700	-0.76976600
C	5.87140400	1.01879500	-0.32146100
H	6.18868000	1.18639800	-1.36722200
C	5.07586000	2.21967100	0.13282700
C	5.06566300	2.65870900	1.46433500
H	5.66359400	2.13143700	2.19907300
C	4.30756700	3.76818900	1.84152400
H	4.31899800	4.09743300	2.87754300
C	3.53864200	4.45222500	0.89896800
H	2.95115700	5.31767500	1.19450500
C	3.53742500	4.01957200	-0.42903400
H	2.94443500	4.54131200	-1.17506600
C	4.30342100	2.91776300	-0.80724700
H	4.30106400	2.59130700	-1.84474500
H	6.33172900	-1.98495400	1.00367500

C 6.77191700 -2.68838000 -0.96680200

C 6.41703800 -4.00180200 -0.63403200

H 5.94369400 -4.20424100 0.32397500

C 6.65896100 -5.05296800 -1.52023200

H 6.38298300 -6.06657600 -1.24038200

C 7.26347100 -4.80639300 -2.75349900

H 7.45732000 -5.62459900 -3.44222000

C 7.62237000 -3.49986900 -3.09313000

H 8.09619400 -3.29728200 -4.05043500

C 7.37833100 -2.44994900 -2.20853100

H 7.67259700 -1.43627600 -2.46105900

C -0.29325000 1.13096000 -0.96683800

C -0.89989700 0.89248000 -2.20844200

H -1.19423700 -0.12119900 -2.46085300

C -1.14406400 1.94236300 -3.09305200

H -1.61807200 1.73973800 -4.05025900

C -0.78506100 3.24889200 -2.75356200

H -0.97901800 4.06707000 -3.44228600

C -0.18031000 3.49551500 -1.52041900

H 0.09576100 4.50912800 -1.24068100

C 0.06173900 2.44439200 -0.63420700

H 0.53525600 2.64687000 0.32370800

H 0.14705700 0.42766900 1.00364900

Table D-3. Optimized XYZ Coordinates of TPPB BDP **3**.

C 0.00000000 0.00000000 0.00000000

P -1.49117000 -1.01355800 0.50277200

C -0.37357600 -2.52155500 0.71714500

N 0.84703400 -2.25864700 -0.04472000

N 0.95237700 -0.95123700 -0.55230000

C 1.94349500 -0.56752300 -1.39260500

O 1.94099600 0.51829300 -1.91062200

C 3.04755600 -1.54544500 -1.56615100

C 4.08985700 -1.25035400 -2.43526000

H 4.04958800 -0.34391900 -3.00753200

C 5.15867500 -2.11932400 -2.53376900

H 5.96710900 -1.89891400 -3.20702900

C 5.19818100 -3.27377900 -1.75877100

H 6.03559600 -3.94300900 -1.83840200

C 4.16670500 -3.56529300 -0.88767600

H 4.17617400 -4.45226100 -0.28439100

C 3.08513700 -2.69899200 -0.79534800

C 1.94807000 -3.04922700 0.09772600

O 1.95385700 -4.00499600 0.82152400

H -0.11535500 -2.52960100 1.76962900

C -1.01929000 -3.85499300 0.39057600

C -1.64474700 -4.56074100 1.40930700

H -1.64301900 -4.16822600 2.41079600

C -2.26473100 -5.77307200 1.15380800

H -2.73812600 -6.30732400 1.95797000

C -2.26137900 -6.29872700 -0.12727700

H -2.73120700 -7.24539800 -0.32695400

C -1.63654400 -5.60067000 -1.14865800

H -1.62400900 -6.00200300 -2.14629100

C -1.02165200 -4.38743800 -0.89264000

H -0.53705300 -3.86087000 -1.69267800

C -2.36717400 -1.29097400 -1.11779400

C -1.72526200 -1.10256500 -2.34112600

H -0.69252700 -0.82014300 -2.37150100

C -2.38597100 -1.27762200 -3.54359500

H -1.85964000 -1.12578000 -4.46881200

C -3.71441200 -1.65421200 -3.54360100

H -4.24076100 -1.80596400 -4.46882400

C -4.37510500 -1.82936700 -2.34113800

H -5.40785200 -2.11173900 -2.37151500

C -3.73316900 -1.64109000 -1.11780000

P -4.60914500 -1.91858600 0.50276100

C -5.72690600 -0.41070600 0.71704300

N -6.94742400 -0.67373200 -0.04492100

N -7.05265300 -1.98122900 -0.55234600

C -6.10019700 -2.93233500 0.00003400

H -5.82652600 -3.61575000 -0.78710700

C -6.65458000 -3.73885800 1.16644500

C -7.58909200 -3.22168300 2.05364500

H -7.97459200 -2.22746300 1.92232900

C -8.04861300 -3.98338700 3.11742700

H -8.77470500 -3.56732700 3.79273900

C -7.57949000 -5.27065200 3.30860200

H -7.93845800 -5.86178500 4.13184900

C -6.64743600 -5.79436500 2.42613200

H -6.28301900 -6.79739800 2.55953500

C -6.19053500 -5.03454500 1.36442900

H -5.47013100 -5.45149700 0.68331500

C -8.04384600 -2.36518000 -1.39247600

O -8.04128100 -3.45106700 -1.91033200

C -9.14802600 -1.38740200 -1.56605300

C -9.18567500 -0.23377400 -0.79536900

C -8.04859300 0.11667000 0.09759600

O -8.05445700 1.07248600 0.82132900

C -10.2673430 0.63239400 -0.88770900

H -10.2768700 1.51942600 -0.28451800

C -11.2988580 0.34067200 -1.75869600

H -12.1363510 1.00980400 -1.83832700

C -11.2592870 -0.81386200 -2.53356500

H -12.0677400 -1.03443300 -3.20674800

C -10.1903600 -1.68270300 -2.43504500

H -10.1500430 -2.58920000 -3.00721300

H -5.98520800 -0.40264400 1.76951000

C -5.08121800 0.92275200 0.39050400

C -4.45552300 1.62833300 1.40920800

H -4.45701400 1.23565600 2.41063500

C -3.83553200 2.84066700 1.15374800

H -3.36191600 3.37477000 1.95787900

C -3.83918600 3.36653300 -0.12725100

H -3.36938800 4.31322800 -0.32688300

C -4.46429000 2.66866200 -1.14859200

H -4.47705300 3.07015300 -2.14615800

C	-5.07914200	1.45539300	-0.89262700
H	-5.56394800	0.92896600	-1.69263100
H	-0.27357300	0.68339100	-0.78719700
C	0.55442200	0.80658300	1.16636100
C	1.48871500	0.28933100	2.05376300
H	1.87402900	-0.70498700	1.92264200
C	1.94826600	1.05109500	3.11748200
H	2.67418100	0.63498000	3.79295100
C	1.47940000	2.33849700	3.30840600
H	1.83838400	2.92967200	4.13161600
C	0.54758200	2.86228200	2.42574200
H	0.18337000	3.86541600	2.55894300
C	0.09064000	2.10239500	1.36409400
H	-0.62957700	2.51941300	0.68282000

Table D-4. Optimized XYZ Coordinates of red-TPPB BDP **4**.

C	0.00000000	0.00000000	0.00000000
P	-0.98944000	-1.62352300	-0.10929700
C	-2.55819400	-0.62754800	0.35153100
N	-2.16636000	0.79271400	0.45123900
N	-0.75661800	0.90192500	0.88014700
C	-0.35966800	2.29777400	0.62164400
H	-0.38079500	2.49854000	-0.46600800
H	0.67498000	2.41355900	0.95786300
C	-1.25961700	3.28529500	1.32575400
C	-0.82965600	4.59085700	1.58801300

H	0.18165000	4.88531600	1.31461500
C	-1.68199500	5.51229500	2.19338300
H	-1.33587600	6.52286900	2.39308200
C	-2.97937300	5.13033400	2.54457200
H	-3.65146900	5.84269500	3.01547100
C	-3.41078500	3.83065600	2.28671000
H	-4.42066200	3.52994200	2.55891800
C	-2.55819400	2.90361300	1.67747300
C	-3.00294800	1.47952100	1.44106100
H	-2.99875600	0.93377400	2.40446500
H	-4.03070500	1.45569400	1.06214700
H	-2.89664800	-1.01785100	1.32346000
C	-3.68095800	-0.81040700	-0.65311400
C	-3.75784900	-0.03189500	-1.81601000
H	-3.01773800	0.74539200	-1.97589000
C	-4.78434900	-0.23365400	-2.73876000
H	-4.83096000	0.38186400	-3.63367300
C	-5.74996200	-1.21733000	-2.51605300
H	-6.55123700	-1.37149200	-3.23406200
C	-5.68143300	-1.99660900	-1.36007600
H	-6.43214400	-2.75977600	-1.17072900
C	-4.65614700	-1.79279400	-0.43572000
H	-4.61129200	-2.40681700	0.46091900
C	-0.60955000	-2.47882600	1.51096500
C	-0.81929500	-1.83617600	2.74689200
H	-1.14414800	-0.80112600	2.75722200
C	-0.59133800	-2.48521000	3.95656800

H	-0.75734300	-1.95929300	4.89349400
C	-0.15103600	-3.80868600	3.95656800
C	0.07692100	-4.45772000	2.74689200
C	-0.13282400	-3.81507000	1.51096500
P	0.24706600	-4.67037300	-0.10929700
C	-0.74237400	-6.29389600	0.00000000
N	0.01424400	-7.19582100	0.88014700
N	1.42398600	-7.08661000	0.45123900
C	2.26057400	-7.77341700	1.44106100
C	1.81582000	-9.19750900	1.67747300
C	0.51724300	-9.57919100	1.32575400
C	-0.38270600	-8.59167000	0.62164400
H	-0.36157900	-8.79243600	-0.46600800
H	-1.41735400	-8.70745500	0.95786300
C	0.08728200	-10.8847530	1.58801300
H	-0.92402400	-11.1792120	1.31461500
C	0.93962100	-11.8061910	2.19338300
H	0.59350200	-12.8167650	2.39308200
C	2.23699900	-11.4242300	2.54457200
H	2.90909500	-12.1365910	3.01547100
C	2.66841100	-10.1245520	2.28671000
H	3.67828800	-9.82383800	2.55891800
H	2.25638200	-7.22767000	2.40446500
H	3.28833100	-7.74959000	1.06214700
C	1.81582000	-5.66634800	0.35153100
H	2.15427400	-5.27604500	1.32346000
C	2.93858400	-5.48348900	-0.65311400

C 3.01547500 -6.26200100 -1.81601000

H 2.27536400 -7.03928800 -1.97589000

C 4.04197500 -6.06024200 -2.73876000

H 4.08858600 -6.67576000 -3.63367300

C 5.00758800 -5.07656600 -2.51605300

H 5.80886300 -4.92240400 -3.23406200

C 4.93905900 -4.29728700 -1.36007600

H 5.68977000 -3.53412000 -1.17072900

C 3.91377300 -4.50110200 -0.43572000

H 3.86891800 -3.88707900 0.46091900

H -0.69560500 -6.66879400 -1.03992500

C -2.19582300 -6.13803400 0.38288900

C -3.12983200 -5.80685900 -0.60958000

H -2.79681300 -5.68376800 -1.63762200

C -4.47722300 -5.63318600 -0.29525900

H -5.18204700 -5.37493100 -1.08083900

C -4.91741000 -5.79881600 1.01990100

H -5.96889300 -5.67529700 1.26593000

C -3.99686800 -6.13463400 2.01385000

H -4.32888600 -6.27088100 3.03997200

C -2.64660300 -6.29863600 1.70075900

H -1.93493900 -6.56306700 2.47481600

H 0.40177400 -5.49277000 2.75722200

H 0.01496900 -4.33460300 4.89349400

H -0.04676900 0.37489800 -1.03992500

C 1.45344900 -0.15586200 0.38288900

C 2.38745800 -0.48703700 -0.60958000

H	2.05443900	-0.61012800	-1.63762200
C	3.73484900	-0.66071000	-0.29525900
H	4.43967300	-0.91896500	-1.08083900
C	4.17503600	-0.49508000	1.01990100
H	5.22651900	-0.61859900	1.26593000
C	3.25449400	-0.15926200	2.01385000
H	3.58651200	-0.02301500	3.03997200
C	1.90422900	0.00474000	1.70075900
H	1.19256500	0.26917100	2.47481600

Table D-5. Optimized XYZ Coordinates of TPSB BDPE **5**.

C	0.00000000	0.00000000	0.00000000
P	-1.29624800	-1.38076900	0.16287400
C	-2.07384500	-0.78500400	-1.47301500
N	-1.02441300	-0.06315900	-2.20383200
N	0.14998400	0.19714700	-1.43552100
C	1.34964300	0.46328800	-2.05486400
O	2.39599100	0.55428600	-1.42955700
C	1.19315200	0.71668900	-3.54722500
H	1.16914900	-0.24888600	-4.07019500
H	2.08100100	1.25565900	-3.88475400
C	-0.10026400	1.50056600	-3.81829900
H	-0.04842000	2.48821100	-3.33932300
H	-0.26894800	1.66910600	-4.88482400
C	-1.31966400	0.76661000	-3.27495100
O	-2.43925600	0.81874700	-3.75645800

H -2.84759100 -0.06255700 -1.18067700

C -2.74590000 -1.89542100 -2.25845000

C -2.16669200 -2.48476500 -3.38602200

H -1.20933800 -2.12503200 -3.74761200

C -2.81988900 -3.52163500 -4.05664100

H -2.36806500 -3.94972800 -4.94840900

C -4.05054100 -3.99533200 -3.59934700

H -4.55879500 -4.80106300 -4.12147700

C -4.63292800 -3.41348600 -2.47106900

H -5.59251200 -3.77005800 -2.10770900

C -3.98962700 -2.36669800 -1.81356500

H -4.45771300 -1.90793100 -0.94536200

C -0.20373800 -2.83121000 -0.33913800

C -0.94252600 -4.18323800 -0.33913800

P 0.14998400 -5.63367900 0.16287400

C -1.14626400 -7.01444800 0.00000000

N -1.29624800 -7.21159500 -1.43552100

N -0.12185100 -6.95128900 -2.20383200

C 0.17340000 -7.78105800 -3.27495100

O 1.29299200 -7.83319500 -3.75645800

C -1.04600000 -8.51501400 -3.81829900

C -2.33941600 -7.73113700 -3.54722500

C -2.49590700 -7.47773600 -2.05486400

O -3.54225500 -7.56873400 -1.42955700

H -2.31541300 -6.76556200 -4.07019500

H -3.22726500 -8.27010700 -3.88475400

H -1.09784400 -9.50265900 -3.33932300

H -0.87731600 -8.68355400 -4.88482400
C 0.92758100 -6.22944400 -1.47301500
H 1.70132700 -6.95189100 -1.18067700
C 1.59963600 -5.11902700 -2.25845000
C 1.02042800 -4.52968300 -3.38602200
H 0.06307400 -4.88941600 -3.74761200
C 1.67362500 -3.49281300 -4.05664100
H 1.22180100 -3.06472000 -4.94840900
C 2.90427700 -3.01911600 -3.59934700
H 3.41253100 -2.21338500 -4.12147700
C 3.48666400 -3.60096200 -2.47106900
H 4.44624800 -3.24439000 -2.10770900
C 2.84336300 -4.64775000 -1.81356500
H 3.31144900 -5.10651700 -0.94536200
H -2.10807000 -6.64247500 0.36257900
C -0.76786500 -8.26451800 0.77757500
C 0.05729900 -9.26114200 0.24096200
H 0.42413600 -9.17765200 -0.77783900
C 0.40773600 -10.3780890 1.00143300
H 1.04613900 -11.1430570 0.56756100
C -0.05815200 -10.5136950 2.30938300
H 0.21385900 -11.3843510 2.89964500
C -0.88155200 -9.52541600 2.85222800
H -1.25824700 -9.62479800 3.86667400
C -1.23285700 -8.41174200 2.09091800
H -1.88225200 -7.65061000 2.51783200
H -1.44967400 -4.35338600 -1.29289500

H	-1.72200800	-4.18144900	0.43560000
H	0.30341000	-2.66106200	-1.29289500
H	0.57574400	-2.83299900	0.43560000
C	-0.37839900	1.25007000	0.77757500
C	-1.20356300	2.24669400	0.24096200
H	-1.57040000	2.16320400	-0.77783900
C	-1.55400000	3.36364100	1.00143300
H	-2.19240300	4.12860900	0.56756100
C	-1.08811200	3.49924700	2.30938300
H	-1.36012300	4.36990300	2.89964500
C	-0.26471200	2.51096800	2.85222800
H	0.11198300	2.61035000	3.86667400
C	0.08659300	1.39729400	2.09091800
H	0.73598800	0.63616200	2.51783200
H	0.96180600	-0.37197300	0.36257900

Table D-6. Optimized XYZ Coordinates of red-TPSB BDPE **6**.

C	0.00000000	0.00000000	0.00000000
P	-0.37720100	0.04567000	-1.87446800
C	-1.22106400	1.73477400	-1.62237800
N	-1.48968000	1.84719700	-0.18040100
N	-0.26291300	1.36502800	0.48746400
C	-0.49300600	1.35372100	1.94019200
H	0.39833800	0.91999200	2.40305800
H	-1.35535200	0.70447400	2.18298700
C	-0.74552300	2.76813300	2.46221700

H -0.94760100 2.73272600 3.53962100

H 0.16119700 3.36920500 2.31655000

C -1.91375200 3.39678200 1.69846300

H -2.03315300 4.45568300 1.95802000

H -2.84982300 2.88684100 1.96140000

C -1.67682400 3.26091600 0.19460300

H -2.53484600 3.63374400 -0.37182400

H -0.78866800 3.84981500 -0.09907400

H -0.44649200 2.46481400 -1.91918500

C -2.44454300 1.94867800 -2.48367600

C -2.29116500 2.44096100 -3.78816700

H -1.29672000 2.69386600 -4.14970300

C -3.39509200 2.60969200 -4.62357600

H -3.25415100 2.99095000 -5.63165000

C -4.67648600 2.29940900 -4.16388800

H -5.53832800 2.43512600 -4.81174500

C -4.84164700 1.81805800 -2.86410400

H -5.83484900 1.57569200 -2.49496600

C -3.73588500 1.63985500 -2.03162500

H -3.86306600 1.26923800 -1.01975600

C -1.83720700 -1.13636200 -1.91295300

C -1.35573100 -2.59771200 -1.91295300

P -2.81573700 -3.77974400 -1.87446800

C -3.19293800 -3.73407400 0.00000000

N -2.93002500 -5.09910200 0.48746400

N -1.70325800 -5.58127100 -0.18040100

C -1.51611400 -6.99499000 0.19460300

C	-1.27918600	-7.13085600	1.69846300
C	-2.44741500	-6.50220700	2.46221700
C	-2.69993200	-5.08779500	1.94019200
H	-3.59127600	-4.65406600	2.40305800
H	-1.83758600	-4.43854800	2.18298700
H	-2.24533700	-6.46680000	3.53962100
H	-3.35413500	-7.10327900	2.31655000
H	-1.15978500	-8.18975700	1.95802000
H	-0.34311500	-6.62091500	1.96140000
H	-0.65809200	-7.36781800	-0.37182400
H	-2.40427000	-7.58388900	-0.09907400
C	-1.97187400	-5.46884800	-1.62237800
H	-2.74644600	-6.19888800	-1.91918500
C	-0.74839500	-5.68275200	-2.48367600
C	0.54294700	-5.37392900	-2.03162500
H	0.67012800	-5.00331200	-1.01975600
C	1.64870900	-5.55213200	-2.86410400
H	2.64191100	-5.30976600	-2.49496600
C	1.48354800	-6.03348300	-4.16388800
H	2.34539000	-6.16920000	-4.81174500
C	0.20215400	-6.34376600	-4.62357600
H	0.06121300	-6.72502400	-5.63165000
C	-0.90177300	-6.17503500	-3.78816700
H	-1.89621800	-6.42794000	-4.14970300
H	-2.48172300	-3.01653900	0.44754200
C	-4.60400700	-3.29290800	0.32828900
C	-4.84164700	-2.01374400	0.84666500

H	-4.00164800	-1.35089000	1.04527300
C	-6.14154200	-1.58183100	1.11924100
H	-6.30525400	-0.58582200	1.52275900
C	-7.22368100	-2.43017500	0.88501300
H	-8.23611300	-2.09826900	1.09948900
C	-6.99601500	-3.71262600	0.37839600
H	-7.83316300	-4.38214800	0.19761200
C	-5.69870500	-4.13963300	0.10076200
H	-5.51785000	-5.13937000	-0.28188600
H	-0.68444300	-2.80057000	-1.07040800
H	-0.78732400	-2.80062700	-2.82738000
H	-2.50849500	-0.93350400	-1.07040800
H	-2.40561400	-0.93344700	-2.82738000
C	1.41106900	-0.44116600	0.32828900
C	2.50576700	0.40555900	0.10076200
H	2.32491200	1.40529600	-0.28188600
C	3.80307700	-0.02144800	0.37839600
H	4.64022500	0.64807400	0.19761200
C	4.03074300	-1.30389900	0.88501300
H	5.04317500	-1.63580500	1.09948900
C	2.94860400	-2.15224300	1.11924100
H	3.11231600	-3.14825200	1.52275900
C	1.64870900	-1.72033000	0.84666500
H	0.80871000	-2.38318400	1.04527300
H	-0.71121500	-0.71753500	0.44754200

Table D-7. Optimized XYZ Coordinates of TNSB BDP **7**.

P	0.00000000	0.00000000	0.00000000
P	2.97543100	-1.31276800	-0.00004800
O	-3.78708000	0.58260300	-2.52292500
O	-1.75639000	4.05940000	1.01556300
O	4.73153000	-5.37255100	1.01492300
O	6.76184500	-1.89553200	-2.52373000
N	-2.18050000	1.19161400	-1.03106600
N	-1.54158900	2.23222700	-0.32520500
N	4.51678700	-3.54518400	-0.32564500
N	5.15600700	-2.50440300	-1.03099200
C	-3.82441900	-1.47773800	0.47951300
C	-4.16999400	-2.05480300	-0.77585400
H	-3.65699500	-1.73723000	-1.67445000
C	-5.19747100	-2.96538200	-0.88554000
H	-5.44270700	-3.38022000	-1.85936700
C	-5.94480600	-3.35479000	0.25000800
H	-6.75128200	-4.07603000	0.14848000
C	-5.65779000	-2.80172700	1.47596300
H	-6.23606800	-3.07593700	2.35534300
C	-4.60920300	-1.85376400	1.62554100
C	-4.33542000	-1.27152300	2.89066000
H	-4.94556400	-1.56112200	3.74295800
C	-3.31960300	-0.35795800	3.03380500
H	-3.11130300	0.09140100	4.00061200
C	-2.52020400	-0.01372500	1.92140500
H	-1.69844500	0.67861500	2.08000300

C	-2.73934100	-0.55083000	0.66394600
C	-1.83756300	-0.14045600	-0.49738900
H	-1.91137500	-0.84999400	-1.31837200
C	-3.24375700	1.45941600	-1.86476900
C	-3.69640200	2.91217000	-1.80900600
H	-4.69661800	2.95929100	-2.24501300
H	-3.03416700	3.53345900	-2.42697000
C	-3.66634200	3.39985400	-0.35055400
H	-4.35537300	2.80341900	0.26245700
H	-3.96772600	4.44567700	-0.25700000
C	-2.26009600	3.27919300	0.22441900
C	-0.15602400	1.94137400	0.04579700
H	-0.06609900	2.22153700	1.09917200
C	0.87245500	2.72241200	-0.75045900
C	0.54827100	3.27929100	-1.97112000
H	-0.45394300	3.14867400	-2.36537900
C	1.48398800	4.03375800	-2.71465300
H	1.18696600	4.45959400	-3.66915800
C	2.75342500	4.23174600	-2.22932500
H	3.47864700	4.81603900	-2.79044600
C	3.14077900	3.67645200	-0.98112800
C	4.44963300	3.87029200	-0.46562600
H	5.15471700	4.45695400	-1.04983300
C	4.82895100	3.32474300	0.73930900
H	5.83813600	3.46920100	1.11337100
C	3.90483500	2.55744900	1.48422800
H	4.20940800	2.11675900	2.42900100

C 2.62431600 2.35317000 1.01534900

H 1.94221000 1.75068600 1.60530200

C 2.19557500 2.90254700 -0.22544600

C 0.84609600 -0.35207800 -1.62600500

C 0.22985800 -0.07359600 -2.85860900

H -0.75434200 0.38112600 -2.88086800

C 0.85357500 -0.36785400 -4.06812600

H 0.35091800 -0.14024900 -5.00429600

C 2.12211400 -0.94400000 -4.06816700

H 2.62483400 -1.17133600 -5.00436800

C 2.74577300 -1.23855200 -2.85869000

H 3.73000600 -1.69318300 -2.88100500

C 2.12945800 -0.96040300 -1.62605100

C 3.13136000 -3.25413600 0.04572200

H 3.04163100 -3.53428200 1.09912200

C 2.10263800 -4.03502400 -0.75035500

C 2.42652500 -4.59174200 -1.97116300

H 3.42867900 -4.46117000 -2.36559600

C 1.49059900 -5.34602300 -2.71462500

H 1.78739600 -5.77169600 -3.66927500

C 0.22125300 -5.54399600 -2.22906500

H -0.50412800 -6.12816300 -2.79011100

C -0.16580500 -4.98888000 -0.98068900

C -1.47455300 -5.18274100 -0.46493700

H -2.17981300 -5.76923000 -1.04910100

C -1.85357500 -4.63738700 0.74018000

H -2.86268400 -4.78188000 1.11442800

C	-0.92927900	-3.87024900	1.48501700
H	-1.23363800	-3.42966300	2.42990900
C	0.35114100	-3.66593500	1.01588200
H	1.03336800	-3.06351000	1.60575100
C	0.77960400	-4.21515300	-0.22508500
C	5.23522000	-4.59233800	0.22379300
C	6.64126900	-4.71321300	-0.35161500
H	6.94238700	-5.75915100	-0.25845300
H	7.33065000	-4.11718000	0.26139300
C	6.67109200	-4.22514800	-1.80993900
H	7.67120800	-4.27233300	-2.24617800
H	6.00863800	-4.84617200	-2.42793200
C	6.21868000	-2.77229300	-1.86535900
C	4.81304500	-1.17241800	-0.49724900
H	4.88702600	-0.46279400	-1.31815300
C	5.71467100	-0.76215300	0.66427300
C	5.49513100	-1.29907600	1.92173000
H	4.67322800	-1.99127400	2.08019400
C	6.29427800	-0.95482900	3.03430100
H	6.08565800	-1.40404600	4.00110400
C	7.31026400	-0.04141800	2.89132700
H	7.92020500	0.24819900	3.74376500
C	7.58448400	0.54060500	1.62620500
C	8.63327500	1.48837500	1.47678800
H	9.21131100	1.76264400	2.35630800
C	8.92076100	2.04118500	0.25083800
H	9.72739100	2.76227300	0.14942600

C	8.17370700	1.65169900	-0.88487300
H	8.41933200	2.06632400	-1.85869000
C	7.14602500	0.74133700	-0.77536000
H	6.63325500	0.42369200	-1.67406500
C	6.79996900	0.16454000	0.48000900

Table D-8. Optimized XYZ Coordinates of red-TNSB BDP **8**.

C	0.00000000	0.00000000	0.00000000
P	0.57549700	-1.74492400	0.55630200
C	-1.26494900	-2.27038400	0.59921500
N	-1.98417200	-1.31884700	-0.26844700
N	-1.47395100	0.00684400	0.13799900
C	-2.06125300	1.03279000	-0.73680500
H	-1.81153600	0.82694000	-1.79444700
H	-1.60314700	1.98761400	-0.46214500
C	-3.57901400	1.08867500	-0.56399600
H	-4.00218200	1.82886900	-1.25400600
H	-3.80901700	1.41999300	0.45673300
C	-4.17377800	-0.30078300	-0.80428900
H	-5.24148200	-0.32364600	-0.55429000
H	-4.07968700	-0.57014400	-1.86462800
C	-3.42884300	-1.33376000	0.04105800
H	-3.58350200	-1.11994600	1.11405000
H	-3.79679600	-2.34202300	-0.16222000
H	-1.54979800	-2.06934800	1.64556300
C	-1.54768700	-3.71934500	0.27844900

C -1.93548400 -4.09423300 -0.99556000

H -2.00985300 -3.33182800 -1.76271300

C -2.26394900 -5.43288800 -1.30711400

H -2.57205600 -5.68327300 -2.31894500

C -2.20404300 -6.40444700 -0.33800700

H -2.45910000 -7.43605300 -0.56560000

C -1.79340200 -6.07855900 0.98151400

C -1.72181800 -7.07468600 1.99154300

H -1.98610400 -8.09569400 1.72843800

C -1.31153200 -6.76576300 3.26744000

H -1.25566000 -7.53934500 4.02840600

C -0.94578100 -5.43772800 3.58391300

H -0.60411900 -5.19717500 4.58708800

C -1.00872700 -4.44634500 2.62932100

H -0.69657700 -3.44282700 2.89620900

C -1.44372200 -4.72303300 1.30225400

C 1.21665200 -2.45041800 -1.05658100

C 0.64770700 -2.08716100 -2.29254100

H -0.25931200 -1.49191700 -2.30315600

C 1.20489500 -2.48948500 -3.50345100

H 0.73715800 -2.19574900 -4.43993500

C 2.36730900 -3.25953500 -3.50345100

C 2.92449700 -3.66185900 -2.29254100

C 2.35555200 -3.29860200 -1.05658100

P 2.99670700 -4.00409600 0.55630200

C 3.57220400 -5.74902000 0.00000000

N 5.04615500 -5.75586400 0.13799900

N	5.55637600	-4.43017300	-0.26844700
C	7.00104700	-4.41526000	0.04105800
C	7.74598200	-5.44823700	-0.80428900
C	7.15121800	-6.83769500	-0.56399600
C	5.63345700	-6.78181000	-0.73680500
H	5.38374000	-6.57596000	-1.79444700
H	5.17535100	-7.73663400	-0.46214500
H	7.57438600	-7.57788900	-1.25400600
H	7.38122100	-7.16901300	0.45673300
H	8.81368600	-5.42537400	-0.55429000
H	7.65189100	-5.17887600	-1.86462800
H	7.15570600	-4.62907400	1.11405000
H	7.36900000	-3.40699700	-0.16222000
C	4.83715300	-3.47863600	0.59921500
H	5.12200200	-3.67967200	1.64556300
C	5.11989100	-2.02967500	0.27844900
C	5.50768800	-1.65478700	-0.99556000
H	5.58205700	-2.41719200	-1.76271300
C	5.83615300	-0.31613200	-1.30711400
H	6.14426000	-0.06574700	-2.31894500
C	5.77624700	0.65542700	-0.33800700
H	6.03130400	1.68703300	-0.56560000
C	5.36560600	0.32953900	0.98151400
C	5.29402200	1.32566600	1.99154300
H	5.55830800	2.34667400	1.72843800
C	4.88373600	1.01674300	3.26744000
H	4.82786400	1.79032500	4.02840600

C	4.51798500	-0.31129200	3.58391300
H	4.17632300	-0.55184500	4.58708800
C	4.58093100	-1.30267500	2.62932100
H	4.26878100	-2.30619300	2.89620900
C	5.01592600	-1.02598700	1.30225400
H	3.29112800	-5.86310400	-1.05177600
C	2.98275400	-6.88500400	0.82007600
C	3.43312800	-7.07385500	2.11479300
H	4.18894300	-6.39928300	2.50349400
C	2.96812500	-8.13578700	2.91906300
H	3.34701700	-8.24512000	3.93181000
C	2.05542700	-9.03266500	2.41689500
H	1.70193400	-9.86483600	3.02135600
C	1.56225400	-8.89128400	1.09450800
C	0.63622900	-9.82750900	0.55996600
H	0.31818500	-10.6555640	1.18977400
C	0.15397400	-9.70120900	-0.72188700
H	-0.54781200	-10.4296600	-1.11964600
C	0.57383700	-8.61356100	-1.52230800
H	0.18246300	-8.50346300	-2.53008900
C	1.46911400	-7.68725800	-1.03513100
H	1.74780700	-6.85405700	-1.67033500
C	2.00995000	-7.79295800	0.27892600
H	3.83151600	-4.25710300	-2.30315600
H	2.83504600	-3.55327100	-4.43993500
H	0.28107600	0.11408400	-1.05177600
C	0.58945000	1.13598400	0.82007600

C	0.13907600	1.32483500	2.11479300
H	-0.61673900	0.65026300	2.50349400
C	0.60407900	2.38676700	2.91906300
H	0.22518700	2.49610000	3.93181000
C	1.51677700	3.28364500	2.41689500
H	1.87027000	4.11581600	3.02135600
C	2.00995000	3.14226400	1.09450800
C	2.93597500	4.07848900	0.55996600
H	3.25401900	4.90654400	1.18977400
C	3.41823000	3.95218900	-0.72188700
H	4.12001600	4.68064000	-1.11964600
C	2.99836700	2.86454100	-1.52230800
H	3.38974100	2.75444300	-2.53008900
C	2.10309000	1.93823800	-1.03513100
H	1.82439700	1.10503700	-1.67033500
C	1.56225400	2.04393800	0.27892600